Journal of Applied Mathematics

Mathematical and Numerical Modeling of Flow and Transport 2012

Guest Editors: Shuyu Sun, Mohamed Fathy El-Amin, Zhangxing Chen, and Hiroshi Kanayama

Mathematical and Numerical Modeling of Flow and Transport 2012

Journal of Applied Mathematics

Mathematical and Numerical Modeling of Flow and Transport 2012

Guest Editors: Shuyu Sun, Mohamed Fathy El-Amin, Zhangxing Chen, and Hiroshi Kanayama

Editorial Board

Contents

Mathematical and Numerical Modeling of Flow and Transport 2012, Shuyu Sun, Mohamed Fathy El-Amin, Zhangxing Chen, and Hiroshi Kanayama
Volume 2012, Article ID 318496, 4 pages

Effects of Regional Magnetic Field on Rotating MHD Flow Field of Unity Magnetic Prandtl Number, Sheng Lun Hung and Jik Chang Leong
Volume 2012, Article ID 804105, 17 pages

A Numerical Study on Flow around Nonuniform Porous Fences, Long-Ming Huang, H. C. Chan, and Jung-Tai Lee
Volume 2012, Article ID 268371, 12 pages

Mathematical Analysis of Inclusion Removal from Liquid Steel by Gas Bubbling in a Casting Tundish, H. Arcos-Gutierrez, J. de J. Barreto, S. Garcia-Hernandez, and A. Ramos-Banderas
Volume 2012, Article ID 534275, 16 pages

Characteristics of Wave Reflection for Vertical and Slit Caissons with Porous Structures, Tae-Hwa Jung, Sung-Jae Lee, and Yong-Sik Cho
Volume 2012, Article ID 972650, 15 pages

Natural Convection in an Inclined Porous Cavity with Spatial Sidewall Temperature Variations, M. S. Selamat, R. Roslan, and I. Hashim
Volume 2012, Article ID 939620, 10 pages

Flow Simulations Using Two Dimensional Thermal Lattice Boltzmann Method, Saeed J. Almalowi and Alparslan Oztekin
Volume 2012, Article ID 135173, 12 pages

Influence of Secondary Currents on Solute Dispersion in Curved Open Channels, Myung Eun Lee and Gunwoo Kim
Volume 2012, Article ID 781695, 18 pages

Numerical Simulation of Oil Spill in Ocean, Yong-Sik Cho, Tak-Kyeom Kim, Woochang Jeong, and Taemin Ha
Volume 2012, Article ID 681585, 15 pages

FEM Analyses for T-H-M-M Coupling Processes in Dual-Porosity Rock Mass under Stress Corrosion and Pressure Solution, Yu-Jun Zhang, Chao-Shuai Yang, and Gang Xu
Volume 2012, Article ID 983718, 21 pages

A Stabilized Incompressible SPH Method by Relaxing the Density Invariance Condition, Mitsuteru Asai, Abdelraheem M. Aly, Yoshimi Sonoda, and Yuzuru Sakai
Volume 2012, Article ID 139583, 24 pages

Nonlinear Fluid Models for Biofluid Flow in Constricted Blood Vessels under Body Accelerations: A Comparative Study, D. S. Sankar and Atulya K. Nagar
Volume 2012, Article ID 950323, 27 pages

Thermal Diffusion and Diffusion Thermo Effects on MHD Thermosolutal Marangoni Convection Boundary Layer Flow over a Permeable Surface, R. A. Hamid, W. M. K. A. Wan Zaimi, N. M. Arifin, N. A. A. Bakar, and B. Bidin
Volume 2012, Article ID 750939, 14 pages

Viscous Flow over Nonlinearly Stretching Sheet with Effects of Viscous Dissipation, Javad Alinejad and Sina Samarbakhsh
Volume 2012, Article ID 587834, 10 pages

Modelling Considerations in the Simulation of Hydrogen Dispersion within Tunnel Structures, Idris Ismail, Hisayoshi Tsukikawa, and Hiroshi Kanayama
Volume 2012, Article ID 846517, 13 pages

Evaluation of Congestion Relief Proposals in a Capital City, Sudhir C. Fowdur and Soonil D. D. V. Rughooputh
Volume 2012, Article ID 420195, 13 pages

GMM Estimator: An Application to Intraindustry Trade, Nuno Carlos Leitão
Volume 2012, Article ID 857824, 12 pages

Airflow and Heat Transfer in the Slot-Vented Room with Radiant Floor Heating Unit, Xiang-Long Liu, Guang-Cai Gong, Heng-Sheng Cheng, and Li-Xing Ding
Volume 2012, Article ID 287271, 12 pages

Upscaling of Permeability Field of Fractured Rock System: Numerical Examples, Kai Bao, Amgad Salama, and Shuyu Sun
Volume 2012, Article ID 546203, 20 pages

The Technique of MIEELDLD in Computational Aeroacoustics, A. R. Appadu
Volume 2012, Article ID 783101, 30 pages

1D and 2D Numerical Modeling for Solving Dam-Break Flow Problems Using Finite Volume Method, Szu-Hsien Peng
Volume 2012, Article ID 489269, 14 pages

A New Direct Method for Solving Nonlinear Volterra-Fredholm-Hammerstein Integral Equations via Optimal Control Problem, M. A. El-Ameen and M. El-Kady
Volume 2012, Article ID 714973, 10 pages

Numerical Investigation of Nanofluid Forced Convection in Channels with Discrete Heat Sources, Payam Rahim Mashaei, Seyed Mostafa Hosseinalipour, and Mehdi Bahiraei
Volume 2012, Article ID 259284, 18 pages

Viscoelastic Flow through an Axisymmetric Contraction Using the Grid-by-Grid Inversion Method, H. M. Park
Volume 2012, Article ID 420189, 15 pages

A Platoon Dispersion Model Based on a Truncated Normal Distribution of Speed, Ming Wei, Wenzhou Jin, and Lvou Shen
Volume 2012, Article ID 727839, 13 pages

Contents

Theoretical Analysis and Semianalytical Solutions for a Turbulent Buoyant Hydrogen-Air Jet,
M. F. El-Amin, Shuyu Sun, and Amgad Salama
Volume 2012, Article ID 710172, 12 pages

Hindawi Publishing Corporation
Journal of Applied Mathematics
Volume 2012, Article ID 318496, 4 pages
doi:10.1155/2012/318496

Editorial

Mathematical and Numerical Modeling of Flow and Transport 2012

Shuyu Sun,[1] Mohamed Fathy El-Amin,[1,2] Zhangxing Chen,[3] and Hiroshi Kanayama[4]

[1] *Computational Transport Phenomena Laboratory (CTPL), Division of Physical Sciences and Engineering (PSE), King Abdullah University of Science and Technology (KAUST), Thuwal 23955-6900, Saudi Arabia*
[2] *Mathematics Department, Faculty of Science, Aswan University, Aswan 81528, Egypt*
[3] *Schulich School of Engineering, University of Calgary, 2500 University Drive NW, Calgary, AB, Canada T2N 1N4*
[4] *Department of Mechanical Engineering, Kyushu University, 744 Motooka, Nishi-ku, Fukuoka 819-0395, Japan*

Correspondence should be addressed to Shuyu Sun, shuyu.sun@kaust.edu.sa

Received 18 September 2012; Accepted 18 September 2012

1. Introduction

Modeling of flow and transport is an essential component of many scientific and engineering applications, with increased interests in recent years. Application areas vary widely and include groundwater contamination, carbon dioxide sequestration, air pollution, petroleum exploration and recovery, weather prediction, and chemical separation processes However, accurate mathematical and numerical simulation of flow and transport remains a challenging topic from many aspects of physical modeling, numerical analysis, and scientific computation. An important step of its numerical solution procedure is to apply advanced discretization methods (e.g., finite elements, finite volumes, and finite differences) to the governing equations. Another important solution step is the design of fast and accurate solvers for the large-scale linear and nonlinear algebraic equation systems that result from discretization. Solution techniques of interest include multiscale algorithms, mesh adaptation, parallel algorithms and implementation, and efficient splitting or decomposition schemes.

2. Overview of Work Presented in This Annual Issue

This annual special issue covers a number of developing topics in mathematical modeling and numerical simulations of flow and transport phenomena for a variety of applications.

The issue effectively blends theoretical, numerical, modeling, and simulation aspects of flow and transport problems that are usually encountered in many research areas. From biological applications to the steel industry, and all the way to nanofluids applications, the 25 papers of this annual issue serve as state-of-the-art important reference for any mathematician or engineer working in a field related to modeling and simulation of flow and transport problems. The topics of this special issue may be divided into eight sections of complex flow and transport: (1) fluid flow problems, (2) flow in porous media, (3) fluid flow and heat transfer, (4) nano- and biofluids, (5) traffic problems, (6) selected problems of industrial challenges, (7) hydrogen safety issues, and (8) integration techniques for flow and transport. We outline each of the eight areas below.

The first group of papers addresses various issues in the area of flow of fluids. A stabilized incompressible smoothed particle hydrodynamics is proposed in the paper "*A stabilized incompressible SPH method by relaxing the density invariance condition*" to simulate free surface flow. The modification appears in the source term of pressure Poisson equation, and the idea is similar to the recent development in Moving Particle Semi-implicit method (MPS). In a paper entitled "*Viscoelastic flow through an axisymmetric contraction using the grid-by-grid inversion method*," by H. Park, the grid-by-grid inversion algorithm is developed to simulate viscoelastic flow through an axisymmetric contraction. S. Peng has introduced a paper entitled "*1D and 2D numerical modeling for solving dam-break flow problems using finite volume method*" to model the flow movement in an idealized dam-break configuration. One-dimensional and two-dimensional motion of a shallow flow over a rigid inclined bed was considered in this study. In the paper "*Effects of regional magnetic field on rotating MHD flow field of unity magnetic Prandtl number*" S. Hung and J. Leong studied the flow pattern of a magnetic fluid filled within an annulus with moving inner cylinder at a constant rotational speed and stationary outer cylinder under influence of a nonuniform external magnetic field. M. Lee and G. Kim introduced the dispersion coefficient tensor including off-diagonal components of the flow with secondary currents, namely, skewed shear flow dispersion (SSFD) coefficient tensor, in the paper "*Influence of secondary currents on solute dispersion in curved open channels*."

The second group concerns with flow in porous media. In "*FEM analyses for T-H-M-M coupling processes in dual-porosity rock mass under stress corrosion and pressure solution*" Y. J. Zhang et al. have introduced the models of stress corrosion and pressure solution into the 2D FEM code of thermo-hydro-mechanical-migratory coupling analysis for dual-porosity medium. The effects of a porous fence with a nonuniform porosity on flow fields are investigated numerically by L. M. Huang et al. in a paper entitled "*A numerical study on flow around nonuniform porous fences*." In the paper "*Natural convection in an inclined porous cavity with spatial sidewall temperature variations*" M. Selamat et al. have studied the natural convection in a porous cavity with a nonuniform hot wall temperature and a uniform cold wall temperature. In the paper "*Upscaling of permeability field of fractured rock system: numerical examples*" by K. Bao et al., several numerical examples have been considered to calculate effective hydraulic properties for a given fractured porous medium domain. Several scenarios of fractured systems have been considered starting with two fractures up to 800 fractures. T. H. Jung et al. have introduced a numerical experiment in their paper "*Characteristics of wave reflection for vertical and slit caissons with porous structures*" to investigate the characteristics of a reflected wave from a porous structure located in front of a slit caisson.

Coupling of heat and fluid flow is covered by the third group. S. Almalowi and A. Oztekin presented numerical simulation of two-dimensional convective heat transfer problem using two-dimensional, nine directional D2Q9 thermal lattice Boltzmann arrangements, in the paper entitled "*Flow simulations using two-dimensional thermal lattice*

Boltzmann method." In the paper entitled "*Thermal diffusion and diffusion thermoeffects on MHD thermosolutal Marangoni convection boundary layer flow over a permeable surface*" by R. Hamid et al., the problem of thermal diffusion and diffusion thermoeffects on thermosolutal Marangoni convection flow of an electrically conducting fluid over a permeable surface is investigated. The paper entitled "*Airflow and heat transfer in the slot-vented room with radiant floor heating unit*" presents numerical simulation of floor radiant heating system with three types of slot ventilation, namely, lateral slot ventilation (LSV), ceiling slot ventilation (CSV) and no slot ventilation (NSV). J. Alinejad and S. Samar bakhsh in their paper, "*Viscous flow over nonlinearly stretching sheet with effects of viscous dissipation*" have presented an analysis to study the flow and heat transfer phenomenon in a viscous fluid over a nonlinearly stretching sheet by considering the effects of heat dissipation.

The next group of papers is devoted to flow and transport of nanofluids and biofluids. In the paper "*Numerical investigation of nanofluid forced convection in channels with discrete heat sources*" the flow and heat transfer characteristics of channel flow with discrete heat sources for base fluid (distilled water) and a nanofluid that is composed of distilled water and Al_2O_3 nanoparticles are numerically investigated by Mashaei et al. The paper entitled "*Nonlinear fluid models for biofluid flow in constricted blood vessels under body accelerations: a comparative study*" by D. Sankar and A. Nagar presents a mathematical analysis that represents various interesting rheological properties of blood when it flows through narrow stenosed arteries with body acceleration, treating it as different non-Newtonian fluid models with yield stress such as Herschel-Bulkley fluid model and Casson fluid model.

The fifth group concerns with some traffic problems. The paper "*Evaluation of congestion relief proposals in a capital city*" aims at analyzing three different solutions suggested for traffic congestion relief in Port Louis, the busiest city of Mauritius. Three alternatives use light rail transit (LRT) as an alternative mode of transport, the construction of a ring road around Port Louis, and the upgrading of the current bus network into a bus rapid transit (BRT) system. Assuming that platoon speed follows a truncated normal distribution, ranging from minimum speed to maximum speed, the paper "*A platoon dispersion model based on a truncated normal distribution of speed*" by M. Wei et al. develops a piecewise density function that describes platoon dispersion characteristics as the platoon moves from an upstream to a downstream intersection.

Selected problems from industry have been covered in the sixth group. The objective of the paper "*Mathematical analysis of inclusion removal from liquid steel by gas bubbling in a casting tundish*" is to analyze and improve the understanding of the alumina inclusion removal rate by bubble attachment and by gas bubbling fluid dynamics effects. In a paper entitled "*Numerical simulation of oil spill in ocean*," a numerical model is employed to solve a two-dimensional advection-diffusion-reaction equation. The model is based on a standard split operator (fractional step) approach. N. Leitão has introduced a paper entitled "*GMM estimator: an application to intraindustry trade*" to investigate the determinants of intraindustry trade (IIT), horizontal IIT (HIIT), and vertical IIT (VIIT) in the automobile industry in Portugal. The GMM system is applied to solve the problems of serial correlation and the endogeneity of some explanatory variables.

The seventh group is devoted to hydrogen safety issues. In the paper "*Theoretical analysis and semianalytical solutions for a turbulent buoyant hydrogen-air jet*" semianalytical solutions are developed by M. El-Amin et al. for turbulent hydrogen-air plume. Analytical expressions are derived for plume centerline variables (radius, velocity, and density deficit) in terms of a single universal function. I. Ismail et al. have investigated the effect of wind speed and tunnel geometry on the flow and dispersion of hydrogen within tunnel structures

in a paper entitled "*Modelling considerations in the simulation of hydrogen dispersion within tunnel structures.*"

Finally, in the eighth group some integration techniques for flow and transport are introduced. In the paper "*The technique of MIEELDLD in computational aeroacoustics,*" Appadu has used the technique of minimised integrated exponential error for low dispersion and Low Dissipation (MIEELDLD) in a computational aeroacoustics framework to obtain modifications to optimized spatial schemes constructed in a previous work. A new method for solving nonlinear Volterra-Fredholm-Hammerstein (VFH) integral equations is presented in the paper "*A new direct method for solving nonlinear Volterra-Fredholm-Hammerstein integral equations via optimal control problem.*" The method is based on reformulation of VFH to the simple form of Fredholm integral equations and hence converting it to optimal control problem.

3. Conclusions

Improvement of computer hardware and numerical algorithms in recent years had made more accurate and higher-resolution simulations of flow and transport possible, which yielded a better and deeper understanding of flow and transport and their interaction with other physical, chemical, biological, and sociological processes. This special issue focuses on eight important areas of flow and transport and it highlights new applications and new challenges. Like the previous issue, this issue is not intended to be an exhaustive collection nor a survey of all of the current trends in flow and transport research; many additional significant research areas of flow and transport still exist and remain to be explored, but multidisciplinary research effort is a clear trend.

Acknowledgments

The authors would like to thank the participants of the special issue for their inspiring contributions, and the anonymous reviewers for their diligent work, which led to the high quality of the special issue. The lead guest editor S. Sun would like to acknowledge KAUST Faculty Baseline Research Fund (BRF) for supporting his research in flow and transport.

Shuyu Sun
Mohamed Fathy El-Amin
Zhangxing Chen
Hiroshi Kanayama

Hindawi Publishing Corporation
Journal of Applied Mathematics
Volume 2012, Article ID 804105, 17 pages
doi:10.1155/2012/804105

Research Article

Effects of Regional Magnetic Field on Rotating MHD Flow Field of Unity Magnetic Prandtl Number

Sheng Lun Hung and Jik Chang Leong

Department of Vehicle Engineering, National Pingtung University of Science and Technology, Pingtung 912, Taiwan

Correspondence should be addressed to Jik Chang Leong, jcleong@mail.npust.edu.tw

Received 29 January 2012; Revised 30 March 2012; Accepted 16 April 2012

Academic Editor: Hiroshi Kanayama

This work numerically studies the flow pattern of a magnetic fluid filled within an annulus whose inner cylinder is moving at a constant rotational speed, while the outer cylinder is stationary but under the influence of a nonuniform external magnetic field. The magnetic field consists of four basic configurations, that is, completely circular, semicircular, quarter circular, and alternately quarter circular. The strength of the external magnetic field is characterized using a reference Hartmann number. As the reference Hartmann number increases, the fluid elements need to overcome greater resistance to enter the region with magnetic field. Hence, there always exists an apparent recirculation cell within the region without externally applied magnetic field. The strength and size of the recirculation cell depend on the reference Hartmann number, the number and size of the discrete regions without external magnetic field. Only the shear stress on the moving cylinder always increases in magnitude with the reference Hartmann number and the span of the single external magnetic field region. Splitting and separating the external magnetic field may increase the magnitude of the shear stress on the moving inner cylinder but decrease that on the stationary outer cylinder. If the magnitude of the shear stress on the outer cylinder reduces beyond zero, a shear stress in the opposite sense will increase in magnitude with Hartmann number.

1. Introduction

The study of magnetohydrodynamics (MHD) has recently become a topic of study which has attracted a lot of attention. In the 1960s, Papell of NASA mixed very fine magnetite particles below 10 nm with appropriate surfactant so that the nanomagnetite could be effectively dispersed in nonpolar solvents [1]. He then successfully produced a magnetic fluid which had demonstrated many very distinctive physical behaviors. In general, magnetic fluid can

be classified as either conducting or nonconducting depending on their nature of electric conductivity. Under the influence of an external magnetic field, a conducting magnetic fluid in motion will produce an electromotive force that causes an induced electric current to flow. The presence of this induced electric field then in turn produces an induced magnetic field. At the same time, the induced electric field interacts with the overall magnetic field to produce Lorentz force that acts on the fluid elements. Since the Lorentz force acts to oppose the mechanisms that create it, it therefore generally serves to reduce the magnitude of fluid element velocity field.

As a matter of fact, Hartmann, way ahead of Papell's study, had successfully investigated the nature of magnetic Poiseuille flow based on experimental and theoretical approaches as early as 1937 [2]. His study was later referred to as the well-known Hartmann flow and the dimensionless parameter appeared in the problem was named after him as the Hartmann number. This parameter basically represents the relative importance between the magnetic and the inertial forces. In 1970, Finlayson [3] performed a theoretical study of a magnetic fluid behavior under the influence of perpendicular uniform external magnetic field.

Chang and Lundgren [4] have also performed a rather complete investigation on Hartmann flow. In their paper, they pointed out that the flow at the middle between the upper and lower surfaces tends to become flatter as Ha increases. Not only so, the overall velocity of the fluid decreases with Ha. In 1999, Yamaguchi et al. [5] studied the instability of magnetic fluid in a two-dimensional enclosure subjected to an external magnetic field through experimental and numerical simulations. As of this moment, magnetic fluid is widely employed in various engineering applications.

(a) Medical Therapy

For cancer detection, magnetic fluids are commonly used as the MRI contrast agents. Moreover, magnetic fluid is also used in experimental cancer treatments named magnetic hyperthermia.

(b) Seals for Electronic Devices

Magnetic fluids are used to form liquid seals surrounding the driver shafts in hard disk drives. A small amount of oil-based magnetic fluid can be injected into the gap between the magnet and the rotating shaft. The magnetic attraction holds the fluid in place forming a protection that prevents dusts from entering the hard disk drive.

(c) Lubrication

Oil-based magnetic fluids are also excellent lubricants. They can be injected into the gaps between moving mechanical parts of distinctive speeds. During operation, the leakage of the fluid can be prevented under the influence of magnetism. This feature is highly valued in the industry for it greatly reduces the hassle for consistent lubricant refill [6].

(d) Transportation

Magnetic fluids are now widely used in the magnetorheological damper, a kind of active suspension system surrounded with an electromagnet. The viscosity of the magnetic fluid in

this kind of vehicle damper can be dramatically varied to account for the driver preference or the vehicle overall weight. More importantly, its viscosity may be dynamically regulated to improve overall vehicle stability control because the damping factor of the active suspension system can be adjusted once every millisecond in response to actual road conditions. As a matter of fact, magnetorheological dampers are also used in helicopter cockpit seats as safety devices which serve to significantly decrease the rate of permanent injury during a crash.

(e) Energy Conversion

The energy conversion device using magnetic fluid is attractive for space use or in a situation where no maintenance is required. Yamaguchi et al. [7] have designed and constructed a direct-heat-to-power energy conversion device that makes use of temperature-sensitive magnetic fluid.

For a very long period of time, fluid behaviors between a pair of independently rotating cylinders have been investigated extensively. Perhaps all studies in rotational MHD flow trace back to the work by Taylor [8, 9] who has investigated both theoretically and experimentally the stability of the classical Couette-Taylor flow. Shortly after Taylor's discovery of the onset of axisymmetric Taylor vortices, Jeffreys [10] has extended the concept of Couette-Taylor flow and shown that the earth rotational motion has a negligible influence on the mantle convective motion. On the other hand, Meksyn [11] has investigated a similar problem using a different asymptotic method of integration. Later, Coles and van Atta [12–14] disclose nonaxisymmetric spiral vortices as a result of counter-rotating cylinders. Since then, just to name a few, many monumental studies [15–27] mostly deal with flow instability have been reported laying a solid foundation and inspiration for numerous future research topics and activities.

As a matter fact, Chandrasekhar [27] has recognized the need for further understanding of magnetic fluid instability associated to rotating cylinders. He extended the work by Taylor, Jeffreys, and Meksyn and considered an electrically conducting under the influence of an axial magnetic field. There are several factors affecting the effectiveness of the magnetic field in suppressing the onset of thermal instability. However, instability suppression due to the presence of the magnetic field is always more pronounced for rotational motion than for differential heating from below. While there were many research works related to a disk configuration, Donnelly et al. [28–30], Brahme [31], Ji et al. [32, 33] have contributed to the understanding of megnetorotational instability (MRI) in rotating fluid.

Despite the vast collection of MHD Couette flow problems, rarely found are those not tackling instability problems. Willis and Barenghi [34] investigated the response of a conducting liquid in a three dimensional cylindrical geometry subjected to an imposed axial magnetic field. The patterns of a typical nonlinear steady hydromagnetic flow were shown. Because of the magnetic field, the Taylor cells found in classical Coutte-Taylor flow are apparently elongated in the axial direction.

Szklarski and Rüdiger [35, 36] have actually simulated a magnetorotational MHD Taylor-Couette flow with an external helical magnetic field at small Prandtl number limits. Through plots of stream function contour, they showed the existence of drifting vortex pairs within an infinitely long annular space. For an enclosure with a motionless bottom endplate and a rotating upper endplate, a traveling wave propagates in the upward axial direction dramatically distorting the drifting vortex pairs observed in infinitely long annulus. The formation of Ekman-Hartmann layer is observed near the endplates where a Hartmann current exists and penetrates the bulk of the conducting fluid.

The purpose of this paper is to numerically study the flow pattern of a magnetic fluid filled within an annulus under the influence of different nonuniform externally applied magnetic field configurations. Based on the flow field obtained for different magnetic field configurations and field strengths, the shear stress along the moving cylinder is evaluated.

The description for the formulation of the magnetic fluid confined within a pair of infinitely long cylinders is given in Section 2. The governing equations along with the appropriate boundary conditions were made dimensionless and numerical approach was employed to solve the equations. The flow patterns of the magnetic fluid under the influence of the nonuniform externally applied magnetic field are investigated in Section 3. It is shown that the flow pattern depend strongly on the Hartmann number, that is, the strength of the external magnetic field. In particular, it is shown that the configuration of the external magnetic field plays a very important role in local acceleration and deceleration of the magnetic fluid. The change in shear stress due to the change in flow pattern is also documented. Finally, some important findings are reported in Section 4.

2. Governing Equations

Current work numerically simulates the flow field of a two-dimensional cylindrical magnetic Couette flow. The polar coordinate system is represented by (r,θ), while the velocity and external magnetic fields are represented by (u_r,u_θ) and (B_r,B_θ), respectively. The radii of the inner and outer cylinders are represented by r_i and r_o. Also, the inner cylinder rotates at a constant speed Ω.

The behaviors of electromagnetism are governed by the Maxwell's equations. As a matter of fact, these equations are a collection of four fundamental governing equations individually known as the Gauss's law, the Gauss's law for magnetism, the Faraday's law of induction, and the Ampère's law with Maxwell's correction. Together with the so-called material equations, these equations are mathematically given as [37]

$$\nabla\cdot\vec{B}=0, \tag{2.1}$$

$$\nabla\times\vec{E}=-\frac{\partial\vec{B}}{\partial t}, \tag{2.2}$$

$$\nabla\times\vec{H}=\vec{j}, \tag{2.3}$$

$$\nabla\cdot\vec{D}=0, \tag{2.4}$$

where the above parameters are interrelated through the following relationships:

$$\vec{H}=\frac{1}{\mu}\vec{B}, \tag{2.5}$$

$$\vec{j}=\sigma\left(\vec{E}+\vec{V}\times\vec{B}\right), \tag{2.6}$$

$$\vec{D}=\varepsilon\,\vec{E}\,. \tag{2.7}$$

Combining (2.1), (2.2), (2.3), (2.5), and (2.6), the general magnetic field equation for any magnetic fluid can be obtained in the following form:

$$\frac{\partial \vec{B}}{\partial t} + \left(\vec{V}\cdot\nabla\right)\vec{B} + \left(\nabla\cdot\vec{V}\right)\vec{B} = \left(\vec{B}\cdot\nabla\right)\vec{V} + \frac{1}{\mu\sigma}\nabla^2\vec{B}. \tag{2.8}$$

Although one can clearly understand the relationships and behaviors between the magnetic and electric fields, the theory of electromagnetism has also suggested that an electromagnetic force namely the Lorentz force will be produced in the magnetic fluid as it flows in the region under the influence of magnetic field. This force later tends to influence the motion of the fluid elements. For this reason, the magnetic, electric, and flow fields are interinfluential. The conservations of mass and momentum of the fluid are governed by the continuity and Navier-Stokes equation as

$$\begin{aligned} \frac{D\rho}{Dt} &= 0, \\ \frac{D\left(\rho\vec{V}\right)}{Dt} &= -\nabla p + \rho\vec{g} + \frac{1}{\mu}\left(\nabla\times\vec{B}\right)\times\vec{B} + \mu\nabla^2\vec{V}. \end{aligned} \tag{2.9}$$

Current study assumes that the magnetic fluid is steady, incompressible, and laminar while the gravitational acceleration is negligible. Equation (2.9) simplifies as

$$\nabla\cdot\vec{V} = 0, \tag{2.10}$$

$$\left(\vec{V}\cdot\nabla\right)\vec{V} = -\frac{1}{\rho}\nabla p + \vec{g} + \frac{1}{\mu\rho}\left(\nabla\times\vec{B}\right)\times\vec{B} + \nu\nabla^2\vec{V}. \tag{2.11}$$

With the help of continuity equation, (2.8) can be further simplified to give

$$\left(\vec{V}\cdot\nabla\right)\vec{B} = \left(\vec{B}\cdot\nabla\right)\vec{V} + \frac{1}{\mu\sigma}\nabla^2\vec{B}. \tag{2.12}$$

The external magnetic field varies as a function of radial direction, that is, B_0/r, where B_0 will then be used to define the reference Hartmann number in current study. The dynamical state of the magnetic fluid can therefore be determined by solving (2.10)–(2.12) simultaneously. This set of equations is apparently too complicated to be solved directly. To further simplify it, stream function ψ is introduced to eliminate the continuity equation and thus to reduce the number of equation needed to solve simultaneously. The stream function ψ is defined such that

$$u_r = \frac{1}{r}\frac{\partial\psi}{\partial\theta}, \qquad u_\theta = -\frac{\partial\psi}{\partial r}, \tag{2.13}$$

where u_r and u_θ are the dimensionless radial and azimuthal components of velocity. On the other hand, the following dimensionless parameters are also introduced to normalize the remaining set of equations:

$$r^* = \frac{r}{r_i}, \qquad \psi^* = \frac{\psi}{\nu}, \qquad \Omega^* = \frac{\Omega}{\nu/r_i^2},$$
$$\omega^* = \frac{\omega}{\nu/r_i^2}, \qquad A^* = \frac{A}{B_0}, \qquad \mathrm{Ha} = \frac{B_0 a}{r_i}\sqrt{\frac{\sigma}{\rho\nu}}. \tag{2.14}$$

The parameter Ha is referred to as the reference Hartmann number because the term B_0/r_i is actually the amount of reference external magnetic field density at r_i. Clearly, a larger Ha indicates a stronger external magnetic field B_0. The parameters appeared within the square root are merely electrical and mechanical properties of the magnetic fluid. To simplify the formulation, the distribution of the magnetic potential A is more frequently solved to replace the magnetic field density. The magnetic potential A is defined similar to the stream function and is given as below for a two-dimensional formulation

$$B_r = \frac{1}{r}\frac{\partial A}{\partial \theta}, \qquad B_\theta = -\frac{\partial A}{\partial r}. \tag{2.15}$$

Neglecting displacement currents, induced magnetic field, dissipation, and Joule heating, the Navier-Stokes equations can be transformed into the following nondimensional stream function-vorticity form after dropping the asterisk in (2.14) for simplicity:

$$\frac{1}{r}\frac{\partial}{\partial r}\left(\omega\frac{\partial \psi}{\partial \theta}\right) - \frac{1}{r}\frac{\partial}{\partial \theta}\left(\omega\frac{\partial \psi}{\partial r}\right)$$
$$= \frac{1}{r}\frac{\partial}{\partial r}\left(r\frac{\partial \omega}{\partial r}\right) + \frac{1}{r^2}\frac{\partial^2 \omega}{\partial \theta^2} - \frac{\mathrm{Ha}^2}{r^2}\left(\frac{\partial A}{\partial \theta}\frac{\partial}{\partial r} - \frac{\partial A}{\partial r}\frac{\partial}{\partial \theta}\right)\left[\frac{\partial}{\partial r}\left(r\frac{\partial A}{\partial r}\right) + \frac{1}{r}\frac{\partial^2 A}{\partial \theta^2}\right], \tag{2.16}$$

where the definition of dimensionless vorticity is given below without asterisk

$$\frac{1}{r}\frac{\partial}{\partial r}\left(r\frac{\partial \psi}{\partial r}\right) + \frac{1}{r^2}\frac{\partial^2 \psi}{\partial \theta^2} = -\omega. \tag{2.17}$$

To be consistent, the dimensional magnetic field equation, (2.12), was also nondimensionalized and simplified after some manipulation to yield

$$\frac{1}{r}\frac{\partial}{\partial r}\left(A\frac{\partial \psi}{\partial \theta}\right) - \frac{1}{r}\frac{\partial}{\partial \theta}\left(A\frac{\partial \psi}{\partial r}\right)$$
$$= \frac{1}{r}\frac{\partial}{\partial r}\left(\omega\frac{\partial A}{\partial \theta}\right) - \frac{1}{r}\frac{\partial}{\partial \theta}\left(\omega\frac{\partial A}{\partial r}\right) + \frac{1}{P_m}\left[\frac{1}{r}\frac{\partial}{\partial r}\left(r\frac{\partial A}{\partial r}\right) + \frac{1}{r^2}\frac{\partial^2 A}{\partial \theta^2}\right], \tag{2.18}$$

where P_m is the magnetic Prandtl number defined as $P_m = \mu\sigma\nu$.

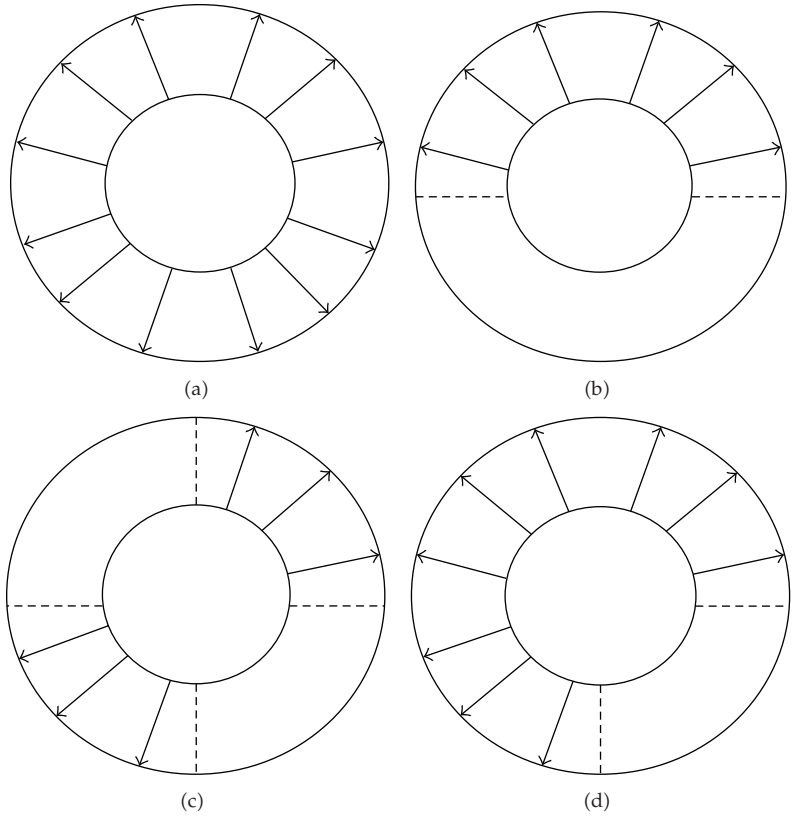

Figure 1: Distribution of externally applied magnetic fields: (a) uniform, (b) a semicircular, (c) two-quarter circular, and (d) a three-quarter circular.

Appropriate boundary conditions for the velocity field are imposed by specifying the values of dimensionless stream function on the surface of the inner and outer cylinders. After dropping the asterisk, they are given in terms of dimensionless rotational speed of the inner cylinder as

Inner cylinder,

$$\psi = \frac{r_o - r_i}{r_i}\Omega \quad \text{at } r = 1, \tag{2.19a}$$

Outer cylinder,

$$\psi = 0 \quad \text{at } r = \frac{r_o}{r_i}. \tag{2.20a}$$

Other than the above velocity boundary conditions, an external magnetic field must be imposed on the magnetic fluid. The various configurations of the externally applied magnetic field considered in this study are shown in Figure 1. The dimensionless magnetic

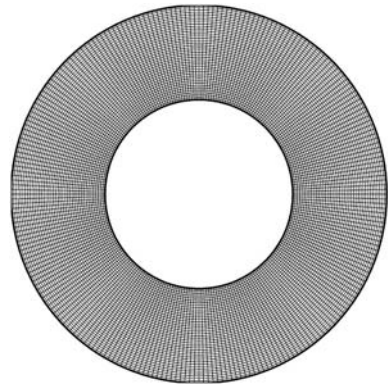

Figure 2: Grid distribution.

potential within the region $\mathcal{R}$ including its inner and outer bounds where the magnetic field is externally applied is given as

Region with magnetic field,

$$A = \theta \quad \text{for } 1 \le r \le \frac{r_o}{r_i},\ \theta \subset \mathcal{R}, \tag{2.21a}$$

Region without magnetic field,

$$A = 0 \quad \text{for } 1 \le r \le \frac{r_o}{r_i},\ \theta \not\subset \mathcal{R}. \tag{2.22a}$$

In the present work, a finite difference method was employed. The governing equations (2.16)–(2.18) were approximated by algebraic equations at the nodal points over the computational domain. A finite volume was constructed surrounding each nodal point. The governing differential equations were then integrated over the control volume. This ensures that the conservation laws were satisfied both over the control volume as well as the computational domain. This numerical method has been successfully employed by the authors [38]. The geometry and grid system of the annular space was constructed using a structured orthogonal mesh system. The grid distribution in this work was 40 × 260, as shown in Figure 2. Under- and over-relaxation was employed for most of the calculations to ensure the efficiency and accuracy of the numerical results. The reference Hartmann number investigated in this work includes 1, 3, 5, 10, 20, 30, 40, and 50. A grid refinement test had been performed and it was found that there was no significant improvement on present computational results even if the number of grid was increased up to 8 times denser than the current one.

3. Results and Discussion

Since the magnetic fluid flow in the annular space is subjected to an external magnetic field, its fluid elements experience either a local acceleration or a local deceleration. It has long

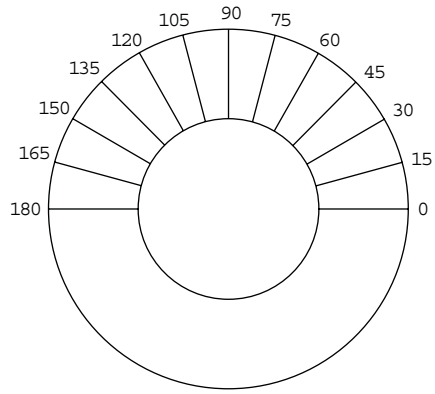

Figure 3: Locations where the velocity profiles are displayed.

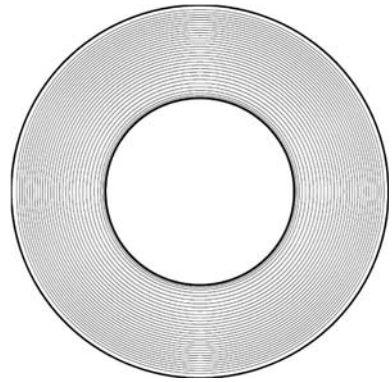

Figure 4: Distribution of the contours of stream function for a uniform external magnetic fluid of Ha = 30 ($\Delta\psi = 0.0025$).

been recognized through various studies that as Ha increases, the velocity close to the inner cylinder decelerates while that close to the outer cylinder accelerates. Not only so, the velocity gradient at the surfaces of both the inner and outer cylinders increases with Ha. In current study in which the external magnetic field is regional, it is found that the velocity gradient becomes relatively more obvious when Ha > 20. For this reason, the discussion that follows will only focus on the scenario where Ha = 30 and 50. In order to further examine these phenomena, this paper divides the upper half section of annulus (i.e., $0° \leq \theta \leq 180°$) into 12 sections which are 15° wide. These cross-sections between these sections are shown in Figure 3.

The contour of stream functions for Ha = 30 is presented in Figure 4. Since the external magnetic field is completely circular within the annular space, the flow patterns are certainly axis-symmetrical. This fact is evident from the distribution of stream function contours. It can be seen that the contours of stream functions appear to be a family of concentric circles. In other words, the magnetic fluid is merely a swirl flow under the influence of the complete circular external magnetic field proving the fact that the flow field is completely one-dimensional and angular independent.

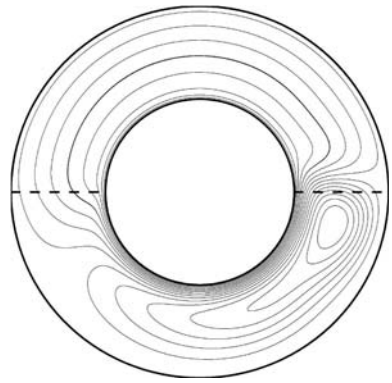

Figure 5: Distribution of the contours of stream function for a semicircular external magnetic fluid of Ha = 30 ($\Delta\psi = 0.0025$).

Figure 5 shows the contours of stream functions for the magnetic fluid subjected to a semicircular external magnetic field of Ha = 30. Unlike the previous case, there exists in the lower portion of the annular space an additional recirculation cell rotating in the clockwise direction. The eye of the cell is located to the right side of the annulus in the region without external magnetic field. Clearly, the flow pattern is no longer axis-symmetrical. Remember that the magnetic field is only applied in the upper half of the annulus. In this region with an external magnetic field, the magnetic fluid simply flows in the counterclockwise direction. In the lower half where the external magnetic field is absent, the region is mostly occupied by a recirculation cell. The formation of the recirculation cell is solely due to the presence of the external magnetic field in the upper half region. In the upper half region, the fluid elements generally slow down under the influence of the Lorentz force. Prior to entering the upper half region, the fluid elements in the lower half region has experienced a considerable flow resistance. Hence, some of the fluid elements are forced to flow radially outward similar to the phenomena discovered for flow impingement. This radially outward flow eventually forms the recirculation cell. It is remarkable to see that only a very thin layer of magnetic fluid right next to the inner rotating cylinder is capable of penetrating the upper half region because the flow momentum at this region is continuously supplied by the rotation of the inner cylinder. Once it enters the upper region where the recirculation cell is no longer present, it expands almost radially and therefore fills the entire gap between the inner and outer cylinders. As it leaves the upper half region and returns to the lower half region, its fluid elements are squeezed radially inwards by the recirculation cell. Even though the phenomena of magnetic fluid entering and leaving the upper half region is somewhat similar (but in a reversed fashion), the change in velocity field is more abrupt for the magnetic fluid elements entering than leaving the region subjected to an external magnetic field.

In Figure 6, $R^* = 0$ and $R^* = 1$ indicate the locations of the inner and outer cylinders, respectively. Here, the aforementioned radial coordinate was scaled through $R^* = (r - r_i)/(r_o - r_i)$. Similarly, the angular velocity component u_θ of the magnetic fluid was calculated through (2.10) and then normalized by the linear velocity of the inner cylinder, that is, $V^* = u_\theta/\omega r_i$. Apparently, the fluid elements on the inner cylinder move at a finite tangential velocity while those on the outer cylinder remain motionless. Furthermore, there exists a section close to the outer cylinder whose angular velocity component is less than zero at $\theta = 0^\circ$ indicating that the fluid elements at this section actually flow in the direction opposite to the direction

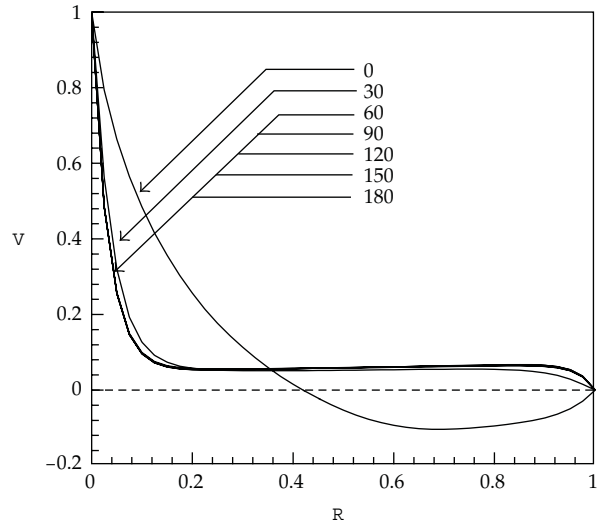

Figure 6: Angular velocity profiles at $0° \leq \theta \leq 180°$ subjected to a semicircular external magnetic field.

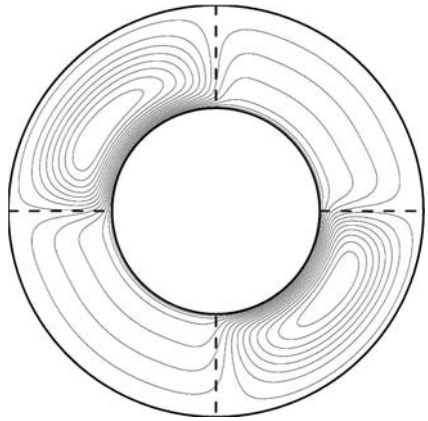

Figure 7: Distribution of the contours of stream function for two-quarter circular external magnetic fluids of Ha = 30 ($\Delta\psi = 0.00025$).

of the rotating inner cylinder. At other locations, that is, $30° \leq \theta \leq 180°$, the angular velocity profiles are almost identical. Based on this figure, it is not difficult to see that the magnitude of the normalized angular velocity V^* in the region corresponding to $0.12 \leq R^* \leq 0.84$ and $30° \leq \theta \leq 180°$ is about 0.06. This implies that the rotational speed in this region is inversely proportional to its radial distance.

If the external magnetic field is applied at the first and third quadrants, the flow patterns can be expected to bear some resemblances with that for a semicircular magnetic field. Since there are two discrete regions without external magnetic field in this case, there surely exist two recirculation cells within these regions, as clearly displayed in Figure 7. However, the strength of these two cells is actually weaker than the single cell for the case shown in Figure 5. This can be imagined as if the single recirculation cell in Figure 5 is forced to split into two recirculation cells by the presence of the additional region with external

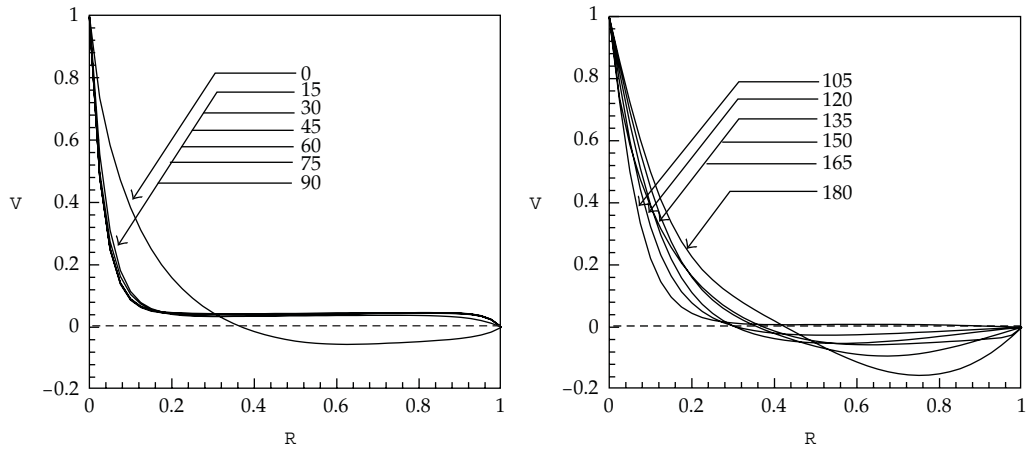

Figure 8: Angular velocity profiles subjected to two-quarter circular external magnetic fields at (a) $0° \leq \theta \leq 90°$ and (b) $105° \leq \theta \leq 180°$.

magnetic field. As the single larger recirculation cell splits into two smaller cells, their strength apparently weakens. This means the fluid elements in Figure 7 circulate at a lower velocity. In the regions with external magnetic fields, the distribution of stream function contours in general is less dense in Figure 7 in comparison with those depicted in Figure 5. This clearly suggests that, except in the vicinity very close to the rotating inner cylinder, the majority fluid elements flow slower if the single region with an external magnetic field is split and separated. This phenomenon implies the decrease in flow kinetic energy in the annular space is attributed to the effect of additional flow deceleration and acceleration prior to crossing the interface between the regions with and without external magnetic field. Based on a careful comparison, it was also found that the flow in this case has to squeeze itself through a slightly narrower gap between the recirculation cell and the surface of the inner rotating cylinder.

To further understand the nature of the magnetic fluid flow, the velocity profiles in the upper half region of the annulus are plotted in Figure 8. It is observed that at $\theta = 0°$, there is a large section where flow reversal takes place. Among the various velocity profiles demonstrated, the angular velocity component is all greater than 0 for $15° \leq \theta \leq 120°$. Although the external magnetic field is only applied at $0° \leq \theta \leq 90°$, the upstream recirculation cell actually stretches beyond the interface at $\theta = 0°$ while the counter-clockwise swirl flow extends over $\theta = 105°$ which is beyond the other interface at $\theta = 90°$. In this region, the velocity profiles at $30° \leq \theta \leq 90°$ are almost the same.

The flow pattern of the magnetic fluid in the annular space under the influence of a three-quarter-circular external magnetic field is shown in Figure 9. In this scenario, only the forth quadrant is not subjected to an external magnetic field. In Figure 9(a), the strength of the external magnetic field is associated to $\mathrm{Ha} = 30$. The flow patterns of fluid elements entering the region subjected to an external magnetic field are very similar to the previous cases. However, the flow pattern of the fluid elements leaving the region is very distinctive. Under the influence of the external magnetic field spanning over the upper half region as in Figure 5, the fluid elements are enormously squeezed so that they manage to complete a cycle. If the external magnetic field is split, separated, and applied alternatively over the upper and lower half semiannular spaces as in Figure 7, the fluid elements still need to force

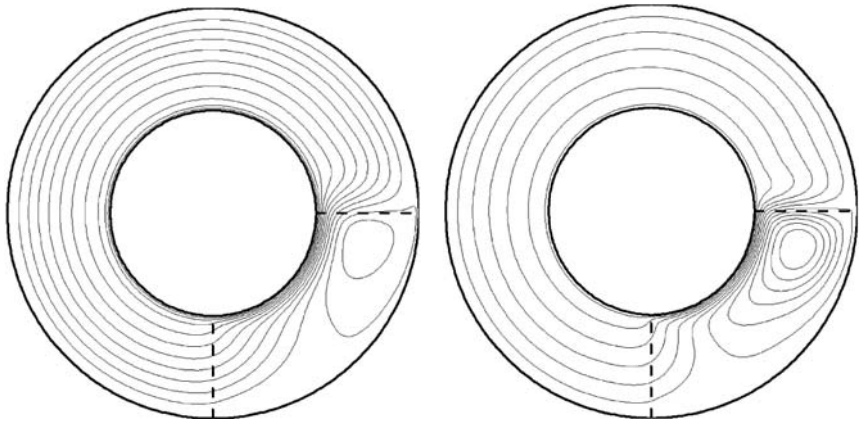

Figure 9: Distributions of the contours of stream function for a three-quarter-circular external magnetic fluids of (a) Ha = 30 and (b) Ha = 50 ($\Delta\psi = 0.0025$).

their way through the annular space. When an additional external magnetic field is applied at the second quadrant as in Figure 9(a), the fluid elements actually experience less resistance when flowing through the region without external magnetic field.

Based upon these figures, it is remarkable to find that the strength and size of the recirculation cell are strongly dependent on the number of the discrete regions without external magnetic field and their span in the angular direction. Among these three external magnetic field configurations, the recirculation cell is the weakest when only a quarter of the annular space is free of external magnetic field. As the span of this region without external magnetic field is doubled, the strength of the cell increases due to the decrease in Lorentz force, as evidently shown in Figure 5. If the second and third quadrants of a semicircular external magnetic field (in Figure 5) are interchanged to form the two quarter-circular external magnetic fields, the recirculation cell is also split into two individual cells whose strengths are apparently less than the previous one.

Figure 9(b) shows the flow pattern for the same conditions except that Ha is increased to 50. The flow pattern is quite similar to that in Figure 9(a) except at the regions in the vicinity of the recirculation cell. Because of the increase in the reference Hartmann number, the corresponding recirculation cell grows in strength and as a result it leaves the swirl flow less space to go around. Also for this reason, the change in flow direction prior to the formation of the recirculation cell is much more dramatic for Ha = 50 than for Ha = 30. This also clearly proves that the strength of the recirculation cell for Ha = 50 is greater between the two cases. As the fluid elements enter the region with an external magnetic field of Ha = 50, they also tend to change their flow directions more rapidly under the influence of stronger Lorentz force.

If the external magnetic field conditions shown in Figure 9 are interchanged to form a quarter circular magnetic field, the general flow patterns interchange between the regions with and without external magnetic field. As shown in Figure 10, the strength of the recirculation cell actually increases tremendously as evidently depicted by the denser distribution of the contours surrounding the eye of the recirculation cell. More surprisingly,

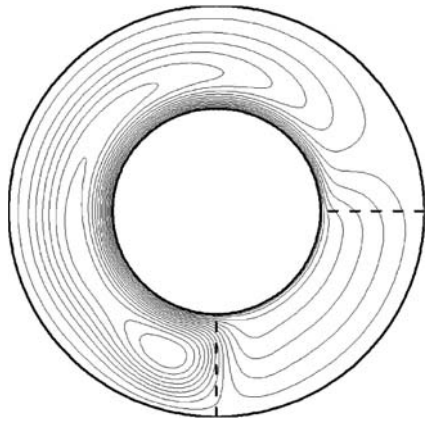

Figure 10: Distributions of the contours of stream function for a quarter-circular external magnetic fluids of Ha = 30 ($\Delta\psi = 0.0025$).

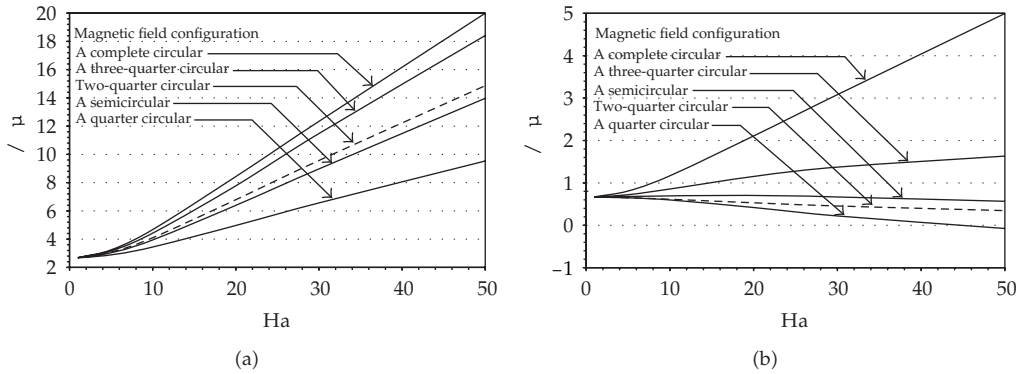

Figure 11: Variation of dimensionless shear stress on cylindrical surface: (a) inner and (b) outer.

this recirculation cell is even stronger than the one shown in Figure 9(b), which corresponds to Ha = 50.

The shear stress τ on the inner and outer cylinders were nondimensionalized by the product of the inner cylinder rotational speed ω and the fluid dynamic viscosity μ. The dependence of these dimensionless shear stresses on the external magnetic field configuration and Ha are displayed in Figure 11. As Ha increases, the shear stress on the inner cylinder always increases but that on the outer cylinder does not necessarily follows this rule. In fact, the formation of the recirculation cell in the region without external magnetic field serves to reverse the shear stress the outer cylinder surface experiences. For this reason, it is found there exists a critical reference Hartmann number beyond which the shear stress on the outer cylinder acts on the opposite direction if only an external magnetic field is applied to a quarter of the annular space. Not only so, whenever the external magnetic field covers less than half of the annular space, the magnitude of the shear stress on the outer cylinder will tends to decreases and will eventually replaced by a growing shear stress in the opposite sense if the Hartman number is large enough. Also in these figures, the effect of splitting and separating the external magnetic field on the shear stress on the inner and outer cylinders is investigated. The shear stress associated with the semicircular magnetic field is found to

increase in magnitude on the inner cylinder but to decrease in magnitude on the outer one as it is split to form two quarter-circular magnetic field (represented by the broken lines). As the Hartmann number is increases, this magnitude continues to reduce to zero. Then, a shear stress in the opposite sense is anticipated to grow in magnitude. Again, this is strictly related to the nature of the recirculation cells. As the magnetic field is split, the recirculation cell corresponding to the semicircular magnetic field is also split to form two weaker recirculation cells. Because of the presence of these two recirculation cells, the shear flow next to the inner cylinder is more difficult to squeeze through the annular space leading to an increase in shear stress magnitude. On the other hand, the two weaker recirculation cells exert greater reversed friction force and therefore reduce the magnitude of the shear stress on the outer cylinder.

4. Summary

A computational study of magnetic fluid in an annular space subjected to a rotating inner cylinder and nonuniform external magnetic fields is accomplished in this work. Based on current investigation, the following conclusions can be drawn.

(1) The presence and absence of the external magnetic field brake the fluid elements prior to entering the region with external magnetic field. This leads to the generation of a recirculation cell.

(2) In the annular space, a recirculation cell always occupies every discrete region without external magnetic field.

(3) The strength and size of the recirculation cell depend on the strength of the external magnetic field, the number of discrete regions without external magnetic field, and their span.

(4) The strength of the recirculation cell is inversely proportional to the span in the angular direction of the region subjected to external magnetic field.

(5) The shear stress on the moving inner cylinder increases with the reference Hartmann number and the span of the single external magnetic field region.

(6) The magnitude of the shear stress on the stationary outer cylinder may increase or decrease with the reference Hartmann number depending on the external magnetic field configuration.

(7) Splitting and separating an external magnetic field may cause the magnitude of the shear stress on the moving inner cylinder to increase but that on the stationary outer cylinder to decrease.

Nomenclature

A : Magnetic scalar potential, A
a: Gap width between cylinders, m
B: Magnetic field density, T
B_0: External magnetic field density, T
D: Electric displacement field, C/m^2
E: Electric field, V/m

H: Magnetized field, A/m
Ha: Hartmann number,—
j: Current density, A/m^2
P_m: Magnetic Prandtl number,—
q: Electric charge, C
r: Radial coordinate, m
t: Time, s
u_r: Radial velocity, m/s
u_θ: Angular velocity, m/s.

Greek Symbols

ε: Permittivity, F/m
ν: Fluid kinematic viscosity, m^2/s
μ: Fluid dynamic viscosity, kg/m·s
θ: Angular coordinate,—
ρ: Fluid density, kg/m^3
σ: Electric conductivity, Ω^{-1} m^{-1}
ω: Rotational speed of the inner cylinder, rad/s.

References

[1] S. S. Papell, Low viscosity magnetic fluid obtained by the colloidal suspension of magnetic particles, U.S. Patent No. 3215527, 1965.
[2] J. Hartmann, "Hg dynamics I. Theory of the laminar flow of an electrically conductive liquid in a homogeneous magnetic," *FieldMathematisk-Fysiske Meddelelser*, vol. 15, no. 6, pp. 1–27, 1937.
[3] B. A. Finlayson, "Convective instability of ferromagnetic fluids," *Journal of Fluid Mechanics*, vol. 40, no. 4, pp. 753–767, 1970.
[4] C. C. Chang and T. S. Lundgren, "Duct flow in magnetohydrodynamics," *Zeitschrift Fuangewandte Mathematik and Physik*, vol. 12, pp. 100–114, 1961.
[5] H. Yamaguchi, I. Kobori, and Y. Uehata, "Heat transfer in natural convection of magnetic fluids," *Journal of Thermophysics and Heat Transfer*, vol. 13, no. 4, pp. 501–507, 1999.
[6] R. E. Rosensweig, "An introduction to ferrohydrodynamics," *Chemical Engineering Communications*, vol. 67, no. 1, pp. 1–18, 1988.
[7] H. Yamaguchi, A. Sumiji, S. Shuchi, and T. Yonemura, "Characteristics of thermo-magnetic driven motor using magnetic fluid," *Journal of Magnetism and Magnetic Materials*, vol. 272–276, no. 3, pp. 2362–2364, 2004.
[8] G. I. Taylor, "Stability of a viscous liquid contained between two rotating cylinders," *Philosophical Transactions of the Royal Society A*, vol. 223, pp. 289–343, 1923.
[9] G. I. Taylor, "Fluid friction between rotating cylinders," *Proceedings of the Royal Society A*, vol. 157, pp. 546–564, 1936.
[10] H. Jeffreys, "Some cases of instability in fluid motion," *Proceedings of the Royal Society A*, vol. 118, pp. 195–208, 1928.
[11] D. Meksyn, "Stability of viscous flow between rotating cylinders. I," *Proceedings of the Royal Society. London. Series A*, vol. 187, pp. 115–128, 1946.
[12] D. Coles, "Transition in circular Couette flow," *Journal of Fluid Mechanics*, vol. 21, pp. 385–425, 1965.
[13] D. Coles and C. van Atta, "Measured distortion of a laminar circular Couette flow by end effects," *Journal of Fluid Mechanics*, vol. 25, pp. 513–521, 1966.
[14] C. van Atta, "Exploratory measurements in spiral turbulence," *Journal of Fluid Mechanics*, vol. 25, pp. 495–512, 1966.
[15] E. R. Krueger, A. Gross, and R. C. DiPrima, "On the relative importance of Taylor-vortex and non-axisymmetric modes in flow between rotating cylinders," *Journal of Fluid Mechanics*, vol. 24, pp. 521–538, 1966.

[16] H. A. Snyder, "Stability of rotating Couette flow. I. Asymmetric waveforms," *Physics of Fluids*, vol. 11, no. 4, pp. 728–734, 1968.
[17] H. A. Snyder, "Stability of rotating Couette flow. II. Comparison with numerical results," *Physics of Fluids*, vol. 11, no. 8, pp. 1599–1605, 1968.
[18] H. A. Snyder, "Waveforms in rotating Couette flow," *International Journal of Non-Linear Mechanics*, vol. 5, no. 4, pp. 659–685, 1970.
[19] R. C. Diprima and P. M. Eagles, "Amplification rates and torques for Taylor-vortex flows between rotating cylinders," *Physics of Fluids*, vol. 20, no. 2, pp. 171–175, 1977.
[20] P. R. Fenstermacher, H. L. Swinney, and J. P. Gollub, "Dynamical instabilities and the transition to the chaotic Taylor vortex flow," *Journal of Fluid Mechanics*, vol. 94, no. 1, pp. 103–128, 1979.
[21] K. Park, G. L. Crawford, and R. J. Donnelly, "Determination of transition in couette flow in finite geometries," *Physical Review Letters*, vol. 47, no. 20, pp. 1448–1450, 1981.
[22] K. Park and R. J. Donnelly, "Study of the transition to Taylor vortex flow," *Physical Review A*, vol. 24, no. 4, pp. 2277–2279, 1981.
[23] C. A. Jones, "On flow between counter-rotating cylinders," *Journal of Fluid Mechanics*, vol. 120, pp. 433–450, 1982.
[24] C. D. Andereck, R. Dickman, and H. L. Swinney, "New flows in a circular Couette system with co-rotating cylinders," *Physics of Fluids*, vol. 26, no. 6, pp. 1395–1401, 1983.
[25] P. S. Marcus, "Simulation of Taylor-Couette flow. Part 1. Numerical methods and comparison with experiment," *Journal of Fluid Mechanics*, vol. 146, pp. 45–64, 1984.
[26] C. D. Andereck, S. S. Liu, and H. L. Swinney, "Flow regimes in a circular Couette system with independently rotating cylinders," *Journal of Fluid Mechanics*, vol. 164, pp. 155–183, 1986.
[27] S. Chandrasekhar, "The stability of viscous flow between rotating cylinders in the presence of a magnetic field," *Proceedings of the Royal Society. London. Series A*, vol. 216, pp. 293–309, 1953.
[28] R. J. Donnelly and M. Ozima, "Hydromagnetic stability of flow between rotating cylinders," *Physical Review Letters*, vol. 4, no. 10, pp. 497–498, 1960.
[29] R. J. Donnelly and M. Ozima, "Experiments on the stability of flow between rotating cylinders in the presence of magnetic field," *Proceedings of the Royal Society A*, vol. 266, pp. 272–286, 1962.
[30] R. J. Donnelly and D. R. Caldwell, "Experiments on the stability of hydromagnetic Couette flow," *Journal of Fluid Mechanics*, vol. 19, pp. 257–263, 1964.
[31] A. Brahme, "On the hydromagnetic stability of a nonuniformly rotating fluid," *Physica Scripta*, vol. 2, pp. 108–112, 1970.
[32] H. Ji, J. Goodman, and A. Kageyama, "Magnetorotational instability in a rotating liquid metal annulus," *Monthly Notices of the Royal Astronomical Society*, vol. 325, no. 2, pp. L1–L5, 2001.
[33] J. Goodman and H. Ji, "Magnetorotational instability of dissipative Couette flow," *Journal of Fluid Mechanics*, vol. 462, pp. 365–382, 2002.
[34] A. P. Willis and C. F. Barenghi, "Hydromagnetic Taylor-Couette flow: numerical formulation and comparison with experiment," *Journal of Fluid Mechanics*, vol. 463, pp. 361–375, 2002.
[35] J. Szklarski and G. Rüdiger, "Nonlinear simulations of magnetic Taylor-Couette flow with current-free helical magnetic field," *Astronomische Nachrichten*, vol. 327, no. 9, pp. 844–849, 2006.
[36] J. Szklarski and G. Rüdiger, "Ekman-Hartmann layer in a magnetohydrodynamic Taylor-Couette flow," *Physical Review E*, vol. 76, no. 6, Article ID 066308, p. 8, 2007.
[37] J. D. Jackson, *Classical Electrodynamics*, John Wiley & Sons, New York. NY, USA, 2nd edition, 1975.
[38] J. C. Leong, N. M. Brown, and F. C. Lai, "Mixed convection from an open cavity in a horizontal channel," *International Communications in Heat and Mass Transfer*, vol. 32, no. 5, pp. 583–592, 2005.

Hindawi Publishing Corporation
Journal of Applied Mathematics
Volume 2012, Article ID 268371, 12 pages
doi:10.1155/2012/268371

Research Article

A Numerical Study on Flow around Nonuniform Porous Fences

Long-Ming Huang,[1] H. C. Chan,[1] and Jung-Tai Lee[2]

[1] *Department of Soil and Water Conservation, National Chung Hsing University, Taichung 40227, Taiwan*
[2] *Sinotech Engineering Consultants, Ltd., 12th Floor, 171 Nanking E. Road. Section 5, Taipei 10570, Taiwan*

Correspondence should be addressed to Jung-Tai Lee, lee2406@mail.sinotech.com.tw

Received 15 February 2012; Accepted 27 May 2012

Academic Editor: Shuyu Sun

The effects of a porous fence with a nonuniform porosity on flow fields are investigated numerically. First, an experiment with a non-uniform porous fence located in a wind tunnel is performed to obtain a reference data set. Then, a numerical model that utilizes the finite volume scheme with a weakly compressible-flow method to solve the continuity and momentum equations is developed. The numerical simulation is compared to experimental measurements for validation purposes. As a result, the numerical predictions show good agreements with the experimental data. Finally, the numerical investigations of the flow fields around porous fences with various combinations of upper and lower fence porosity are also presented. When the upper porosity is greater than the lower porosity, the Protection Index $PI_{0.1}$, $PI_{0.3}$ and $PI_{0.5}$, representing the adverse sheltering effect, decreases compared to that of the uniform porous fence. When the upper porosity is less than the lower porosity, the $PI_{0.5}$ increases and the variations of the $PI_{0.1}$ and $PI_{0.3}$, depend on the upper porosity, compared to that of the uniform porous fence. The results show that the porous fence with the upper fence porosity $\varepsilon_U = 0\%$ and the lower fence porosity $\varepsilon_L = 30\%$ gives the best sheltering effect among the porous fences in this study.

1. Introduction

Various kinds of fences have been used as windbreaks to reduce the wind erosion effectively. A fence blocks the oncoming flow and reduces the mean velocity of the flow behind the fence. Flows around a fence are of complex characteristics. Flow separation from fences results in strong shear layers, along which turbulence intensities are large. *The high turbulence level and the shear layer of the recirculation flow in the near wake region.* Variations of fence porosity are not only to modify the flow velocity but also to control the turbulence structure around the fence. In order to evaluate the sheltering effect properly and efficiently, a deeper understanding of the underlying dynamics of the turbulent structures is required.

The characteristics of turbulent flows around porous fences have been reported in several studies [1–4]. Raine and Stevenson [3] measured the mean and turbulent

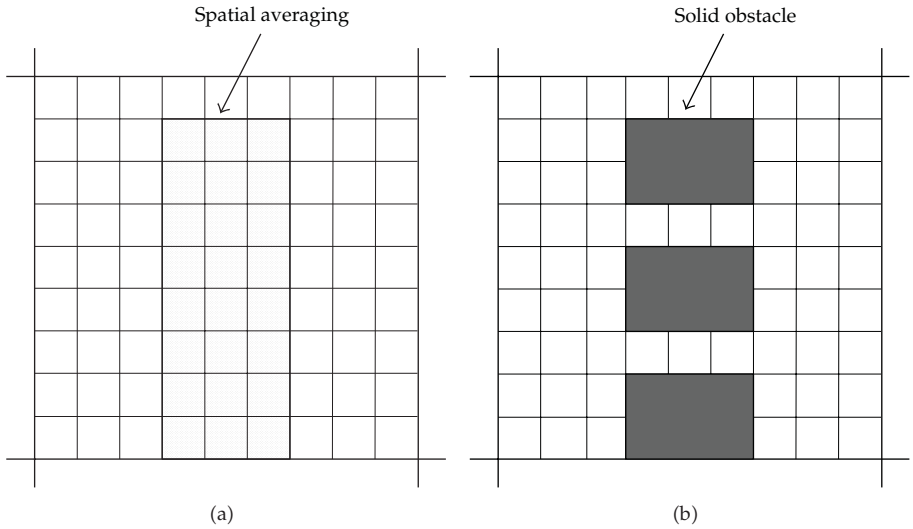

Figure 1: How to handle the porous fence. (a) Reproduced as a drag law. (b) Directly reproduced configuration.

characteristics of wake flow behind various porous fences. They classified the wake flow into two regions: the bleed flow dominant region and the displacement flow dominant region. Additionally, porous fences with low to medium porosities were more effective in reducing the mean velocity more than the solid one. Perera [1] experimentally investigated the flow around various porous fences immersed in a simulated atmospheric boundary layer. The porosity of the fence was the most significant parameter on the recirculation characteristics behind the fence, compared to other factors required for the fence design. Castro [2] and Perera [1] showed that the recirculation flow behind the porous fence disappeared when the fence porosity was more than $\varepsilon = 30\%$. Yaragal et al. [4] measured the flow fields downstream of both solid and porous fences. The fluctuating pressure of the porous fence with $\varepsilon = 60\%$ was by about 50% less than that of the solid fence. By measuring the mean velocity and turbulence intensity profiles, Lee et al. [5] found that the porous wind fence with porosity $\varepsilon = 30\%$ was most effective in abating windblown sand particles.

The above experimental results demonstrated that the characteristics of turbulent flow downstream of the porous fence significantly depended on the porosities. Hence, the numerical model will meet some considerable both in modeling the fluid dynamics of the recirculation flow and the porous effects. Usually, practical engineers used a drag law to represent the porous effects due to low computational cost [6–9]. With such a drag law, only the spatial averaged flow structures around porous fences are provided (Figure 1(a)). *The application of drag law needs to correctly acquire drag coefficients in the momentum equation.* However, very little drag data of porous fences are available. Application of the numerical model with a drag law to predicate the local flows around porous fences is rather difficult. In other previous studies, the flows around porous fences were solved at a local level [10]. The computational grids lie well inside the holes of porous fences and hence flow characteristics are calculated both inside and around the holes (Figure 1(b)). The primary application of these models is to model the interactions between the flow through the holes and the recirculation flow.

The above literature demonstrates the detailed investigation of the flow structures around porous fences, and the role played by the porosity has been emphasized. However,

data for the cases of a porous fence with a nonuniform porosity are limited. An elevated fence constructed in a road becomes nonuniform when support structures create a gap between the bottom of the fence and the ground. Also, the solid fences act as nonuniform porous fences when it receives a strong wind during its construction. Cho [11] pointed out that a fence with a bottom gap was cost effective in reducing the surface shear stress behind a porous fence. Park and Lee [12] experimentally investigated the turbulent flow behind the porous fences with nonuniform porosities. In their study, they focused on the effects of fence gap on the surface pressure characteristics behind the fences rather than exhibiting the flow structures and their interactions with the porous fences.

The main objective of this study is to numerically investigate the effects of porous fences with nonuniform porosities on flow structures, by varying the porosity in the upper and lower halves of a fence. We recognized in literature survey that no experimental data was available for examining the performance of a model predicting flow through a nonuniform porous fence. Therefore, experimental results with a nonuniform porous fence are presented to provide a reference data set for validating the numerical model. The validated numerical model is used to study the sheltering effect of a nonuniform porous fence. The Protection Index described by Van et al. [13], evaluated from the area of the reduced mean streamwise velocity behind a fence, is introduced to examine the performance of a porous fence. The present findings are expected to provide proper guidance in the design of porous fences with nonuniform porosities.

2. Experimental Apparatus and Methods

The experiments were conducted in an open-suction-type wind tunnel with a test section of 0.6 W × 0.6 H × 8.0 L (m^3). Spires and roughness elements were installed in front of the test section to create a thermally neutral atmospheric boundary layer. A porous fence with a nonuniform porosity was tested. The porosity of the lower half of the porous fence (ε_L) was 30%, while the upper half was solid and upper porosity (ε_U) was 0%. The porous fence had a height (H) of 6.0 cm and a flat end at the fence top. The porous fence extended the full width of the wind tunnel test section. Since the aspect ratio (height/width) of the porous fence is small (1/10), the model fence used in this study can be assumed to be two-dimensional (2D) one. The porous fence was installed at a position 6.0 m downstream of the inlet of the test section. A schematic diagram of the porous fence model and coordinate system used in this study is shown in Figure 2. The uniform inlet velocity U_0 was 10.60 m/sec and the Reynolds number Re_H based on the fence height H was about 4.1×10^4. A hot-wire anemometer (TSI IFA-300) with a probe (TSI 1241-T1.5) were used to measure the velocity profiles. A computer-controlled translation system was used to precisely locate and move the probe. The measurements were made at 36 points in the vertical, with distance from the bottom wall ranging from $0.05H$ to $7.5H$. The measurements at each location were instantaneous at a sampling frequency of 2 kHz for 20,000 data. These data were used to compute the statistical properties and would be compared with the corresponding numerical simulation.

3. Numerical Simulation

The flow characteristics depicted in Figure 1 can be carried out under a simplified condition. The porous fence extended the full width of the wind tunnel test section. It involves the 2-D turbulent flows around a porous fence. The governing equations are the continuity and

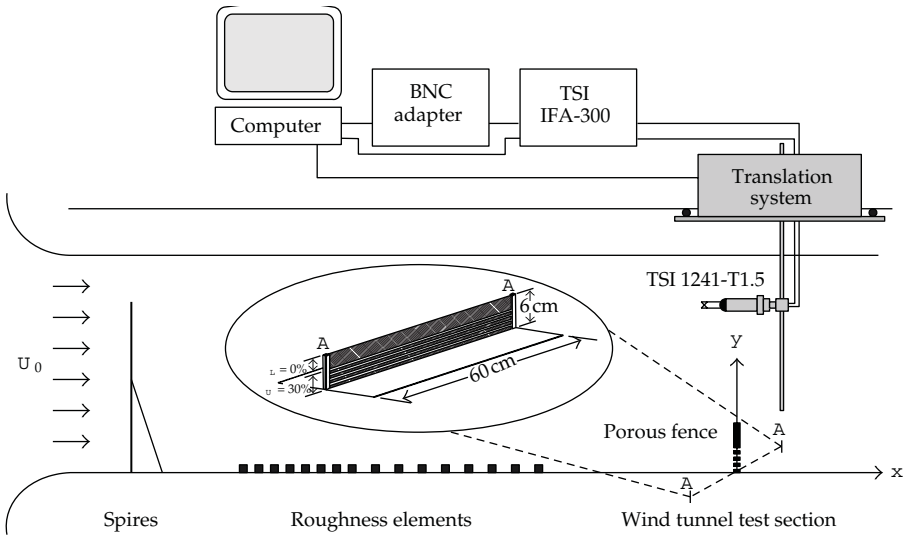

Figure 2: Schematic diagram of the porous fence and coordinate system.

momentum equations. The LES form of the dynamic subgrid-scale model by Germano et al. [14] is employed to take the turbulent effects into account. The numerical method used for the solution of the governing equations is developed on the basis of the finite volume scheme with a weakly compressible-flow method [15] in a Cartesian coordinate system. The governing equations of continuity and momentum are as follows:

$$\begin{aligned} \frac{\partial p}{\partial t} + k\nabla \cdot V &= 0 \\ \frac{\partial V}{\partial t} + V \cdot \nabla V &= -\nabla \frac{p}{\rho} + \nabla \cdot [(\nu + \nu_t)\nabla V], \end{aligned} \tag{3.1}$$

where p is the pressure; V denotes velocity components on each axis on the Cartesian coordinates; t is the time; k is the bulk modulus of elasticity of air; ν is the kinematic viscosity; ν_t is the turbulent eddy viscosity. The turbulent eddy viscosity is expressed as

$$\nu_t = (C_S \Delta)^2 \quad \overline{2S_{ij}S_{ij}} \quad \text{where } S_{ij} = \frac{1}{2} \quad \frac{\partial u_i}{\partial x_j} + \frac{\partial u_j}{\partial x_i} \quad , \tag{3.2}$$

where C_S is the Smagorinsky coefficient; Δ denotes the characteristic length of the computational grid and the strain tensor S_{ij}. Based on the dynamic subgrid-scale model [14], two filters (grid and test filters) are used in the model calculations. The C_S, at the next time step, is determined through the comparison between the turbulent shear stresses resulting from different filters in a certain time step. The computational domain used in terms of the fence height H is $40H$ long and $10H$ high. The geometric characteristics used in the equations are the same ones used in the experiments. Figure 3 depicts an example of the grid system used in this study. Mesh distributions are all geometric progressions away from the regions of steep gradients, such as those close to the walls and around the holes of the fences. The

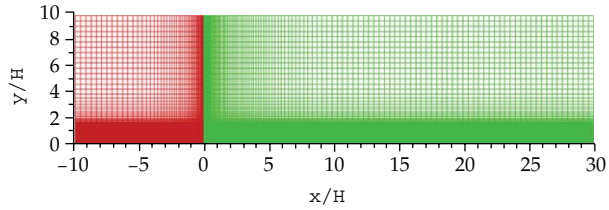

Figure 3: Grid system used in this study (green grids showing downstream of the fence; red grids showing upstream of the fence).

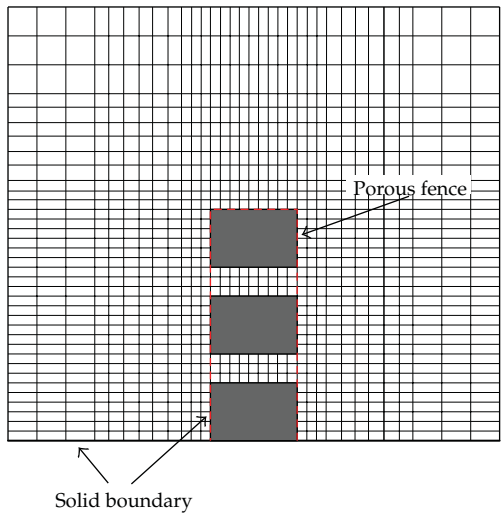

Figure 4: Computational grid local to the porous fence.

grid structure local to the porous region is shown in Figure 4. In this study, the numerical simulation particularly investigates the flow near a porous fence, which is difficult to be represented by treating the porous fence as a uniform area with a drag law. In order to reflect the physical nature of the boundaries, *the following boundary conditions are used in this study: a power-law velocity profile at the entrance; a reference pressure at the exit; a no-slip condition at the wall and the surface of the porous fence.*

4. Model Testing and Validation

Figure 5 shows the measured mean velocity profiles around the porous fence. The approaching flow is divided into two parts just in front of the fence. The deflected flow moves upward and passes above the fence top. In addition, the bleed flow passes through the holes of the lower half of the porous fence. A recirculation region with negative velocities exists behind the porous fence. Velocity profiles behind the porous fence show large velocity gradients existing at two vertical locations, one just above the structures and the other near the location of $y/H = 0.5$. The higher part indicates the separation from the top edge of the fence. The lower part attributes to the interaction between the bleed flow and the wall boundary layer. Meanwhile, the numerical model in this study was employed to simulate

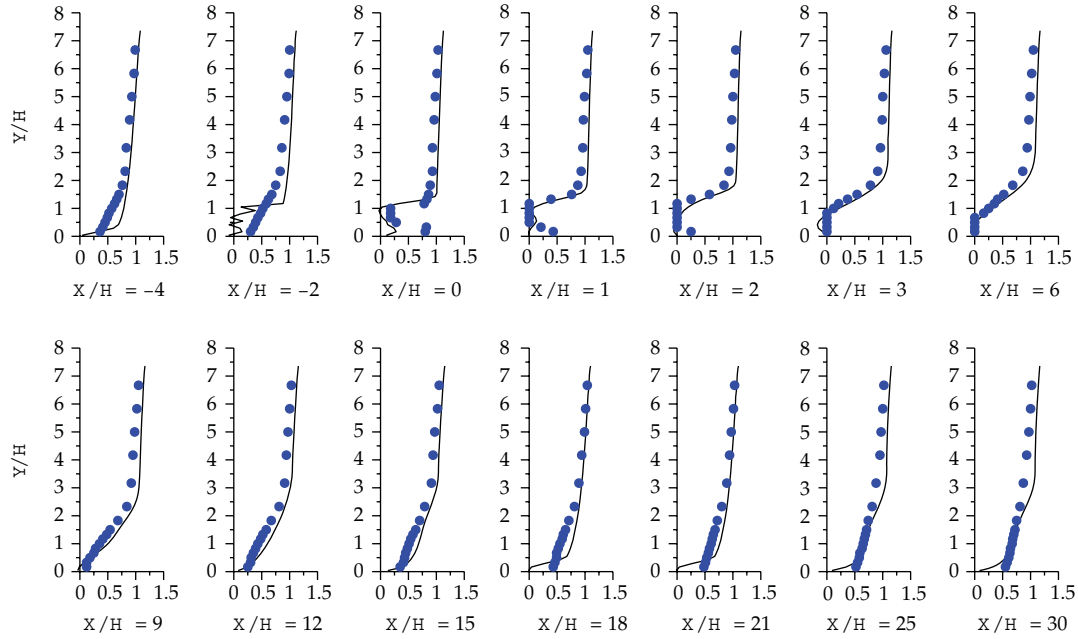

Figure 5: Comparison between calculated results and measured data of mean streamwise velocity profiles around the nonuniform porous fence (ε_U = 0% and ε_L = 30%): (full line) numerical simulation, ( ) experiment.

the flow fields around nonuniform porous fences. The first run was performed under the experimental condition. *The numerical results were tested for grid independence by comparing the velocities obtained for* 301 × 46 *and* 351 × 51 *grid cells.* With these two grids, the results are quite close while the streamwise velocities near the porous fence reveal an averaged discrepancy of 1.2%. Therefore, all the following computations are carried out using a grid size of 351 × 51, and are expected to be grid independent. Figure 4 also shows the detailed comparison between the measured data and the corresponding computed results. Behind the porous fence, the bleed flow passing through the porous fence pushes the recirculation flow resulting in positive velocities near the wall, and the reversed flow phenomena disappear in the region $6 < x/H < 9$. This mixing interaction between the bleed flow and the recirculation flow is well-predicted using the present model. *The model gives slightly higher values than the measured data in the recirculation region. However, the general trends of velocity profiles and the locations of the peak value are well reproduced. The velocity distributions are in good agreement and measures can be evaluated for the main recirculation zone behind the fence. As shown in Figure 2, therefore, the porous fence was arranged in the wind tunnel with two vertical blocks from side walls. The LES is considered to be sufficiently validated to carry out the numerical simulations of turbulent flow passing through a porous fence.*

5. Results and Discussion

The numerical model in this study was validated by comparing the computed results with the experimental data. Future applications of the numerical model were to be the numerical analysis of the manipulated flow cases. The computational conditions, including the boundary conditions and model parameters, of the experiment in the previous section

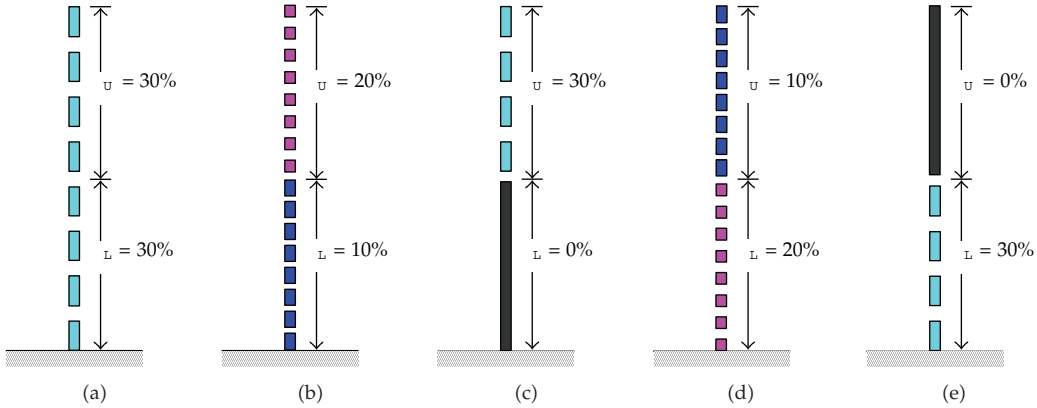

Figure 6: Porous fences: (a) $\varepsilon_U = 30\%$ and $\varepsilon_L = 30\%$; (b) $\varepsilon_U = 20\%$ and $\varepsilon_L = 10\%$; (c) $\varepsilon_U = 30\%$ and $\varepsilon_L = 0\%$; (d) $\varepsilon_U = 10\%$ and $\varepsilon_L = 20\%$; (e) $\varepsilon_U = 0\%$ and $\varepsilon_L = 30\%$.

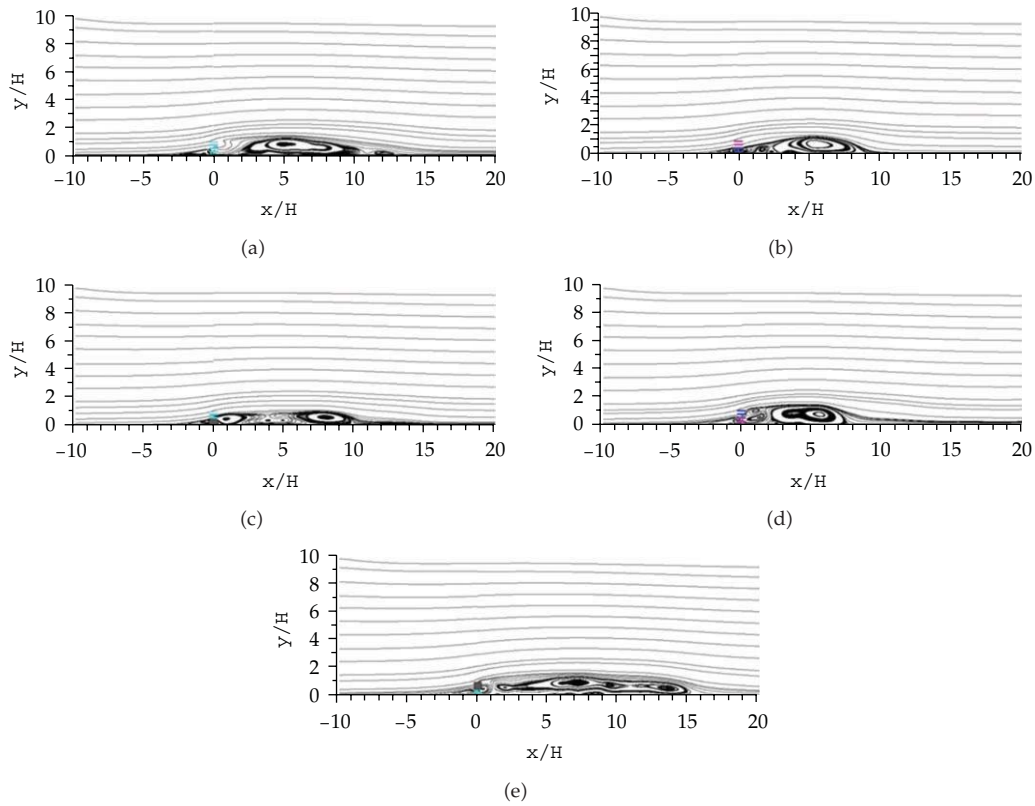

Figure 7: Comparison between calculated streamline patterns around various porous fences.

were used as the basis for the following numerical analysis. Various combinations of upper and lower fence porosity were numerically studied. Five porous fences and the combinations of upper and lower fence porosity used in this study are shown in Figure 6. *Figure 7 presents the mean streamline patterns around various porous fences.* For all the porous fences, the

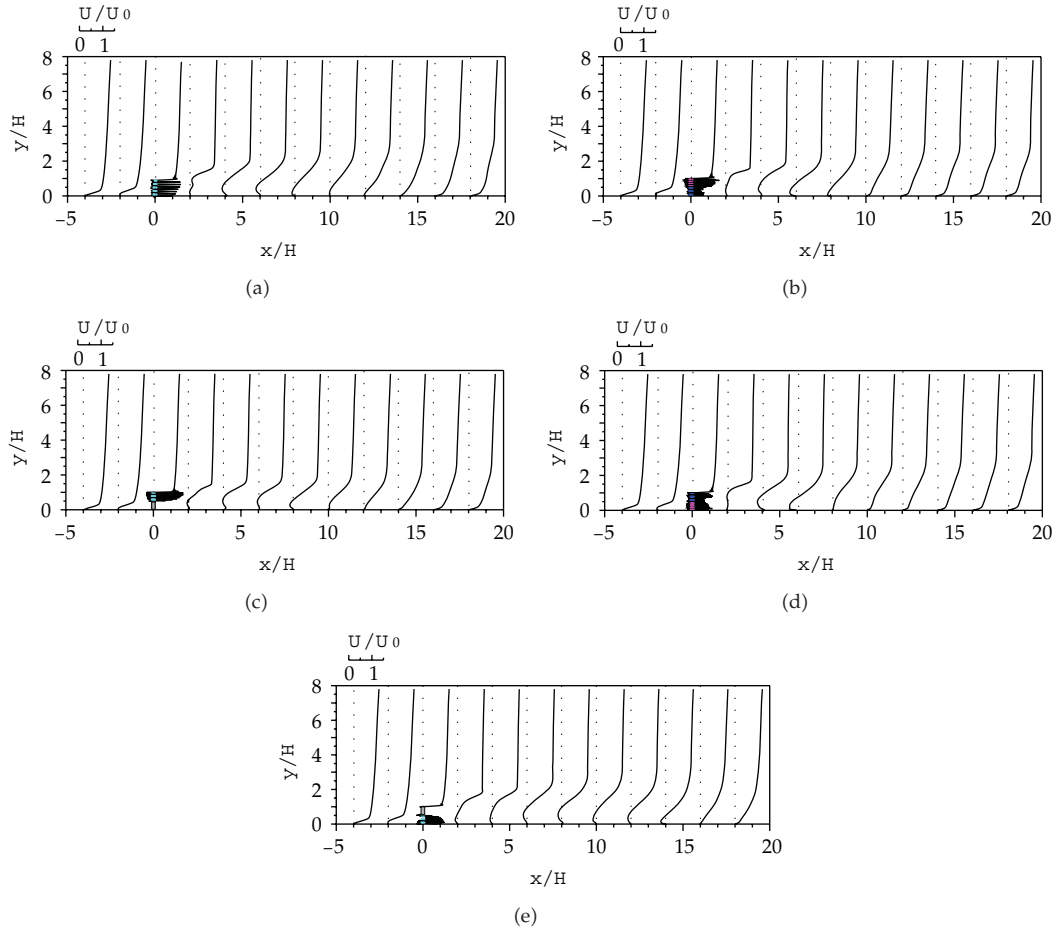

Figure 8: Variations of calculated mean streamwise velocity profiles around various porous fences.

streamlines are shifted and there is a recirculation flow region behind the fence. When the porous fence is nonuniform, the bleed flow has a velocity gradient in the vertical direction. This effect produces extra mixing interaction as the fluid passes through the fence holes. Therefore, the recirculation region is highly dependent of the combinations of fence porosity. This indicates that the manipulation of the bleed flow at either the upper or lower parts of the fence has a significant effect on the recirculation region but the mechanisms involved are different. Besides, the recirculation region behind the porous fence of case E is considerably larger than the other cases. Figures 8 and 9 show the variations of mean streamwise and vertical velocity profiles around porous fences. The results give the qualitative and quantitative observations of flow patterns passing through the porous fences. The bleed flow passing through porous holes facilitate jets toward the recirculation flow at high velocities. When the upper porosity is greater than the lower porosity, the bleed flow passing through the upper half of the fence increases. The strong bleed flow of the upper fence mixes with the shear layer separated from the top edge of the fence. Hence, the downward motion of the entrained shear flow is reduced. In cases B and C, the mean vertical velocities are smaller than that of the uniform porous fence. When the porosity of the upper half of the fence is

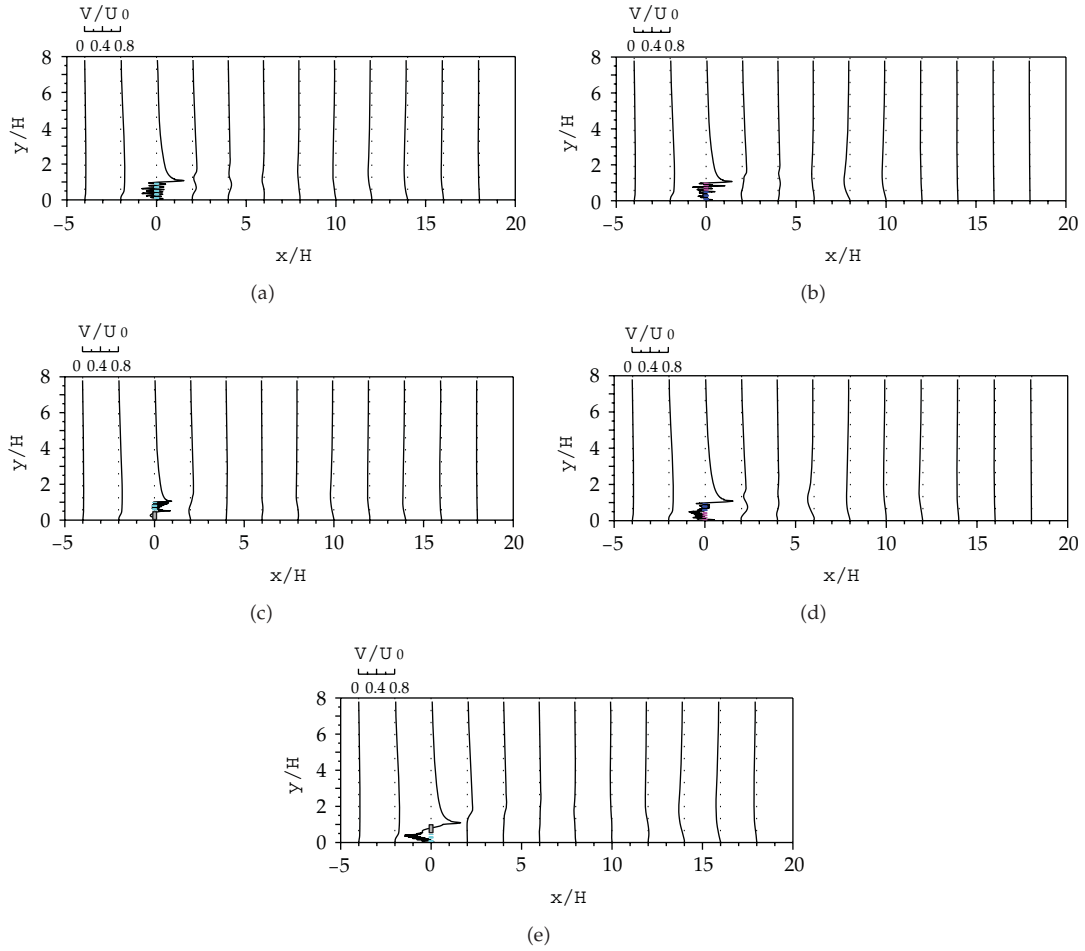

Figure 9: Variations of calculated mean vertical velocity profiles around various porous fences.

less than that of the lower half, the bleed flow passing through the lower fence becomes strong and gradually pushes up the recirculation flow. In cases D and E, the recirculation flow displays high vertical velocities in the region of $y/H < 0.5$. Contour plots of the mean streamwise velocity for the different fences are shown in Figure 10. For all porous fences, the approaching flow decelerates behind the fence. The optimal design of porous fences is determined by engineer's own purpose. For the main purpose of mean velocity reduction, Van et al. [13] had proposed a shelter parameter to quantify the sheltering effect of the fence. This index was evaluated from the areas under the $U/U_0 = 0.5$ contour line of the reduced mean streamwise velocity behind the fence. However, this index reflected only the streamwise mean velocity at one certain value. Although the areas under the other velocity level are relatively small compared to the areas under the $U/U_0 = 0.5$ contour line, it must be considered in addition to obtain an accurate shelter parameter. Therefore, this study takes into account three streamwise velocity levels. The contour lines are the best fit curves with a second-order polynomial. The corresponding areas under $U/U_0 = 0.1, 0.3$ and 0.5 behind the fences are represented by $PI_{0.1}$, $PI_{0.3}$, and $PI_{0.5}$, respectively, and summarized in Table 1.

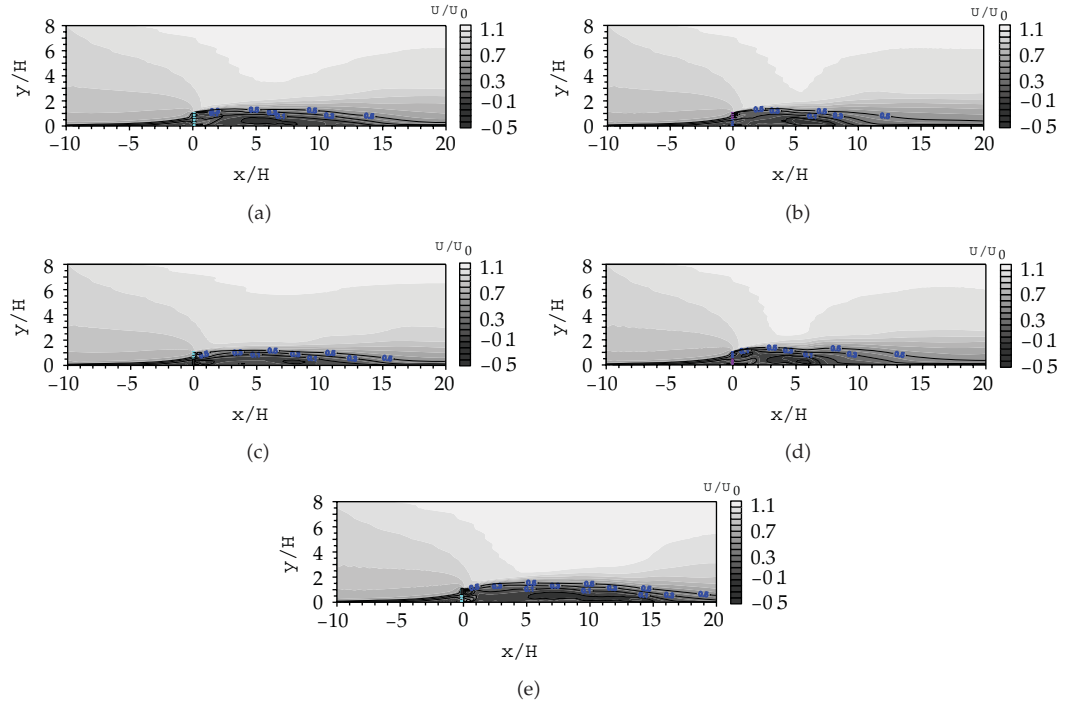

Figure 10: Contour plots of the calculated mean streamwise velocity for various porous fences.

Table 1: Areas under contours $U/U_0 = 0.1, 0.3$ and 0.5 behind the fences.

Protection Index (H^2)	Case				
	A	B	C	D	E
$PI_{0.1}$	9.44	7.44	8.56	7.78	14.49
$PI_{0.3}$	16.67	13.05	13.63	14.26	21.33
$PI_{0.5}$	22.97	21.92	20.96	24.06	28.37

The effects of nonuniform porosity are clearly shown in terms of the values of $PI_{0.1}$, $PI_{0.3}$, and $PI_{0.5}$. In the cases of the upper porosity being greater than the lower porosity, the values of $PI_{0.1}$, $PI_{0.3}$, and $PI_{0.5}$ are slightly smaller than that of the uniform fence (case A). This may be attributed to the downward shear flow affected by the bleed flow which reduces the length of the recirculation flow. The velocity contours are sensitive when the upper porosity is less than the lower porosity. In case D, $PI_{0.1}$ and $PI_{0.3}$ decrease but $PI_{0.5}$ increases, comparison with the respective ones of the uniform fence. In case E, however, all of the areas under the three velocity contours significantly increase. These clearly reveal that the manipulation of the bleed flow at the lower locations of the porous fence has a significant effect on the sheltering effect. The values of $PI_{0.5}$ increase by about 5% and 24% for cases D and E, respectively, compared to that of the uniform fence. case E has the highest value of $PI_{0.5}$ among the porous fences in this study.

6. Conclusion

Flows around nonuniform porous fences are numerically investigated. The numerical model developed in this work is based on the finite volume scheme with a weakly-compressible-flow method. Additionally, the experimental data of a nonuniform porous fence are presented mainly for the validation of the numerical model. As a result, the numerical model is shown to be useful and appropriate for predicting the flows around a nonuniform porous fence. The computation results are consistent with the experimental data. The effect of nonuniform porous fence on flow fields are simulated by varying the combinations of upper and lower fence porosity. The bleed flow passing through a nonuniform porous fence has a velocity gradient in the vertical direction. This manipulation of the bleed flow of the porous fence has a significant effect on the sheltering effect evaluated by the Protection Index. In the porous fences with the upper porosity being greater than the lower porosity, the Protection Index decreases compared to that of the uniform porous fence. Additionally, the porous fences with the upper porosity being less than the lower porosity effectively enhance the sheltering effect. The porous fence with the porosity of the upper half of fence is 0% and the lower half of fence is 30% demonstrates best performance in sheltering effect among the porous fences in this study.

Acknowledgments

The authors gratefully acknowledge Ching-Hua Yang, former master student of the National Chung Hsing University (Taiwan), who carried out the wind tunnel measurements. The J.-T. Lee would also like to thank the National Science Council (Taiwan) for providing financial support (NSC 100-2626-M-005-004-MY3) during preparing this paper.

References

[1] M. D. A. E. S. Perera, "Shelter behind two-dimensional solid and porous fences," *Journal of Wind Engineering and Industrial Aerodynamics*, vol. 8, no. 1-2, pp. 93–104, 1981.

[2] I. P. Castro, "Wake characteristics of two-dimensional perforated plates normal to an air-stream," *The Journal of Fluid Mechanics*, vol. 46, pp. 599–609, 1971.

[3] J. K. Raine and D. C. Stevenson, "Wind protection by model fences in a simulated atmospheric boundary layer," *Journal of Industrial Aerodynamics*, vol. 2, no. 2, pp. 159–180, 1977.

[4] S. C. Yaragal, H. S. Govinda Ram, and K. Keshava Murthy, "An experimental investigation of flow fields downstream of solid and porous fences," *Journal of Wind Engineering and Industrial Aerodynamics*, vol. 66, no. 2, pp. 127–140, 1997.

[5] S. J. Lee, K. C. Park, and C. W. Park, "Wind tunnel observations about the shelter effect of porous fences on the sand particle movements," *Atmospheric Environment*, vol. 36, no. 9, pp. 1453–1463, 2002.

[6] A. R. Packwood, "Flow through porous fences in thick boundary layers: comparisons between laboratory and numerical experiments," *Journal of Wind Engineering and Industrial Aerodynamics*, vol. 88, no. 1, pp. 75–90, 2000.

[7] S. J. Lee and H. C. Lim, "A numerical study on flow around a triangular prism located behind a porous fence," *Fluid Dynamics Research*, vol. 28, no. 3, pp. 209–221, 2001.

[8] R. H. Shaw and U. Schumann, "Large-eddy simulation of turbulent flow above and within a forest," *Boundary-Layer Meteorology*, vol. 61, no. 1-2, pp. 47–64, 1992.

[9] T. Maruyama, "Large eddy simulation of turbulent flow around a windbreak," *Journal of Wind Engineering and Industrial Aerodynamics*, vol. 96, no. 10-11, pp. 1998–2006, 2008.

[10] S. Alhajraf, "Computational fluid dynamic modeling of drifting particles at porous fences," *Environmental Modelling and Software*, vol. 19, no. 2, pp. 163–170, 2004.

[11] H. M. Cho, *Wind-tunnel and numerical simulation of flow over porous fences and particle saltation in atmospheric boundary layer [Ph.D. thesis]*, Department of Mechanical and Aeronautical Engineering, University of California at Davis, Davis, Calif, USA, 1996.

[12] C. W. Park and S. J. Lee, "The effects of a bottom gap and non-uniform porosity in a wind fence on the surface pressure of a triangular prism located behind the fence," *Journal of Wind Engineering and Industrial Aerodynamics*, vol. 89, no. 13, pp. 1137–1154, 2001.

[13] E. J. Van, R. Karschon, L. A. Razumova, and G. W. Roberts, "Windbreaks and Shelterbelts," W. M. O. Technical note no. 59, Geneva, Switzerland, 1964.

[14] M. Germano, U. Piomelli, P. Moin, and W. H. Cabot, "A dynamic subgrid-scale eddy viscosity model," *Physics of Fluids A*, vol. 3, no. 7, pp. 1760–1765, 1991.

[15] C. C. S. Song and M. Yuan, "A weakly compressible flow model and rapid convergence methods," *Journal of Fluids Engineering*, vol. 110, pp. 441–455, 1988.

Hindawi Publishing Corporation
Journal of Applied Mathematics
Volume 2012, Article ID 534275, 16 pages
doi:10.1155/2012/534275

Research Article

Mathematical Analysis of Inclusion Removal from Liquid Steel by Gas Bubbling in a Casting Tundish

H. Arcos-Gutierrez, J. de J. Barreto, S. Garcia-Hernandez, and A. Ramos-Banderas

Instituto Tecnologico de Morelia, Metallurgy Graduate Center, Av. Tecnologico No. 1500, 58120-Morelia, Michoacan, Mexico

Correspondence should be addressed to S. Garcia-Hernandez, iq_sagahz@hotmail.com

Received 5 February 2012; Revised 16 April 2012; Accepted 27 April 2012

Academic Editor: M. F. El-Amin

The mechanism of inclusion removal from liquid steel by gas bubbling and bubble attachment in the tundish is complex due to the great number of variables involved, and it is even more difficult to study because of the turbulent flow conditions. The main objective of this work is to analyze and improve the understanding of the alumina inclusion removal rate by bubble attachment and by gas bubbling fluid dynamics effects. The results show that the inclusion collection probability mainly depends on the attachment mechanism by collision. This parameter was determined by calculating the induction time, which is shorter when the rupture time and the formation time of a stable three phases contact (particle/liquid/gas) are ignored than when it is fully considered, affecting the attachment probability. In addition, to achieve acceptable inclusion removal, a smaller bubble diameter is required, such as 1 mm. This consideration is almost impossible to achieve during tundish operation; a more realistic bubble diameter around 10 mm is employed, resulting in a very inefficient inclusion removal process by bubble attachment. Nevertheless, in a real casting tundish the inclusion removal rate employing argon bubbling is efficient; is mainly due to the fluid flow pattern changes rather than bubble attachment. Consequently, it is imperative to consider the summation of both removal mechanisms to compute a better approximation of this important operation.

1. Introduction

Due to the stringent control on the cleanliness of the steel, many steel casting shops around the world have studied extensively the tundish systems employed, not only to maximize the benefits of increasing the residence time by flow control and reduce contamination, but also to have better and faster assimilation of the non metallic inclusions by the slag. The most recent research reported in the open literature on the subject of inclusion removal in tundish can

be grouped in three main subjects: the effect of the fluidynamics on the inclusion trajectories [1–5], the mechanisms of inclusions assimilation by the slag [6, 7], and the mechanisms of inclusion removal by bubble flotation [4, 8–28].

Argon bubbling is a very attractive technology used as a flow control and inclusion removal, it strongly affects the fluid flow patterns in the tundish by reducing the dead flow zones and by increasing the plug flow together with the mean residence time [22–24, 27]. In addition, it has been found by industrial trial that the implementation of this operation improves the inclusion removal rate by decreasing the final range of inclusion size, and the inclusion ratio in the final product [25, 28]. Furthermore, there are some works focusing on the main variables that control the particle-bubble flotation mechanisms [16–19]. Even with all this research, there is a gap in the knowledge of the inclusion-bubble interaction in the tundish and its effect on the removal rate. A few efforts have been done to study this subject, such as the work done by Rogler et al. [20], where the porous zone width effect on the inclusion removal in the tundish was studied. However, in this work many assumptions were taken, for instance considering constant the collection probability. Another important effort was developed by Zhang and Taniguchi [4] where the silica inclusion removal by bubble flotation in the ladle was determined by using the oscillation model.

Equally important is to consider the detrimental effect of the submerged entry nozzle clogging by alumina inclusions in the tundish and the limited understanding on the subject. Therefore, the objective of this work is to analyze mathematically and analytically the alumina inclusion removal rate before they get to the submerge entry nozzle by bubble attachment mechanism, considering attachment by oscillation or sliding models and the collection probability as a function of complete induction time, and by the bubbling fluidynamic effects.

2. Model Development

A fluidynamics mathematical model was developed based on a previous published work by the authors [9] and an analytical model was developed to understand the attachment mechanism for inclusion removal in the tundish. The fundamental equations and mechanisms are described as follows.

2.1. Mechanisms for Particle-Bubble Interaction

The mechanism for inclusion attachment to the bubble can take place by collision (if $t_c > t_{\text{fr}}$) or by sliding (if $t_s > t_{\text{fr}}$). Both are considered in this work. This mechanism has been widely studied and it is composed of six steps [14]:

(1) inclusion approximation to the bubble;

(2) liquid film formation between inclusion and bubble;

(3) oscillation or sliding of the inclusion on the bubble surface;

(4) drainage and rupture of the film to achieve the three phase contact (TPC);

(5) stabilization of the system particle-bubble against external stresses;

(6) flotation of the stable system inclusion-bubble.

This mechanism is influenced by many parameters, where the system is very sensitive. Those parameters are as follows.

Collision time (t_c) is calculated by Evans' model [13],

$$t_c = \left(\frac{\pi^2 \rho_p}{12\sigma_L}\right)^{1/2} d_p^{3/2}. \tag{2.1}$$

Drainage time (t_{fr}) is determined by Schulze's model [19],

$$t_{\mathrm{fr}} = \frac{3}{64}\left(\frac{\pi}{180}\right)^2 \frac{b_\alpha^2 (32 u_R t_c)^{2m_a} \mu_L d_p^3}{\sigma_L k h_{\mathrm{crit}}^2}. \tag{2.2}$$

Critical film thickness (h_{crit}) is calculated by Sharma and Ruckenstein Hole Formation model [13]. This model considers irregular inclusion shapes,

$$h_{\mathrm{crit}} = -2\sigma_l + \frac{\left(4\sigma_l^2 + 2\rho_L g \sigma_l (1 - \cos\theta) r^2\right)^{1/2}}{\rho_L g r}. \tag{2.3}$$

Sliding time (t_s) is calculated by Nguyen's model [17, 18],

$$t_s = \frac{d_P + d_B}{2u_B(1 - B^2)A} \ln\left\{ \frac{\tan(\theta_c/2)}{\tan(\theta_0/2)} \left[\frac{\operatorname{cosec}\theta_c + B\cot\theta_c}{\operatorname{cosec}\theta_0 + B\cot\theta_0}\right]^B \right\}. \tag{2.4}$$

Bubble diameter (d_b) is calculated as a function of Orifice Reynolds number,

$$N_{\mathrm{Re},O} = \frac{u d_0 \rho_g}{\mu_L} = \frac{4Q_g\rho_g}{\pi d_0 \mu_L}$$
$$N_{\mathrm{Re},0} < 500 \longrightarrow d_B = \left[\frac{6 d_0 \sigma_L}{g(\rho_L - \rho_G)}\right]^{1/3} \text{ and to } N_{\mathrm{Re},0} > 5000 \longrightarrow d_B = \frac{1.3 Q_g^{6/5}}{g^{3/5}}. \tag{2.5}$$

Bubble velocity (u_b), Davies and Taylor's model is used for bubbles of spherical cap shape with a bigger diameter than 6 mm [22], and the Stokes model for the bubble diameter smaller than 1 mm,

$$u_B = 1.02\left(\frac{g d_B}{2}\right)^{1/2}, \qquad u_B = \frac{d_B^2}{18\mu_L} g(\rho_L - \rho_G). \tag{2.6}$$

Induction Time (t_i) is determined by the complete Nguyen's model [18],

$$t_i = \frac{d_P + d_B}{2u_B(1 - B^2)A} \ln\left\{ \frac{1/\sqrt{P_{\mathrm{at}}} + \sqrt{1/P_{\mathrm{at}} + D^2 - 1}}{\left(1/\sqrt{P_{\mathrm{at}}} + B\sqrt{1/P_{\mathrm{at}} + D^2 - 1}\right)^B} \times \frac{(1 + BD)^B}{1 + D} \right\}. \tag{2.7}$$

The induction time is a relatively new parameter that has not been fully studied.

2.2. Inclusion Collection Probability

The overall probability (2.8) is the product of the attachment probability (Equation (2.9), Yoon's model [14]), the collision probability (Equation (2.10), Nguyen's semianalytic model [17, 18]), and one minus the detachment probability, which is considered equal to zero,

$$P = P_C \cdot P_{\text{at}}(1 - P_{\text{det}}) \tag{2.8}$$

$$P_{\text{at}} = \text{sen}^2\left[2\arctan\exp\left(-\frac{2t_{\text{fr}}}{d_b + d_p}X\right)\right] \tag{2.9}$$

$$X = \left[\left\{\left[1 - \frac{3}{4x_E} - \frac{1}{4x_E^3} + \frac{\text{Re}_B^{0.72}}{15}\left(-\frac{2}{x_E^4} + \frac{1}{x_E^3} + \frac{1}{x_E}\right)\right]u_b - u_p\right\}\right], \quad x_E = 1 + k_2,\ k_2 = \frac{d_p}{d_b}$$

$$P_C = \frac{2u_B D}{9(u_B + u_P)Y}\left(\frac{d_P}{d_B}\right)^2\left[\sqrt{(X + C)^2 + 3Y^2} + 2(X + C)\right]^2. \tag{2.10}$$

The model proposed by Rogler et al. is used [20] to study the alumina inclusion removal rate in the tundish. In this model the inclusion concentration is a function of the residence time and it is given by

$$-\frac{dn}{dt} = N_T = kn, \quad \text{where } N_T = N_{CC} \cdot N_B = \frac{3q_G P T_F}{2d_B T_0} \cdot n = k \cdot n, \tag{2.11}$$

where: $n = n_0 e^{-k\tau}$.

The inclusion removal efficiency is expressed for

$$\varepsilon = \left(1 - e^{k\tau}\right) \cdot 100. \tag{2.12}$$

2.3. Mathematical Model Considerations and Boundary Conditions

The fluidynamic model consists-of the fundamental Navier-Stokes equations, together with the k-ε turbulence model and the discrete phase model [9] embedded in the commercial CFD code FLUENT. The liquid steel flowing in the tundish is assumed to have Newtonian behavior, under isothermal and steady state conditions. Both turbulent and laminar flows coexist in the tundish; however, only laminar flow is present close to solid walls. Consequently, typical nonslipping conditions were applied to all solid surfaces. Wall functions were used at the nodes close to any wall. The gravity force was considered to act over the y-coordinate. No slag layer was considered, instead a plane surface was assumed where the velocity gradients, turbulent kinetic energy, and its dissipation rate are taken as zero.

To study the macroscopic flow effect, the simulated inclusions were assumed to have a spherical rigid shape with the physical properties of alumina. No interaction among the inclusions was considered; therefore, agglomeration and collision were not simulated. The only inclusion removal mechanism considered was Stoke's flotation. Inclusion trajectories

were calculated using a Langrangian particle-tracking approach, which solves a transport equation for each inclusion as they travel through the previous calculated velocity field of liquid steel. This approach assumes that the interaction between steel and the inclusion is one-way coupled, that is, only the steel affects the trajectories of inclusions but these do not affect the steel flow. The boundary conditions for inclusion removal were as follows: any inclusion that reached the free surface was considered removed and the rest was considered as escaped.

2.4. Analytical Model Description and Considerations

The argon bubbles have a constant size, and they are uniformly distributed in the bubble region. The bubble-bubble and inclusion-inclusion interactions are ignored. The inclusion-inclusion collision as well as the agglomeration is not considered, and the inclusion size does not affect the bubble trajectory. The removal mechanisms considered are bubble flotation and buoyancy forces.

For the calculation of the inclusion removal rate by bubble attachment, five main programs were developed, for those the dimensionless constants (A, B, C, D, X, Y all these constants were calculated with the equations proposed by Nguyen et al. [17, 18]) were calculated as a function of the Re_b. Program I: calculate d_b, u_b, t_i, P_a, P_c, E_{ri}, t_c, t_{fr}, h_{crit} using small increments of the gas flow rate and the diameter of the pore in the porous plug. Program II: calculate u_p, P_c, P_a, E_{ri}, t_c, t_i, t_{fr}, h_{cri} using different width of the bubble region, but considering constant the resident time of the steel, the bubble diameter, the gas flow rate, and the diameter of the pore in the porous region. Program III: calculate P_c, P_a, t_c, t_{fr}, h_{crit} using constant the inclusion diameter and the bubble diameter. Program IV: calculate d_b, u_b, P_a, P_c, E_{ri}, t_c, t_{fr}, h_{crit} but employing constant the gas flow rate and the diameter of the pore in the porous plug. Program V: calculate P, P_a, P_c, t_s, t_c, t_{fr}, t_i, h_{crit} for different bubble and inclusion diameters. This has been summarized in Table 1.

3. Results and Discussion

3.1. Analytical Analysis

The first variable calculated was the Critical Film Thickness (h_{cr}) for alumina inclusions, this variable was predicted using the hole formation and oscillation models, and the Schulze and Birzer empirical relationship. The results are shown in Figure 1(a), where h_{cr} for this inclusion type has values between 0.015–452 nm. Consequently, the dominant forces for the film draining and rupture are the Van der Waals forces. It was also observed that h_{cr} value is bigger when it is calculated using the hole formation model indicating that the liquid film rupture takes place easier by the formation of a hole. Since this work is focused on inclusion sizes ranging between 1–40 microns, it can be observed that the predicted values for h_{cr} are in the zone of the experimental results in water systems. Furthermore, Figure 1(b) shows the h_{cr} results for silica inclusions reported by Zhang and Taniguchi [4], who established that h_{cr} value is 3 to 5 times higher for the hole formation model than the values obtained by oscillation model, concluding that the film rupture is easier by the formation of a hole. These authors suggested that for alumina inclusions the film drainage and rupture may occur by the formation of a hole, which is corroborated by the present results and it was concluded

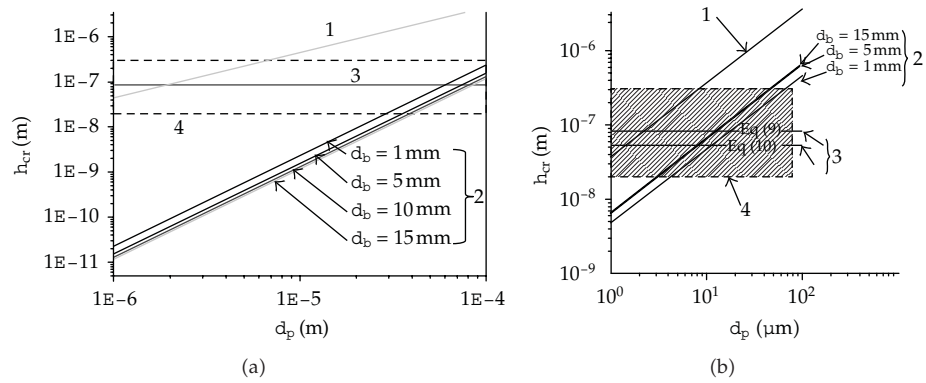

Figure 1: The critical film thickness (h_{cr}) calculated as a function of the inclusion diameter (d_p), (a) alumina inclusion and (b) silica inclusion [13].

Table 1: Variables, parameters, and equations for each program developed.

Program	Variables calculated	Parameters modified	Equation numbers employed	Dimensionless constants
I	$d_b, u_b, P_a, P_c, E_{\text{ri}}, t_i, t_c, t_{\text{fr}}, h_{\text{crit}}$	d_p, n_0, τ, d_0, Q_g	1, 2, 3, 5, 6, 7, 9, 10, 11	A, B, C, D, X, Y
II	$u_p, P_c, P_a, E_{\text{ri}}, t_c, t_{\text{fr}}, t_i, h_{\text{cri}}$	$d_p, n_0, \tau, d_0, Q_g, d_b$	1, 2, 3, 5, 7, 9, 10, 11	A, B, C, D, X, Y
III	$P_c, P_a, t_c, t_{\text{fr}}, h_{\text{crit}}$	d_p, d_b	1, 2, 3, 10, 11	C, D, X, Y
IV	$d_b, u_b, P_a, P_c, E_{\text{ri}}, t_c, t_{\text{fr}}, h_{\text{crit}}$	d_p, n_0, d_0, Q_g	1, 2, 3, 6, 7, 9, 10, 11	A, B, C, D, X, Y
V	$P, P_a, P_c, t_s, t_c, t_{\text{fr}}, t_i, h_{\text{crit}}$	d_p, d_b	1, 2, 3, 4, 5, 6, 7, 9, 10, 11	A, B, C, D, X, Y

that h_{cr} is dependent of the inclusion type, and the film rupture will take place by the hole formation mechanism, which will be the model to be considered further on.

It is well known that the inclusion attachment mechanisms to a bubble can be by collision or by sliding. For such reason, it is required to know the collision time (t_c), the sliding time (t_s), and the induction time (t_i), since the controlling attachment mechanism is determined through these three variables. The induction time is the time required to achieve the drainage and rupture of the film, in order to reach a stable three phase contact (TPC). In previous research works, some of the considerations were taken to predict the induction time results in smaller values, for instance, Wang et al. [14] calculated $t_i = t_{\text{fc}}$ without considering TPC rupture time and the time for the formation of the stable TPC; however, the authors advice that this assumption is not exact; this hypothesis was also considered by Rogler et al. [20]. Nevertheless, due to its importance, in the present work it has been fully calculated using Nguyen's model (2.7). The numerical values of these three time variables calculated for alumina inclusions are shown in Figure 2(a). Where it should be taken into account that if $t_c > t_i$, the inclusion attachment is by collision if $t_c < t_i$, the inclusion does not attach if $t_s > t_i$, the inclusion attachment is by sliding and if $t_s < t_i$ the inclusion slide; but it does not attach. Considering this as a reference, the results show that in general $t_i > t_c$ for the studied bubble diameters; consequently, the alumina inclusion attachment occurs by sliding

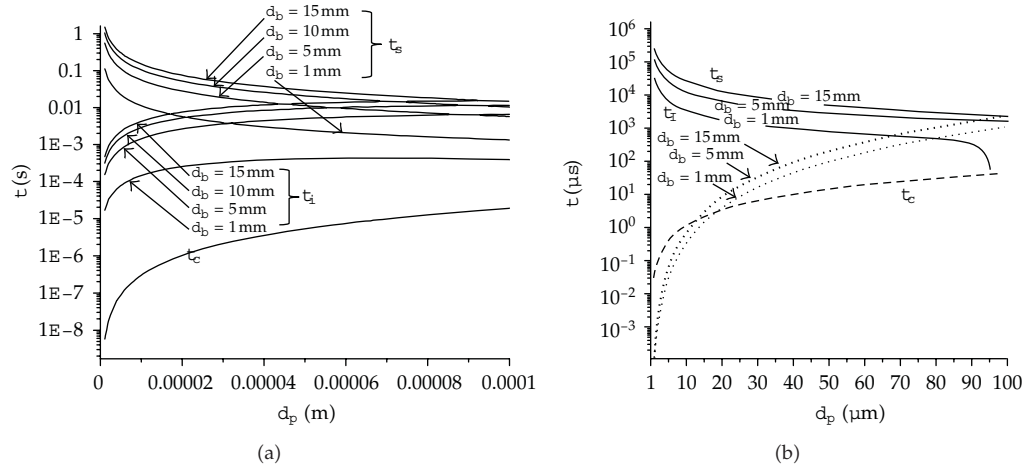

Figure 2: Relationship of the Inclusion Diameter to the collision, sliding and induction times. (a) t_i calculated using the Nguyen's equation and (b) t_i reported by Zhang and Taniguchi [13].

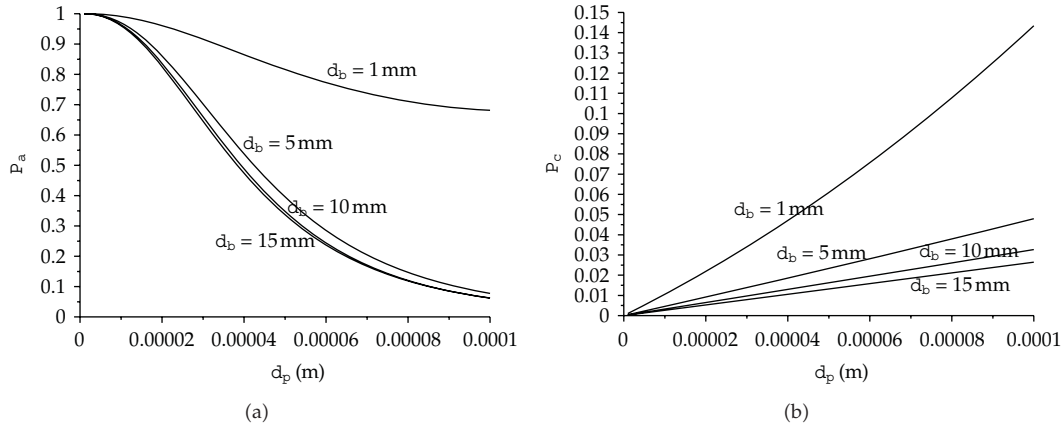

Figure 3: (a) Attachment Probability and (b) Collision Probability.

or bouncing back, but it will not take place by collision. About the variable t_s when the bubble size is 1 mm $t_s > t_i$, meaning that the inclusion attaches by sliding, and when the bubbles size is 5 mm $t_s > t_i$ but only for particles diameters up to 83 μm. Figure 2(a) also shows the limit for inclusion diameter that may attach to a bubble, which is identified by the intersecting point of t_s and t_i. The present results show bigger t_i values and therefore smaller limits compared to those obtained previously by Zhang and Taniguchi [13]. Therefore, it is essential to select adequately the model used for compute t_i.

To predict the inclusion removal rate in the tundish, it is required the collection probability which depends on the attachment and collision probabilities; for this reason, these probabilities are first analyzed. Figure 3(a) shows the calculated P_{att} values as a function of the bubble and particle diameters, where it can be seen that for $d_p < 10$ microns the values obtained are close to unity, independently of the d_b. This indicates that any inclusion that impacts a bubble will be removed. On the other hand, for $d_p > 10$ microns the P_{att} becomes a function of d_b, for example for $d_b = 1$ mm the P_{att} is high; nevertheless, for $d_b = 5$ mm

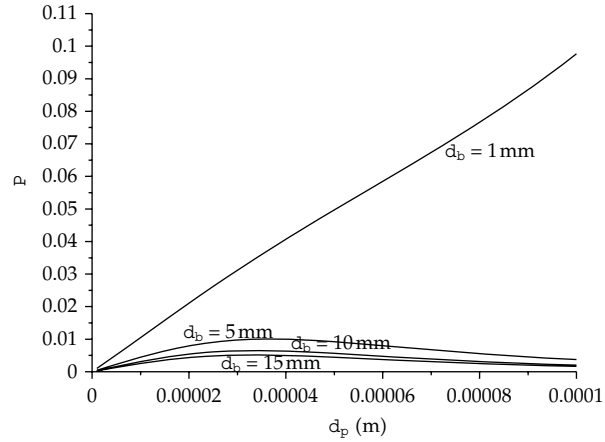

Figure 4: Collection Probability.

the P_{att} decreases exponentially. Moreover, for bigger bubble diameters such as 10 or 15 mm, the P_{att} shows values and a declined profile similar to $d_b = 5$ mm. These results are in accordance to previous works published in the open literature [13, 14, 20], which means that the present model predicts correctly the P_{att} and allows to conclude that it is necessary to have $d_b < 5$ mm to remove efficiently small alumina inclusions in the range of 1–40 microns.

Figure 3(b) shows that, in general, the collision probability is very low independently of the bubble and inclusion sizes. It is important to state that if an inclusion collides with a bubble, the removal probability will be high. In order to improve the collision probability considering the above inclusion size range, it is required that bubble diameters be smaller than 1 mm. However, in the liquid steel flowing inside the tundish it is extremely difficult to get argon bubble diameters as small as 1 mm; therefore, the P_c will be very low and consequently the collection probability will be even smaller, this can be observed in Figure 4. Taken into consideration the calculated information, the inclusion removal rate in the tundish by bubble attachment may not be as efficient as can be expected and it is perhaps more dependent on other variables. According to this hypothesis, it is required to calculate the inclusion removal rate (R_E) of a typical two-strand tundish. To determin this variable, it was necessary to define some parameters, such as the width of the porous media considering both sides (L_B), the tundish mean residence time (T_R) and the mean residence time inside the bubble zone (T_{RB}); the last two are directly related with the steel level which was set as constant implicating that T_R is constant, and T_{RB} depends only on the L_B variable. With these conditions, R_E was calculated using the Rogler and Heaslip model [20] and the results are shown in Figure 5(a). In this figure, the requirement of small bubble diameters to get an efficient inclusion removal is evident once more. Through these results the declared hypothesis in Figure 4 is confirmed, since R_E values are smaller than 30% for inclusion in the interest range with 10 mm argon bubble diameter.

In spite of the small values mentioned above, it is necessary to find out the controlling variable on R_E. In order to achieve this goal, some variations were considered and their effects were analyzed against the R_E value of 21% for $d_p = 30$ microns and $b_d = 10$ mm. First, the T_R was decreased from 600 to 400 seconds, Figure 5(b). This change turned out in a 33% decrease of T_{RB}, consequently a 34% decrease of R_E reference value was observed. Second, reducing by half L_B and keeping T_R constant, Figure 5(c), the T_{RB} value was diminished to

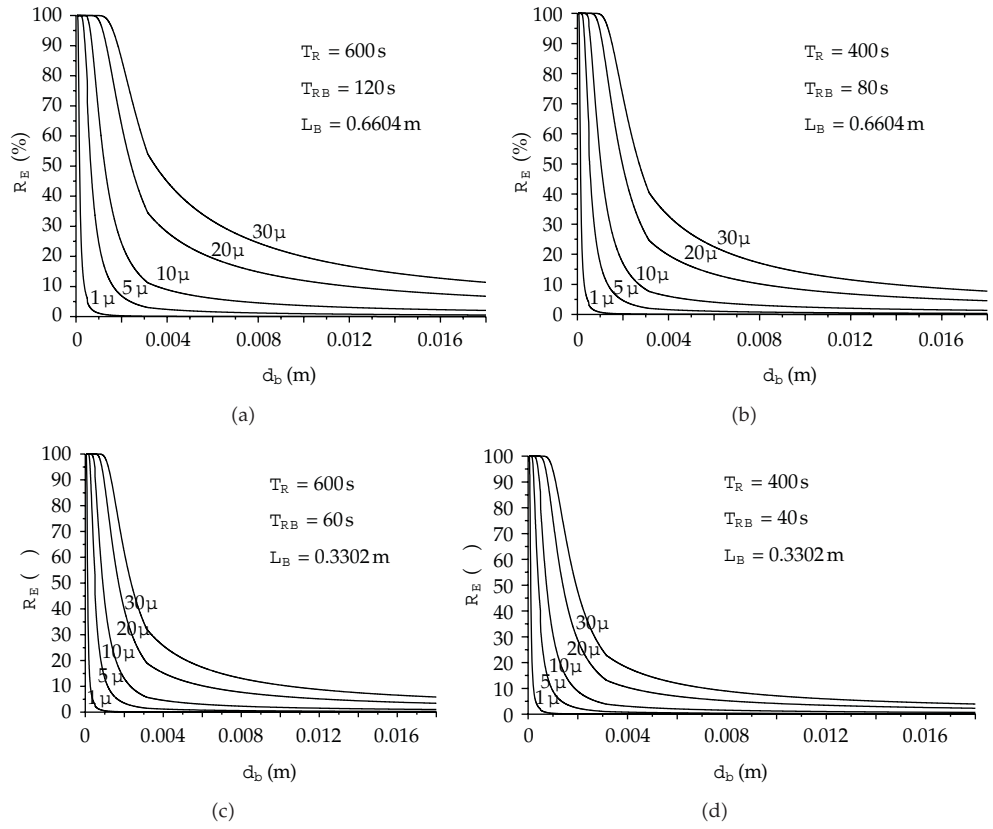

Figure 5: Prediction of the inclusion removal rate in a continuous casting tundish, (a) Constant T_R and L_B, (b) Decrease of T_R in 200 s, (c) Decrease of L_B by half, and (d) Decrease of T_R and decrease of L_B by half.

50% causing a drop of 52% on R_E. Finally, the two previous reductions were put together, Figure 5(d), and resulted in a T_{RB} decrease of 66% inducing an R_E value of 6%. According to these results, R_E is a direct function of T_{RB}. As in the majority of the tundish systems L_B, T_R, and T_{RB} are constants, R_E depends exclusively on the bubble attachment mechanism which is a very inefficient process as has been shown above. However, to explain the benefices reported from other modelling studies [8, 9, 26] and those observed in practice [8, 28], where the argon bubbling helps a lot the inclusion removal, it is necessary to consider additionally the fluidynamics analysis of the system. This need is focused in the strong modification of the flow patterns produced by the argon bubbling; first of all, the bubble curtain redirects the flow towards the free surface, and secondly, the leaving flow from the curtain shows a plug behavior promoting a bigger inclusion uncoupling. As a consequence of these patterns, it is possible to obtain a considerable improvement on the inclusion removal.

3.2. Mathematical Analysis

In order to confirm the last hypothesis, a mathematical simulation of the fluidynamics in a tundish equipped with a turbulence inhibitor and under argon bubbling was carried out, in which R_E was only calculated by fluidynamics effects (Stoke's flotation). Since there are many

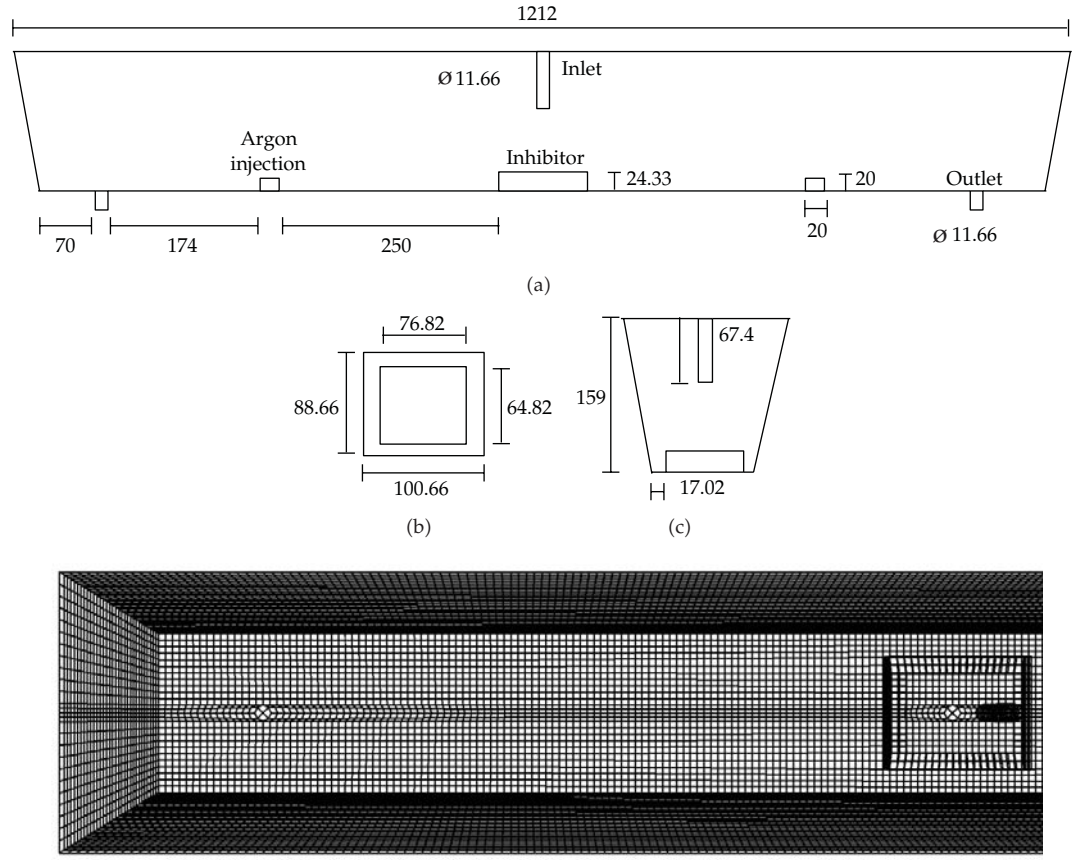

Figure 6: Characteristic dimensions of the continuous casting tundish (a) Frontal view, (b) Turbulence Inhibitor (TI) upper view, (c) Lateral view, and (d) Computational grid.

different tundish configurations, it was considered a typical slab tundish configuration and the numerical assumptions employed in a previous published work [9]. The characteristic dimensions of the tundish and the mesh used in this study are presented in Figure 6.

It should be taken into account that the inclusions are only removed when they reach the free surface; consequently, when the movement of the steel towards the free surface is acquired, a better removal percentage can be expected. It is important to notice that R_E could be anticipated to be bigger than the one calculated by attachment since the area of removal is also bigger; due to the difference of densities the uncoupling mechanism is easier than the bubble attachment mechanism.

Observing the flow pattern changes in Figures 7 and 8, it can be seen that when argon is not injected, the fluid flow is directed by the turbulence inhibitor towards the free surface inducing a better removal efficiency since it promotes a redirection of the inclusion to the steel-slag interface. However, nearly at half of the distance between the inlet and the outlet, the steel moves downwards; this change has as a consequence that the inclusions move far from the interface, because of that, most of the inclusions are removed mainly at the first half of the tundish. Nevertheless, when the argon is injected, the flow patterns have

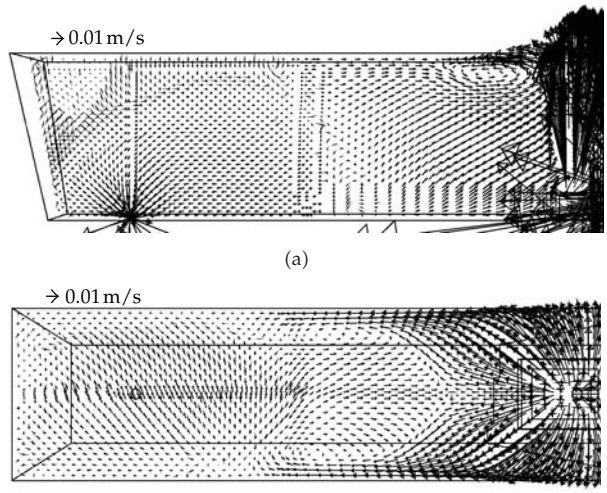

Figure 7: Velocity profiles inside the tundish without argon injection, (a) At the symmetric-longitudinal plane and (b) At the tundish steel level.

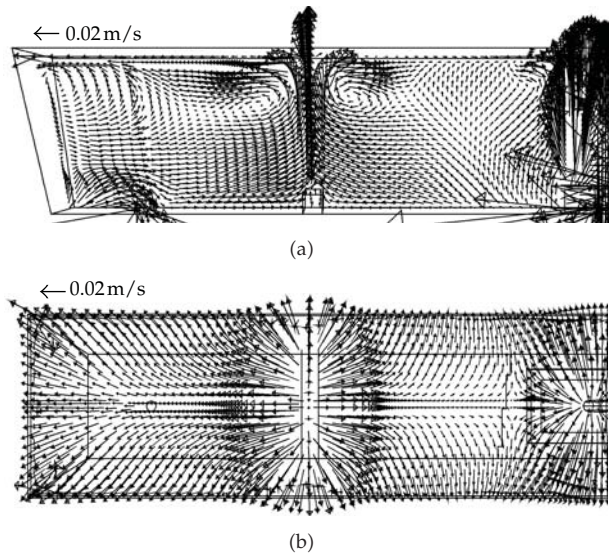

Figure 8: Velocity profiles inside the tundish with argon injection, (a) At the symmetric-longitudinal plane and (b) At the tundish steel level.

a strong change since two recirculation patterns are produced before and after the argon bubbling zone. These two changes generate a major removal percentage of inclusion due to the recirculation patterns.

For this study, the alumina inclusions were fed in the tundish entry nozzle and it was considered that the removed inclusions were only those that reach the tundish steel-slag interface. Since the most difficult inclusion removal size are those smaller than 30 microns, the results for that range are shown in Figure 9, where it can be observed that without argon,

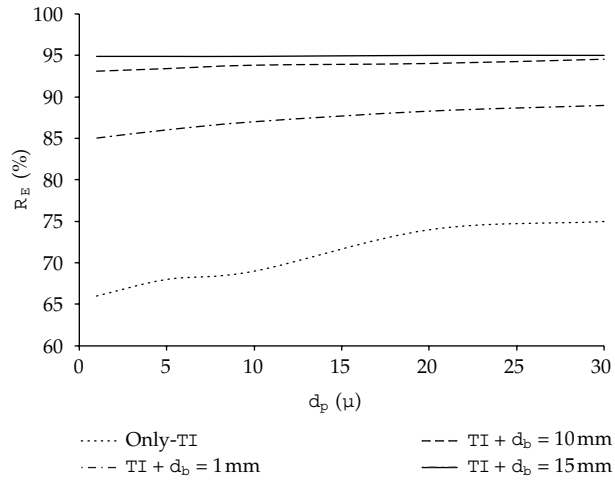

Figure 9: Non metallic Inclusion removal rate considering only the fluidynamics effect.

bubbling R_E is near to 70% only by fluid flow. Now, if it is considered argon injection with $d_b = 1$ mm, R_E is improved by a further 15% just for fluidynamics, even more, if we add the theoretical R_E by bubble attachment (Figure 5(a)) the total R_E should be close to 100%. Nevertheless, for more regular bubble diameters such as $d_b = 10$ mm or bigger like 15 mm, the bubble curtain effects on steel movement is larger inducing a major displacement of the fluid to the interface steel-slag; consequently, R_E must increase as actually is happening since R_E achieves values close to 90%. Thus, even R_E by bubble attachment is quite low (near to 21%), the total R_E should be bigger than 90%. It is important to notice that the total R_E is not only a direct sum of both percentages. Figure 10 shows the combination of the two mechanisms and shows the increasing of the total R_E.

With these results it can be concluded that the inclusion removal rate in the tundish is efficient, employing argon bubbling mainly by the fluid flow pattern changes rather than by bubble attachment. Additionally, it can be established that it is imperative to consider the summation of both removal mechanisms to compute a better approximation of this important operation.

Finally, it is important to mention that these higher values of R_E are a close approximation, since many of the inclusions that reach the interface never get absorbed by the slag and some others get back to the steel flow again, due to the strong turbulence of the liquid steel; consequently, this removal percentage is a powerful indicative of the way a tundish reactor is working on the inclusion removal, but until now it still impossible to establish that these results are definitive.

4. Conclusions

The non metallic inclusion removal mechanism by argon bubbling effects in a continuous casting tundish operation is analyzed analytically and by mathematical simulation involving a great number of variables. After analyzing the alumina inclusion removal rate by bubble attachment and by bubble fluidynamics effects the following conclusions can be drawn.

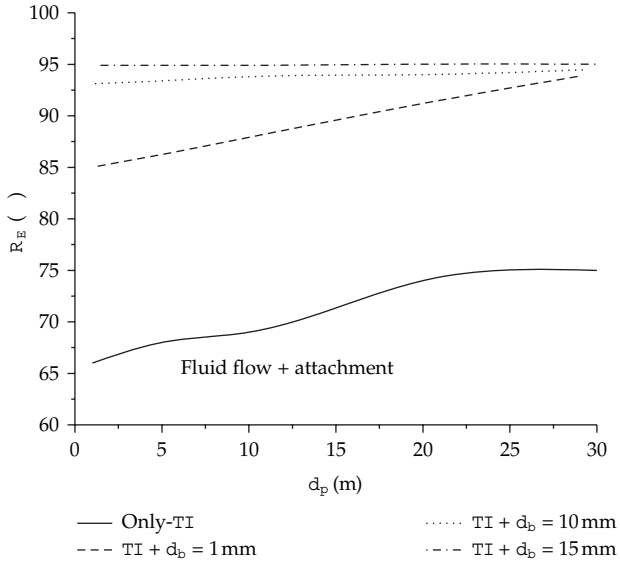

Figure 10: Non metallic Inclusion removal rate considering the sum of the fluidynamics effect and the bubble attachment.

(1) The results show that the film rupture between the inclusion and the bubble is easier by the formation of a hole and this mechanism has a dependency of the inclusion type.

(2) Since the current results show bigger t_i values, this work demonstrates that the model used to calculate t_i is important and as a consequence smaller attachment limits are obtained. At the same time, these increased values of t_i turn out in smaller percentage of the alumina inclusion collection probability.

(3) The removal rate (R_E) shows more dependency on other variables such as T_R and L_B; those variables show an indirect effect on R_E since it affects directly T_{RB}, which represents the controlling variable on the inclusion removal by bubble attachment.

(4) The results indicate that it is required to have very small bubble diameters to achieve acceptable R_E percentages, however, in the real process, this consideration is almost impossible to get, and the real bubble diameters are around 10 mm resulting in a very inefficient inclusion removal process in the tundish by bubble attachment.

(5) Despite of conclusion four, the inclusion removal rate in the tundish is efficient employing argon bubbling, mainly by the fluid flow patterns changes rather than by bubble attachment. Then, it can be established that is imperative to consider the summation of both removal mechanisms, to compute a better approximation of this important operation.

Nomenclature

A : Dimensionless parameters which are functions of the Reynolds bubble
B: Dimensionless parameters which are functions of the Reynolds bubble
C: Dimensionless parameters which are functions of the Reynolds bubble
D: Dimensionless parameters which are functions of the Reynolds bubble
d_p: Particle diameter
d_b: Bubble diameter
d_0: Porous diameter
g: Gravity
h_{crit}: Critical film thickness
k: Shape factor = 4
n_o: Initial inclusion concentration
n: Inclusion concentration
$N_{\text{Re,O}}$: Reynolds bubble
P: Collection probability
P_{att}: Attachment probability
P_c: Collision probability
P_{det}: Detachment probability
Q_g: Gas flow rate
R_E: Inclusion removal rate
t_i: Induction time
t_c: Collision time
t_{fr} : Drainage time
t_s: Sliding time
t_{fc} : Film drainage and rupture time during collision
T_F: Steel temperature (1800 K)
T_0: Gas temperature (300 K)
u_p: Particle velocity
u_B: Bubble velocity.

Greek symbols

ρ_p: Particle density
ρ_g: Gas density
σ_L: Superficial tension
μ_L: Liquid viscosity
θ: Polar angle
θ_c: Polar angle at the end of the interaction slidingcontact
θ_0: Polar angle at the beginning of the interaction slidingcontact
τ: Resident time of the steel in the bubble region in the tundish
ε: The inclusion removal efficiency.

Acknowledgments

The authors give thanks to the following institutions: DGEST, ITM, PROMEP, and SNI for their permanent support to the Academic Research Group on Mathematical Simulation of Materials Processing and Fluid Dynamics.

References

[1] Y. Sahai and T. Emi, "Melt flow characterization in continuous casting tundishes," *ISIJ International*, vol. 36, no. 6, pp. 667–672, 1996.

[2] L. Zhang, S. Taniguchi, and K. Cai, "Fluid flow and inclusion removal in continuous casting tundish," *Metallurgical and Materials Transactions B*, vol. 31, no. 2, pp. 253–266, 2000.

[3] C. M. Fan, R. J. Shie, and W. S. Hwang, "Studies by mathematical and physical modelling of fluid flow and inclusion removal phenomena in slab tundish for casting stainless steel using various flow control device designs," *Ironmaking and Steelmaking*, vol. 30, no. 5, pp. 341–347, 2003.

[4] L. Zhang and S. Taniguchi, "Fundamentals of inclusion removal from liquid steel by attachment to rising bubbles," *ISS Transactions*, vol. 28, no. 9, pp. 55–79, 2001.

[5] S. Garcia-Hernandez, J. J. de Barreto, J. A. Ramos-Banderas, and G. Solorio-Diaz, "Modeling study of the vortex and short circuit flow effect on inclusion removal in a slab tundish," *Steel Research International*, vol. 81, no. 36, pp. 453–460, 2010.

[6] J. Strandh, K. Nakajima, R. Eriksson, and P. Jonsson, "A mathematical model to study liquid inclusion behavior at the steel-slag interface," *ISIJ International*, vol. 45, no. 12, pp. 1838–1847, 2005.

[7] M. Valdez, G. S. Shannon, and S. Sridhar, "The ability of slags to absorb solid oxide inclusions," *ISIJ International*, vol. 46, no. 3, pp. 450–457, 2006.

[8] Q. Hou, Q. Yue, H. Wang, Z. Zou, and A. Yu, "Modelling of inclusion motion and flow patterns in swirling flow tundishes with symmetrical and asymmetrical structures," *ISIJ International*, vol. 48, no. 6, pp. 787–792, 2008.

[9] A. Ramos-Banderas, R. D. Morales, J. D. J. Barreto, and G. Solorio-Diaz, "Modelling study of inclusions removal by bubble flotation in the tundish," *Steel Research International*, vol. 77, no. 5, pp. 325–335, 2006.

[10] L. T. Wang, Q. Y. Zhang, S. H. Peng, and Z. B. Li, "Mathematical model for growth and removal of inclusion in a multi-tuyere ladle during gas-stirring," *ISIJ International*, vol. 31, no. 3, pp. 331–337, 2005.

[11] L. T. Wang, Q. Y. Zhang, S. H. Peng, and Z. B. Li, "Mathematical model for removal of inclusion in molten steel by injecting gas at ladle shroud," *ISIJ International*, vol. 45, no. 8, pp. 1138–1144, 2005.

[12] L. Zhang, S. Taniguchi, and K. Matsumoto, "Water model study on inclusion removal from liquid steel by bubble flotation under turbulent conditions," *Ironmaking and Steelmaking*, vol. 29, no. 5, pp. 326–336, 2002.

[13] L. Zhang and S. Taniguchi, "Fundamentals of inclusion removal from liquid steel by bubble flotation," *International Materials Reviews*, vol. 45, no. 2, pp. 59–82, 2000.

[14] L. Wang, H. G. Lee, and P. Hayes, "Prediction of the optimum bubble size for inclusion removal from molten steel by flotation," *ISIJ International*, vol. 36, no. 1, pp. 7–16, 1996.

[15] M. Iguchi, H. Kawabata, Y. Ito, K. Nakajima, and Z. I. Morita, "Continuous measurements of bubble characteristics in a molten iron bath with Ar gas injection," *ISIJ International*, vol. 34, no. 12, pp. 980–985, 1994.

[16] G. S. Dobby and J. A. Finch, "Particle size dependence in flotation derived from a fundamental model of the capture process," *International Journal of Mineral Processing*, vol. 21, no. 3-4, pp. 241–260, 1987.

[17] A. V. Nguyen and S. Kmet, "Probability of collision between particles and bubbles in flotation: the theoretical inertialess model involving a swarm of bubbles in pulp phase," *International Journal of Mineral Processing*, vol. 40, no. 3-4, pp. 155–169, 1994.

[18] A. V. Nguyen, J. Ralston, and H. J. Schulze, "On modelling of bubble-particle attachment probability in flotation," *International Journal of Mineral Processing*, vol. 53, no. 4, pp. 225–249, 1998.

[19] H. J. Schulze, "Hydrodynamics of bubble-mineral particle collisions," *Mineral Processing and Extractive Metallurgy Review*, vol. 5, pp. 43–67, 1989.

[20] J. P. Rogler, L. J. Heaslip, and M. Mehrvar, "Inclusion removal in a tundish by gas bubbling," *Canadian Metallurgical Quarterly*, vol. 43, no. 3, pp. 407–416, 2004.

[21] H. Arai, K. Matsumoto, S. I. Shimasaki, and S. Taniguchi, "Model experiment on inclusion removal by bubble flotation accompanied by particle coagulation in turbulent flow," *ISIJ International*, vol. 49, no. 7, pp. 965–974, 2009.

[22] A. Vargas-Zamora, R. D. Morales, M. Diaz-Cruz, J. Palafox-Ramos, and J. D. J. Barreto-Sandoval, "Inertial and buoyancy driven water flows under gas bubbling and thermal stratification conditions in a tundish model," *Metallurgical and Materials Transactions B*, vol. 35, no. 2, pp. 247–257, 2004.

[23] A. Ramos-Banderas, R. D. Morales, L. García-Demedices, and M. Díaz-Cruz, "Mathematical simulation and modeling of steel flow with gas bubbling in trough type tundishes," *ISIJ International*, vol. 43, no. 5, pp. 653–662, 2003.

[24] L. C. Zhong, L. Y. Li, B. Wang, L. Zhang, L. X. Zhu, and Q. F. Zhang, "Fluid flow behaviour in slab continuous casting tundish with different configurations of gas bubbling curtain," *Ironmaking and Steelmaking*, vol. 35, no. 6, pp. 436–440, 2008.

[25] D. S. Kumar, T. Rajendra, R. Prasad, A. Sarkar, and M. Ranjan, "Forced flotation of inclusions in tundish," *Ironmaking and Steelmaking*, vol. 36, no. 6, pp. 470–475, 2009.

[26] A. Cwudzinski, "Numerical simulation of liquid steel flow and behaviour of non-metallic inclusions in one-strand slab tundish with subflux turbulence controller and gas permeable barrier," *Ironmaking and Steelmaking*, vol. 37, no. 3, pp. 169–180, 2010.

[27] K. Chattopadhyay, M. Hasan, M. Isac, and R. I. L. Guthrie, "Physical and mathematical modeling of inert gas-shrouded ladle nozzles and their role on slag behavior and fluid flow patterns in a delta-shaped, four-strand tundish," *Metallurgical and Materials Transactions B*, vol. 41, no. 1, pp. 225–233, 2010.

[28] C. Marique, A. Dong, and J. P. Mahieu, "Bubbling of inert gas into the tundish. A means to improve steel cleanliness," *Iron and Steelmaker*, vol. 17, no. 9, p. 15, 1990.

Hindawi Publishing Corporation
Journal of Applied Mathematics
Volume 2012, Article ID 972650, 15 pages
doi:10.1155/2012/972650

Research Article

Characteristics of Wave Reflection for Vertical and Slit Caissons with Porous Structures

Tae-Hwa Jung,[1] Sung-Jae Lee,[2] and Yong-Sik Cho[2]

[1] *Department of Civil Engineering, Hanbat National University, San 16-1, Duckmyoung-dong, Daejeon 305-719, Republic of Korea*
[2] *Department of Civil and Environmental Engineering, Hanyang University, 222 Wangsimni-ro, Seongdong-gu, Seoul 133-791, Republic of Korea*

Correspondence should be addressed to Yong-Sik Cho, ysc59@hanyang.ac.kr

Received 3 January 2012; Accepted 16 March 2012

Academic Editor: M. F. El-Amin

Offshore structures are occasionally located at a relatively deep water region, the outside of breakwater. In this case, these structures may be damaged by the supposition of incident and reflected waves from a vertical breakwater. To prevent the damage, the reflected waves are controlled by installing porous structures at the face of the vertical breakwater. In this study, numerical experiments are carried out to identify the characteristics of wave reflection from the porous structures installing in front of a vertical or slit caisson.

1. Introduction

Offshore structures such as oil buoys or floating structures are sometimes required to be located outside of a breakwater. These structures may be damaged by the reflected waves from a vertical breakwater as well as incident waves. Thus, it is important to reduce the energy of reflected waves from a vertical breakwater to secure the stability of offshore structures. One possible way to reduce reflected waves is dissipating wave energy by adding porous structures at the face of a vertical breakwater.

Few studies regarding numerical experiments have been paying attention to the wave reflection from a vertical breakwater with a frontally porous structure because of complexities of interaction between porous flow and nonlinear waves. The mechanism of wave energy dissipation and reflection due to a porous structure is not yet clearly understood. Therefore, the energy dissipation efficiency of a permeable structure was assessed by measuring the wave reflection from the breakwater. Sollit and Cross [1] performed the study on wave

reflection and transmission through a porous structure using the linear wave theory and the linearized friction equation for flows in porous media. Following Sollit and Cross [1], several researches were carried out on wave and porous structure interaction [2, 3]. However, these studies were less practical because they assumed linear wave, constant depth, or integrated over the depth. The applicability of numerical study on water waves and porous structures was much improved by adopting the Navier-Stokes equation [4].

In this study, a numerical experiment was carried out to investigate the characteristics of a reflected wave from a porous structure located in front of a slit caisson. For numerical experiment, CADMAS-SURF [5, 6] was used. The irregular wave based on Bretschneider-Mitsuyasu's frequency spectrum was used, and the three-point method was used to decompose the incident and reflected waves.

2. Numerical Model

2.1. Governing Equations

CADMAS-SURF based on the Navier-Stokes equations is composed of the continuity, momentum, VOF, and turbulence equations.

Continuity equation:

$$\frac{\partial \gamma_x u}{\partial x} + \frac{\partial \gamma_z w}{\partial z} = S_\rho. \tag{2.1}$$

Momentum equation:

$$\begin{aligned}
\lambda_v \frac{\partial u}{\partial t} + \frac{\partial \lambda_x uu}{\partial x} + \frac{\partial \lambda_z wu}{\partial z} = & -\frac{\gamma_v}{\rho}\frac{\partial p}{\partial x} + \frac{\partial}{\partial x}\left\{\gamma_x v_e\left(2\frac{\partial u}{\partial x}\right)\right\} + \frac{\partial}{\partial z}\left\{\gamma_z v_e\left(\frac{\partial u}{\partial z} + \frac{\partial w}{\partial x}\right)\right\} \\
& - D_x u + S_v - R_x, \\
\lambda_v \frac{\partial w}{\partial t} + \frac{\partial \lambda_x uw}{\partial x} + \frac{\partial \lambda_z ww}{\partial z} = & -\frac{\gamma_v}{\rho}\frac{\partial p}{\partial x} + \frac{\partial}{\partial x}\left\{\gamma_x v_e\left(\frac{\partial w}{\partial x} + \frac{\partial u}{\partial z}\right)\right\} + \frac{\partial}{\partial z}\left\{\gamma_z v_e\left(2\frac{\partial w}{\partial z}\right)\right\} \\
& - D_z w + S_w - R_z - \gamma_v q,
\end{aligned} \tag{2.2}$$

where t is the time, x and z are the horizontal and vertical coordinates, u, w are the horizontal and vertical velocity components, ρ is the density of fluid, p is the pressure, v_e is the summation of molecular kinematic viscosity and eddy kinematic viscosity, g is the gravitational acceleration, γ_v is the volume porosity (fraction of the volume of voids over the total volume), γ_x andγ_z are the surface porosity (fraction of the area of voids over the total area) components in the x and z projections, S_ρ, S_u, and S_w are wave generation source, and D_x and D_z are the coefficients for sponge layer.

Using the inertia coefficient C_m, and γ_v, γ_x, and γ_z the inertia force effects from structure, λ_v, λ_x, and λ_z are written as follows:

$$\begin{aligned}\lambda_v &= \gamma_v + (1-\gamma_v)C_m,\\ \lambda_x &= \gamma_x + (1-\gamma_x)C_m,\\ \lambda_z &= \gamma_z + (1-\gamma_z)C_m.\end{aligned} \tag{2.3}$$

With the drag coefficient, C_D, the resistance force due to porous media R_x and R_z are defined by the following equations:

$$\begin{aligned}R_x &= \frac{1}{2}\frac{C_D}{\Delta x}(1-\gamma_x)u\sqrt{u^2+w^2},\\ R_z &= \frac{1}{2}\frac{C_D}{\Delta z}(1-\gamma_z)w\sqrt{u^2+w^2}.\end{aligned} \tag{2.4}$$

Free Surface Equation (VOF)

The VOF method was used to represent the interface boundary between the water and air, known as free surface [7]. The method introduces a volume of fluid function $F(x,z,t)$ to define the fluid region. The physical meaning of F is the fractional volume of a cell occupied by water. A unit value of F corresponds to a cell full of water, and a zero value indicates that the cell contains no water. Cells with F value between zero and one must then contain a free surface. The advection of free surface is represented by a convective equation of F extended for porous media as follows:

$$\gamma_v\frac{\partial F}{\partial t} + \frac{\partial \gamma_x uF}{\partial x} + \frac{\partial \gamma_z wF}{\partial z} = S_F, \tag{2.5}$$

where S_F is a source term for the wave generation source method.

Turbulence Model

In the turbulent model, a closure k-ε turbulence model is adopted. In the closure k-ε turbulence model, the turbulent kinetic energy k and the rate of dissipation of turbulent

kinetic energy ε are defined in (2.6) and (2.7) using the amount of fluctuation $u';w'$ and derived from the advection-diffusion equation shown in (2.8) and (2.9):

$$k = \frac{1}{2}\left(u'^2 + w'^2\right), \tag{2.6}$$

$$\varepsilon = \nu\left\{2\left(\frac{\partial u'}{\partial x}\right)^2 + 2\left(\frac{\partial w'}{\partial z}\right)^2 + \left(\frac{\partial w'}{\partial x} + \frac{\partial u'}{\partial z}\right)^2\right\}, \tag{2.7}$$

$$\gamma_v\frac{\partial k}{\partial t} + \frac{\partial \gamma_x uk}{\partial x} + \frac{\partial \gamma_z wk}{\partial z} = \frac{\partial}{\partial x}\left\{\gamma_x v_k\left(\frac{\partial k}{\partial x}\right)\right\} + \frac{\partial}{\partial z}\left\{\gamma_z v_k\left(\frac{\partial k}{\partial z}\right)\right\} + \gamma_v G_s - \gamma_v\varepsilon, \tag{2.8}$$

$$\gamma_v\frac{\partial \varepsilon}{\partial t} + \frac{\partial \gamma_x u\varepsilon}{\partial x} + \frac{\partial \gamma_z w\varepsilon}{\partial z} = \frac{\partial}{\partial x}\left\{\gamma_x v_\varepsilon\left(\frac{\partial \varepsilon}{\partial x}\right)\right\} + \frac{\partial}{\partial z}\left\{\gamma_z v_\varepsilon\left(\frac{\partial \varepsilon}{\partial z}\right)\right\} + \gamma_v C_1\frac{\varepsilon}{k}G_s - \gamma_v C_2\frac{\varepsilon^2}{k}, \tag{2.9}$$

$$G_s = \nu_t\left\{2\left(\frac{\partial u}{\partial x}\right)^2 + 2\left(\frac{\partial w}{\partial z}\right)^2 + \left(\frac{\partial w}{\partial x} + \frac{\partial u}{\partial z}\right)^2\right\}, \tag{2.10}$$

where the eddy kinematic viscosity ν_t and the diffusion coefficient, and ν_k and ν_ε are described as follows:

$$\begin{aligned}\nu_t &= \frac{C_\mu k^2}{\varepsilon},\\ \nu_k &= \nu + \frac{\nu_t}{\sigma_k},\\ \nu_\varepsilon &= \nu + \frac{\nu_t}{\sigma_\varepsilon}\end{aligned} \tag{2.11}$$

2.2. Boundary Conditions

To treat outgoing waves effectively, two boundary conditions are employed.

Radiation Boundary Condition

Sommerfeld's open boundary condition is employed as follows:

$$\frac{\partial f}{\partial t} + C\frac{\partial f}{\partial x} = 0, \tag{2.12}$$

where f is the wave property such as a mean velocity or mean free surface displacement, and C is the phase velocity. In the case of a regular wave, it is easy to apply because the phase velocity C is known in advance. In the case of irregular waves, however, it is difficult to satisfy a nonreflection condition because the phase velocity C is not clear.

Absorbing Boundary Condition

Because it is difficult to satisfy Sommerfeld's open boundary condition, sponge layer technique, which gradually attenuates wave energy, is used. The attenuation effect is

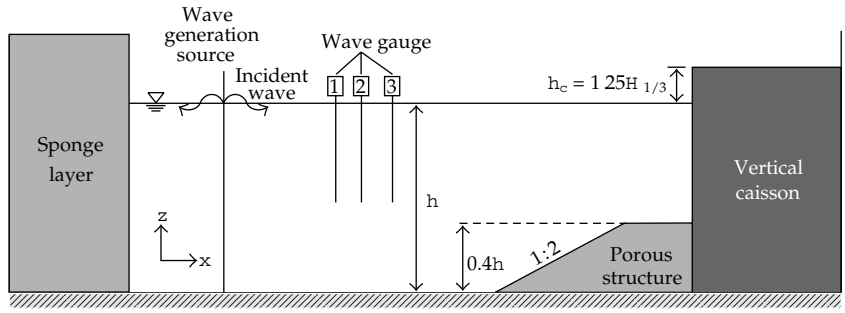

(a) Combination of the vertical caisson and the porous structure

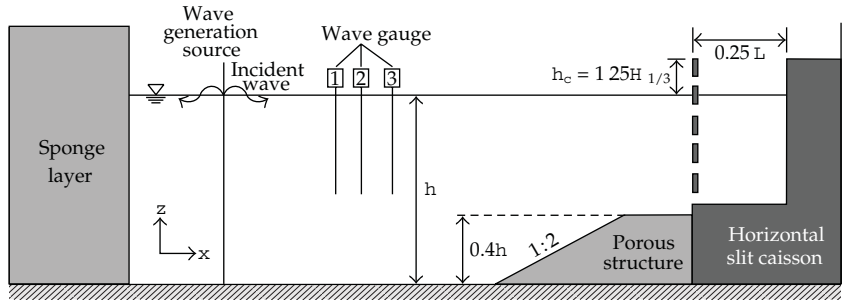

(b) Combination of the slit caisson and the porous structure

Figure 1: Schematic diagram of the numerical wave flume.

represented by $-D_x u$ and $-D_z u$ in the momentum equations of (2.2). Coefficients D_x and D_z are defined as follows:

$$D_x = \theta_x \sqrt{\frac{g}{h}}(N+1)\left(\frac{x-x_0}{l}\right)^N,$$
$$D_z = \theta_z \sqrt{\frac{q}{h}}(N+1)\left(\frac{x-x_0}{l}\right)^N, \tag{2.13}$$

where h is the water depth, l and x_0 are the width of a sponge layer and starting point, N is the order of the distribution function, and θ_x and θ_z are the nondimensional coefficients.

3. Numerical Experiments

3.1. Numerical Conditions

The numerical wave flume used in this study is shown in Figure 1. The length of wave flume changed according to the width of the sponge layer, equivalent to $2L$, where L is the incident wave length. The water depth h was set to 0.5 m. In the sponge layer, the wave amplitude decreased exponentially, thus it became small enough to be applied Sommerfeld's radiation condition at the both ends of wave flume. To generate expected target waves unaffected by the sponge layer, the waves are generated inside the computational domain (internal wave generation technique [8]). To analyze wave transformation, three wave gauges were placed

Table 1: Numerical conditions.

Number	Variable	Notation	Range
(1)	Type of wave		Regular wave and irregular wave
(2)	Significant wave height	$H_{1/3}$	2 cm, 3 cm, and 4 cm
(3)	Significant wave period	$T_{1/3}$	1.5 sec., 2.0 sec., and 2.5 sec.
(4)	Type of upright breakwater		Vertical caisson and slit caisson
(5)	Shape of the porous structure		Rectangle, triangle, and trapezoid
(6)	Height of the porous structure		$0.4h$ and $0.8h$
(7)	Water depth	h	$0.5m$
(8)	Wave chamber width	B	$0.25L$

as shown in Figure 2. The distances from the gauges to the porous structure were $1L$, $1L$ + 0.2 m, and $1L + 0.56$ m. That is, the distances between the wave gauges were 0.2 m and 0.36 m. Four combination of the porous structure and the caisson were considered: (1) the vertical caisson only; (2) the vertical caisson and the porous structure; (3) the slit caisson only; (4) the slit caisson and the porous structure. When it comes to the shape of the porous structure, the rectangular, triangular, and trapezoidal shapes were used. The heights of the porous structure were set to $0.4h$ and $0.8h$. The crown height h_c of two kinds of vertical breakwater was set to $1.25H_{1/3}$. Since the ratio of distance of wave chamber to wave length $B/L = 0.25$ is known that it gave the minimum wave reflection [9], a constant value of 0.25 was applied to the wave chamber. In which, the wave chamber means the space between a slit and a vertical wall in the caisson. The significant wave periods of the incident waves were 1.5, 2.0, and 2.5 sec. The significant wave heights of the incident waves were 2.0, 3.0, and 4.0 cm. These conditions are summarized in Table 1.

3.2. Incident Wave

One regular wave and nine irregular waves were used as an incident wave condition. The irregular waves were generated by using following equations:

$$\eta(t) = \sum_{m=1}^{M} a_m \cos\left(2\pi f_m t - \varepsilon_m\right),$$

$$u(z,t) = \sum_{m=1}^{M} 2\pi f_m \frac{\cosh k_m(h+z)}{\sinh k_m h} a_m \cos\left(2\pi f_m t - \varepsilon_m\right), \tag{3.1}$$

$$w(z,t) = \sum_{m=1}^{M} 2\pi f_m \frac{\sinh k_m(h+z)}{\sinh k_m h} a_m \sin\left(2\pi f_m t - \varepsilon_m\right),$$

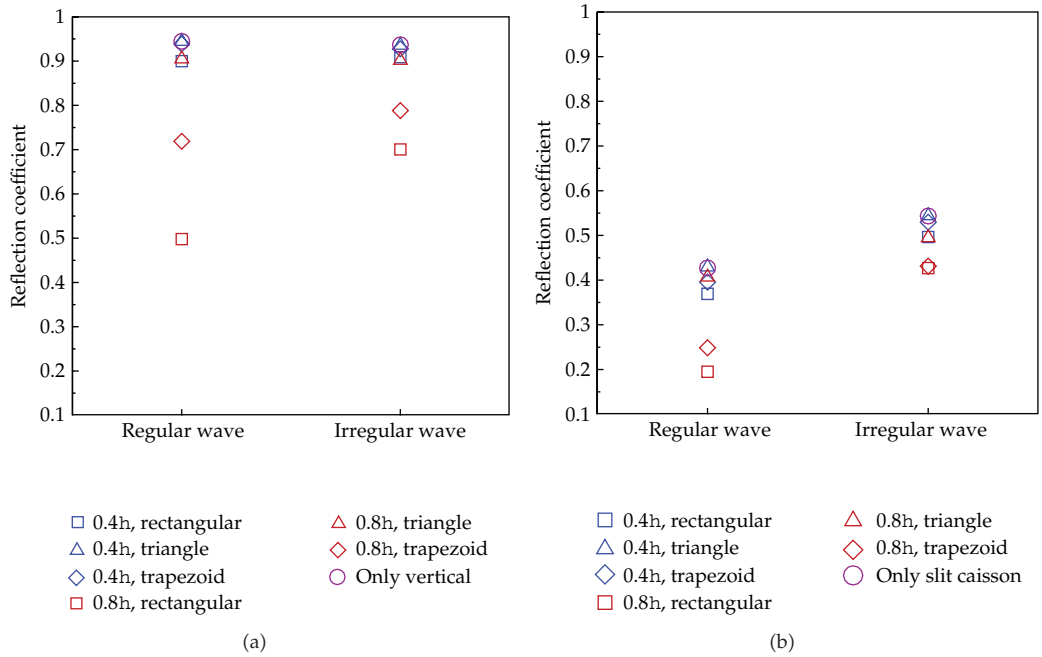

Figure 2: Reflection coefficients of the regular and irregular waves.

where M is a number of frequency, subscript m is mth component, f_m is the corresponding frequency, ε_m is the corresponding random phase angle, k_m is the corresponding wavenumber, and a_m is the corresponding wave amplitude obtained from (3.2):

$$a_m = \sqrt{2S(f)\Delta f}, \tag{3.2}$$

where Δf is the frequency interval, and $S(f)$ is the Bretschneider-Mitsuyasus frequency spectrum given by:

$$S(f) = 0.257 H_{1/3}^2 T_{1/3} (T_{1/3} f)^{-5} \exp\left[-1.03 (T_{1/3} f)^{-4}\right], \tag{3.3}$$

where f is wave frequency, and $H_{1/3}$ and $T_{1/3}$ are the significant wave height and period, respectively.

3.3. Wave Decomposition

The three-point method suggested by Suh et al. [10] was used to decompose the waves into the incident and reflected waves. A brief description of this method is as follows. Incident and reflected waves can be given by

$$\begin{aligned}\eta_i(t) &= \frac{H_i}{2}\cos\left(k_i x - \omega t + \phi_i\right),\\ \eta_r(t) &= \frac{H_r}{2}\cos\left(k_r x + \omega t + \phi_r\right),\end{aligned} \tag{3.4}$$

where H is the wave height, k is the wavenumber, ϕ is the random phase angle, and ω is the angular frequency. The surface elevation at the n-point can be expressed as follows:

$$\eta_n(t) = \eta_i(t) + \eta_r(t) = \frac{H_i}{2}\cos\left(k_i x_n - \omega t + \phi_i\right) + \frac{H_r}{2}\cos\left(k_r x_n + \omega t + \phi_r\right) + \mathrm{e}_n(t) \tag{3.5}$$

or

$$\begin{aligned}\eta_n(t) = {} & X_1\cos(\omega t - k_i x_n) + X_2\cos(\omega t - k_r x_n)\\ & + X_3\sin(\omega t - k_i x_n) - X_4\sin(\omega t - k_r x_n) + e_n(t),\end{aligned} \tag{3.6}$$

where x_n is the distance from the first measuring point to the nth location, e_n is error due to signal noise, $X_i (i = 1 \sim 4)$ are unknown coefficients expressed in terms of the height and phase of the incident and reflected waves. The squared error is

$$\varepsilon^2 = \sum_{n=1}^{N}\int_0^T [e_n(t)]^2 dt \tag{3.7}$$

and, the unknowns in (3.6) can be determined by using the least-square method:

$$\frac{\partial \varepsilon^2}{\partial X_j} = 0, \quad j = 1, 2, 3, 4. \tag{3.8}$$

Finally, the incident and reflected wave heights can be calculated using following relation:

$$H_i = \frac{2(X_1 + X_3)}{\cos\phi_i + \sin\phi_i}, \qquad H_r = \frac{2(X_2 + X_4)}{\cos\phi_r + \sin\phi_r}. \tag{3.9}$$

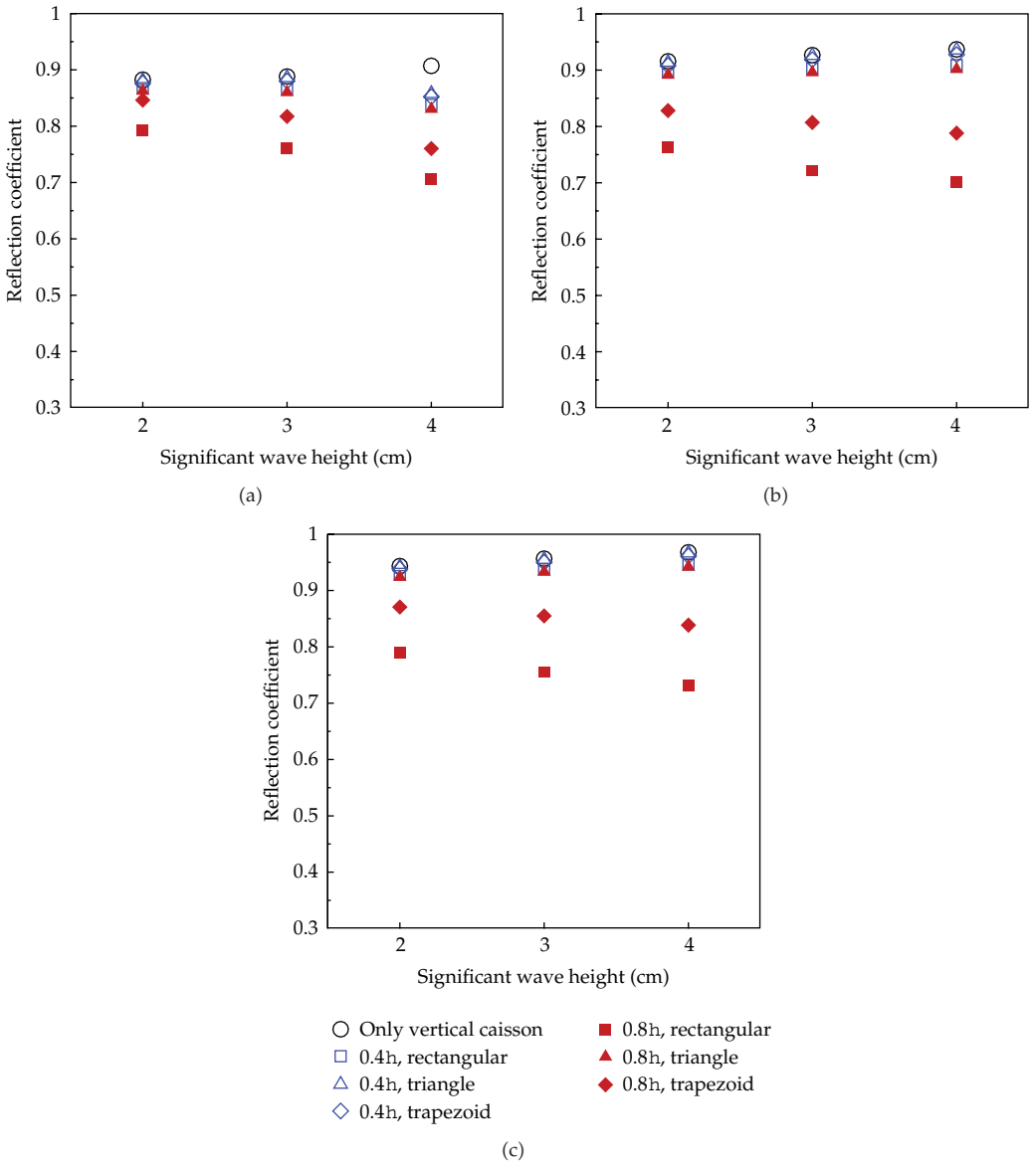

Figure 3: Reflection coefficient for vertical caisson with different significant wave heights.

Since the energies of the incident and reflected waves are proportional to the squares of their heights, the reflection coefficient can be estimated from

$$R = \sqrt{\frac{E_r}{E_i}}, \tag{3.10}$$

where E_i and E_r are the energies of the incident and reflected waves, respectively.

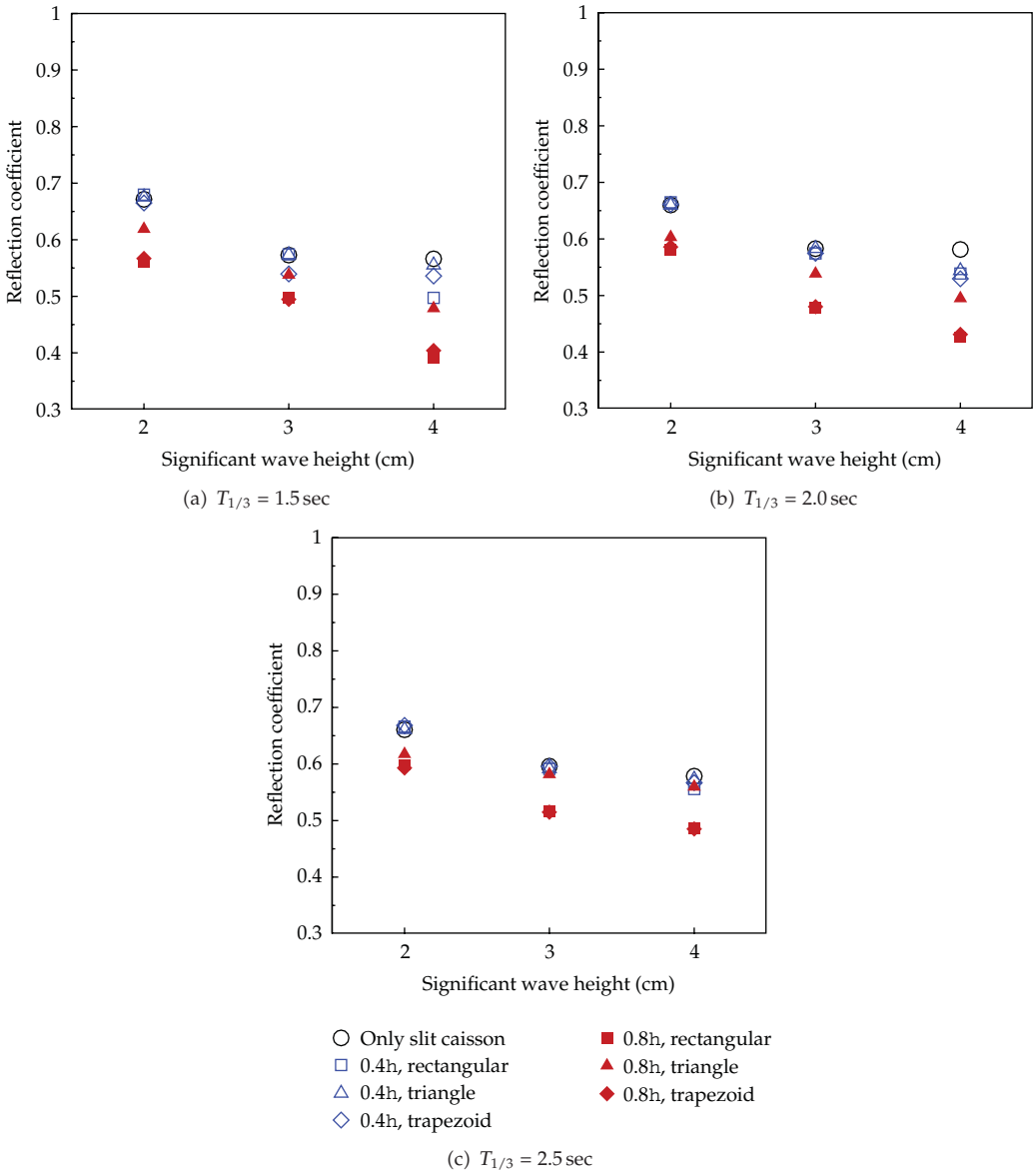

Figure 4: Reflection coefficient for slit caisson with different significant wave heights.

4. Results and Discussion

Figure 2 showed the reflection coefficients of the regular and irregular waves for the vertical and slit caissons, respectively. The reflection coefficient decreased as the height of the porous structure increased when the porous structure was installed in front of the vertical caisson or the slit caisson. In the case of the regular wave, the reflection coefficient was significantly reduced, whereas the reflection of the irregular waves was slightly reduced. This may be due to fixed width of wave chamber. That is, the width of wave chamber using in the present study referred to the previous study for regular waves. Therefore, it may not be effective

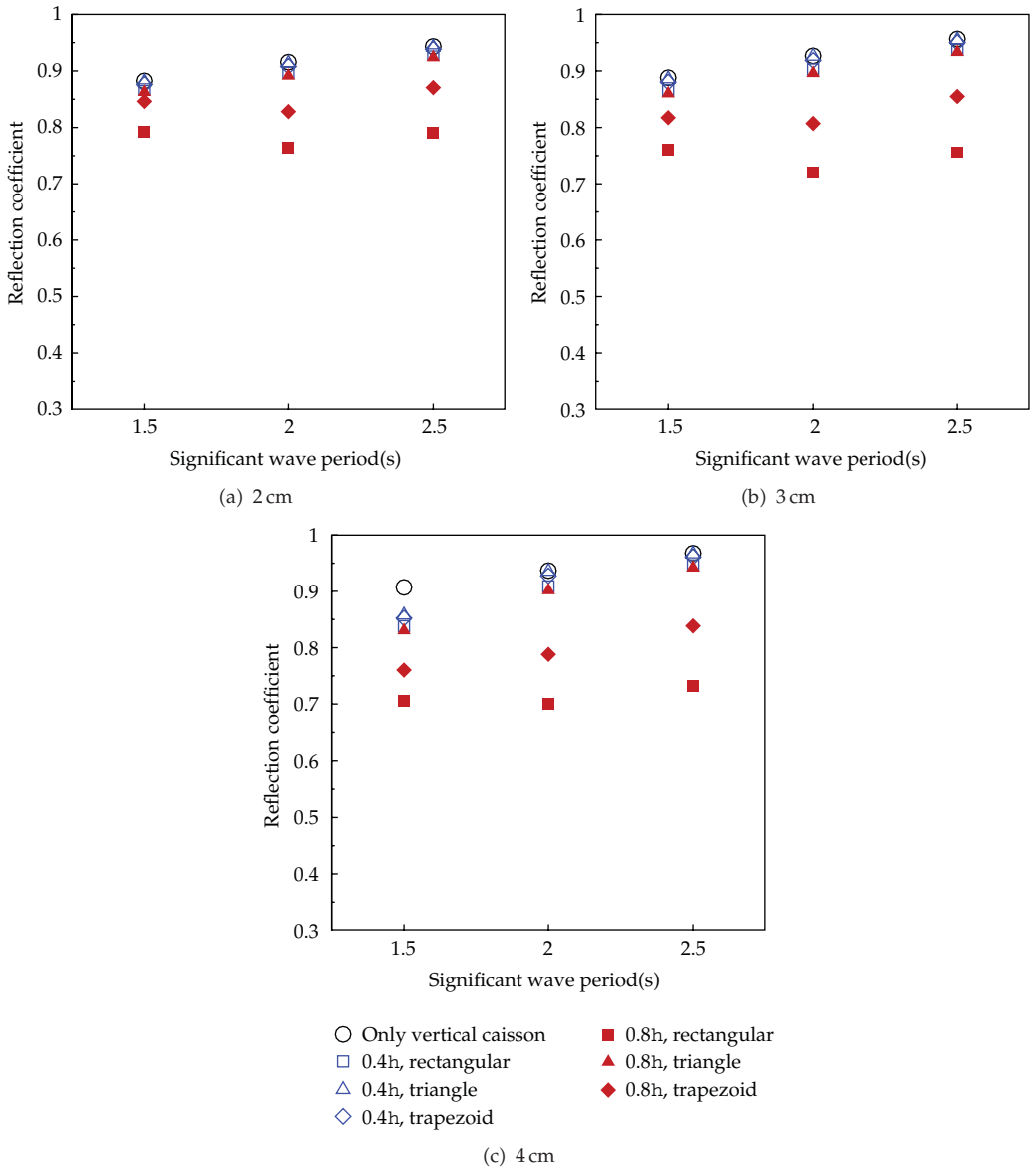

Figure 5: Reflection coefficient for vertical caisson with different significant wave periods.

for irregular waves because there are many regular components, and some of them are less affected by the width of wave chamber.

Figures 3 and 4 showed the reflection coefficients for different significant wave heights. It was observed that the reflection coefficient decreased as the height of porous structure increased when the porous structure was located in front of the vertical caisson or the slit caisson. As the height of the significant waves increased, the reflection coefficient decreased. The waves at the slit caisson were more dissipated than those at the vertical caisson.

Figures 5 and 6 showed the reflection coefficients for different significant wave periods. As the height of a porous structure increased, the reflection coefficient decreased

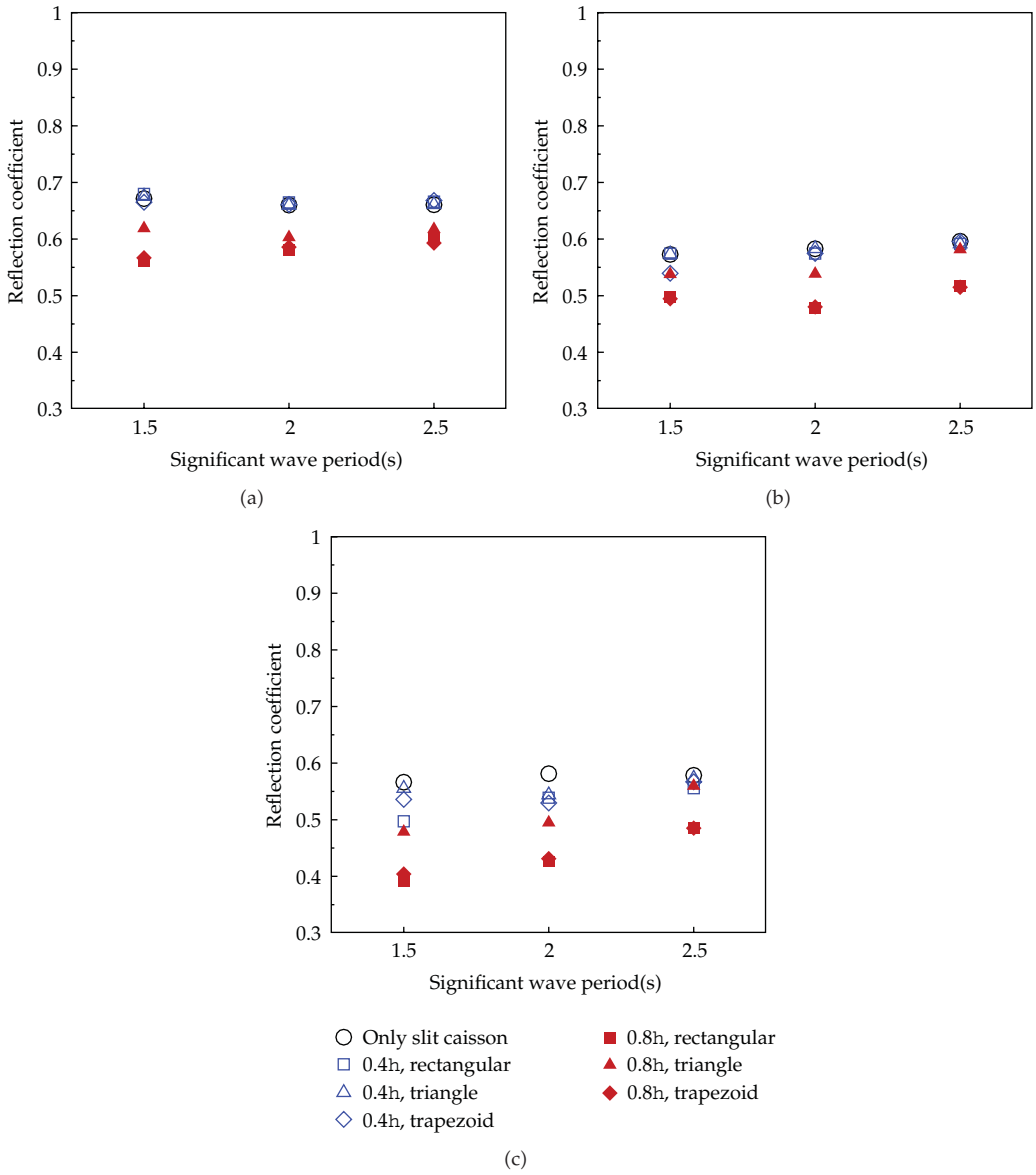

Figure 6: Reflection coefficient for slit caisson with different significant wave periods.

when the porous structure was located in front of the caisson. The reflection coefficients for a slit caisson were much smaller than those for a vertical caisson. However, the significant wave period rarely affected to the wave reflection. That is, the variation of reflection coefficient due to significant wave period was very small compared to other parameters.

Figures 7 and 8 showed the reflection coefficient for different shapes of porous structure. As the height of porous structure increased, the reflection coefficient decreased. As for the estimated wave coefficients based on the shape of the porous structure, the rectangular and trapezoidal porous structure showed obvious energy dissipation. On the other hand, the

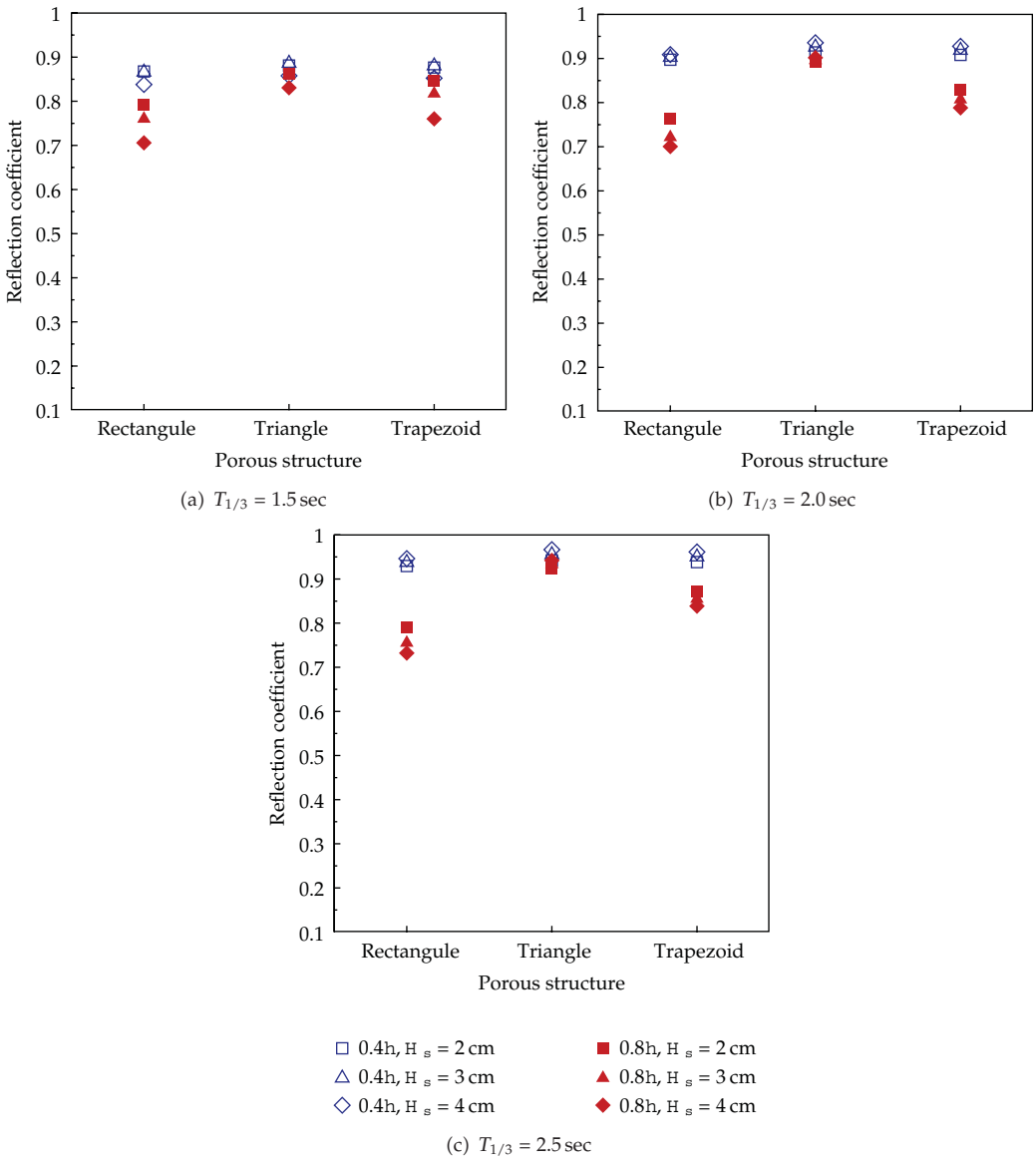

Figure 7: Reflection coefficient for vertical caisson with different shapes of porous structure.

triangular porous structure showed little reduction effect on the slit caisson and almost no reduction on the vertical caisson.

5. Concluding Remarks

In this study, the wave reflection of a vertical and slit caissons with porous structures was analyzed using the number model based on the Navier-Stokes equations. Both of regular and irregular waves were used as incident waves. In the case of regular waves, the reflection coefficient was significantly reduced, whereas the reflection coefficient for irregular

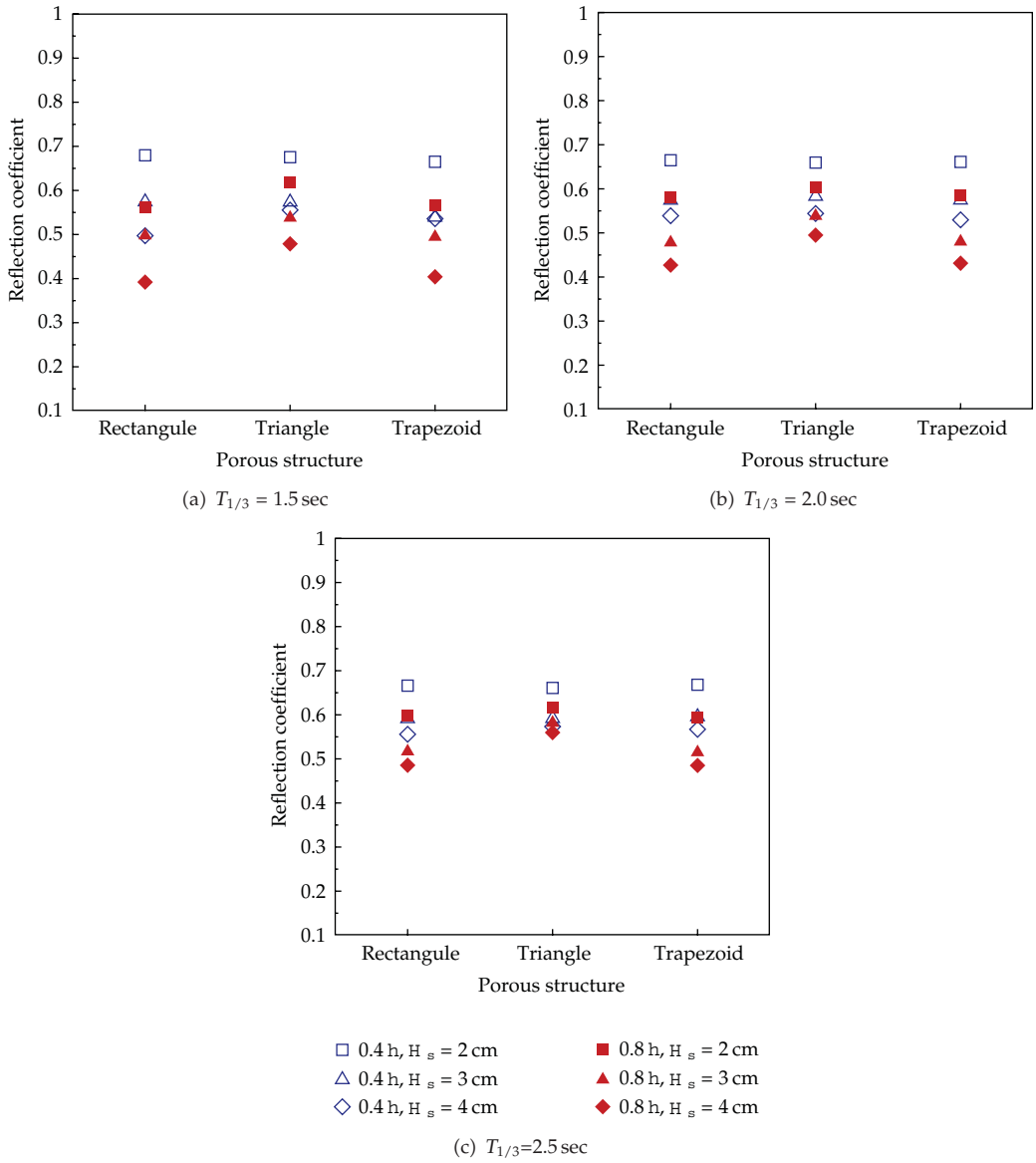

(a) $T_{1/3}$ = 1.5 sec

(b) $T_{1/3}$ = 2.0 sec

(c) $T_{1/3}$=2.5 sec

Figure 8: Reflection coefficient for slit caisson with different shapes of porous structure.

waves reduced by a relatively small amount. As the wave height increased, the reflection coefficient decreased for both vertical and slit caissons. The waves were more dissipated at the slit caisson than the vertical caisson. The reflection coefficient was rarely affected by the variation of significant wave period. The rectangular and trapezoidal porous structures showed obvious energy dissipation, whereas the triangular porous structure showed a little reduction effect on the slit caisson and almost no reduction on the vertical caisson. Because porous structure with low height is not able to dissipate wave energy effectively, a proper height is required for efficiency. Although rectangular and trapezoidal porous structures

showed almost same energy dissipation, the trapezoidal structure is more preferred because it has superiority in the workability and stability.

Acknowledgments

This research was supported by the Basic Science Research Program through the National Research Foundation of Korea funded by the Ministry of Education, Science and Technology (no. 2010-0022337).

References

[1] C. K. Sollit and R. H. Cross, "Wave transmission through permeable breakwaters," in *Proceedings of the 13th International Conference on Coastal Engineering, ASCE*, pp. 1827–1846, 1972.
[2] R. Silva, P. Salles, and A. Palacio, "Linear waves propagating over a rapidly varying finite porous bed," *Coastal Engineering*, vol. 44, no. 3, pp. 239–260, 2002.
[3] H. B. Chen, C. P. Tsai, and J. R. Chiu, "Wave reflection from vertical breakwater with porous structure," *Ocean Engineering*, vol. 33, no. 13, pp. 1705–1717, 2006.
[4] M. F. Karim and T. Tingsanchali, "A coupled numerical model for simulation of wave breaking and hydraulic performances of a composite seawall," *Ocean Engineering*, vol. 33, no. 5-6, pp. 773–787, 2006.
[5] CDIT, *Research and Development of Numerical Channel*, CDIT library, Coastal Development Institute of Technology, 2001.
[6] The Study Group for the Development of CADMAS-SUR, *CADMAS-SURF User's Manual (in Korean)*, 2003.
[7] C. W. Hirt and B. D. Nichols, "Volume of fluid (VOF) method for the dynamics of free boundaries," *Journal of Computational Physics*, vol. 39, no. 1, pp. 201–225, 1981.
[8] J. Larsen and H. Dancy, "Open boundaries in short wave simulations–a new approach," *Coastal Engineering*, vol. 7, no. 3, pp. 285–297, 1983.
[9] M. Fugazza and L. Natale, "Hydraulic design of perforated breakwaters," *Journal of Waterway, Port, Coastal and Ocean Engineering*, vol. 118, no. 1, pp. 1–14, 1992.
[10] K. D. Suh, W. S. Park, and B. S. Park, "Separation of incident and reflected waves in wave-current flumes," *Coastal Engineering*, vol. 43, no. 3-4, pp. 149–159, 2001.

Hindawi Publishing Corporation
Journal of Applied Mathematics
Volume 2012, Article ID 939620, 10 pages
doi:10.1155/2012/939620

Research Article

Natural Convection in an Inclined Porous Cavity with Spatial Sidewall Temperature Variations

M. S. Selamat,[1] R. Roslan,[2] and I. Hashim[3]

[1] *Department of Mathematics & Statistics, Faculty of Computer & Mathematical Sciences, Universiti Teknologi MARA Pahang, 62400 Bandar Jengka, Malaysia*
[2] *Faculty of Science, Technology and Human Development, Universiti Tun Hussein Onn Malaysia, Batu Pahat, Johor, 86400 Parit Raja, Malaysia*
[3] *School of Mathematical Sciences and Solar Energy Research Institute, Faculty of Science and Technology, Universiti Kebangsaan Malaysia, Selangor, 43600 Bangi, Malaysia*

Correspondence should be addressed to I. Hashim, ishak_h@ukm.my

Received 4 February 2012; Accepted 18 March 2012

Academic Editor: Hiroshi Kanayama

The natural convection in an inclined porous square cavity is investigated numerically. The left wall is assumed to have spatial sinusoidal temperature variations about a constant mean value, while the right wall is cooled. The horizontal walls are considered adiabatic. A finite difference method is used to solve numerically the nondimensional governing equations. The effects of the inclination angle of the cavity, the amplitude and wave numbers of the heated sidewall temperature variation on the natural convection in the cavity are studied. The maximum average Nusselt number occurs at different wave number. It also found that the inclination could influence the Nusselt number.

1. Introduction

Convective heat transfer has attracted significant attention due to wide applications in engineering such as operation of solar collectors, cooling systems in electronics equipments, insulations of buildings and so forth. Many studies with application to the above research areas may be found in the book by Nield and Bejan [1].

The problem of natural convection in an enclosure has been studied extensively by many researchers such as Weber [2], Bejan [3], Bradean et al. [4], Goyeau et al. [5], Guo and Bathe [6] and Saeid and Pop [7]. Saeid and Mohamad [8] studied numerically the natural convection in a porous cavity with spatial sidewall temperature variation. They found that the average Nusselt number is dependent on the amplitude and the wave number of the spatial sinusoidal temperature. Saeid and Yaacob [9] investigated the natural convection in

a square cavity filled with a pure air with a nonuniform side wall temperature. They found that the average Nusselt number along the hot wall varies sinusoidally based on the hot wall temperature.

Most of the studies on natural convection are devoted to the classical Rayleigh-Benard model (hot bottom wall and cold top wall) or to the case of rectangular or square cavity with one vertical wall heated and the opposite one cooled. However, in some engineering applications, enclosures are inclined to the direction of gravity. Hence, the flow structure and the heat transfer within the enclosure are modified by the components of buoyancy forced. The effects of inclination on natural convection in an enclosure have been discussed by several investigators. For example Hart [10] studied the stability of the flow in an inclined box. Holst and Aziz [11] and Ozoe et al. [12] studied three- and two-dimensional natural convection in porous media, respectively. A good review on the study the inclination of natural convection can be seen in Yang [13]. Rasoul and Prinos [14] studied the effect of the inclination angle on steady natural convection in a square cavity for the Raleigh number ranging from 10^3 to 10^6 and the Prandtl number from 0.02 to 4000. Baytaşc [15] investigated entropy generation distribution according to inclination angle for saturated porous cavity by using the second law of thermodynamics. Kalabin et al. [16] investigated the influence of inclination angle and oscillation frequency on heat transfer through the square enclosure. Meanwhile, Chamkha and Al-Mudhaf [17] studied the double-diffusive natural convection in inclined porous cavities with the presence of temperature-dependent heat generation or absorption. They concluded that the heat and mass transfer and the flow characteristics inside the cavity are strongly dependent on the buoyancy ratio, inclination angle, and the heated generations or absorption effect. A numerical study has been carried out by Wang et al. [18] for the natural convection heat transfer in an inclined porous cavity with time-periodic boundary condition. They found that, if the inclination angle is maintained at a fixed value and the oscillating approaches infinity, the oscillating temperature on a sidewall has a little effect on the temperature near the opposite sidewall.

In this paper we study the natural convection in a porous cavity with a non-uniform hot wall temperature and a uniform cold wall temperature. The heated wall is assumed to have spatial sinusoidal temperature variations about a constant mean value which is higher than the cold sidewall temperature. This work extends in particular the work of Saeid and Mohamad [8] to the more general setup of an inclined cavity.

2. Mathematical Formulation

The heat transfer by natural convection across porous media is considered as shown in Figure 1. The top and bottom horizontal walls are adiabatic, and the right sidewall is maintained at a constant cold temperature T_c. The temperature of opposing sidewall is assumed to have spatial sinusoidal temperature variations about a constant mean value which is higher than the cold sidewall temperature.

Applying Darcy's flow model and the Boussinesq approximation, the governing equations are [8]

$$\frac{\partial u}{\partial x} + \frac{\partial v}{\partial y} = 0,$$

$$\frac{\partial u}{\partial y} - \frac{\partial v}{\partial x} = \frac{g\beta K}{\nu}\left(\frac{\partial T}{\partial y}\cos\phi - \frac{\partial T}{\partial x}\sin\phi\right),$$

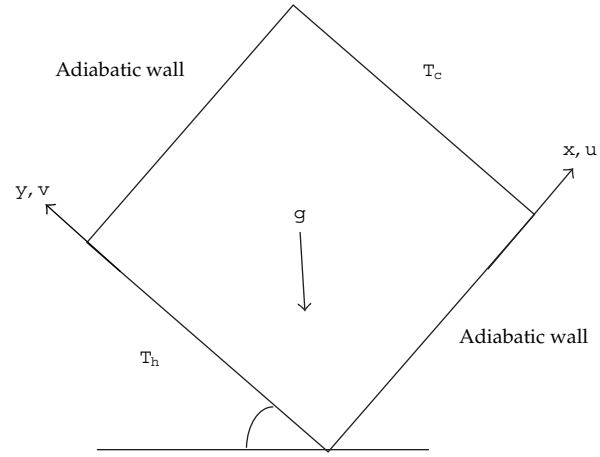

Figure 1: Schematic diagram of the physical model and coordinate system.

$$u\frac{\partial T}{\partial x} + v\frac{\partial T}{\partial y} = \alpha\left(\frac{\partial^2 T}{\partial x^2} + \frac{\partial^2 T}{\partial y^2}\right), \tag{2.1}$$

where u and v are the velocity components along the x- and y-axes, respectively, T is the fluid temperature, g is the gravitational acceleration, K is the permeability of the porous medium, α is the effective thermal diffusivity, β is the coefficient of thermal expansion, and ν is the kinematic viscosity of the fluid. The temperature of the hot wall is assumed to have a sinusoidal variation about a minimum value of $\overline{T}_h$ in the form

$$T_h(y) = \overline{T}_h + \varepsilon\left(\overline{T}_h - T_c\right)\left[1 - \cos\left(\frac{2\pi\kappa y}{L}\right)\right], \tag{2.2}$$

where L is the cavity height/width, κ is the wave number, and ε is the nondimensional amplitude.

Equations (2) are subject to the following boundary conditions:

$$\begin{aligned} u(0,y) = v(0,y) = 0, &\qquad T(0,y) = T_h(y), \\ u(L,y) = v(L,y) = 0, &\qquad T(L,y) = T_c, \\ u(x,0) = v(x,0) = 0, &\qquad \frac{\partial T(x,0)}{\partial y} = 0, \\ u(x,L) = v(x,L) = 0, &\qquad \frac{\partial T(x,L)}{\partial y} = 0. \end{aligned} \tag{2.3}$$

Using the stream functions defined by $u = \partial\psi/\partial y$ and $v = -\partial\psi/\partial x$ and nondimensional variables

$$X = \frac{x}{L}, \qquad Y = \frac{y}{L}, \qquad \theta = \frac{T - T_0}{\overline{T}_h - T_c}, \qquad \Psi = \frac{\psi}{\alpha}, \tag{2.4}$$

where $T_0 = (\overline{T}_h + T_c)/2$, the governing equations (2) and boundary conditions (2.3) can be written in dimensionless forms:

$$\frac{\partial^2\Psi}{\partial X^2} + \frac{\partial^2\Psi}{\partial Y^2} = \mathrm{Ra}\left(\frac{\partial\theta}{\partial Y}\cos\phi - \frac{\partial\theta}{\partial X}\sin\phi\right), \tag{2.5}$$

$$\frac{\partial^2\theta}{\partial X^2} + \frac{\partial^2\theta}{\partial Y^2} = \frac{\partial\Psi}{\partial Y}\frac{\partial\theta}{\partial X} - \frac{\partial\Psi}{\partial X}\frac{\partial\theta}{\partial Y}, \tag{2.6}$$

$$\Psi(0, Y) = 0, \qquad \theta(0, Y) = 0.5 + \varepsilon[1 - \cos(2\pi\kappa Y)], \tag{2.7}$$

$$\Psi(1, Y) = 0, \qquad \theta(1, Y) = -0.5, \tag{2.8}$$

$$\Psi(X, 0) = 0, \qquad \frac{\partial\theta(X, 0)}{\partial Y} = 0, \tag{2.9}$$

$$\Psi(X, 1) = 0, \qquad \frac{\partial\theta(X, 1)}{\partial Y} = 0, \tag{2.10}$$

where Ra is the Rayleigh number defined as

$$\mathrm{Ra} = \frac{g\beta K\left(\overline{T}_h - T_c\right)L}{\nu\alpha}. \tag{2.11}$$

The local Nusselt numbers along the hot and cold wall are given, respectively, by

$$\begin{aligned} \mathrm{Nu}_h &= \frac{hY}{\lambda} = \left(-\frac{\partial\theta}{\partial X}\right)_{X=0}, \\ \mathrm{Nu}_c &= \frac{hY}{\lambda} = \left(-\frac{\partial\theta}{\partial X}\right)_{X=1}, \end{aligned} \tag{2.12}$$

where h is the heat transfer coefficient and λ is the thermal conductivity of the porous media.

Table 1: Comparison of the average Nusselt number, $\overline{\mathrm{Nu}}$, against some previous results for isothermal vertical walls in a square cavity in the case $\phi = 90°$.

References	Mesh size	Ra = 100		Ra = 1000	
		$\overline{\mathrm{Nu}}_h$	$\overline{\mathrm{Nu}}_c$	$\overline{\mathrm{Nu}}_h$	$\overline{\mathrm{Nu}}_c$
[3]		4.200		15.800	
[5]		3.110		13.470	
[8]	(20 × 20)	3.081	3.081	12.890	12.890
[8]	(40 × 40)	3.099	3.099	13.431	13.431
[8]	(80 × 80)	3.108	3.107	13.531	13.531
[8]	(160 × 160)	3.110	3.110	13.592	13.592
Present work	(20 × 20)	3.005	3.005	9.865	9.864
Present work	(40 × 40)	3.080	3.080	12.157	12.154
Present work	(80 × 80)	3.100	3.100	13.180	13.178
Present work	(160 × 160)	3.106	3.106	13.498	13.494

The average Nusselt number is defined as

$$\overline{\mathrm{Nu}_i} = \frac{hL}{\lambda} = \int_0^1 \mathrm{Nu}\, dY, \tag{2.13}$$

where Nu_i is Nu_h or Nu_c, respectively.

3. Numerical Scheme

The coupled system of (2.5) and (2.6) subject to boundary conditions (2.7)–(2.10) is solved numerically using a finite difference method. The central difference method was applied for discretizing the equations. The resulting algebraic equations were solved by using the Gauss-Seidel iteration with a relaxation method. The unknowns Ψ and θ are calculated until the following convergence criterium is fulfilled:

$$\frac{\sum_{i,j}\left|\zeta_{i,j}^{n+1} - \zeta_{i,j}^{n}\right|}{\sum_{i,j}\left|\zeta_{i,j}^{n+1}\right|} \leq \epsilon, \tag{3.1}$$

where ζ is either Ψ or θ, n represents the iteration number, and ϵ is the convergence criterium. In this study, the convergence criterium was set at $\epsilon = 10^{-6}$.

The numerical code was validated in a square porous cavity with constant isothermal vertical walls ($\varepsilon = 0$) using different mesh sizes, 20 × 20, 40 × 40, 80 × 80, and 160 × 160. The average Nusselt numbers along the hot wall and cold wall of the cavity are calculated and compared with the results by different authors for Ra = 100 and Ra = 1000 as shown in Table 1. From Table 1, the error between $\overline{\mathrm{Nu}}_c$ and $\overline{\mathrm{Nu}}_h$ is found less than 0.004 percent for Ra = 100, and it is less than 0.03 percent for Ra = 1000 which reflects the accuracy of the present results. Also, Table 1 shows the good agreement between our result and the existing results for a porous square enclosure for $\phi = 90°$.

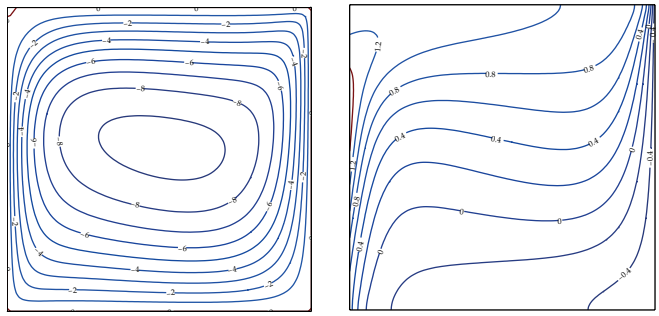

(a) $\phi = 50°$

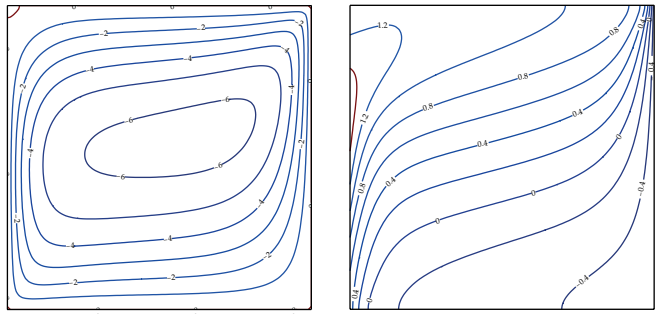

(b) $\phi = 90°$

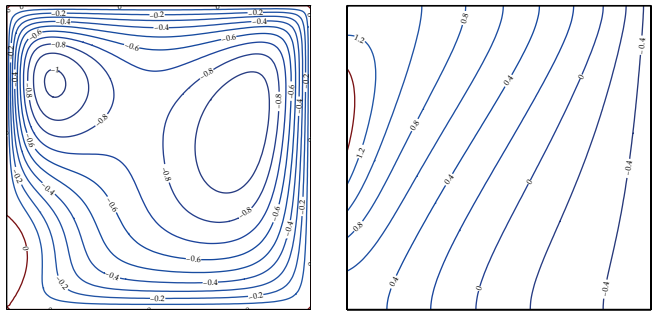

(c) $\phi = 150°$

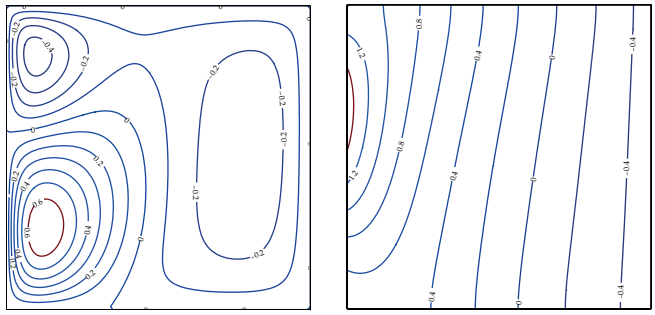

(d) $\phi = 170°$

Figure 2: Effects of inclination angle ϕ on streamlines (left) and isotherms (right) for $\varepsilon = 0.5$, $\kappa = 0.75$, and Ra = 100.

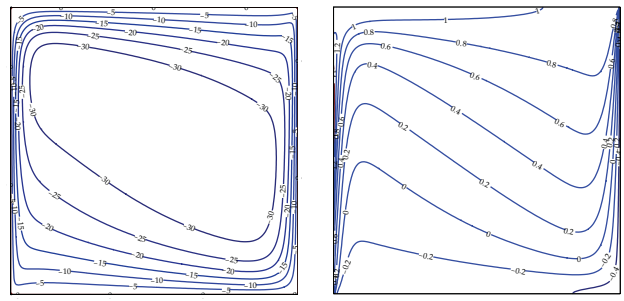

(a) $\phi = 50°$

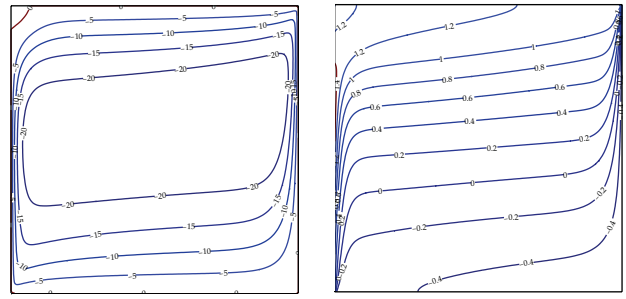

(b) $\phi = 90°$

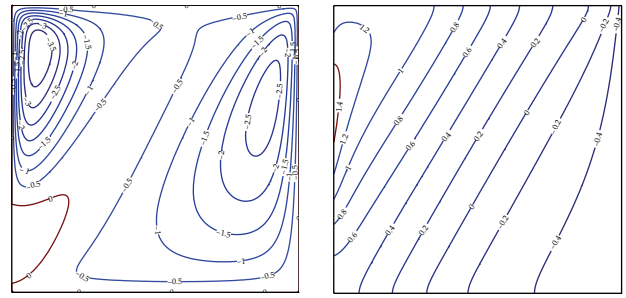

(c) $\phi = 150°$

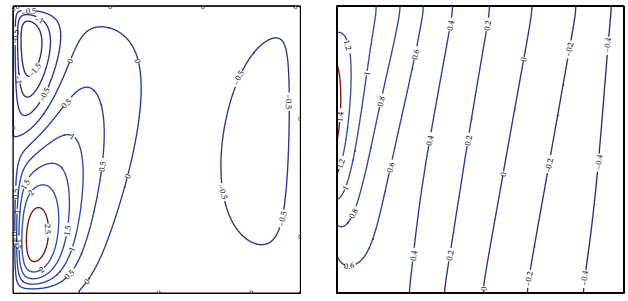

(d) $\phi = 170°$

Figure 3: Effects of inclination angle ϕ on streamlines (left) and isotherms (right) for $\varepsilon = 0.5$, $\kappa = 0.75$, and Ra = 1000.

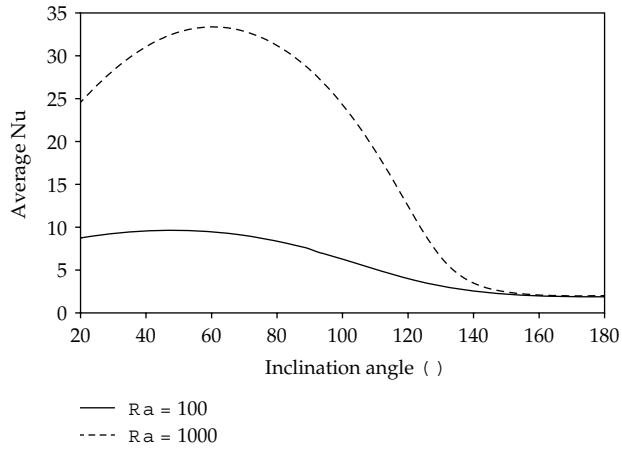

Figure 4: Average Nusselt number versus inclination angle.

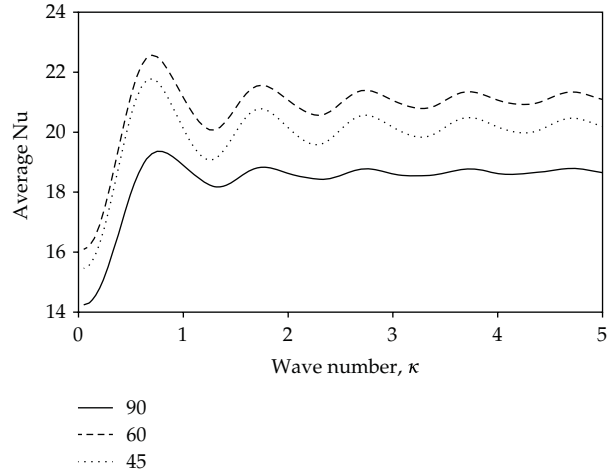

Figure 5: Variation of the Nusselt number with the wavenumber for the case $\varepsilon = 0.2$ and Ra = 1000. The solid line for the case $\phi = 90°$ is the recomputed results of Saeid and Mohamad [8].

A grid independence test has been performed in the case of maximum amplitude ($\varepsilon = 1$) and maximum wavenumber ($\kappa = 5$) for Ra = 1000. The 80 × 80 mesh gives $\overline{\mathrm{Nu}}_h = 40.7623$ and $\overline{\mathrm{Nu}}_c = 41.0717$, and the 120 × 120 mesh gives $\overline{\mathrm{Nu}}_h = 42.9346$ and $\overline{\mathrm{Nu}}_c = 43.7658$. Meanwhile, the 100 × 100 mesh gives $\overline{\mathrm{Nu}}_h = 42.0375$ and $\overline{\mathrm{Nu}}_c = 42.6741$. Therefore, the 100 × 100 mesh will give grid-independent solution for our study of sidewall temperature variations and thus has been chosen in all the calculations in this paper.

4. Results and Discussion

Investigation is carried out for the case Ra = 100 and Ra = 1000 with $\varepsilon = 0.5$ and $\kappa = 0.75$ for selected inclination angles, ϕ between 0° and 180°. The effects of inclination angle on the flow patterns and temperature fields are presented as streamline and isotherms in Figures

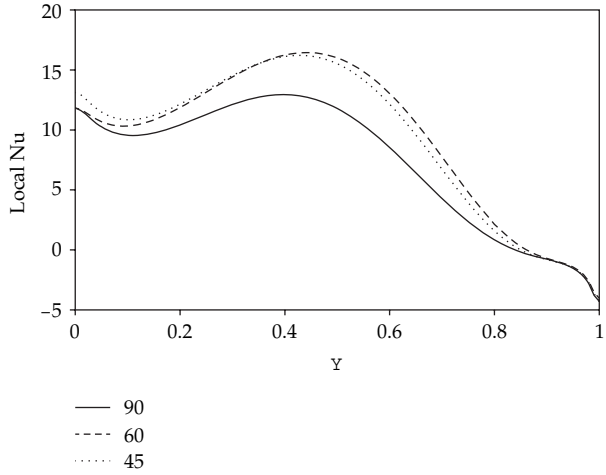

Figure 6: Variation of the local Nusselt number along the hot wall for $\varepsilon = 0.5$, $\kappa = 0.75$ and Ra = 1000. The solid line for the case $\phi = 90°$ is the recomputed results of Saeid and Mohamad [8].

2 and 3. At $\phi = 0°$, the hot wall is horizontal and at the bottom. As the cavity is inclined, the gravity components started to assist and accelerate the flow motion until the maximum Nusselt number is reached at $\phi = 50°$ for Ra = 100 and $\phi = 60°$ for Ra = 1000. For ϕ close to 180°, two and three cells are formed along the hot walls as shown in Figures 2(c) and 2(d) and Figures 3(c) and 3(d), indicating that the fluid from hot wall and cold wall rotates back to the same wall. For $\phi = 170°$, the isotherms far from the hot wall are almost perpendicular to the gravitational vector and the gradients are relatively small, implying the small value in the Nusselt number along the walls.

The influence of the inclination angles on the average Nusselt number is demonstrated in Figure 4. It is clear that the maximum average Nusselt number is attained at about $\phi = 50°$ for Ra = 100 and $\phi = 60°$ for Ra = 1000. Beyond that angle, the Nusselt number decreases until it reaches the condition where the Nusselt number has its minimum point or close to the pure conduction value. In general, the Nusselt number increases with increasing in Ra.

Figure 5 shows the variations of the average Nusselt number along the hot wall for Ra = 1000 and $\varepsilon = 0.2$. It can be seen from Figure 5 that the average Nusselt number varies spatially with increasing the wave number. Also, we found that the maximum average Nusselt numbers occur at $\kappa = 0.6$, 0.65, and 0.75 for $\phi = 45°$, 60°, and 90°, respectively.

As comparison with the work by Saied and Mohamad [8], we plotted the variation of the local Nusselt number along the hot wall for Ra = 1000, $\varepsilon = 0.5$, and $\kappa = 0.75$ in Figure 6. It is found that the value of local Nusselt numbers became negative near the upper portion of the hot wall which means that heat transfer occurred from the higher temperature parts to the lower temperature parts of the hot wall.

5. Conclusion

In this work, the natural convection in an inclined porous cavity has been investigated numerically using a finite difference approach. The effects of the inclination angle of the cavity are investigated. The numerical results indicate that the maximum natural convection

is dependent on the inclination angle, where the maximum Nusselt number occurs at different wave numbers for different inclination angle.

Acknowledgments

The first author gratefully acknowledged the financial support from the Ministry of Higher Education of Malaysia and the Universiti Teknologi MARA.

References

[1] D. A. Nield and A. Bejan, *Convection in Porous Media*, Springer, New York, NY, USA, 2nd edition, 1999.
[2] J. E. Weber, "The boundary-layer regime for convection in a vertical porous layer," *International Journal of Heat and Mass Transfer*, vol. 18, no. 4, pp. 569–573, 1975.
[3] A. Bejan, "On the boundary layer regime in a vertical enclosure filled with a porous medium," *Letters in Heat and Mass Transfer*, vol. 6, no. 2, pp. 93–102, 1979.
[4] R. Bradean, D. B. Ingham, P. J. Heggs, and I. Pop, "Free convection fluid flow due to a periodically heated and cooled vertical flat plate embedded in a porous media," *International Journal of Heat and Mass Transfer*, vol. 39, no. 12, pp. 2545–2557, 1996.
[5] B. Goyeau, J.-P. Songbe, and D. Gobin, "Numerical study of double-diffusive natural convection in a porous cavity using the Darcy-Brinkman formulation," *International Journal of Heat and Mass Transfer*, vol. 39, no. 7, pp. 1363–1378, 1996.
[6] Y. Guo and K. Bathe, "A numerical study of a natural convection flow in a cavity," *International Journal for Numerical Methods in Fluids*, vol. 40, no. 8, pp. 1045–1057, 2002.
[7] N. H. Saeid and I. Pop, "Transient free convection in a square cavity filled with a porous medium," *International Journal of Heat and Mass Transfer*, vol. 47, no. 8-9, pp. 1917–1924, 2004.
[8] N. H. Saeid and A. A. Mohamad, "Natural convection in a porous cavity with spatial sidewall temperature variation," *International Journal of Numerical Methods for Heat and Fluid Flow*, vol. 15, no. 6, pp. 555–566, 2005.
[9] N. H. Saeid and Y. Yaacob, "Natural convection in a square cavity with spatial side-wall temperature variation," *Numerical Heat Transfer A*, vol. 49, no. 7, pp. 683–697, 2006.
[10] J. E. Hart, "Stability of the flow in a differentially heated inclined box," *The Journal of Fluid Mechanics*, vol. 47, no. 3, pp. 547–576, 1971.
[11] P. H. Holst and K. Aziz, "Transient three-dimensional natural convection in confined porous media," *International Journal of Heat and Mass Transfer*, vol. 15, no. 1, pp. 73–90, 1972.
[12] H. Ozoe, K. Yamamoto, H. Sayama, and S. W. Churchill, "Natural convection in an inclined rectangular channel heated on one side and cooled on the opposing side," *International Journal of Heat and Mass Transfer*, vol. 17, no. 12, pp. 1209–1217, 1974.
[13] K. T. Yang, "Transitions and bifurcations in laminar bouyant flows in confined enclosures," *Journal of Heat Transfer*, vol. 110, no. 4, pp. 1191–1204, 1998.
[14] J. Rasoul and P. Prinos, "Natural convection in an inclined enclosure," *International Journal of Numerical Methods for Heat and Fluid Flow*, vol. 7, no. 5, pp. 438–478, 1997.
[15] A. C. Baytaşc, "Entropy generation for natural convection in an inclined porous cavity," *International Journal of Heat and Mass Transfer*, vol. 43, no. 12, pp. 2089–2099, 2000.
[16] E. V. Kalabin, M. V. Kanashina, and P. T. Zubkov, "Natural-convective heat transfer in a square cavity with time-varying side-wall temperature," *Numerical Heat Transfer A*, vol. 47, no. 6, pp. 621–631, 2005.
[17] A. J. Chamkha and A. Al-Mudhaf, "Double-diffusive natural convection in inclined porous cavities with various aspect ratios and temperature-dependent heat source or sink," *Heat and Mass Transfer/Waerme- und Sto uebertragung*, vol. 44, no. 6, pp. 679–693, 2008.
[18] G. Wang, Q. Wang, M. Zeng, and H. Ozoe, "Numerical study of natural convection heat transfer in an inclined porous cavity with time-periodic boundary conditions," *Transport in Porous Media*, vol. 74, no. 3, pp. 293–309, 2008.

Hindawi Publishing Corporation
Journal of Applied Mathematics
Volume 2012, Article ID 135173, 12 pages
doi:10.1155/2012/135173

Research Article

Flow Simulations Using Two Dimensional Thermal Lattice Boltzmann Method

Saeed J. Almalowi and Alparslan Oztekin

Department of Mechanical Engineering and Mechanics, Lehigh University, 27 Memorial Drive West, Bethlehem, PA 18015, USA

Correspondence should be addressed to Alparslan Oztekin, alo2@lehigh.edu

Received 13 February 2012; Accepted 9 April 2012

Academic Editor: Shuyu Sun

Lattice Boltzmann method is implemented to study hydrodynamically and thermally developing steady laminar flows in a channel. Numerical simulation of two-dimensional convective heat transfer problem is conducted using two-dimensional, nine directional D2Q9 thermal lattice Boltzmann arrangements. The velocity and temperature profiles in the developing region predicted by Lattice Boltzmann method are compared against those obtained by ANSYS-FLUENT. Velocity and temperature profiles as well as the skin friction and the Nusselt numbers agree very well with those predicted by the self-similar solutions of fully developed flows. It is clearly shown here that thermal lattice Boltzmann method is an effective computational fluid dynamics (CFD) tool to study nonisothermal flow problems.

1. Introduction

Historically, the Lattice Boltzman method (LBM) evolves from Lattice Gas Cellular Automata. In 1988, LBM is proposed to be used to simulate flows for the first time. The LBM is a branch of statistics of mechanics which is an ideal approach to simulate flows in simple or complex geometries. Recently, LBM has been modified to solve nonlinear partial differential equations to model complex fluid flows. Different approaches of the LBM have been discussed by several investigators [1]. However a successfully LBM simulation rests on the correct implementation of the boundary conditions, where unknown distribution function originated from the operation. As it is stated in several literatures, the implementation of the boundary conditions in LBM is the key to successfully model flow problems. Each type of boundary condition requires different technique and has different degree of accuracy as well.

LBM has been used to model flows in various geometries by several research groups, but only few investigators compare LBM model against other numerical methods for computational fluid dynamics (CFD). Recently Chen et al. and Begum and Basit [2, 3]

had proposed models to be applied to simulate complex flows. It has been shown that LBM can easily be implemented to study single- and multiphase flows. The equations governing conservation of mass and momentum are satisfied at each lattice nodes. The LBM approximation is a linear discretized equation which has two terms: streaming and collision terms. The collision term in the LBM has been approximated to be a linear term using models introduced by Bhatngar, Gross, and Krook (BGK) [4]. Recent study by Shi et al. [5] has shown that the LBM is a promising tool to study microscopic flows. Present work is to illustrate that LBM can be an effective CFD tool and in order to demonstrate that 2D developing nonisothermal flows in a channel is studied by implementing LBM method. The results predicted by LBM have been compared against those obtained using ANSYS-FLUENT and those obtained by self-similar solutions in the developed region for validation.

2. Lattice Boltzmann Governing Equation

Ludwig Eduard Boltzmann (1844–1906), the Austrian physicist, had the greatest achievement in the development of statistical mechanics. This approach has been used to predict macroscopic properties of matter such as the viscosity, thermal conductivity, and diffusion coefficient from the microscopic properties of atoms and molecules [6–8]. The probability of finding particles within certain range of velocities at a certain range of locations replaces tagging each particle as in molecular dynamics simulation. The lattice Boltzmann transportation can be governed by distribution function which represents particles at location $\mathbf{r}(x, y)$ at time t, and the particle will be displaced by (dx, dy) in time dt with the application force $\mathbf{F}$ on the liquid molecules [9]. The equation governing the distribution function $f(\mathbf{r}, \mathbf{c}, t)$ has two terms, the streaming step and the collision term. Here, x and y are spatial coordinates, t is the time, and $\mathbf{c}$ is the lattice discrete velocity.

The collision takes place between the molecules; there will be a net difference between the numbers of molecules in the interval $d\mathbf{r}d\mathbf{c}$. The rate of change of the distribution function is expressed as

$$\frac{f(\mathbf{r} + d\mathbf{r}, \mathbf{c} + \mathbf{F}dt/m, t + dt) - f(\mathbf{r}, \mathbf{c}, t)}{dt} = \frac{\partial f}{\partial t} + c_x \frac{\partial f}{\partial x} + c_y \frac{\partial f}{\partial y} + \frac{\mathbf{F}}{m} \cdot \frac{\partial f}{\partial \mathbf{c}} = \varphi(f). \tag{2.1}$$

Here, $\mathbf{F}$ denotes external forces applied, and $\varphi(f)$ is the source or the collision term. With the absence of the external forces, (2.1) becomes

$$\frac{\partial f_i}{\partial t} + \mathbf{c} \cdot \nabla f_i = \varphi(f_i). \tag{2.2}$$

Equation (2.2) is known as the lattice Boltzmann governing equation. The right hand side of equation is called a source and is approximated by BGK as

$$\varphi(f_i) = \frac{1}{\tau}\left(f_i^{\mathrm{eq}} - f_i\right). \tag{2.3}$$

Here $\omega = 1/\tau$ is the relaxation frequency and the τ is the relaxation time f^{eq} is the equilibrium value of distribution function and is written as

$$f_i^{\mathrm{eq}} = w_i \rho \left[1 + \frac{3\mathbf{c}_i \cdot \mathbf{V}}{{c_s}^2} + 4.5 \frac{(\mathbf{c}_i \cdot \mathbf{V})^2}{{c_s}^4} - 1.5 \frac{\mathbf{V} \cdot \mathbf{V}}{{c_s}^2} \right], \tag{2.4}$$

where $\mathbf{c}_i$ is the discrete velocities vector, $\mathbf{V}$ is the bulk fluid velocity, c_s is the lattice sound speed and w_i is the weight factor, one has

$$\mathbf{c}_i = \begin{cases} (0,0) & i = 1 \\ \mathbf{c}\left(\left[\dfrac{\sin(i-1)\pi}{2} \right], \left[\dfrac{\cos(i-1)\pi}{2} \right] \right) & i = 2,3,4,5 \\ \mathbf{c}\left(\sqrt{2} \left[\dfrac{\cos(2i-11)\pi}{4} \right], \sqrt{2} \left[\dfrac{\sin(2i-11)\pi}{4} \right] \right) & i = 6,7,8,9, \end{cases}$$

$$w_i = \begin{cases} \dfrac{4}{9} & i = 1 \\ \dfrac{1}{9} & i = 2,3,4,5 \\ \dfrac{1}{36} & i = 6,7,8,9. \end{cases} \tag{2.5}$$

Equation (2.3) becomes

$$f_i(\mathbf{r} + d\mathbf{r}, t + dt) = (1 - \omega) f_i(\mathbf{r}, t) + \omega f_i^{\mathrm{eq}}. \tag{2.6}$$

3. Lattice Boltzmann Arrangements (D2Q9)

Lattice Boltzmann is relatively recent technique that has been shown to be as accurate as traditional CFD methods having ability to integrate arbitrarily complex geometries. LBM can be used for different arrangements such as D1Q2, D2Q4, D2Q9, D3Q15, D3Q19, or D3Q27 [10]. However, in this paper, we only use D2Q9 which implies the two-dimensional and nine velocity components as shown in Figure 1.

Each distribution function has position ($\mathbf{r}$), velocity ($\mathbf{c}$), and weight factor (w).

4. Momentum Lattice Boltzmann Model

The momentum LBM represents the particles velocity [4]. For instance, for D2Q9 lattice arrangements, the particle at the origin is at rest and the remaining particles move in different directions with different speed. Each velocity vector denotes a lattice per unit step. These velocities are exceptionally convenient in that all x and y components are either 0 or ±1.

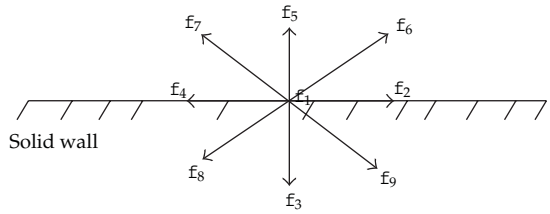

Figure 1: D2Q9 LBM arrangement.

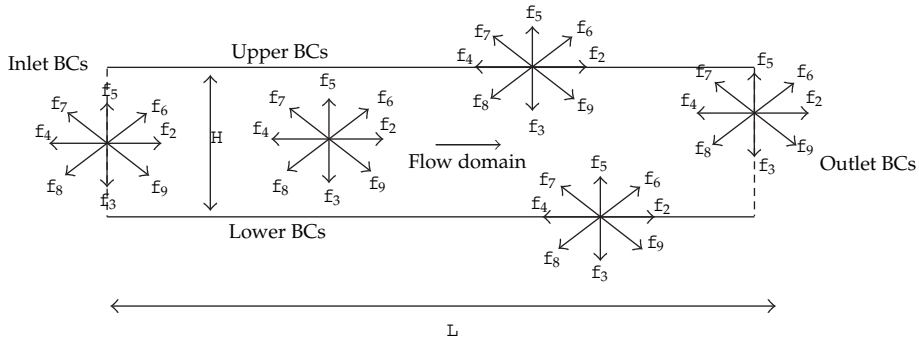

Figure 2: D2Q9 momentum lattice arrangements at boundaries and inside the flow domain.

Mass of particle is taken as unity uniformly throughout the flow domain. The macroscopic fluid density, ρ, is governed by conservation of mass

$$\rho = \sum_{i=1}^{9} f_i. \tag{4.1}$$

The bulk fluid velocity ($\mathbf{V} = (u, v)$) is the average of microscopic lattice-directional velocity ($\mathbf{c} = (c_x, c_y)$) and the directional density and is governed by conservation of momentum

$$\mathbf{V} = \frac{1}{\rho} \sum_{i=1}^{9} f_i \mathbf{c}_i. \tag{4.2}$$

Here $c_x = dx/dt$, $c_y = dy/dt$ are x and y components of the lattice directional velocity. Conservation of mass and momentum is also applied at each boundary, at the inlet and the outlet as shown in Figure 2 for the D2Q9 lattice arrangement for nodes placed on boundaries.

The uniform inlet velocity is U_{in}, the length of channel is L, and the gap between plates is H. u is measured in units of U_{in} ($U = u/U_{\text{in}}$), x and y are measured in units of L and H ($X = x/L$ and $Y = y/H$), respectively. Scaled inlet velocity becomes $U = 1$, and the flow domain (X, Y) becomes $0 \le Y \le 1$, and $0 \le X \le 1$.

5. Thermal Lattice Boltzmann Model

There has been rapid progress in developing the construction of stable thermal lattice Boltzmann equation models to study heat transfer problems. McNamara and Zanetti

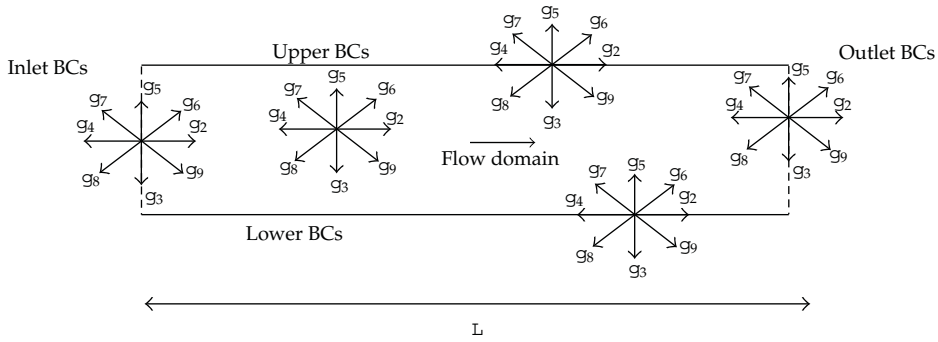

Figure 3: D2Q9 thermal lattice arrangements at boundaries and inside the flow domain.

successfully applied multispeed thermal fluid lattice Boltzmann method to solve heat transfer problems [6]. At the outlet, bounce back or extrapolation boundary conditions are considered as the thermal and flow boundary conditions. Bounce back type boundary conditions are proven to provide more accurate numerical approximations [11] and are used by the present work. The temperature at each wall is specified; however, the temperatures which are pointing to the flow domain are unknowns, and they can be evaluated from streaming and collision steps. The thermal lattice arrangement is illustrated in Figure 3.

The rate of change of the thermal distribution function is written as

$$g_i(\mathbf{r} + d\mathbf{r}, t + dt) = (1 - \omega) g_i(\mathbf{r}, t) + \omega g_i^{\mathrm{eq}}. \tag{5.1}$$

With normalized temperature $\theta = (T - T_w)/[T_{\mathrm{in}}(H/2) - T_w]$, the equilibrium value of the thermal distribution function g^{eq} is given by

$$g_i^{\mathrm{eq}} = \omega_i \theta \left[1 + \frac{3\mathbf{c}_i \cdot \mathbf{V}}{{c_s}^2} + 4.5 \frac{(\mathbf{c}_i \cdot \mathbf{V})^2}{{c_s}^4} - 1.5 \frac{\mathbf{V} \cdot \mathbf{V}}{{c_s}^2} \right]. \tag{5.2}$$

For simplicity the relaxation frequency of the thermal and momentum distribution function is selected as the same. Hence the kinematic viscosity, υ, and the thermal diffusivity, α, are the same and are expressed by

$$\upsilon = \alpha = \frac{(dx)^2}{3dt} \left(\frac{1}{\omega} - \frac{1}{2} \right). \tag{5.3}$$

Here, T_w is the wall temperature, and $T_{\mathrm{in}}(y)$ is the temperature distribution at the inlet. The Prandtl number $\mathrm{Pr} = \upsilon/\alpha = 1$. The temperature of the fluid is governed by the conservation of energy

$$T = \sum_{i=1}^{9} g_i. \tag{5.4}$$

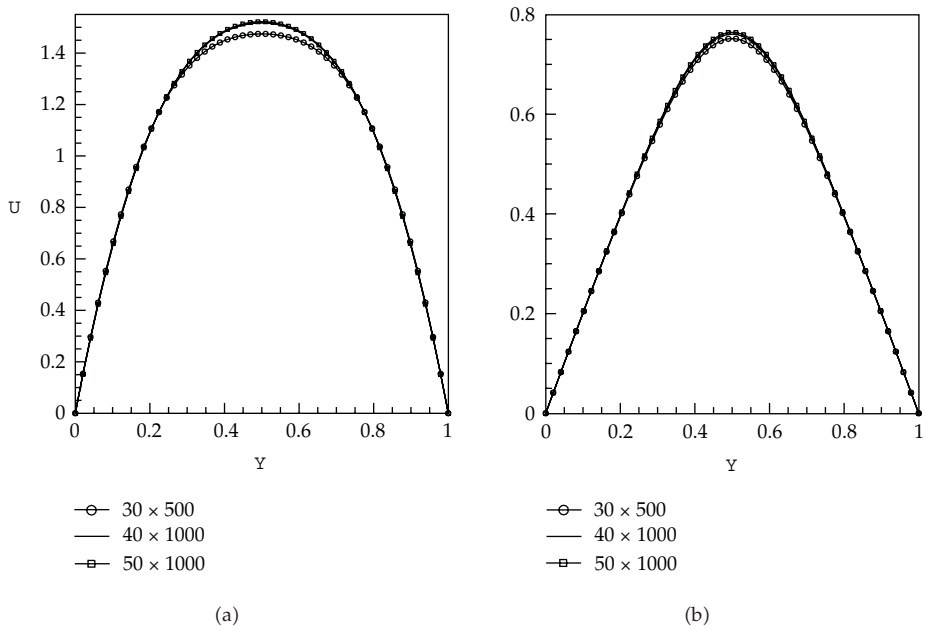

Figure 4: (a) Velocity and (b) temperature profiles at $X = 0.2$ plotted for various N and M.

6. Results and Discussion

The discretized equations (2.6) and (5.1) for momentum and thermal distribution f and g for $M \times N$ nodes in x and y directions, respectively, are solved by employing Gauss-Siedel iterations. For boundary nodes the detailed discretized equations for f and g are described in Appendices A and B. The results are presented for steady incompressible two-dimensional laminar flows in an entrance region of a channel. Flow develops hydrodynamically and thermally in a 1 m long and 0.02 m height channel with the aspect ratio AR of 50. At the inlet the flow is uniform ($U_{\text{in}} = 0.02\,\text{m/sec}$), and the temperature of the fluid satisfies $\theta_{\text{in}} = 4 \times (Y - Y^2)$. Boundary conditions imposed on the velocity field at $Y = 0$ and 1 are no-slip and no-penetration, and the thermal boundary conditions applied on each surface are $\theta = 0$. The physical properties are considered to be constant and are determined for water at 300 K—($\rho = 999.1\,\text{kg/m}^3$ and $\mu = 855 \times 10^{-3}\,\text{N} \cdot \text{s/m}^2$). For the example illustrated in this paper, the flow rate considered is 0.4 kg/s and the corresponding Reynolds number $\text{Re} = \rho 2HU_{\text{in}}/\mu = 800$.

Spectral convergence is checked for LBM to ensure that the results predicted by the LBM are not dependent on the number of nodes selected for the numerical simulations. Nodes ($M \times N$) are placed uniformly in the direction of x (M nodes) and y (N nodes). The convergence test is displayed in Figure 4 as the velocity and temperature profile at $X = 0.2$ plotted for various M and N. It is shown that the (50 × 1000) mesh provides satisfactory spectral convergence and numerical accuracy and is thereby chosen for the numerical simulation results predicted by LBM.

The velocity and temperature profiles are displayed at various cross-sections in the developing region. The profiles that are obtained by LBM are compared against those obtained by ANSYS-FLUENT at the same conditions. The boundary conditions at the inlet and the outlet and on the surface of the plates are selected as the same for both methods.

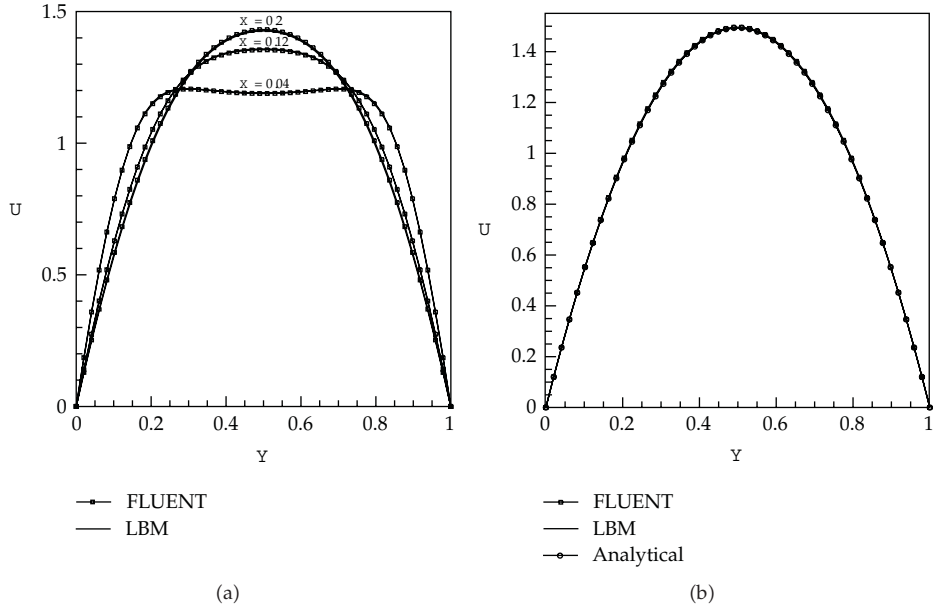

Figure 5: (a) Velocity profiles at various cross-sections predicted by LBM and FLUENT. (b) Velocity profile at $X = 0.725$ predicted by LBM and FLUENT and the self-similar solution for the fully developed laminar channel flow.

The velocity and temperature field are considered to be converged when the error tolerance is less than 10^{-3}.

The velocity profiles predicted by LBM and FLUENT at various cross-sections are shown in Figure 5. The solid lines denote the prediction obtained by LBM while the symbols denote the predictions obtained by FLUENT. The velocity profiles at all cross-section predicted by LBM agree very well with those predicted by FLUENT, as shown in Figure 5(a). The development length for velocity field at Re = 800 in this flow is expected to be $x/H = 47.4$. The thermal field has the same development length as the hydrodynamic field since Pr is selected to be unity. The nearly fully developed velocity profile obtained by both methods at $X = 0.725$ also agrees very well with each other. They also agree well with the analytical solution, $U = 6(Y - Y^2)$, obtained by the self-similar solution for fully developed laminar flow in a channel, as shown in Figure 5(b).

The temperature profiles predicted by LBM and FLUENT at various cross-sections are shown in Figure 6. The solid lines denote the prediction obtained by LBM, and the symbols denote the predictions obtained by FLUENT. The temperature profiles predicted by LBM agree very well with those predicted by FLUENT.

Wall shear stress and heat transfer coefficient are predicted at various cross-sections in the developing region. The local value of skin friction, C_f, and the Nusselt number, Nu, are determined from the numerical solution as

$$C_f(X) = \frac{\mu}{1/2\rho U_{\text{in}}^2}\frac{\partial u}{\partial y}(x,0) = \frac{4}{\text{Re}}\frac{\partial U}{\partial Y}(X,0), \qquad \text{Nu}(X) = 2\frac{T_{\text{in}} - T_w}{T_m - T_w}\frac{\partial \theta}{\partial Y}(X,0), \tag{6.1}$$

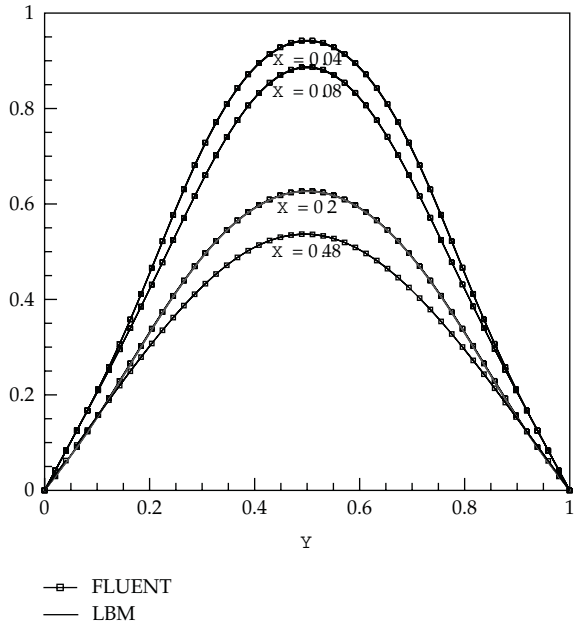

Figure 6: Temperature profile at various cross-sections predicted by LBM and FLUENT.

where T_m is the bulk temperature of the fluid and is calculated at each cross-section as

$$T_m = \frac{1}{\int U dA} \int [T_w + (T_{\text{in}}(0.5H) - T_w)\theta] U dA. \tag{6.2}$$

The skin friction and the Nusselt number predicted by LBM are plotted in Figure 7 as a function $x/2H$. $\text{Re}\, C_f$ tends to 24 as the fully developed region is approached. Similarly, Nusselt number tends to 7.54 as the thermally fully developed region is approached, as shown in Figure 7(b). These values are in perfect agreement with the fully developed values of C_f and Nu as well documented in the literature.

7. Conclusion

Hydrodynamically and thermally developing laminar steady flow in a channel is considered as an example to illustrate that Lattice Boltzmann method is a promising computational fluid dynamics tool. D2Q9 lattice arrangement is used to predict both velocity and temperature field. Profiles obtained by LBM-D2Q9 and ANSYS-FLUENT agree very well. Away from the inlet as the fully developed region is approached, and the profiles tend to self-similar solutions of developed laminar channel flows. That is confirmed by prediction of the skin friction and Nusselts number. As full-developed region is approached away from the inlet both the skin friction coefficient and the Nusselt number tend to well-documented values in the literature. Extension of LBM method to three-dimensional unsteady complex multiphase flows is natural, and the implementation of LBM to tackle such problems is underway.

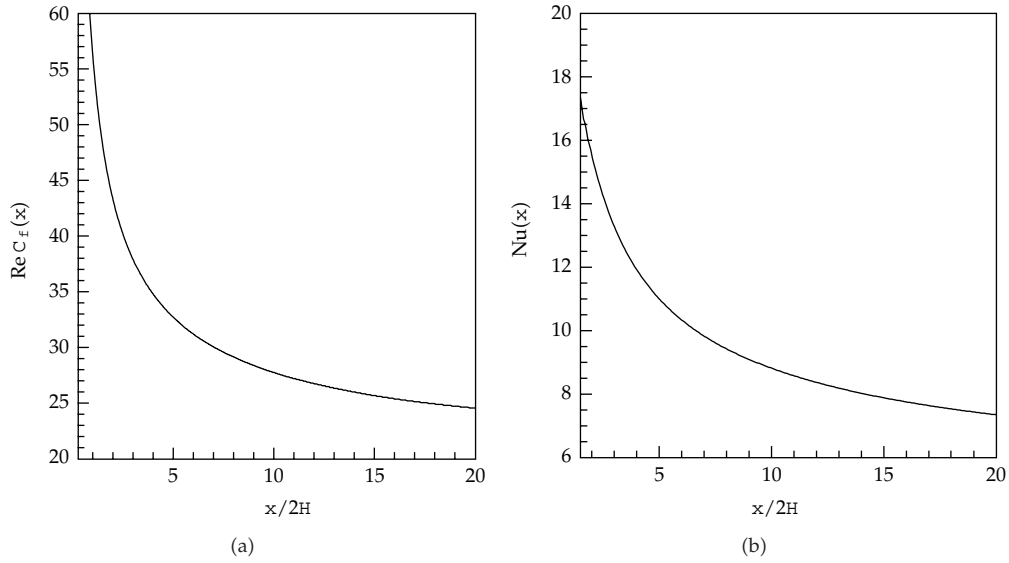

Figure 7: (a) Skin friction and (b) Nusselt number plotted as a function of $x/2H$.

Appendices

A. Discretized LB Equations for the Velocity Field at the Inlet, the Outlet, and at the Surface of Plates

With indices k denoting 9 directions of LB D2Q9 arrangements, i denoting the nodes placed in the x-direction and j denoting the nodes placed in the y-directions, the distribution functions for velocity, f, and temperature field, g, are represented by three-dimensional arrays $f(k,i,j)$, and $g(k,i,j)$ for $k = 1$ to 9, $i = 1, M$ and $j = 1, N$.

At the inlet ($i = 1$; $j = 2$ to $N - 1$), the conservation of mass and momentum yield

$$\rho(1,i,j) = \frac{\left(f(1,i,j) + f(5,i,j) + f(3,i,j) + 2 \times \left(f(4,i,j) + f(7,i,j) + f(8,i,j)\right)\right)}{\left(1 - u(1,i,j)\right)},$$

$$f(2,i,j) - f^{\mathrm{eq}}(2,i,j) = f(4,i,j) - f^{\mathrm{eq}}(4,i,j),$$

$$f(2,i,j) = f(4,i,j) + \frac{2}{3}\rho(1,i,j) \times u(1,i,j), \tag{A.1}$$

$$f(9,i,j) = f(6,i,j) + \frac{1}{6}\rho(1,i,j) \times u(1,i,j),$$

$$f(5,i,j) = f(7,i,j) + \frac{1}{6}\rho(1,i,j) \times u(1,i,j).$$

The boundary conditions at the surface of the lower plate ($i = 1, M-1;\ j = 1$) imposed on the velocity field give

$$\begin{aligned}
\rho(1,i,j) &= \frac{\left(f(1,i,j)+f(5,i,j)+f(2,i,j)+2\times\left(f(3,i,j)+f(9,i,j)+f(8,i,j)\right)\right)}{\left(1-v(1,i,j)\right)},\\
f(5,i,j) &= f(3,i,j)+\frac{2}{3}\rho(1,i,j)\times v(1,i,j), \qquad f(3,i,j)-f^{\mathrm{eq}}(3,i,j) = f(5,i,j)-f^{\mathrm{eq}}(5,i,j),\\
f(6,i,j) &= f(8,i,j)+\frac{1}{2}\left(f(4,i,j)-f(2,i,j)\right)+\frac{1}{6}\rho(1,i,j)\times v(1,i,j)+\frac{1}{2}\rho(1,i,j)\times u(1,i,j),\\
f_7 &= f_9-\frac{1}{2}\left(f_4-f_2\right)+\frac{1}{6}\rho(1,i,j)\times v(1,i,j)-\frac{1}{2}\rho(1,i,j)\times u(1,i,j).
\end{aligned} \tag{A.2}$$

At the top surface ($i = 1, M-1;\ j = N$), the velocity boundary conditions yield

$$\begin{aligned}
\rho(1,i,j) &= \frac{\left(f(1,i,j)+f(2,i,j)+f(4,i,j)+2\times\left(f(5,i,j)+f(7,i,j)+f(6,i,j)\right)\right)}{\left(1+v(1,i,j)\right)},\\
f(3,i,j) &= f(5,i,j)-\frac{2}{3}\rho_u(1,i,j)\times v(1,i,j),\\
f(8,i,j) &= f(6,i,j)-\frac{1}{2}\left(f(4,i,j)-f(2,i,j)\right)-\frac{1}{6}\rho(1,i,j)\times v(1,i,j)-\frac{1}{2}\rho(1,i,j)\times u(1,i,j),\\
f(9,i,j) &= f(7,i,j)+\frac{1}{2}\left(f(4,i,j)-f(2,i,j)\right)-\frac{1}{6}\rho(1,i,j)\times v(1,i,j)+\frac{1}{2}\rho(1,i,j)\times u(1,i,j).
\end{aligned} \tag{A.3}$$

The outlet conservation of mass and momentum is approximated by using second-order extrapolation which yields

$$f(k,M,j) = 2f(k,M-1,j)-f(k,M-2,j) \quad \text{where } k = 2,6,9,\ j = 2,N-1. \tag{A.4}$$

B. Discretized LB Equations for the Temperature Field at the Inlet, the Outlet, and at the Surface of Plates

The inlet ($i = 1;\ j = 2$ to $N-1$) conservation of energy gives

$$\begin{aligned}
g(3,i,j)-g^{\mathrm{eq}}(3,i,j) &= g(5,i,j)-g^{\mathrm{eq}}(5,i,j),\\
g(2,i,j) &= \theta_{\mathrm{in}}(1,i,j)\left(w(4)+w(2)\right)-g(4,i,j),\\
g(6,i,j) &= \theta_{\mathrm{in}}(1,i,j)\left(w(6)+w(8)\right)-g(8,i,j),\\
g(9,i,j) &= \theta_{\mathrm{in}}(1,i,j)\left(w(7)+w(9)\right)-g(7,i,j).
\end{aligned} \tag{B.1}$$

With $\theta_w = 0$ the thermal boundary condition at the surface of the lower plate ($i = 1, M-1;\ j = 1$) gives

$$\begin{aligned} g(7,i,j) &= -g(7,i,j), \\ g(5,i,j) &= -g(3,i,j), \\ g(6,i,j) &= -g(4,i,j), \\ g(2,i,j) &= -g(4,i,j). \end{aligned} \tag{B.2}$$

With $\theta_w = 0$ the thermal boundary condition at the surface of the upper plate ($i = 1, M-1;\ j = N$) gives

$$\begin{aligned} g(3,i,j) - g^{\mathrm{eq}}(3,i,j) &= g(5,i,j) - g^{\mathrm{eq}}(5,i,j), \\ g(9,i,j) &= -g(7,i,j), \\ g(8,i,j) &= -g(6,i,j), \\ g(3,i,j) &= -g(5,i,j), \\ g(2.i.j) &= -g(4,i,j). \end{aligned} \tag{B.3}$$

The outlet conservation of energy is approximated by the second-order extrapolation which yields

$$g(k,M,j) = 2g(k,M-1,j) - g(k,M-2,j) \quad \text{where } k = 2,6,9,\ j = 2,N-1. \tag{B.4}$$

Nomenclature

f:	Density distribution function
f^{eq}:	Local equilibrium density distribution function
g:	Temperature distribution function
g^{eq}:	Local equilibrium temperature distribution function
$\mathbf{c} = (c_x, c_y)$:	Lattice discrete velocity, c_x and c_y are x and y components
$\mathbf{V} = (u, v)$:	Bulk velocity of the fluid, u and v are x and y components
U:	Normalized x component of the fluid velocity
θ:	Normalized temperature
ω:	Dimensionless relaxation frequency
w:	Weight factor
T_w:	Wall temperature in (°C)
c_s:	Lattice sound speed
τ:	Dimensionless collision relaxation time
$\mathbf{r}$:	Position vector
(X, Y):	Dimensionless x and y coordinate
U_{in}:	Fluid speed at the inlet
T_{in}:	Temperature profile at the inlet in (°C), $T_{\mathrm{in}}(y)$
ρ:	Density of fluid, kg/m^3
υ:	Kinematic viscosity of fluid, m^2/sec
α:	Thermal diffusivity of fluid, m^2/sec
Pr:	Prandtl number

Re: Reynolds number
T: Bulk temperature in (°C).

Acknowledgment

One of the authors of this paper is grateful to Saudi Arabia government for its support toward his graduate education.

References

[1] X. D. Niu, C. Shu, and Y. T. Chew, "A thermal lattice Boltzmann model with diffuse scattering boundary condition for micro thermal flows," *Computers and Fluids*, vol. 36, no. 2, pp. 273–281, 2007.
[2] S. Chen, D. Martínez, and R. Mei, "On boundary conditions in lattice Boltzmann methods," *Physics of Fluids*, vol. 8, no. 9, pp. 2527–2536, 1996.
[3] R. Begum and M. A. Basit, "Lattice Boltzmann method and its applications to fluid flow problems," *European Journal of Scientific Research*, vol. 22, no. 2, pp. 216–231, 2008.
[4] Q. Zou and X. He, "On pressure and velocity boundary conditions for the lattice Boltzmann BGK model," *Physics of Fluids*, vol. 9, no. 6, pp. 1591–1596, 1997.
[5] Y. Shi, T. S. Zhao, and Z. L. Guo, "Finite difference-based lattice Boltzmann simulation of natural convection heat transfer in a horizontal concentric annulus," *Computers and Fluids*, vol. 35, no. 1, pp. 1–15, 2006.
[6] G. R. McNamara and G. Zanetti, "Use of the boltzmann equation to simulate lattice-gas automata," *Physical Review Letters*, vol. 61, no. 20, pp. 2332–2335, 1988.
[7] M. C. Sukop and D. T. Thorne Jr., *Lattice Boltzmann Modeling an Introduction for Geosceintific and Engineers*, Springer, Berlin, Germany, 2010.
[8] A. J. C. Ladd and R. Verberg, "Lattice-Boltzmann simulations of particle-fluid suspensions," *Journal of Statistical Physics*, vol. 104, no. 5-6, pp. 1191–1251, 2001.
[9] M. Sbragaglia and S. Succi, "Analytical calculation of slip flow in lattice boltzmann models with kinetic boundary conditions," *Physics of Fluids*, vol. 17, no. 9, Article ID 093602, 8 pages, 2005.
[10] S. Succi, *The Lattice Boltzmann Equation for Fluid Dynamics and Beyond*, Numerical Mathematics and Scientific Computation, The Clarendon Press/Oxford University Press, New York, NY, USA, 2001.
[11] Q. Liao and T.-C. Jen, "Application of Lattice Boltzmann method in fluid flow and heat transfer," in *Computational Fluid Dynamics Technologies and Applications*, InTech.

Hindawi Publishing Corporation
Journal of Applied Mathematics
Volume 2012, Article ID 781695, 18 pages
doi:10.1155/2012/781695

Research Article

Influence of Secondary Currents on Solute Dispersion in Curved Open Channels

Myung Eun Lee[1] and Gunwoo Kim[2]

[1] *Department of Civil and Environmental Engineering, Seoul National University, Seoul 151-742, Republic of Korea*
[2] *Department of Ocean Civil & Plant Construction Engineering, Mokpo National Maritime University, Mokpo, Jeollanamdo 530-729, Republic of Korea*

Correspondence should be addressed to Gunwoo Kim, gwkim@mmu.ac.kr

Received 25 December 2011; Accepted 17 April 2012

Academic Editor: Shuyu Sun

The dispersion coefficient tensor including off-diagonal components was introduced in the flow with secondary currents, which is called skewed shear flow dispersion (SSFD) coefficient tensor, in this paper. To observe the detailed effect of cross-dispersion terms in SSFD model on solute dispersion, mathematical analysis of eigenvalue problem with respect to the equation with SSFD coefficient tensor was performed. The analysis results show the several differences of SSFD model compared to CSFD (conventional shear flow dispersion) model: the oblique direction of principal dispersion with respect to the streamline, the increase of peak concentration, and the change in the eccentricity of elliptical tracer cloud. SSFD coefficient tensor in a streamwise curvilinear coordinate system of curved channel was transformed to those components of fixed Cartesian coordinate system, and 2D numerical model with finite element method was established in the Eulerian-Cartesian coordinate. Through this process, the transformation equation using the depth-averaged velocity field was derived. Several numerical tests were performed to assure the results obtained in the mathematical analysis and to show the applicability of the derived transformation equation on the flow with continuously changing flow direction.

1. Introduction

The advection and dispersion of passive solutes in open channels—which includes pollutant transport in artificial canals, natural streams, and rivers—is an important topic in environmental hydraulics. In open channels, once vertical mixing is completed in the initial period of solute transport, the vertical shear velocity profile increases the longitudinal spreading in the streamline direction [1]. As a result, in flows where the longitudinal flow is

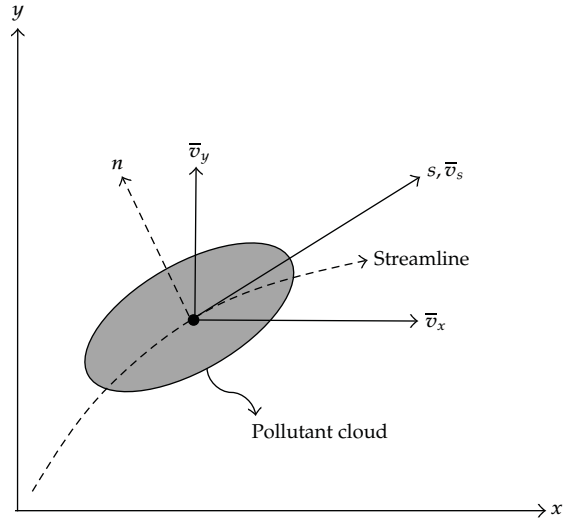

Figure 1: Schematic diagram for CSFD model: x, y: coordinate axes of the Eulerian-Cartesian coordinate system; $\overline{v}_x, \overline{v}_y$: components of depth-averaged velocities on the x, y axes.

dominant, such as straight open-channel flows, solute spreading is commonly described with longitudinal shear dispersion and transverse turbulent diffusion:

$$\frac{\partial C}{\partial t} + \frac{\partial(\overline{v}_s C)}{\partial s} = \frac{\partial}{\partial s}\left(D_{ss}\frac{\partial C}{\partial s}\right) + \frac{\partial}{\partial n}\left(\varepsilon_n \frac{\partial C}{\partial n}\right), \tag{1.1}$$

where s is the coordinate axis coinciding with the streamline direction; n is local coordinate axis that is normal to the streamline; C the depth-averaged concentration; $\overline{v}_s$ the longitudinal depth-averaged velocity; D_{ss} the longitudinal dispersion coefficient; ε_n the transverse turbulent diffusion coefficient. In (1.1), the axis of the longitudinal dispersion always coincides with the streamline of the principal flow. Thus, the distribution of concentration shows axisymmetry with respect to the (s, n) axes, as shown in Figure 1.

However, the secondary current around pronounced curvatures in many open channels introduces a large magnitude of transverse circulation combined with the principal longitudinal flow. Hence, the solute dispersion by the secondary current cannot be described by only the dispersion in the longitudinal direction; there is a dispersion effect in the transverse direction that is much more effective than the transverse turbulent diffusion. A flow with secondary currents, as that in Figure 2, has a structure with skewed shear profiles having different velocity profiles in two orthogonal directions.

Fischer [2] proposed that the cross-dispersion terms should be included in the 2D depth-averaged dispersion equation, to deal with the effect of skewed vertical profiles on the horizontal dispersion process:

$$\frac{\partial C}{\partial t} + \frac{\partial(\overline{v}_s C)}{\partial s} = \frac{\partial}{\partial s}\left(D_{ss}\frac{\partial C}{\partial s} + D_{sn}\frac{\partial C}{\partial n}\right) + \frac{\partial}{\partial n}\left(D_{ns}\frac{\partial C}{\partial s} + D_{nn}\frac{\partial C}{\partial n}\right), \tag{1.2}$$

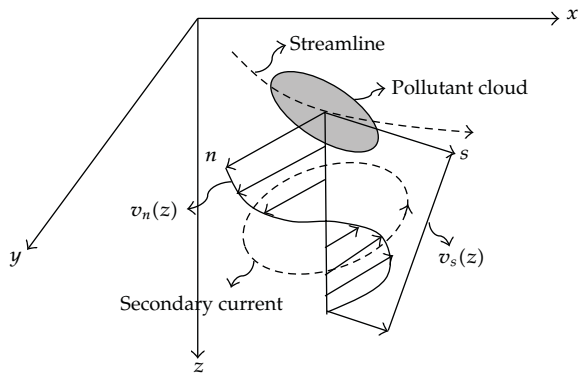

Figure 2: Schematic diagram for SSFD model: v_s, v_n: horizontal velocities on the s, n axes; z: coordinate axis of the vertical direction.

where D_{ss}, D_{sn}, D_{ns}, and D_{nn} are components of the full dispersion coefficient tensor and D_{nn} denotes the transverse dispersion coefficient. The additional cross-dispersion terms $D_{sn}(\partial C/\partial s)$ and $D_{ns}(\partial C/\partial n)$ indicate mass transport in the longitudinal direction caused by the concentration gradient in the transverse direction and vice versa. These terms rotate a dispersing tracer cloud away from symmetry on the s and n axes. Once the open-channel flow with secondary currents is regarded as the skewed shear flow, the off-diagonal components D_{sn} and D_{ns} should be clearly considered on the solute dispersion in a curved flow. However, most studies and pollutant transport models related to the role of secondary currents in the dispersion process only focused on activation of the transverse dispersion that only increases D_{nn} [3–9]. Neglecting cross-dispersion terms, solute dispersion on a curved flow with secondary currents is still described with only the longitudinal and transverse dispersion coefficients in the widely used 2D environmental mixing models:

$$\frac{\partial C}{\partial t} + \frac{\partial(\overline{v}_s C)}{\partial s} = \frac{\partial}{\partial s}\left(D_{ss}\frac{\partial C}{\partial s}\right) + \frac{\partial}{\partial n}\left(D_{nn}\frac{\partial C}{\partial n}\right). \tag{1.3}$$

Hereafter, we call this kind of model as a conventional shear flow dispersion (CSFD) model.

In this study, we introduced the full dispersion coefficient tensor to the solute dispersion model with respect to the stream wise curvilinear frame of reference as described in (1.2), and we call this the skewed shear flow dispersion (SSFD) model. This model describes the skewed shear flow dispersion process in a flow with a secondary current that induces strong interaction between the longitudinal and transverse dispersions. For detailed study with respect to the effect of the off-diagonal terms on the passive solute dispersion, the dispersion equation with the SSFD coefficient tensor was mathematically analyzed by solving the eigenvalue problem and comparing the results with the CSFD model. The finite element formulation in fixed Cartesian coordinates was selected for computational modeling to test the SSFD model in curved open channels. To deal with the governing equation on a fixed Cartesian coordinate, a transformation equation for SSFD tensor, originally defined in the stream wise curvilinear coordinate system, was derived using the depth-averaged velocity field.

2. Analysis of SSFD Model

Two-dimensional advection-dispersion equation is simply expressed below in (2.1) with a substantial derivative in the stream-wise curvilinear frame of reference

$$\frac{dC}{dt} = \nabla \cdot (\mathbf{D}\nabla C) = \nabla^T \mathbf{D}\nabla C, \qquad \nabla = \left[\frac{\partial}{\partial s} \quad \frac{\partial}{\partial n}\right]^T. \tag{2.1}$$

By the above expression, the full dispersion coefficient tensor $\mathbf{D}$ of the SSFD model is expressed in a 2×2 matrix to correspond to (1.2) as follows:

$$\mathbf{D} = \begin{bmatrix} D_{ss} & D_{sn} \\ D_{ns} & D_{nn} \end{bmatrix}. \tag{2.2}$$

However in the CSFD model represented by (1.3), $\mathbf{D}$ in (2.1) is replaced by the diagonal dispersion coefficient tensor $\mathbf{D}_c$

$$\frac{dC}{dt} = \nabla \cdot (\mathbf{D}_c \nabla C) = \nabla^T \mathbf{D}_c \nabla C, \qquad \mathbf{D}_c = \begin{bmatrix} D_{ss} & 0 \\ 0 & D_{nn} \end{bmatrix}. \tag{2.3}$$

In order to analyze the effect of off-diagonal components on the full dispersion coefficient tensor of the SSFD model, we performed a mathematical analysis to solve eigenvalue problems related to the dispersion tensor and equation.

Because $\nabla^T \mathbf{D} \nabla$ in (2.1) is in quadratic form, we may replace $\mathbf{D}$ with the symmetric matrix $\overline{\mathbf{D}}$ by taking off-diagonal components together in pairs and writing the result as a sum of two equal terms [10]:

$$\frac{dC}{dt} = \nabla^T \overline{\mathbf{D}} \nabla C, \qquad \overline{\mathbf{D}} = \begin{bmatrix} D_{ss} & \overline{D}_{sn} \\ \overline{D}_{sn} & D_{nn} \end{bmatrix}, \tag{2.4}$$

where $\overline{D}_{sn} = (D_{sn} + D_{ns})/2$. Symmetric dispersion coefficient matrices such as $\overline{\mathbf{D}}$ have an orthonormal basis of eigenvectors. Thus, if we take these as column vectors, we obtain a matrix $\mathbf{X}$ that is orthogonal—so that $\mathbf{X}^T = \mathbf{X}^{-1}$. According to the theory of orthogonal eigenvectors of a specified symmetric matrix, a certain diagonal matrix $\overline{\mathbf{D}}'$ is obtained by the following relationship:

$$\overline{\mathbf{D}} = \mathbf{X}\mathbf{D}'\mathbf{X}^{-1} = \mathbf{X}\mathbf{D}'\mathbf{X}^T. \tag{2.5}$$

It should be noted that $\mathbf{D}'$ is a similar matrix of $\overline{\mathbf{D}}$ by orthogonal transformation: $\mathbf{D}' = \mathbf{X}^{-1}\overline{\mathbf{D}}\mathbf{X}$. Substituting (2.5) into (2.4) transforms the quadratic form $\nabla^T \overline{\mathbf{D}} \nabla$ to the principal axes form:

$$\frac{dC}{dt} = \nabla^T \mathbf{X}\mathbf{D}'\mathbf{X}^T \nabla C\Big|_{(s,n)} = \nabla \cdot \left(\mathbf{D}'\nabla C\right)\big|_{(x',y')}, \tag{2.6}$$

where $\mathbf{X}^T\nabla|_{(s,n)} = \nabla|_{(x',y')} = [\partial/\partial x' \ \partial/\partial y']^T$ denotes the gradient in the coordinates of the principal axes (x', y'). As a result, (2.1) is finally transformed to the equation with the principal dispersion coefficient tensor $\mathbf{D}'$ in the rotated (x', y')-coordinate system. Because $\mathbf{D}'$ is a diagonal matrix, the symmetric axes of the equiconcentration line should be parallel to the directions of the x' and y' axes. Because the directions of the x' and y' axes are rotated from the original s and n axes by the amounts of orthogonal transformations, the axisymmetric concentration should also be rotated from the s and n axes. We estimated the magnitude of the rotated angle by solving the following eigenvalue problem:

$$\overline{\mathbf{D}}\nabla C = \lambda_i \nabla C, \tag{2.7}$$

where λ_i $(i = 1, 2)$ is eigenvalue of the corresponding eigenvector in $\mathbf{X}$, and each value can be derived as follows:

$$\lambda_1, \lambda_2 = \frac{D_{ss} + D_{nn}}{2} \pm \sqrt{\left(\frac{D_{ss} - D_{nn}}{2}\right)^2 + \overline{D}_{sn}{}^2}. \tag{2.8}$$

The obtained eigenvalues in (2.8) are the diagonal components of $\mathbf{D}'$:

$$\mathbf{D}' = \begin{bmatrix} \lambda_1 & 0 \\ 0 & \lambda_2 \end{bmatrix} \tag{2.9}$$

by the calculation of $\mathbf{D}' = \mathbf{X}^{-1}\overline{\mathbf{D}}\mathbf{X}$. Because the principal dispersion coefficients always have to be positive, the following is the relationship between each component of $\overline{\mathbf{D}}$:

$$\sqrt{D_{ss}D_{nn}} > \overline{D}_{sn}. \tag{2.10}$$

By (2.10), we can find the eigenvectors corresponding to λ_1 and λ_2 that are the column vectors of $\mathbf{X}$, and the directions of eigenvectors whose directions coincide with the directions of the x' and y' axes can be derived. The angle of the counterclockwise rotation φ of the x' and y' axes from the s and n axes is obtained by

$$\varphi = \arctan\left[-\frac{D_{ss} - D_{nn}}{2\overline{D}_{sn}} \pm \sqrt{\left(\frac{D_{ss} - D_{nn}}{2\overline{D}_{sn}}\right)^2 + 1}\right]. \tag{2.11}$$

Therefore, the angles of φ represent orthogonal rotation of the axes of symmetry: (x', y') from the axes of (s, n)-coordinates.

Another remarkable effect of the off-diagonal terms in the SSFD model is the difference in the resultant peak concentration. When we present the analytical solution of the instantaneously dumped point mass with respect to the (x', y')-coordinates, it is given by

$$C(x', y', t) = \frac{M}{4\pi ht\sqrt{\lambda_1\lambda_2}} \exp\left[-\frac{x'^2}{4\lambda_1 t} - \frac{y'^2}{4\lambda_2 t}\right], \tag{2.12}$$

where M is the total mass of tracer. With this solution, the equiconcentration curves are ellipses with $\sqrt{\lambda_1}$ and $\sqrt{\lambda_2}$ as the lengths of semimajor and minor axes. Using (2.12), the peak concentration at time t is inversely proportional to $\sqrt{\lambda_1\lambda_2}$, which is given by

$$\sqrt{\lambda_1\lambda_2} = \sqrt{D_{ss}D_{nn} - \overline{D}_{sn}^{\,2}} \leq \sqrt{D_{ss}D_{nn}}. \tag{2.13}$$

According to (2.12) and (2.13), the peak concentration with off-diagonal terms $M/(4\pi ht\sqrt{D_{ss}D_{nn} - \overline{D}_{sn}^{\,2}})$ is always larger than the peak concentration neglecting off-diagonal terms $M/(4\pi ht\sqrt{D_{ss}D_{nn}})$. Thus, if the off-diagonal components in the SSFD condition are ignored, the dilution degree of the pollutant is likely to be overestimated. Assuming that the corresponding CSFD and SSFD models have the same diagonal components for each dispersion coefficient tensor, the ratio of the overestimated dilution degree due to neglect of the off-diagonal components by applying the CSFD model is

$$\frac{C_p(\mathbf{D}_c, t)}{C_p\left(\overline{\mathbf{D}}, t\right)} = \frac{M/\left(4\pi ht\sqrt{D_{ss}D_{nn}}\right)}{M/\left(4\pi ht\sqrt{D_{ss}D_{nn} - \overline{D}_{sn}^{\,2}}\right)} = \frac{\sqrt{D_{ss}D_{nn} - \overline{D}_{sn}^{\,2}}}{\sqrt{D_{ss}D_{nn}}} < 1, \tag{2.14}$$

where C_p is the peak concentration. Although (2.14) is valid only in the case of instantaneous release of mass at $t = 0$ in a uniform flow field, the above analytical analysis provides the knowledge of possible overestimation in dilution degree when the CSFD model is wrongly applied to a skewed shear flow field of secondary currents.

The final characteristic of the SSFD model compared to the CSFD model is the change in the eccentricity of ellipses. The dispersive scale in the direction of the symmetric axes of concentration depends on the pair of principal dispersion coefficients, which are λ_1, λ_2 for the SSFD model and D_{ss}, D_{nn} for CSFD. Therefore, the comparison between the magnitudes of the principal dispersion coefficients accounts for the difference in the shapes of the ellipses by $\overline{\mathbf{D}}$ and $\mathbf{D}_c$. The ellipses of the concentration in the SSFD model have larger eccentricity than that of the corresponding CSFD model by the relation:

$$\begin{aligned} \max\{\lambda_1, \lambda_2\} &= \frac{D_{ss} + D_{nn}}{2} + \sqrt{\left(\frac{D_{ss} - D_{nn}}{2}\right)^2 + \overline{D}_{sn}^{\,2}} \geq \max\{D_{ss}, D_{nn}\}, \\ \min\{\lambda_1, \lambda_2\} &= \frac{D_{ss} + D_{nn}}{2} - \sqrt{\left(\frac{D_{ss} - D_{nn}}{2}\right)^2 + \overline{D}_{sn}^{\,2}} \leq \min\{D_{ss}, D_{nn}\}. \end{aligned} \tag{2.15}$$

Including (2.15), three characteristics of the SSFD model that contrast with the CSFD model have been pointed out by the eigenvalue problem solved in this section; the rotation of the major dispersion axis about the streamline, the larger peak concentration, and the larger eccentricity of the elliptical concentration. These results show that the application of the CSFD model to flows with a secondary current is not accurate because skewed vertical profiles clearly exist in the secondary current combined with the principal flow along the curves. The oblique direction of the principal dispersion with respect to the streamline and other characteristics related to the peak concentration and shape of the equiconcentration curves

were demonstrated in a numerical experiment that used the computational model established in the Eulerian coordinate system, as presented in the next section.

3. Coordinate Transformation

To deal with diverse flow directions in natural streams and rivers with irregular boundaries, conventional river hydrodynamics and mass transport models are usually established in a fixed Eulerian coordinate system, where implementing a horizontal unstructured grid is convenient. In computational models established for such curved channels with continuously changing flow directions, the principal direction of anisotropic dispersion is usually not parallel to the axes of the Cartesian coordinates. Therefore, in commonly used CSFD models, components of $\mathbf{D}_c$ constantly defined in a stream-wise curvilinear frame of reference (s, n) are transformed into nodal dispersion parameters with respect to the Eulerian-Cartesian coordinates [11–15]. The dispersion coefficient tensor $\mathbf{D}_c$ of (s, n)-coordinates is related to nodal parameters in (x, y)-coordinates through the Jacobian matrix expressed with a nodal velocity vector.

$$\mathbf{J} = \begin{bmatrix} \dfrac{\partial x}{\partial s} & \dfrac{\partial x}{\partial n} \\ \dfrac{\partial y}{\partial s} & \dfrac{\partial y}{\partial n} \end{bmatrix} = \begin{bmatrix} \dfrac{\overline{v}_x}{|\overline{v}_s|} & -\dfrac{\overline{v}_y}{|\overline{v}_s|} \\ \dfrac{\overline{v}_y}{|\overline{v}_s|} & \dfrac{\overline{v}_x}{|\overline{v}_s|} \end{bmatrix}, \tag{3.1}$$

where $\overline{v}_x$, $\overline{v}_y$ are depth-averaged velocity components in the x and y directions, respectively. Because (3.1) is orthogonal matrix, the inverse of $\mathbf{J}$ is equal to $\mathbf{J}^T$, which results in $\nabla|_{(s,n)} = \mathbf{J}^T \nabla|_{(x,y)}$. Thus, both (2.1) and (2.3) can then be transformed into equations with respect to fixed Cartesian coordinate system; by applying $\nabla|_{(s,n)} = \mathbf{J}^T \nabla|_{(x,y)}$ to (2.3),

$$\frac{dC}{dt} = \left(\mathbf{J}^T \nabla\right)^T \mathbf{D}_c \left(\mathbf{J}^T \nabla\right) C = \nabla^T \left(\mathbf{J}\mathbf{D}_c \mathbf{J}^T\right) \nabla C. \tag{3.2}$$

$\mathbf{D}_c$ is transformed into the nodal dispersion coefficients with respect to Eulerian-Cartesian coordinates: $\mathbf{J}\mathbf{D}_c\mathbf{J}^T$, where each component of $\mathbf{J}\mathbf{D}_c\mathbf{J}^T$ can be written as

$$D_{xx} = D_{nn} + (D_{ss} - D_{nn}) \frac{\overline{v}_x{}^2}{\overline{v}_s{}^2}, \tag{3.3a}$$

$$D_{xy} = D_{yx} = (D_{ss} - D_{nn}) \frac{\overline{v}_x\, \overline{v}_y}{\overline{v}_s{}^2}, \tag{3.3b}$$

$$D_{yy} = D_{nn} + (D_{ss} - D_{nn}) \frac{\overline{v}_y{}^2}{\overline{v}_s{}^2}, \tag{3.3c}$$

where D_{xx}, D_{xy}, D_{yx}, and D_{yy} are Cartesian components of the nodal dispersion coefficient tensor. As we describe for the commonly used CSFD model, (3.3a), (3.3b), and (3.3c) are the conventional way to determine nodal dispersion parameters by the longitudinal and transverse dispersion coefficients D_{ss} and D_{nn} constantly specified in a global domain.

The full dispersion coefficient tensor introduced by Fischer [2] also include D_{ns} and D_{sn} as cross-dispersion coefficients that can be specified by physical considerations as well as D_{ss} and D_{nn}:

$$
\begin{aligned}
D_{ss} &= -\frac{1}{h}\int_0^h v_s' \int_0^z \frac{1}{\varepsilon(z)} \int_0^z v_s' \, dz\, dz\, dz, \\
D_{sn} &= -\frac{1}{h}\int_0^h v_s' \int_0^z \frac{1}{\varepsilon(z)} \int_0^z v_n' \, dz\, dz\, dz, \\
D_{ns} &= -\frac{1}{h}\int_0^h v_n' \int_0^z \frac{1}{\varepsilon(z)} \int_0^z v_s' \, dz\, dz\, dz, \\
D_{nn} &= -\frac{1}{h}\int_0^h v_n' \int_0^z \frac{1}{\varepsilon(z)} \int_0^z v_n' \, dz\, dz\, dz,
\end{aligned}
\tag{3.4}
$$

where h is flow depth; ε is the vertical turbulent diffusion coefficient; v_s', v_n' the vertical deviations of the point velocities with respect to depth-averaged velocities in the s and n directions, respectively. Because the tensor dispersion coefficients proposed by Fischer [2] is expressed in fixed coordinates, the same transformation as did in (3.3a), (3.3b), and (3.3c) is needed for components of SSFD tensor to be applied in a flow where the flow direction continuously changes as in a curved stream: the components of $\mathbf{JDJ}^T$ in SSFD model, which is analogous to $\mathbf{JD}_c\mathbf{J}^T$ of CSFD model, are derived as follows:

$$
\begin{aligned}
D_{xx} &= D_{ss}\frac{\overline{v}_x{}^2}{\overline{v}_s{}^2} - (D_{sn}+D_{ns})\frac{\overline{v}_x\overline{v}_y}{\overline{v}_s{}^2} + D_{nn}\frac{\overline{v}_y{}^2}{\overline{v}_s{}^2}, \\
D_{xy} &= (D_{ss}-D_{nn})\frac{\overline{v}_x\overline{v}_y}{\overline{v}_s{}^2} + D_{sn}\frac{\overline{v}_x{}^2}{\overline{v}_s{}^2} - D_{ns}\frac{\overline{v}_y{}^2}{\overline{v}_s{}^2}, \\
D_{yx} &= (D_{ss}-D_{nn})\frac{\overline{v}_x\overline{v}_y}{\overline{v}_s{}^2} - D_{sn}\frac{\overline{v}_y{}^2}{\overline{v}_s{}^2} + D_{ns}\frac{\overline{v}_x{}^2}{\overline{v}_s{}^2}, \\
D_{yy} &= D_{ss}\frac{\overline{v}_y{}^2}{\overline{v}_s{}^2} + (D_{sn}+D_{ns})\frac{\overline{v}_x\overline{v}_y}{\overline{v}_s{}^2} + D_{nn}\frac{\overline{v}_x{}^2}{\overline{v}_s{}^2}.
\end{aligned}
\tag{3.5}
$$

Obviously, (3.5) reduces to (3.3a), (3.3b), and (3.3c) if D_{sn}, D_{ns} are assumed to be zero. Through (3.5), the coefficients of the SSFD tensor in (s,n)-coordinates are transformed into nodal dispersion coefficients in Eulerian (x,y)-coordinates (Figure 2).

Using the transformed component of the nodal CSFD and SSFD coefficient tensor with respect to the global coordinate system, we present expanded the Cartesian forms of (2.1) and (2.3) as follows:

$$
\frac{\partial C}{\partial t} + \frac{\partial(\overline{v}_x C)}{\partial x} + \frac{\partial(\overline{v}_y C)}{\partial y} = \frac{\partial}{\partial x}\left(D_{xx}\frac{\partial C}{\partial x} + D_{xy}\frac{\partial C}{\partial y}\right) + \frac{\partial}{\partial y}\left(D_{yx}\frac{\partial C}{\partial x} + D_{yy}\frac{\partial C}{\partial y}\right). \tag{3.6}
$$

For complex geometries of curved streams with irregular boundaries, an unstructured grid with the finite element or finite volume method is more useful than a numerical method with a structure grid. Therefore, we solve (3.6) by the finite element model established in the Eulerian coordinate system [16]. In this model, the Petrov-Galerkin approximation with a bilinear shape function is applied for spatial discretization, and the Crank-Nicolson type of discrete time marching is used for transient term. For each nodal point, the components of the dispersion tensor are determined by (3.3a), (3.3b), and (3.3c) in the CSFD model and by (3.5) in the SSFD model.

4. Test for the Direction of Principal Dispersion

In order to observe the oblique direction of the principal dispersion with respect to the longitudinal streamline, a solute mixing in uniform oscillatory flow was simulated by the established CSFD and SSFD models. The direction of the oscillatory flow was varied at $\theta = 0°$, 30°, and 45° counterclockwise with respect to the x-axis, to test the applicability of the derived (3.5) for various flow directions. Each result of the SSFD model was compared with that of the corresponding CSFD model with the same D_{ss} and D_{nn}. The velocity of the uniform oscillatory flow was defined by a cosine curve with respect to time as

$$(\overline{v}_x, \overline{v}_y) = (\overline{v}_s \cos \phi t \cos \theta, \overline{v}_s \cos \phi t \sin \theta), \tag{4.1}$$

where $\overline{v}_s = 0.25\,\mathrm{m/s}$ and $\phi = 2\pi/(12\,\mathrm{h})$. In this flow field, the concentration distribution with a two-dimensional Gaussian profile was given as the initial concentration at the center of a 20 km × 20 km rectangular computational domain; this is the conventional test condition for the advection-dispersion problem [17]. The initial Gaussian distribution was obtained by the analytic solution after 1 day of pure diffusion of point mass $M = 5 \times 10^4\,\mathrm{kg/m}$ with constant isotropic diffusion coefficient $k = 5\,\mathrm{m}^2/\mathrm{s}$:

$$C(x, y, 0) = \frac{M}{4\pi k \tau} \exp\left[-\frac{x^2}{4k} - \frac{y^2}{4k}\right]\Bigg|_{\tau = 1\,\mathrm{day}}. \tag{4.2}$$

By (4.2), the initial peak concentration was 9.21 ppm. A rectangular element was chosen as a finite element grid of the test case due to its simplicity. The grid and time step sizes were determined as $\Delta x = \Delta y = 1\,\mathrm{km}$ and $\Delta t = 900\,\mathrm{sec}$. The maximum Courant number was $(\overline{v}_s \Delta t)/\Delta x = 0.225$, which guaranteed a stable solution. The initial concentration was spread under oscillatory flow conditions over 960 time steps, which covered a period of 6 days. Diagonal components of the SSFD and CSFD coefficient tensors of this case were arbitrarily determined as $D_{ss} = 10$ and $D_{nn} = 1\,\mathrm{m}^2/\mathrm{s}$. With these longitudinal and transverse coefficients, the off-diagonal components of the SSFD coefficient were determined as $D_{sn} = D_{ns} = 3.125\,\mathrm{m}^2/\mathrm{s}$, following the dispersion tensor for the application example in Fischer [2]:

$$\mathbf{D} = \frac{h^2}{\varepsilon} \begin{bmatrix} \dfrac{U_o{}^2}{120} & \dfrac{5U_oV_o}{192} \\ \dfrac{5U_oV_o}{192} & \dfrac{V_o{}^2}{12} \end{bmatrix}, \tag{4.3}$$

where U_o, V_o are magnitude of the longitudinal and transverse velocity deviation defined in Figure 3. The dispersion coefficient in (4.3) was derived from the approximated mean velocity profile of a continental shelf, as given in Figure 3. When we assume a skewed shear flow structure for secondary currents as shown in Figure 3, the intensity of the secondary current is maximized for the same transverse velocity deviation. The diagonal dispersion coefficient tensor with eigenvalues of $\mathbf{D}$ is $\mathbf{D}' = \begin{bmatrix} 10.979 & 0 \\ 0 & 0.021 \end{bmatrix}$ m^2/s by (2.8) and (2.9), and the coefficient tensor of the corresponding CSFD model is $\mathbf{D}_c = \begin{bmatrix} 10 & 0 \\ 0 & 1 \end{bmatrix}$ m^2/s.

In Figure 3, the concentration distributions of the SSFD model $C(\mathbf{D}, t)$ at $t = 6$ days are compared to those of the corresponding CSFD model $C(\mathbf{D}_c, t)$. In the results from the CSFD model, which are given in Figures 4(a), 4(c), and 4(e), the direction of the principal dispersion coincided with the oscillatory flow direction of each case. However, the differences in the symmetric axes of the concentration by SSFD model and the corresponding oscillatory flow direction were found to be $\psi = 17.4°$, as shown in Figures 4(b), 4(d), and 4(f). This difference confirmed the eigenvalue analysis results given in the previous section. The directions of the eigenvectors of $\mathbf{D} = \begin{bmatrix} 10 & 3.125 \\ 3.125 & 1 \end{bmatrix}$ m^2/s were computed (2.11) to be oriented toward 17.4° and −72.6° with respect to the s axis.

The results in Figure 4 also show the applicability of (3.5); the coordinate transformation of dispersion tensor by (3.5) successfully introduced the full SSFD coefficient tensor in the numerical grid of Eulerian coordinates. When we consider solute transport in complex flow with continuously changing flow direction such as meandering streams, the whole problem is effectively solved in one domain based on the Eulerian frame of reference using (3.5). As presented in the next section, two flows with secondary currents case studies for application are considered. Through those examples, other aspects of the SSFD model—the increase in peak concentration and eccentricity of the tracer ellipse—were examined.

5. Application in Flows with Secondary Currents

In order to investigate the performance of the SSFD model in a flow field with secondary currents, an example case similar to the classic teacup experiment was considered. First, we assumed a solid-body rotation of water in a coaxial cylindrical container, as in Figure 5, to produce a so-called forced vortex. In this kind of fluid rotation, there is a pressure gradient from the perimeter toward the center. When we stop the rotation of the container abruptly, this pressure gradient coupled with the slower speed near the bottom boundary layer causes the secondary flow that makes the boundary layer spiral inward to the axis of circulation. Except for near the side wall and bottom, the fluid continues to rotate as before. Thus, a rotating flow field of vortex with a constant angular velocity can be assumed for a while in the container. We assume that a certain passive solute is dropped as an instantaneous point source as soon as the container is stopped. For this case, both dispersion models were applied to observe the difference in modeling results: SSFD model accounted for the effect of the secondary flow and CSFD neglected the secondary flow effect.

The outer and inner cylinders had radii of 10 and 3 m, respectively, and the container rotated at an angular speed of $\omega = 2\pi/(3 \text{ min})$. The plan view of the container and grid for the simulation are presented in Figure 6; the grid sizes in the radial and tangential directions were 0.5 m and $\pi r/40$, respectively, where r is the distance from the axis of rotation. The simulation was performed by the SSFD model with an arbitrarily determined $\mathbf{D} = \begin{bmatrix} 0.01 & -0.002 \\ -0.002 & 0.001 \end{bmatrix}$ m^2/s of which the magnitude of the off-diagonal component was smaller than those of (4.3). The negative sign in the off-diagonal components of $\mathbf{D}$ was determined by

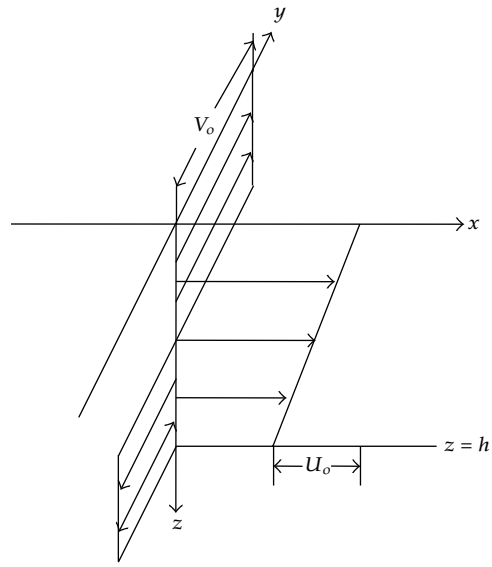

Figure 3: Representation of the shear flow on the continental shelf of the middle Atlantic bight [2].

(3.3b) and (3.3c) and the circulating direction of the secondary current, which was negative n-direction in the upper part of the flow and positive n-direction in the lower part. The dispersion coefficient tensor of the corresponding CSFD model was $\mathbf{D}_c = \begin{bmatrix} 0.01 & 0 \\ 0 & 0.001 \end{bmatrix} \mathrm{m}^2/\mathrm{s}$. An initial concentration of 100 was dropped at the nodal point $(x, y) = (6.5\,\mathrm{m}, 0)$.

The simulation results at $t = 36, 72, \ldots, 180\,\mathrm{sec}$ for both CSFD and SSFD model are given in Figure 7. Figure 7(a) shows that the curvilinear axis of the principal dispersion direction in $C(\mathbf{D}_c, t)$ coincided with the circular streamline of the rotating flow. However, in Figure 7(b), the result of $C(\mathbf{D}, t)$ shows that the direction of the major dispersion axis spiraled outward to the perimeter of the outer cylinder due to the rotation of the symmetric axis of the tracer cloud. As pointed out in Section 2, the peak concentration of $C(\mathbf{D}, t)$ was computed to be larger than that of $C(\mathbf{D}_c, t)$; when the tracer cloud rotated for one complete round at 180 s, $C_p(\mathbf{D}_c, t)$ and $C_p(\mathbf{D}, t)$ were founded to be 3.305 and 3.851, respectively. Along with the larger peak concentration, the SSFD model increased the eccentricity of the ellipse of the tracer cloud. The tracer clouds in Figure 7(b) are longer and narrower than those in Figure 7(a).

For another example case of flow with secondary currents, the dispersion problem in a strongly curved channel with secondary flow was solved by the SSFD and CSFD modes. The famous experiments provided by Rozovski [18] were chosen as an example problem, in which the velocity field was measured along the bend of a U-shaped laboratory channel with a rectangular cross-section. The width of the channel was 0.8 m with inner and outer bend radii of 0.4 and 1.2 m, respectively, and the water flowed on the zero-slope bottom with a mean velocity of 0.25 m/s for his experimental case Run 8.

The velocity field in the whole domain was reproduced by the commonly used depth-averaged flow analysis model RMA-2 in TABS-MD [19]. Figure 8 compares the computed velocities against the measured data of Rozovski [18] at five cross-sections in the bend and shows that the computational result described the flow field along the channel bend well. When water flowed along the bend of the rectangular channel, the usual path of velocity maxima is located near the inner bend at the entrance to the bend and shift to near the outer

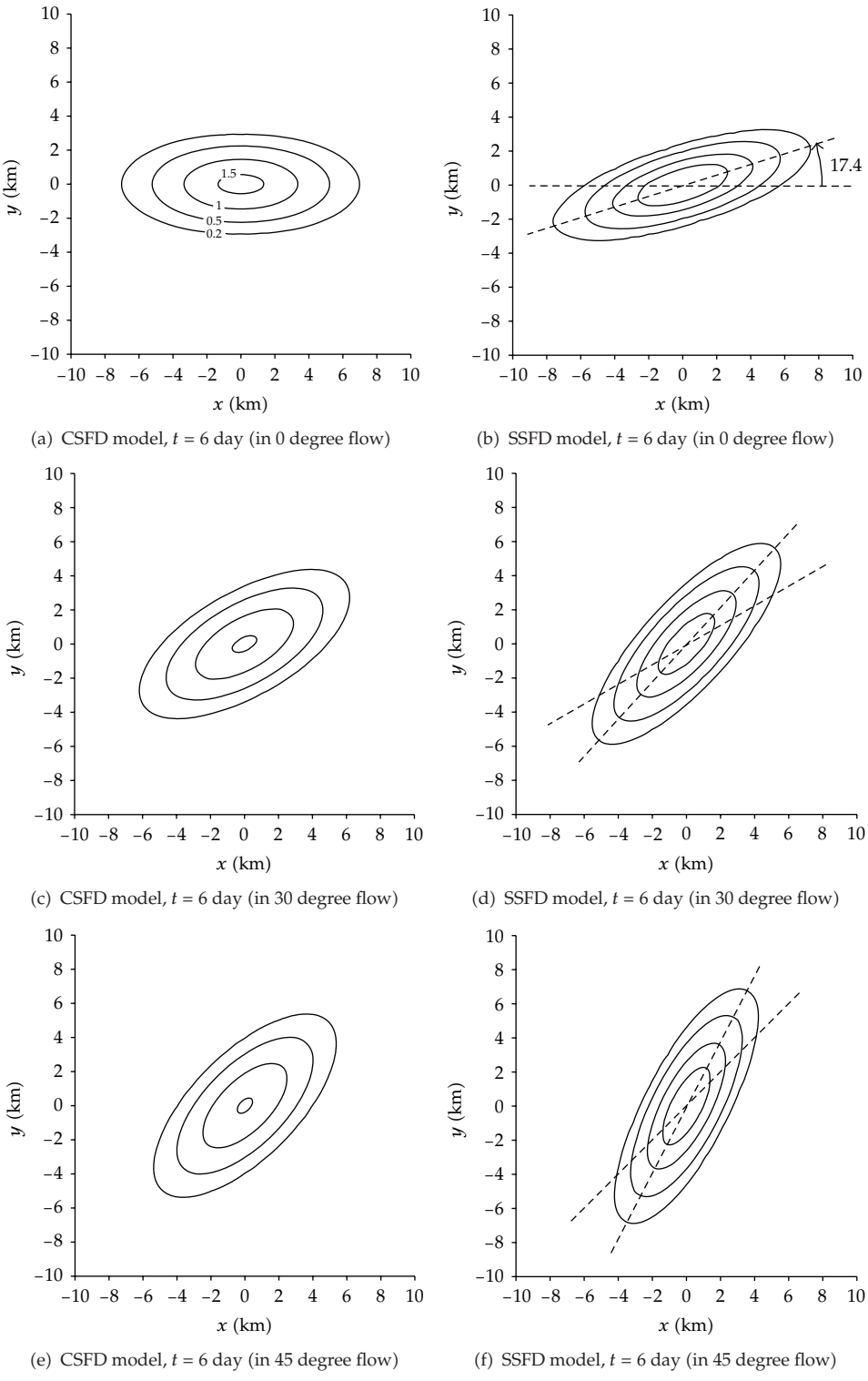

(a) CSFD model, t = 6 day (in 0 degree flow)

(b) SSFD model, t = 6 day (in 0 degree flow)

(c) CSFD model, t = 6 day (in 30 degree flow)

(d) SSFD model, t = 6 day (in 30 degree flow)

(e) CSFD model, t = 6 day (in 45 degree flow)

(f) SSFD model, t = 6 day (in 45 degree flow)

Figure 4: Concentration distribution in uniform oscillatory flow (unit: ppm).

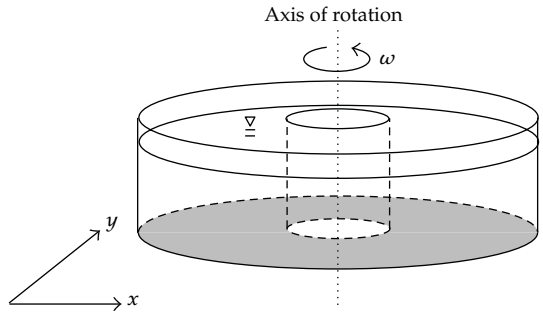

Figure 5: Rotating water in coaxial cylindrical container.

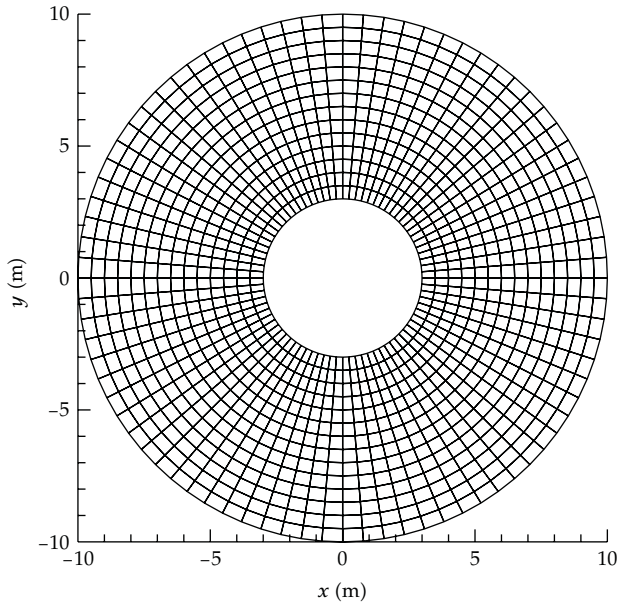

Figure 6: Grid system for coaxial cylindrical container.

bank at the exit as shown in the measurement of longitudinal velocity in curved channels [20–22] as observed in Figure 8. This is due to the increase of the water elevation at the outer bank and the decrease at the inner bank by centrifugal forces in curved channels [23]. The principal flow following the velocity maxima along the bend is accompanied by the secondary flow by which the path line is partly downstream and partly across the channel from the outer bank toward the inner bank at the bottom. To observe the solute spreading around the bend, the initial concentration of 100 was defined at the centered point of bend entrance $(x, y) = (6\,\text{m}, -5.75\,\text{m})$. A dispersion coefficient tensor with $\mathbf{D} = \begin{bmatrix} 0.005 & -0.002 \\ -0.002 & 0.001 \end{bmatrix} \text{m}^2/\text{s}$ was arbitrarily selected for the SSFD model, and $\mathbf{D}_c = \begin{bmatrix} 0.005 & 0 \\ 0 & 0.001 \end{bmatrix} \text{m}^2/\text{s}$ was used for the corresponding CSFD model.

Concentration distributions at $t = 4$ and $8\,\text{s}$ were presented in Figures 9 and 10, respectively. According to Figures 9 and 10, advection by a lateral nonuniform flow coupled with the skewed shear flow dispersion causes the remarkable change in the shape of tracer cloud compared to the CSFD model: the elliptical curves of the equiconcentration computed

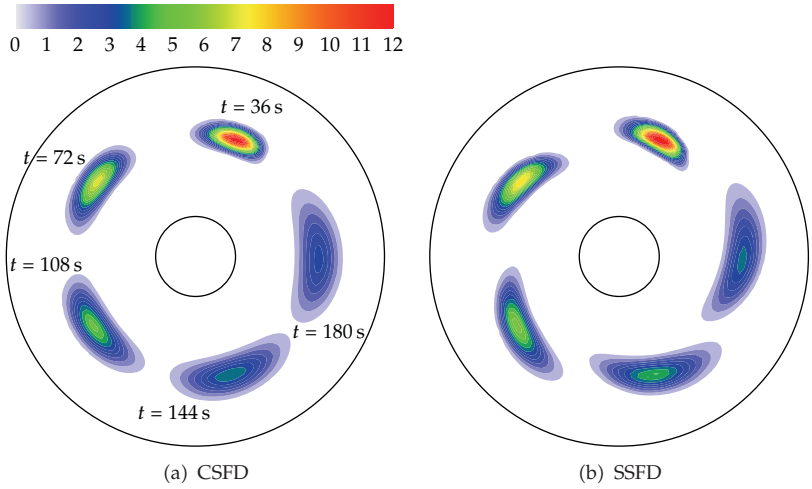

Figure 7: Concentration distribution in coaxial cylindrical container.

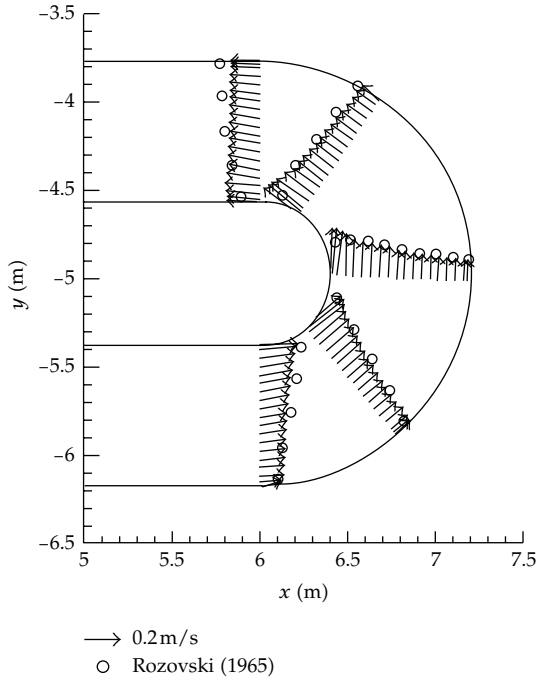

Figure 8: Comparison between computed and measured flow fields in Rozovski's channel.

by the CSFD model maintained the elongated shape along the streamline until the total mass exited the bend, whereas those of the SSFD model were much shorter. These results seem to be opposite to the elongated shape of the tracer cloud by the SSFD model shown in the previous example of a force vortex. The mechanism for the generation of the clustered concentration by the SSFD model in this example is explained as follows. When the SSFD coefficient tensor is applied, the direction of the major dispersion axis becomes oblique clockwise with respect to the streamlines; this is the typical mechanism for skewed shear flow dispersion as well as

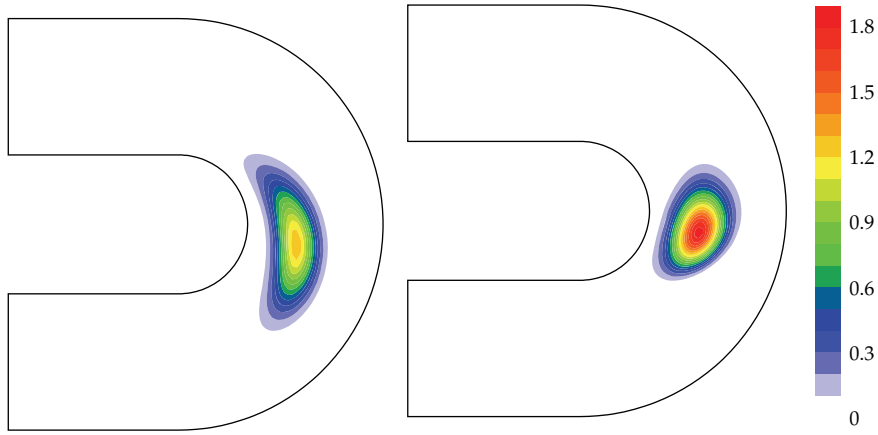

(a) CSFD (b) SSFD

Figure 9: Concentration distribution in Rozovski's channel at $t = 4$ s.

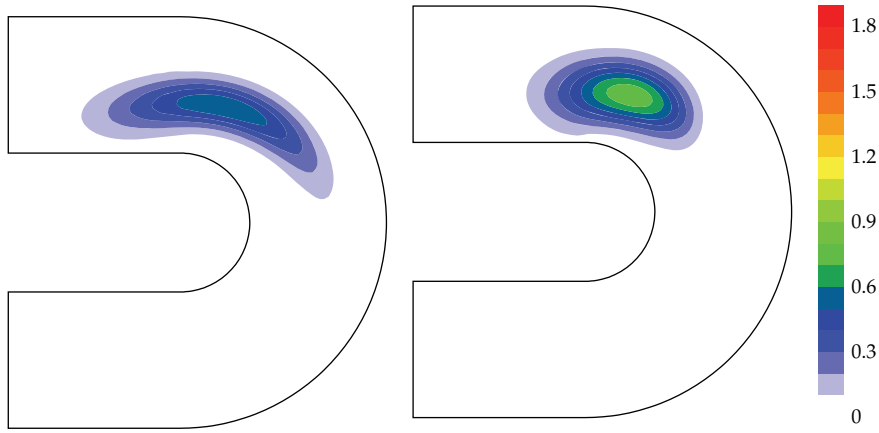

(a) CSFD (b) SSFD

Figure 10: Concentration distribution in Rozovski's channel at $t = 8$ s.

the previous example. However, in contrast to the force vortex, the nonuniform longitudinal velocities of the channel bend shift each particle in the skewed tracer cloud with different speeds along each streamline; the particles near the inner bank move faster than the particles near the outer bank. As a result, the dispersed particles in the tracer cloud skewed about streamlines are centered into the mean displacement of the moving fluids. In particular, at $t = 4$ s, the shape of the equiconcentration curve appeared to be rounded and concentrated.

The rotation of the major dispersion axis in the SSFD model and the nonuniform advection along the curved streamline had a combined effect on the increase in the peak concentration. The peak concentrations at $t = 8$ s, as given in Figure 10, were found to be 0.60 and 0.78 for the CSFD and SSFD models, respectively. This shows that the application of the CSFD model in the curved channel with a strong secondary current—instead of the SSFD model—may underestimate the peak concentration of the transported pollutant from upstream. Although the secondary current is known to activate transverse dispersion and

increase the dilution effect, the results in this study indicate that the skewed vertical shear profile of the secondary current may offset the enhancement of dilution caused by the large transverse dispersion.

6. Conclusion

In this study, it was proposed that the SSFD coefficient tensor should be applied for 2D passive solute transport modeling in the flow with secondary current because of its vertically skewed shear flow structure. Mathematical analysis of eigenvalue problem pointed out several significant effects of the off-diagonal terms of dispersion tensor: the rotation of principal direction of dispersion with respect to the streamline, the increase of peak concentration, and the change in eccentricity of elliptical concentration. To apply full dispersion coefficient tensor defined in a stream-wise curvilinear coordinate system to the numerical model on the Eulerian-Cartesian coordinates, transformation relationship was derived with given depth-averaged velocity field. With the derived transformation equation, 2D numerical model was established with finite element method on the Eulerian coordinate system. Numerical tests show that the coordinate transformation relationship derived in this study successfully introduced the SSFD coefficient tensor in the numerical grid of Eulerian coordinates. It was also shown that there is a possibility of overestimation in dilution of pollutant if CSFD model was applied instead of SSFD model in the dispersion process affected by secondary currents. The conventional 2D solute mixing modules equipped in the various hydrodynamic modeling packages are expected to predict more reliable mixing patterns of pollutants by including off-diagonal terms as in SSFD model, when it is applied to flow field with secondary currents.

Nomenclature

C:	Depth-averaged concentration
C_p:	Peak concentration
D_{ss}, D_{sn}, D_{ns}, and D_{nn}:	Components of the full dispersion coefficient tensor defined in stream-wise curvilinear coordinates
$\overline{D}_{sn}$:	Mean value of D_{sn} and D_{ns}
D_{xx}, D_{xy}, D_{yx}, and D_{yy}:	Components of the nodal dispersion coefficient tensor in the Eulerian-Cartesian coordinates
$\mathbf{D}$:	Matrix notation of SSFD coefficient tensor in curvilinear coordinates
$\mathbf{D}_c$:	Matrix notation of CSFD coefficient tensor in curvilinear coordinates
$\overline{\mathbf{D}}$:	Symmetric version of SSFD coefficient tensor, which takes $\overline{D}_{sn}$ as off-diagonal entries
$\mathbf{D}'$:	Principal dispersion coefficient tensor, which takes eigenvalues λ_1, λ_2 as entries
h:	Flow depth
$\mathbf{J}$:	Jacobian matrix for coordinate transformation
k:	Isotropic diffusion coefficient
M:	Total mass of tracer

n: Axis normal to the streamline in the stream-wise curvilinear coordinate system
s: Axis along the streamline in the stream-wise curvilinear coordinate system
t: Time
Δt: Discretization size in time
U_o, V_o: Magnitude of longitudinal and transverse velocity deviations in Figure 3
$v_s,\ v_n$: Horizontal velocities on the s-, n-axis
$\overline{v}_s$: Longitudinal depth-averaged velocity
$v_s',\ v_n'$: Vertical deviations of the point velocities with respect to depth-averaged $v_s,\ v_n$
$\overline{v}_x,\ \overline{v}_y$: Ddepth-averaged velocity components in the x and y directions
$x,\ y$: Axes of the Eulerian-Cartesian coordinate system
$x',\ y'$: Axes with identical directions as the principal axes of $\overline{\mathbf{D}}$
Δx: Discretization size in the x direction
Δy: Discretization size in the y direction
$\mathbf{X}$: Matrix that takes the eigenvectors of $\overline{\mathbf{D}}$ as column vectors
z: Axis of the vertical direction
ε_n: Transverse turbulent diffusion coefficient
ε: Vertical turbulent diffusion coefficient
ϕ: Angular frequency of oscillatory flow
θ: Angle of oscillatory direction with respect to the x-direction
$\lambda_1,\ \lambda_2$: Eigenvalues of $\overline{\mathbf{D}}$
ω: Angular speed of rotation of coaxial cylindrical container
ψ: Angle of counterclockwise rotation from the s axis of the principal dispersion axes.

References

[1] G. I. Taylor, "Dispersion of soluble matter in solvent flowing slowly through a tube," *Proceedings of the Royal Society A*, vol. 219, pp. 186–203, 1953.

[2] H. B. Fischer, "On the tensor form of the bulk dispersion coefficient in a bounded skewed shear flow," *Journal of Geophysical Research*, vol. 83, no. C5, pp. 2373–2375, 1978.

[3] C. W. Almquist and E. R. Holley, "Transverse mixing in meandering laboratory channels with rectangular and naturally varying cross sections," Tech. Rep. CRWR-205, University of Texas, Austin, Texas, 1985.

[4] K. O. Baek, I. W. Seo, and S. J. Jeong, "Evaluation of dispersion coefficients in meandering channels from transient tracer tests," *Journal of Hydraulic Engineering*, vol. 132, no. 10, pp. 1021–1032, 2006.

[5] J. B. Boxall and I. Guymer, "Analysis and prediction of transverse mixing coefficients in natural channels," *Journal of Hydraulic Engineering*, vol. 129, no. 2, pp. 129–139, 2003.

[6] J. B. Boxall, I. Guymer, and A. Marion, "Transverse mixing in sinuous natural open channel flows," *Journal of Hydraulic Research*, vol. 41, no. 2, pp. 153–165, 2003.

[7] Y. C. Chang, *Lateral mixing in meandering channels*, Ph.D. thesis, University of Iowa, Iowa City, Iowa, USA, 1971.

[8] B. G. Krishnappan and Y. L. Lau, "Transverse mixing in meandering channels with varying bottom topography," *Journal of Hydraulic Research*, vol. 15, no. 4, pp. 351–371, 1977.

[9] A. Marion and M. Zaramella, "Effects of velocity gradients and secondary flow on the dispersion of solutes in a meandering channel," *Journal of Hydraulic Engineering*, vol. 132, no. 12, pp. 1295–1302, 2006.

[10] E. Kreyszig, *Advanced Engineering Mathematics*, John Wiley & Sons, 9th edition, 2006.

[11] V. Alavian, "Dispersion tensor in rotating flows," *Journal of Hydraulic Engineering*, vol. 112, no. 8, pp. 771–777, 1986.

[12] D. Liang, X. Wang, R. A. Falconer, and B. N. Bockelmann-Evans, "Solving the depth-integrated solute transport equation with a TVD-MacCormack scheme," *Environmental Modelling and Software*, vol. 25, no. 12, pp. 1619–1629, 2010.

[13] M. Piasecki and N. D. Katopodes, "Identification of stream dispersion coefficients by adjoint sensitivity method," *Journal of Hydraulic Engineering*, vol. 125, no. 7, pp. 714–724, 1999.

[14] R. W. Preston, "The representation of dispersion in two-dimensional shallow water flow," Report TPRD/L/278333/N84, Central Electricity Research Laboratories, Leatherhead, England, 1985.

[15] A. Younes and P. Ackerer, "Solving the advection-diffusion equation with the Eulerian-Lagrangian localized adjoint method on unstructured meshes and non uniform time stepping," *Journal of Computational Physics*, vol. 208, no. 1, pp. 384–402, 2005.

[16] I. W. Seo, M. E. Lee, and K. O. Baek, "2D modeling of heterogeneous dispersion in meandering channels," *Journal of Hydraulic Engineering*, vol. 134, no. 2, pp. 196–204, 2008.

[17] R. T. Cheng, V. Casulli, and S. N. Milford, "Eulerian-Lagrangian solution of the convection-dispersion equation in natural co-ordinates," *Water Resources Research*, vol. 20, no. 7, pp. 944–952, 1984.

[18] I. L. Rozovski, *Flow of Water in Bends of Open Channels*, Israel Program for Scientific Translation, Jerusalem, Israel, 1965.

[19] I King, B. P. Donnell, J. V. Letter, W. H. McAnally, W. A. Thomas, and C. LaHatte, "RMA2 users guide 4.5x," US Army, Engineer Research and Development Center, Waterways Experiment Station, Coastal and Hydraulics Laboratory, 2006.

[20] Y. C. Chang, *Lateral mixing in meandering channels*, Ph.D. thesis, University of Iowa, Iowa City, Iowa, USA, 1971.

[21] H. J. DeVriend, "Flow measurements in a curved rectangular channel," Internal Report number 9-79, Delft University of Technology, Department of Civil Engineering, Laboratory of Fluid Mechanics, 1979.

[22] S. Fukuoka, *Longitudinal dispersion in sinuous channels*, Ph.D. thesis, University of Iowa, Iowa City, Iowa, USA, 1971.

[23] A. O. Demuren and W. Rodi, "Calculation of flow and pollutant dispersion in meandering channels," *Journal of Fluid Mechanics*, vol. 172, pp. 63–92, 1986.

Hindawi Publishing Corporation
Journal of Applied Mathematics
Volume 2012, Article ID 681585, 15 pages
doi:10.1155/2012/681585

Research Article

Numerical Simulation of Oil Spill in Ocean

Yong-Sik Cho,[1] Tak-Kyeom Kim,[1] Woochang Jeong,[2] and Taemin Ha[1]

[1] *Department of Civil and Environmental Engineering, Hanyang University, 222 Wangsimni-ro, Seongdong-gu, Seoul 133-791, Republic of Korea*
[2] *Department of Civil Engineering, Kyungnam University, 449 Wolyoung-dong, Masan 631-701, Republic of Korea*

Correspondence should be addressed to Taemin Ha, kevin4324@hanyang.ac.kr

Received 4 January 2012; Revised 29 March 2012; Accepted 2 April 2012

Academic Editor: Shuyu Sun

The spreading of oil in an open ocean may cause serious damage to a marine environmental system. Thus, an accurate prediction of oil spill is very important to minimize coastal damage due to unexpected oil spill accident. The movement of oil may be represented with a numerical model that solves an advection-diffusion-reaction equation with a proper numerical scheme. In this study, the spilled oil dispersion model has been established in consideration of tide and tidal currents simultaneously. The velocity components in the advection-diffusion-reaction equation are obtained from the shallow-water equations. The accuracy of the model is verified by applying it to a simple but significant problem. The results produced by the model agree with corresponding analytical solutions and field-observed data. The model is then applied to predict the spreading of an oil spill in a real coastal environment.

1. Introduction

In an ocean environment, a spilled oil due to an unexpected accident may cause a serious damage. Thus, an accurate prediction of behaviors of split oil is very significant to keep coastal environmental system. The area of oil spreading can be predicted numerically by solving the proper equations governing the flow field and the associated mass transport phenomenon. The most reasonable choice is probably an advection-diffusion equation consisted of both advection and diffusion. The equation is difficult to solve numerically because it is represented by both hyperbolic- and parabolic-type partial differential equations. A standard split operator approach is a plausible and practical choice for solving the advection-diffusion-type partial differential equation [1]. The hyperbolic (advection) and parabolic (diffusion) components of the equation are solved separately using methods that

properly and simply simulate the physical behaviors. Numerical solutions obtained from the advection and diffusion equations are then combined.

An oil spill accident is regarded as a kind of a disaster because it causes not only fatal destruction of the marine environment but also enormous cost of the disaster prevention and the damage compensation. Thus, it is important to accurately predict the spread range of the spilled oil as an early stage countermeasure against a disaster. In the last three decades, many investigators have studied the transport processes of oil spills based on the trajectory method [2–4]. Those methods have been applied in river-lake system [5–7] and seas [8–11]. Some commercial oil spill models, such as, COZOIL [12], NOAA [13], OILMAP [14], WOSM [15], have been used to determine the oil movement and distribution in the water body. However, transport of oil spills has been conducted considering tidal currents simultaneously in only few researches. Furthermore, oil spills processes in a field of strong tide and tidal currents have not been investigated.

In this study, the spilled oil dispersion model has been established in consideration of tide and tidal currents simultaneously. The Hebei Spirit oil spill that occurred on December 7, 2007 is the largest oil spill accident occurred in the Yellow Sea. In the Yellow Sea, tidal currents are very strong and should be considered to investigate related coastal processes. Therefore, the accuracy of the model for predicting tide and tidal currents is very important to investigate oil spreading in this area. Subsequently, by computing the diffusion distribution on the Hebei Spirit oil spill considering tidal currents simultaneously, verification has been made through comparison of the diffusion distribution and the field-observed data between at 8 p.m. on December 7, 2007 when the spilled oil flowed into the whole Manripo and Sinduri seashore and at 11 a.m. on December 11, 2007 when the satellite photographs exist. Also, this study aims to prepare for a possible accident in the future and provide the basic materials for establishing the disaster prevention of the oil spill pollution.

In the following section, the governing equations are described first. The numerical model is then presented and detailed description is followed. Numerical simulations of tide and tidal currents are conducted to test the applicability of the spilled oil spreading model in the Yellow Sea, and the verification has been made comparing numerical results with the field observed data. Also, the model is verified conducting the numerical calculations on the simple diffusion distribution problem. The model is then applied to predict the Hebei Spirit oil spill in a real coastal environment. Finally, concluding remarks are made.

2. Governing Equations

The behaviors of tide and tidal currents may be described by the following nonlinear shallow-water equations [16, 17]:

$$\frac{\partial \eta}{\partial t} + \frac{\partial P}{\partial x} + \frac{\partial Q}{\partial y} = 0, \tag{2.1}$$

$$\frac{\partial P}{\partial t} + \frac{\partial}{\partial x}\left(\frac{P^2}{H}\right) + \frac{\partial}{\partial y}\left(\frac{PQ}{H}\right) + gH\frac{\partial \eta}{\partial x} + \frac{\tau_x}{\rho} = 0, \tag{2.2}$$

$$\frac{\partial Q}{\partial t} + \frac{\partial}{\partial x}\left(\frac{PQ}{H}\right) + \frac{\partial}{\partial y}\left(\frac{Q^2}{H}\right) + gH\frac{\partial \eta}{\partial y} + \frac{\tau_y}{\rho} = 0. \tag{2.3}$$

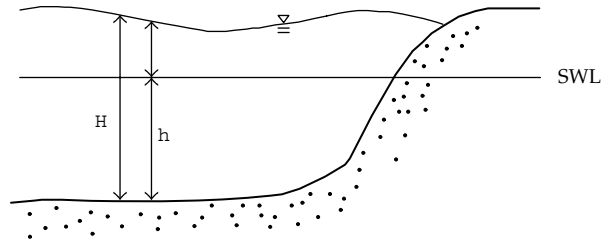

Figure 1: A definition sketch of the free surface displacement and local water depth.

In (2.1)–(2.3), η represents the free surface displacement and H is the total water depth defined as $H = \eta + h$ with h being a local still water depth (Figure 1), P and Q are volume flux components along the x- and y-axis directions defined as $P = uH$ and $Q = vH$ with u and v being the depth-integrated velocity components in the x- and y-axis directions, and τ_x and τ_y are bottom frictional effects of the x- and y-axis directions, respectively.

The study is focused to investigate the oil spreading in a limited area in the Southern part of the Korean Peninsula and thus the Cartesian coordinate system is then employed. The boundary conditions along the offshore are provided by a large-scale numerical model [18]. The bottom frictional effects may play a significant role in the very shallow zone. Thus, the Manning's empirical formula is employed in the study given as:

$$\begin{aligned} \frac{\tau_x}{\rho} &= \frac{gn^2}{H^{7/3}} P\sqrt{P^2 + Q^2}, \\ \frac{\tau_y}{\rho} &= \frac{gn^2}{H^{7/3}} Q\sqrt{P^2 + Q^2}. \end{aligned} \tag{2.4}$$

In (2.4), n is the Manning's roughness coefficient. In this study, the Manning coefficient of $n = 0.013$ has been used.

It is well known that the change of sea level is very complicated and affected by many physical phenomena such as waves, tides, and others. Among these, the tide may be the most dominant force for the oil spreading in the Yellow Sea. In this study, therefore, the tide is only investigated in a very limited area without considering any interaction with other physical phenomena.

In this study, a source or sink can be described to a following equation [19]:

$$S(C) = \frac{dS}{dt} = \frac{dS}{dC}\frac{dC}{dt}, \tag{2.5}$$

in which C represents the concentration of the oil in the sea. The source or sink $S(C)$ is assumed to be nonlinear and is linearized using the Newton-Raphson iterative technique [20] as:

$$S = S^* + \left.\frac{dS}{dC}\right|^* (C - C^*), \tag{2.6}$$

in which the superscript $(*)$ represents a previous step and the sedimentation rate, k can be derived as the following relation [21]:

$$k = \left.\frac{dS}{dC}\right|^{*}. \tag{2.7}$$

By applying an operator splitting approach to (2.1), the following advection equation can first be obtained by:

$$\frac{\partial C}{\partial t} + \frac{\partial (CU)}{\partial x} + \frac{\partial (CV)}{\partial y} = 0, \tag{2.8}$$

and the diffusion-reaction equation can then be derived by

$$\frac{\partial C}{\partial t} = \frac{1}{H}\frac{\partial}{\partial x}\left[HD_{xx}\frac{\partial C}{\partial x} + HD_{xy}\frac{\partial C}{\partial y}\right] + \frac{1}{H}\frac{\partial}{\partial y}\left[HD_{yx}\frac{\partial C}{\partial x} + HD_{yy}\frac{\partial C}{\partial y}\right] + S, \tag{2.9}$$

in which D_{xx}, D_{xy}, D_{yx}, D_{yy} represent the diffusion coefficients.

3. Numerical Model

The continuity and momentum equations given by (2.1)–(2.3) are solved by the finite difference approximations. The detailed description of the finite difference method can be found in literatures [2, 3] and is not repeated here. Firstly, the advection equation can be discretized by using the SOWMAC (second-order wave equation method for advective calculation) scheme based on the characteristic method and is given as [22]

$$\begin{aligned}(1-\chi)\left(C_{i-1}^{n+1} - 2C_{i-1}^{n} + C_{i-1}^{n}\right) + \chi\left(C_{i}^{n+1} - 2C_{i}^{n} + C_{i}^{n-1}\right) \\ + \alpha^2\left[\theta\left(C_{i+1}^{n+1} - 2C_{i}^{n+1} + C_{i-1}^{n+1}\right) + (1-\theta)\left(C_{i+1}^{n} - 2C_{i}^{n} + C_{i-1}^{n}\right)\right] = 0,\end{aligned} \tag{3.1}$$

in which α is the Courant number defined as $\alpha = U\Delta t/\Delta x$, and superscript n and subscript i are time level and computational point, respectively. χ and θ are weighting factors of the finite difference scheme.

An unnecessary wave propagates upstream if the initial concentration distributions at both $t = 0$ and $t = -\Delta t$ are not consistent with the downstream advection progress. To overcome this difficulty, the values of the concentration at time step $(n-1)$ can be employed as shown in Figure 2 instead of time step $(n-1)$. Drawing the characteristic curves which go downstream through points (i, n) and $(i+1, n)$, time step $(n-1)$ can be introduced corresponding to time $(n\Delta t - \Delta x/U)$ when each characteristic curve intersects the $(i-1$-$)$axis

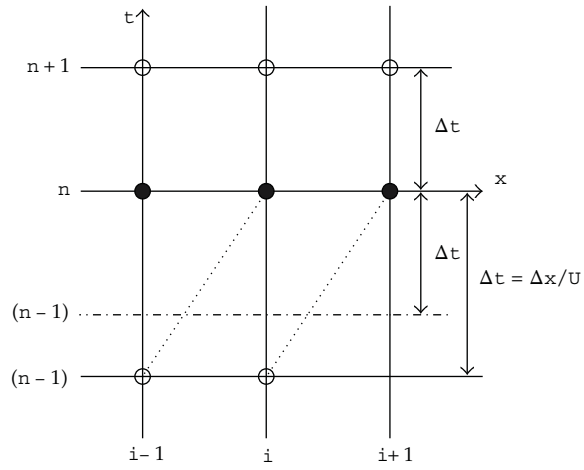

Figure 2: Estimation of concentration at a previous time step.

or i-axis. According to the concept of characteristics for a pure advection, the concentrations are conserved between two time steps and are given as follows:

$$C_{i-1}^{(n-1)'} = C_i^n,$$
$$C_i^{(n-1)'} = C_{i+1}^n. \tag{3.2}$$

Using (3.2), (3.1) can be rewritten as

$$2(1-\chi)\left(C_{i-1}^{n+1} - 2C_{i-1}^n + \alpha C_i^n\right) + 2\chi\left[C_i^{n+1} - (\alpha+1)C_i^n + \alpha C_{i+1}^n\right]$$
$$= \alpha(\alpha+1)\theta\left(C_{i+1}^{n+1} - 2C_i^{n+1} + C_{i-1}^{n+1}\right) + \alpha(\alpha+1)(1-\theta)\left(C_{i+1}^n - 2C_i^n + C_{i-1}^n\right). \tag{3.3}$$

The optimal values of χ and θ in (3.3) do not seem to be constant, but instead are dependent on the Courant number α. To obtain the functional relationship of χ and θ to α, the Taylor series expansion on (3.3) may be employed [22].

The final expression of the advection equation can be written as follows:

$$p_1 C_{i-1}^{n+1} + p_2 C_i^{n+1} + p_3 C_{i+1}^{n+1} = p_4 C_{i-1}^n + p_5 C_i^n + p_6 C_{i+1}^n, \tag{3.4}$$

in which the coefficients are given by

$$\begin{aligned}
p_1 &= 0.3776\alpha_{0+} + 0.3152\alpha_{0-} - 0.5467\alpha_{1+} + 0.4843\alpha_{1-} + 0.1691\alpha^2,\\
p_2 &= 1.3072 + 0.0624|\alpha| - 0.3382\alpha^2,\\
p_3 &= 0.3152\alpha_{0+} + 0.3776\alpha_{0-} + 0.4843\alpha_{1+} - 0.5467\alpha_{1-} + 0.1691\alpha^2,\\
p_4 &= 0.3776\alpha_{0+} + 0.3152\alpha_{0-} + 0.5157\alpha_{1+} - 0.4533\alpha_{1-} + 0.1381\alpha^2,\\
p_5 &= 1.3072 - 0.0624|\alpha| - 0.2762\alpha^2,\\
p_6 &= 0.3152\alpha_{0+} + 0.3776\alpha_{0-} - 0.4553\alpha_{1+} + 0.5157\alpha_{1-} + 0.1383\alpha^2.
\end{aligned} \tag{3.5}$$

The values of α_{0+}, α_{0-}, α_{1+} and α_{1-} are defined as:

$$\begin{aligned}
\alpha_{0+} &= \mathrm{AINT}\left\{\frac{\alpha+1}{|\alpha|+1}\right\},\\
\alpha_{0-} &= \mathrm{AINT}\left\{\frac{1-\alpha}{1+|\alpha|}\right\},\\
\alpha_{1+} &= \frac{|\alpha|+\alpha}{2},\\
\alpha_{1-} &= \left|\frac{\alpha-|\alpha|}{2}\right|,
\end{aligned} \tag{3.6}$$

in which AINT is one of the intrinsic functions in FORTRAN that carries out the function of truncating decimals.

Secondly, the diffusion-reaction equation can be written as:

$$\frac{\partial C}{\partial t} = \frac{\partial}{\partial x}\left[D_{xx}\frac{\partial C}{\partial x} + D_{xy}\frac{\partial C}{\partial y}\right] + \frac{\partial}{\partial y}\left[D_{yx}\frac{\partial C}{\partial x} + D_{yy}\frac{\partial C}{\partial y}\right] + kC. \tag{3.7}$$

The diffusion-reaction equation is discretized by a three-level locally implicit scheme with reference to the computational grid, as shown in Figure 3 [23].

Equation (3.7) contains two dimensions and is different from the form derived in Hobson et al. [23]. However, their numerical scheme can be easily extended to the y-direction

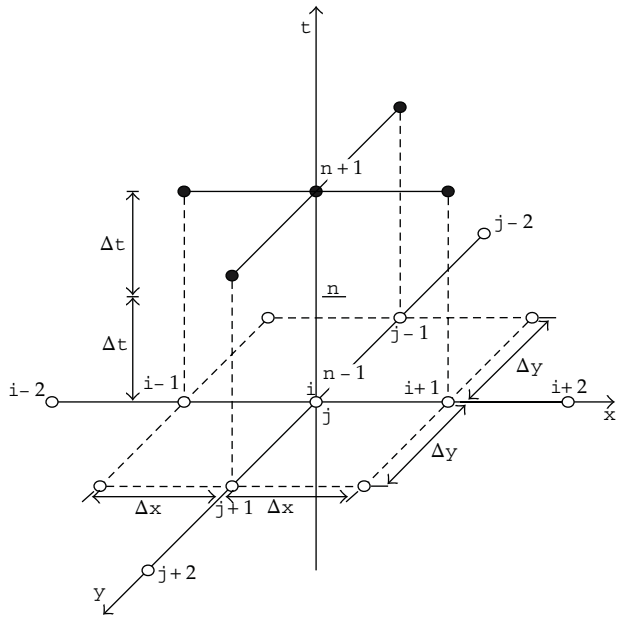

Figure 3: Computational mesh for the diffusion-reaction term.

in a similar manner and the final form of discretized equations using the finite difference approximation is given as:

$$\begin{aligned}
&\left[1+(4\alpha+4)K+(16\alpha-4\beta)K^2\right]\frac{C_{i,j}^{n+1}-C_{i,j}^{n-1}}{2\Delta t}\\
&\quad=D\left[K\left\{4\left(\frac{C_{i+2,j}^{n-1}+C_{i,j+2}^{n-1}+C_{i-2,j}^{n-1}+C_{i,j-2}^{n-1}-4C_{i,j}}{(2\Delta x)^2}\right)\right.\right.\\
&\qquad+2\left(\frac{C_{i+1,j+1}^{n-1}+C_{i+1,j-1}^{n-1}+C_{i-1,j+1}^{n-1}+C_{i-1,j-1}^{n-1}-4C_{i,j}^{n-1}}{(2\Delta x)^2}\right)\\
&\qquad\left.\left.-4(1-\alpha)\left(\frac{C_{i+1,j+1}^{n-1}+C_{i+1,j-1}^{n-1}}{(\Delta x)^2}+\frac{C_{i-1,j+1}^{n-1}+C_{i-1,j-1}^{n-1}-4C_{i,j}^{n-1}}{(\Delta x)^2}\right)\right\}\right.\\
&\quad\left.+\left(\frac{C_{i+1,j+1}^{n-1}+C_{i+1,j-1}^{n-1}+C_{i-1,j+1}^{n-1}+C_{i-1,j-1}^{n-1}-4C_{i,j}^{n-1}}{(\Delta x)^2}\right)\right.\\
&\quad\left.+2\Delta t(4K+4\alpha K+1)kC\right],
\end{aligned}\tag{3.8}$$

in which $K = 2D\Delta t/(\Delta x)^2$ is used and the diffusion coefficients are assumed as a constant value, D. In (3.8), α and β are the artificial values which are determined to give the correct

amount of diffusion and avoid any time lag problems. In general, a whole family of diffusion schemes can be obtained by changing the values of α and β. The optimum scheme of this type is the one which exhibits no time lag and is the most numerically stable.

In this study, (3.8) is solved by a two-dimensional three-level locally implicit scheme with second-order accuracy [23]. Equation (3.8) can be rewritten for $C_{i,j}^{n+1}$ as follows:

$$\begin{aligned} C_{i,j}^{n+1} = {} & A\left(C_{i+2,j}^{n-1} + C_{i,j+2}^{n-1} + C_{i-2,j}^{n-1} + C_{i,j-2}^{n-1}\right) \\ & + B\left(C_{i+1,j+1}^{n-1} + C_{i+1,j-1}^{n-1} + C_{i-1,j+1}^{n-1} + C_{i-1,j-1}^{n-1}\right) \\ & + E\left(C_{i+1,j}^{n-1} + C_{i,j+1}^{n-1} + C_{i-1,j}^{n-1} + C_{i,j-1}^{n-1}\right) + FC_{i,j}^{n-1} + G(kC), \end{aligned} \tag{3.9}$$

in which A, B, E, F and G are given as:

$$\begin{aligned} A &= \frac{K^2}{\left[1 + (4\alpha + 4)K + (16\alpha - 4\beta)K^2\right]}, \\ B &= \frac{2K^2}{\left[1 + (4\alpha + 4)K + (16\alpha - 4\beta)K^2\right]}, \\ E &= \frac{K[1 - 4(1 - \alpha)K]}{\left[1 + (4\alpha + 4)K + (16\alpha - 4\beta)K^2\right]}, \\ F &= \frac{\left[1 + 4\alpha K + 4(1 - \beta)K^2\right]}{\left[1 + (4\alpha + 4)K + (16\alpha - 4\beta)K^2\right]}, \\ G &= \frac{2\Delta t(4K + 4\alpha K + 1)}{\left[1 + (4\alpha + 4)K + (16\alpha - 4\beta)K^2\right]}. \end{aligned} \tag{3.10}$$

Since a first-order sink and zero-order reaction cannot generate numerical stability alone, this study is concerned only with the presence of a first-order term. Thus, the zero-order sedimentation rate, k_0, is assumed to be zero, and the first-order sedimentation rate of a suspended material, k_1, is described as:

$$k_1 = -\frac{\lambda W_s}{H}, \tag{3.11}$$

and a first-order sink is defined as:

$$\text{sink} = k_1 C, \tag{3.12}$$

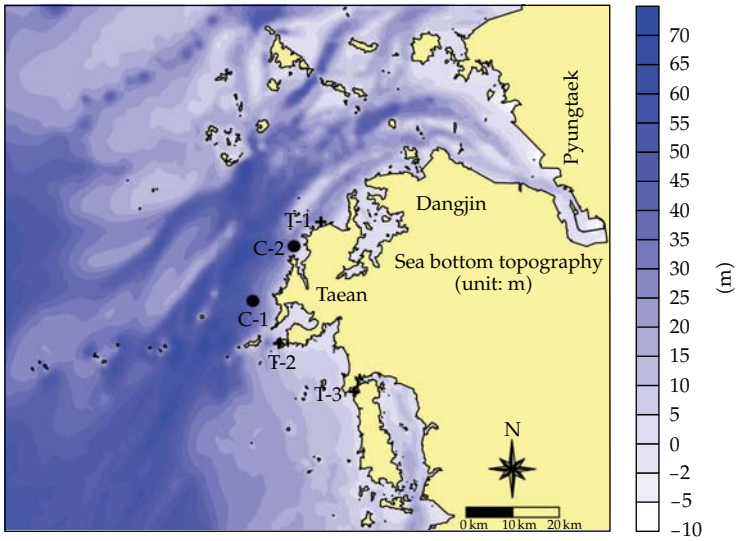

Figure 4: Computational domain and sea bottom topography.

in which λ is a coefficient for calculation of the concentration at the bottom and, for convenience, is assumed to be 1, and W_s is the sedimentation rate, assumed to be 0.08 mm/sec.

4. Verification of the Numerical Model

The numerical model developed in this study is employed to simulate the change of tide and tidal currents near the accident area of the Hebei Spirit oil spill occurred on December 7, 2007. The Hebei Spirit oil spill is the largest oil spill accident occurred in the Yellow Sea located between Korea and China. In general, tide effects play a dominant role in coastal processes in the Yellow Sea, which is well known for the strongest tidal currents in the world. Therefore, the accuracy of the model for predicting tide and tidal currents is very important to investigate oil spreading in this area. To verify the model, free surface elevations and tidal ellipses at several points are computed and compared with the corresponding observed data.

Figure 4 shows the computational domain and sea level observation points. Sea bottom topography is also shown in the figure. Numerical simulations of tide and tidal currents were conducted during 16 days (December 7 ~ 22, 2007) and the harmonic analysis for computed results is presented. Table 1 displays a comparison of observed data and computed results using harmonic analysis. Computed results represent both amplitudes and phase differences very well. Figure 5 shows a comparison of numerically obtained free surface profiles and corresponding observed measurements at points of T-1, T-2, and T-3. The agreement between the numerical solutions and field measurements is quite reasonable.

Tidal currents are very strong in the Yellow Sea and those may play an important role in oil spreading. In Figure 6, tidal ellipses at points of C-1 and C-2 are computed and compared with field-observed data to verify the accuracy of the numerical model. The numerical model represents well-strong tidal currents observed in this area.

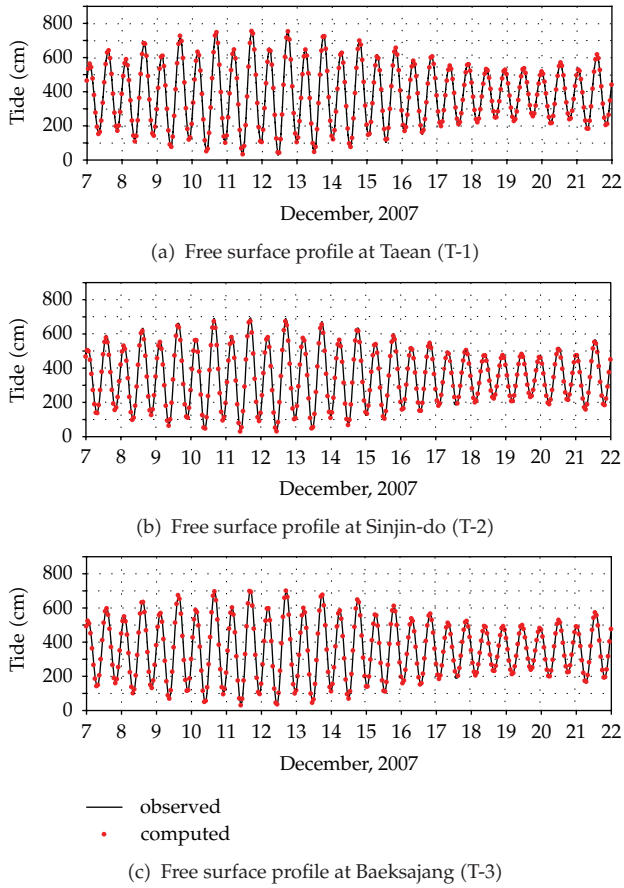

(a) Free surface profile at Taean (T-1)

(b) Free surface profile at Sinjin-do (T-2)

(c) Free surface profile at Baeksajang (T-3)

Figure 5: Comparison of observed and computed free surfaces of tides.

5. Application of the Model

The spilled oil dispersion model as established in previous sections is applied to predict the diffusion distribution on the Hebei Spirit oil spill. Subsequently, by conducting the numerical calculations on the diffusion distribution considering tide and tidal currents simultaneously, the prediction has been made through the comparison of the diffusion distribution observation between at 8 p.m. on December 7, 2007 when the spilled oil flowed into the whole Manripo and Sindu-ri seashore and at 11 a.m. on December 11, 2007 when the satellite photographs exist (Figure 7). In Figure 7, a target area of the numerical simulation is also described.

Figures 8(a) and 8(b) show distribution of simulated tidal currents field, 8(a) flood phase and 8(b) ebb phase, where the Hebei Spirit was stranded on duration of a spring tide. The results show that the tide current reaches the maximum speed in the northern area from the accident and mainly flows not perpendicular to the coastline but parallel to that. As a result, strong invasion of the oil spill to the coastline is not represented in the numerical simulation.

Figures 9(a) and 9(b) show numerically obtained diffusion distribution at 8 p.m. on December 7, 2007 and 11 a.m. on December 11, 2007. Figure 9(a) shows diffusion distribution

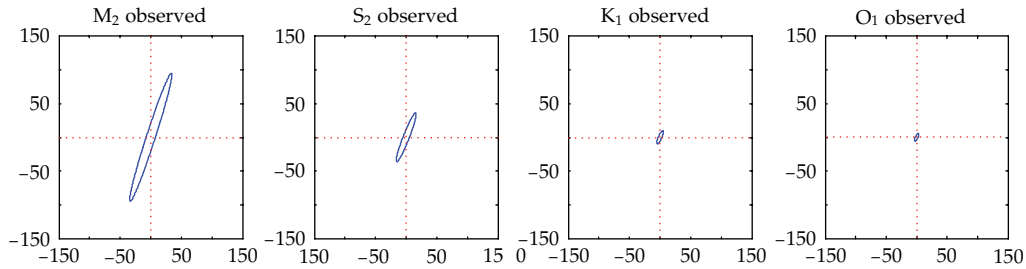

(a) C-1 (observed data)

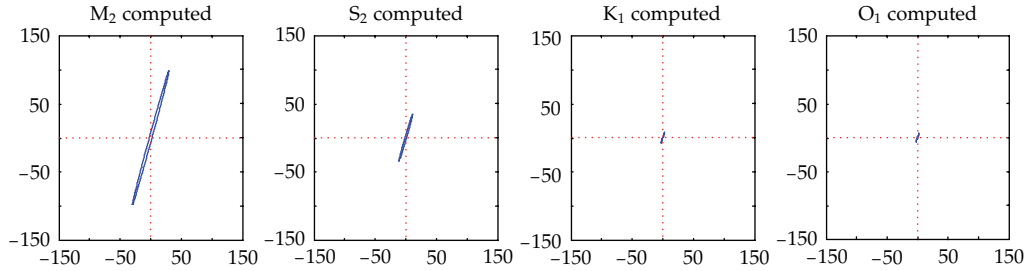

(b) C-1 (numerical model)

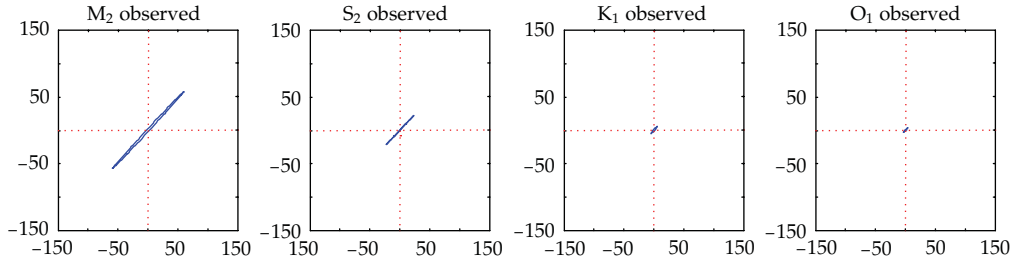

(c) C-2 (observed data)

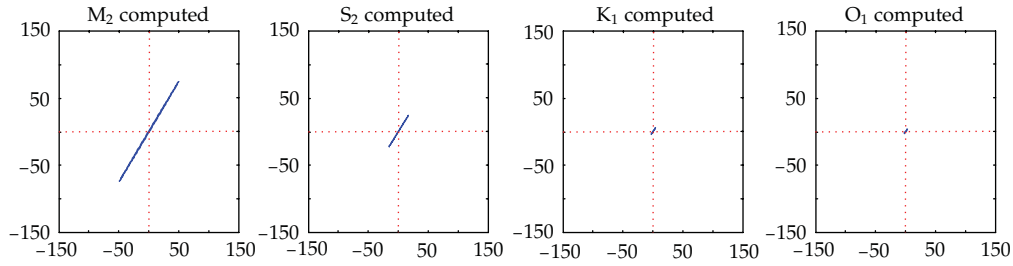

(d) C-2 (numerical model)

Figure 6: Comparison of observed and predicted tidal ellipses.

after 13 hours since the Hebei Spirit had been stranded. The south-western currents on a flood phase and north-eastern currents on ebb phase are well reproduced and those are well reflected in the shape of oil distribution.Therefore, the numerical result shows similar

Table 1: Observed data and computed results using harmonic analysis.

Data	Pts.	Amplitude (cm)		Phase (deg.)	
		Observed	Computed	Observed	Computed
T-1	M_2	231.6	231.8	106.6	115.5
	S_2	90.1	88.1	155.1	160.9
	K_1	34.7	36.2	287.0	288.0
	O_1	28.5	27.3	257.0	260.3
T-2	M_2	211.1	207.5	95.4	94.2
	S_2	81.0	78.7	138.8	137.8
	K_1	35.8	33.3	280.1	278.8
	O_1	26.8	24.4	252.1	250.6
T-3	M_2	215.7	215.5	90.0	89.3
	S_2	83.3	81.7	133.7	133.8
	K_1	35.2	34.1	277.5	275.7
	O_1	26.3	25.2	249.4	247.5

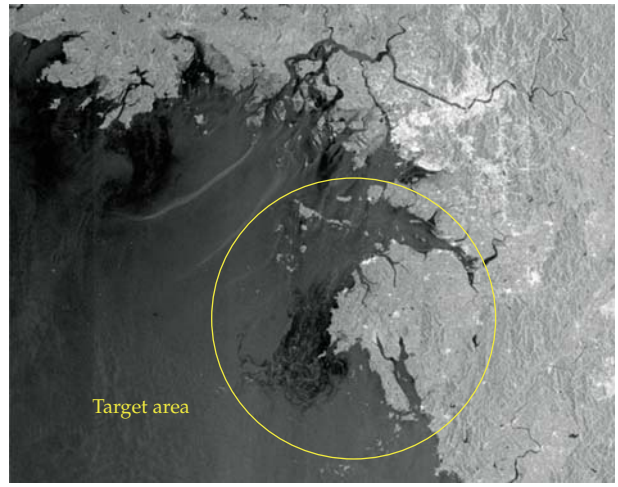

Figure 7: Satellite image of the Hebei Spirit oil spill (December 11, 2007).

distribution of the oil spreading with the satellite photograph (Figure 7). Since there is lack of quantitative observed data near the target area, numerical results are compared with a satellite image only in a qualitative viewpoint. On the other hand, by comparing the satellite photograph and Figure 9(b), numerical results do not represent strong invasion of the oil spill to the coastline. It may be occurred because effects of wind wave were neglected in the numerical simulation. Nevertheless, it is obvious that the model represents well the whole processes of the oil spreading, and the model can be applied to predict the oil spreading in a real coastal environment.

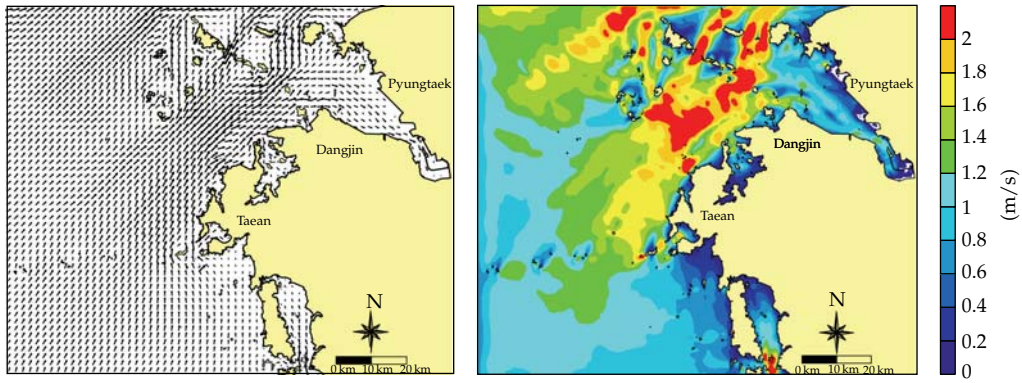

(a) Flood current at a spring tide

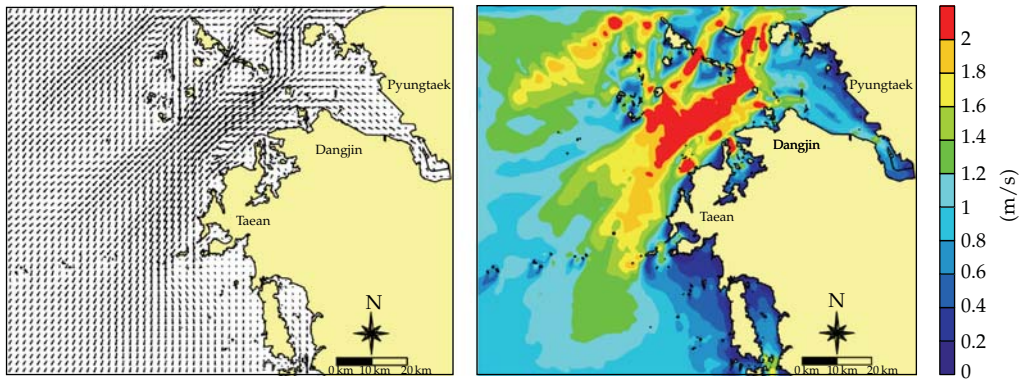

(b) Ebb current at a spring tide

Figure 8: Distribution of tidal currents near the target area.

6. Concluding Remarks

In this study, a numerical model is employed to solve a two-dimensional advection-diffusion-reaction equation. The model is based on a standard split operator (fractional step) approach. Thus, the hyperbolic (advection) and parabolic (diffusion) portions of the equation are solved separately by using techniques describing properly the physical behaviors of each. In the model, the advection step is solved by using the SOWMAC scheme, while the diffusion-reaction step is done by a three-level locally implicit scheme.

The numerical model is first applied to an idealized problem to verify its accuracy. The model produces results agreeable with corresponding analytical solutions and field observed data. The model is then employed to investigatethe behavior of the oil spreading in a coastal

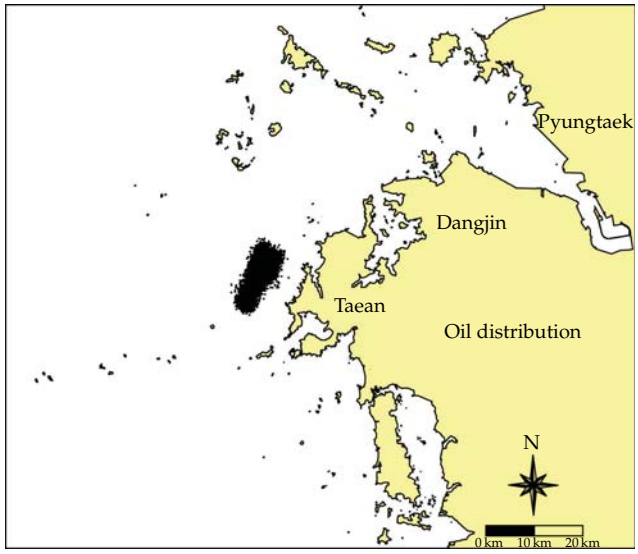

(a) 8 p.m. on December 7, 2007

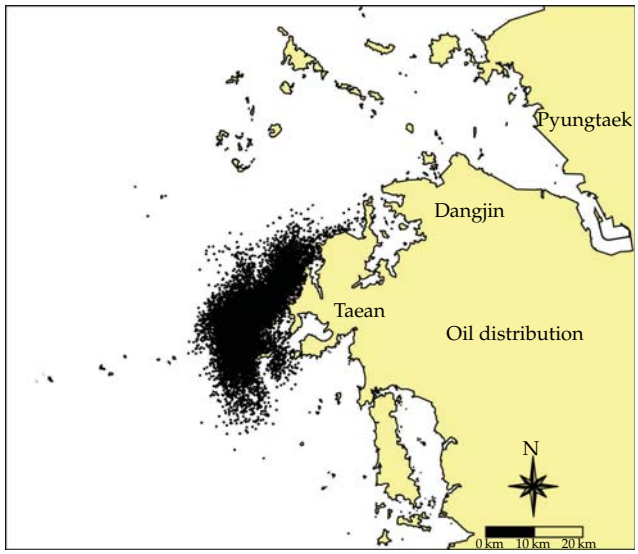

(b) 11 a.m. on December 11, 2007

Figure 9: Computed diffusion distribution of the Hebei Spirit oil spreading.

environment. The model yields reasonable results. The employed model could be used to forecast the behaviors of oil spreading in various practical situations.

Acknowledgment

This research was supported by Basic Science Research Program through the National Research Foundation of Korea(NRF) funded by the Ministry of Education, Science and Technology (2011-0015386).

References

[1] B. Lin and R. A. Falconer, "Tidal flow and transport modeling using ultimate quickest scheme," *Journal of Hydraulic Engineering*, vol. 123, no. 4, pp. 303–314, 1997.

[2] D. Mackay, S. Paterson, and K. Trudel, "A mathematical model of oil spill behavior," Environmental Protection Service, Fisheries and Environment Canada.

[3] J. C. Huang, "A review of the state-of-the-art of oil spill fate/behavior models," in *Proceedings of the Oil Spill Conference*, pp. 313–322, Washington, 1983.

[4] M. L. Spaulding, "Oil spill trajectory and fate modeling: state-of-the art review," in *Proceedings of the 2nd International Oil Spill Research and Development Forum,*, London, UK, 1995.

[5] H. T. Shen and P. Yapa, "Oil slick transport in rivers," *Journal of Hydraulic Engineering*, vol. 114, no. 5, pp. 529–543, 1988.

[6] H. T. Shen, P. D. Yapa, and M. E. Petroski, "Simulation of oil slick transport in Great Lakes connecting channels," Report Nos. 86-1 to 4, vols. I-IV, Department of Civil and Environmental Engineering, Clarkson University, Potsdam, NY, USA, 1986.

[7] P. D. Yapa, H. T. Shen, and K. S. Angammana, "Modeling oil spills in a river-lake system," *Journal of Marine Systems*, vol. 4, no. 6, pp. 453–471, 1994.

[8] S. A. Lonin, "Lagrangian model for oil spill diffusion at Sea," *Spill Science and Technology Bulletin*, vol. 5, no. 5-6, pp. 331–336, 1999.

[9] X. Chao, N. J. Shankar, and H. F. Cheong, "Two- and three-dimensional oil spill model for coastal waters," *Ocean Engineering*, vol. 28, no. 12, pp. 1557–1573, 2001.

[10] S. D. Wang, Y. M. Shen, and Y. H. Zheng, "Two-dimensional numerical simulation for transport and fate of oil spills in seas," *Ocean Engineering*, vol. 32, no. 13, pp. 1556–1571, 2005.

[11] S. D. Wang, Y. M. Shen, Y. K. Guo, and J. Tang, "Three-dimensional numerical simulation for transport of oil spills in seas," *Ocean Engineering*, vol. 35, no. 5-6, pp. 503–510, 2008.

[12] M. Reed, E. Gundlach, and T. Kana, "A coastal zone oil spill model: development and sensitivity studies," *Oil and Chemical Pollution*, vol. 5, no. 6, pp. 411–449, 1989.

[13] J. A. Galt, G. Y. Watabayashi, D. L. Payton, and J. C. Petersen, "Trajectory analysis for the Exxon Valdez: Hindcast study," in *International Oil Spill Conference (IOSC '91)*, pp. 629–634, Washington, DC, USA, 1991.

[14] E. Howlett, K. Jayko, and M. L. Spaulding, "Interfacing real-time information with OILMAP," in *Proceedings of the 16th Arctic and Marine Oil Spill Program Technical Seminar*, pp. 517–527, 1993.

[15] V. S. Kolluru, M. L. Spaulding, and E. L. Anderson, "A three-dimensional oil dispersion model using a particle based approach," in *Proceedings of the 17th Arctic and Marine Oil Spill Program Technical Seminar*, pp. 867–894, 1994.

[16] Y. S. Cho and P. L. F. Liu, "Crest-length effects in nearshore tsunami run-up around islands," *Journal of Geophysical Research C*, vol. 104, no. 4, pp. 7907–7913, 1999.

[17] Y. S. Cho and H. J. Kim, "Sea level change due to typhoons in Korean peninsula," *Journal of Coastal Research*, vol. 22, no. 3, pp. 678–682, 2006.

[18] B. H. Choi, H. M. Eum, and S. B. Woo, "Modeling of coupled tide-wave-surge process in the Yellow Sea," *Ocean Engineering*, vol. 30, no. 6, pp. 739–759, 2003.

[19] P. L. Brezonik, *Chemical Kinetics and Process Dynamics in Aquatic Systems*, Lewis Publishers, 1994.

[20] S. V. Patankar, "Numerical Heat Transfer and Fluid Flow," Hemisphere Publishing Coporation, 1980.

[21] D. L. Stefanovic and H. G. Stefan, "Accurate two-dimensional simulation of advective-diffusive-reactive transport," *Journal of Hydraulic Engineering*, vol. 127, no. 9, pp. 728–737, 2001.

[22] T. Komatsu, K. Ohgushi, and K. Asai, "Refined numerical scheme for advective transport in diffusion simulation," *Journal of Hydraulic Engineering*, vol. 123, no. 1, pp. 41–50, 1997.

[23] J. M. Hobson, N. Wood, and P. J. Mason, "A new finite-difference diffusion scheme," *Journal of Computational Physics*, vol. 125, no. 1, pp. 16–25, 1996.

Hindawi Publishing Corporation
Journal of Applied Mathematics
Volume 2012, Article ID 983718, 21 pages
doi:10.1155/2012/983718

Research Article

FEM Analyses for T-H-M-M Coupling Processes in Dual-Porosity Rock Mass under Stress Corrosion and Pressure Solution

Yu-Jun Zhang,[1] Chao-Shuai Yang,[2] and Gang Xu[1]

[1] *State Key Laboratory of Geomechanics and Geotechnical Engineering, Institute of Rock and Soil Mechanics, The Chinese Academy of Sciences, Wuhan 430071, China*
[2] *Technology Centre, China Railway Tunnel Group Co. Ltd., Luoyang 471009, China*

Correspondence should be addressed to Chao-Shuai Yang, yangchaoshuai2008@126.com

Received 31 January 2012; Accepted 28 March 2012

Academic Editor: Zhangxing Chen

The models of stress corrosion and pressure solution established by Yasuhara et al. were introduced into the 2D FEM code of thermo-hydro-mechanical-migratory coupling analysis for dual-porosity medium developed by the authors. Aiming at a hypothetical model for geological disposal of nuclear waste in an unsaturated rock mass from which there is a nuclide leak, two computation conditions were designed. Then the corresponding two-dimensional numerical simulation for the coupled thermo-hydro-mechanical-migratory processes were carried out, and the states of temperatures, rates and magnitudes of aperture closure, pore and fracture pressures, flow velocities, nuclide concentrations and stresses in the rock mass were investigated. The results show: the aperture closure rates caused by stress corrosion are almost six orders higher than those caused by pressure solution, and the two kinds of closure rates climb up and then decline, furthermore tend towards stability; when the effects of stress corrosion and pressure solution are considered, the negative fracture pressures in near field rise very highly; the fracture aperture and porosity are decreases in the case 1, so the relative permeability coefficients reduce, therefore the nuclide concentrations in pore and fracture in this case are higher than those in case 2.

1. Introduction

The rock mass below thousands of meters from the ground surface, which is dual-porosity medium with pore and fracture as the conduits of transporting, will be the site for the recovery of energy resources and minerals, and for the safe isolation and storage of high level radioactive wastes, CO_2, and so forth. So, the changes in the ambient stress and temperature conditions may affect the permeability characteristics of these conduits combined effects. Stress corrosion [1–4] and pressure solution [5–8], which are corresponding to the fractures,

may result in the sealing and degradation of permeability through compaction driven by fracturing (or crushing) of the propping asperities and by dissolution at contacting asperities, respectively.

When local tensile stresses result from the compressive loading of contacting asperities, "subcritical" or "quasistatic" cracking may occur, leading to a time-dependent or progressive failure. Specifically, sub-critical crack growth in the presence of water is believed to be facilitated by chemical reaction, and the resulting process is termed stress corrosion. Pressure solution incorporates three serial processes: mineral dissolution at stressed contacts, diffusive transport of this material along the intervening thin film of water, and ultimate deposition of the mineral matter at the pore wall.

Dove [9] rigorously investigated the dissolution kinetics of quartz under the wide range of temperature and pH conditions and defined an empirical expression of mode I crack velocity resulted from chemical dissolution. Based on the experimental data, Yasuhara and Elsworth [10] investigated the evolution of fracture aperture within a sample of novaculite containing a natural fracture, and they also presented the models which separately account for stress corrosion and pressure solution to describe this response. Taron and Elsworth [11] introduced a kind of coupled thermo-hydro-mechanical-chemical model of dual-porosity medium, in which the influence of pressure solution, shrinkage and dilation of T-H-M, and precipitation and dissolution of mineral on the opening and closure of apertures was considered by simplification. Subsequently, on the basis of modifying permeability and porosity, the characteristics and change mechanisms of permeability within a rock mass containing natural fractures with TOUGHREACT and FLAC^{3D} were investigated. Taron and Elsworth [12, 13] developed a new model of pressure solution and applied it for numerical simulation of coupled mechanical and chemical processes in engineered geothermal reservoirs with dynamic permeability. Using simplified expression developed by Min et al. [14], the author improved the FEM code of T-H-M coupling of dual-porosity medium, modified the aperture timely and established the evolution of fracture permeability with pressure solution. Aiming at a hypothetical nuclear waste repository in an unsaturated dual-porosity rock mass as the calculation example, the relative numerical simulation [15] was carried out for three cases with different apertures. However, the concentration field of solute was not involved. It is well known that the leakage and diffusion of nuclide from nuclear waste repository are required to study [16]. Consequently, it is imperative to improve the existing model and FEM code, and to perform the analyses of T-H-M-M coupling based on the above work.

The author introduced primarily the models of stress corrosion and pressure solution by Yasuhara into the governing equations presented in [15], and the concentration of solute was involved as well. That is, in the dual-porosity rock mass, the stress field and the temperature field were single, but the water pressures both in pore and fracture are different as well as the concentrations. Therefore, the corresponding simulation for T-H-M-M coupling was constructed. And then, aiming at a hypothetical model for geological disposal of nuclear waste in an unsaturated dual-porosity rock mass, two computation cases were designed: (1) the fracture apertures were changed with the stress corrosion and pressure solution (the porosity of intact rock was also a function of stress); (2) the fracture aperture and the porosity of matrix rock were constants. The corresponding FEM analyses were performed under certain initial conditions of temperature, pore water pressure, in situ stress, and nuclide release intensity, and both the distributions and the changes of temperatures, pore pressures, flow rates, saturations, nuclide concentrations, and stresses in the near field of repository were investigated. Some conclusions were obtained.

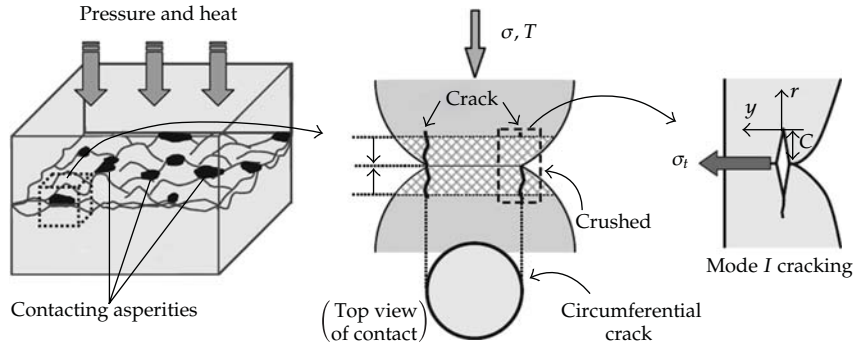

Figure 1: Schematic of fracture compaction induced by microcrack propagation [10].

2. Modification of Fracture Permeability

2.1. Effect of Stress Corrosion on Aperture

Assume that the asperity contacts of brittle materials, schematically shown in Figure 1, within a fracture are in Hertzian contacts, and that a circumferential crack at or outside the contact may be induced by the tensile stress σ_t. And this crack is described as stress corrosion. Mode I crack velocity for quartz was defined by Dove, given as [9]

$$\begin{aligned} v_{\mathrm{Si–O}} = {} & A_{\mathrm{H_2O}} \exp\left(\frac{-\Delta H_{\mathrm{H_2O}}}{RT}\right) \exp\left(b^*_{\mathrm{H_2O}} K_1\right) \left(\theta^{\mathrm{H_2O}}_{\mathrm{Si–O}}\right) \\ & + A_{\mathrm{OH^-}} \exp\left(\frac{-\Delta H_{\mathrm{OH^-}}}{RT}\right) \exp\left(b^*_{\mathrm{OH^-}} K_1\right) \left(\theta^{\mathrm{OH^-}}_{\mathrm{Si–O}}\right), \end{aligned} \tag{2.1}$$

where $v_{\mathrm{Si–O}}$ is mode I crack velocity caused by chemical dissolution; $A_{\mathrm{H_2O}}$ and $A_{\mathrm{OH^-}}$ are the experimentally-determined factor related to temperature; $\Delta H_{\mathrm{H_2O}}$ and $\Delta H_{\mathrm{OH^-}}$ are activation enthalpies; R is the gas constant; T is temperature; $b^*_{\mathrm{H_2O}}$ and $b^*_{\mathrm{OH^-}}$ are the experimentally determined constants derived from the geometry of crack tip; K_1 is the stress intensity factor; $\theta^{\mathrm{H_2O}}_{\mathrm{Si–O}}$ and $\theta^{\mathrm{OH^-}}_{\mathrm{Si–O}}$ always satisfying $\theta^{\mathrm{H_2O}}_{\mathrm{Si–O}} + \theta^{\mathrm{OH^-}}_{\mathrm{Si–O}} = 1$ are the fraction of Si–O reacting with molecular water or hydroxyl ions, and there will be $\theta^{\mathrm{H_2O}}_{\mathrm{Si–O}} = 1$ and $\theta^{\mathrm{OH^-}}_{\mathrm{Si–O}} = 0$ at low pH, and $\theta^{\mathrm{H_2O}}_{\mathrm{Si–O}} = 0$ and $\theta^{\mathrm{OH^-}}_{\mathrm{Si–O}} = 0$ at the high one. Consequently, the closure rate of fracture mechanical aperture due to stress corrosion, given by Yasuhara and Elsworth [10], is as follows:

$$\begin{aligned} \frac{dE^s}{dt} &= -(1 - R_c) \cdot v_{\mathrm{Si–O}}, \\ K_1 &\approx \sigma_t \sqrt{2\pi r}, \\ \sigma_t &= -\frac{(1 - 2\mu)}{2} \sigma_a, \\ \sigma_a &= \frac{\overline{R}}{R_c} \overline{\sigma}, \end{aligned} \tag{2.2}$$

where r is the distance parallel to the long axis direction of mode I crack caused by σ_t, and it is assumed to be infinitesimal as well as initial length of crack; μ is the Poisson's ratio of material; σ_t is the tensile stress induced by σ_a which reaches the maximum value just at the edge of the contact; σ_a is the real stress exerted over the contact area; $\overline{\sigma}$ is average macroscopic effective stress. $\overline{R}$ is the nominal area of the fracture (taking unit value); R_c is the contact-area ratio, and $R_c \leq \overline{R}$.

R_c can be calculated via the expression below:

$$E^s = E_r + (E_0 - E_r)\exp[-(R_c - R_{c0})a], \tag{2.3}$$

where E^s and E_r are the mean and residual apertures caused by stress corrosion, respectively; E_0 is the initial aperture; R_{c0} is the relative contact-area ratio at the reference stress; a is empirical constant.

Therefore, the evolution of fracture mechanical aperture derived from stress corrosion is

$$E^s_{t+\Delta t} = E^s_t + \frac{dE^s}{dt}\Delta t. \tag{2.4}$$

2.2. Effect of Pressure Dissolution on Aperture

The dissolution defined by Yasuhara and Elsworth [10] is expressed as

$$\frac{dM_{\text{diss}}}{dt} = \frac{3\pi V_m^2(\sigma_a - \sigma_c)k_+\rho_g d_c^2}{4RT}, \tag{2.5}$$

where dM_{diss}/dt is the rate of addition of dissolved mass into solution at the interface; V_m is molar volume of the solid; σ_c is the critical stress that defines stress state where the compaction will effectively halt and reach equilibrium while σ_a is equal to σ_c; k_+ is the dissolution rate constant of the solid; ρ_g is the density of solid; d_c is the diameter of the asperity contact.

And

$$\begin{aligned} k_+ &= k_+^0 \exp\left(-\frac{E_a}{RT}\right), \\ \sigma_c &= \frac{E_m(1 - T/T_m)}{4V_m}, \end{aligned} \tag{2.6}$$

where k_+^0 is constant factor; E_a is the activation energy; E_m and T_m are the heat and temperature of fusion, respectively.

The closure rate of fracture mechanical aperture caused by pressure solution is

$$\frac{dE^p}{dt} = -\frac{dM_{\text{diss}}}{dt}\cdot\frac{1}{\rho_g}\cdot\frac{1 - R_c}{(\pi/4)d_c^2} = -\frac{3V_m^2 k_+^0(1 - R_c)(\sigma_a - \sigma_c)}{RT}\exp\left(-\frac{E_a}{RT}\right). \tag{2.7}$$

And the evolution of fracture mechanical aperture due to pressure solution can be expressed as

$$E^p_{t+\Delta t} = E^p_t + \frac{dE^p}{dt}\Delta t. \tag{2.8}$$

2.3. Fracture Permeability

The fracture spacing in rock mass is assumed to be s, and then the total mechanical aperture for a single fracture at the time of $t + \Delta t$ is expressed as

$$E_{t+\Delta t} = \left(E_0 + \sum_{\Delta t} dE^s + \sum_{\Delta t} dE^p\right). \tag{2.9}$$

So, the hydraulic aperture for a single fracture is [17]

$$e_{t+\Delta t} = \frac{E^2_{t+\Delta t}}{\mathrm{JRC}^{2.5}}, \tag{2.10}$$

where JRC is the roughness coefficient of fractures.

Consequently, the equivalent permeability coefficient of fracture in rock mass is [18]:

$$K_{t+\Delta t} = \frac{g e^3_{t+\Delta t}}{12 v s}, \tag{2.11}$$

where g is gravitational acceleration (9.81 $\mathrm{m/s^2}$) and v is kinematics viscosity (the magnitude relative to purified water at 20°C is 1.0×10^{-6} $\mathrm{m^2/s}$).

2.4. Effect of Stress on Permeability of Rock Matrix

According to the empirical expression presented by J. P. Davies and D. K. Davies [19], the porosity and permeability of the rock matrix, when the stress in rock matrix changes, can be modified as

$$\begin{aligned} \phi &= \phi_r + (\phi_0 - \phi_r)\exp\left(f \cdot \sigma'_m\right), \\ k &= k_0 \exp\left[c \cdot \left(\frac{\phi}{\phi_0} - 1\right)\right] = F_{\phi k} k_0, \end{aligned} \tag{2.12}$$

where ϕ_0 and k_0 are the porosity and permeability of rock matrix at the stress state of zero, respectively; ϕ_r is the residual porosity of rock matrix at a high stress state; σ'_m is average effective stress; f and c are the experimentally determined parameters, respectively; $F_{\phi k}$ is the modification factor of pore permeability.

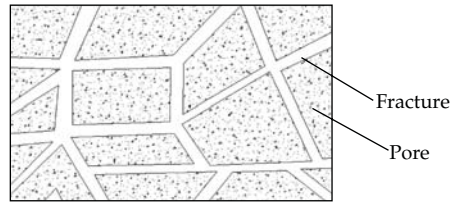

Figure 2: Porous-fractured media.

3. Thermo-Hydro-Mechanical-Migratory Coupling Equations for Dual-Porosity Medium

For the dual-porosity medium shown in Figure 2, it can be thought that there exist pore water pressure and fracture water pressure, pore concentration and fracture concentration, but stress field and temperature field are single in the medium. So, one kind of three-dimensional model for coupled thermo-hydro-mechanical-migratory process is created. By omitting the complex deriving steps, the governing equations are given as follows.

3.1. Equilibrium Stress Equation

Supposing there are n sets of fractures in a fractured porous rock mass, the equilibrium stress equation can be written in the global coordinate system as below:

$$\begin{aligned}\frac{d\sigma}{dt} = D\Bigg[\frac{d\varepsilon}{dt} - m\left(C_1 - \frac{1}{3K_s}\right)\left(s_{w1} + D_{s1}p_{w1}\right)\frac{dp_{w1}}{dt} \\ -m\left(C_2 - \frac{1}{3K_s}\right)\left(s_{w2} + D_{s2}p_{w2}\right)\frac{dp_{w2}}{dt} - m\frac{\beta_S}{3}\frac{dT}{dt}\Bigg],\end{aligned} \tag{3.1}$$

where σ and ε are the total stress and total stain, respectively; $D = (C_1 + C_2)^{-1}$ is the elastic matrix; $m^T = [1\ \ 1\ \ 0]$ is the unit normal column matrix; K_s, β_S, and T are the bulk modulus, synthesized thermal expansion coefficient, and temperature of the fractured porous rock mass, respectively; s_{w1}, p_{w1}, D_{s1}, C_1 and s_{w2}, p_{w2}, D_{s2}, C_2 are the saturation degree, water pressure, specific moisture content, and flexibility matrix of rock matrix and fractured network, respectively; t is the time.

3.2. Continuity Equation for Groundwater

On the basis of the principle of mass balance, the water volume flowing into an object during a time increment of dt is equal to the rate of water accumulation within the object. Assuming that the seepage of water can be expressed by Darcy law, the continuity equation for rock matrix is expressed by

$$\begin{aligned}-\nabla^T\left\{k_1\frac{k_{rw1}}{\mu_w}\nabla\left(p_{w1} + \gamma_w z\right)\right\} + \frac{\overline{\alpha}k_1k_{rw1}}{\mu_w}\left(p_{w1} - p_{w2}\right) \\ + A_1\frac{\partial\varepsilon}{\partial t} + B_1\frac{\partial p_{w1}}{\partial t} + E_1\frac{\partial p_{w2}}{\partial t} + F_1\frac{\partial T}{\partial t} - \nabla^T D_{t1}\nabla T = 0,\end{aligned} \tag{3.2}$$

where k_1 and k_{rw1} are the intrinsic permeability tensor and relative permeability of rock matrix, respectively; ρ_w, μ_w, and γ_w are the density, dynamic viscosity and unit weight of water, respectively; z is the head above some arbitrary datum; $\overline{\alpha}$ is a parameter determined by the aperture and geometry of fracture; D_{t1} is the thermal water diffusivity of rock matrix; and A_1, B_1, E_1, and F_1 are the constant matrixes.

For the fractured medium, the continuity equation of groundwater is:

$$\begin{aligned} &-\nabla^T\left\{k_2\frac{k_{rw2}}{\mu_w}\nabla\left(p_{w2}+\gamma_w z\right)\right\}-\frac{\overline{\alpha}k_1k_{rw1}}{\mu_w}\left(p_{w1}-p_{w2}\right)\\ &\quad+A_2\frac{\partial\varepsilon}{\partial t}+B_2\frac{\partial p_{w2}}{\partial t}+E_2\frac{\partial p_{w1}}{\partial t}+F_2\frac{\partial T}{\partial t}-\nabla^T D_{t2}\nabla T=0, \end{aligned} \tag{3.3}$$

where k_2 and k_{rw2} are the intrinsic permeability tensor and relative permeability of fractured medium, respectively; A_2, B_2, E_2 and F_2 can be obtained by replacing subscripts 1 and 2 in expressions of A_1, B_1, E_1 and F_1 with subscripts 2 and 1; D_{t2} is the thermal water diffusivity of fractured medium.

3.3. Energy Conservation Equation

In accordance with the principle of energy conservation, the rate of heat flowing into an object equals the increase of the internal energy within the object. The temperature field is single, and the energy conservation equation takes the form below:

$$\begin{aligned} &-\nabla^T\lambda\nabla T+\left(\mathrm{s_{w1}}\phi_1\mathrm{V}_1^a+\mathrm{s_{w2}}\phi_2\mathrm{V}_2^a\right)\rho_w C_w\left(\nabla^T T\right)\\ &\quad+\left[\left(1-\varphi_1\right)C_sT\frac{\rho_s}{K_s}\varphi_1C_wT\frac{\rho_w}{K_w}\right]\left(s_{w1}+D_{s1}p_{w1}\right)\frac{\partial p_{w1}}{\partial t}\\ &\quad-\left\{\left(1-\varphi_1\right)C_sT\rho_s\beta_s+\left(\varphi_1+\varphi_2\right)C_wT\rho_w\beta_w-\left[\left(1-\varphi_1\right)\rho_sC_s+\left(\varphi_1+\varphi_2\right)\rho_wC_w\right]\right\}\frac{\partial T}{\partial t}\\ &\quad+\frac{1}{2}\left(1-\phi_1\right)\beta_sT\frac{\partial}{\partial t}\left(u_{i,j}+u_{j,i}\right)\delta_{ij}=0, \end{aligned} \tag{3.4}$$

where C_w is the specific heat of water; C_s, ρ_s, and λ are the specific heat, density and thermal conductivity matrix of fractured porous rock mass, respectively; V_1^a and V_2^a are the apparent flow velocities of pore water and fracture water, respectively; u_i and u_j are the displacement components; δ_{ij} is the Kronecker's delta.

3.4. Percolation-Migration Equation

The percolation-migration equation in [20] was improved by us with the new meaning of adding the solute exchange between rock matrix and fractured network due to concentration

difference. The new percolation-migration equation is derived from the old one as follows:

$$R_i\theta_i\rho_w\frac{\partial c_i}{\partial t} = \nabla^T\theta_i\rho_w D_i\nabla c_i - \theta_i\rho_w V_i\nabla c_i - R_i\theta_i\rho_w\chi c_i + (-1)^{i+1}\overline{\omega}\theta_i\rho_w D_1(C_1 - C_2) - Q_{ci}, \quad (3.5)$$

where $i = 1, 2$ correspond to rock matrix and fractured network, respectively; R_i is the retardation coefficient and is defined as $R_i = V_i/V_i^* = (1 + (\rho_{\mathrm{di}}/\theta_i)K_{\mathrm{di}})$; V_i is the apparent velocity of groundwater; V_i^* is the transport velocity of radioactive nuclide; ρ_{di} is the dry density of rock matrix or fractured network; K_{di} is the distribution coefficient for saturated media; V_i is the apparent velocity of groundwater; θ_i the volumetric water content; D_i is the diffusion tensor; c_i is the concentration of solute; V_i is the apparent velocity vector of groundwater; χ is the radioactive decay constant; $\overline{\omega}$ is the coefficient which depends on the fracture aperture and geometry; Q_{ci} is the source term.

The diffusion tensor can be given by

$$D_{i\alpha\beta} = \alpha_{iT}|V_i|\delta_{\alpha\beta} + (\alpha_{iL} - \alpha_{iT})\frac{V_{i\alpha}V_{i\beta}}{|V_i|} + \alpha_{im}\tau_i\delta_{\alpha\beta}, \quad (3.6)$$

where α_{iT} is the transversal dispersivity; α_{iL} is the longitudinal dispersivity; $|V_i|$ is the absolute value of the apparent flow velocity; α_{im} is the molecular diffusion coefficient; τ_i is the tortuosity coefficient; $\delta_{\alpha\beta}$ is the Kronecker's delta.

The discretizations both in space and time domains are carried out for the equilibrium equation, the continuity equation, the energy conservation equation, and the percolation-migration equation by Galerkin method, and then the FEM pattern can be obtained.

The models of stress corrosion and pressure dissolution developed by Yasuhare et al. were introduced into the governing equations above for T-H-M coupling in dual-porosity rock mass by the author, and the corresponding algorithm was consulted in [21, 22].

4. Computation Example

The computation model in laboratory scale is shown in Figure 3. A canister filled with the vitrified radioactive nuclear waste is disposed at a certain depth beneath the ground surface, and the surrounding rock mass is quartzite which is also an unsaturated dual-porosity medium. As an approximate simplification, it is treated to be a plane strain problem. A computation region with a horizontal length of 4 m and a vertical length of 8 m is taken. There are 800 elements and 861 nodes in the mesh. From the midpoint at the right margin of the vitrified waste to right, the node numbers are 432, 433, 434, 435, and 436, respectively. The boundary conditions are as follows.

The free displacement is allowed for the top of computation domain over which the vertical distributed load of $\sigma_v = 26.7$ MPa is exerted; both the left and right sides are fixed horizontally; the bottom face is fixed vertically; on all the boundary faces the pore pressure, fracture pressure, and temperature are constant with values of −4.59 MPa, −0.46 MPa, and 20°C, respectively. There exist one set of horizontal fractures and one group of vertical ones in the rock matrix, separately. The state of coupled T-H-M is to act as the role of stress corrosion and pressure solution on the fracture aperture. The relative calculating parameters are tabulated in Tables 1, 2 (The parameter values in these two tables are assumed by the authors, but they have reasonable orders.), and Table 3 (All the parameters in this table are taken from

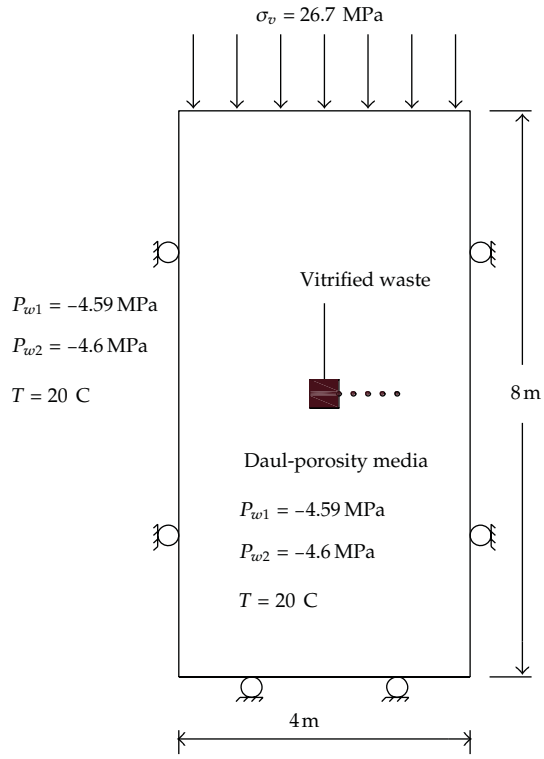

Figure 3: Computation model.

[10] except R_{c0}, $\overline{R}$, and JRC.). The saturations of rock matrix and fracture system are 0.44 and 0.01, respectively, and the temperature of rock mass is the uniform value of 20°C at the initial state. The waste continuously releases heat with a constant power of 1000 W during a period of 4 years [23].

The water retention curves of both porous and fracture media conform to the Van Genuchten model, that is,

$$s_w = (s_{ws} - s_{wr})\left(1 + \left|\alpha\psi\right|^n\right)^{-m} + s_{wr}, \tag{4.1}$$

where $\alpha = 3.86 \times 10^{-6}\,\mathrm{m}^{-1}$, $n = 1.41$ for the rock matrix; $\alpha = 5.26 \times 10^{-4}\,\mathrm{m}^{-1}$, $n = 2.55$ for the fracture system; $m = 1 - 1/n$; ψ is the water potential head; s_{ws} is the maximum saturation with a value of 1.0 while s_{wr} is the minimum saturation of which the values are 0.19 for the rock mass and 0.01 for the fracture system, respectively.

The relationship between relative permeability and saturation degree is

$$k_{rw} = s_w^{2.0}. \tag{4.2}$$

Both the thermal water diffusivities of the rock matrix and fracture system are taken as

$$D_t = 2.5 \times 10^{-10}\,\mathrm{m}^2/\mathrm{s}^\circ\mathrm{C}. \tag{4.3}$$

Table 1: Main computation parameters.

Property	Rock mass	Vitrified waste
Density, ρ (kN·m^{-3})	26.7	25.0
Porosity, ϕ_1	0.11	0.0
Permeability, k_1/μ_w (m^2·Pa^{-1}·s^{-1})	1.24×10^{-13}	1.0×10^{-27}
Young's modulus, E (GPa)	37.0	53.0
Poisson's ratio, μ	0.3	0.25
Specific heat, C (kJ·kg^{-1} · °C^{-1})	1.0	0.7
Thermal expan. coeff., β (°C^{-1})	8.8×10^{-6}	1.0×10^{-5}
Thermal conductivity, λ (W·m^{-1} · °C^{-1})	2.8	5.3

Table 2: Parameters for fracture sets used in calculation.

Parameter	Horizontal fracture	Vertical fracture
Spacing, S (m)	0.3	0.3
Continuity ratio, l	1	1
Dip angle, θ(°)	0	90
Normal stiffness, k_n (MPa/m)	1000.0	2000.0
Shearing stiffness, k_s (MPa/m)	500.0	1000.0
Porosity, ϕ_2	0.01	0.01
Permeability, k_2/μ_w (m^2/Pa·s)	9.7×10^{-9}	9.7×10^{-9}

Table 3: Parameters for stress corrosion and pressure solution.

Parameter	Unit	Values
Empirical constant, a	—	5.0
Origin asperity contact-area ratio, R_{c0}	—	0.1
Nominal asperity contact-area ratio, $\overline{R}$	—	1.0
Roughness coefficient of fracture, JRC	—	2.5
Factor, A_{H_2O}	ms^{-1}	1.12×10^{-4} T
Factor, A_{OH^-}	ms^{-1}	2.51×10^{3} T
Origin aperture, E_0	m	0.0125
Residual aperture, E_r	m	0.0025
Constant, $b^*_{H_2O}$	N^{-1} m$^{3/2}$	2.69×10^{-5} (quartz)
Constant, $b^*_{OH^-}$	N^{-1} m$^{3/2}$	1.78×10^{-5} (quartz)
Activation energy, E_a	J·mol^{-1}	7.0×10^{4} (quartz)
Heat of fusion, E_m	J·mol^{-1}	8.57×10^{3} (quartz)
Activation enthalpy for H_2O, ΔH_{H_2O}	J·mol^{-1}	6.6×10^{4}
Activation enthalpy for OH^-, ΔH_{OH^-}	J·mol^{-1}	8.27×10^{4}
Reference dissolution rate constant, k^0_+	mol·m^{-2} s^{-1}	1.59
Infinitesimal distance from crack tip, r	m	1.0×10^{-6}
Gas constant, R	J·mol^{-1} K^{-1}	8.31
Temperature of fusion, T_m	K	1883 (quartz)
Molar volume, V_m	m^3 mol^{-1}	2.27×10^{-5} (quartz)
Fraction of Si–O reacting with H_2O, $\theta^{H_2O}_{Si-O}$	—	0.99921 (pH = 7)
Fraction of Si–O reacting with OH^-, $\theta^{OH^-}_{Si-O}$	—	0.00079 (pH = 7)

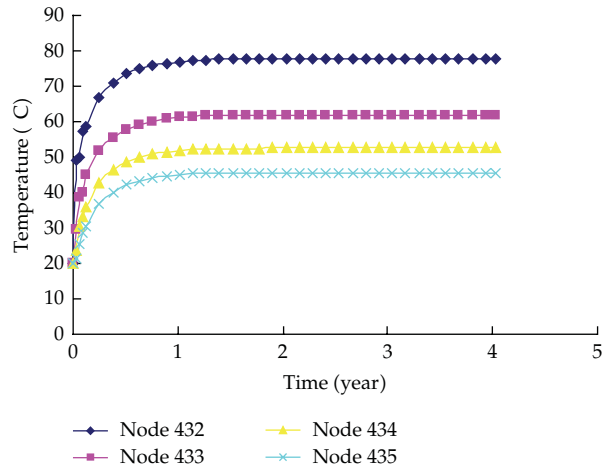

Figure 4: Temperatures versus time at some nodes for case 1.

The vitrified waste is the source term with a diffusive mass flux of radioactive nuclides $Q_{c1} = 1.44 \times 10^{-10}$ mol·kg/m^3·s^{-1}. The constants used in the computation concerned with the percolation-migration of nuclide are supposed as follows: the tortuosity coefficients τ_1, τ_2 are 0.4 and 0.8, respectively; the dispersivities in the longitudinal direction α_{1L} and α_{2L} are 1.0 m and 2.0 m, respectively; the dispersivities in the transversal direction are $\alpha_{iT} = \alpha_{iL}/10$; the molecular diffusion coefficients α_{1m} and α_{2m} are 1.0×10^{-9} m^2/s and 2.0×10^{-9} m^2/s, respectively; the distribution coefficients K_{d1} and K_{d2} are 8.0 mL/g and 5.3 mL/g, respectively; the dry densities ρ_{d1} and ρ_{d2} are 23.0 kg/m^3 and 21.0 kg/m^3, respectively; the parameter $\overline{\omega}$ is 100.0 m^{-2}; the radioactive decay constant $\chi = \ln 2/T_{\text{half}}$, where T_{half} is the half life of radioactive nuclide and is taken as 1000 years in the computation. The waste radiates continuously heat with a power of 1000 W during a period of 4 years, and the time step is taken as 100000 s.

For the two cases with different evolutions of fracture aperture above, the change and distribution of the temperatures, displacements, pore pressures, nuclide concentrations and stresses in the rock mass are studied. The analyses of the main computation results are as follows.

The changes of temperatures in calculation region for case 1 and 2 are basically the same. Taking case 1 for instance, the temperatures versus time at nodes 432, 433, 434, and 435 are shown in Figure 4. In the early 0.1 a, the temperature of buffer increases fast, then it grows slowly. At the termination of computation, the temperatures of nodes 432, 433, 434, and 435 are 77.8°C, 62.0°C, 52.5°C, and 45.7°C, respectively.

Induced by the stress corrosion and pressure dissolution, the aperture closure rates of the horizontal fracture and the vertical fracture at the midpoint on the right edge of the canister versus time are plotted in Figures 5 and 6, respectively. It can be seen that both the rates due to these two factors climb up, then decline after the peak, and furthermore tend towards stability slowly. The aperture closure rates caused by stress corrosion are almost six orders higher than those caused by pressure solution. This response is similar with the conclusions presented in [10]. Meanwhile, the aperture closure rates of horizontal fractures are larger than those of vertical fractures, and the reason is that the vertical stresses are higher than the horizontal ones in rock mass. The apertures and the asperity contact-area ratios of

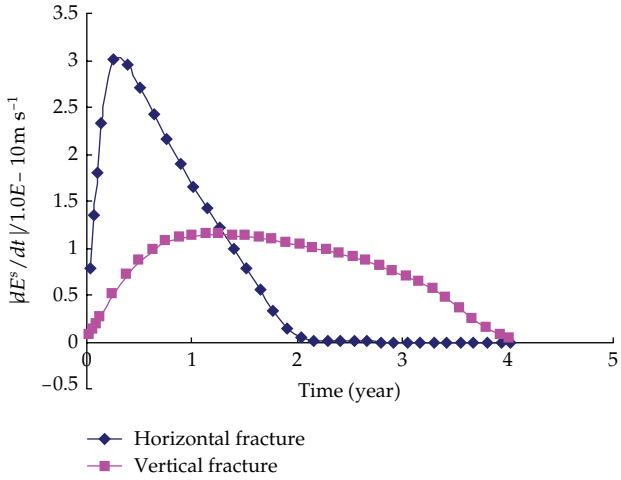

Figure 5: $|dE^s/dt|$ caused by stress corrosion versus time at middle point of right margin of vitrified waste.

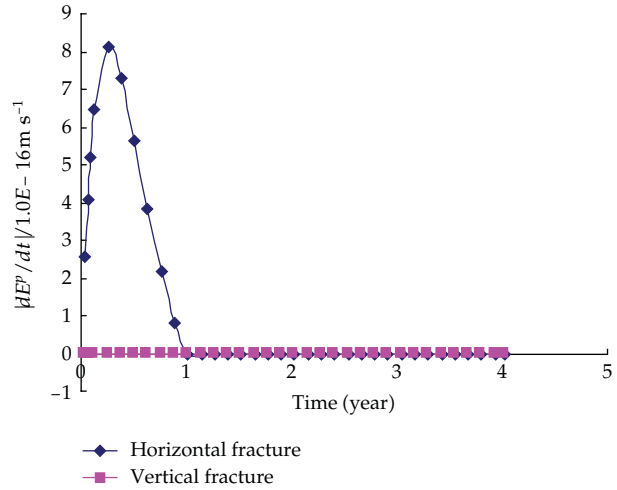

Figure 6: $|dE^p/dt|$ caused by pressure solution versus time at middle point of right margin of vitrified waste.

the horizontal fracture and the vertical fracture at the midpoint mentioned above versus time are presented in Figures 7 and 8, respectively. For the former, the apertures decrease from the original value and then tend towards the residual value. The contact-area ratios of asperities increase also from initial value then towards the nominal value (unit value), and the changes of the values corresponding to the horizontal fractures are more significant. It can be seen in Figure 9 that stress intensity factor ratio on vertical crack is much larger than that on horizontal crack at this midpoint, and both of them reduce over time. It is shown in Figure 10 that at this midpoint, the critical stresses of horizontal fracture and vertical fracture are equal. They decline rapidly at the beginning, and then tend towards constant. This phenomenon is just due to the combined effects of temperature, stress, and chemistry.

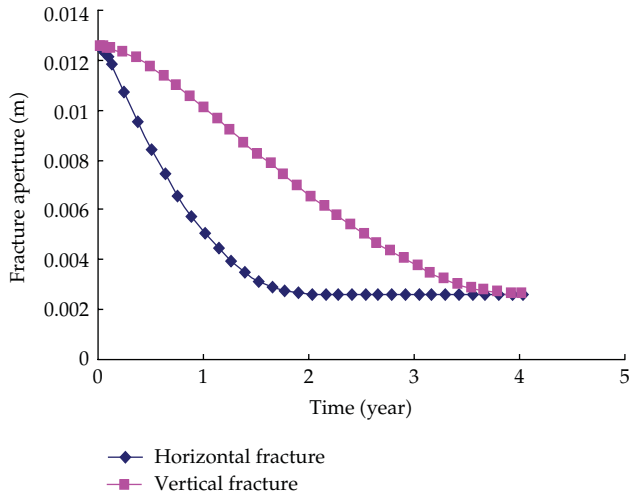

Figure 7: Fracture apertures versus time at middle point of right margin of vitrified waste.

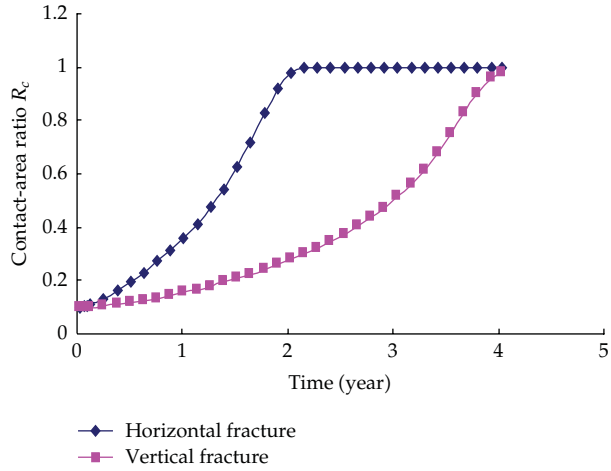

Figure 8: Contact-area ratios versus time at middle point of right margin of vitrified waste.

Pore and fracture pressures at nodes 432, 433, 434, and 435 versus time for case 1 and case 2 are presented in Figures 11 and 12, respectively. It can be seen that negative pore and fracture pressures rise higher for case 1 than those for case 2. Particularly, at node 432 where the effects of stress corrosion and pressure solution are the most intense, the negative fracture pressure reaches a quite large value. The reason of this response is that the reduction of stress corrosion and pressure dissolution on the fracture apertures and the change of pore permeability with time are considered for case 1, while the fracture apertures and the pore permeability remain constants for case 2. The negative pore and fracture pressures at node 432 at 4 a are −12.25 MPa, −7.95 MPa for case 1 and −6.03 MPa, −0.66 MPa for case 2, respectively. Contours of pore and fracture pressures within a range of 2 m × 2 m around the canister at 4 years for case 1 and case 2 are described in Figures 13 and 14, respectively. It is found that the

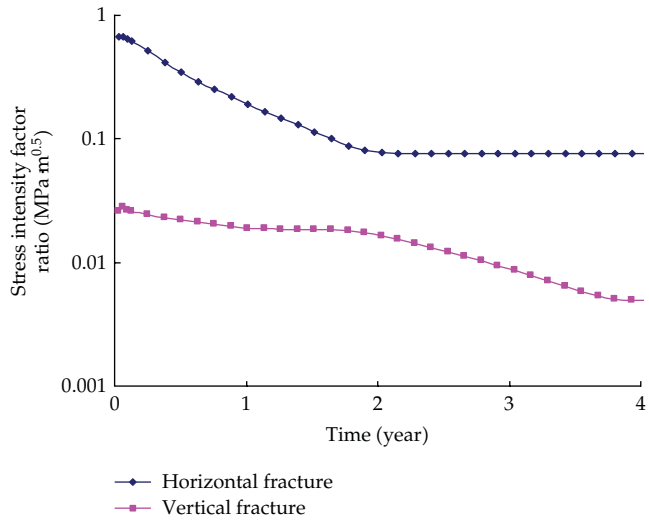

Figure 9: Stress intensity factor ratios versus time at middle point of right margin of vitrified waste.

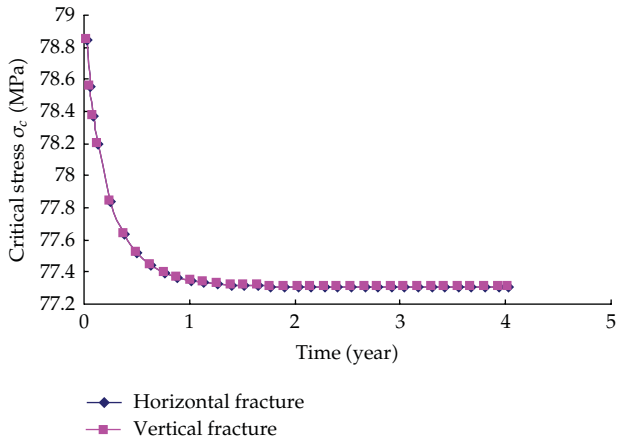

Figure 10: Critical stresses versus time at middle point of right margin of vitrified waste.

fracture pressures affected by the stress corrosion and pressure dissolution for case 1 have a significant growth around the canister as compared with case 2.

The flow vector distributions of pore and fracture water in calculation domain at 4 a for the two cases are presented in Figure 15. The fracture flow vectors for case 1, on which the effects of stress corrosion and pressure dissolution are considered, are quite distinguished from those for case 2, especially in the vicinity of canister. Taking the node 432 for instance, flow velocities of pore and fracture are 3.40×10^{-8} m/s, 1.52×10^{-8} m/s for case 1 and 2.32×10^{-8} m/s, 2.77×10^{-8} m/s for case 2, respectively.

Pore and fracture concentrations at nodes 432, 433, 434, and 435 versus time for the two cases are presented in Figures 16 and 17, respectively. Compared with case 2 in which all of the aperture, porosity, and pore permeability are constants, the nuclides both in fracture and pore are gathered largely in case 1 for the reason that both the reduction of aperture

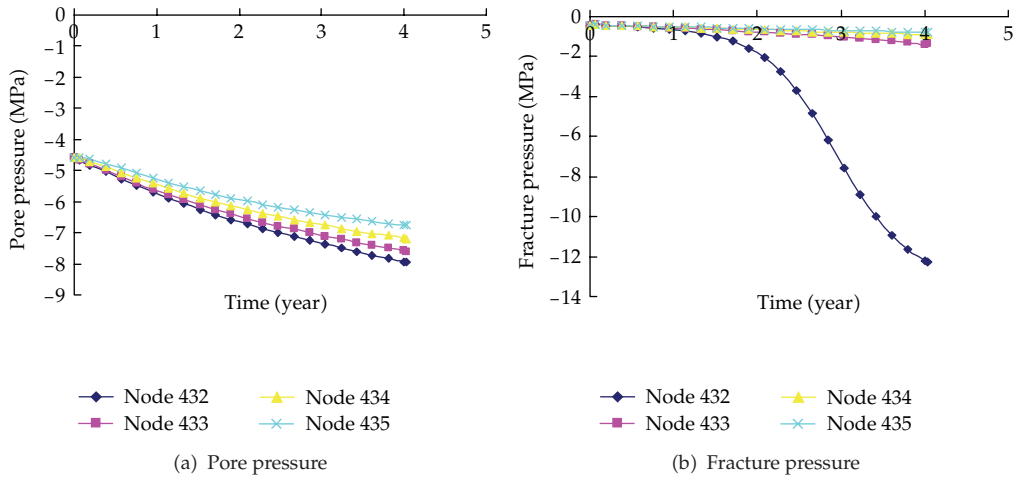

(a) Pore pressure (b) Fracture pressure

Figure 11: Pore and fracture water pressures versus time at some nodes for case 1.

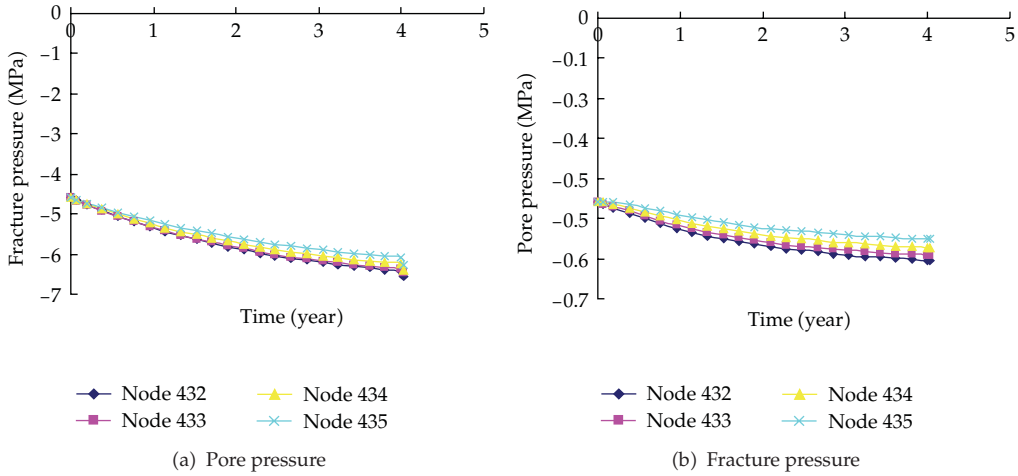

(a) Pore pressure (b) Fracture pressure

Figure 12: Pore and fracture water pressures versus time at some nodes for case 2.

due to stress corrosion and pressure dissolution and the compression of porosity due to mean effective stress lead to decreasing the permeabilities of pore and fracture. The nuclide concentrations at nodes 432, 433, 434, and 435 at 4 a for the two cases are 20.18/6.82, 15.42/3.60, 12.06/2.55 and 9.36/1.76 for rock matrix, and 10.86/8.44, 8.39/6.82, 6.28/5.54 and 5.00/4.63 for fracture system, respectively, (the values in the left and right of "/" are for case 1 and 2, resp., and their units are 10^{-3} mol/m^3). Contours of pore and fracture concentrations within a range of 2 m × 2 m around the canister at 4 years for case 1 and case 2 are described in Figures 18 and 19, respectively.

The differences between the magnitudes and distributions of stresses within the rock mass in the two cases are quite small for the reason that the impacts of negative pore pressure and negative fracture pressure on the mechanical balance are not considered [24]. For instance, normal stress contours in calculation domain at 4 a for case 1 are given in Figure 20.

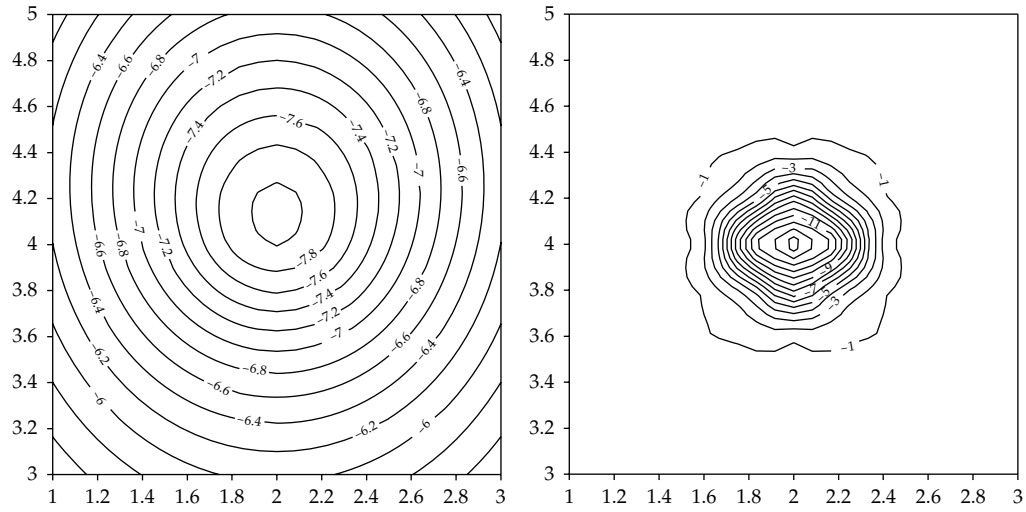

(a) Pore pressure (b) Fracture pressure

Figure 13: Contours of pore and fracture pressures in a 2 m × 2 m area at 4 years for case 1 (MPa).

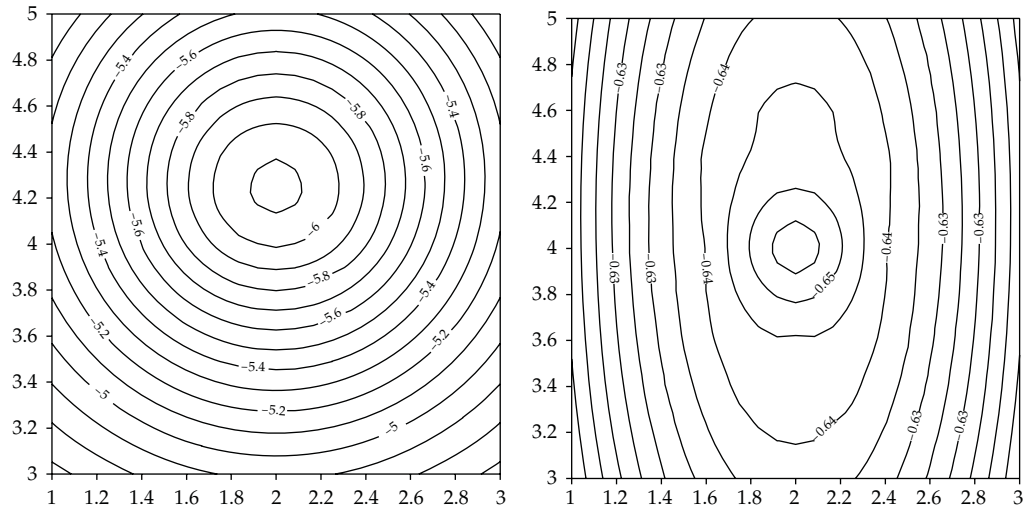

(a) Pore pressure (b) Fracture pressure

Figure 14: Contours of pore and fracture pressures in a 2 m × 2 m area at 4 years for case 2 (MPa).

It can be known that the stress fields, influenced by the existence of the vitrified waste and the effect of radiating heat, are distinguished from those caused only by the gravity of rock mass (the contours of the latter are the horizons). At 4 a, the horizontal stress and vertical stress at the midpoint on the right edge of the canister are −0.124 MPa and −26.75 MPa, respectively. The compressive effect is not to be analyzed in this paper.

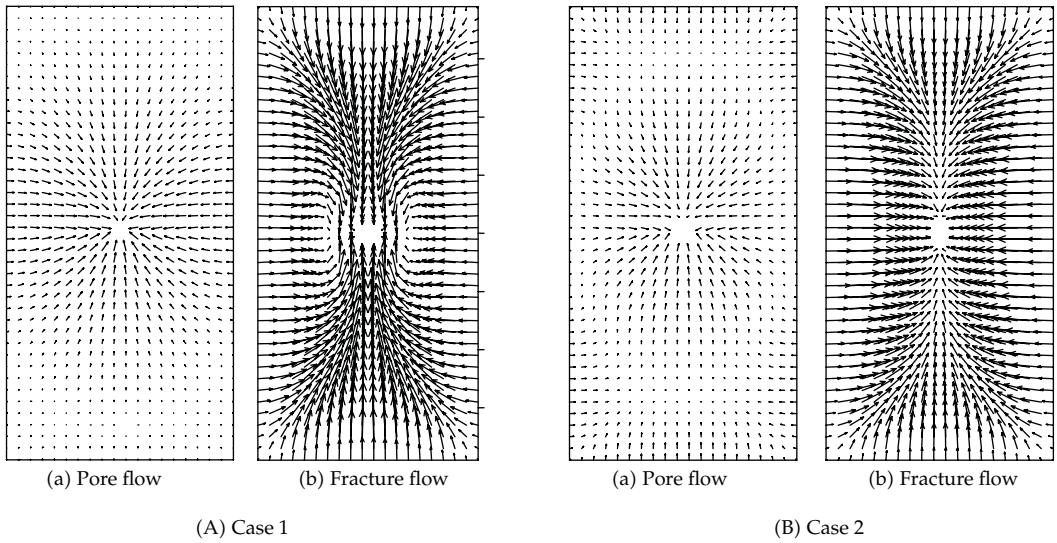

Figure 15: Flow vectors of pore and fracture water in calculation domain at 4 years.

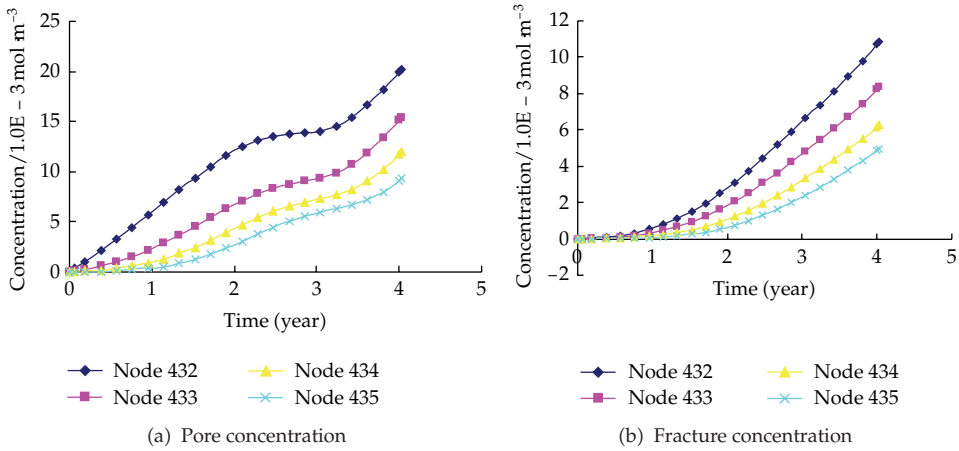

Figure 16: Nuclide concentrations versus time at some nodes for case 1.

5. Concluding Remarks

Based on the introduction of stress corrosion and pressure dissolution of fracture aperture as well as the concentration field of solute, the existing governing equations for T-H-M coupling in dual-porosity rock mass were developed to a model for T-H-M-M coupling. Taking a hypothetical model for geological disposal of nuclear waste with a nuclide leakage in an unsaturated dual-porosity rock mass as a calculation example, on the basis of the two cases whether the changes of fracture apertures with stress corrosion and pressure dissolution are considered or not (meanwhile whether the porosity of rock matrix is the stress function or not), the change and distribution of temperatures, rates and magnitudes of aperture closure, pore pressures, flow velocities, nuclide concentrations, and stresses in rock mass were

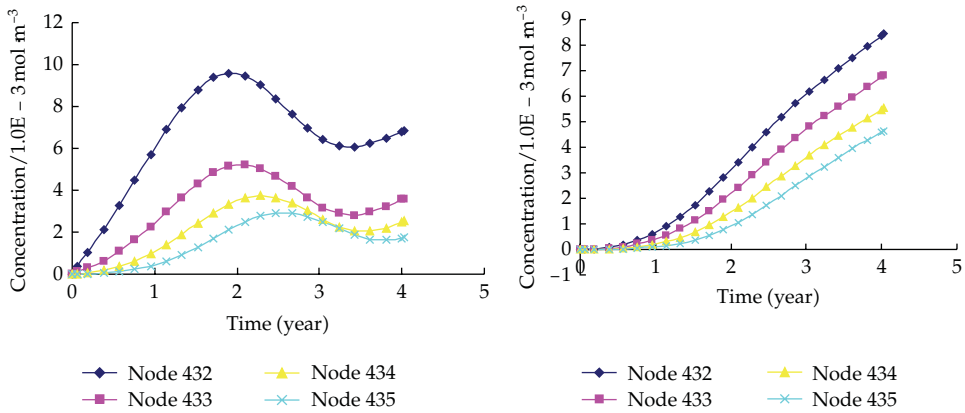

(a) Pore concentration (b) Fracture concentration

Figure 17: Nuclide concentrations versus time at some nodes for case 2.

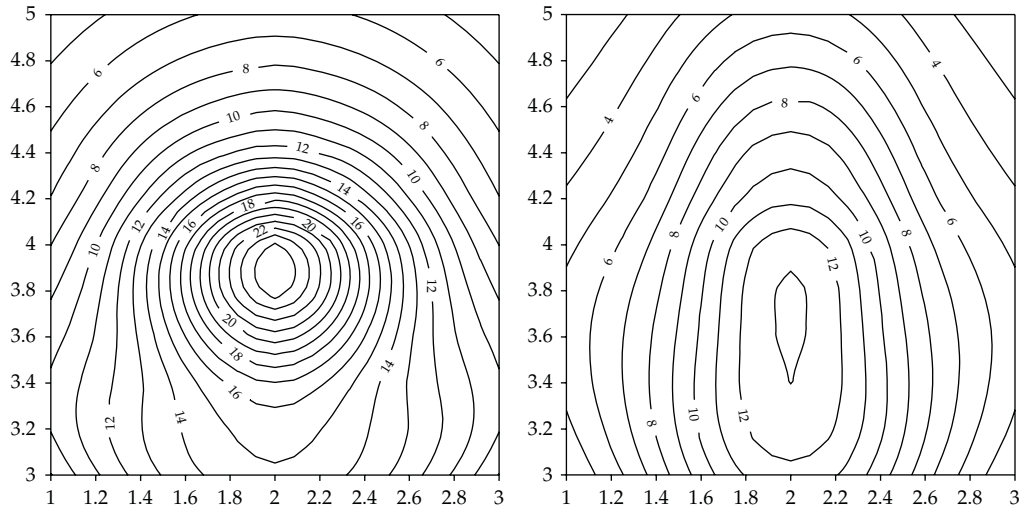

(a) Pore concentration (b) Fracture concentration

Figure 18: Contours of nuclide concentration in a 2 m × 2 m area at 4 years for case 1 (10^{-3} mol/m^3).

investigated by the two-dimensional FEM simulation for the coupled T-H-M-M processes. It is shown from the computing results that the temperature differences between case 1 and case 2 are not large, and the temperature in near field can reach 30.0~80.0°C at the end of calculation (4 a); the aperture closure rates caused by stress corrosion are almost six orders higher than those produced by pressure solution, and the two kinds of closure rates rise and then reduce, and furthermore tend towards stability; the fracture apertures decrease from the original value and tend towards the residual value while the contact-area ratios of asperities increase from the original value and tend towards the nominal value; the tensile stress and critical stress exerted over cracks decline over time and then tend towards constants; the negative fracture pressures for the case in which the effects of stress corrosion and pressure solution are considered in near field rise more highly than those for the case in which the

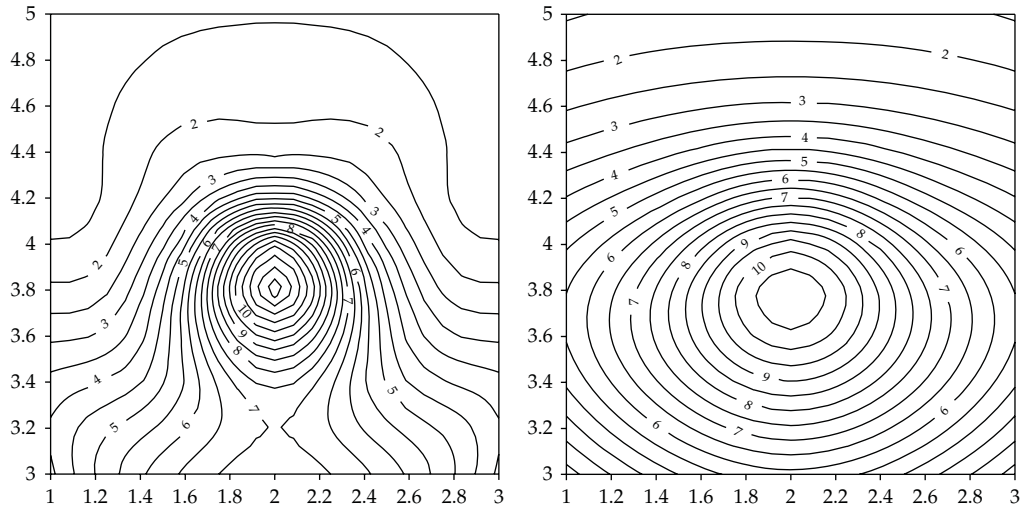

(a) Pore concentration (b) Fracture concentration

Figure 19: Contours of nuclide concentration in a 2 m × 2 m area at 4 years for case 2 (10^{-3} mol/m^3).

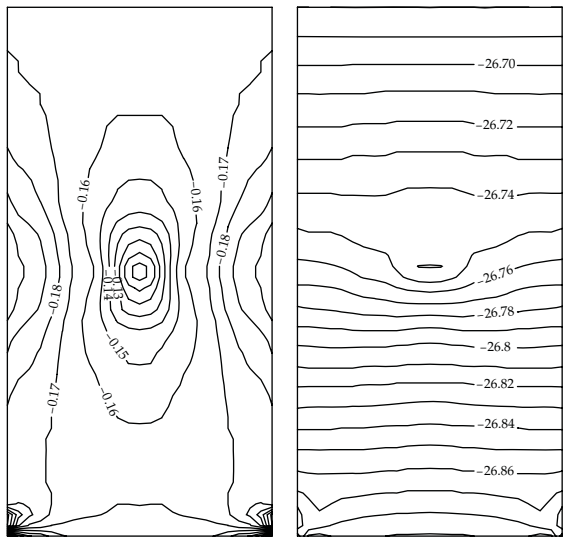

(a) Horizontal stress (b) Vertical stress

Figure 20: Normal stress contours in calculation domain at 4 years for case 1 (MPa).

corresponding effects are not considered, and the differences of flow vectors between the two cases are quite large; the permeabilities of fracture and pore decline resulted from stress corrosion, pressure dissolution, and mean effective stress in case 1, while they are constants in case 2, so the concentrations both in fracture and pore for the former are larger than those for the latter. but the differences between the magnitudes and distributions of stresses within the rock mass in two cases are very small.

However, the models of stress corrosion and pressure solution by Yasuhara et al. are based on the laboratory test for small scale rock, and the application of them in large-scale rock mass engineering remain to be examined. They are applied on FEM analysis with THMM coupling for a hypothetical model of geological disposal of nuclear waste in an unsaturated rock mass by the authors, and the reliability of it is limited in a certain extent. The further research remains to be carried out in the future.

Acknowledgments

This paper is supported by the National Key Basic Research and Development Program of China (973 Project) (Grant no. 2010CB732101), the National Natural Science Foundation of China (Grant no. 51079145), and the National Key Technology R&D Program (Grant no. 2009-BAK53B03).

References

[1] B. K. Atkinson, "A fracture mechanics study of subcritical tensile cracking of quartz in wet environments," *Pure and Applied Geophysics*, vol. 117, no. 5, pp. 1011–1024, 1979.

[2] P. M. Dove, "The dissolution kinetics of quartz in sodium chloride solutions at 25° to 300°C," *American Journal of Science*, vol. 294, no. 6, pp. 665–712, 1994.

[3] J. S. Chester, S. C. Lenz, F. M. Chester, and R. A. Lang, "Mechanisms of compaction of quartz sand at diagenetic conditions," *Earth and Planetary Science Letters*, vol. 220, no. 3-4, pp. 435–451, 2004.

[4] Y. Nara and K. Kaneko, "Study of subcritical crack growth in andesite using the Double Torsion test," *International Journal of Rock Mechanics and Mining Sciences*, vol. 42, no. 4, pp. 521–530, 2005.

[5] P. Y. F. Robin, "Pressure solution at grain-to-grain contacts," *Geochimica et Cosmochimica Acta*, vol. 42, no. 9, pp. 1383–1389, 1978.

[6] T. Dewers and A. Hajash, "Rate laws for water-assisted compaction and stress-induced water- rock interaction in sandstones," *Journal of Geophysical Research*, vol. 100, no. 7, pp. 13–112, 1995.

[7] A. Revil, "Pervasive pressure-solution transfer: a poro-visco-plastic model," *Geophysical Research Letters*, vol. 26, no. 2, pp. 255–258, 1999.

[8] H. Yasuhara, D. Elsworth, and A. Polak, "Evolution of permeability in a natural fracture: significant role of pressure solution," *Journal of Geophysical Research B*, vol. 109, no. 3, pp. B03204–11, 2004.

[9] P. M. Dove, "Geochemical controls on the kinetics of quartz fracture at subcritical tensile stresses," *Journal of Geophysical Research*, vol. 100, no. 11, pp. 22–359, 1995.

[10] H. Yasuhara and D. Elsworth, "Compaction of a rock fracture moderated by competing roles of stress corrosion and pressure solution," *Pure and Applied Geophysics*, vol. 165, no. 7, pp. 1289–1306, 2008.

[11] J. Taron and D. Elsworth, "Thermal-hydrologic-mechanical-chemical processes in the evolution of engineered geothermal reservoirs," *International Journal of Rock Mechanics and Mining Sciences*, vol. 46, no. 5, pp. 855–864, 2009.

[12] J. Taron and D. Elsworth, "Coupled mechanical and chemical processes in engineered geothermal reservoirs with dynamic permeability," *International Journal of Rock Mechanics and Mining Sciences*, vol. 47, no. 8, pp. 1339–1348, 2010.

[13] J. Taron and D. Elsworth, "Constraints on compaction rate and equilibrium in the pressure solution creep of quartz aggregates and fractures: controls of aqueous concentration," *Journal of Geophysical Research B*, vol. 115, no. 7, Article ID B07211, 2010.

[14] K. B. Min, J. Rutqvist, and D. Elsworth, "Chemically and mechanically mediated influences on the transport and mechanical characteristics of rock fractures," *International Journal of Rock Mechanics and Mining Sciences*, vol. 46, no. 1, pp. 80–89, 2009.

[15] Y. J. Zhang and W. Q. Zhang, "Finite element analysis of influence of pressure solution of fracture aperture on T-H-M coupling in dual-porosity medium," *Yantu Lixue/Rock and Soil Mechanics*, vol. 31, no. 4, pp. 1269–1275, 2010 (Chinese).

[16] E. Sonnenthal, A. Ito, N. Spycher et al., "Approaches to modeling coupled thermal, hydrological, and chemical processes in the drift scale heater test at Yucca Mountain," *International Journal of Rock Mechanics and Mining Sciences*, vol. 42, no. 5-6, pp. 698–719, 2005.

[17] R. Olsson and N. Barton, "An improved model for hydromechanical coupling during shearing of rock joints," *International Journal of Rock Mechanics and Mining Sciences*, vol. 38, no. 3, pp. 317–329, 2001.

[18] D. T. Snow, "Anisotropic permeability of fractured media," *Water Resources Research*, vol. 5, no. 6, pp. 1273–1289, 1969.

[19] J. P. Davies and D. K. Davies, "Stress-dependent permeability: characterization and modeling," in *Proceedings of the SPE Annual Technical Conference and Exhibition*, SPE 56813, Houston, Tex, USA, 1999.

[20] M. Nishigaki, "Density dependent transport analysis saturateds-unsaturated porous media—3 dimensional eulerian lagrangian method," Okayama University, 2001.

[21] Y. Zhang and W. Zhang, "3D thermo-hydro-mechanical-migratory coupling model and FEM analyses for dual-porosity medium," *Science China Technological Sciences*, vol. 53, no. 8, pp. 2172–2182, 2010.

[22] Y.-J. Zhang and C.-S. Yang, "coupled hermo-hydro-mechanical—migratory model for dual-porosity medium and numerical analysis," *Journal of Central South University of Technology*, vol. 18, no. 4, pp. 1256–1262, 2011.

[23] J. Rutqvist, B. Freifeld, K. B. Min, D. Elsworth, and Y. Tsang, "Analysis of thermally induced changes in fractured rock permeability during 8 years of heating and cooling at the Yucca Mountain Drift Scale Test," *International Journal of Rock Mechanics and Mining Sciences*, vol. 45, no. 8, pp. 1373–1389, 2008.

[24] M. Chijimatsu, H. Kurikami, A. Ito, and Y. Sugita, "Implication of THM coupling on the near-field of a nuclear waste repository in a homogeneous rock mass," DECOVALES III-Task3-Bench Mark Test 1(BMT1)-Subtask BMT1-B, pp.1–43, 2002.

Hindawi Publishing Corporation
Journal of Applied Mathematics
Volume 2012, Article ID 139583, 24 pages
doi:10.1155/2012/139583

Research Article

A Stabilized Incompressible SPH Method by Relaxing the Density Invariance Condition

Mitsuteru Asai,[1] Abdelraheem M. Aly,[1] Yoshimi Sonoda,[1] and Yuzuru Sakai[2]

[1] *Department of Civil Engineering, Kyushu University, 744 Motooka, Nishi–ku, Fukuoka 819-0395, Japan*
[2] *Faculty of Education and Human Science, Yokohama National University, 79-1 Tokiwadai, Hodogaya-ku, Yokohama 240-8501, Japan*

Correspondence should be addressed to Mitsuteru Asai, asai@doc.kyushu-u.ac.jp

Received 5 January 2012; Accepted 16 March 2012

Academic Editor: Hiroshi Kanayama

A stabilized Incompressible Smoothed Particle Hydrodynamics (ISPH) is proposed to simulate free surface flow problems. In the ISPH, pressure is evaluated by solving pressure Poisson equation using a semi-implicit algorithm based on the projection method. Even if the pressure is evaluated implicitly, the unrealistic pressure fluctuations cannot be eliminated. In order to overcome this problem, there are several improvements. One is small compressibility approach, and the other is introduction of two kinds of pressure Poisson equation related to velocity divergence-free and density invariance conditions, respectively. In this paper, a stabilized formulation, which was originally proposed in the framework of Moving Particle Semi-implicit (MPS) method, is applied to ISPH in order to relax the density invariance condition. This formulation leads to a new pressure Poisson equation with a relaxation coefficient, which can be estimated by a preanalysis calculation. The efficiency of the proposed formulation is tested by a couple of numerical examples of dam-breaking problem, and its effects are discussed by using several resolution models with different particle initial distances. Also, the effect of eddy viscosity is briefly discussed in this paper.

1. Introduction

The meshless particle methods have been applied in many engineering applications including the free-surface fluid flows. In the particle methods, the state of a system is represented by a set of discrete particles, without a fixed connectivity; hence, such methods are inherently well suited for the analysis of moving discontinuities and large deformations such as the free-surface fluid flows with breaking and fragmentation.

The SPH technique was originally proposed by Lucy [1] and further developed by Gingold and Monaghan [2] for treating astrophysical problems. Its main advantage is

the absence of a computational grid or mesh since it is spatially discretized into Lagrangian moving particles. This allows the possibility of easily modeling flows with a complex geometry or flows where large deformations or the appearance of a free surface occurs. At the present time, it is being exploited for the solution of problems appearing in different physical processes. Monaghan [3] has provided a fairly extensive review of SPH methods. The SPH method had been applied into compressible and incompressible viscous flow problems [4–7]. The SPH is originally developed in compressible flow, and then some special treatment is required to satisfy the incompressible condition. One approach is to run the simulations in the quasi-incompressible limit, that is, by selecting the smallest possible speed of sound which still gives a very low Mach number ensuring density fluctuations within 1% [4, 5]. This method is known as the Weakly Compressible Smooth Particle Hydrodynamics (WCSPH). In the WCSPH, the artificial viscosity, which is originally developed by Monaghan, has been widely used not only for the energy dissipation but also for preventing unphysical penetration of particles. Recently, a proposal for constructing an incompressible SPH model has been introduced, whose pressure is implicitly calculated by solving a discretized pressure Poisson equation at every time step [8–17].

Lee et al. [13] presented comparisons of a semi-implicit and truly incompressible SPH (ISPH) algorithm with the classical WCSPH method, showing how some of the problems encountered in WCSPH have been resolved by using ISPH to simulate incompressible flows. They used the function of temporal velocity divergence for discretized source terms of Poisson equation of pressure to ensure truly incompressible flow. Khayyer et al. [14, 15] proposed a corrected incompressible SPH method (CISPH) derived based on a variational approach to ensure the angular momentum conservation of ISPH formulations to improve the pressure distribution by improvement of momentum conservation and the second improvement is achieved by deriving and employing a higher-order source term based on a more accurate differentiation.

The source term in pressure Poisson equation (PPE) for ISPH is not unique; it has several formulations in the literature; one of them as a function of density variation and the other utilizes velocity divergence condition to formulate the source term. The former formulation with the density variation can keep a uniform particle distribution, although evaluated pressure include high unrealistic fluctuation. On the other hand, the formulation of the divergence-free condition evaluates much smoother pressure distribution, but density errors may occur due to particle clustering. Then, modified schemes have been proposed to satisfy the above two conditions: density invariant and divergence-free condition. Pozorski and Wawrenczuk [9] proposed a modified scheme, in which both the PPEs are solved separately at two intermediate states in each time step. Hu and Adams [16, 17] introduced internal iterations to satisfy both conditions accurately at the same moment. These modified schemes need to solve multiple PPEs in each time step, and these computational costs become expense compared to the conventional ISPH.

Recently, in the framework of MPS, there is a trend to introduce a higher-order source term in the PPE. Kondo and Koshizuka [18] proposed a new formulation with a source term composed by three parts; one is main part and another two terms related to error-compensating parts. Tanaka and Masunaga [19] introduced a similar high-order source term with two components incorporated with quasi-compressibility. Note that the number of PPEs per time step in their higher-order source term formulations is just one and its numerical cost is almost same as the original scheme. In this study, we reformulate a source term of the PPE which contains both contributions from velocity-divergence-free and density invariance conditions. Only one PPE per time step should be solved as the recent development in

the MPS, but our formulation with a relaxation coefficient is unique. Note that, the relaxation coefficient depends on the initial particle distance, and a suitable relaxation coefficient can be obtained from the hydrostatic pressure calculations as a preanalysis. The accuracy and the efficiency of the proposed model are investigated in a couple of examples which are previously selected in published papers.

The turbulence models in the SPH are also important issue and the effects in the WCSPH have been nicely investigated by Violeau and Issa [20]. Lee et al. have introduced the same turbulence model such as k-ε model into ISPH. Gotoh et al. [21] and Shao and Gotoh [22] introduced the static Smagorinsky model into the ISPH, and he discussed the effect of additional eddy viscosity shortly. In this paper, we also discuss the effect of eddy viscosity from our simulation results.

2. Typical Incompressible Smoothed Particle Hydrodynamics (ISPHs) Formulation

In this section, typical ISPH formulation, which is similar procedure in moving particle semi-implicit method (MPS) proposed by Koshizuka and Oka [24], is summarized. The main feature is that semi-implicit integration scheme is applied into particle discretized equations for the incompressible flow problem. The original idea of the semi-implicit scheme is called by projection method, which has been widely used in the finite difference method and in the finite element method. After the basic application of projection method into SPH is described here, several similar schemes will be categorized by the difference of treatment of PPE in the next section.

2.1. The Governing Equations for Incompressible Flow

In the Lagrange description, the continuity equation and the Navier-Stokes equations can be written as

$$\frac{D\rho}{Dt} + \rho\nabla\cdot\mathbf{u} = 0, \tag{2.1}$$

$$\frac{D\mathbf{u}}{Dt} = -\frac{1}{\rho}\nabla P + \upsilon\nabla^2\mathbf{u} + \mathbf{g} + \frac{1}{\rho}\nabla\cdot\boldsymbol{\tau}, \tag{2.2}$$

where ρ and υ are density and kinematic viscosity of fluid, $\mathbf{u}$ and P are a velocity vector and pressure of fluid, respectively, $\mathbf{g}$ is gravity acceleration, and t indicates time. The turbulence stress $\boldsymbol{\tau}$ is necessary to represent the effects of turbulence with coarse spatial grids, and its application into the particle simulation has been initially developed by Gotoh et al. [21]. In the most general incompressible flow approach, the density is assumed by a constant value with its initial value ρ^0. Then, the aforementioned governing equations lead to

$$\nabla\cdot\mathbf{u} = 0, \tag{2.3}$$

$$\frac{D\mathbf{u}}{Dt} = -\frac{1}{\rho^0}\nabla P + \upsilon\nabla^2\mathbf{u} + \mathbf{g} + \frac{1}{\rho^0}\nabla\cdot\boldsymbol{\tau}. \tag{2.4}$$

2.2. Projection Method

In the projection method [25], the velocity-pressure-coupled problem has been solved separately for velocity and pressure. Here, all the state variables may update from a previous time step to current time step. Below, superscripts (n) and $(n+1)$ indicate previous and current time step, respectively. In the first predictor step, intermediate state without pressure gradient is assumed, and its velocity field is indicated by $\mathbf{u}^*$. The intermediate velocity field can be evaluated by solving the following equation:

$$\frac{\mathbf{u}^* - \mathbf{u}^n}{\Delta t} = \upsilon \nabla^2 \mathbf{u}^n + \mathbf{g} + \frac{1}{\rho^0} \nabla \cdot \boldsymbol{\tau}, \tag{2.5}$$

$$(\text{Predictor}) : \mathbf{u}^* = \mathbf{u}^n + \Delta t \left(\upsilon \nabla^2 \mathbf{u}^n + \mathbf{g} + \frac{1}{\rho^0} \nabla \cdot \boldsymbol{\tau} \right), \tag{2.6}$$

Then, the following corrector step introduces an effect of remaining "current" pressure gradient term as follows:

$$\frac{\mathbf{u}^{n+1} - \mathbf{u}^*}{\Delta t} = -\frac{1}{\rho^0} \nabla P^{n+1}, \tag{2.7}$$

$$(\text{Corrector}) : \mathbf{u}^{n+1} = \mathbf{u}^* + \Delta \mathbf{u}^* = \mathbf{u}^* - \Delta t \left(\frac{1}{\rho^0} \nabla P^{n+1} \right), \tag{2.8}$$

where $\Delta \mathbf{u}^*$ indicates the incremental velocity from the predicted velocity $\mathbf{u}^*$.

The key point here is the evaluation of "current" pressure value. By taking the divergence of correction step (2.7) as

$$\nabla \cdot \left(\frac{\mathbf{u}^{n+1} - \mathbf{u}^*}{\Delta t} \right) = -\nabla \cdot \left(\frac{1}{\rho^0} \nabla P^{n+1} \right). \tag{2.9}$$

Then, the incompressible condition (2.3) leads to

$$\nabla \cdot \frac{\mathbf{u}^{n+1}}{\Delta t} = 0. \tag{2.10}$$

By substituting (2.10) into (2.9), this leads to the following pressure Poisson equation (PPE):

$$\nabla^2 P^{n+1} = \rho^0 \frac{\nabla \cdot \mathbf{u}^*}{\Delta t}. \tag{2.11}$$

The above corrector step can be implemented by substituting the pressure gradient with the solution of PPE.

2.3. The SPH Methodology

A spatial discretization using scattered particles, which is based on the SPH, is summarized. First, a physical scalar function $\phi(x_i,t)$ at a sampling point x_i can be represented by the following integral form:

$$\phi(x_i,t) = \int W(x_i - x_j,h)\phi(x_j,t)dv = \int W(r_{ij},h)\phi(x_j,t)dv, \tag{2.12}$$

where W is a weight function called by smoothing kernel function in the SPH literature. In the smoothing kernel function, $r_{ij} = |x_i - x_j|$ and h are the distance between neighbor particles and smoothing length, respectively. For SPH numerical analysis, the integral equation (2.12) is approximated by a summation of contributions from neighbor particles in the support domain.

$$\phi(x_i,t) \approx \langle \phi_i \rangle = \sum_j \frac{m_j}{\rho_j} W(r_{ij},h)\phi(x_j,t), \tag{2.13}$$

where the subscripts i and j indicate positions of labeled particle, and ρ_j and m_j mean density and representative mass related to particle j, respectively. Note that the triangle bracket $\langle \phi_i \rangle$ means SPH approximation of a function ϕ. The gradient of the scalar function can be assumed by using the above defined SPH approximation as follows:

$$\nabla\phi(x_i) \approx \langle \nabla\phi_i \rangle = \frac{1}{\rho_i}\sum_j m_j(\phi_j - \phi_i)\nabla W(r_{ij},h). \tag{2.14}$$

Also, the other expression for the gradient can be represented by

$$\nabla\phi(x_i) \approx \langle \nabla\phi_i \rangle = \rho_i \sum_j m_j \left(\frac{\phi_j}{\rho_j^2} + \frac{\phi_i}{\rho_i^2}\right)\nabla W(r_{ij},h). \tag{2.15}$$

In this paper, quintic spline function [26] is utilized as a kernel function.

$$W(r_{ij},h) = \beta_d \begin{cases} \left(3 - \dfrac{r_{ij}}{h}\right)^5 - 6\left(2 - \dfrac{r_{ij}}{h}\right)^5 + 15\left(1 - \dfrac{r_{ij}}{h}\right)^5, & 0 \le r_{ij} < h, \\ \left(3 - \dfrac{r_{ij}}{h}\right)^5 - 6\left(2 - \dfrac{r_{ij}}{h}\right)^5, & h \le r_{ij} < 2h, \\ \left(3 - \dfrac{r_{ij}}{h}\right)^5, & 2h \le r_{ij} < 3h, \\ 0, & r_{ij} \ge 3h, \end{cases} \tag{2.16}$$

where β_d is $7/478\pi h^2$ and $3/358\pi h^3$, respectively, in two- and three-dimensional space. It has been observed that a cubic spline produces fluctuations in the pressure and velocity fields for fluid dynamics simulation, and the quintic spline shown in (2.16) gives more stable solutions.

2.4. Projection-Based ISPH Formulations

Here, the projection method for incompressible fluid problem, which is summarized in Section 2.2, is descretized into particle quantities based on the SPH methodology. For this purpose, the gradient of pressure and the divergence of velocity are approximated as follows:

$$\nabla p(x_i) \approx \langle \nabla p_i \rangle = \rho_i \sum_j m_j \left(\frac{p_j}{\rho_j^2} + \frac{p_i}{\rho_i^2} \right) \nabla W(r_{ij}, h), \tag{2.17}$$

$$\nabla \cdot \mathbf{u}(x_i) \approx \langle \nabla \cdot \mathbf{u}_i \rangle = \frac{1}{\rho_i} \sum_j m_j \left(\mathbf{u}_j - \mathbf{u}_i \right) \cdot \nabla W(r_{ij}, h). \tag{2.18}$$

Although the Laplacian could be derived directly from the original SPH approximation of a function in (2.17), this approach may lead to a loss of resolution. Then, the second derivative of velocity for the viscous force and the Laplacian of pressure have been proposed by Morris et al. [5] by an approximation expression as follows:

$$\nabla \cdot (\upsilon \nabla \mathbf{u})(x_i) \approx \langle \nabla \cdot (\upsilon \nabla \cdot \mathbf{u}_i) \rangle = \sum_j m_j \left(\frac{\rho_i \upsilon_i + \rho_j \upsilon_j}{\rho_i \rho_j} \frac{r_{ij} \nabla W(|r_i - r_j|, h)}{r_{ij}^2 + \eta^2} \right) \mathbf{u}_{ij}, \tag{2.19}$$

where η is a parameter to avoid a zero dominator, and its value is usually given by $\eta^2 = 0.0001\, h^2$. For the case of $\upsilon_i = \upsilon_j$ and $\rho_i = \rho_j$, the Laplacian term is simplified as

$$\langle \nabla \cdot (\upsilon \nabla \cdot \mathbf{u}_i) \rangle = \frac{2\upsilon_i}{\rho_i} \sum_j m_j \left(\frac{r_{ij} \nabla W(|r_i - r_j|, h)}{r_{ij}^2 + \eta^2} \right) \mathbf{u}_{ij}. \tag{2.20}$$

Similarly, the Laplacian of pressure in pressure Poisson equation (PPE) is given by

$$\nabla^2 p(x_i) \approx \left\langle \nabla^2 p_i \right\rangle = \frac{2}{\rho_i} \sum_j m_j \left(\frac{p_{ij} r_{ij} \nabla W(|r_i - r_j|, h)}{r_{ij}^2 + \eta^2} \right). \tag{2.21}$$

The PPE after SPH interpolation is solved by a preconditioned (diagonal scaling) Conjugate Gradient (PCG) method [27] with a convergence tolerance ($= 1.0 \times 10^{-9}$).

2.5. Modeling of the Turbulence Stress

When dealing with the turbulent flows, the turbulent stress in (2.2), which are called by sub-particle scale stress in the particle simulations, needs to be modeled. In this paper, a large eddy simulation approach [21, 22] is used for modeling the turbulent stress as

$$\frac{\tau_{IJ}}{\rho_0} = 2\upsilon_T S_{IJ} - \frac{2}{3} k \delta_{IJ}, \tag{2.22}$$

where υ_T and k are the turbulence eddy viscosity and the turbulence kinetic energy, respectively. S_{IJ} indicates the strain rate of the mean flow, and δ_{IJ} is the Kronecker delta. It is

assumed in this paper that the eddy viscosity is modeled by the static Smagorinsky model as $\upsilon_T = (C_s\Delta)^2|\overline{S}|$, in which $C_s = 0.2$ is the Smagorinsky constant (taken as the analytical value in this paper), the constant Δ is taken as $2h$, in which h is the smoothing length defined in (2.12). The local strain rate $|\overline{S}| = (2S_{IJ}S_{IJ})^{1/2}$ can be calculated in the SPH formulation as Violeau and Issa [20].

2.6. Treatment of No-Slip Boundary Condition

The boundary condition on the rigid bodies has an important role to prevent penetration and to reduce error related to truncation of the kernel function. Takeda et al. [28] and Morris et al. [5] have introduced a special wall particle which can satisfy imposed boundary conditions. Recently, Bierbrauer et al. [29] described a consistent treatment of boundary conditions, utilizing the momentum equation to obtain approximations to velocity of image particles.

In our research, dummy particles technique, in which dummy particles are regularly distributed at the initial state and have zero velocity through the whole simulation process, is utilized just for simplicity in the implementation. In the following simulation, the pressure Poisson equation is solved for all particles including these dummy particles to get an enough repulsive force preventing penetration.

3. Stabilizations of Pressure Evaluation in Pressure Poisson Equation

Here, the pressure Poisson equation is reconsidered to overcome the error of artificial pressure fluctuation in the ISPH. The key points are related to the accuracy of density representation in SPH formulation and the treatment of pressure Poisson equation.

3.1. Keeping Divergence Free Scheme

Divergence free condition in the projection-based ISPH has been initially proposed by Cummins and Rudman [8]. Lee et al. [13] has applied it into the Reynolds turbulence model which uses an averaging in time. They called by "truly" incompressible SPH since the initial density ρ^0 is assumed constant for each particle. Then the divergence of the intermediate velocity has been used to calculate the PPE as mentioned above in (2.11). The PPE can be written in SPH approximation by substituting (2.18) and (2.21) as follows:

$$\left\langle \nabla^2 p_i^{n+1} \right\rangle = \frac{\rho^0}{\Delta t}\langle \nabla \cdot \mathbf{u}_i^* \rangle. \tag{3.1}$$

3.2. Keeping Density Invariance Scheme

The alternative scheme can be derived by using a density invariance condition [14, 15]. Here, the "particle" density in the SPH is evaluated by

$$\rho(x_i) \approx \langle \rho_i \rangle = \sum_j m_j W(r_{ij}, h) = \sum_j m_j W_{ij}. \tag{3.2}$$

The particle position updates after each predictor step in the density invariance scheme and the particle density is updated on the intermediate particle positions. The intermediate

particle density is indicated by $\langle \rho_i^* \rangle$. By assuming incompressibility condition with $\langle \rho_i^{n+1} \rangle = \rho^0$, the mass conservation law (2.1) can be rewritten for each particle as follows:

$$\frac{\langle \rho_i^* \rangle - \rho^0}{\Delta t} + \rho^0 \langle \nabla \cdot \mathbf{u}_i^* \rangle = 0. \tag{3.3}$$

By substituting (3.3) into (2.11) and using the SPH form, the PPE for ISPH can be approximately redefined by

$$\langle \nabla^2 p_i^{n+1} \rangle = \frac{\rho^0 - \langle \rho_i^* \rangle}{\Delta t^2}. \tag{3.4}$$

The main difference between the keeping divergence-free and keeping density-invariance scheme appeared in the source term of the PPE. Note that this keeping density-invariance scheme is analogous to the formulation in the MPS, although the MPS utilizes a "particle number" density instead of the particle density. The above two schemes have a relationship. Ataie-Ashtiani and Shobeyri [30] has converted from a PPE in the keeping density invariance scheme to a PPE in the keeping divergence-free scheme.

3.3. Combination Scheme of Both Divergence-Free and Density-Invariance Condition

A notable scheme was proposed by Hu and Adams [16]. The divergence-free and density-invariance conditions are sufficiently satisfied in their scheme. As they discussed, the divergence-free scheme calculates a smoothed pressure field but a large density variation will appear. Hu and Adams's scheme includes an internal iteration at each step, and two kinds of PPEs should be solved until both the divergence-free and density-invariance conditions are approximately satisfied. According to Xu et al. [31], this scheme shows accurate and robust solutions, but total calculation time shows 4-5 times higher than that of the above two scheme.

3.4. Relaxed Density Invariance Scheme Incorporated with Divergence-Free Condition

Here, we proposed an efficient and robust ISPH scheme using both conditions without internal iterations. In the sense of physical observation, physical density should keep its initial value for incompressible flow. However, during numerical simulation, the "particle" density may change slightly from the initial value because the particle density is strongly dependent on particle locations in the SPH method. If the particle distribution can keep almost uniformity, the difference between "physical" and "particle" density may be vanishingly small. In other words, accurate SPH results in incompressible flow need to keep the uniform particle distribution. For this purpose, the different source term in pressure Poisson equation can be derived using the "particle" density. The SPH interpolations are introduced into the original mass conservation law before the perfect compressibility condition is applied

$$\left\langle \nabla \cdot \mathbf{u}_i^{n+1} \right\rangle = -\frac{1}{\rho^0} \frac{\langle \rho_i^{n+1} \rangle - \langle \rho_i^n \rangle}{\Delta t}. \tag{3.5}$$

By substituting (3.5) into (2.9) and using SPH form, the PPE can be represented by

$$\left\langle \nabla^2 p_i^{n+1} \right\rangle = \frac{\rho^0}{\Delta t} \left\langle \nabla \cdot \mathbf{u}_i^* \right\rangle + \frac{\left\langle \rho_i^{n+1} \right\rangle - \left\langle \rho_i^n \right\rangle}{\Delta t^2}. \tag{3.6}$$

Here, it is assumed that the current particle density is "hopefully" closed to initial density and the incremental particle density $\langle \Delta \rho_i^n \rangle$ are defined by

$$\left\langle \rho_i^{n+1} \right\rangle = \left\langle \rho_i^n \right\rangle + \left\langle \Delta \rho_i^n \right\rangle \approx \rho^0, \tag{3.7}$$

$$\left\langle \Delta \rho_i^n \right\rangle := \alpha \left(\rho^0 - \left\langle \rho_i^n \right\rangle \right), \tag{3.8}$$

where the above integration scheme is called by the method of coordinate descent with a relaxation coefficient α $(0 \le \alpha \le 1)$, and the PPE is modified as follows:

$$\left\langle \nabla^2 p_i^{n+1} \right\rangle = \frac{\rho^0}{\Delta t} \left\langle \nabla \cdot \mathbf{u}_i^* \right\rangle + \alpha \frac{\rho^0 - \left\langle \rho_i^n \right\rangle}{\Delta t^2}. \tag{3.9}$$

The similar equation, in which the density is replaced by a particle number density, was proposed by Losasso et al. [32], but they did not introduce the relaxation coefficient. Note that our proposed scheme couples the divergence-free and a relaxed density-invariance condition, and a special case using $\alpha = 0$ leads to the original divergence-free scheme. The effect of the relaxation coefficient will be tested in the later examples. Figure 1 shows the flow charts of these schemes to show the difference between existing and our proposed scheme. Similar modifications in the source term of PPE have been proposed in the MPS by Tanaka and Masunaga [19]. Recently, Khayyer and Gotoh [33] proposed a different higher-order source term without the unknown coefficient like the relaxation coefficient in this paper. It is important that the relaxation coefficient is strongly dependent on the initial particle distance, and the optimum value can be calibrated by a simple hydrostatic pressure test with the same initial particle distance as the final simulation model. The hydrostatic pressure test is called by preanalysis in this paper.

3.5. Tracking the Free Surface Boundary

Detection of free surface has an important role in the ISPH for free surface flow, because the pressure values on free surface particles should be equal to zero as Dirichlet boundary conditions of PPE. The method how to track the free surface may differ in each ISPH scheme.

Usually in the keeping density-invariance scheme, surface particles have been detected by referring the current particle density $\langle \rho_i \rangle$. The details have been discussed by Gotoh et al. [21], Shao and Gotoh [22], and Khayyer et al. [14, 15]. On the other hand, in the keeping divergence-free scheme, Lee et al. [13] proposed a new treatment with the divergence of a particle position vector. If the particle density keeps around its initial value, the former free surface detection method can be utilized. In our simulation, surface particles are simply judged by the total number of neighboring particles.

G. R. Liu and M. B. Liu [34] have investigated the number of neighboring particles to estimate an efficient variable smoothing length for the adaptive analysis. In the case of

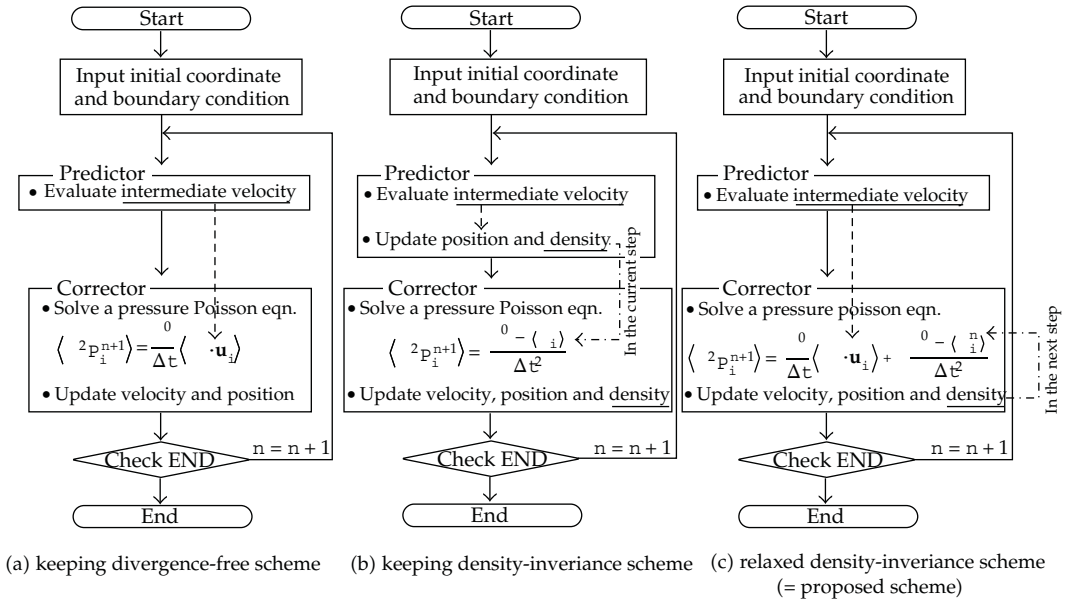

(a) keeping divergence-free scheme (b) keeping density-inveriance scheme (c) relaxed density-inveriance scheme (= proposed scheme)

Figure 1: Flow charts in the ISPH schemes.

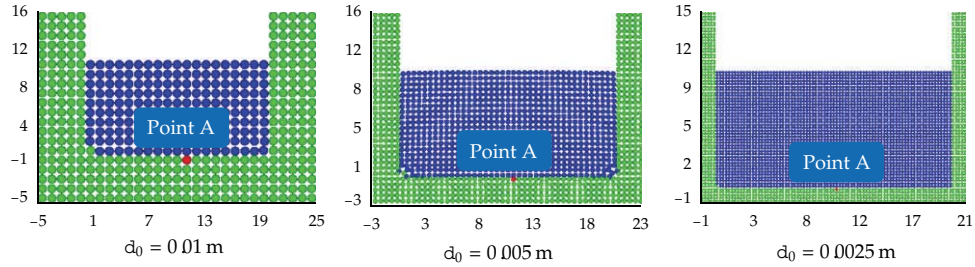

$d_0 = 0.01$ m $d_0 = 0.005$ m $d_0 = 0.0025$ m

Figure 2: Schematic diagram of hydrostatic pressure at point A for three values of particle sizes.

a simply cubic patterned lattice, h is usually chosen as larger than 1.2 times of the initial particle distance d_0. They showed that the number of neighboring particle within the support domain kh with $k = 2$ for cubic spline kernel function should be about 21 in two-dimensional simulations. We checked a threshold for judging free surface particles for quintic spline kernel function with $k = 3$, and the threshold should be about 28 and 190 in 2D and 3D, respectively.

4. Preanalysis to Determine an Efficient Relaxation Coefficient

In this section, hydrostatic pressure evaluations are performed to investigate the effects of relaxation coefficient and to determine a suitable range of its value with reference to an initial particle distance.

The three particle models have been generated with different initial particles distances $d_0 = 0.01$, 0.005, and 0.0025 m as shown in Figure 2. The theoretical hydrostatic pressure is given by a law: $p = \rho g h$ $(= 980\,\mathrm{N/m^2})$ with water density $\rho = 1000\,\mathrm{kg/m^3}$ and a water height $h = 0.1$ m. Figure 3 shows pressure histories with different relaxation coefficients for

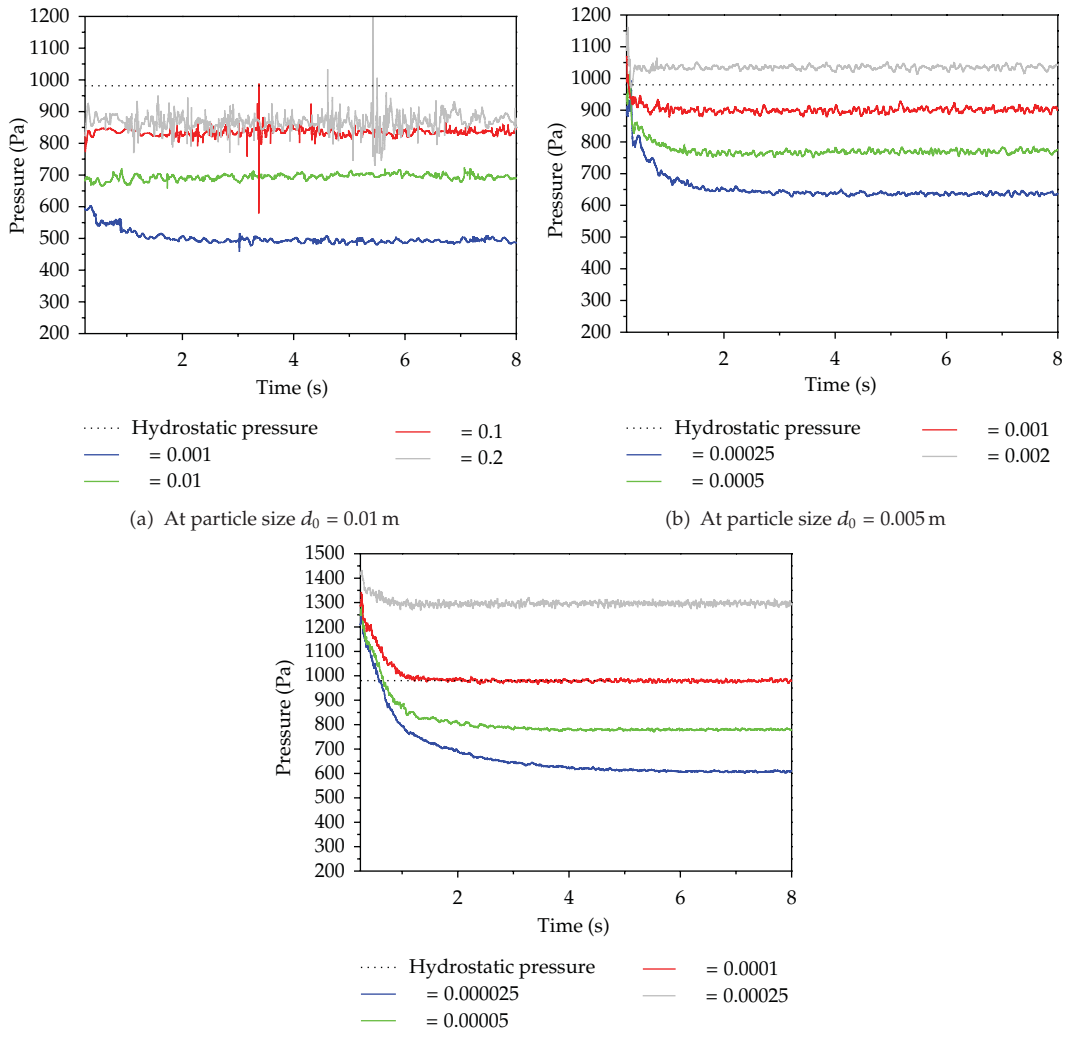

(a) At particle size $d_0 = 0.01$ m

(b) At particle size $d_0 = 0.005$ m

(c) At particle size $d_0 = 0.0025$ m

Figure 3: Time history for pressure distributions under the effect of relaxation coefficient at different particle size models $d_0 = 0.01$, 0.005, and 0.0025 m, respectively.

each model. From this figure, the proper ranges of relaxation coefficient α with initial particle distances $d_0 = 0.01$, 0.005, and 0.0025 m are approximately about (0.1 : 0.2), (0.0005 : 0.002) and (0.00005 : 0.0002), respectively. In this paper, a constant time is chosen by $\Delta t = 0.1\, d_0$ corresponding to Khayyer et al. [15]. Here note that the optimum parameter calibrated from this preanalysis can use the same value in the later examples if the model has the same particle resolution.

5. Numerical Examples

Here, several numerical examples are solved by the current scheme with an efficient relaxation coefficient, which are calibrated by the hydrostatic pressure evaluation in the previous section.

5.1. The Effect of Relaxation Coefficient during Dam Break Simulation

A two-dimensional dam break analysis is performed to compare the proper relaxation coefficient between hydrostatic pressure and dam break simulation with the same particle distance. The geometry of a 2D dam break is shown in Figure 4, where the particle distance $d_0 = 0.01\,\text{m}$, the water width $L = 0.20\,\text{m}$, water height $H_w = 2.5\,\text{L}$, and the wall width $W_l = 5\,\text{L}$.

At first, Figure 5 shows the results of free surface detection by using the number of neighbors. It is seen that this simple free surface detection scheme is sufficiently accurate to determine the Dirichlet boundary conditions of the pressure Poisson equation and it is also suitable for any formulation of the pressure Poisson equation. The effects of relaxation coefficient are investigated by the density errors. Two boundary particles A and B, which position is marked in Figure 4, are selected to output an evaluated numerical density. Figure 6 shows the time histories of the density at particles A and B. From this observation with a particle distance $d_0 = 0.01\,\text{m}$, it seems that, too low relaxation coefficient (below 0.01) the density errors are high. A proper range of relaxation coefficient $\alpha = 0.1\sim0.25$ leads to a stable solution. In addition, the density error fluctuations become serious when the relaxation coefficient is larger than this proper range. In the same way, the suitable ranges of relaxation coefficient for different particles distances $d_0 = 0.005,\ 0.0025\,\text{m}$ are evaluated by $(0.0005 : 0.0025)$ and $(0.00005 : 0.0001)$, respectively. Note that these proper ranges for each initial particle distance are close to the preevaluated proper ranges calibrated with the hydrostatic pressure test. Finally, the optimum values of relaxation coefficient in 2D dam break analysis for particle sizes $d_0 = 0.01,\ 0.005$, and $0.0025\,\text{m}$ are determined by 0.15, 0.001, and 0.00006, respectively.

Figure 7 shows the pressure distributions for three models with different initial particle distances $d_0 = 0.01,\ 0.005,$ and $0.0025\,\text{m}$. A suitable relaxation coefficient is utilized for each model. The first water impact at the right wall generates highest pressure, and it returns in the form of a jet. Then, it becomes a stable state after two more water impacts act on both side walls. The snapshots for water impact, after the first water impact, reversing jet and water stable state are captured from each model with different particle distance. These snapshots at the same time show similar water shape. The pressure histories at the right corner are plotted in Figure 8. Although unrealistic pressure fluctuation appears in the case of lowest resolution model with $d_0 = 0.01\,\text{m}$, a similar tendency of pressure history can get from different resolution models. Adjusting suitable relaxation coefficient can increase the pressure smoothness. The hydrostatic pressure after this dam break analysis is analytically evaluated by $1000\,\text{N/m}^2$, and our evaluated pressure after 4 seconds looks to converge into the analytical hydrostatic value. In this example, water front speed is plotted in Figure 9. Our results shows a good agreement with the experimental results obtained by Koshizuka and Oka [24] and Martin and Moyce [35], moreover the numerical results obtained by Lee et al. [23].

5.2. Comparison of Configurations and Pressure during Dam Break Simulation

Next, water configurations and pressure distribution are compared with an experimental data by Zhou et al. [36] and with a result by original incompressible SPH, which is the same as a special case of our proposed scheme with $\alpha = 0$. The schematic diagram is the same as Zhou's experiment is shown in Figure 10, and the pressure measuring point is located at

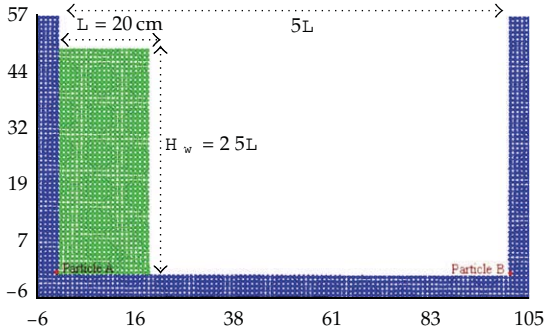

Figure 4: Dam break analysis (unit: cm).

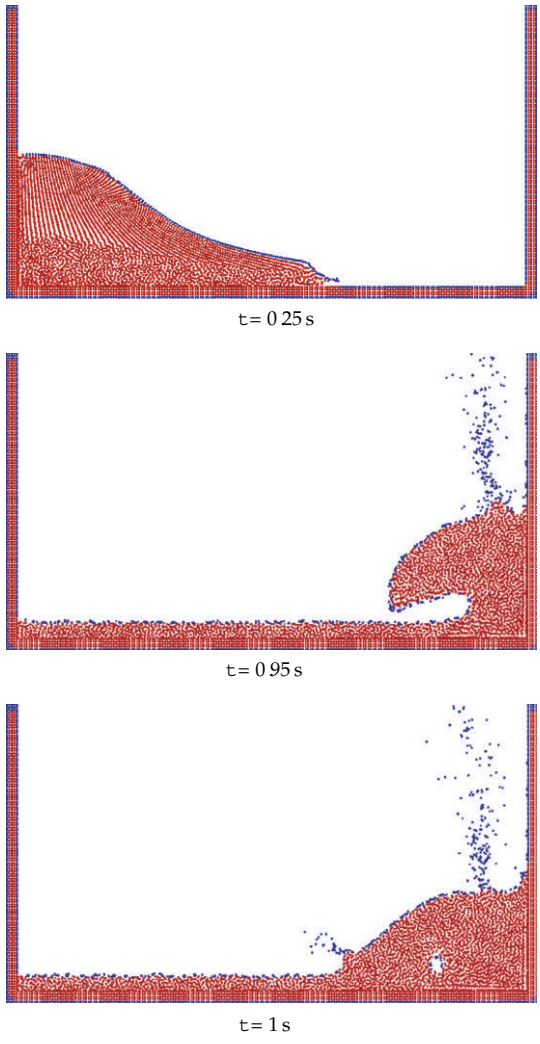

Figure 5: Detect free surface numerically using the number of neighbouring particles for using $k = 3$ and $h = 1.2\, d_0$ for quintic spline kernel function at initial particle size $d_0 = 0.005$ m.

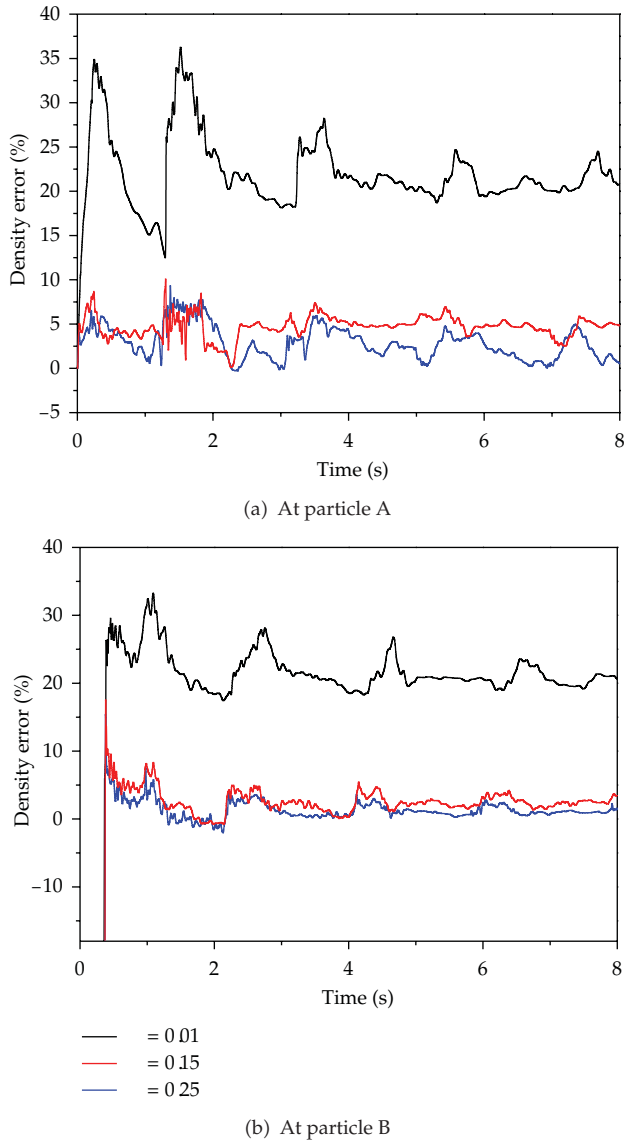

Figure 6: Effect of relaxation coefficient on the density evaluation error at (a) particles A and (b) Particle B, respectively.

a point on the right wall (0.16 m). The particle initial distance is selected as $d_0 = 0.005$ m. A proper relaxation coefficient for this resolution is selected by $\alpha = 0.001$ which is the same optimum value in the hydrostatic pressure test, and then the numerical solution is compared to the truly incompressible scheme with $\alpha = 0$. Figure 11 shows the comparison results of the snapshots with pressure distribution from the initial state to the final stable state. The snapshots from each scheme are captured at the first water impact, running up along the right wall reversing development of splash-up and the stable state. Although the wave configurations show similarities, the pressure value from the truly incompressible scheme is less than that from our proposed scheme. In addition, the total volume of the water at

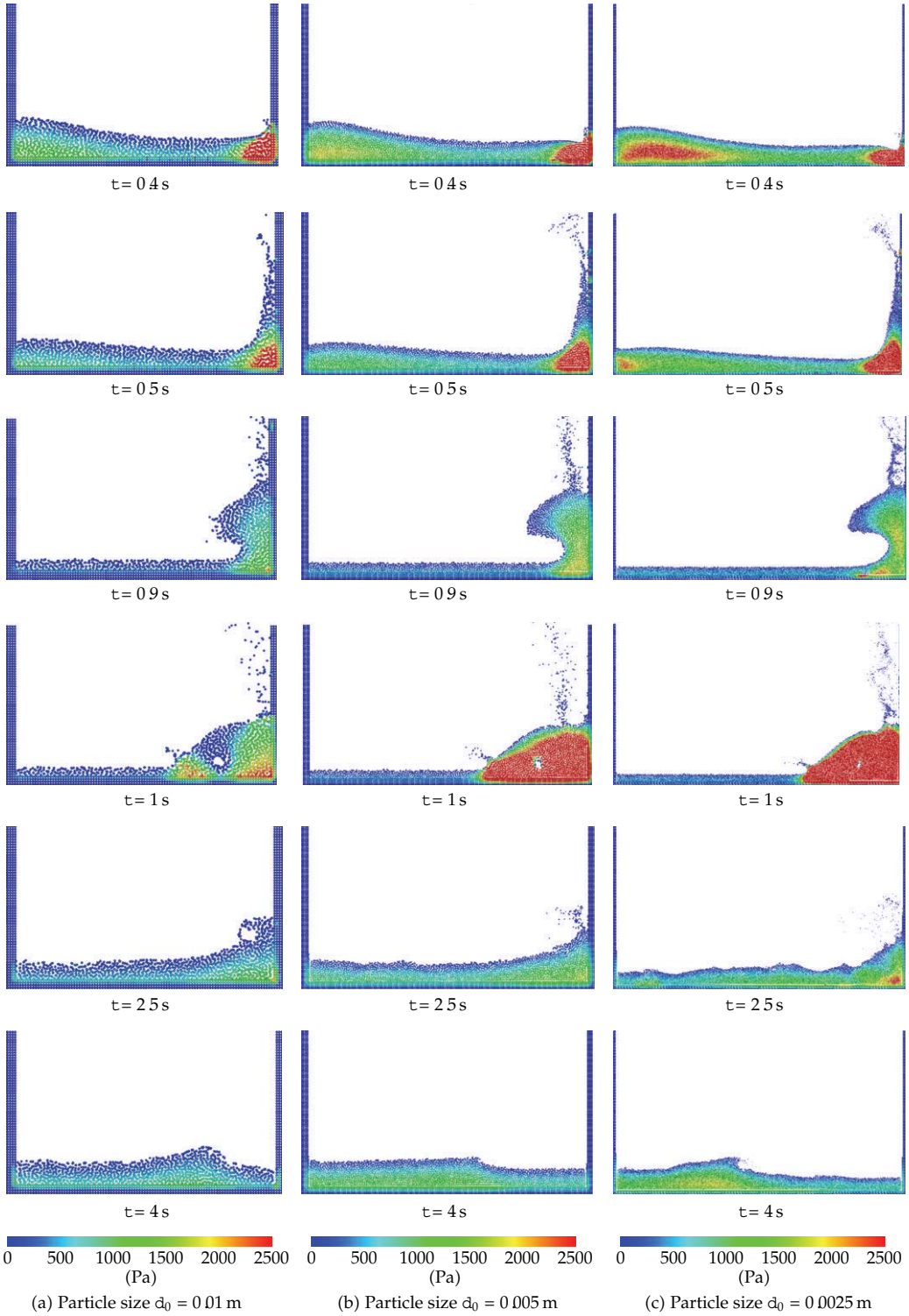

Figure 7: Pressure distributions for dam break analysis from different particle size models $d_0 = 0.01,\ 0.005,$ and 0.0025 m, respectively.

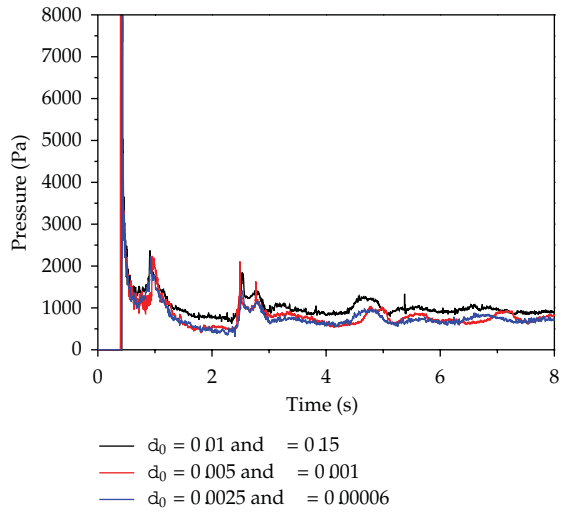

Figure 8: Time history for pressure distribution at different particle sizes with proper relaxation coefficient.

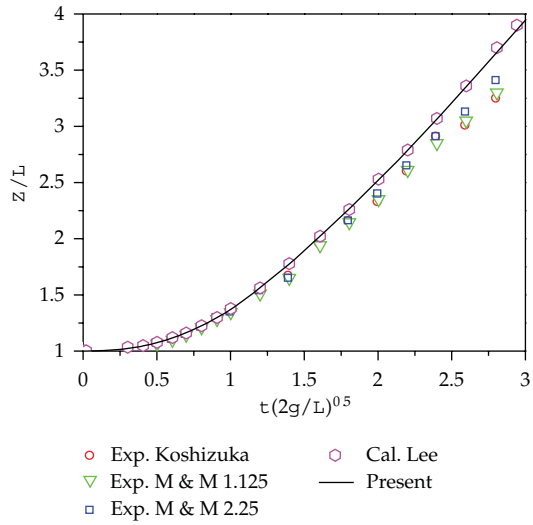

Figure 9: Comparison on dam break fronts in the dam break analysis.

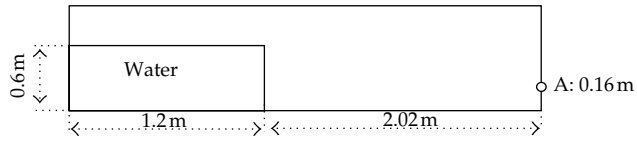

Figure 10: Dam break simulation corresponding to experiment by Zhou et al. [36].

the final stable state is compared between the proposed scheme and truly incompressible scheme using the water height. It seems that the proposed scheme conserves the total volume compared to the theoretical value of height about 0.22 m, while the truly incompressible

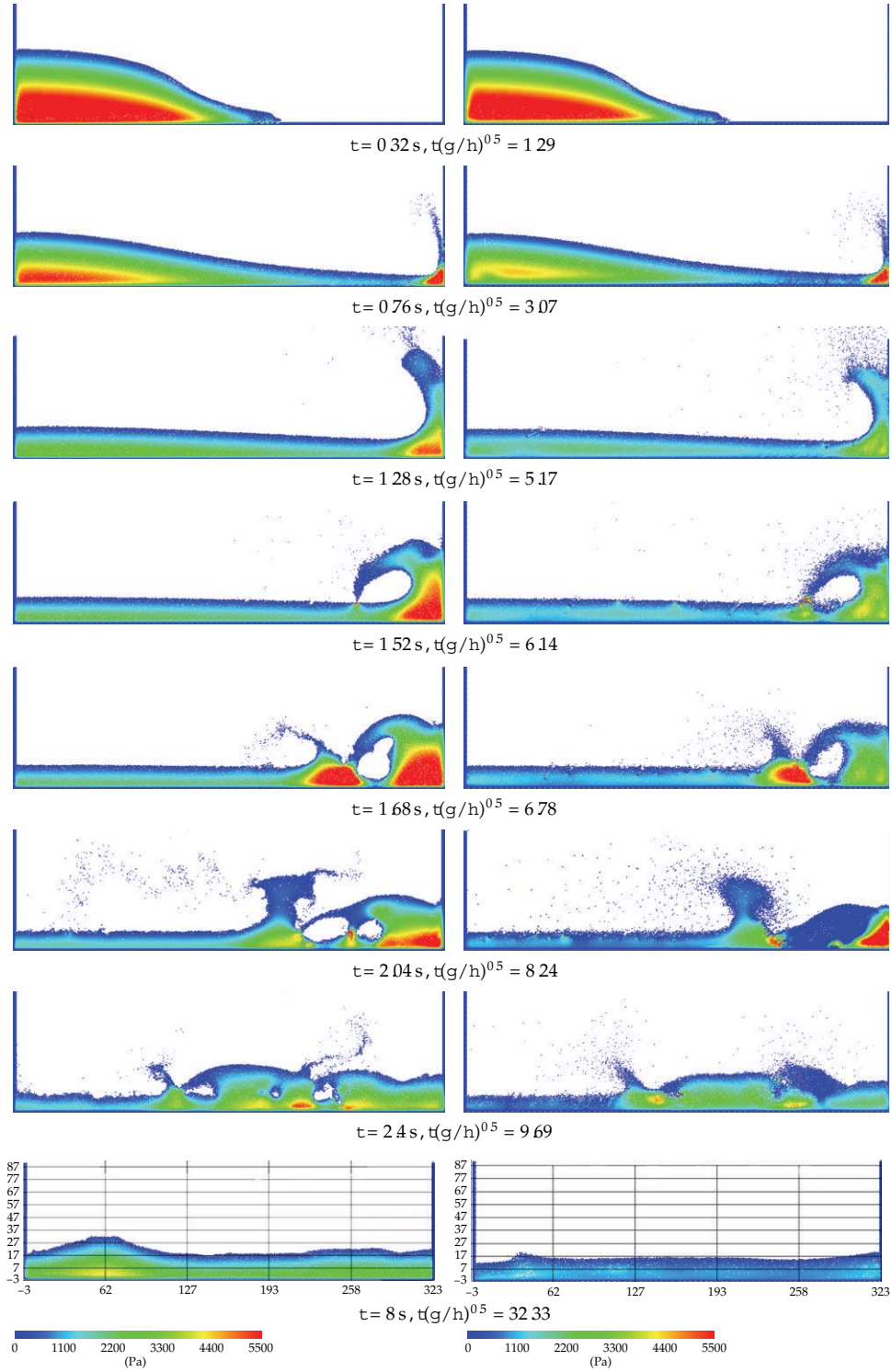

Figure 11: Pressure distribution for dam break analysis by (a) stabilized ISPH with eddy viscosity effect, and (b) original ISPH ($\alpha = 0$) without eddy viscosity effect, respectively.

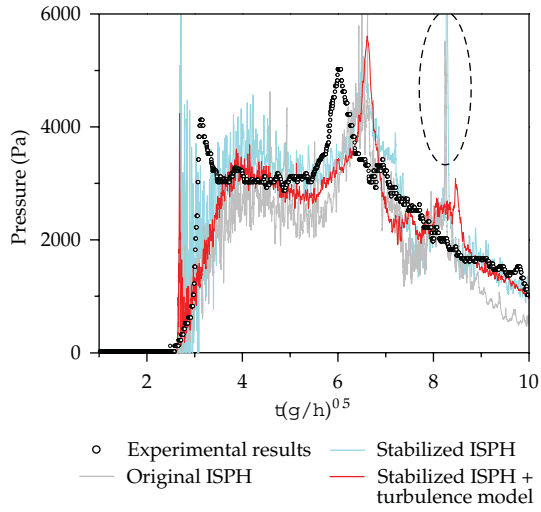

Figure 12: (a) Comparison between the current stabilized model including/excluding eddy viscosity, divergence-free scheme condition, and experimental data by Zhou et al. [36].

scheme cannot conserve the volume at the final stable state. Figure 12 shows the comparison of pressure history at the right corner among our proposed scheme result with a proper relaxation coefficient, result from the truly incompressible scheme, and experimental data by Zhou et al. [36]. Although the pressure level from the truly incompressible scheme ($\alpha = 0$) is lower than the experimental data in the entire simulation period, the evaluated pressure from our proposed scheme shows a good agreement with the experimental data. In this figure, imaginary pressure peak is evaluated around $t = 2.04$ $(t(g/h)^{0.5} = 8.24)$ in the results without turbulence model. The combination with the proposed stabilized ISPH and turbulence model generates smoothed and accurate pressure distribution.

5.3. 3D Dam Break Flow with an Obstacle

The last application is one of the benchmark test suggested by SPH European Research Interest Community (SPHERIC). The experimental tests on a dam break flow with an obstacle was carried out at the Maritime Research Institute Netherlands (MARIN) as reported by Kleefsman et al. [37].

Figures 13 and 14 show geometry of the experimental test and locations of pressure sensor, respectively. While ps_1 to ps_8 sensors were used in the experimental test, here only odd numbers of pressure sensor are utilized for the comparison. In the numerical modeling, the initial particle distance is fixed at 0.01 m for both regions of water and wall. The total number of particles is about 1.4 millions, and 0.67 million particles are located in the water. In order to evaluate an efficient relaxation coefficient, the same procedure as two-dimensional cases is applied. First, the hydrostatic pressure test has been implemented by using the same initial particle distance $d_0 = 0.01$ m and time increment $\Delta t = 0.001$ s in the 3D dam break problem. Then the optimum relaxation coefficient α was fixed by 0.1.

The pressure time history on the front (ps_1 and ps_3) and top (ps_5 and ps_7) is shown in Figure 15. Figures 16 and 17 show the snapshots with particle pressure values and labels related to free surface, respectively. In Figure 16, the numerical solutions by our

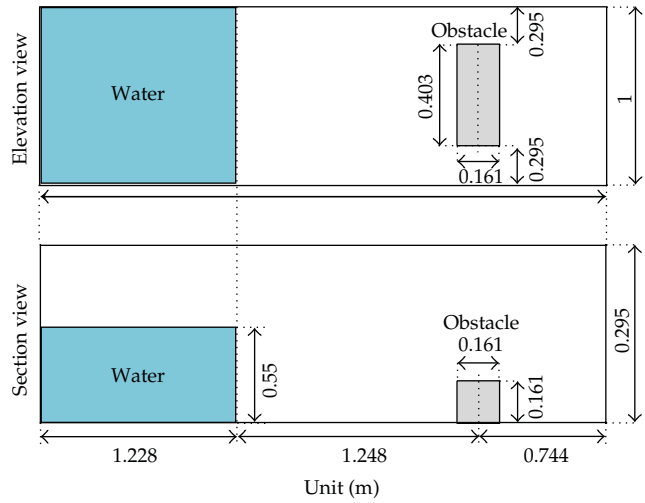

Figure 13: Geometry of the 3D dam break experiment.

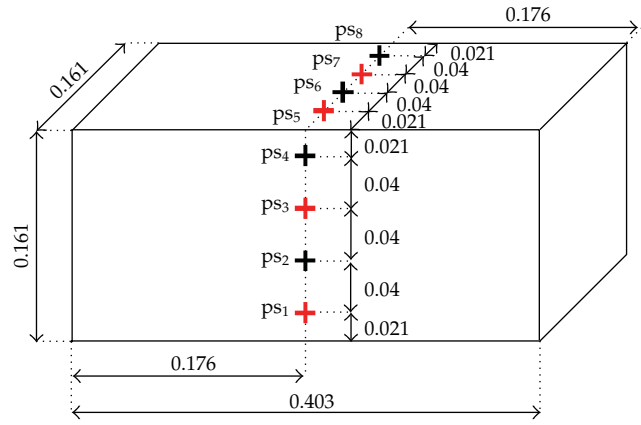

Figure 14: Locations of the pressure sensor on the obstacle.

proposed relaxed density invariant scheme (stabilizes ISPH) are compared with Kleefsman's experimental results and numerical results by the keeping divergence-free scheme with $\alpha = 0$ (original ISPH). The first impact occurred at about 0.42 s both in the numerical and experimental test, although the time of secondary hit has about 0.5 s difference (0.45 s and 0.50 s, resp.). That is, our solution shows small delay as the time goes. The pressure resulting from the keeping divergence-free scheme shows lower value during the simulation, although a smooth pressure distribution can be generated as in Figure 16. It seems that the keeping divergence scheme cannot keep the total volume of water. On the other hand, except for the local pressure oscillation especially at ps_5 and ps_7, the pressure histories by our proposed scheme show good agreement with the experimental results.

Lee et al. [38] has been simulated to the same problem, and they have discussed the difference between weakly compressible SPH and their proposed truly incompressible SPH that is one of the keeping divergence-free scheme. According to their result, the weakly compressible SPH shows a critical error in the pressure and their truly incompressible SPH

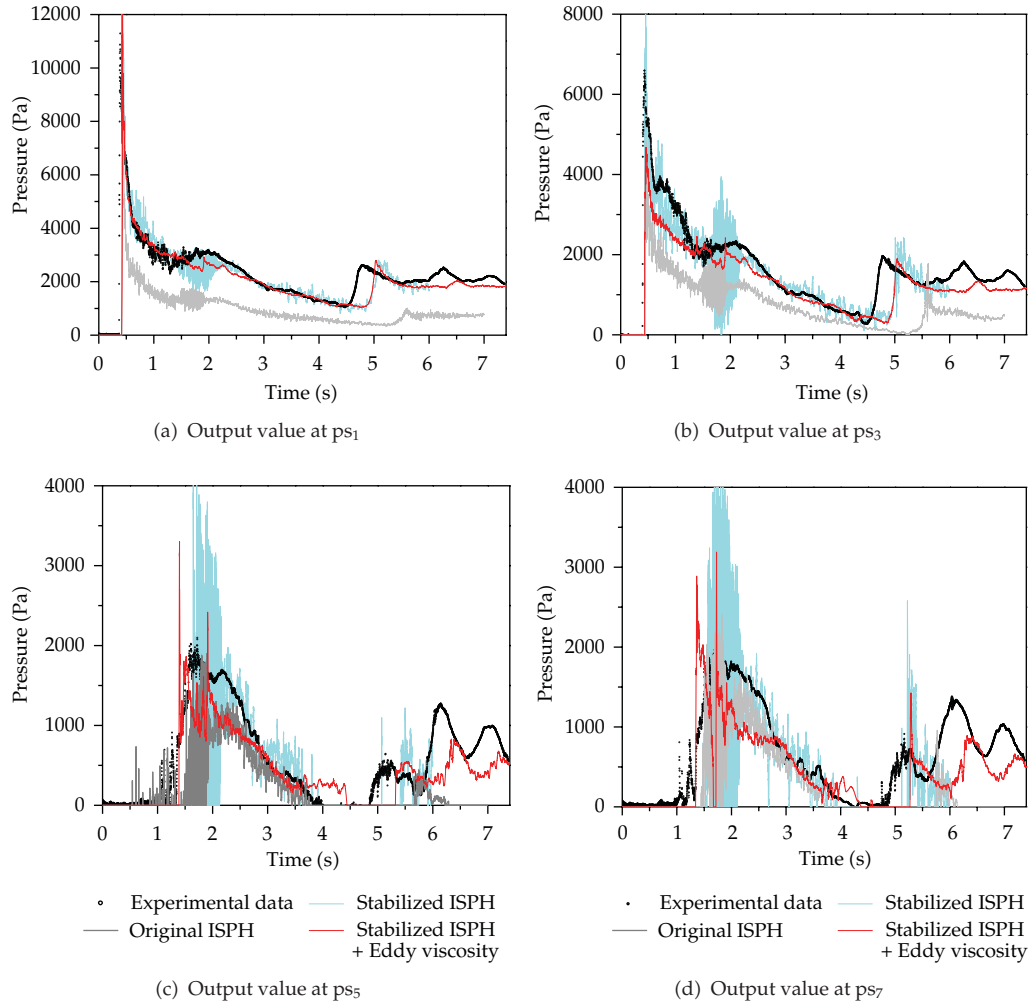

(a) Output value at ps_1

(b) Output value at ps_3

(c) Output value at ps_5

(d) Output value at ps_7

Figure 15: Time history of Pressure for 3D dam break at ps_1, ps_3, ps_5, and ps_7.

solution has the similar tendency as our results. However, the original ISPH scheme cannot keep the total volume as far as we have checked.

6. Conclusion

A stabilized incompressible smoothed particle hydrodynamics is proposed to simulate free surface flow. The modification is appeared in the source term of pressure Poisson equation, and the idea is similar to the recent development in Moving Particles Semi-implicit method (MPS). Although only one set of linear equations should be solved to evaluate pressure at each particle, both the velocity divergence-free condition and the density invariance condition can be approximately satisfied. The additional parameter is the relaxation coefficient, and its value can be calibrated by a simple hydrostatic simulation with a regular initial particle distribution. It has a uniform tendency that the relaxation coefficient becomes smaller due to decrease in the initial particle distance. The efficiency and its accuracy

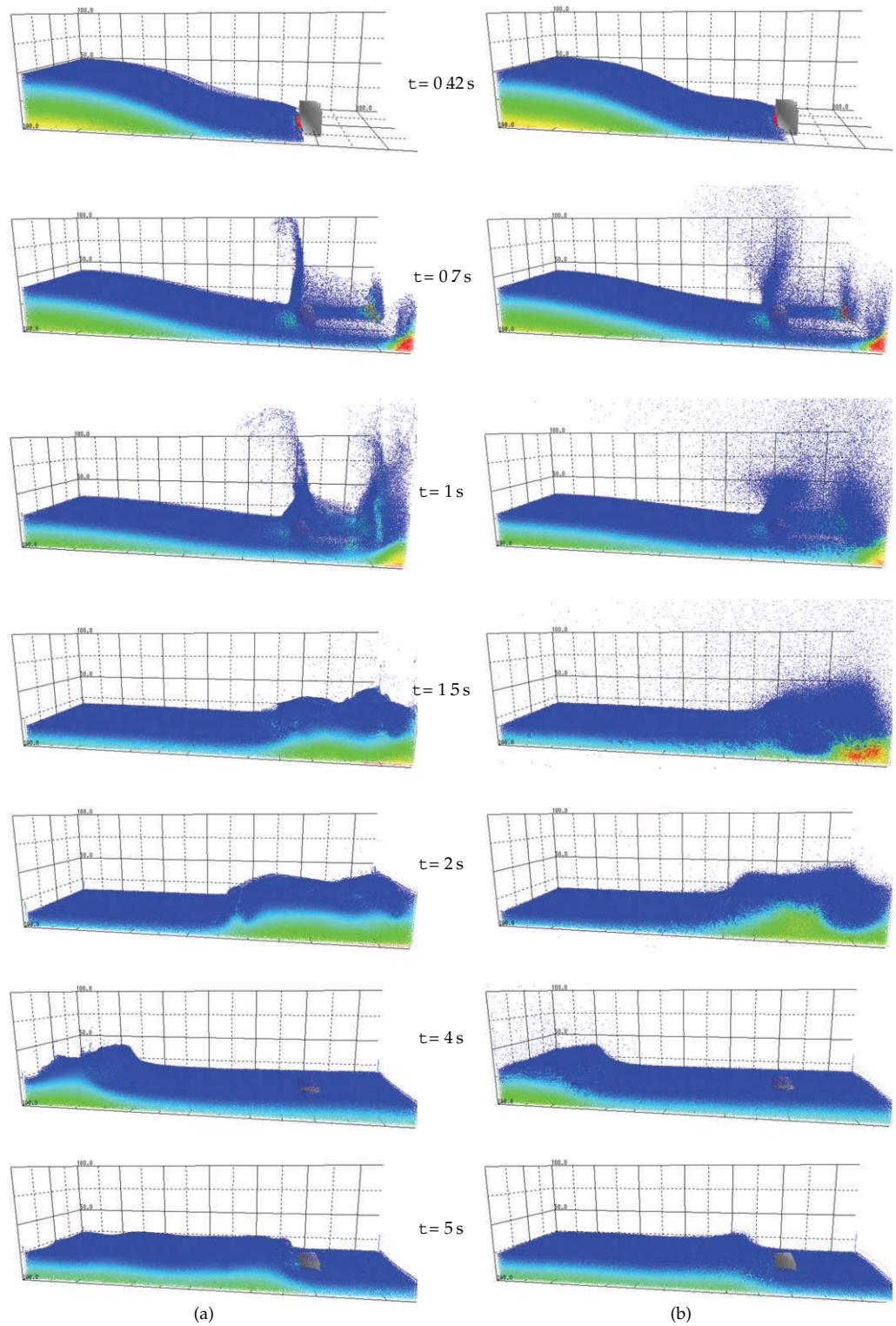

Figure 16: Time sequence of 3D dam break simulation by (a) stabilized ISPH method with eddy viscosity effect and (b) without eddy viscosity effect.

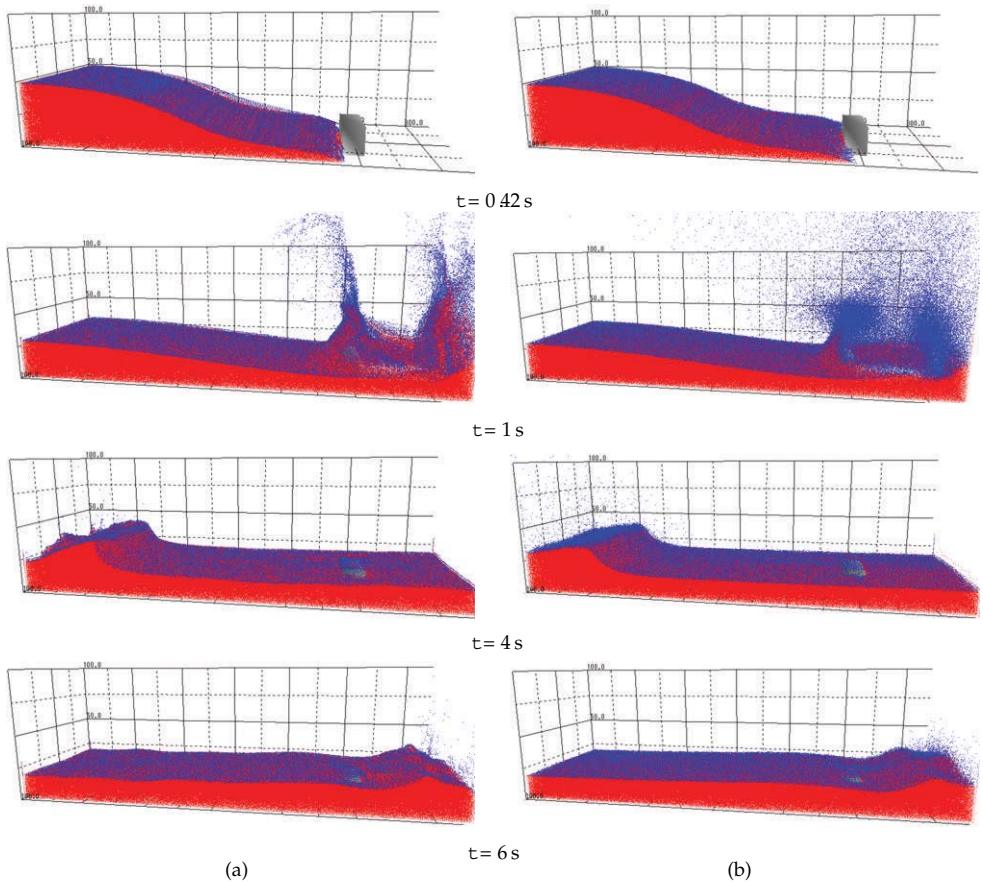

Figure 17: Time sequence for detection free surface in 3D dam break simulation by (a) stabilized ISPH method with eddy viscosity effect and (b) without eddy viscosity effect.

have been tested by the dam break in two- and three-dimension simulations compared to their reference solutions. Our proposed scheme shows the clear advantage to keep the total volume by comparing the original ISPH, and it may contribute to have an accurate pressure value. However, it still has an artificial oscillation in the pressure value with original viscosity. The additional viscosity based on the Subparticle Scale turbulence model shows an important role to generate smoother pressure distribution and to decrease the number of isolated particles after the splash in the dam break problems.

Acknowledgments

The first author is partially supported by the Ministry of Education, Science, Sports and Culture of Japan (Grant-in-Aid for Young Scientist (B) 2176036).

References

[1] L. B. Lucy, "A numerical approach to the testing of the fusion process," *Astronomical Journal*, vol. 88, pp. 1013–1024, 1977.

[2] R. A. Gingold and J. J. Monaghan, "Smoothed particle hydrodynamics: theory and application to non-spherical stars," *Monthly Notices of the Royal Astronomical Society*, vol. 181, pp. 375–389, 1977.
[3] J. J. Monaghan, "Smoothed particle hydrodynamics," *Annual Review of Astronomy and Astrophysics*, vol. 30, no. 1, pp. 543–574, 1992.
[4] J. J. Monaghan, "Simulating free surface flows with SPH," *Journal of Computational Physics*, vol. 110, no. 2, pp. 399–406, 1994.
[5] J. P. Morris, P. J. Fox, and Y. Zhu, "Modeling low Reynolds number incompressible flows using SPH," *Journal of Computational Physics*, vol. 136, no. 1, pp. 214–226, 1997.
[6] J. J. Monaghan, "Heat conduction with discontinuous conductivity," in *Applied Mathematics Reports and Preprints*, Monash University, 1995.
[7] N. Okahci, A. Hirota, S. Izawa, Y. Fukunishi, and H. Higuchi, "SPH simulation of pulsating pipe flow at a junction," in *Proceedings of the 1st International Symposium on Advanced Fluid Information*, pp. 388–391, 2001.
[8] S. J. Cummins and M. Rudman, "An SPH projection method," *Journal of Computational Physics*, vol. 152, no. 2, pp. 584–607, 1999.
[9] J. Pozorski and A. Wawrenczuk, "SPH computation of incompressible viscous flows," *Journal of Theoretical and Applied Mechanics*, vol. 40, pp. 917–937, 2002.
[10] S. Shao and E. Y. M. Lo, "Incompressible SPH method for simulating Newtonian and non-Newtonian flows with a free surface," *Advances in Water Resources*, vol. 26, no. 7, pp. 787–800, 2003.
[11] X. Y. Hu and N. A. Adams, "Angular-momentum conservative smoothed particle dynamics for incompressible viscous flows," *Physics of Fluids*, vol. 18, no. 10, Article ID 101702, 4 pages, 2006.
[12] M. Ellero, M. Serrano, and P. Espanol, "Incompressible smoothed particle hydrodynamics," *Journal of Computational Physics*, vol. 226, no. 2, pp. 1731–1752, 2007.
[13] E.-S. Lee, C. Moulinec, R. Xu, D. Violeau, D. Laurence, and P. Stansby, "Comparisons of weakly compressible and truly incompressible algorithms for the SPH mesh free particle method," *Journal of Computational Physics*, vol. 227, no. 18, pp. 8417–8436, 2008.
[14] A. Khayyer, H. Gotoh, and S. Shao, "Corrected incompressible SPH method for accurate water-surface tracking in breaking waves," *Coastal Engineering*, vol. 55, no. 3, pp. 236–250, 2008.
[15] A. Khayyer, H. Gotoh, and S. Shao, "Enhanced predictions of wave impact pressure by improved incompressible SPH methods," *Applied Ocean Research*, vol. 31, no. 2, pp. 111–131, 2009.
[16] X. Y. Hu and N. A. Adams, "An incompressible multi-phase SPH method," *Journal of Computational Physics*, vol. 227, no. 1, pp. 264–278, 2007.
[17] X. Y. Hu and N. A. Adams, "A constant-density approach for incompressible multi-phase SPH," *Journal of Computational Physics*, vol. 228, no. 6, pp. 2082–2091, 2009.
[18] M. Kondo and S. Koshizuka, "Improvement of stability in moving particle semi-implicit method," *International Journal for Numerical Methods in Fluids*, vol. 65, no. 6, pp. 638–654, 2011.
[19] M. Tanaka and T. Masunaga, "Stabilization and smoothing of pressure in MPS method by quasi-compressibility," *Journal of Computational Physics*, vol. 229, no. 11, pp. 4279–4290, 2010.
[20] D. Violeau and R. Issa, "Numerical modelling of complex turbulent free-surface flows with the SPH method: an overview," *International Journal for Numerical Methods in Fluids*, vol. 53, no. 2, pp. 277–304, 2007.
[21] H. Gotoh, S. Shao, and T. Memita, "SPH-LES model for numerical investigation of wave interaction with partially immersed breakwater," *Coastal Engineering Journal*, vol. 46, no. 1, pp. 39–63, 2004.
[22] S. Shao and H. Gotoh, "Turbulence particle models for tracking free surfaces," *Journal of Hydraulic Research*, vol. 43, no. 3, pp. 276–289, 2005.
[23] B. H. Lee, J. C. Park, M. H. Kim, S. J. Jung, M. C. Ryu, and Y. S. Kim, "Numerical simulation of impact loads using a particle method," *Ocean Engineering*, vol. 37, no. 2-3, pp. 164–173, 2010.
[24] S. Koshizuka and Y. Oka, "Moving-particle semi-implicit method for fragmentation of incompressible fluid," *Nuclear Science and Engineering*, vol. 123, no. 3, pp. 421–434, 1996.
[25] A. J. Chorin, "Numerical solution of the Navier-Stokes equations," *Mathematics of Computation*, vol. 22, pp. 745–762, 1968.
[26] I. J. Schoenberg, "Contributions to the problem of approximation of equidistant data by analytic functions," *Quarterly of Applied Mathematics*, vol. 4, pp. 45–99, 1946.
[27] J. A. Meijerink and H. A. van der Vorst, "An iterative solution method for linear systems of which the coefficient matrix is a symmetric M-matrix," *Mathematics of Computation*, vol. 31, no. 137, pp. 148–162, 1977.
[28] H. Takeda, S. Miyama, and M. Sekiya, "Numerical simulation of viscous flow by smoothed particle hydrodynamics," *Progress of Theoretical Physics*, vol. 92, no. 5, pp. 939–960, 1994.

[29] F. Bierbrauer, P. C. Bollada, and T. N. Phillips, "A consistent reflected image particle approach to the treatment of boundary conditions in smoothed particle hydrodynamics," *Computer Methods in Applied Mechanics and Engineering*, vol. 198, no. 41–44, pp. 3400–3410, 2009.

[30] B. Ataie-Ashtiani and G. Shobeyri, "Numerical simulation of landslide impulsive waves by incompressible smoothed particle hydrodynamics," *International Journal for Numerical Methods in Fluids*, vol. 56, no. 2, pp. 209–232, 2008.

[31] R. Xu, P. Stansby, and D. Laurence, "Accuracy and stability in incompressible SPH (ISPH) based on the projection method and a new approach," *Journal of Computational Physics*, vol. 228, no. 18, pp. 6703–6725, 2009.

[32] F. Losasso, J. O. Talton, N. Kwatra, and R. Fedkiw, "Two-way coupled SPH and particle level set fluid simulation," *IEEE Transactions on Visualization and Computer Graphics*, vol. 14, no. 4, pp. 797–804, 2008.

[33] A. Khayyer and H. Gotoh, "Enhancement of stability and accuracy of the moving particle semi-implicit method," *Journal of Computational Physics*, vol. 230, no. 8, pp. 3093–3118, 2011.

[34] G. R. Liu and M. B. Liu, *Smoothed Particle Hydrodynamic, a Meshfree Particle Method*, World Scientific, 2003.

[35] J. C. Martin and W. J. Moyce, "An experimental study of the collapse of liquid columns on a rigid horizontal plane," *Philosophical Transactions of the Royal Society of London A*, vol. 244, no. 882, pp. 312–324, 1952.

[36] Z. Q. Zhou, J. O. De Kat, and B. Buchner, "A nonlinear 3-D approach to simulate green water dynamics on deck," in *Proceedings of the 7th International Conference on Numerical Ship Hydrodynamics*, Nantes, France, July 1999.

[37] K. M. T. Kleefsman, G. Fekken, A. E. P. Veldman, B. Iwanowski, and B. Buchner, "A volume-of-fluid based simulation method for wave impact problems," *Journal of Computational Physics*, vol. 206, no. 1, pp. 363–393, 2005.

[38] E. S. Lee, D. Violeau, R. Issa, and S. Ploix, "Application of weakly compressible and truly incompressible SPH to 3-D water collapse in waterworks," *Journal of Hydraulic Research*, vol. 48, no. 1, pp. 50–60, 2010.

Hindawi Publishing Corporation
Journal of Applied Mathematics
Volume 2012, Article ID 950323, 27 pages
doi:10.1155/2012/950323

Research Article

Nonlinear Fluid Models for Biofluid Flow in Constricted Blood Vessels under Body Accelerations: A Comparative Study

D. S. Sankar[1] and Atulya K. Nagar[2]

[1] *School of Mathematical Sciences, University Science Malaysia, 11800 Penang, Malaysia*
[2] *Centre for Applicable Mathematics and Systems Science, Department of Computer Science, Liverpool Hope University, Hope Park, Liverpool L16 9JD, UK*

Correspondence should be addressed to D. S. Sankar, sankar_ds@yahoo.co.in

Received 3 January 2012; Accepted 12 February 2012

Academic Editor: M. F. El-Amin

Pulsatile flow of blood in constricted narrow arteries under periodic body acceleration is analyzed, modeling blood as non-Newtonian fluid models with yield stress such as (i) Herschel-Bulkley fluid model and (ii) Casson fluid model. The expressions for various flow quantities obtained by Sankar and Ismail (2010) for Herschel-Bulkley fluid model and Nagarani and Sarojamma (2008), in an improved form, for Casson fluid model are used to compute the data for comparing these fluid models. It is found that the plug core radius and wall shear stress are lower for H-B fluid model than those of the Casson fluid model. It is also noted that the plug flow velocity and flow rate are considerably higher for H-B fluid than those of the Casson fluid model. The estimates of the mean velocity and mean flow rate are considerably higher for H-B fluid model than those of the Casson fluid model.

1. Introduction

Atherosclerosis is an arterial disease in large and medium size blood vessels which involve in the complex interactions between the artery wall and blood flow and is caused by intravascular plaques leading to malfunctions of the cardiovascular system [1]. The intimal thickening of an artery is the initial process in the development of atherosclerosis and one of the most wide spread diseases in humans [2]. In atherosclerotic arteries, the lumen is typically narrowed and the wall is stiffened by the buildup of plaque with a lipid core and a fibromuscular cap, and the narrowing of lumen of the artery by the deposit of fats, lipids, cholesterol, and so forth is medically termed as stenosis formation [3]. Different shapes of

stenoses are formed in arteries like axisymmetric, asymmetric, overlapping, and multiple and even sometimes it may be arbitrary in shape [4–7]. Once stenosis develops in an artery, its most serious consequences are the increased resistance and the associated reduction of blood flow to the vascular bed supplied by the artery [8, 9]. Thus, the presence of a stenosis leads to the serious circulatory disorder. Hence, it is very useful to mathematically analyze the blood flow in stenosed arteries.

In many situations of our day to day life, we are exposed to body accelerations or vibrations, like swinging of kids in a cradle, vibration therapy applied to a patient with heart disease, travel of passengers in road vehicles, ships and flights, sudden movement of body in sports activities, and so forth [10, 11]. Sometime, our whole body may be subjected to vibrations, like a passenger sitting in a bus/train, and so forth, while in some other occasions, specific part of our body might be subjected to vibrations, for example, in the operation of jack hammer or lathe machine, driver of a car, and so forth [12–14]. Prolonged exposure of our body to high level unintended external body accelerations causes serious health hazards due to the abnormal blood circulation [15–17]. Some of the symptoms which result from prolonged exposure of body acceleration are headache, abdominal pain, increase in pulse rate, venous pooling of blood in the extremities, loss of vision, hemorrhage in the face, neck, eye-sockets, lungs, and brain [18–20]. Thus, an adequate knowledge in this field is essential to the diagnosis and therapeutic treatment of some health problems, like vision loss, joint pain, and vascular disorder, and so forth, and also in the design of protective pads and machines. Hence, it is important to mathematically analyze and also to quantify the effects of periodic body accelerations in arteries of different diameters.

Due to the rheological importance of the body accelerations and the arterial stenosis, several theoretical studies were performed to understand their effects on the physiologically important flow quantities and also their consequences [15–20]. Blood shows anomalous viscous properties. Blood, when it flows through larger diameter arteries at high shear rates, it shows Newtonian character; whereas, when it flows in narrow diameter arteries at low shear rates, it exhibits remarkable non-Newtonian behavior [21, 22]. Many studies pertaining to blood flow analysis treated it as Newtonian fluid [4, 15, 23]. Several researchers used non-Newtonian fluids models for mathematical analysis of blood flow through narrow arteries with different shapes of stenosis under periodic body accelerations [24–27]. Casson and Herschel-Bulkley (H-B) fluid models are some of the non-Newtonian fluid models with yield stress and are widely used in the theoretical analysis of blood flow in narrow arteries [28, 29]. The advantages of using H-B fluid model rather than Casson fluid model for modeling of blood flow in narrow arteries are mentioned below.

Chaturani and Samy [8] emphasized the use of H-B fluid model for blood flow modeling with the argument that when blood flows in arteries of diameter 0.095 mm, it behaves like H-B fluid rather than other non-Newtonian fluids. Tu and Deville [21] pronounced that blood obeys Casson fluid's constitutive equation only at moderate shear rates, whereas H-B fluid model can be used still at low shear rates and represents fairly closely what is occurring in blood. Iida [30] reports "the velocity profiles of blood when it flows in the arterioles having diameter less than 0.1 mm are generally explained fairly by Casson and H-B fluid models. However, the velocity profiles of blood flow in the arterioles whose diameters are less than 0.065 mm do not conform to the Casson fluid model, but, can still be explained by H-B fluid model." Moreover, Casson fluid's constitutive equation has only one parameter, namely, the yield stress, whereas the H-B fluid's constitutive equation has one more parameter, namely, the power law index "n" and

thus one can obtain more detailed information about blood flow characteristics by using the H-B fluid model rather than Casson fluid model [31]. Hence, it is appropriate to treat blood as H-B fluid model rather than Casson fluid model when it flows through narrow arteries.

Sankar and Ismail [32] investigated the effects of periodic body accelerations in blood flow through narrow arteries with axisymmetric stenosis, treating blood as H-B fluid model. Nagarani and Sarojamma [33] mathematically analyzed the pulsatile flow of Casson fluid for blood flow through stenosed narrow arteries under body acceleration. The pulsatile flow of H-B fluid model and Casson fluid model for blood flow through narrow arteries with asymmetric stenosis under periodic body acceleration has not been studied so far, to the knowledge of the authors. Hence, in the present study, a comparative study is performed for the pulsatile flow H-B and Casson fluid models for blood flow in narrow arteries with asymmetric shapes of stenoses under periodic body acceleration. The expressions obtained in Sankar and Ismail [32] for shear stress, velocity distribution, wall shear stress, and flow rate are used to compute data for the present comparative study. The aforesaid flow quantities obtained by Nagarani and Sarojamma [33] for Casson fluid model in the corrected form are used in this study to compute data for performing the present comparative study. The layout of the paper is as follows.

Section 2 mathematically formulates the H-B and Casson fluid models for blood flow and applies the perturbation method of solution. In Section 3, the results of H-B fluid model and Casson fluid model for blood flow in axisymmetric and asymmetrically stenosed narrow arteries are compared. Some possible clinical applications to the present study are also given in Section 3. The main results are summarized in the concluding Section 4.

2. Mathematical Formulation

Consider an axially symmetric, laminar, pulsatile, and fully developed flow of blood (assumed to be incompressible) in the axial ($\overline{z}$) direction through a circular narrow artery with constriction. The constriction in the artery is assumed as due to the formation of stenosis in the lumen of the artery and is considered as mild. In this study, we consider the shape of the stenosis as asymmetric. The geometry of segment of a narrow artery with asymmetric shape of mild stenosis is shown in Figure 1(a). For different values of the stenosis shape parameter m, the asymmetric shapes of the stenoses are sketched in Figure 1(b). In Figure 1(b), one can notice the axisymmetric shape of stenosis when the stenosis shape parameter $m = 2$. The segment of the artery under study is considered to be long enough so that the entrance, end, and special wall effects can be neglected. Due to the presence of the stenosis in the lumen of the segment of the artery, it is appropriate to treat the segment of the stenosed artery under study as rigid walled. Assume that there is periodical body acceleration in the region of blood flow and blood is modeled as non-Newtonian fluid model with yield stress. In this study, we use two different non-Newtonian fluid models with yield stress for blood flow simulations such as (i) Herschel-Bulkley (H-B) fluid and (ii) Casson fluid. Note that for particular values of the parameters, H-B fluid model's constitutive equation reduces to the constitutive equations of Newtonian fluid, power law fluid, and Bingham fluid. Also it is to be noted that Casson fluid model's constitutive equation reduces to the constitutive equation of Newtonian fluid when the yield stress parameter becomes zero. The cylindrical polar coordinate system $(\overline{r}, \overline{\varphi}, \overline{z})$ has been used to analyze the blood flow.

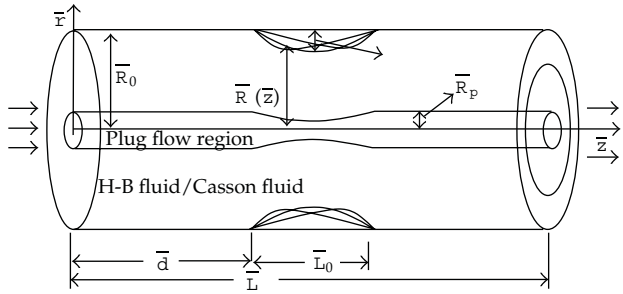

(a) Geometry of the stenosed artery in cylindrical polar coordinate system

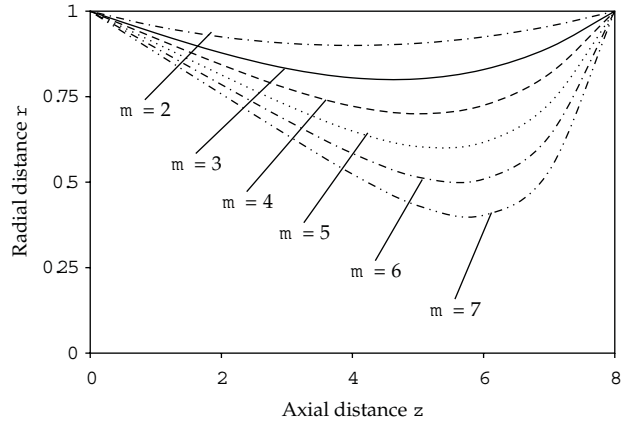

(b) Shapes of the arterial stenosis for different values of the stenosis shape parameter m

Figure 1: Pictorial description of segment of the artery with asymmetric stenosis.

2.1. Herschel-Bulkley Fluid Model

2.1.1. Governing Equations and Boundary Conditions

It has been reported that the radial velocity is negligibly small and can be neglected for a low Reynolds number flow in a narrow artery with mild stenosis. The momentum equations governing the blood flow in the axial and radial directions simplify, respectively, to [32]

$$\overline{\rho}_H \frac{\partial \overline{u}_H}{\partial \overline{t}} = -\frac{\partial \overline{p}}{\partial \overline{z}} - \frac{1}{\overline{r}} \frac{\partial}{\partial \overline{r}} \left(\overline{r}\overline{\tau}_H\right) + \overline{F}\left(\overline{t}\right), \tag{2.1}$$

$$0 = \frac{\partial \overline{p}}{\partial \overline{r}}, \tag{2.2}$$

where $\overline{\rho}_H$, $\overline{u}_H$ are the density and axial component of the velocity of the H-B fluid, respectively; $\overline{p}$ is the pressure; $\overline{t}$ is the time; $\overline{\tau}_H = |\overline{\tau}_{\overline{r}\overline{z}}| = -\overline{\tau}_{\overline{r}\overline{z}}$ is the shear stress of the H-B fluid; $\overline{F}(\overline{t})$ is the term which represents the effect of body acceleration and is given by

$$\overline{F}\left(\overline{t}\right) = \overline{a}_0 \cos\left(\overline{\omega}_b \overline{t} + \phi\right), \tag{2.3}$$

where $\overline{a}_0$ is the amplitude of the body acceleration, $\overline{\omega}_b = 2\pi \overline{f}_b$, $\overline{f}_b$ is the frequency in Hz and is assumed to be small so that the wave effect can be neglected [14], ϕ is the lead angle of $\overline{F}(\overline{t})$ with respect to the heart action. Since, the blood flow is assumed as pulsatile, it is appropriate to assume the pressure gradient as a periodic function as given below [25]:

$$-\frac{\partial \overline{p}}{\partial \overline{z}}\left(\overline{z}, \overline{t}\right) = \overline{A}_0 + \overline{A}_1 \cos\left(\overline{\omega}_p \overline{t}\right), \tag{2.4}$$

where $\overline{A}_0$ is the steady component of the pressure gradient, $\overline{A}_1$ is the amplitude of the pulsatile component of the pressure gradient, and $\overline{\omega}_p = 2\pi \overline{f}_p$, $\overline{f}_p$ is the pulse frequency in Hz [23]. The constitutive equation of the H-B fluid (which represents blood) is given by

$$\begin{aligned} \overline{\tau}_H &= \overline{\mu}_H^{1/n} \left(\frac{-\partial \overline{u}_H}{\partial \overline{r}} \right)^{1/n} + \overline{\tau}_y \quad \text{if } \tau_H \geq \tau_y, \\ \frac{\partial \overline{u}_H}{\partial \overline{r}} &= 0 \quad \text{if } \overline{\tau}_H \leq \overline{\tau}_y, \end{aligned} \tag{2.5}$$

where, $\overline{\tau}_y$ is the yield stress of the H-B fluid and $\overline{\mu}_H$ is the coefficient of viscosity of H-B fluid with dimension $(ML^{-1}T^{-2})^n T$. The geometry of the asymmetric shape of stenosis in the arterial segment is mathematically represented by the following equation [34]:

$$\frac{\overline{R}(\overline{z})}{\overline{R}_0} = \begin{cases} 1 - \overline{G}\left[\overline{L}_0^{m-1}\left(\overline{z} - \overline{d}\right) - \left(\overline{z} - \overline{d}\right)^m\right] & \text{if } \overline{d} \leq \overline{z} \leq \overline{d} + \overline{L}_0, \\ 1 & \text{otherwise,} \end{cases} \tag{2.6}$$

where $\overline{G} = (\overline{\delta}/\overline{R}_0\overline{L}_0)m^{(m/m-1)}$; $\overline{\delta}$ denotes the maximum height of the stenosis at $\overline{z} = \overline{d} + (\overline{L}_0/m^{(m/m-1)})$ such that $\overline{\delta}/\overline{R}_0 \ll 1$; $\overline{L}_0$ is the length of the stenosis; $\overline{d}$ denotes its location; $\overline{R}(\overline{z})$ is the radius of the artery in the stenosed region; $\overline{R}_0$ is the radius of the normal artery. It is to be noted that (2.6) also represents the geometry of segment of the artery with axisymmetric stenosis when the stenosis shape parameter $m = 2$. We make use of the following boundary conditions to solve the system of momentum and constitutive equations for the unknown velocity and shear stress:

$$\begin{aligned} &\overline{\tau}_H \text{ is finite at } \overline{r} = 0, \\ &\overline{u}_H = 0 \quad \text{at } \overline{r} = \overline{R}(\overline{z}). \end{aligned} \tag{2.7}$$

2.1.2. Nondimensionalization

Let us introduce the following nondimensional variables:

$$z = \frac{\overline{z}}{\overline{R}_0}, \quad R(z) = \frac{\overline{R}(\overline{z})}{\overline{R}_0}, \quad r = \frac{\overline{r}}{\overline{R}_0}, \quad t = \overline{t}\overline{\omega}, \quad \omega = \frac{\overline{\omega}_b}{\overline{\omega}_p}, \quad \delta = \frac{\overline{\delta}}{\overline{R}_0}, \quad u_H = \frac{\overline{u}_H}{\left(\overline{A}_0 \overline{R}_0{}^2/4\overline{\mu}_0\right)},$$
$$\tau_H = \frac{\overline{\tau}_H}{\left(\overline{A}_0\overline{R}_0/2\right)}, \quad \theta = \frac{2\overline{\tau}_y}{\overline{A}_0\overline{R}_0}, \quad \alpha_H^2 = \frac{\overline{R}_0{}^2\overline{\omega}\,\overline{\rho}_H}{\overline{\mu}_0}, \quad e = \frac{\overline{A}_1}{\overline{A}_0}, \quad B = \frac{\overline{a}_0}{\overline{A}_0}, \tag{2.8}$$

where $\overline{\mu}_0 = \overline{\mu}_H(2/\overline{R}_0\overline{A}_0)^{n-1}$ having dimension as that of Newtonian fluid's viscosity [22, 34]; α_H is the generalized Wormersly frequency parameter or pulsatile Reynolds number, and when $n = 1$, it reduces to the Newtonian fluid's pulsatile Reynolds number. Using nondimensional variables defined in (2.8), the momentum and constitutive equations (2.1) and (2.5) can be simplified to the following equations:

$$\alpha_H^2 \frac{\partial u_H}{\partial t} = 4(1 + e\cos t) + 4B\cos(\omega t + \phi) - \frac{2}{r}\frac{\partial}{\partial r}(r\tau_H), \tag{2.9}$$

$$\tau_H = \left(-\frac{1}{2}\frac{\partial u_H}{\partial r}\right)^{1/n} + \theta \quad \text{if } \tau_H \geq \theta, \tag{2.10}$$

$$\frac{\partial u_H}{\partial r} = 0 \quad \text{if } \tau_H \leq \theta. \tag{2.11}$$

The geometry of the asymmetric shape of the stenosis in the arterial segment in the nondimensional form reduces to the following equation:

$$R(z) = \begin{cases} 1 - G\left[L_0^{m-1}(z-d) - (z-d)^m\right] & \text{if } d \leq z \leq d + L_0, \\ 1 & \text{otherwise,} \end{cases} \tag{2.12}$$

where $G = (\overline{\delta}/\overline{R}_0\overline{L}_0)m^{(m/m-1)}$. The boundary conditions in the nondimensional form are

$$\begin{aligned} &\tau_H \text{ is finite at } r = 0, \\ &u_H = 0 \quad \text{at } r = R. \end{aligned} \tag{2.13}$$

The volume flow rate in the nondimensional is given by

$$Q(z,t) = 4\int_0^{R(z)} u_H(z,r,t)r\,dr, \tag{2.14}$$

where $Q(z,t) = \overline{Q}(\overline{z},\overline{t})/[\pi\overline{R}_0^4\overline{A}_0/8\overline{\mu}_0]$, $\overline{Q}$ is the volumetric flow rate.

2.1.3. Perturbation Method of Solution

Since, (2.9) and (2.10) form the system of nonlinear partial differential equations, it is not possible to get an exact solution to them. Thus, perturbation method is used to solve this system of nonlinear partial differential equations. Since, the present study deals with slow flow of blood (low Reynolds number flow) where the effect of pulsatile Reynolds number α_H is negligibly small and also it occurs naturally in the nondimensional form of the momentum equation, it is more appropriate to expand the unknowns u_H and τ_H in (2.9) and (2.10) in the perturbation series about α_H^2. Let us expand the velocity u_H in the perturbation series about the square of the pulsatile Reynolds number α_H^2 as below (where $\alpha_H^2 \ll 1$):

$$u_H(r,z,t) = u_{H0}(r,z,t) + \alpha_H^2 u_{H1}(r,z,t) + \cdots . \tag{2.15}$$

Similarly, one can expand the shear stress $\tau_H(r,z,t)$, the plug core radius $R_p(z,t)$, the plug core velocity $u_p(z,t)$, and the plug core shear stress $\tau_p(z,t)$ in terms of α_H^2. Substituting the perturbation series expansions of u_H and τ_H in (2.9) and then equating the constant term and α_H^2 term, we get

$$\begin{aligned} \frac{\partial}{\partial r}(r\tau_{H0}) &= 2r\left[(1 + e\cos t) + B\cos(\omega t + \phi)\right], \\ \frac{\partial u_{H0}}{\partial t} &= -\frac{2}{r}\frac{\partial}{\partial r}(r\tau_{H1}). \end{aligned} \tag{2.16}$$

Using the binomial series approximation in (2.10) (assuming $(\theta/\tau)^2 \ll 1$) and then applying the perturbation series expansions of u_H and τ_H in the resulting equation and then equating the constant term and α_H^2 term, one can obtain

$$\begin{aligned} -\frac{\partial u_{H0}}{\partial r} &= 2\tau_{H0}^{n-1}[\tau_{H0} - n\theta], \\ -\frac{\partial u_{H1}}{\partial r} &= 2n\tau_{H0}^{n-2}\tau_{H1}[\tau_{H0} - (n-1)\theta]. \end{aligned} \tag{2.17}$$

Applying the perturbation series expansions of u_H and τ_H in the boundary conditions (2.13), we obtain

$$\begin{aligned} &\tau_{H0}, \tau_{H1} \text{ are finite at } r = 0, \\ &u_{H0} = 0, \quad u_{H1} = 0 \quad \text{at } r = 0. \end{aligned} \tag{2.18}$$

Solving (2.16)–(2.17) with the help of the boundary conditions (2.18) for the unknowns τ_{P0}, τ_{P1}, τ_{H0}, τ_{H1}, u_{P0}, u_{P1}, u_{H0}, and u_{H1}, one can get the following expressions (detail of obtaining these expressions is given in [32]):

$$\tau_{P0} = g(t)R_{0p},$$

$$\tau_{H0} = g(t)r,$$

$$u_{H0} = 2\left[g(t)R\right]^n R\left[\frac{1}{(n+1)}\left\{1-\left(\frac{r}{R}\right)^{n+1}\right\}-\left(\frac{q^2}{R}\right)\left\{1-\left(\frac{r}{R}\right)^{n}\right\}\right],$$

$$u_{0p} = 2\left[g(t)R\right]^n R\left[\frac{1}{(n+1)}\left\{1-\left(\frac{q^2}{R}\right)^{n+1}\right\}-\left(\frac{q^2}{R}\right)\left\{1-\left(\frac{q^2}{R}\right)^{n}\right\}\right],$$

$$\tau_{P1} = -\left[g(t)R\right]^n DR^2\left[\frac{n}{2(n+1)}\left(\frac{q^2}{R}\right)-\frac{(n-1)}{2}\left(\frac{q^2}{R}\right)^2-\frac{n}{2(n+1)}\left(\frac{q^2}{R}\right)^{n+2}\right],$$

$$\begin{aligned}\tau_{H1} = -\left[g(z)R\right]^n DR^2\Bigg[&\frac{n}{(n+1)(n+3)}\left\{\left(\frac{n+3}{2}\right)\left(\frac{r}{R}\right)-\left(\frac{r}{R}\right)^{n+2}\right\}\\&-\frac{(n-1)}{(n+2)}\left(\frac{q^2}{R}\right)\left\{\left(\frac{n+2}{2}\right)\left(\frac{r}{R}\right)-\left(\frac{r}{R}\right)^{n+1}\right\}\\&-\frac{3\left(n^2+2n-2\right)}{2(n+2)(n+3)}\left(\frac{q^2}{R}\right)^{n+3}\left(\frac{R}{r}\right)\Bigg],\end{aligned}$$

$$\begin{aligned}u_{H1} = -2n\left[g(t)R\right]^{2n-1} DR^3\Bigg[&\frac{n}{2(n+1)^2(n+3)}\left\{(n+2)-(n+3)\left[\frac{r}{R}\right]^{n+1}+\left[\frac{r}{R}\right]^{2n+2}\right\}\\&+\frac{(n-1)}{2(n+1)(n+2)(n+3)(2n+1)}\left[\frac{q^2}{R}\right]\\&\times\Bigg\{(n+2)(n+3)(2n+1)\left[\left(\frac{r}{R}\right)^n+\left(\frac{r}{R}\right)^{n+1}\right]\\&\quad-2\left[\left(2n^3+9n^2+11n+3\right)+\left(2n^2+6n+3\right)\left[\frac{r}{R}\right]^{2n+1}\right]\Bigg\}\\&+\frac{(n-1)^2}{2n(n+2)}\left(\frac{q^2}{R}\right)^2\left\{(n+1)-(n+2)\left[\frac{r}{R}\right]^n+\left[\frac{r}{R}\right]^{2n}\right\}\end{aligned}$$

$$
\begin{aligned}
&+\frac{3\left(n^2+2n-2\right)}{2(n-1)(n+2)(n+3)}\left(\frac{q^2}{R}\right)^{n+3}\left\{\left(\frac{r}{R}\right)^{n-1}-1\right\}\\
&+\frac{3\left(n^2+2n-2\right)(n-1)}{2(n-2)(n+2)(n+3)}\left(\frac{q^2}{R}\right)^{n+4}\left\{1-\left[\frac{r}{R}\right]^{n-2}\right\}\Bigg],\\
u_{P1}=-2n\left[g(t)R\right]^{2n-1}DR^3&\Bigg[\frac{n}{2(n+1)^2(n+3)}\left\{(n+2)-(n+3)\left[\frac{q^2}{R}\right]^{n+1}+\left[\frac{q^2}{R}\right]^{2n+2}\right\}\\
&+\frac{(n-1)}{2(n+1)(n+2)(n+3)(2n+1)}\left[\frac{q^2}{R}\right]\\
&\times\left\{(n+2)(n+3)(2n+1)\left[\left(\frac{q^2}{R}\right)^{n}+\left(\frac{q^2}{R}\right)^{n+1}\right]\right.\\
&\quad\left.-2\left[\left(2n^3+9n^2+11n+3\right)+\left(2n^2+6n+3\right)\left[\frac{q^2}{R}\right]^{2n+1}\right]\right\}\\
&+\frac{(n-1)^2}{2n(n+2)}\left(\frac{q^2}{R}\right)^{2}\left\{(n+1)-(n+2)\left[\frac{q^2}{R}\right]^{n}+\left[\frac{q^2}{R}\right]^{2n}\right\}\\
&+\frac{3\left(n^2+2n-2\right)}{2(n-1)(n+2)(n+3)}\left(\frac{q^2}{R}\right)^{n+3}\left\{\left(\frac{q^2}{R}\right)^{n-1}-1\right\}\\
&+\frac{3\left(n^2+2n-2\right)(n-1)}{2(n-2)(n+2)(n+3)}\left(\frac{q^2}{R}\right)^{n+4}\left\{1-\left[\frac{q^2}{R}\right]^{n-2}\right\}\Bigg],
\end{aligned}
\tag{2.19}
$$

where $q^2=(\theta/g(t))$, $r|_{\tau_{0p}=\theta}=R_{0p}=\theta/g(t)=q^2$, $g(t)=(1+e\cos t)+B\cos(\omega t+\phi)$, and $D=(1/g)(dg/dt)$. The wall shear stress τ_w is a physiologically important flow quantity which plays an important role in determining the aggregate sites of platelets [3]. The expression for wall shear stress τ_w is given by [32]

$$
\begin{aligned}
\tau_w&=\left(\tau_{H0}+\alpha_H^2\tau_{H1}\right)_{r=R}\\
&=\left[g(t)R\right]\\
&\quad\times\left[1-\frac{\left(g(t)R\right)^{n-1}\alpha^2R^2B}{2(n+2)(n+3)}\right.\\
&\qquad\left.\times\left\{n(n+2)-(n-1)n(n+3)\left(\frac{q^2}{R}\right)-3\left(n^2+2n-2\right)\left(\frac{q^2}{R}\right)^{n+3}\right\}\right].
\end{aligned}
\tag{2.20}
$$

The expression for volumetric flow rate $Q(z,t)$ is obtained as below (see [32] for details):

$$\begin{aligned}
Q(z,t) &= 4\left[\left(\int_0^{R_{0p}} ru_{0p}dr + \int_{R_{0p}}^{R} ru_0 dr\right) + \alpha^2\left(\int_0^{R_{0p}} ru_{1p}dr + \int_{R_{0p}}^{R} ru_1 dr\right)\right] \\
&= \frac{4[g(t)R]^{n}R^3}{(n+2)(n+3)}\left[\left\{(n+2) - n(n+3)\left(\frac{q^2}{R}\right) + \left(n^2+2n-2\right)\left(\frac{q^2}{R}\right)^{n+3}\right\}\right. \\
&\qquad - \alpha^2[g(t)R]^{n-1}\left(\frac{nDR^2}{4}\right) \\
&\qquad \times \left\{n - \frac{2n(n-1)(4n^2+12n+5)}{(2n+1)(2n+3)}\left(\frac{q^2}{R}\right)\right. \\
&\qquad\quad + \frac{n(n-1)^2(n+3)}{(n+1)}\left(\frac{q^2}{R}\right)^2 + \frac{(n^3-2n^2-11n+6)}{(n+1)}\left(\frac{q^2}{R}\right)^{n+3} \\
&\qquad\quad - \frac{(n-1)(n^3-2n^2-11n+6)}{n}\left(\frac{q^2}{R}\right)^{n+4} \\
&\qquad\quad \left.\left. - \frac{(4n^5+14n^4-8n^3-45n^2-3n+18)}{n(n+1)(2n+3)}\left(\frac{q^2}{R}\right)^{2n+4}\right\}\right].
\end{aligned} \tag{2.21}$$

The expression for the plug core radius is obtained as below [32]:

$$R_p = q^2 + \alpha^2[g(t)R]^{n-1}\left(\frac{nDR^3}{2(n+1)}\right)\left[\left(\frac{q^2}{R}\right) - \left(\frac{n^2-1}{n}\right)\left(\frac{q^2}{R}\right)^2 - \left(\frac{q^2}{R}\right)^{n+2}\right]. \tag{2.22}$$

The longitudinal impedance to flow in the artery is defined as

$$\Lambda = \frac{P(t)}{Q(z,t)}, \tag{2.23}$$

where

$$P(t) = 4[1 + e\cos(t)] \tag{2.24}$$

is the pressure gradient in the nondimensional form.

2.2. Casson Fluid Model

2.2.1. Governing Equations and Boundary Conditions

The momentum equations governing the blood flow in the axial and radial directions simplify, respectively, to [33]

$$\overline{\rho}_C \frac{\partial \overline{u}_C}{\partial \overline{t}} = -\frac{\partial \overline{p}}{\partial \overline{z}} - \frac{1}{\overline{r}} \frac{\partial}{\partial \overline{r}} (\overline{r}\,\overline{\tau}_C) + \overline{F}\left(\overline{t}\right), \tag{2.25}$$

$$0 = \frac{\partial \overline{p}}{\partial \overline{r}}, \tag{2.26}$$

where $\overline{u}_C$ and $\overline{\rho}_C$ are the axial component of the velocity and density of Casson fluid; $\overline{p}$ is the pressure; $\overline{t}$ is the time; $\overline{\tau}_C = |\overline{\tau}_{\overline{r}\overline{z}}| = -\overline{\tau}_{\overline{r}\overline{z}}$ is the shear stress of Casson fluid. Equations (2.3) and (2.4) which define mathematically the body acceleration term $\overline{F}(\overline{t})$ and pressure gradient $-(\partial \overline{p}/\partial \overline{z})$ are assumed in this subsection. Similarly, (2.6) which mathematically describes the geometry of the axisymmetric shape of stenosis and asymmetric shape of stenosis in the segment of the stenosed artery is also assumed in this subsection (the details of these assumptions can be found in Section 2.1.1) The constitutive equation of the Casson fluid model (which models blood) is defined as below:

$$\sqrt{\overline{\tau}_C} = \sqrt{\overline{\mu}_C \left(\frac{-\partial \overline{u}_C}{\partial \overline{r}} \right)} + \sqrt{\overline{\tau}_y} \quad \text{if } \tau_C \geq \tau_y, \tag{2.27}$$

$$\frac{\partial \overline{u}_C}{\partial \overline{r}} = 0 \quad \text{if } \overline{\tau}_C \leq \overline{\tau}_y, \tag{2.28}$$

where $\overline{\tau}_y$ is the yield stress of Casson fluid and $\overline{\mu}_C$ is the coefficient of viscosity of Casson fluid with dimension $ML^{-1}T^{-1}$. The appropriate boundary conditions to solve the system of momentum and constitutive equations (2.25), (2.27), and (2.28) for the unknown velocity and shear stress are

$$\begin{aligned} &\overline{\tau}_C \text{ is finite at } \overline{r} = 0, \\ &\overline{u}_C = 0 \quad \text{at } \overline{r} = \overline{R}(\overline{z}). \end{aligned} \tag{2.29}$$

2.2.2. Nondimensionalization

Similar to (2.8), let us introduce the following nondimensional variables for the Casson fluid flow modeling as follows:

$$z = \frac{\overline{z}}{\overline{R}_0}, \quad R(z) = \frac{\overline{R}(\overline{z})}{\overline{R}_0}, \quad r = \frac{\overline{r}}{\overline{R}_0}, \quad t = \overline{t}\overline{\omega}, \quad \omega = \frac{\overline{\omega}_b}{\overline{\omega}_p}, \quad \delta = \frac{\overline{\delta}}{\overline{R}_0}, \quad u_C = \frac{\overline{u}_C}{\left(\overline{A}_0\overline{R}_0^2/4\overline{\mu}_C\right)},$$
$$\tau_C = \frac{\overline{\tau}_C}{\left(\overline{A}_0\overline{R}_0/2\right)}, \quad \theta = \frac{2\overline{\tau}_y}{\overline{A}_0\overline{R}_0}, \quad \alpha_C^2 = \frac{\overline{R}_0^2\overline{\omega\rho}_C}{\overline{\mu}_C}, \quad e = \frac{\overline{A}_1}{\overline{A}_0}, \quad B = \frac{\overline{a}_0}{\overline{A}_0}, \tag{2.30}$$

where α_C is the Wormersly frequency parameter or pulsatile Reynolds number of Casson fluid model. Use of the above nondimensional variables reduces the momentum and constitutive equations (2.25), (2.27), and (2.28), respectively, to the following equations:

$$\alpha_C^2\frac{\partial u_C}{\partial t} = 4(1 + e\cos t) + 4B\cos\left(\omega t + \phi\right) - \frac{2}{r}\frac{\partial}{\partial r}(r\tau_C), \tag{2.31}$$

$$\sqrt{\tau_C} = \sqrt{-\frac{1}{2}\frac{\partial u_C}{\partial r}} + \sqrt{\theta} \quad \text{if } \tau_C \geq \theta, \tag{2.32}$$

$$\frac{\partial u_C}{\partial r} = 0 \quad \text{if } \tau_C \leq \theta. \tag{2.33}$$

Equation (2.12) which mathematically defines the nondimensional form of the geometry of the asymmetric shapes of stenosis in the arterial segment is assumed in this sub-section. The boundary conditions in the nondimensional form are

$$\begin{aligned} &\tau_C \text{ is finite at } r = 0, \\ &u_C = 0 \quad \text{at } r = R. \end{aligned} \tag{2.34}$$

The volume flow rate in the nondimensional is given by

$$Q = 4\int_0^{R(z)} u_C(z, r, t) r\, dr, \tag{2.35}$$

where $Q = \overline{Q}/[\pi\overline{R}_0^4\overline{A}_0/8\overline{\mu}_C]$, $\overline{Q}$ is the volumetric flow rate.

2.2.3. Perturbation Method of Solution

As described in Section 2.1.3, perturbation method is applied to solve the system of nonlinear partial differential equations (2.31) and (2.32). Let us expand the velocity u_C in the perturbation series about the square of the pulsatile Reynolds number α_C^2 as below (where $\alpha_C^2 \ll 1$):

$$u_C(r,z,t) = u_{C0}(r,z,t) + \alpha_C^2 u_{C1}(r,z,t) + \cdots . \tag{2.36}$$

Similarly, one can expand the shear stress $\tau_C(r,z,t)$, the plug core radius $R_p(z,t)$, the plug core velocity $u_p(z,t)$, and the plug core shear stress $\tau_p(z,t)$ in terms of α_C^2. Substituting the perturbation series expansions of $u_C$and τ_C in (2.31) and then equating the constant term and α_C^2 term, one can obtain

$$\begin{gathered}\frac{\partial}{\partial r}(r\tau_{C0}) = 2r\left[(1 + e\cos t) + B\cos(\omega t + \phi)\right], \\ \frac{\partial u_{C0}}{\partial t} = -\frac{2}{r}\frac{\partial}{\partial r}(r\tau_{C1}).\end{gathered} \tag{2.37}$$

Applying the perturbation series expansions of u_C and τ_C in (2.32) and then equating the constant term and α_C^2 term, we get

$$\begin{aligned}-\frac{\partial u_{C0}}{\partial r} &= 2\left[\tau_{C0} - 2\sqrt{\left(\frac{\theta}{\tau_{C0}}\right)} + \theta\right], \\ -\frac{\partial u_{C1}}{\partial r} &= 2\tau_{C1}\left[1 - \sqrt{\left(\frac{\theta}{\tau_{C0}}\right)}\right].\end{aligned} \tag{2.38}$$

Applying the perturbation series expansions of u_C and τ_C in the boundary conditions (2.34) and then equating the constant terms and α_C^2 terms, one can get

$$\begin{gathered}\tau_{C0},\ \tau_{C1} \text{ are finite at } r = 0, \\ u_{C0} = 0, \quad u_{C1} = 0 \quad \text{at } r = 0.\end{gathered} \tag{2.39}$$

Solving (2.37)–(2.38) with the help of the boundary conditions (2.39) for the unknowns τ_{P0}, τ_{P1}, τ_{C0}, τ_{C1}, u_{P0}, u_{P1}, u_{C0}, and u_{C1}, one can get the following expressions as in [33], but in a corrected form ((2.40)–(2.50)):

$$\tau_{P0} = g(t)R_{0p}, \tag{2.40}$$

$$\tau_{C0} = g(t)r, \tag{2.41}$$

$$u_{C0} = g(t)R^2\left[\left\{1-\left(\frac{r}{R}\right)^2\right\}-\frac{8}{3}\left(\frac{q}{\sqrt{R}}\right)\left\{1-\left(\frac{r}{R}\right)^{3/2}\right\}+\frac{2q^2}{R}\left\{1-\left(\frac{r}{R}\right)\right\}\right], \tag{2.42}$$

$$u_{P0} = g(t)R^2\left[1-\frac{8}{3}\left(\frac{q}{\sqrt{R}}\right)+2\left(\frac{q^2}{R}\right)-\frac{1}{3}\left(\frac{q^2}{R}\right)^2\right], \tag{2.43}$$

$$\tau_{P1} = -\frac{g(t)DR^5}{12}\left(\frac{q^2}{R}\right)\left[3-4\sqrt{\frac{q^2}{R}}+\left(\frac{q^2}{R}\right)^2\right], \tag{2.44}$$

$$\begin{aligned}\tau_{C1} = {} & \frac{g(t)DR^3}{8} \\ & \times\left[2\left(\frac{r}{R}\right)-\left(\frac{r}{R}\right)^3-\left(\frac{q^2}{R}\right)^4\left(\frac{R}{r}\right)-\frac{8}{21}\sqrt{\frac{q^2}{R}}\left\{7\left(\frac{r}{R}\right)-4\left(\frac{r}{R}\right)^{5/2}-3\left(\frac{q^2}{R}\right)^{7/2}\left(\frac{R}{r}\right)\right\}\right],\end{aligned} \tag{2.45}$$

$$\begin{aligned}u_{C1} = -g(t)DR^4\Bigg[& -\frac{1}{12}\left\{1-\left(\frac{r}{R}\right)^2\right\}-\frac{1}{3}\sqrt{\frac{q^2}{R}}\left\{1-\left(\frac{r}{R}\right)^{3/2}\right\} \\ & -\frac{1}{16}\left\{1-\left(\frac{r}{R}\right)^4\right\}+\frac{53}{294}\sqrt{\frac{q^2}{R}}\left\{1-\left(\frac{r}{R}\right)^{7/2}\right\} \\ & +\frac{4}{9}\left(\frac{q^2}{R}\right)\left\{1-\left(\frac{r}{R}\right)^{3/2}\right\}-\frac{8}{63}\left(\frac{k^2}{R}\right)\left\{1-\left(\frac{r}{R}\right)^3\right\} \\ & -\frac{1}{28}\left(\frac{q^2}{R}\right)^4\log\left(\frac{r}{R}\right)+\frac{1}{14}\left(\frac{q^2}{R}\right)^{9/2}\left\{1-\sqrt{\frac{R}{r}}\right\}\Bigg],\end{aligned} \tag{2.46}$$

$$\begin{aligned}u_{P1} = -g(t)DR^4\Bigg[& -\frac{7}{48}+\frac{15}{98}\sqrt{\left(\frac{q^2}{R}\right)}-\frac{20}{63}\left(\frac{q^2}{R}\right)+\frac{5}{12}\left(\frac{q^2}{R}\right)^2 \\ & -\frac{4}{9}\left(\frac{q^2}{R}\right)^{5/2}-\frac{439}{7056}\left(\frac{q^2}{R}\right)^4+\frac{1}{14}\left(\frac{q^2}{R}\right)^{9/2}-\frac{1}{28}\left(\frac{q^2}{R}\right)^4\log\left(\frac{q^2}{R}\right)\Bigg],\end{aligned} \tag{2.47}$$

where $q^2 = (\theta/g(t))$, $r|_{\tau_{0p}=\theta} = R_{0p} = \theta/g(t) = q^2$, $g(t) = (1 + e\cos t) + B\cos(\omega t + \phi)$, and $D = (1/g)(dg/dt)$. Using (2.41) and (2.45), the expression for wall shear stress τ_w is obtained as below:

$$\tau_w = \left(\tau_{C0} + \alpha_C^2\tau_{C1}\right)_{r=R} = g(t)R\left[1 - \frac{\alpha_C^2R^2D}{8}\left\{1 - \frac{8}{7}\left(\frac{q}{\sqrt{R}}\right) + \frac{1}{7}\left(\frac{q^2}{R}\right)^4\right\}\right]. \tag{2.48}$$

The expression for volumetric flow rate $Q(z,t)$ is obtained as below:

$$\begin{aligned} Q(z,t) &= 4\left[\left(\int_0^{R_{0P}} ru_{0p}dr + \int_{R_{0P}}^{R} ru_0dr\right) + \alpha^2\left(\int_0^{R_{0P}} ru_{1p}dr + \int_{R_{0P}}^{R} ru_1dr\right)\right] \\ &= g(t)R^4\left[1 - \frac{16}{7}\left(\frac{q}{\sqrt{R}}\right) + \frac{4}{3}\left(\frac{q^2}{R}\right) - \frac{1}{21}\left(\frac{q^2}{R}\right)^4 - \alpha_C^2R^6g(t)D\right. \\ &\quad \times \left\{\frac{1}{6} - \frac{30}{77}\left(\frac{q}{\sqrt{R}}\right) + \frac{8}{35}\left(\frac{q^2}{R}\right) - \frac{1}{3}\left(\frac{q^2}{R}\right)^{5/2} + \frac{1}{14}\left(\frac{q^2}{R}\right)^{9/2}\right. \\ &\quad \left.\left. - \frac{41}{770}\left(\frac{q^2}{R}\right)^6 - \frac{1}{14}\left(\frac{q^2}{R}\right)^6\log\left(\frac{q^2}{R}\right) + \frac{1}{14}\left(\frac{q^2}{R}\right)^4\left(1 - \left(\frac{q^2}{R}\right)^2\right)\log(q)\right\}\right]. \end{aligned} \tag{2.49}$$

The expression for the plug core radius is obtained as below [33]:

$$R_p = q^2 - \frac{D\alpha_C^2R^3}{4}\left[\left(\frac{q^2}{R}\right) - \frac{4}{3}\left(\frac{q^2}{R}\right)^{3/2} + \frac{1}{3}\left(\frac{q^2}{R}\right)^3\right]. \tag{2.50}$$

The longitudinal impedance to flow in the artery is defined as

$$\Lambda = \frac{P(t)}{Q(z,t)}. \tag{2.51}$$

3. Numerical Simulation of the Results

The main objective of the present mathematical analysis is to compare the H-B and Casson fluid models for blood flow in constricted arteries and spell out the advantageous of using H-B fluid model rather than Casson fluid for the mathematical modeling of blood flow in a narrow artery with asymmetric stenosis. It is also aimed to bring out the effect of body acceleration, stenosis shape parameter, yield stress, and pressure gradient on the physiologically important flow quantities such as plug core radius, plug flow velocity, velocity distribution, flow rate, wall shear stress, and longitudinal impedance to flow. The different parameters used in this analysis and their range of values are given below [32–35].

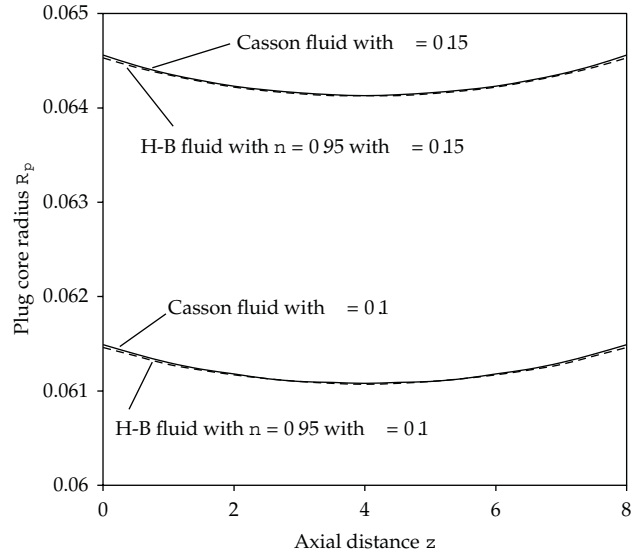

Figure 2: Variation of plug core radius with axial distance for H-B and Casson fluid models with different values of yield stress θ and with $\delta = 0.15$, $\alpha_H = \alpha_C = 0.2$, $B = 2$, $e = \phi = 0.7$, and $t = 45°$.

Yield stress θ: 0–0.3; power law index n: 0.95–1.05; pressure gradient e: 0-1; body acceleration B: 0–2; frequency parameter ω: 0-1; pulsatile Reynolds numbers α_H and α_C: 0.2–0.7; lead angle ϕ: 0.2–0.5; asymmetry parameter m: 2–7; stenosis depth δ: 0–0.2.

3.1. Plug Core Radius

The variation of the plug core with axial distance in axisymmetric stenosed artery ($m = 2$) for different values of the yield stress of H-B and Casson fluid models with $\delta = 0.15$, $B = 2$, $\alpha_H = \alpha_C = 0.2$, $e = \phi = 0.7$ and $t = 45°$ is shown in Figure 2. It is observed that the plug core radius decreases slowly when the axial variable z increases from 0 to 4 and then it increases when z increases further from 4 to 8. The plug core radius is minimum at the centre of the stenosis ($z = 4$), since the stenosis is axisymmetric. The plug core radius of the H-B fluid model is slightly lower than that of the Casson fluid model. One can note that the plug core radius increases very significantly when the yield stress of the flowing blood increases. Figure 3 sketches the variation of plug core radius with pressure gradient ratio in asymmetrically stenosed artery ($m = 4$) for H-B and Casson fluid models and for different values of the body acceleration parameter with $\theta = \delta = 0.1$, $t = 60°$, $\phi = 0.7$, $m = 4$, and $z = 4$. It is noticed that the plug core radius decreases rapidly with the increase of the pressure gradient ratio e from 0 to 0.5 and then it decreases slowly with the increase of the pressure gradient ratio e from 0.5 to 1. It is seen that plug core radius increases significantly with the increase of the body acceleration parameter B. Figures 2 and 3 bring out the influence of the non-Newtonian behavior of blood and the effects of body acceleration and pressure gradient on the plug core radius when blood flows in asymmetrically stenosed artery.

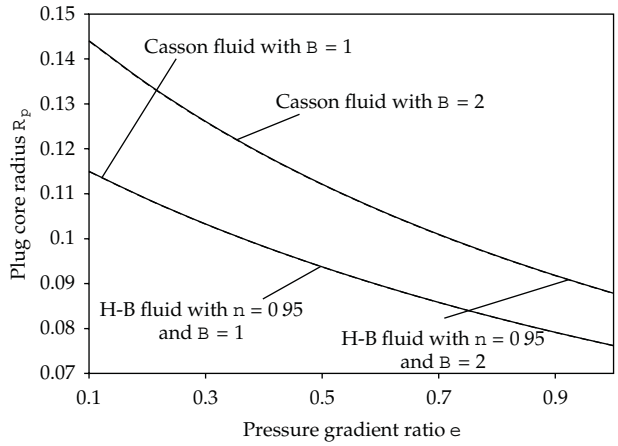

Figure 3: Variation of plug core radius with pressure gradient for H-B and Casson fluids and for different values of body acceleration parameter B with $\theta = \delta = 0.1$, $t = 60°$, $\phi = 0.7$, $m = 4$, and $z = 4$.

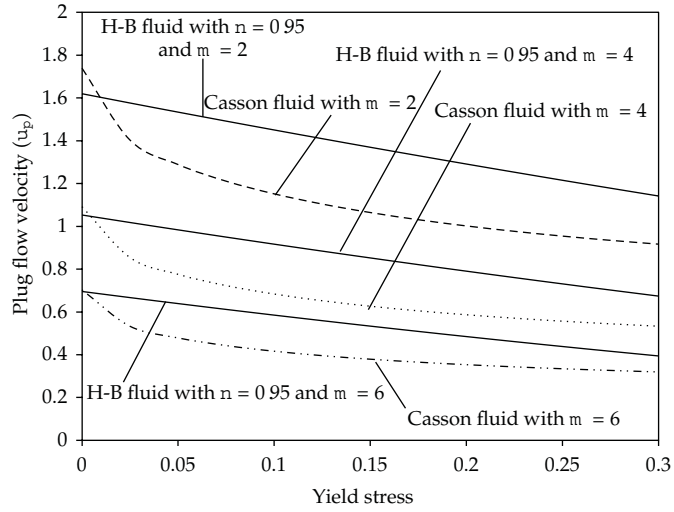

Figure 4: Variation of plug flow velocity with yield stress for H-B and Casson fluid models and for different values of stenosis shape parameter m with $e = 0.5$, $\phi = 0.2$, $t = 60°$, $z = 4$, $\omega = 0.5$, $B = 1$, and $\delta = 0.1$.

3.2. Plug Flow Velocity

Figure 4 shows the variation of the plug flow velocity with yield stress for H-B and Casson fluid models and for different values of the stenosis shape parameter with $e = 0.5$, $\phi = 0.2$, $z = 4$, $t = 60°$, $\omega = 0.5$, $B = 1$, and $\delta = 0.1$. It is noted that for H-B fluid model, the plug flow velocity decreases very slowly with the increase of the yield stress, whereas, in the case of Casson fluid model, it decreases rapidly when the yield stress θ increases from 0 to 0.05 and then it decreases slowly with the increase of the yield stress from 0.05 to 0.3. It is seen that the plug flow velocity is considerably higher for H-B fluid model than that of the Casson fluid model. One can easily observe that the plug flow velocity decreases significantly with the increase of the stenosis shape parameter m. The variation of plug flow velocity with axial

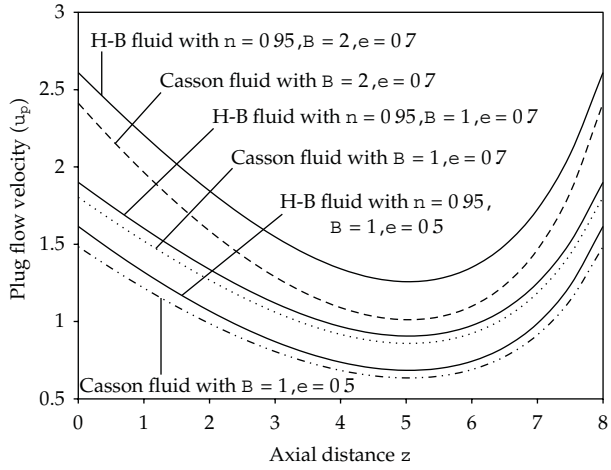

Figure 5: Variation of plug flow velocity with axial distance for H-B and Casson fluids and for different values of B and e with $\delta = \theta = 0.1$, $m = 4$, $t = 60°$, $\phi = 0.2$, and $\omega = 0.5$.

distance for H-B and Casson fluid models and for different values of the body acceleration B and pressure gradient ratio e with $\delta = \theta = 0.1$, $m = 4$, $t = 60°$, $\phi = 0.2$, and $\omega = 0.5$ is depicted in Figure 5. It is seen that the plug flow velocity skews more to the right-hand side in the axial direction which is attributed by the skewness of the stenosis. It is clear that the plug flow velocity increases considerably with the increase of the body acceleration parameter B and pressure gradient ratio e. Figures 4 and 5 show the non-Newtonian character of blood and effects of body acceleration, pressure gradient, and asymmetry of the stenosis on the plug flow velocity of blood when it flows through a constricted artery.

3.3. Velocity Distribution

Figure 6 sketches the velocity distribution for H-B and Casson fluid models and for different values of yield stress θ, stenosis depth δ with $m = 2$, $e = 0.2$, $\alpha_H = \alpha_C = 0.5$, $\phi = 0.2$, $\omega = 1$, $t = 60°$, and $B = 1$. It is observed that the velocity of H-B fluid model is considerably higher than that of Casson fluid model. It is also found that the velocity of the blood flow decreases with the increase of the yield stress θ and stenosis depth δ. But the decrease in the velocity is considerable when the stenosis depth δ increases, whereas it decreases significantly with the increase of the yield stress. It is of interest to note that the velocity distribution of H-B fluid with $\delta = 0.2$ and $\theta = 0.05$ and $B = 0$ is in good agreement with the corresponding plot in Figure 6 of Sankar and Lee [34]. It is also to be noted that the velocity distribution of Casson fluid with $\delta = 0.2$, $\theta = 0.01$, and $B = 0$ is in good agreement with the corresponding plot in Figure 6 of Siddiqui et al. [35].

3.4. Flow Rate

The variation of flow rate with pressure gradient ratio for H-B and Casson fluid models and for different values of the power law index n, body acceleration parameter B, and stenosis shape parameter m with $\theta = \delta = 0.1$, $\alpha_H = \alpha_C = \phi = 0.2$, $z = 4$, $t = 60°$, and $\omega = 1$ is shown

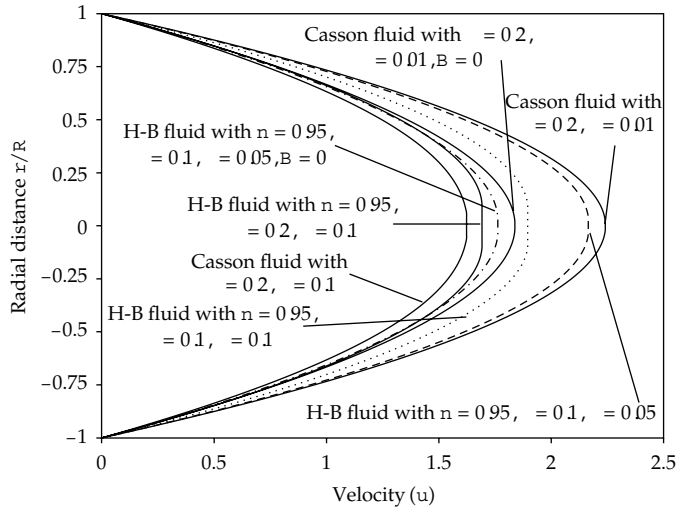

Figure 6: Velocity distribution for different fluid models with $e = 0.2$, $\alpha_H = \alpha_C = 0.5$, $\phi = 0.2$, $\omega = 1$, $t = 60°$, and $B = 1$.

in Figure 7. It is seen that the flow rate increases with the pressure gradient ratio e. But the increase in the flow rate is linear for H-B fluid model and almost constant for Casson fluid model. For a given set of values of the parameters, the flow rate for H-B fluid model is considerably higher than that of the Casson fluid model. It is also clear that for a given set of values of n and m, the flow rate increases considerably with the increase of the body acceleration parameter B. One can observe that for fixed values of n and B, the flow rate decreases significantly with the increase of the stenosis shape parameter m. When the power law index n increases from 0.95 to 1.05 and all the other parameters were held constant, the flow rate decreases slightly when the range of the pressure gradient ratio e is 0–0.5 and this behavior is reversed when the range of the pressure gradient ratio e is 0.5 to 1. Figure 7 brings out the effects of body acceleration and stenosis shape on the flow rate of blood when it flows through narrow artery with mild stenosis.

3.5. Wall Shear Stress

Figure 8 shows the variation of wall shear stress with frequency ratio for H-B and Casson fluid models and for different values of the ϕ (lead angle), α_H (pulsatile Reynolds number for H-B fluid model), and α_C (pulsatile Reynolds number of Casson fluid model) with $m = 2$, $\theta = \delta = 0.1$, $e = 0.5$, $B = 1$, $z = 4$, and $t = 60°$. It is seen that the wall shear stress decreases slightly nonlinearly with frequency ratio for lower values of the pulsatile Reynolds numbers α_H and α_C and lead angle ϕ, and it decreases linearly with frequency ratio for higher values of the pulsatile Reynolds numbers α_H and α_C and lead angle ϕ. It is found that for a given set of values of the parameters, the wall shear stress is marginally lower for H-B fluid model than that of the Casson fluid model. Also, one can note that for fixed value of the lead angle ϕ, the wall shear stress decreases significantly with the increase of the pulsatile Reynolds numbers α_H and α_C. It is also observed that the wall shear stress decreases marginally with the increase of the lead angle ϕ when all the other parameters were kept as invariables. Figure 8 spells out

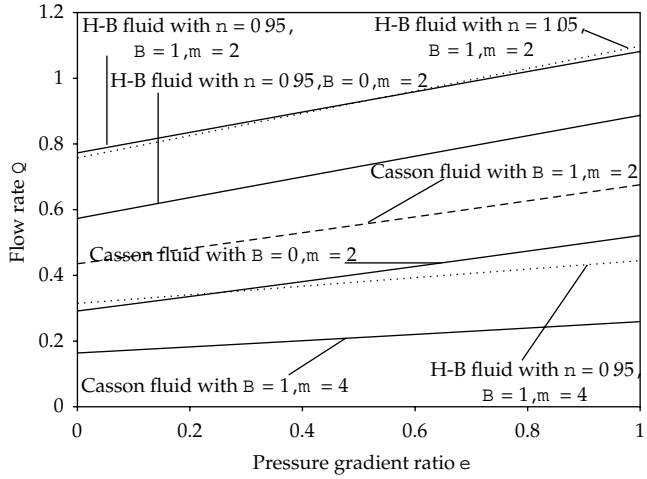

Figure 7: Variation of flow rate with pressure gradient for H-B and Casson fluid models and for different values of B and m with $\theta = \delta = 0.1$, $\alpha_H = \alpha_C = \phi = 0.2$, $z = 4$, $t = 60°$, and $\omega = 1$.

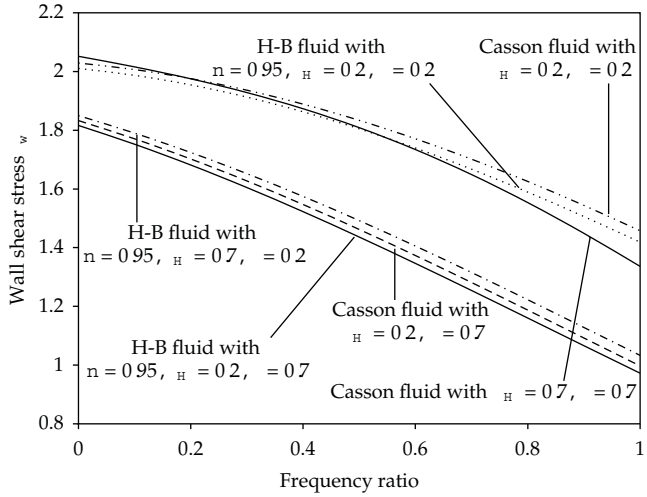

Figure 8: Variation of wall shear stress with frequency ratio for H-B and Casson fluids and for different values of α_H, α_C and ϕ with $\theta = \delta = 0.1$, $m = 2$, $e = 0.5$, $B = 1$, $z = 4$, and $t = 60°$.

the effects of pulsatility and non-Newtonian character of blood on the wall shear stress when it flows in a narrow artery with mild stenosis.

3.6. Longitudinal Impedance to Flow

The variation of the longitudinal impedance to flow with axial distance for different values of the stenosis shape parameter m and body acceleration parameter B with $\theta = \delta = 0.1$, $t = 60°$, $\alpha_H = \alpha_C = \phi = 0.2$, $e = 0.5$, and $\omega = 1$ is depicted in Figures 9(a) (for H-B fluid model) and 9(b) (Casson fluid model). It is noticed that the longitudinal impedance to flow increases with the increase of the axial variable z from 0 to the point where the stenosis depth is maximum

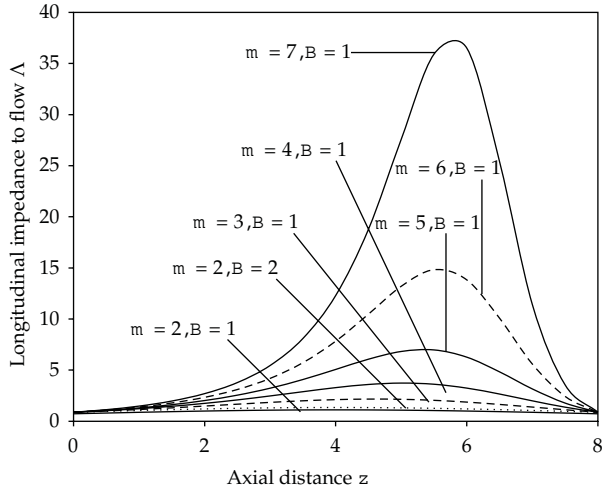

(a) Herschel-Bulkley fluid with $n = 0.95$

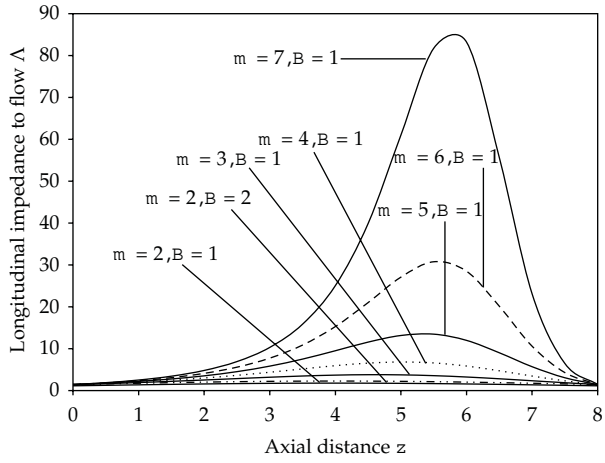

(b) Casson fluid

Figure 9: Variation of longitudinal impedance to flow with axial distance for H-B and Casson fluid models and for different values of m and B with $\theta = \delta = 0.1$, $t = 60°$, $\alpha_H = \alpha_C = \phi = 0.2$, $e = 0.5$, and $\omega = 1$.

and then it decreases as the axial variable z increases further from that point to 8. One can see the significant increase in the longitudinal impedance to flow when the stenosis shape parameter m increases and marginal increase in the longitudinal impedance to flow when the body acceleration parameter B increases. It is also clear that for the same set of values of the parameters, the longitudinal impedance to flow is significantly lower for H-B fluid model than that of the Casson fluid model. Figures 9(a) and 9(b) bring out the effects of body acceleration and asymmetry of the stenosis shape on the longitudinal impedance to blood flow.

The increase in the longitudinal impedance to blood flow due to the asymmetry shape of the stenosis is defined as the ratio between the longitudinal impedance to flow of a fluid model for a given set of values of the parameters in an artery with asymmetric stenosis and the longitudinal impedance of the same fluid model and for the same set of values

Table 1: Estimates of the increase in the longitudinal impedance to flow due to the increase in the stenosis shape parameter and body acceleration with $\delta = \theta = 0.1$, $e = 0.5$, $\omega = 1$, $\alpha_H = \alpha_C = \phi = 0.2$, $z = 4$, and $t = 60°$.

m	H-B fluid model			Casson fluid model		
	$B = 0$	$B = 1$	$B = 2$	$B = 0$	$B = 1$	$B = 2$
3	1.5759	1.5698	1.5657	1.6401	1.6282	1.6202
4	2.4616	2.4419	2.4289	2.6690	2.6289	2.6022
5	3.8118	3.7642	3.7331	4.3105	4.2098	4.1433
6	5.9191	5.8153	5.7484	6.9964	6.7688	6.6201
7	9.3531	9.1338	8.9944	11.6016	11.1022	10.7803

Table 2: Physiological data for different arteries.

S. no.	Artery	Radius ($\times 10^{-2}$ m)	A_0 ($\times 10$ Kg m^{-2} s^{-1})	A_1 ($\times 10$ Kg m^{-2} s^{-1})
1	Aorta	1.0	7.3	1.46
2	Femoral	0.5	32.0	6.4
3	Carotid	0.4	50.0	10.0
4	Coronary	0.15	698.65	139.74
5	Arteriole	0.008	2000.0	400

of the parameters in that artery with axisymmetric stenosis. The estimates of the increase in the longitudinal impedance to flow are computed in Table 1 for different values of the stenosis shape parameter m and body acceleration parameter B with $\delta = \theta = 0.1$, $e = 0.5$, $\omega = 1$, $z = 4$, $\alpha_H = \alpha_C = \phi = 0.2$, and $t = 60°$. It is observed that the estimates of the increase in the longitudinal impedance to flow increase considerably when the stenosis shape parameter m increases and they decrease slightly when the body acceleration parameter B increases. Hence, the longitudinal impedance to flow is significantly higher in the arteries with asymmetric shape of the stenosis compared to that in the arteries with axisymmetric stenosis. It is also noted that the presence of the body acceleration decreases the longitudinal impedance to blood flow considerably.

3.7. Some Possible Clinical Applications

To discuss some possible clinical applications of the present study, the data (for different types of arteries, their corresponding radii, steady and pulsatile pressure gradient values) reported by Chaturani and Wassf Issac [23] are given in Table 2 and are used in this applications part of our study. For these clinical data (given in Table 2), the estimates of the mean velocity of H-B and Casson fluid models for different values of the stenosis shape parameter m and different values of the body acceleration parameter B with $\theta = \delta = 0.1$, $t = 60°$, $\omega = 1$, $z = 4$, $\phi = 0.2$, $\alpha_H = \alpha_C = 0.2$, and $e = 0.2$ are computed in Table 3. It is recorded that the estimates of the mean velocity increase significantly with the increase of the artery radius, except in arterioles. It is also found that the estimates of the mean velocity of H-B fluid model are marginally higher than those of the Casson fluid model. It is noted that the mean velocity increases considerably with the increase of the body acceleration parameter B and the reverse behavior is found when the stenosis shape parameter m increases.

For the clinical data given in Table 2, the estimates of the mean flow rate of H-B and Casson fluid models are computed in Table 4 for different values of the stenosis shape parameter m and different values of the body acceleration parameter B with $\theta = \delta = 0.1$, ω

Table 3: Estimates of mean velocity of H-B and Casson fluid models for different values of m and B in arteries with different radii with $\theta = \delta = 0.1$, $t = 60°$, $\omega = 1$, $z = 4$, $e = 0.2$, and $\alpha_H = \alpha_C = \phi = 0.2$.

S. no.	Artery type	H-B fluid model ($\times 10^{-2}$ m s^{-1})				Casson fluid model ($\times 10^{-2}$ m s^{-1})			
		$m = 2$		$m = 4$		$m = 2$		$m = 4$	
		$B = 0$	$B = 1$	$B = 0$	$B = 1$	$B = 0$	$B = 1$	$B = 0$	$B = 1$
1	Aorta	40.28	46.25	36.35	41.82	37.46	42.89	33.18	37.88
2	Femoral	46.78	52.38	40.22	45.41	42.55	49.67	37.69	42.47
3	Carotid	46.78	52.38	40.22	45.41	42.55	49.67	37.69	42.47
4	Coronary	93.85	97.55	89.45	93.48	89.24	94.38	86.12	90.59
5	Arteriole	0.62	0.75	0.55	0.68	0.57	0.69	0.51	0.63

Table 4: Estimates of mean flow rate of H-B and Casson fluid models for different values of m and B in arteries with different radii with $\theta = \delta = 0.1$, $t = 60°$, $\omega = 1$, $z = 4$, $e = 0.2$, and $\alpha_H = \alpha_C = \phi = 0.2$.

S. no.	Artery type	H-B fluid model ($\times 10^{-2}$ m s^{-1})				Casson fluid model ($\times 10^{-2}$ m s^{-1})			
		$m = 2$		$m = 4$		$m = 2$		$m = 4$	
		$B = 0$	$B = 1$	$B = 0$	$B = 1$	$B = 0$	$B = 1$	$B = 0$	$B = 1$
1	Aorta	65.43	72.54	61.42	68.72	61.49	66.58	55.24	62.66
2	Femoral	14.87	20.38	12.66	17.41	11.57	16.93	10.41	15.28
3	Carotid	9.56	13.15	8.43	11.85	7.94	11.27	6.25	9.49
4	Coronary	3.12	3.55	2.85	3.25	2.75	3.15	2.37	2.84
5	Arteriole	70.8E−6	82.5E−6	67.3E−6	74.6E−6	65.8E−6	75.61	61.8E−6	69.7E−6

$= 1$, $t = 60°$, $z = 4$, $\phi = 0.2$, $\alpha_H = \alpha_C = 0.2$, and $e = 0.2$. It is observed that the estimates of the mean flow rate decrease very significantly with the increase of the artery radius. It is also found that the estimates of the mean flow rate of H-B fluid model are considerably higher than those of the Casson fluid model. It is noted that the estimates of the mean flow rate increase significantly with the increase of the body acceleration parameter B and the reverse behavior is recorded when the stenosis shape parameter m increases.

4. Conclusions

The present mathematical analysis brings out various interesting rheological properties of blood when it flows through narrow stenosed arteries with body acceleration, treating it as different non-Newtonian fluid models with yield stress such as (i) Herschel-Bulkley fluid model and (ii) Casson fluid model. By the use of appropriate mathematical expression for the geometry of segment of the stenosed artery, both axisymmetric and asymmetric shapes of stenoses are considered to study the effects of stenosis shape and size on the physiologically important quantities. Some major findings of this mathematical analysis are summarized below.

(i) The plug core radius, wall shear stress, and longitudinal impedance to flow are marginally lower for H-B fluid model than those of the Casson fluid model.

(ii) The plug flow velocity, velocity distribution, and flow rate are considerably higher for H-B fluid model than those of the Casson fluid model.

(iii) The plug core radius and longitudinal impedance to flow increase significantly with the increase of the stenosis shape parameter, and the reverse behavior is observed for plug flow velocity, velocity distribution, and flow rate.

(iv) The estimates of the mean velocity and mean flow rate are considerably higher for H-B fluid model than those of the Casson fluid model.

(v) The estimates of the mean velocity and mean flow rate increase considerably with the increase of the body acceleration, and this behavior is reversed when the stenosis shape parameter increases.

Based on these results, one can note that there is substantial difference between the flow quantities of H-B fluid model and Casson fluid model, and thus it is expected that the use of H-B fluid model for blood flow in diseased artery may provide better results which may be useful to physicians in predicting the effects of body accelerations and different shapes and sizes of stenosis in the artery on the physiologically important flow quantities. Also, it is hoped that this study may provide some useful information to surgeons to take some crucial decisions regarding the treatment of patients, whether the cardiovascular disease can be treated with medicines or should the patient undergo a surgery. Hence, it is concluded that the present study can be treated as an improvement in the mathematical modeling of blood flow in narrow arteries with mild stenosis under the influence of periodic body accelerations.

Nomenclature

$\bar{r}$: Radial distance
r: Dimensionless radial distance
$\bar{z}$: Axial distance
z: Dimensionless axial distance
n: Power law index
$\bar{p}$: Pressure
p: Dimensionless pressure
P: Dimensionless pressure gradient
$\overline{Q}$: Flow rate
Q: Dimensionless flow rate
$\overline{R}_0$: Radius of the normal artery
$\overline{R}(\bar{z})$: Radius of the artery in the stenosed region
$R(z)$: Dimensionless radius of the artery in the stenosed region
$F(\bar{t})$: Body acceleration function
a_0: Amplitude of the body acceleration
$\overline{R}_P$: Plug core radius
R_P: Dimensionless plug core radius
$\overline{u}_H$: Axial velocity of Herschel-Bulkley fluid
u_H: Dimensionless axial velocity of Herschel-Bulkley fluid
$\overline{u}_C$: Axial velocity of Casson fluid
u_C: Dimensionless axial velocity of Casson fluid
$\overline{A}_0$: Steady component of the pressure gradient
$\overline{A}_1$: Amplitude of the pulsatile component of the pressure gradient

$\overline{L}$: Length of the normal artery
$\overline{L}_0$: Length of the stenosis
m: Stenosis shape parameter
L_0: Dimensionless length of the stenosis
$\overline{d}$: Location of the stenosis
d: Dimensionless location of the stenosis
$\overline{t}$: Time
t: Dimensionless time.

Greek Letters

Λ: Dimensionless longitudinal impedance to flow
ϕ: Azimuthal angle
$\dot{\gamma}$: Shear rate
$\overline{\tau}_y$: Yield stress
θ: Dimensionless yield stress
$\overline{\tau}_H$: Shear stress of the Herschel-Bulkley fluid
τ_H: Dimensionless shear stress of Herschel-Bulkley fluid
$\overline{\tau}_C$: Shear stress for Casson fluid
τ_C: Dimensionless shear stress of Casson fluid
τ_w: Dimensionless wall shear stress
$\overline{\rho}_H$: Density of Herschel-Bulkley fluid
$\overline{\rho}_C$: Density of Casson fluid
$\overline{\mu}_H$: Viscosity of Herschel-Bulkley fluid
$\overline{\mu}_C$: Viscosity of the Casson fluid
α_H: Pulsatile Reynolds number of Herschel-Bulkley fluid
α_C: Pulsatile Reynolds number of Casson fluid
$\overline{\delta}$: Depth of the stenosis
δ: Dimensionless depth of the stenosis
$\overline{\omega}$: Angular frequency of the blood flow
ϕ: Lead angle.

Subscripts

w: Wall shear stress (used for τ)
H: Herschel-Bulkley fluid (used for $\overline{u}, u, \overline{\tau}, \tau$)
C: Newtonian fluid (used for $\overline{u}, u, \overline{\tau}, \tau$).

Acknowledgments

This research work was supported by the Research University Grant of Universiti Sains Malaysia, Malaysia (RU Grant ref. no. 1001/PMATHS/811177). The authors thank the reviewers for their valuable comments which helped to improve the technical quality of this research article.

References

[1] S. Cavalcanti, "Hemodynamics of an artery with mild stenosis," *Journal of Biomechanics*, vol. 28, no. 4, pp. 387–399, 1995.

[2] M. E. Clark, J. M. Robertson, and L. C. Cheng, "Stenosis severity effects for unbalanced simple-pulsatile bifurcation flow," *Journal of Biomechanics*, vol. 16, no. 11, pp. 895–906, 1983.

[3] D. Liepsch, M. Singh, and M. Lee, "Experimental analysis of the influence of stenotic geometry on steady flow," *Biorheology*, vol. 29, no. 4, pp. 419–431, 1992.

[4] G. T. Liu, X. J. Wang, B. Q. Ai, and L. G. Liu, "Numerical study of pulsating flow through a tapered artery with stenosis," *Chinese Journal of Physics*, vol. 42, no. 4 I, pp. 401–409, 2004.

[5] P. R. Johnston and D. Kilpatrick, "Mathematical modelling of flow through an irregular arterial stenosis," *Journal of Biomechanics*, vol. 24, no. 11, pp. 1069–1077, 1991.

[6] K. C. Ang and J. Mazumdar, "Mathematical modelling of triple arterial stenoses," *Australasian Physical and Engineering Sciences in Medicine*, vol. 18, no. 2, pp. 89–94, 1995.

[7] D. Kilpatrick, S. D. Webber, and J. P. Colle, "The vascular resistance of arterial stenoses in series," *Angiology*, vol. 41, no. 4, pp. 278–285, 1990.

[8] P. Chaturani and R. P. Samy, "Pulsatile flow of Casson's fluid through stenosed arteries with applications to blood flow," *Biorheology*, vol. 23, no. 5, pp. 499–511, 1986.

[9] D. S. Sankar and K. Hemalatha, "Pulsatile flow of Herschel-Bulkley fluid through stenosed arteries-A mathematical model," *International Journal of Non-Linear Mechanics*, vol. 41, no. 8, pp. 979–990, 2006.

[10] J. C. Misra and B. Pal, "A mathematical model for the study of the pulsatile flow of blood under an externally imposed body acceleration," *Mathematical and Computer Modelling*, vol. 29, no. 1, pp. 89–106, 1999.

[11] S. Chakravarty and P. K. Mandal, "Two-dimensional blood flow through tapered arteries under stenotic conditions," *International Journal of Non-Linear Mechanics*, vol. 35, no. 5, pp. 779–793, 2000.

[12] V. K. Sud and G. S. Sekhon, "Arterial flow under periodic body acceleration," *Bulletin of Mathematical Biology*, vol. 47, no. 1, pp. 35–52, 1985.

[13] R. Usha and K. Prema, "Pulsatile flow of particle-fluid suspension model of blood under periodic body acceleration," *Zeitschrift fur Angewandte Mathematik und Physik*, vol. 50, no. 2, pp. 175–192, 1999.

[14] P. K. Mandal, S. Chakravarty, A. Mandal, and N. Amin, "Effect of body acceleration on unsteady pulsatile flow of non-newtonian fluid through a stenosed artery," *Applied Mathematics and Computation*, vol. 189, no. 1, pp. 766–779, 2007.

[15] N. Mustapha, S. Chakravarty, P. K. Mandal, and N. Amin, "Unsteady response of blood flow through a couple of irregular arterial constrictions to body acceleration," *Journal of Mechanics in Medicine and Biology*, vol. 8, no. 3, pp. 395–420, 2008.

[16] M. El-Shahed, "Pulsatile flow of blood through a stenosed porous medium under periodic body acceleration," *Applied Mathematics and Computation*, vol. 138, no. 2-3, pp. 479–488, 2003.

[17] V. P. Rathod, S. Tanveer, I. S. Rani, and G. G. Rajput, "Pulsatile flow of blood under periodic body acceleration and magnetic field through an exponentially diverging vessel," *Proceedings National Conference Advanced, Fluid Dynamics*, pp. 106–117, 2004.

[18] S. Chakravarty and A. K. Sannigrahi, "An analytical estimate of the flow-field in a porous stenotic artery subject to body acceleration," *International Journal of Engineering Science*, vol. 36, no. 10, pp. 1083–1102, 1998.

[19] P. Chaturani and V. Palanisamy, "Pulsatile flow of blood with periodic body acceleration," *International Journal of Engineering Science*, vol. 29, no. 1, pp. 113–121, 1991.

[20] S. N. Majhi and V. R. Nair, "Pulsatile flow of third grade fluids under body acceleration-Modelling blood flow," *International Journal of Engineering Science*, vol. 32, no. 5, pp. 839–846, 1994.

[21] C. Tu and M. Deville, "Pulsatile flow of Non-Newtonian fluids through arterial stenoses," *Journal of Biomechanics*, vol. 29, no. 7, pp. 899–908, 1996.

[22] D. S. Sankar and K. Hemalatha, "Pulsatile flow of Herschel-Bulkley fluid through catheterized arteries—a mathematical model," *Applied Mathematical Modelling*, vol. 31, no. 8, pp. 1497–1517, 2007.

[23] P. Chaturani and A. S. A. Wassf Isaac, "Blood flow with body acceleration forces," *International Journal of Engineering Science*, vol. 33, no. 12, pp. 1807–1820, 1995.

[24] G. Sarojamma and P. Nagarani, "Pulsatile flow of Casson fluid in a homogenous porous medium subject to external acceleration," *International Journal of Non-Linear Di erential Equations*, vol. 7, pp. 50–64, 2002.

[25] P. Chaturani and V. Palanisamy, "Casson fluid model for pulsatile flow of blood under periodic body acceleration," *Biorheology*, vol. 27, no. 5, pp. 619–630, 1990.

[26] P. Chaturani and V. Palanisamy, "Pulsatile flow of power-law fluid model for blood flow under periodic body acceleration," *Biorheology*, vol. 27, no. 5, pp. 747–758, 1990.

[27] S. Chakravarty and P. K. Mandal, "A nonlinear two-dimensional model of blood flow in an overlapping arterial stenosis subjected to body acceleration," *Mathematical and Computer Modelling*, vol. 24, no. 1, pp. 43–58, 1996.

[28] Y. C. Fung, *Biomechanics: Mechanical Properties of Living Tissues*, Springer, Berlin, Germany, 1981.

[29] J. N. Kapur, *Mathematical Models in Biology and Medicine*, Affiliated East-West Press Pvt. Ltd., New Delhi, India, 1992.

[30] N. Iida, "Influence of plasma layer on steady blood flow in micro vessels," *Japanese Journal of Applied Physics*, vol. 17, pp. 203–214, 1978.

[31] D. S. Sankar and K. Hemalatha, "A non-Newtonian fluid flow model for blood flow through a catheterized artery-Steady flow," *Applied Mathematical Modelling*, vol. 31, no. 9, pp. 1847–1864, 2007.

[32] D. S. Sankar and A. I. M. Ismail, "Effect of periodic body acceleration in blood flow through stenosed arteries—a theoretical model," *International Journal of Nonlinear Sciences and Numerical Simulation*, vol. 11, no. 4, pp. 243–257, 2010.

[33] P. Nagarani and G. Sarojamma, "Effect of body acceleration on pulsatile flow of casson fluid through a mild stenosed artery," *Korea Australia Rheology Journal*, vol. 20, no. 4, pp. 189–196, 2008.

[34] D. S. Sankar and U. Lee, "Mathematical modeling of pulsatile flow of non-Newtonian fluid in stenosed arteries," *Communications in Nonlinear Science and Numerical Simulation*, vol. 14, no. 7, pp. 2971–2981, 2009.

[35] S. U. Siddiqui, N. K. Verma, S. Mishra, and R. S. Gupta, "Mathematical modelling of pulsatile flow of Casson's fluid in arterial stenosis," *Applied Mathematics and Computation*, vol. 210, no. 1, pp. 1–10, 2009.

Hindawi Publishing Corporation
Journal of Applied Mathematics
Volume 2012, Article ID 750939, 14 pages
doi:10.1155/2012/750939

Research Article

Thermal Diffusion and Diffusion Thermo Effects on MHD Thermosolutal Marangoni Convection Boundary Layer Flow over a Permeable Surface

R. A. Hamid,[1] W. M. K. A. Wan Zaimi,[1] N. M. Arifin,[2] N. A. A. Bakar,[1] and B. Bidin[1]

[1] *Institute of Engineering Mathematics, Universiti Malaysia Perlis, Taman Bukit Kubu Jaya, Jalan Sarawak, 02000 Kuala Perlis, Malaysia*
[2] *Institute for Mathematical Research and Department of Mathematics, Universiti Putra Malaysia, 43400 Serdang, Malaysia*

Correspondence should be addressed to R. A. Hamid, rohanahamid@unimap.edu.my

Received 6 January 2012; Revised 1 March 2012; Accepted 15 March 2012

Academic Editor: Hiroshi Kanayama

The problem of thermal diffusion and diffusion thermo effects on thermosolutal Marangoni convection flow of an electrically conducting fluid over a permeable surface is investigated. Using appropriate similarity transformations, the governing system of partial differential equation is transformed to a set of nonlinear ordinary differential equations, then solved numerically using the Runge-Kutta-Fehlberg method. The effects of thermal diffusion and diffusion thermo, magnetic field parameter, thermosolutal surface tension ratio, and suction/injection parameter on the flow field, heat transfer characteristic, and concentration are thoroughly examined. Numerical results are obtained for temperature and concentration profiles as well as the local Nusselt and Sherwood numbers are presented graphically and analyzed. It is found that these governing parameters affect the variations of the temperature and concentration and also the local Nusselt and Sherwood numbers.

1. Introduction

The study of Marangoni convection has received great consideration in recent years in view of its application in industries. Marangoni convection is predictable to be very useful in wide area especially in crystal growth melts and semiconductor processing. The Marangoni boundary layer term was first initiated by Napolitano [1, 2] when studied the existence of the steady dissipative layers which occur along the liquid-liquid or liquid-gas interfaces. Marangoni convection induced by the surface tension gradient can be due to

gradients of temperature (thermal convection) and/or concentration (solutal convection). A lot of analyses in Marangoni convection have been discovered in various geometries and conditions. Some of experimental works linked to Marangoni convection were discussed in several papers by Arafune and Hirata [3], Arafune et al. [4], Galazka and Wilke [5], Neumann et al. [6], Arendt and Eggers [7], and Xu et al. [8].

The related works to this present study were done by Al-Mudhaf and Chamkha [9] who obtained the similarity solution for MHD thermosolutal Marangoni convection over a flat surface in the presence of heat generation or absorption with fluid suction and injection. Christopher and Wang [10] have analyzed the effects of Prandtl number on Marangoni convection flow over a flat surface. Later, Pop et al. [11] studied numerically the problem of thermosolutal Marangoni forced convection over a permeable surface and this study continued by Hamid et al. [12] who obtained dual solutions of the problem. Chen [13] investigated the flow and the heat transfer characteristics on the forced convection in a power law liquid film under an applied Marangoni convection over a stretching sheet. Magyari and Chamkha [14] found solution for steady MHD thermosolutal Marangoni convection and present analytical solutions for velocity, temperature, and concentration field. Arifin et al. [15] added new dimension to the Marangoni convection problem by considering the steady thermosolutal marangoni mixed convection boundary layer flow under an external pressure gradient. The problem is solved using the shooting method. Most lately, Hamid et al. [16] studied the two-dimensional Marangoni convection flow past a flat plate in the presence of thermal radiation, suction, and injection effects.

Several papers that deal with flows in the presence Dufour or diffusion thermo effect and Soret or thermal diffusion effect are now presented. A brief literature on existence and development of Dufuor and Soret effects can be found in the papers by Kafoussias and Williams [17] and Puvi Arasu et al. [18]. Puvi Arasu et al. [18] investigated the impact of thermophoresis particles deposition on two-dimensional flow over a vertical stretching surface in the presence of chemical reaction and also Dufour and Soret effects taking place in the flow. The temperature gradients and concentration gradients play vital role in producing Dufour and Soret effects. The concentration gradient has generated the heat flux, namely, Dufour effect while mass flux is created by temperature gradients and is known as Soret effects. It is seem that the Charles Soret in 1879 is the first who found that a salt solution contained in a tube with two ends did not remain uniform in composition at different temperature. By this pioneering discovering, the term "Soret effect" officially introduced regarded his contribution on study of this particular effect. Later, the fundamental study on Soret effects remarkably grow over century (Osalusi et al. [19]).

The effects of thermal diffusion and diffusion thermo have been studied widely by several researchers due to its importance contribution in theory and practical. Some numerical studies on thermal diffusion and diffusion thermo effects include Afify [20] who studied the effects of thermal diffusion and diffusion thermo with suction and injection parameter on MHD free convection heat and mass transfer past a stretching sheet. Kafoussias and Williams [17] considered the mixed forced convection boundary layer flow with the effects of thermal diffusion and diffusion thermo in the presence of variable viscosity effect. This similar work continued by Eldabe et al. [21] for non-Newtonian power law fluid with the temperature dependent viscosity in the flow. Later, El-Aziz [22] considered the MHD three-dimensional free convection boundary layer flows past a stretching sheet with suction or injection and radiation in presence of Dufour and Soret effects. Next, Osalusi et al. [19] numerically studied the effects of thermal diffusion and diffusion thermo on combined heat and mass transfer of MHD convective and slip flow due to a rotating disk

with the inclusion of viscous dissipation and Ohmic heating while Rashidi et al. [23] found its analytical solution using the homotopy analysis method (HAM). Most recently, Hayat et al. [24] obtained the series solutions for MHD two-dimensional axisymmetric flow of a second grade fluid with the existence of thermal diffusion and diffusion thermo effects, Joule heating and the chemical reaction effects.

The aim of this paper is to discuss the MHD thermosolutal Marangoni convection boundary layer over a permeable flat surface considering the effects of the thermal diffusion and diffusion thermo. The set of governing equations and boundary equation of the problem that are transformed into a set of nonlinear ordinary differential equation with assisting of similarity transformations are solved using the Runge-Kutta-Fehlberg method. The effects of different physical parameters on the temperature and concentration profiles as well as the local Nusselt and Sherwood numbers are presented. To verify the obtained results, we have compared the present numerical results with previous work by Al-Mudhaf and Chamkha [9]. The comparison results show a good agreement and we are confident that our present numerical results are accurate.

2. Mathematical Formulation

We consider the laminar boundary layer flow of an electrically conducting fluid over a permeable flat surface in the presence of Dufour and Soret effects. It is assumed that the mass flux velocity is v_w with $v_w < 0$ for suction and $v_w > 0$ for injection, respectively. It is also assumed that a uniform magnetic field, B_0 is imposed in the direction normal to the surface. Then, the basic governing equation of the proposed problem (see Al-Mudhaf and Chamkha [9] and Afify [20]):

$$\begin{aligned}
\frac{\partial u}{\partial x} + \frac{\partial v}{\partial y} &= 0,\\
u\frac{\partial u}{\partial x} + v\frac{\partial u}{\partial y} &= \nu\frac{\partial^2 u}{\partial y^2} - \frac{\sigma^* B_0^2}{\rho}u,\\
u\frac{\partial T}{\partial x} + v\frac{\partial T}{\partial y} &= \alpha\frac{\partial^2 T}{\partial y^2} + \frac{D_m k_T}{c_s c_p}\frac{\partial^2 h}{\partial y^2},\\
u\frac{\partial h}{\partial x} + v\frac{\partial h}{\partial y} &= D_m\frac{\partial^2 h}{\partial y^2} + \frac{D_m k_T}{T_m}\frac{\partial^2 T}{\partial y^2}.
\end{aligned} \tag{2.1}$$

The surface tension σ is assumed to vary linearly with the temperature T and concentration h as well as the wall temperature T_w and concentration h_w are presumed to be in quadratic functions of x. Hence, the boundary conditions of (2.1) is (see Al-Mudhaf and Chamkha [9])

$$u = 0, \quad v = v_w, \quad T = T_\infty + Ax^2, \quad h = h_\infty + A^* x^2, \quad \mu\frac{\partial u}{\partial y} = \sigma_T\frac{\partial T}{\partial x} + \sigma_h\frac{\partial h}{\partial x} \text{ on } y = 0, \tag{2.2}$$

$$u \longrightarrow 0,\ T \longrightarrow T_\infty,\ h \longrightarrow h_\infty \text{ as } y \longrightarrow \infty, \tag{2.3}$$

where u, v are the components of velocity, respectively, in the x and y directions, ν is the kinematic viscosity, σ^* is the fluid electrical conductivity, ρ is the fluid density, and α is the thermal diffusivity. Besides, D_m, k_T, c_s, c_p, and T_m are the diffusion coefficient, thermal-diffusion ratio, concentration susceptibility, specific heat at constant pressure, and mean fluid temperature, respectively (see Puvi Arasu et al. [18]). Moreover, μ is the dynamic viscosity, σ_T and σ_h are the rates of change of surface tension with temperature and solutal concentration while A and A^* are the temperature and concentration gradient coefficients, respectively.

The surface tension is defined as follow:

$$\sigma = \sigma_0\ 1 - \gamma_T(T - T_\infty) - \gamma_h(h - h_\infty)\ , \tag{2.4}$$

where

$$\gamma_T = -\frac{\partial\sigma}{\partial T}, \quad \gamma_h = -\frac{\partial\sigma}{\partial h}. \tag{2.5}$$

In order to find the similarity solutions of (2.1) subject to boundary conditions (2.2)-(2.3), we introduced the similarity variables (see Al-Mudhaf and Chamkha [9])

$$\eta = C_1 y, \quad f\ \eta\ = \frac{C_2\psi\ x, y}{x}, \quad \theta\ \eta\ = \frac{(T - T_\infty)}{Ax^2}, \quad H\ \eta\ = \frac{(h - h_\infty)}{A^* x^2}, \tag{2.6}$$

and $\psi(x, y)$ is the stream function defined in usual way as $u = \partial\psi/\partial y$ and $v = -\partial\psi/\partial x$ where

$$C_1 = \sqrt[3]{\frac{\rho A(d\sigma/dT)_h}{\mu^2}}, \quad C_2 = \sqrt[3]{\frac{\rho^2}{\mu A(d\sigma/dT)_h}}, \tag{2.7}$$

are the two similarity transformation coefficients.

Substituting (2.6)-(2.7) into (2.1), we obtained the following nonlinear ordinary differential equations:

$$f''' + ff'' - f'^2 - M^2 f' = 0, \tag{2.8}$$

$$\frac{1}{Pr}\theta'' + f\theta' - 2f'\theta + D_f H'' = 0, \tag{2.9}$$

$$\frac{1}{Sc}H'' + fH' - 2f'H + S_r\theta'' = 0, \tag{2.10}$$

where a prime denotes a differentiation with respect to η, $D_f = D_m k_T(h_w - h_\infty)/c_s c_p \nu(T_w - T_\infty)$ and $S_r = D_m k_T(T_w - T_\infty)/T_m \nu(h_w - h_\infty)$ are the Dufour and Soret numbers, respectively. Here, M is the magnetic field parameter, Pr is the Prandtl number, and Sc is the Schmidt number.

It is important to mention that f is the stream function similarity variable, θ and H are the nondimensional temperature and concentration, respectively. The boundary conditions (2.2)-(2.3) are reduced to

$$\begin{gathered} f(0) = f_0, \quad f''(0) = -2(1+r), \quad \theta(0) = 1, \quad H(0) = 1, \\ f'(\infty) = 0, \quad \theta(\infty) = 0, \quad H(\infty) = 0, \end{gathered} \tag{2.11}$$

where $r = \Delta h(d\sigma/dh)|_T / \Delta T(d\sigma/dT)|_h$ is the thermosolutal surface tension ratio.

The local Nusselt and Sherwood numbers are given by (see Al-Mudhaf and Chamkha [9])

$$\begin{aligned} Nu_x &= \frac{q''(x)x}{\lambda(T_w - T_\infty)} = -C_1 x\theta'(0), \\ Sh_x &= \frac{h''(x)x}{D(T_w - T_\infty)} = -C_1 xH'(0), \end{aligned} \tag{2.12}$$

where D is the mass diffusivity, q'' is the heat flux, and h'' is the mass flux.

3. Results and Discussion

Numerical solutions of the ordinary differential equations (2.8)–(2.10) that subject to boundary conditions (2.11) have been solved using the Runge-Kutta-Fehlberg fourth-fifth order (RKF45) method using Maple 12 and the algorithm RKF45 in Maple has been well tested for its accuracy and robustness (Aziz [25]). In this method, it is most important to choose the appropriate finite value of the edge of boundary layer, $\eta \to \infty$ (say η_∞) that is between 4 to 10, which is in accordance with the standard practice in the boundary layer analysis. The influences of the magnetic field parameter (M), the suction/injection parameter (f_0), the thermosolutal surface tension ratio (r), the combined Dufour number D_f and Soret number S_r on the velocity, temperature and concentration, and the Nusselt and Sherwood numbers are presented in tables and some graphs. These findings are summarized and presented in the Tables 1–4 and Figures 1–9. We have compared the present results with the results attained by Al-Mudhaf and Chamkha [9] when the heat generation/absorption and first-order chemical reaction effects are neglected. It is seen that the results presented in Tables 1–3 are in very well agreement. Hence, this leads the confidence of the present results. It should be mentioned that $f'(0)$, $-\theta'(0)$ and $-H'(0)$ are related to the surface velocity, Nusselt number, and Sherwood numbers, respectively.

Figures 1, 2, and 3 display the velocity, temperature, and concentration profiles for different values of magnetic field parameter M when the other parameters are fixed. An application of a magnetic field within boundary layer has produced resistive-type force which known as Lorentz force. This force acts to retard the fluid motion along surface and

Table 1: Comparison values of $f'(0)$, $-\theta'(0)$ and $-H'(0)$ with different parameter M.

M	$f'(0)$		$-\theta'(0)$		$-H'(0)$	
	Al-Mudhaf and Chamkha [9]	Present	Al-Mudhaf and Chamkha [9]	Present	Al-Mudhaf and Chamkha [9]	Present
0	1.587671	1.587401	1.442203	1.442069	1.220880	1.220731
1	1.315181	1.314596	1.206468	1.205891	1.005541	1.005808
2	0.903945	0.9032119	0.7596045	0.7625145	0.6106418	0.6188354
3	0.6448883	0.6440222	0.4422402	0.4625877	0.3473967	0.37638077
4	0.4933589	0.4924782	0.2728471	0.3114736	0.2127706	0.25873328

Table 2: Comparison values of $f'(0)$, $-\theta'(0)$ and $-H'(0)$ with different parameter f_0.

f_0	$f'(0)$		$-\theta'(0)$		$-H'(0)$	
	Al-Mudhaf and Chamkha [9]	Present	Al-Mudhaf and Chamkha [9]	Present	Al-Mudhaf and Chamkha [9]	Present
−2	2.383451	2.382975	1.251341	1.250618	1.129218	1.128784
−1	2.000379	1.999999	1.336441	1.335853	1.173002	1.173006
0	1.587671	1.58740104	1.442203	1.442067	1.220880	1.220715
1	1.179708	1.17950902	1.634990	1.634360	1.328699	1.327979
2	0.8480268	0.8477075	2.020949	2.019468	1.593570	1.592596

Table 3: Comparison values of $f'(0)$, $-\theta'(0)$ and $-H'(0)$ with different parameter r.

r	$f'(0)$		$-\theta'(0)$		$-H'(0)$	
	Al-Mudhaf and Chamkha [9]	Present (2011)	Al-Mudhaf and Chamkha [9]	Present (2011)	Al-Mudhaf and Chamkha [9]	Present (2011)
0	1.587582	1.587297	1.442247	1.442412	1.220880	1.222427
1	2.520988	2.519819	1.817826	1.816999	1.538960	1.538688
5	5.244303	5.241482	2.621562	2.620417	2.219093	2.218261

Table 4: The values of $-\theta'(0)$ and $-H'(0)$ with different parameters D_f and S_r.

D_f	S_r	$-\theta'(0)$	$-H'(0)$
0.03	2.0	1.624748	−0.00587659
0.06	1.0	1.603973	0.6866464
0.15	0.4	1.541646	1.102160
0.3	0.2	1.437767	1.240664
0.6	0.1	1.230011	1.309917
2.0	0.03	0.260478	1.358394

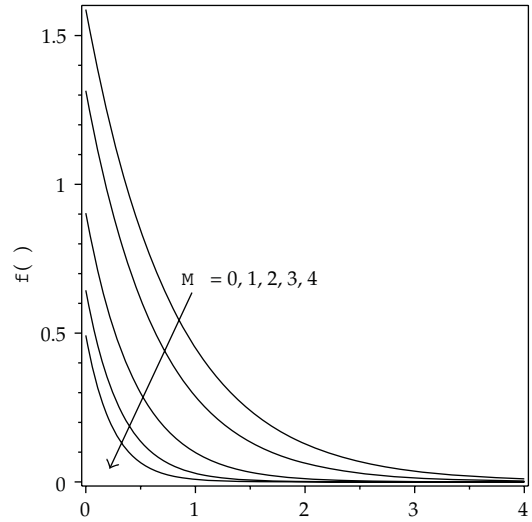

Figure 1: Velocity profiles for different values of M when $Pr = 0.78$, $Sc = 0.6$, $D_f = 0.03$, $S_r = 2$,$r = 0$, and $f_0 = 0$.

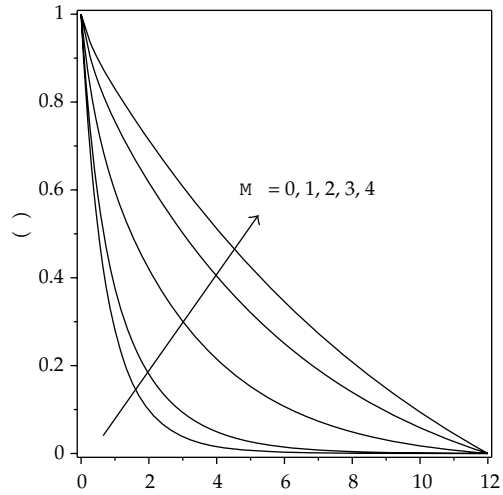

Figure 2: Temperature profiles for different values of M when $Pr = 0.78$, $Sc = 0.6$, $D_f = 0.03$, $S_r = 2$, $r = 0$, and $f_0 = 0$.

simultaneously increases its temperature and concentration values. In addition, the effect of the magnetic parameter of the viscous shearing force and the Lorentz force is given by

$$\nu \frac{u}{\delta_v^2} \approx \frac{\delta^* B_0^2}{\rho} u. \tag{3.1}$$

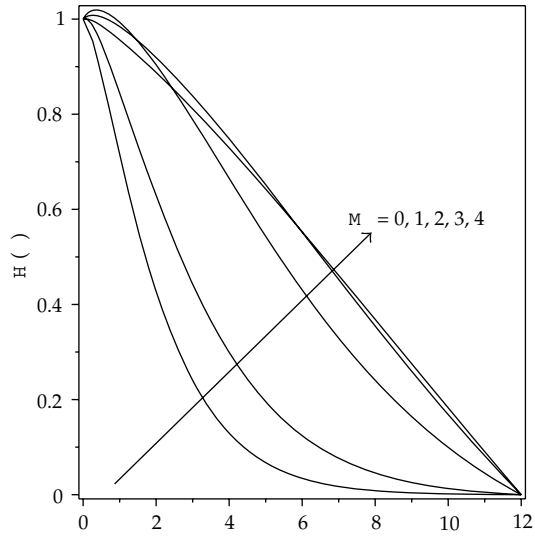

Figure 3: Concentration profiles for different values of M when $Pr = 0.78$, $Sc = 0.6$, $D_f = 0.03$, $S_r = 2$, $r = 0$, and $f_0 = 0$.

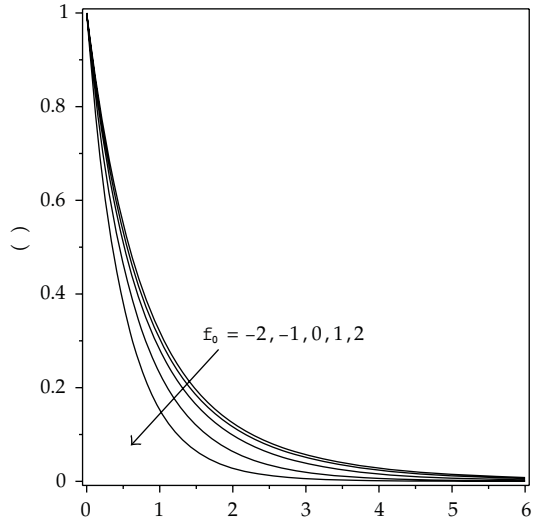

Figure 4: Temperature profiles for different values of f_0 when $Pr = 0.78$, $Sc = 0.6$, $D_f = 0.03$, $S_r = 2$, $r = 0$, and $M = 0$.

Thus, (3.1) gives

$$\eta_V \approx \frac{1}{M}. \tag{3.2}$$

However, the effect of surface tension can be obtained from (2.2) by the relation

$$\nu \frac{u}{\delta_v} \approx (\sigma_T 2Ax + \sigma_h A^* x). \tag{3.3}$$

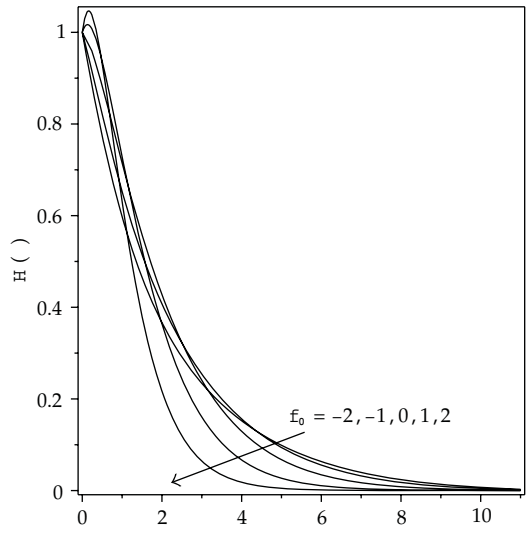

Figure 5: Concentration profiles for different values of f_0 when $Pr = 0.78$, $Sc = 0.6$, $D_f = 0.03$, $S_r = 2$, $r = 0$, and $M = 0$.

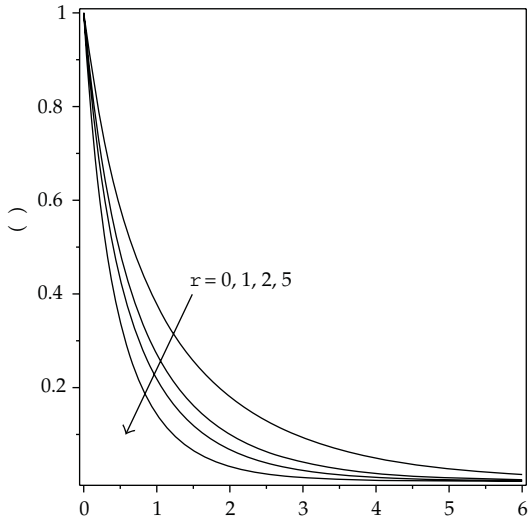

Figure 6: Temperature profiles for different values of r when $Pr = 0.78$, $Sc = 0.6$, $D_f = 0.03$, $S_r = 2$, $M = 1$, and $f_0 = 0$.

Then, (3.3) becomes

$$f'(0) \approx 2(1+r)\eta_V \approx \frac{2(1+r)}{M}. \tag{3.4}$$

Therefore, one can see that the velocity boundary layer thickness decreases with the increase of M as shown in Figure 1. However, the temperature and concentration increase

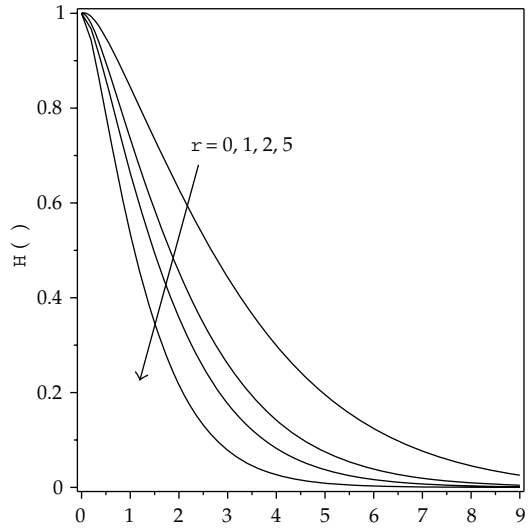

Figure 7: Concentration profiles for different values of r when $Pr = 0.78$, $Sc = 0.6$, $D_f = 0.03$, $S_r = 2$, $M = 1$, and $f_0 = 0$.

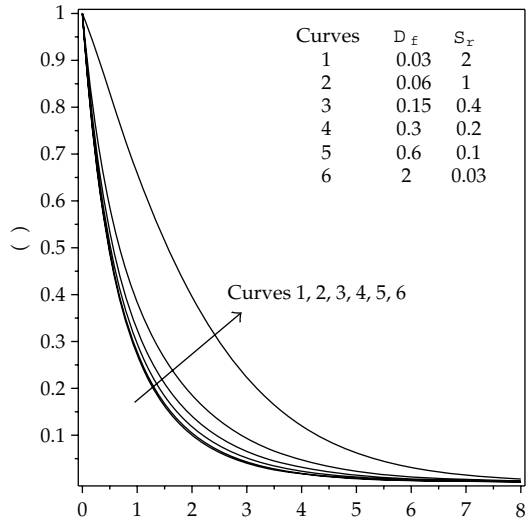

Figure 8: Temperature profiles for different values of D_f and S_r when $Pr = 0.78$, $Sc = 0.6$, $r = 1$, $M = 1$, and $f_0 = 0$.

with the increasing of the magnetic field parameter M. The temperature and concentration profiles are also affected by Pr, Sc, D_f, and S_r. Figures 4 and 5 show the influences of the suction and injection parameter f_0 on the temperature and concentration profiles. The results point out that increasing values in suction parameter ($f_0 > 0$) at the wall tend to decrease the temperature of the flow as shown in the Figure 4. Concurrently, the concentration profiles decrease as well with the inclusion of the suction parameter. This phenomenon is caused by

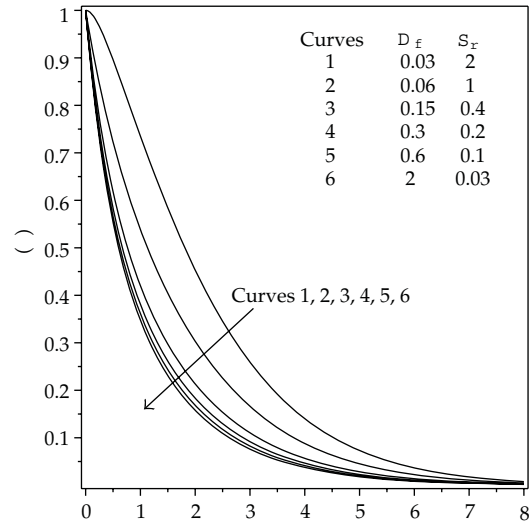

Figure 9: Concentration profiles for different values of D_f and S_r when $Pr = 0.78$, $Sc = 0.6$, $r = 1$, $M = 1$, and $f_0 = 0$.

the fluid moves nearer to the surface and decreases the thermal and concentration boundary layer thickness. Conversely, these observations are found to be opposite in the case of injection ($f_0 < 0$). It is seen that the imposition of the injection parameter will increase the fluid temperature and concentration.

The effect of the inclusion of the thermosolutal surface tension ratio r on the temperature and concentration profiles is illustrated in Figures 6 and 7, respectively. We observed that the parameter r significantly decreases the fluid temperature and concentration. This finding is obtained due to the increase of the Marangoni convection effect as r increases. From physical point of view, by increasing the Marangoni convection effect, more induced flows are produced. As consequences, the resulting flows will propagate within the boundary layers impling the maximum velocity obtained at the wall.

Figures 8 and 9 show the combination effects of the Dufour and Soret numbers on the fluid temperature and concentration. The Dufour D_f and Soret S_r numbers represent the thermal diffusion and diffusion thermal effects in this problem. Moreover, we have to be discriminating in selection of Dufour and Soret numbers in order to guarantee that the product of $S_r D_f$ is kept constant as well as assuming the mean temperature T_m is constant. To be practical, the Dufour and Soret values that are used in the present study are referred to the paper reported by Kafoussias and Williams [17]. Figure 8 specifically shows the influences of the Dufour and Soret number on the variations of the fluid temperature. For the case of increasing Dufour number and decreasing Soret number, it is seen that the temperature profiles show dissimilar increasing on its values. The Dufour term that describes the effect of concentration gradients as underlined in (2.9) plays a vital role in assisting the flow and is able to increase thermal energy in the boundary layer. This is the evident that as the parameter D_f increases and S_r decreases, the fluid temperature will increase.

In Figure 9, increasing Dufour number and simultaneously decreasing Soret number have implied significant effects on the concentration profiles. The Soret term exemplifies the

temperature gradient effects on the variation of concentration as noted in (2.10). It is observed as the Dufour number increases and Soret number is decreased, the concentration values are found to decrease. For a small Soret number $S_r < 0.4$, it is seen that the concentration values decrease steadily and closely to each other with similar pattern. On the other hand, these observations are found to be contrary in the case of $S_r > 1$ when the graph shows large differences in concentration values compared to curves (3–5) with low values of Soret number. The physical reason of this phenomena that occurs is due to a strong concentration overshoot that happens nearly to the surface.

Furthermore, the results in the Figures 8 and 9 agree well with the data in Table 4. We can see that combination effects of the thermal diffussion and diffusion thermo can reduce the surface temperature gradient while increase the surface concentration gradient. Hence, the local Nusselt number decreases and the local Sherwood number increases by increasing the Dufour number and reducing the Soret number.

4. Conclusions

The problem of thermal diffusion and diffusion thermo effects on thermosolutal Marangoni convection boundary layer flow over a flat surface considering the fluid suction and injection in the presence of the magnetic field is studied. The governing partial differential equations associated with the boundary conditions were transformed into nonlinear ordinary differential equations before being solved using the Runge-Kutta-Fehlberg method. The effects of thermal diffusion (Soret number S_r) and diffusion thermo (Dufour number D_f), magnetic field parameter M, thermosolutal surface tension ratio r and suction or injection parameter f_0 on the velocity, temperature and concentration field, and the physical quantities interest in engineering problem such as surface velocity, the local Nusselt number and Sherwood number were plotted, tabulated, and analyzed. It is found that the inclusion of the magnetic field parameter on the flow increased the temperature, and concentration profiles while it decreased the velocity field as well as Nusselt an Sherwood numbers. The analysis also revealed that the same behavior was drawn as thermosolutal surface tension ratio r was decreased. We also observed that increasing the suction parameter f_0 has decreased the fluid velocity, temperature and concentration profiles as it increased the Nusselt and Sherwood numbers. In contrast, the opposite observation was attained for the imposition of the injection parameter. The current analysis also signifies that the temperature profile and Sherwood number increase with the increasing in Dufour number and decreasing in Soret number. Opposite behavior is identified on Nusselt number and concentration profile. We also noticed that the velocity field is insensitive by changing in Dufour and Soret numbers.

Acknowledgment

This work was supported by research grants from the Ministry of Higher Education, Malaysia (project code: FRGS/1/2011/SG/UNIMAP/03/7).

References

[1] L. G. Napolitano, "Microgravity fluid dynamics," in *Proceedings of the 2nd Levitch Conference*, Washington, DC, USA, 1978.

[2] L. G. Napolitano, "Marangoni boundary layers," in *Proceedings of the 3rd European Symposium on Materials Sciences in Space*, Grenoble, France, 1979.
[3] K. Arafune and A. Hirata, "Thermal and solutal marangoni convection in In-Ga-Sb system," *Journal of Crystal Growth*, vol. 197, no. 4, pp. 811–817, 1999.
[4] K. Arafune, K. Yamamoto, and A. Hirata, "Interactive thermal and solutal Marangoni convection during compound semiconductor growth in a rectangular open boat," *International Journal of Heat and Mass Transfer*, vol. 44, no. 13, pp. 2404–2411, 2001.
[5] Z. Galazka and H. Wilke, "Influence of Marangoni convection on the flow pattern in the melt during growth of $Y_3Al_5O_{12}$ single crystals by the Czochralski method," *Journal of Crystal Growth*, vol. 216, no. 1, pp. 389–398, 2000.
[6] H. Neumann, Y. Plevachuk, and F. Allenstein, "Investigation of Marangoni convection in monotectic melts by resistance measurements," *Materials Science and Engineering A*, vol. 361, no. 1-2, pp. 155–164, 2003.
[7] B. Arendt and R. Eggers, "Interaction of Marangoni convection with mass transfer effects at droplets," *International Journal of Heat and Mass Transfer*, vol. 50, no. 13-14, pp. 2805–2815, 2007.
[8] Y. L. Xu, Z. B. Dong, Y. H. Wei, and C. L. Yang, "Marangoni convection and weld shape variation in A-TIG welding process," *Theoretical and Applied Fracture Mechanics*, vol. 48, no. 2, pp. 178–186, 2007.
[9] A. Al-Mudhaf and A. J. Chamkha, "Similarity solutions for MHD thermosolutal Marangoni convection over a flat surface in the presence of heat generation or absorption effects," *Heat and Mass Transfer*, vol. 42, no. 2, pp. 112–121, 2005.
[10] D. M. Christopher and B. Wang, "Prandtl number effects for Marangoni convection over a flat surface," *International Journal of Thermal Sciences*, vol. 40, no. 6, pp. 564–570, 2001.
[11] I. Pop, A. Postelnicu, and T. Groşan, "Thermosolutal Marangoni forced convection boundary layers," *Meccanica*, vol. 36, no. 5, pp. 555–571, 2001.
[12] R. A. Hamid, N. M. Arifin, R. Nazar, F. M. Ali, and I. Pop, "Dual solutions on thermosolutal Marangoni forced convection boundary layer with suction and injection," *Mathematical Problems in Engineering*, vol. 2011, Article ID 875754, 19 pages, 2011.
[13] C. H. Chen, "Marangoni effects on forced convection of power-law liquids in a thin film over a stretching surface," *Physics Letters A*, vol. 370, no. 1, pp. 51–57, 2007.
[14] E. Magyari and A. J. Chamkha, "Exact analytical results for the thermosolutal MHD Marangoni boundary layers," *International Journal of Thermal Sciences*, vol. 47, no. 7, pp. 848–857, 2008.
[15] N. M. Arifin, F. M. Ali, R. Nazar, and I. Pop, "Thermal and solutal marangoni mixed convection boundary layer flow," *WSEAS Transactions on Mathematics*, vol. 9, no. 5, pp. 376–385, 2010.
[16] R. A. Hamid, N. M. Arifin, R. Nazar, and F. M. Ali, "Radiation effects on marangoni convection over a flat surface with suction and injection," *Malaysian Journal of Mathematical Sciences*, vol. 5, no. 1, pp. 13–25, 2011.
[17] N. G. Kafoussias and E. W. Williams, "Thermal-diffusion and diffusion-thermo effects on mixed free-forced convective and mass transfer boundary layer flow with temperature dependent viscosity," *International Journal of Engineering Science*, vol. 33, no. 9, pp. 1369–1384, 1995.
[18] P. Puvi Arasu, P. Loganathan, R. Kandasamy, and I. Muhaimin, "Lie group analysis for thermal-diffusion and diffusion-thermo effects on free convective flow over a porous stretching surface with variable stream conditions in the presence of thermophoresis particle deposition," *Nonlinear Analysis: Hybrid Systems*, vol. 5, no. 1, pp. 20–31, 2011.
[19] E. Osalusi, J. Side, and R. Harris, "Thermal-diffusion and diffusion-thermo effects on combined heat and mass transfer of a steady MHD convective and slip flow due to a rotating disk with viscous dissipation and Ohmic heating," *International Communications in Heat and Mass Transfer*, vol. 35, no. 8, pp. 908–915, 2008.
[20] A. A. Afify, "Similarity solution in MHD: effects of thermal diffusion and diffusion thermo on free convective heat and mass transfer over a stretching surface considering suction or injection," *Communications in Nonlinear Science and Numerical Simulation*, vol. 14, no. 5, pp. 2202–2214, 2009.
[21] N. T. Eldabe, A. G. El-Saka, and A. Fouad, "Thermal-diffusion and diffusion-thermo effects on mixed free-forced convection and mass transfer boundary layer flow for non-Newtonian fluid with temperature dependent viscosity," *Applied Mathematics and Computation*, vol. 152, no. 3, pp. 867–883, 2004.
[22] M. A. El-Aziz, "Thermal-diffusion and diffusion-thermo effects on combined heat and mass transfer by hydromagnetic three-dimensional free convection over a permeable stretching surface with radiation," *Physics Letters A*, vol. 372, no. 3, pp. 263–272, 2008.

[23] M. M. Rashidi, T. Hayat, E. Erfani, S. A. Mohimanian Pour, and A. A. Hendi, "Simultaneous effects of partial slip and thermal-diffusion and diffusion-thermo on steady MHD convective flow due to a rotating disk," *Communications in Nonlinear Science and Numerical Simulation*, vol. 16, no. 11, pp. 4303–4317, 2011.

[24] T. Hayat, M. Nawaz, S. Asghar, and S. Mesloub, "Thermal-diffusion and diffusion-thermo effects on axisymmetric flow of a second grade fluid," *International Journal of Heat and Mass Transfer*, vol. 54, no. 13-14, pp. 3031–3041, 2011.

[25] A. Aziz, "A similarity solution for laminar thermal boundary layer over a flat plate with a convective surface boundary condition," *Communications in Nonlinear Science and Numerical Simulation*, vol. 14, no. 4, pp. 1064–1068, 2009.

Hindawi Publishing Corporation
Journal of Applied Mathematics
Volume 2012, Article ID 587834, 10 pages
doi:10.1155/2012/587834

Research Article

Viscous Flow over Nonlinearly Stretching Sheet with Effects of Viscous Dissipation

Javad Alinejad[1] and Sina Samarbakhsh[2]

[1] *Department of Mechanical Engineering, Sari Branch, Islamic Azad University, Sari 48161-19318, Iran*
[2] *Azmoon Pardazesh Research Institute, No. 2, Malekloo Street, Narmak, Tehran 1483764874, Iran*

Correspondence should be addressed to Javad Alinejad, alinejad_javad@iausari.ac.ir

Received 19 November 2011; Revised 25 January 2012; Accepted 10 February 2012

Academic Editor: M. F. El-Amin

The flow and heat transfer characteristics of incompressible viscous flow over a nonlinearly stretching sheet with the presence of viscous dissipation is investigated numerically. The similarity transformation reduces the time-independent boundary layer equations for momentum and thermal energy into a set of coupled ordinary differential equations. The obtained equations, including nonlinear equation for the velocity field f and differential equation by variable coefficient for the temperature field θ, are solved numerically by using the fourth order of Runge-Kutta integration scheme accompanied by shooting technique with Newton-Raphson iteration method. The effect of various values of Prandtl number, Eckert number and nonlinear stretching parameter are studied. The results presented graphically show some behaviors such as decrease in dimensionless temperature θ due to increase in Pr number, and curve relocations are observed when heat dissipation is considered.

1. Introduction

The study of two-dimensional boundary layer flow, heat, and mass transfer over a nonlinear stretching surface is very important as it finds many practical applications in different areas. Some industrial applications of viscous flow over a stretching sheet are aerodynamic extrusion of plastic sheets, condensation process of metallic plate in a cooling bath, and extrusion of a polymer sheet from a dye. During the manufacture of these sheets, the melt issues from a slit and is subsequently stretched to achieve the desired thickness. The final products of desired characteristics are notably influenced by the stretching rate, the rate of the cooling in the process, and the process of stretching. Viscous dissipation changes the temperature distributions by playing a role like an energy source, which leads to affecting heat transfer rates. The merit of the effect of viscous dissipation depends on whether the sheet is being cooled or heated. The problem of nonlinear stretching sheet for different cases

of fluid flow has also been analyzed by different researchers. Sakiadis [1] initiated the study of boundary layer flow over a continuous solid surface moving with constant speed as result of ambient fluid movement; this boundary flow is generally different from boundary layer flow over a semi-infinite flat plate. Erickson [2] studied this problem to the case in which the transverse velocity at the moving surface is nonzero with the effects of heat and mass transfer being taken in to account. Danberg and Fansler [3], using nonsimilar solution method, studied the flow inside the boundary layer past a wall that is stretched with a velocity proportional to the distance along the wall. P. S. Gupta A. S. Gupta [4], using similar solution method, analyzed heat and mass transfer in the boundary layer over a stretching sheet subject to suction or blowing. The laminar boundary layer on an inextensible continues flat surface moving with a constant velocity in a non-Newtonian fluid characterized by a power-law model is studied by Fox et al. [5], using both exact and approximate methods. Rajagopal et al. [6] studied the flow behavior of viscoelastic fluid over stretching sheet and gave an approximate solution to the flow field. Recently Troy et al. [7] presented an exact solution for Rajagopal problem. Vajravelu and Roper [8] studied the flow and heat transfer in a viscoelastic fluid over a continues stretching sheet with power law surface temperature, including the effects of viscous dissipation, internal heat generation or absorption, and work due to deformation in the energy equation. Vajravelu [9] studied the flow and heat transfer characteristics in a viscous fluid over a nonlinearly stretching sheet without heat dissipation effect. Cortell [10, 11] has worked on viscous flow and heat transfer over a nonlinearly stretching sheet. Raptis and Perdikis [12] studied viscous flow over a nonlinear stretching sheet in the presence of a chemical reaction and magnetic field. Abbas and Hayat [13] addressed the radiation effects on MHD flow due to a stretching sheet in porous space. Cortell [14] investigated the influence of similarity solution for flow and heat transfer of a quiescent fluid over a nonlinear stretching surface. Awang and Hashim [15] obtained the series solution for flow over a nonlinearly stretching sheet with chemical reaction and magnetic field. In the present paper an analysis is carried out to study the flow and heat transfer phenomenon in a viscous fluid over a nonlinearly stretching sheet by considering the effects of heat dissipation. In order to arrive nonlinear ordinary deferential equations, stream function is defined differently (compared to the linear stretching case) and these nonlinear deferential equations along with pertinent boundary condition are solved.

2. Flow and Heat Transfer Analysis

Consider the steady laminar flow of a viscous incompressible over a nonlinearly stretching sheet. The governing boundary layer equations of mass conservation, momentum, and energy with viscous dissipation are

$$\begin{aligned} \frac{\partial u}{\partial x} + \frac{\partial v}{\partial y} &= 0, \\ u\frac{\partial u}{\partial x} + v\frac{\partial u}{\partial y} &= \nu\frac{\partial^2 u}{\partial y^2}, \\ u\frac{\partial T}{\partial x} + v\frac{\partial T}{\partial y} &= \frac{k}{\rho C_p}\frac{\partial^2 T}{\partial y^2} + \frac{\mu}{\rho C_p}\frac{\partial^2 T}{\partial y^2}, \end{aligned} \tag{2.1}$$

where u and v are the velocity components in x and y axes, respectively, T is the temperature, ν the kinematic viscosity, ρ the density, μ the dynamic viscosity, k the thermal conductivity, and C_p the specific heat at constant pressure. The boundary conditions to the case are

$$u = cx^n, \qquad v = 0, \qquad T = T_w \quad \text{at } y = 0, \tag{2.2}$$

$$u \longrightarrow 0, \qquad T \longrightarrow T_\infty \quad \text{as } y \longrightarrow \infty. \tag{2.3}$$

These conditions suggest transforming into the corresponding nonlinear ordinary differential equations by choosing the similarity transformation as given by Vajravelu [9]:

$$\begin{gathered} \eta = y\sqrt{\frac{c(n+1)}{2\nu}}x^{(n-1)/2}, \\ u = cx^n f'(\eta), \\ v = -\sqrt{\frac{c\nu(n+1)}{2}}x^{(n-1)/2}\left[f + \left(\frac{n-1}{n+1}\right)\eta f'\right], \end{gathered} \tag{2.4}$$

where a prime denotes differentiation with respect to η. The transformed nonlinear, coupled ordinary differential equations and boundary conditions are

$$f''' + ff' - \left(\frac{2n}{n+1}\right)(f')^2 = 0, \tag{2.5}$$

$$f' = 1, \qquad f = 0 \quad \text{at } \eta = 0, \tag{2.6}$$

$$\theta'' + \Pr f\theta' + \Pr \mathrm{Ec}(f'')^2 = 0, \tag{2.7}$$

$$\theta = 1 \quad \text{at } \eta = 0, \tag{2.8}$$

$$\theta \longrightarrow 0 \quad \text{as } \eta \longrightarrow \infty, \tag{2.9}$$

where dimensionless parameters are defined as

$$\begin{gathered} \theta(\eta) = \frac{(T - T_\infty)}{T_w - T_\infty}, \\ \mathrm{Ec} = \frac{u^2}{C_P \Delta T} \text{ (Eckert number)}, \\ \Pr = \frac{\mu C_P}{k} \text{ (Prandtl number)}. \end{gathered} \tag{2.10}$$

The shear stress at the surface of the sheet is defined as

$$\tau_w = \mu\left(\frac{\partial u}{\partial y}\right)_{y=0},$$
$$\tau_w = c\mu\sqrt{\frac{c(n+1)}{2\nu}}x^{(3n-1)/2}f''(0). \tag{2.11}$$

And the local wall heat flux is defined as

$$q_w = -k\left(\frac{\partial T}{\partial y}\right)_{y=0},$$
$$q_w = -k(T_w - T_\infty)\sqrt{\frac{c(n+1)}{2\nu}}x^{(n-1)/2}\theta'(0). \tag{2.12}$$

Since there is no exact solution for nonlinearly stretching boundary problem, the differential (2.5) and (2.7) are investigated numerically in accordance with the boundary condition (2.6) and (2.7).

3. Numerical Analysis

The nonlinear boundary value problem represented by (2.5) and (2.7) is solved numerically using fourth-order Runge-Kutta shooting technique. Equations (2.5) and (2.7) have been discretized to five first-order equations as follows:

$$\begin{aligned} y_1' &= y_2, \\ y_2' &= y_3, \\ y_3' &= \left(\frac{2n}{n+1}\right)y_2^2 - y_1y_3, \\ y_4' &= y_5 \\ y_5' &= -\mathrm{Pr}y_1y_5 - \mathrm{PrEc}y_3^2, \end{aligned} \tag{3.1}$$

where $y_1 = f,\ y_2 = f',\ y_3 = f'',\ y_4 = \theta,\ y_5 = \theta'$. Boundary conditions (2.6) and (2.9) become

$$\begin{aligned} y_1 = 0, \quad y_2 = 1, \quad y_4 = 1 \quad \text{at } \eta = 0, \\ y_2 \longrightarrow 0, \quad y_4 \longrightarrow 0 \quad \text{as } \eta \longrightarrow \infty. \end{aligned} \tag{3.2}$$

Regarding the above boundary conditions three values out of five that required initial values are known, and we begin solution procedure by two initial guesses and the procedure corrects them using Newton-Raphson iteration scheme. Initial guesses to initiate the shooting process are very crucial in this process and it should be noted that convergence is not guaranteed,

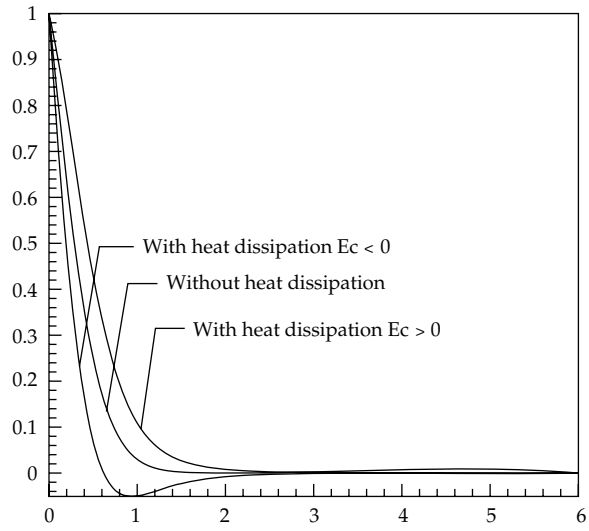

Figure 1: Dimensionless temperature profile θ versus similarity parameter η-Effect of heat dissipation with Pr = 7, $n = 1$.

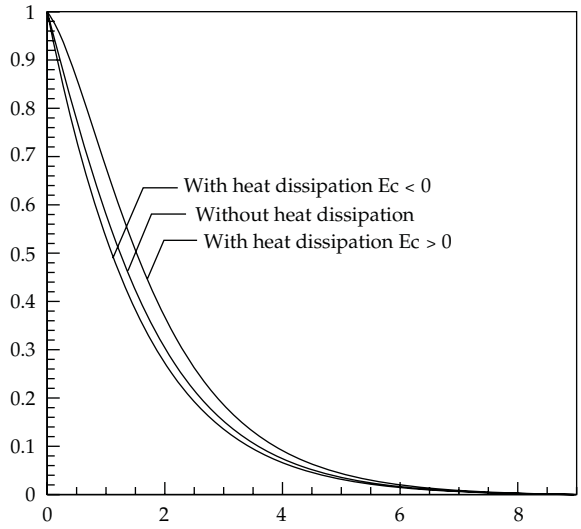

Figure 2: Dimensionless temperature profile θ versus similarity parameter η-Effect of heat dissipation with Pr = 0.71, $n = 1$.

especially if a poor guess for the missing starting boundary values is made. Another challenge to solve this equations system is the values of y_2 and y_4 at $\eta \to \infty$. It is necessary to estimate η by a known value in which dimensionless temperature profile (θ) reaches its asymptotic state.

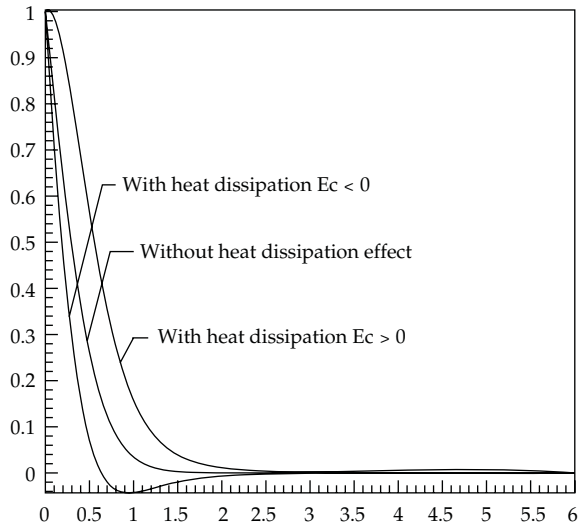

Figure 3: Dimensionless temperature profile θ versus similarity parameter η-Effect of heat dissipation with Pr = 7, n = 5.

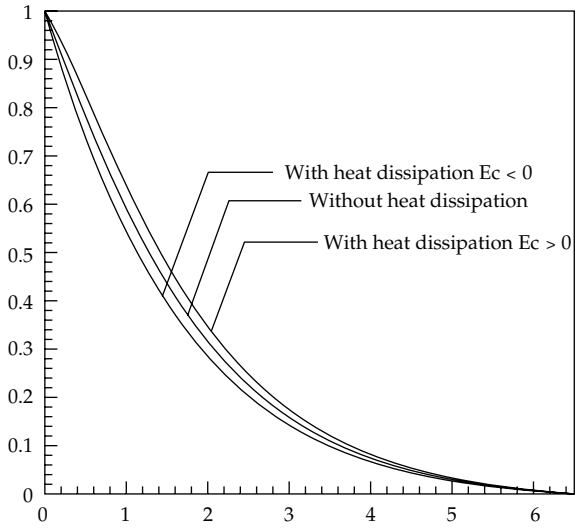

Figure 4: Dimensionless temperature profile θ versus similarity parameter η-Effect of heat dissipation with Pr = 0.71, n = 5.

4. Results and Discussion

Figures 1, 2, 3, 4, 5, and 6 described the behavior of dimensionless temperature profile (θ) versus similarity variable η which are compared for two cases of without heat dissipation and by considering heat dissipation effects. It can be seen that in cases with positive values of the Eckert number, the curves are shifted to the right-hand side and in cases with

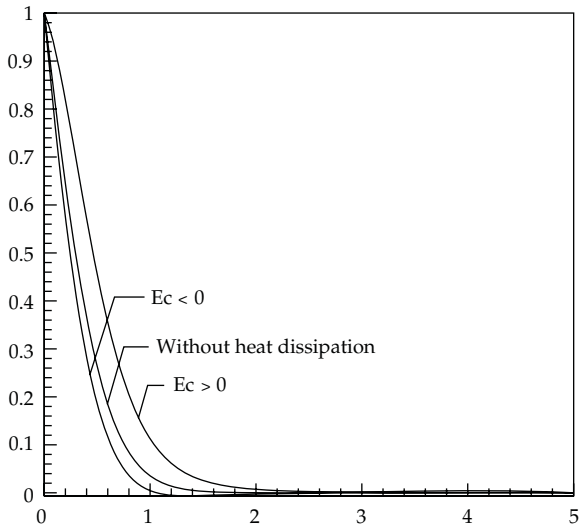

Figure 5: Dimensionless temperature profile θ versus similarity parameter η-Effect of heat dissipation with Pr = 7, n = 10.

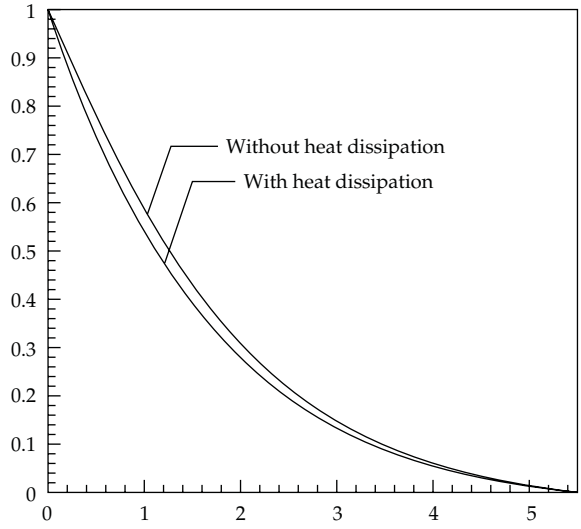

Figure 6: Dimensionless temperature profile θ versus similarity parameter η-Effect of heat dissipation with Pr = 0.71, n = 10.

negative values of the Eckert number the curves are shifted to the left-hand side. This is due to involvement of heat dissipation. Furthermore, it is obvious that the dimensionless temperature θ increases with increases in the nonlinear stretching parameter n (Figures 7 and 8).

It is seen that the dimensionless temperature θ at a point in the flow decreases with an increase in the Prandtl number (Figure 9). Since the Prandtl number is a criterion of relative diffusion effects of momentum and energy in velocity and thermal boundary layer,

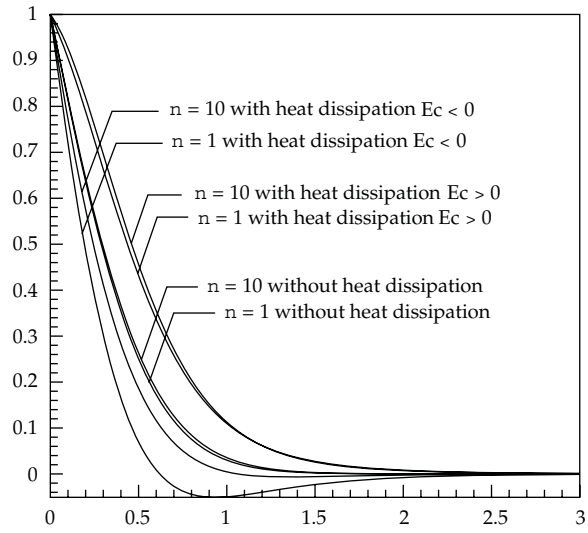

Figure 7: Dimensionless temperature profile θ versus similarity parameter η-Effect of heat dissipation and nonlinear parameter n with Pr = 7.

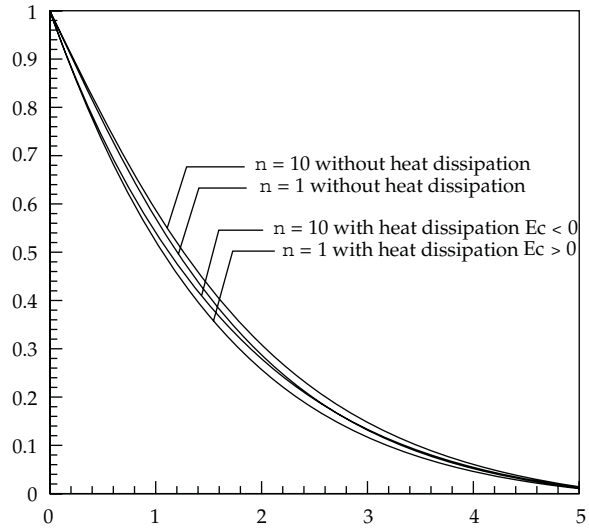

Figure 8: Dimensionless temperature profile θ versus similarity parameter η-Effect of heat dissipation and nonlinear parameter n with Pr = 0.71.

respectively, therefore, this result is consistent with the fact that the thermal boundary layer thickness decreases with an increase in the Prandtl number (see the scales of Figures 1 and 2).

In cases with small Prandtl number (Pr < 1, Figures 2, 4, and 6), there is a very low difference at the end of diagram between the curves with and without heat dissipation (the end of boundary layer thickness) which caused by this fact that, in these cases, the thickness

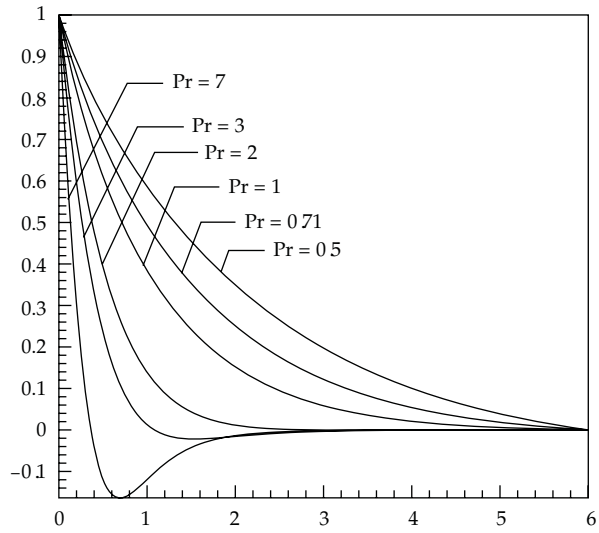

Figure 9: Dimensionless temperature profile θ versus similarity parameter η-Effect of Pr number for $n = 5$, Ec = −1.

of thermal boundary layer is greater than that of velocity boundary layer and at the end of thermal boundary layer in which velocity gradient is reduced to zero, the curves have conformity on each other because the effect of the energy produced by viscosity is destroyed. In cases with large Prandtl number (Pr > 1) and negative Eckert number, the dimensionless temperature θ gains a negative value after reaching zero and, at the end of path, it reaches zero again (Figures 1, 3, and 5). The reason for being negative of θ in a specific domain is the presence of velocity gradient outside the thermal boundary layer. These negative values by considering larger Eckert number are more significant. As soon as velocity gradient is removed (at the end of velocity boundary layer) the θ reaches zero again. In Figure 9, for a constant Eckert number the dimensionless temperature θ is drawn based on different Prandtl number. It is observed that, in larger Prandtl number due to the above-mentioned reasons, θ has smaller value. The dimensionless temperature profiles presented in Figures 1–9 show that the far-field boundary conditions are satisfied asymptotically, which support the validity of the numerical results presented.

References

[1] B. C. Sakiadios, "Boundary layer behaviour on continuous solid surfaces," *American Institute of Chemical Engineers*, vol. 7, pp. 26–28, 1961.

[2] L. E. Erickson, L.T. Fan, and V. G. Fox, "Heat and mass transfer on a moving continuous moving surface," *Industrial & Engineering Chemistry Fundamentals*, vol. 5, pp. 19–25, 1966.

[3] J. E. Danberg and K. S. Fansler, "A nonsimilar moving wall boundary-layer problem," *Quarterly of Applied Mathematics*, vol. 34, pp. 305–309, 1979.

[4] P. S. Gupta and A. S. Gupta, "Heat and mass transfer on a stretching sheet with suction or blowing," *The Canadian Journal of Chemical Engineering*, vol. 55, pp. 744–746, 1977.

[5] V. G. Fox, L. E. Erickson, and L. T. Fan, "Heat and mass transfer on a moving continuous flat plate with suction or injection," *American Institute of Chemical Engineers*, vol. 15, pp. 327–333, 1969.

[6] K. R. Rajagopal, T. Y. Na, and A. S. Gupta, "Flow of a viscoelastic fluid over a stretching sheet," *Rheologica Acta*, vol. 23, no. 2, pp. 213–215, 1984.
[7] W. C. Troy, E. A. Overman, II, G. B. Ermentrout, and J. P. Keener, "Uniqueness of flow of a second-order fluid past a stretching sheet," *Quarterly of Applied Mathematics*, vol. 44, no. 4, pp. 753–755, 1987.
[8] K. Vajravelu and T. Roper, "Flow and heat transfer in a second grade fluid over a stretching sheet," *International Journal of Non-Linear Mechanics*, vol. 34, no. 6, pp. 1031–1036, 1999.
[9] K. Vajravelu, "Viscous flow over a nonlinearly stretching sheet," *Applied Mathematics and Computation*, vol. 124, no. 3, pp. 281–288, 2001.
[10] R. Cortell, "MHD flow and mass transfer of an electrically conducting fluid of second grade in a porous medium over a stretching sheet with chemically reactive species," *Chemical Engineering and Processing*, vol. 46, no. 8, pp. 721–728, 2007.
[11] R. Cortell, "Viscous flow and heat transfer over a nonlinearly stretching sheet," *Applied Mathematics and Computation*, vol. 184, no. 2, pp. 864–873, 2007.
[12] A. Raptis and C. Perdikis, "Viscous flow over a non-linearly stretching sheet in the presence of a chemical reaction and magnetic field," *International Journal of Non-Linear Mechanics*, vol. 41, no. 4, pp. 527–529, 2006.
[13] Z. Abbas and T. Hayat, "Radiation effects on MHD flow in a porous space," *International Journal of Heat and Mass Transfer*, vol. 51, no. 5-6, pp. 1024–1033, 2008.
[14] R. Cortell, "Effects of viscous dissipation and radiation on the thermal boundary layer over a nonlinearly stretching sheet," *Physics Letters, Section A*, vol. 372, no. 5, pp. 631–636, 2008.
[15] S. Awang Kechil and I. Hashim, "Series solution of flow over nonlinearly stretching sheet with chemical reaction and magnetic field," *Physics Letters, Section A*, vol. 372, no. 13, pp. 2258–2263, 2008.

Hindawi Publishing Corporation
Journal of Applied Mathematics
Volume 2012, Article ID 846517, 13 pages
doi:10.1155/2012/846517

Research Article

Modelling Considerations in the Simulation of Hydrogen Dispersion within Tunnel Structures

Idris Ismail, Hisayoshi Tsukikawa, and Hiroshi Kanayama

Department of Mechanical Engineering, Kyushu University, 744, Motooka, Nishi-ku, Fukuoka 819-0395, Japan

Correspondence should be addressed to Hiroshi Kanayama, kanayama@mech.kyushu-u.ac.jp

Received 5 January 2012; Revised 10 March 2012; Accepted 10 March 2012

Academic Editor: M. F. El-Amin

The flow of leaked hydrogen gas in tunnel structures is simulated through a free, open source computational fluid dynamics (CFD) code for incompressible thermal convection flow. A one-fifth scale experimental model of a real tunnel is the target model to be simulated. To achieve this, studies on the effects of different boundary conditions, in particular, the wind speed, are carried out on smaller tunnel structures with the same hydrogen inlet boundary conditions. The results suggest a threshold/limiting value of air speed through tunnel. The target model computed with the most suitable boundary conditions shows some agreement with the experimental ones. A method to compute the buoyancy factor used in the code is also presented.

1. Introduction

The development of hydrogen-fuelled vehicles is currently underway. Car garages and road tunnels—the necessary infrastructure—are partially enclosed spaces, where leaked hydrogen might be constrained from dispersing freely into the atmosphere, and accumulate within the structure. Hydrogen-air gas mixtures have a low ignition energy and large flammability range—from 4 to 75% by volume concentration at room temperature—within which lies a range where detonation is possible, generally taken to be at 18–59% by volume concentration. As such, it is important that the behaviour of leaked hydrogen in partially enclosed spaces is investigated before the widespread use of hydrogen by the public is put in place. However, the inherent dangers in carrying out experiments involving hydrogen necessitate safety measures that can be costly and prohibitive. The solution to this is to use computational fluid dynamics (CFD).

The literature on hydrogen dispersion in partially enclosed spaces is extensive. Basic studies on simple geometries with a hydrogen inlet, and two vents have been carried out both experimentally and with CFD (e.g., [1–6]). Guidelines on the use of hydrogen in confined spaces have also been developed [7]. Works on tunnel-like structures, however, are few, for example, [8, 9]. Most studies, whether experimental or computational, involve overpressure calculations and concentrate on the eventual detonation of hydrogen within the tunnel for example, [10, 11].

This work involves the simulation of tunnel structures using a finite-element code developed in house. The code was written to solve incompressible thermal flow problems. The experimental model studied by Sato et al. [9], HT-5, is taken as the target model to be simulated. In this paper, the effects of the parameters—in particular the wind speed through the tunnel—and boundary conditions are investigated. Using the most appropriate parameters and boundary conditions, the target model is simulated and the results compared with the experimental ones.

We describe the tunnel geometries and the basic equations used in this work in the following section. In Section 3, we state the base boundary conditions used. We present our results and a discussion of these in Section 4. The results for boundary conditions other than the base settings are also presented and discussed. Finally, we state our conclusions in the last section.

2. Tunnel Geometries and Basic Equations

In this work, we limit our investigations to a study of tunnel geometry and ventilation (i.e., wind through the tunnel) speeds and their effects on the hydrogen distribution and flow within the tunnel. We explore the computational settings required to achieve converged results and whether these settings adversely affect the flow.

We use three models in our study—two representative models and a one-fifth scale mockup of a typical tunnel for road transport [9]. The mockup model (Model 3) is the only one where some results on the concentration distribution of hydrogen are available, and is thus our target model. Models 1 and 2 are representative tunnel models, used for parametric studies and to make qualitative, if not quantitative, observations about the flow. Through the results of Models 1 and 2, and trial runs of Model 3, the most appropriate settings and boundary conditions are applied to the computation of Model 3.

The representative tunnel models are shown in Figures 1 and 2. The difference in these models is the tunnel cross sectional area—0.89 m^2 for Model 1 and 1.75 m^2 for Model 2.

The hydrogen inlet is a block of dimensions $0.2 \times 0.2 \times 0.1$ m (length × width × height), giving an inlet surface area of 0.04 m^2. The side from which wind blows is the tunnel entrance; the opposite end is the tunnel exit. The roof cross-section is a semicircle with a diameter equal to the tunnel width. Five sensors are placed downstream from the hydrogen inlet, on the lengthwise axis.

Model 3, shown in Figures 3 and 4, is similar to test HT-5 in [9]. The only difference is the length-test model HT-5 is 78.5 m long, whereas the model here is only 10 m. This difference was due to memory constraints. The tunnel cross sectional area of Model 3 is 3.74 m^2. The hydrogen inlet is of the same dimensions as Models 1 and 2. In [9], only the flow rate was given for HT-5. We use the same flow rate here.

We use ADVENTURE_sFlow Ver0.5b [12], a CFD code written for incompressible viscous flow and thermal convection problems, to carry out the computations. Developed in-house, it is available online as a free open source code. The code uses the finite-element

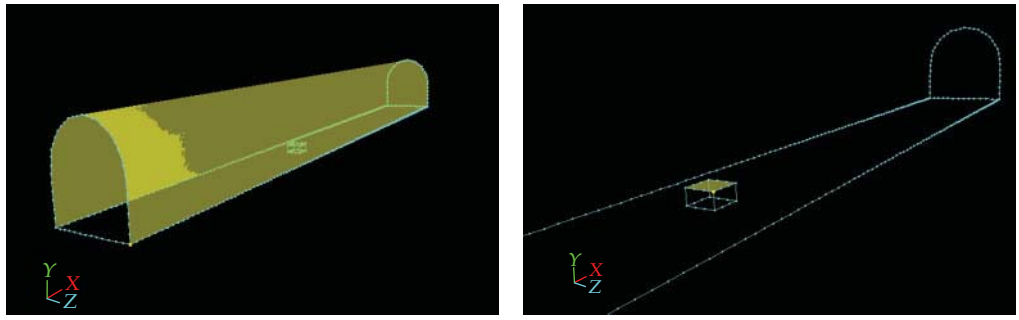

(a) (b)

Figure 1: Model 1 and Model 2. The tunnel roof and side walls are highlighted in (a); the hydrogen inlet is highlighted in (b).

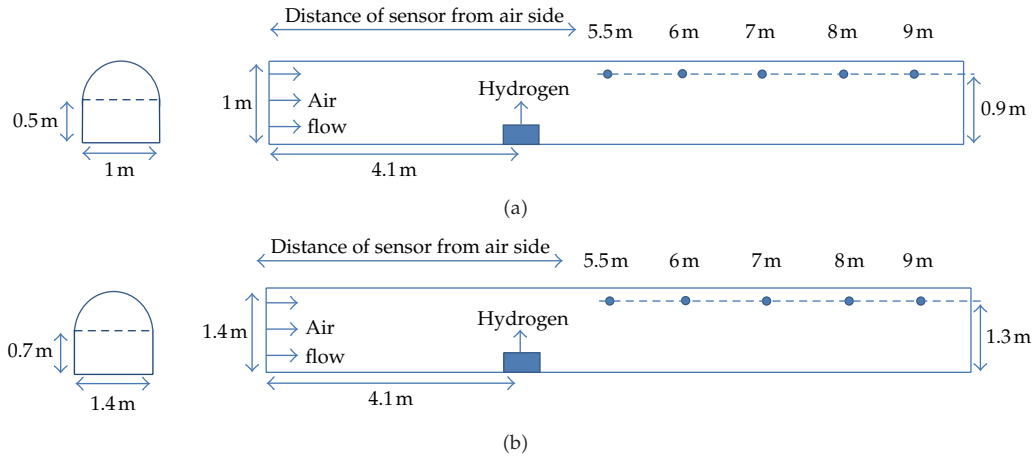

Figure 2: Schematic diagrams of Models 1 and 2 (not to scale).

method to discretize the coupled Navier-Stokes and advection diffusion equations, and the domain decomposition method to enable parallel processing. The code is used for gas dispersion problems through the application of an analogy that relates concentration and temperature. Details regarding the formulations underlying the code, including stabilization methods, can be found in [13]. The code is currently not equipped with any turbulence models. Here, we show the basic equations (the Navier-Stokes and advection-diffusion equations, (2.1)–(2.3)) and initial and boundary conditions used. In addition, we describe methods to compute the buoyancy term and the boundary condition at the hydrogen-air interface, both of which are not described in our previous work:

$$\frac{\partial \mathbf{u}}{\partial t} + (\mathbf{u}\cdot\nabla)\mathbf{u} - 2\nu\nabla\cdot D(\mathbf{u}) + \nabla p = -\beta C g \quad \text{in } \Omega\times(0,T), \tag{2.1}$$

$$\nabla\cdot\mathbf{u} = 0 \quad \text{in } \Omega\times(0,T), \tag{2.2}$$

$$\frac{\partial C}{\partial t} + \mathbf{u}\cdot\nabla C - a\Delta C = S \quad \text{in } \Omega\times(0,T). \tag{2.3}$$

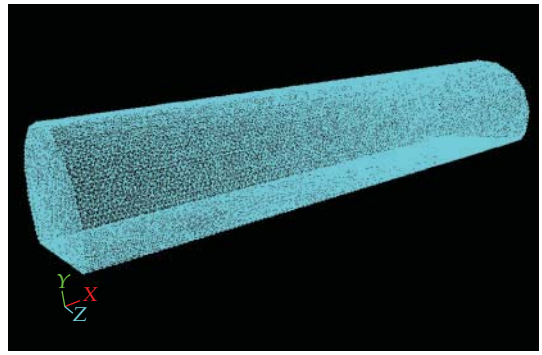

Figure 3: Model 3: geometry and mesh.

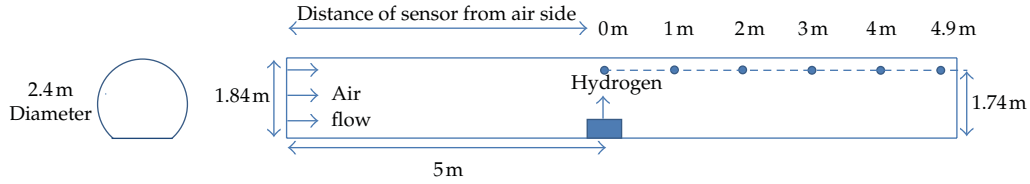

Figure 4: Schematic diagram of Model 3.

The symbols used are as follows. Ω is a three-dimensional polyhedral domain with boundary $\partial\Omega$, $\mathbf{u} = (u_1, u_2, u_3)^T$ is the velocity [m/s], t is time [s], v is the kinematic viscosity coefficient [m^2/s], p is the gas mixture gauge pressure (pressure) normalized by the density [m^2/s^2], $g = (g_1, g_2, g_3)^T$ is gravity [m/s^2], β is, in this case, the analogous coefficient of buoyancy [−], C is the mass concentration of hydrogen [−], a is the hydrogen diffusion coefficient in air [m^2/s], S is the source term [1/s], and D_{ij} is the rate of strain tensor [1/s] defined by

$$D_{ij}(\mathbf{u}) \equiv \frac{1}{2}\left(\frac{\partial u_i}{\partial x_j} + \frac{\partial u_j}{\partial x_i}\right), \quad i, j = 1, 2, 3. \tag{2.4}$$

The following boundary conditions are applied, where Γ_u and Γ_c denote the boundary with specified velocity and concentration, respectively,

$$\begin{aligned} \mathbf{u} &= \hat{\mathbf{u}} \quad \text{on } \Gamma_u \times (0, T), \\ C &= \hat{C} \quad \text{on } \Gamma_c \times (0, T), \\ \sum_{j=1}^{3} \sigma_{ij} n_j &= 0 \quad \text{on } (\partial\Omega - \Gamma_u) \times (0, T), \\ a\frac{\partial C}{\partial \mathbf{n}} &= 0 \quad \text{on } (\partial\Omega - \Gamma_c) \times (0, T), \\ \mathbf{u} = \mathbf{u}^0, &\qquad C = C^0 \quad \text{in } \Omega \text{ at } t = 0, \end{aligned} \tag{2.5}$$

where T is the total time [s], $\mathbf{u}^0$ is the initial velocity [m/s], C^0 is the initial concentration [−], $\hat{\mathbf{u}}$ is the boundary velocity [m/s], $\hat{C}$ is the boundary concentration [−], and $\sigma(u,\ p)$ is the stress tensor normalized by the density [m^2/s^2] defined by

$$\sigma_{ij} = -p\delta_{ij} + 2\nu D_{ij}(\mathbf{u}) \quad i,j = 1,2,3, \tag{2.6}$$

with δ_{ij} being the Kronecker delta and $\mathbf{n}$ being the unit normal vector.

The computation of the analogous coefficient of buoyancy, β in (2.1), is as follows. The ideal gas law may be written as

$$p = \rho RT, \tag{2.7}$$

where p is the pressure [$\mathrm{kg\,m^{-1}\,s^{-2}}$] of the gas, ρ the density [$\mathrm{kg\,m^{-3}}$], R the specific gas constant [$\mathrm{J\,kg^{-1}\,K^{-1}}$], and T the temperature [K]. Taking C as the mass concentration of hydrogen in a hydrogen-air mixture and R_{H_2} and R_{air} as the specific gas constants for hydrogen and air, respectively, substituting these into (2.7) and rearranging gives

$$\rho = \frac{p}{[CR_{H_2} + (1-C)R_{\mathrm{air}}]T}. \tag{2.8}$$

Noting that and $\rho_{H_2} = p/R_{H_2}T$, $\rho_{\mathrm{air}} = p/R_{\mathrm{air}}T$, and substituting these into the equation above gives

$$\rho = \frac{1}{(C/\rho_{H_2}) + ((1-C)/\rho_{\mathrm{air}})}, \tag{2.9}$$

which, when rearranged, give

$$1 - \frac{\rho_{\mathrm{air}}}{\rho} = C\left(1 - \frac{\rho_{\mathrm{air}}}{\rho_{H_2}}\right), \tag{2.10}$$

multiplying throughout by g, the acceleration of gravity [$\mathrm{m\,s^{-2}}$], and equating with the buoyancy force (normalized by gas density) gives

$$\left(1 - \frac{\rho_{\mathrm{air}}}{\rho}\right)g = C\left(1 - \frac{\rho_{\mathrm{air}}}{\rho_{H_2}}\right)g = -\beta C g, \tag{2.11}$$

from which

$$\beta = \frac{\rho_{\mathrm{air}}}{\rho_{H_2}} - 1. \tag{2.12}$$

With $\rho_{H_2} = 0.084\ \mathrm{kg\,m^{-3}}$ and $\rho_{\mathrm{air}} = 1.21\ \mathrm{kg\,m^{-3}}$, (2.12) yields $\beta = 13.4$. This method works for other gas combinations as well; in the case of helium, for example, using $\rho_{\mathrm{He}} = 0.1785\ \mathrm{kg\,m^{-3}}$ yields $\beta = 5.77$.

3. Boundary Conditions and Mesh Details

For the base (reference) settings, we use conditions similar to that used in our simulation of the so-called hallway model [13]. Γ_{inlet}, $\Gamma_{\text{t\_ent}}$, $\Gamma_{\text{t\_ext}}$ and denote the boundary of the hydrogen inlet, the tunnel entrance, and the tunnel exit, respectively. These apply to all three models. At the inlet, hydrogen leaks at a constant rate in the vertical direction. The velocity and the concentration are as follows:

$$\begin{aligned} u_1 = u_3 = 0\,[\mathrm{m/s}], \\ u_2 = 0.1 \text{ or } 0.67\,[\mathrm{m/s}] \quad \text{on } \Gamma_{\text{inlet}}, \\ C = 0.0694\,[-] \quad (= 6.94 \text{ mass\%}). \end{aligned} \tag{3.1}$$

The mass concentration C (=0.0694, or 6.94 by mass%) represents the density ratio between hydrogen and air. The derivation of this value comes from the conservation of hydrogen mass flow [13, 14]. The hydrogen flow velocity of $0.67\,\mathrm{m\,s^{-1}}$ and the inlet surface area of $0.04\,\mathrm{m^2}$ gives a flow rate of $0.0268\,\mathrm{m^3 s^{-1}}$, which is the flow velocity used in test HT-5 of [9]. At the tunnel exit, hydrogen and air are discharged outside freely. At the tunnel entrance, air enters at a constant velocity:

$$\begin{aligned} \sum_{j=1}^{3} \sigma_{ij} n_j = 0\ [\mathrm{m^2/s^2}], \\ a\frac{\partial C}{\partial n} = 0\,[\mathrm{m/s}] \quad \text{on } \Gamma_{\text{t\_ext}}, \\ u_1 = \text{variable}\,[\mathrm{m/s}], \\ u_2 = u_3 = 0\,[\mathrm{m/s}] \quad \text{on } \Gamma_{\text{t\_ent}}, \\ C = 0\,[-]. \end{aligned} \tag{3.2}$$

The other boundaries are effectively non-slip walls, with no inflow or outflow of hydrogen and/or air:

$$\begin{aligned} &u_1 = u_2 = u_3 = 0\ [\mathrm{m/s}] \\ &a\frac{\partial C}{\partial n} = 0\,[\mathrm{m/s}] \end{aligned} \qquad \text{on } \partial\Omega - (\Gamma_{\text{inlet}} + \Gamma_{\text{t\_ent}} + \Gamma_{\text{t\_ext}}). \tag{3.3}$$

The initial conditions are as follows:

$$\begin{aligned} &u_1 = u_2 = u_3 = 0\,[\mathrm{m/s}] \\ &C = 0\,[-] \end{aligned} \qquad \text{in } \Omega. \tag{3.4}$$

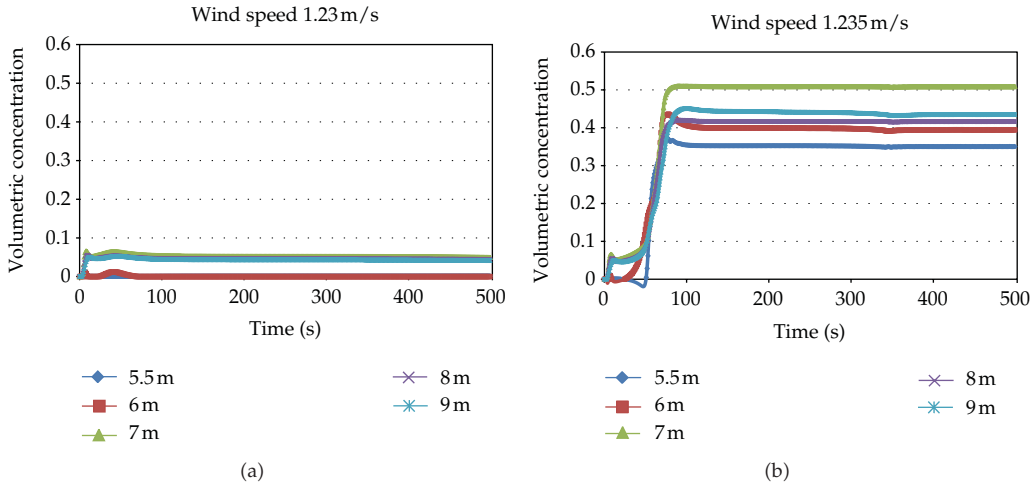

Figure 5: Model 1: plots of volumetric concentration versus time for wind speed 1.23 and 1.235 m s^{-1}.

The numerical parameters are the kinematic viscosity of hydrogen (1.05×10^{-4} [m^2/s]), the diffusion coefficient of hydrogen in air (6.1×10^{-5} [m^2/s]), the analogous coefficient of buoyancy (13.4 [−]), gravity (0, −9.8, 0 [m/s^2]), and the source term (0 [1/s]).

The same mesh density was used for all three tunnel models. This resulted in Model 1 having 100,432 elements (98,715 degrees of freedom), Model 2 with 206,462 (190,580), and Model 3 with 443,695 (391,285). The timestep used was 1 second; this timestep-mesh size combination was determined based on our experience with previous models. Models 1 and 2 were run to 500 s. Steady-state flow was achieved in most cases.

4. Results and Discussion

Model 1 was computed for air inlet velocities ranging from 0.7 to 3 m s^{-1}. Steady-state flow downstream of the hydrogen inlet was observed for all the computations, indicating (but not guaranteeing) that for these models and their respective boundary conditions and numerical parameters, stable flow was reached and therefore the meshsize-timestep combination used was appropriate.

As the wind speed is increased, the computed concentration values tend to drop as expected, but from 1 to 2 m s^{-1}, the concentration values increase suddenly and by almost an order of magnitude. From 2 m s^{-1} and above, the concentration values remain high throughout. Further computations were conducted with wind speeds between 1 to 2 m s^{-1}, and the change in trend was found to have occurred with a mere 0.005 m s^{-1} increase in wind speed (1.23 to 1.235 m s^{-1}). The volumetric concentration profiles at 5 positions measured from the tunnel inlet (Figure 2(a)) of Model 1 for wind speeds 1.23 and 1.235 m s^{-1} are given in Figure 5.

Reverse flow of hydrogen gas (i.e., against the flow of air) was not observed in concentration isosurface plots of the computed models. This indicates that the critical velocity, where the wind speed is sufficient to ensure no reverse flow occurs, is 0.7 m s^{-1} or below for this tunnel configuration.

Figures 6(a)–6(f) show combined velocity vector and concentration isosurface plots for wind speeds 1.23 and 1.235 m s^{-1} at time = 100 s, when steady-state flow has already been

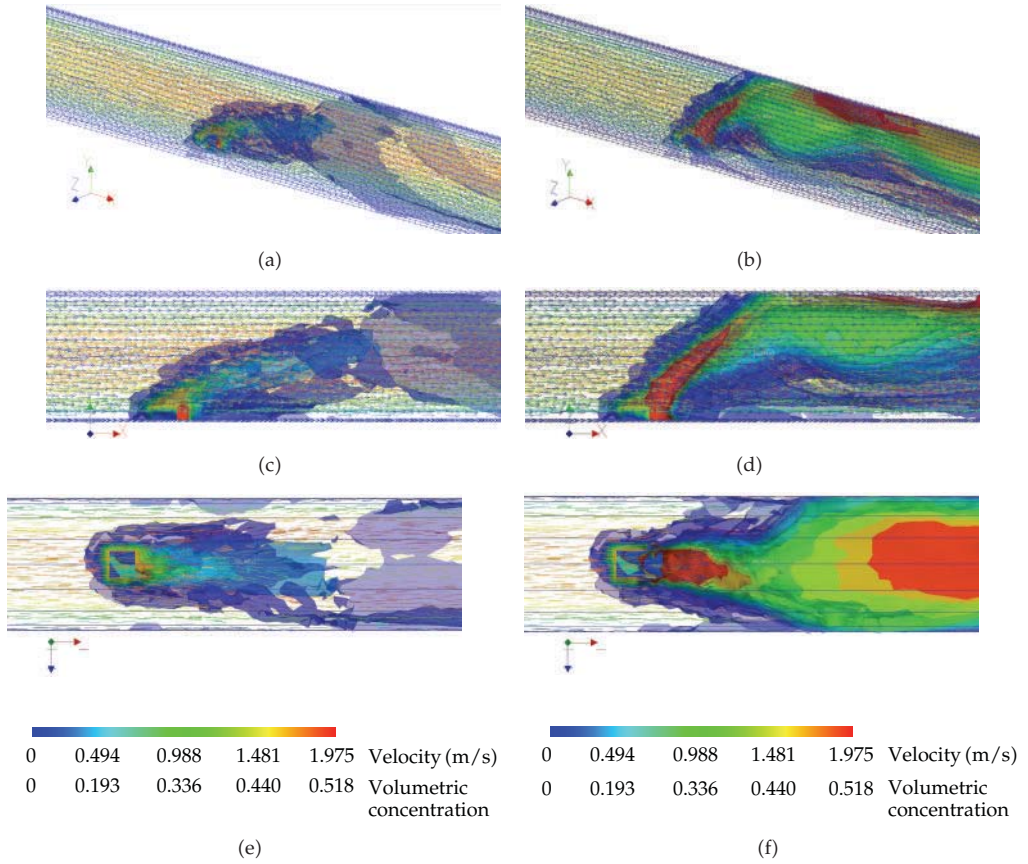

Figure 6: Model 1: combined velocity vector and concentration isosurface plots for wind speeds 1.23 (a, c, e) and 1.235 m s^{-1} (b, d, f) at 100 s elapsed time. The colour plot applies to all 6 figures. (a, b) Orthogonal view. (c, d) Side view. (e, f) Top (plan) view.

reached. Comparing these two, it can be seen that the flow pattern differs significantly: for wind speed 1.23 m s^{-1}, air tends to flow through the hydrogen plume, whereas for the higher wind speed, air tends to flow around the plume. In other words, hydrogen-air mixing is greater at the slower speed than at the higher one. At higher wind speeds, hydrogen "brushes past" the hydrogen plume, and entrainment of hydrogen by air takes place. The existence of threshold values when using CFD to compute this type of flow has been identified. In addition, and as a result of this, the possibility of hydrogen and air mixing at different rates due to different velocities has also been shown.

The volumetric concentration profiles at 5 positions measured from the tunnel inlet (Figure 2(b)) of Model 2 are given for air inlet velocities within the range of 0.7 to 0.95 m s^{-1} in Figure 7.

Some of the hydrogen concentration values obtained for Models 1 and 2 are very high—up to 0.5 (50%) for Model 1 and 0.11 (11%) for Model 2. However, it should be noted that these models have dimensions and boundary conditions that are unrealistic, and therefore the computed results are not truly representative of the concentrations that might occur in situations involving real tunnels.

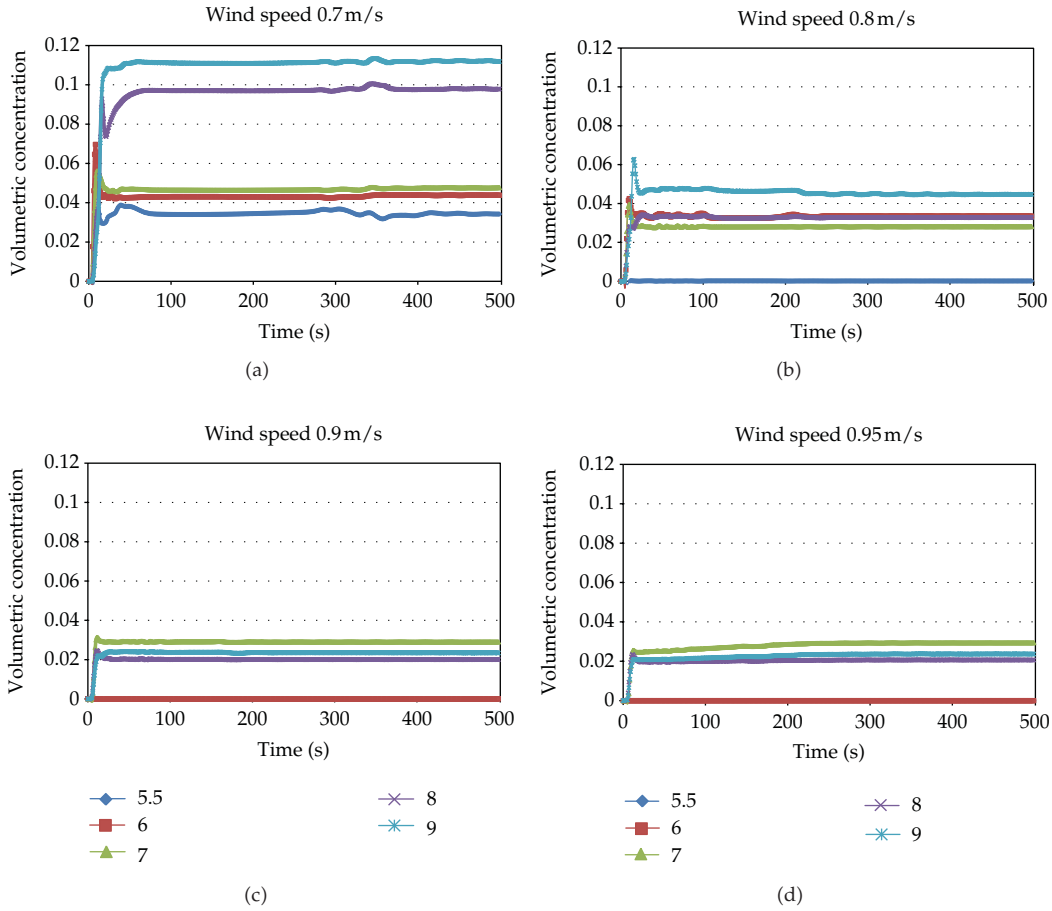

Figure 7: Model 2: volumetric concentration versus time for wind speeds 0.7 to 0.95 m s^{-1}.

The last model (Model 3) was run at a fixed wind speed of 0.26 m s^{-1}. Two hydrogen inlet velocities were used—0.1 and 0.67 m s^{-1}. The value for wind speed was chosen because (i) results of Model 2 hinted that larger cross sectional areas might allow for slower wind speeds, and (ii) 0.26 m s^{-1} was the value used in [9]. Model 3 with 0.1 m s^{-1} was used to study the effects of the boundary condition settings on the computation; the value of 0.1 was chosen because previous experience indicated that this was the "optimal" value for trial purposes given the other settings. The other hydrogen inlet value, 0.67 m s^{-1}, resulted in the same volume flow used in [9]. In this work, two boundary condition settings were explored: the relaxing of non-slip conditions in the mean direction of flow and the introduction of an additional boundary condition at the tunnel exit. Wall boundary conditions with no slip are expressed below:

$$\begin{aligned} u_1 = u_2 = u_3 &= 0\ [\mathrm{m/s}] \\ a\frac{\partial C}{\partial n} &= 0\ [\mathrm{m/s}] \end{aligned} \qquad \text{on } \partial\Omega - (\Gamma_{\text{inlet}} + \Gamma_{t_{\text{ent}}} + \Gamma_{t_{\text{ext}}}). \tag{4.1}$$

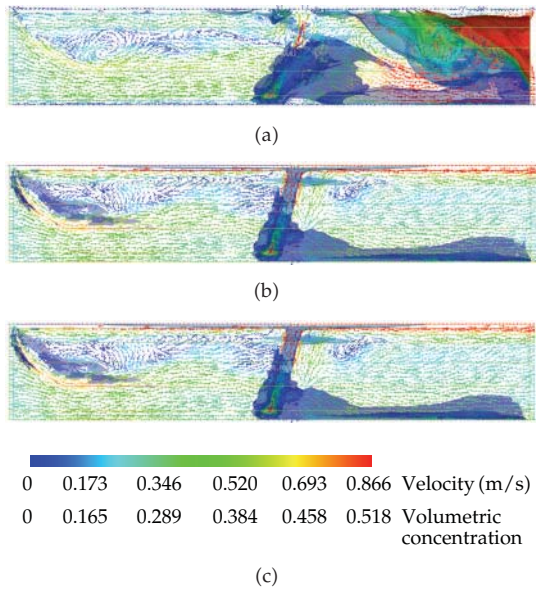

Figure 8: Combined velocity vector and isosurface plots for Model 3 at $t = 55$ s. From top to bottom: boundary conditions as per Section 3 (base settings), slip in the x-direction, slip in the x-direction and $C = 0$ at the tunnel outlet. The colour bar applies to all three figures.

Slip in the direction of mean flow (i.e., the x-direction) is implemented by removing the essential (Dirichlet) boundary condition $u_1 = 0$ from the tunnel walls:

$$\begin{aligned} &\sum_{j=1}^{3} \sigma_{1j} n_j = 0 \left[\mathrm{m}^2/\mathrm{s}^2\right] \\ &u_2 = u_3 = 0 \left[\mathrm{m/s}\right] \qquad \text{on } \partial\Omega - (\Gamma_{\text{inlet}} + \Gamma_{\text{t\_ent}} + \Gamma_{\text{t\_ext}}). \\ &a\frac{\partial C}{\partial n} = 0 \left[\mathrm{m/s}\right] \end{aligned} \tag{4.2}$$

The second condition is attempted by setting $C = 0$ at $\Gamma_{\text{t\_ext}}$:

$$\begin{aligned} &\sum_{j=1}^{3} \sigma_{ij} n_j = 0 \left[\mathrm{m}^2/\mathrm{s}^2\right] \qquad \text{on } \Gamma_{\text{t\_ex}}. \\ &C = 0 \left[\text{mass\%}\right] \end{aligned} \tag{4.3}$$

This setting was used in the hallway model in [13, 14] to simulate air inflow conditions. Both these conditions are believed to have little or no effect on the mean flow pattern.

Figure 8 compares the flow patterns of Model 3 at a hydrogen inlet speed of 0.1 m s^{-1} at three settings—base, slip in the direction of mean flow, and slip in the direction of mean flow combined with $C = 0$ at the tunnel exit—at 55 seconds. Figure 9 compares slip in the

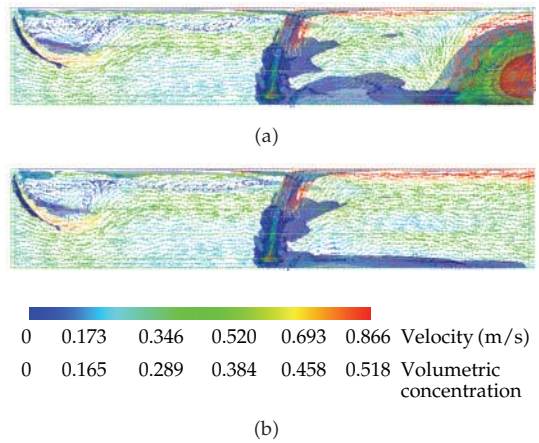

Figure 9: Combined velocity vector and isosurface plots for Model 3 at $t = 127$ s. (a) Slip in the x-direction, (b) slip in the x-direction and $C = 0$ at the tunnel outlet. The colour bar applies both figures.

direction of mean flow and slip in the direction of mean flow combined with $C = 0$ at the tunnel exit at 127 seconds.

We see from Figures 8 and 9 that the upstream flow pattern is the same. The similarity of the flow patterns for all three cases indicate that the changes made to the boundary conditions have little effect on the flow, as believed.

Figure 10 shows a graph of concentration versus time at 6 sensor positions (see Figure 4) for $C = 0$—slip conditions in the direction of mean flow and the hydrogen inlet velocity at 0.67 m s^{-1}—this velocity is the same as the target model in [9]. Steady-state flow was not achieved, unlike Models 1 and 2. However, as mentioned previously, Model 3 has been shortened to 10 metres as compared to 78.5 m in [9]; due to this, we only simulate the early stages of the flow. Hydrogen is first detected in order of sensor distance from the hydrogen inlet, with the exception of sensors at 0 m and 1 m, where the sensor at 1 m picks up hydrogen first. This indicates that, unlike Models 1 and 2, reverse flow has occured, probably due to the low wind speed relative to the hydrogen inlet velocity. Reverse flow was also observed in Model 3 with 0.1 m s^{-1} hydrogen inlet velocity (Figure 9); both models show the same flow patterns, but higher velocity magnitudes are observed with 0.67 m s^{-1}, as expected. The concentration values appear to stabilize at around 0.1 volume concentration. We find that overall, the concentration values obtained for the first 50 seconds are slightly higher than the values suggested in [9]. Longer run times are required to observe the development of concentration profiles within the tunnel; however, this can only be carried out if the tunnel length itself is lengthened or special boundary conditions, as yet undetermined, are applied at the tunnel entrance and exit.

Due to the short run time (50 s) and shortened length of the tunnel, the results obtained here cannot be compared directly with the experimental results given in [9]. The concentration values shown in [9] were taken at 3 points in time when the flow through the tunnel was steady, as opposed to the results shown in Figure 10 (where the flow is clearly unsteady). Nonetheless, it is seen that the computed results, which average around 0.1, or 10%, compare somewhat favourably with the experimental results, which are around 0.03 to 0.07 (3–7%) in the first 5 meters downstream of the hydrogen inlet despite the difference in flow regimes.

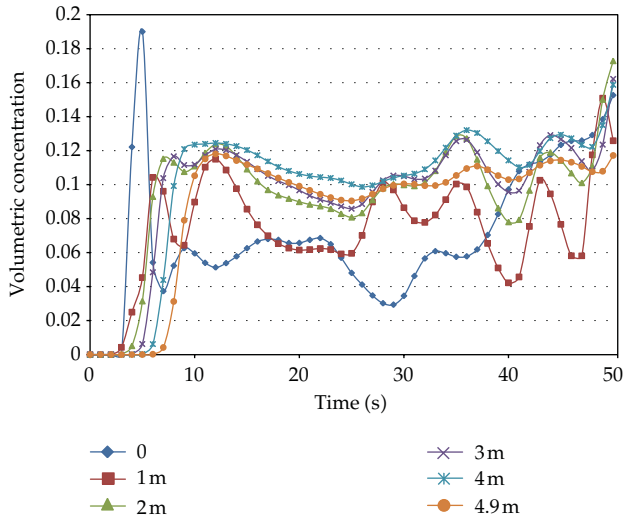

Figure 10: Hydrogen volumetric concentration versus time for Model 3 (hydrogen inlet velocity of 0.67 m s^{-1}) at 6 sensor positions, having slip in the x-direction, and $C = 0$ at the tunnel exit.

5. Conclusions

In this work, we have investigated the effect of wind speed and tunnel geometry on the flow and dispersion of hydrogen within tunnel structures. Our work has suggested the existence of "threshold," or perhaps "limiting" values with regard to CFD modeling of tunnel structures, in this case related to the wind speed. Large variations in entrainment and the rate of hydrogen-air mixing occur when these threshold values (i.e., wind speeds) are crossed. In addition, our findings imply that a change in tunnel cross-sectional area can affect change in the flow pattern within the tunnel, even if all other parameters are maintained. This has implications in the CFD modelling of such structures, as the appropriate computational settings and even boundary conditions have to be reconfirmed.

In this work, we have tested two methods: removal of the non-slip condition in the direction of mean flow, and setting $C = 0$ at the tunnel outlet, and we found that both enable solutions to converge for longer simulation times without changing the mean flow pattern. More work must be done to verify that these findings are applicable to any tunnel structure that is analyzed with CFD. The possibility that other "threshold" values might exist for other variables at certain mesh densities should also be studied. We plan to investigate these in the future.

References

[1] M. R. Swain, E. S. Grilliot, and M. N. Swain, "Risks incurred by hydrogen escaping from containers and conduits," Tech. Rep. NREL/CP-570-25315, NREL, 1998, in *Proceedings of the US DOE Hydrogen Program Review*.

[2] M. R. Swain, P. Filoso, E. S. Grilliot, and M. N. Swain, "Hydrogen leakage into simple geometric enclosures," *International Journal of Hydrogen Energy*, vol. 28, no. 2, pp. 229–248, 2003.

[3] M. Inoue, H. Tsukikawa, H. Kanayama, and K. Matsuura, "Experimental study on leaking hydrogen dispersion in a partially open space," *Journal of Hydrogen Energy Systems Society of Japan*, vol. 33, no. 4, pp. 32–43, 2008 (Japanese).

[4] K. Matsuura, H. Kanayama, H. Tsukikawa, and M. Inoue, "Numerical simulation of leaking hydrogen dispersion behavior in a partially open space," *International Journal of Hydrogen Energy*, vol. 33, no. 1, pp. 240–247, 2008.
[5] K. Matsuura, "Effects of the geometrical configuration of a ventilation system on leaking hydrogen dispersion and accumulation," *International Journal of Hydrogen Energy*, vol. 34, no. 24, pp. 9869–9878, 2009.
[6] K. Prasad, W. Pitts, and J. Yang, "Effect of wind and buoyancy on hydrogen release and dispersion in a compartment with vents at multiple levels," *International Journal of Hydrogen Energy*, vol. 35, no. 17, pp. 9218–9231, 2010.
[7] HYSAFE, "Deliverable D113 Initial Guidance for Using Hydrogen in Confined Spaces—Results from InsHyde," Version 1.1, 2009.
[8] S. Mukai, J. Suzuki, H. Mitsuishi, K. Oyakawa, and S. Watanabe, "CFD simulation on diffusion of leaked hydrogen caused by vehicle accident in tunnels," in *Proceedings of the International Conference on Hydrogen Safety (ICHS '05)*, pp. 8–10, Pisa, Italy, September 2005.
[9] Y. Sato, E. Merilo, M. Groethe et al., "Hydrogen release deflagrations in a sub-scale vehicle tunnel," in *Proceedings of the 16th World Hydrogen Energy Conference*, Lyon, France, June 2006.
[10] W. Breitung, U. Bielert, G. Necker, A. Veser, F. J. Wetzel, and K. Pehr, "Numerical simulation and safety evaluation of tunnel accidents with a hydrogen powered vehicle," in *Proceedings of the 13th World Hydrogen Energy Conference*, Beijing, China, June 2000.
[11] P. Middha and O. R. Hansen, "CFD simulation study to investigate the risk from hydrogen vehicles in tunnels," *International Journal of Hydrogen Energy*, vol. 34, no. 14, pp. 5875–5886, 2009.
[12] The ADVENTURE project, http://adventure.sys.t.u-tokyo.ac.jp/.
[13] H. Kanayama, H. Tsukikawa, and I. Ismail, "Simulation of hydrogen dispersion by the domain decomposition method," *Japan Journal of Industrial and Applied Mathematics*, vol. 28, pp. 43–53, 2011.
[14] H. Kanayama, H. Tsukikawa, S. B. Ndong-Mefane, and O. Sakuragi, "Finite element simulation of hydrogen dispersion by the analogy of the Boussinesq approximation," *Journal of Computational Science and Technology*, vol. 2, no. 4, pp. 643–654, 2008.

Hindawi Publishing Corporation
Journal of Applied Mathematics
Volume 2012, Article ID 420195, 13 pages
doi:10.1155/2012/420195

Research Article

Evaluation of Congestion Relief Proposals in a Capital City

Sudhir C. Fowdur and Soonil D. D. V. Rughooputh

Department of Physics, University of Mauritius, Port Louis 742CU001, Mauritius

Correspondence should be addressed to Sudhir C. Fowdur, chetanfowdur@yahoo.com

Received 28 December 2011; Revised 12 February 2012; Accepted 26 February 2012

Academic Editor: Shuyu Sun

This paper aims at analyzing three different solutions suggested for traffic congestion relief in Port Louis, the busiest city of Mauritius. It evaluates the impact of the three alternatives which are the use of Light Rail Transit (LRT) as an alternative mode of transport, the construction of a Ring road around Port Louis, and the upgrading of the current bus network into a Bus Rapid Transit (BRT) system. The impact of these three solutions has been evaluated by performing Traffic Cellular Automata (TCA) simulations. Our studies reveal that the Ring road will lead to more congestion while introducing the LRT or upgrading the current bus network will reduce congestion significantly.

1. Introduction

Traffic congestion is a condition on road networks which occurs as their use increases. It is characterized by slower speeds, longer trip times, and increased vehicular queuing. Mauritius is an island located in the Indian Ocean with a land area of 1865 km^2. At end of 2010, the population of the Republic of Mauritius stood at 1,283,415. The total road length on the island is of 2066 km. The motorization rate in Mauritius is of 230 and is likely to reach around 350 by the next decade [1]. In Mauritius the congestion cost has been evaluated to be around USD 0.1 billion per year [2]. Increased congestion also implies increased emission of Greenhouse gases (GHG). In 2010, 1323.8 thousand tons of GHG was emitted by the transport sector in Mauritius out of which 1261.2 thousand tons consisted of CO_2. The transport sector contributes 31.9% of the total CO_2 emission in Mauritius. Congestion is now common in both the rural and urban parts of the island. However, the Curepipe-Port Louis corridor, which accounts for nearly one-third of trips, remains the segment of greatest concern.

Traffic simulation techniques are now widely used throughout the world by road traffic planners and engineers to assist in decision making. Simulation in transportation is important because it can study models too complicated for analytical or numerical treatment, can be used for experimental studies, can study detailed relations that might be lost in analytical or numerical treatment, and can produce attractive demos of present and future scenarios. Traffic Cellular Automata (TCA), in recent years, has turned out to be an excellent tool for the simulation of large-scale traffic networks [3–5]. TCA models have been applied in Germany to develop a traffic information system for the freeway traffic in North Rhine-Westphalia, the most populous German state [5]. TCA models have also been used in Belgium for improving current and future traffic conditions [6]. Till now no study of traffic using computer simulations has been carried out in Mauritius [1].

In our work, TCA has been applied to assess the impact of three proposals for reducing the congestion level along the Curepipe-Port Louis corridor. The increased demand for passenger transportation in and around urban areas and the resulting traffic congestion have led many cities to build rapid transit systems and new conventional railway lines [7]. Two proposals from the government are the construction of a Ring road around Port Louis and the introduction of a Light Rail Transit (LRT) system. An additional proposal which we are putting forward is the upgrading of the current bus network in the region to a Bus Rapid Transit (BRT). Previous researchers have attempted to analyse the impact of a transit network for bus and LRT on various transit networks around the world. The simulations in our model have been performed using a multicell TCA model that includes anticipation and probability randomization. Our results indicate that while the Ring road will bring more congestion to traffic flow, the introduction of the LRT or the upgrading of the current bus network will lead to less congested traffic. This paper is organized as follows. Section 2 gives an overview of the region under study and the road network being considered. The methodology employed to implement the simulation model has been explained in Section 3. Section 4 provides the results and discussions. Finally, Section 5 gives the conclusions.

2. Region under Study

Figure 1 shows the road network in Mauritius [6]. The Port Louis to Curepipe corridor (M1) is heavily congested during the morning and afternoon peaks as persons move from their home to workplace and back. An origin-destination survey [8] revealed that 46% of trips amounted to through traffic which only bypassed Port Louis. 25% of traffic enters from the northern region while 21% enters from the southern region.

3. Methodology

3.1. Traffic Cellular Automata

TCA falls in the category of microscopic models which in particular has been very successful in simulating dense networks like cities. The model we implemented in our simulator has been adapted from that proposed by Hafstein et al. [5] which in turn was inspired by the one proposed by Nagel and Schreckenberg [9]. The differences between our model and the one implemented by Nagel and Schreckenberg are as follows:

(i) the model uses smaller cells of length 1.5 m,

(ii) a slow-to-start rule [10] has been applied,

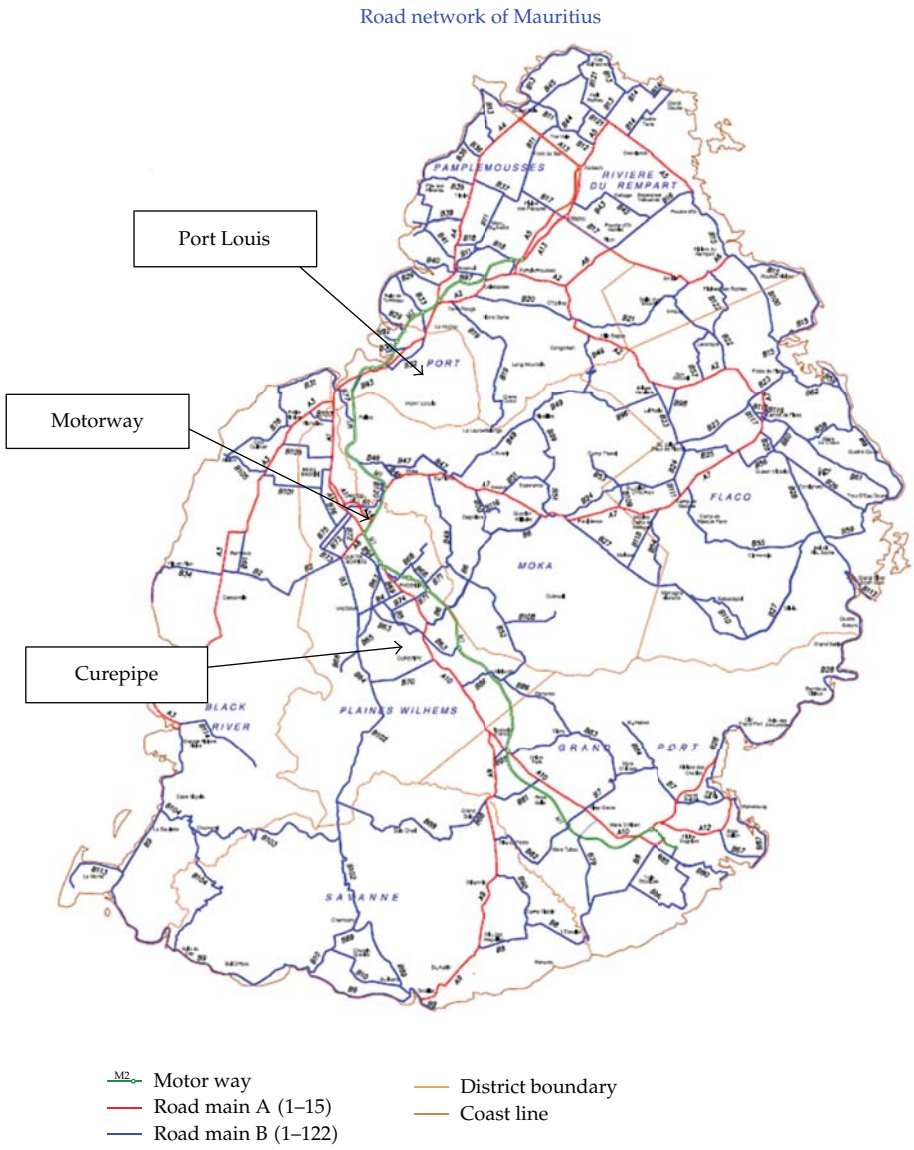

Figure 1: Road network map of Mauritius [6].

(iii) the model includes anticipation [4],

(iv) two classes of vehicles are used. Passenger cars occupy 4 cells while vans, lorries and buses (VLB) occupy 6 cells. The maximum speed of cars is of 17 cells/second (90 km/h) while that of VLB is of 10 cells/second (50 km/h).

Consider three vehicles n, m, and l occupying consecutive positions as shown in Figure 2. The different steps used for vehicle movement can be summarized as follows.

Step 1. Read the values of $v_m(t)$, $d_{n,m}(t)$, and $d_{m,l}(t)$; $v_m(t)$ is the speed of vehicle m, $d_{n,m}(t)$ is the distance between n and m, $d_{m,l}(t)$ is the distance between m and l.

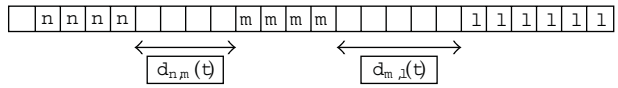

Figure 2: Segment of road occupied by 3 vehicles.

Step 2. Calculate $v^{\min}(t)$ and $d_{\text{eff}}(t)$:

$$\begin{aligned} v^{\min}(t) &= \min(d_{m,l}(t), v_m(t) - 1), \\ d_{\text{eff}}(t) &= d_{n,m}(t) + \max\ v^{\min}(t) - d_s, 0 \end{aligned} \tag{3.1}$$

where d_s is the safety distance taken as 6 cells in our model.

Step 3. Compare d_{eff} to $v_n(t)$.
If $v_n(t) < d_{\text{eff}}$, then

$$v_n(t+1) = \min(v_n(t) + 1, v_{\max}). \tag{3.2}$$

Else $v_n(t+1) = d_{n,m}(t)$.

Step 4 (Probability Randomization). With probability $p = 0.1$, the velocity of each vehicle (if greater than zero) is decreased by one.

Step 4 introduces a slowdown probability parameter. At each time step there is a probability p that all vehicles will slow down to $v_i(t) - 1$. Step 4 introduces the slow-to-start condition whereby at every time step some stopped vehicles have to wait longer before they can continue their journey. This rule introduces individual velocity fluctuations due to delayed acceleration (imperfect driving). Delayed acceleration is a condition generally observed in traffic flow. Vehicle movement is updated in parallel at every time step which makes the model collision-free. At every time step the speed of each individual vehicles can increase by 1 cell/second. This implies that accelerating vehicles have a maximum acceleration of $5.4\,\text{ms}^{-2}$. A more detailed description of the model can be obtained from Fowdur and Rughooputh [11]. In our simulations we restrict to the afternoon peak congestion which is the most severe one in terms of the journey duration.

3.2. Simulation Parameters

3.2.1. The Actual Network

The actual flow of traffic in Port Louis consists of vehicles entering the motorway M1 from Quay D and vehicles generated within Port Louis. Incoming traffic from the North merges with traffic generated within Port Louis and exits Port Louis towards the South. Figure 3 shows the region concerned with the study.

Incoming traffic enters Port Louis at the Quay D roundabout on the M1 as from B30 junction and merges with traffic after 1.1 km (730 cells). The length of the exit road is considered up to the proposed entry point of the Ring Road. An arbitrary number of 300 cells,

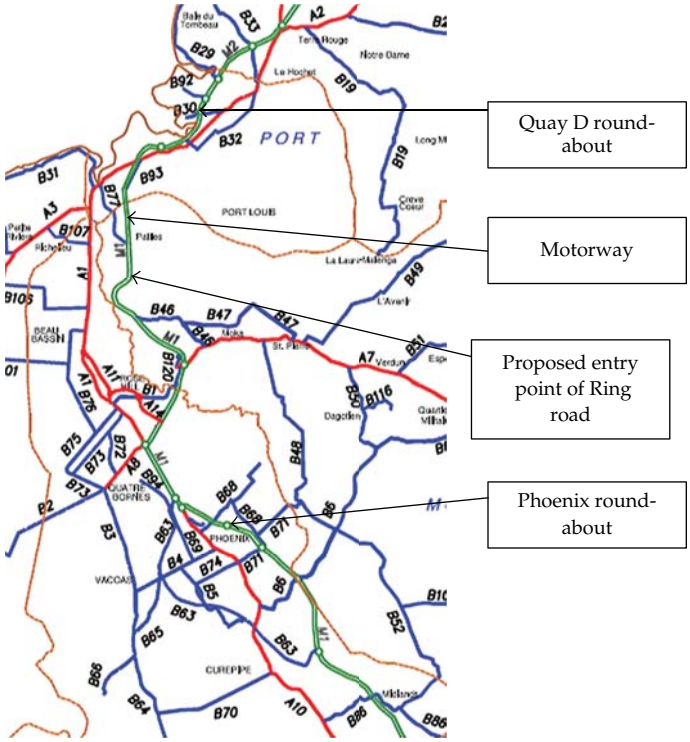

Figure 3: Region under study.

representing a road stretch of 450 m has been assigned to the street from which vehicles merge with those from the North. The implementation of the cellular automata model has been represented in Figure 4.

3.2.2. The Ring Road

The Ring road is a proposed track linking the Quay D roundabout to the motorway at Pailles. The main aim of the Ring road is to provide an alternative path for the actual through traffic in Port Louis. It further aims, through additional entry points, to provide an alternative path for vehicles within Port Louis to leave. Figure 5 shows the track of the Ring road [12].

The length of the Ring road is 10.6 km. Cellular automata implementation of the Ring road will consist of a street of length 7000 cells linking the Quay D roundabout to the motorway. It is estimated that the safe driving speed over it would be around 70 km/h.

3.2.3. The LRT

The LRT has been described as one of the centrepieces of the integrated transport system for Mauritius [6]. Covering a distance of some 25 km, the LRT will have some 13 stations, mainly located in town centres along the route where existing transport terminals already exist. The end-to-end journey time would be approximately 32 minutes and carriages would be air-conditioned, to ensure maximum attraction of car users. Headways would vary by time of

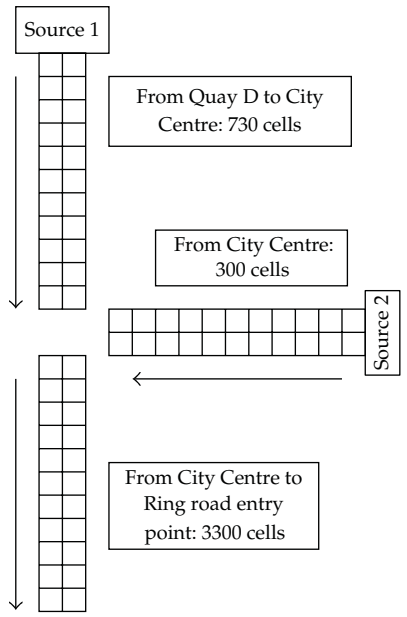

Figure 4: Cellular automata implementation of road network.

Figure 5: Proposed path of Ring road [12].

Table 1: Operating characteristics of the LRT [6].

Characteristic	
Length of line	24.9 km
Average time at stops	20 seconds
Number of stops (stations)	13 stations
Journey time, one way	32 minutes
Time round trip	70 minutes
Commercial speed	43 km/h
Peak train frequency	12 per hour
Vehicle capacity	250 per unit (500 per train)
Vehicle length	30 m per unit (running two units)
Vehicle width	2.65 m
Seating % full	25–30%
Peak pax capacity	6000 per hour/direction
Predicted traffic	93,000 pax (year 2006/working day)
Vehicle required	28 units, 14 trains
Total vehicle required	31 units

day, but are expected to be of the order of 5 minutes in peak periods. Access to stations would be by an integrated system of comfortable and reliable feeder buses [6]. The operating characteristics of the LRT system are summarised in Table 1.

If the LRT is implemented, the road network will remain similar to that of Section 3.2.1 since the LRT network will be an independent one and will not interfere with the current network. In our work we investigate the effect of commuters gradually shifting to the LRT. We independently investigate the effect of 20%, 40%, 60%, 80%, or 100% of commuters choosing the LRT. In such a case, the traffic entering Port Louis from the North will remain the same since the LRT is not being extended to the northern part of the island. However, the traffic generated within Port Louis will decrease since commuters are now expected to use the LRT to travel from Port Louis to Curepipe.

3.2.4. Transition to Bus Network

Here we consider a BRT without any dedicated lane for buses. Hence the road network will remain similar to that of Section 3.2.1. In this case the number of cars both entering Port Louis from the North and generated within Port Louis will decrease. However, an increase in the number of buses will be observed at the expense of cars. It has been estimated that one bus will replace 30 cars. This will lead to a change of the ratio of cars to buses from the actual 8 : 1 to around 3 : 2. Similar to our investigation of the LRT, we investigate the effect if 20%, 40%, 60%, 80%, or 100% commuters gradually shift to the BRT.

4. Results and Discussion

4.1. Maximum Number of Persons Displaced

The three proposed solutions which are the Ring road, the LRT, and the transition to a bus network were compared based on travel times, the maximum number of persons displaced,

Table 2: Total number of vehicles leaving each street.

Simulation	Quay D	Port Louis Centre	Exit at Ring road entry point			
			Cars	Buses	HGV	Total
Actual	1224	1194	1934	242	242	2418
Ring road	491	1826	1925	240	240	2388
LRT20	1316	1050	1886	240	240	2372
LRT40	1472	896	1942	240	240	2426
LRT60	1640	724	1884	240	240	2372
LRT80	1836	554	1910	240	240	2372
LRT100	1996	394	1890	240	240	2380
BRT20	1032	1032	1548	276	240	2066
BRT40	902	902	1160	404	240	1798
BRT60	716	722	776	588	240	1600
BRT80	656	656	388	684	240	1308
BRT100	514	514	0	788	240	1024

and the total number of vehicles entering and leaving each road. The hourly number of vehicles exiting the Quay D, the Port Louis Centre, and the exit at the Ring road entry point is summarised in the Table 2. The terms LRT20, LRT40, LRT60, LRT80, and LRT100 correspond to 20%, 40%, 60%, 80% and 100% of commuters shifting to the LRT, respectively. While the terms BRT20, BRT40, BRT60, BRT80, and BRT100 correspond to 20%, 40%, 60%, 80% and 100% of commuters shifting to the BRT, respectively.

In the actual case, the ratio of cars to buses and Heavy Goods Vehicles (HGV) is of 8 : 1 : 1. The number of passengers per car can be estimated to be 1.5. We can therefore estimate the number of persons displaced per hour as follows:

$$\begin{aligned} &\text{number of persons displaced by car} = 2418 \times 0.8 \times 1.5 = 2902, \\ &\text{number of persons displaced by bus} = 2481 \times 0.1 \times 40 = 9672. \end{aligned} \tag{4.1}$$

The number of heavy goods vehicle (HGV) is of around 240 per hour. HGV's have not been taken into account for the calculation of the number of persons displaced since they are not concerned with public transportation. The maximum number of persons that can be displaced is summarised in the Figure 6.

It is observed that the LRT will be useful only if it can attract at least 60% of users. For the bus transition even if only 20% of users shift to it, the maximum number of users that can use the network will be higher than in the actual case. For the case where more people shift to the BRT, even larger number of persons can be displaced making the option sustainable for future trends.

4.2. Travel Time Analysis

The travel times obtained in the different simulations form the Quay D to the entry point of the Ring road are given in Figures 7 and 8.

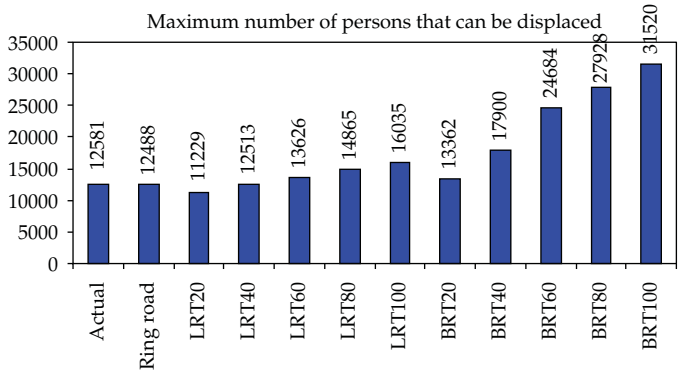

Figure 6: Maximum number of persons displaced.

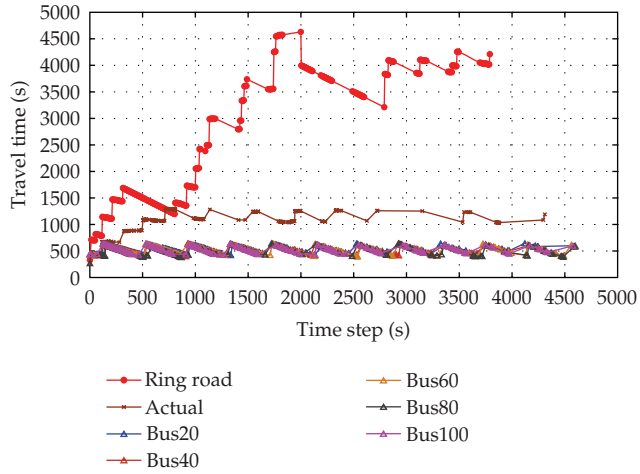

Figure 7: Travel time from Quay D to proposed Ring road entry point for the BRT.

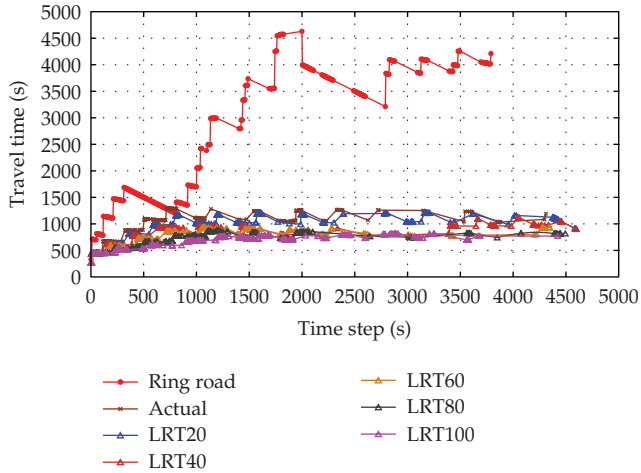

Figure 8: Travel time from Quay D to the proposed Ring road entry point with the LRT.

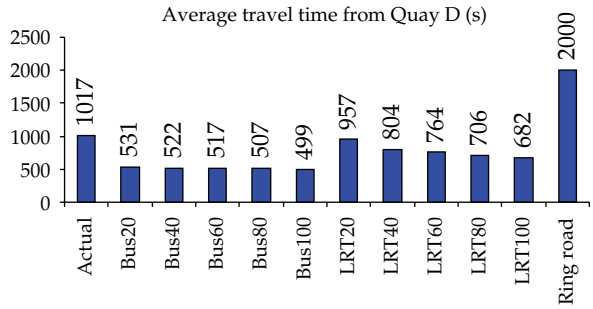

Figure 9: Average travel time from Quay D.

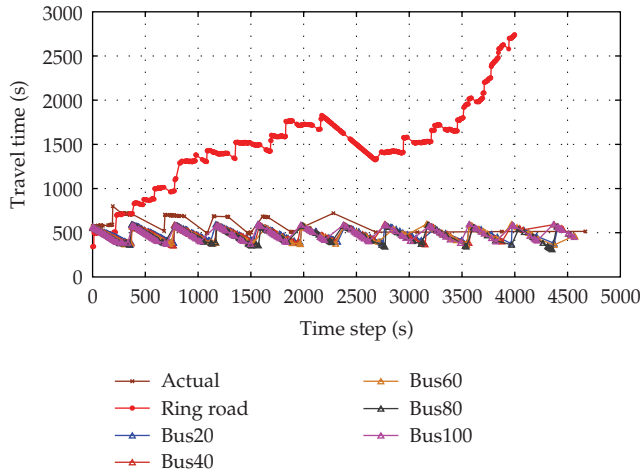

Figure 10: Travel time from the City Centre to proposed Ring road entry point for the BRT.

It is observed that with the BRT, a significant decrease in travel time is obtained. For the LRT, as drivers gradually shift to the LRT, the travel time decreases gradually. This effect can be further observed in Figure 9 which gives the average travel time from Quay D.

Figures 10 and 11 show the travel times obtained from the City Centre. In this case it is observed that the travel time from the City Centre for the BRT decreases while that for the LRT increases. The average travel times are given in Figure 12.

It is therefore observed that with the Ring road, there is a significant increase in travel time for vehicles entering from Quay D as well as those joining the motorway from within Port Louis. The main reason for this is an additional delay introduced at the point where the Ring road merges with the motorway. The average travel time on the Ring road has been calculated to be of 2000 seconds (33.3 minutes) during peak congestion. This time is again far greater than the actual travel times.

With the LRT a decrease in travel time has been achieved for vehicles entering at the Quay D entry point. This has resulted from the fact that with the LRT traffic generated from within Port Louis will drop drastically. As expected, the larger the number of drivers shifting to the LRT, the greater will be the drop in traffic volume. Vehicles entering Port Louis will then face a smaller waiting time at the intersection with the road bringing traffic generated

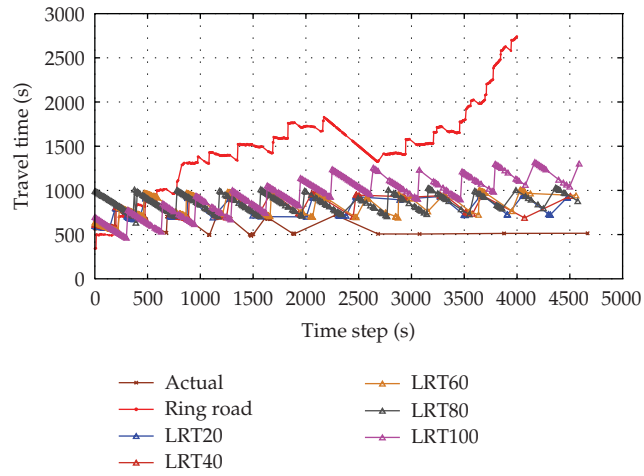

Figure 11: Travel time from the City Centre to proposed Ring road entry point for the LRT.

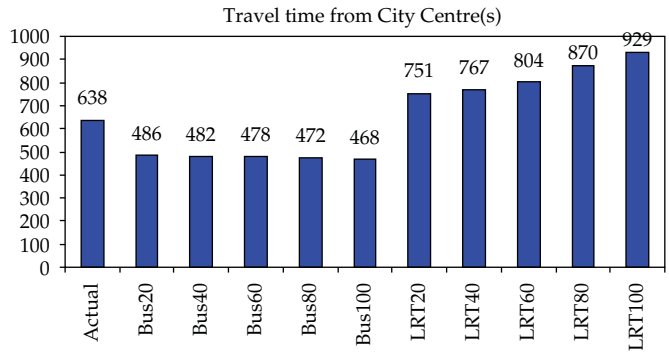

Figure 12: Average travel time from Quay D.

within Port Louis. However, vehicles leaving Port Louis are bound to experience a longer waiting time resulting in an increase in their travel time.

By the BRT a significant decrease in travel time is observed both for vehicles entering from Quay D and vehicles generated within Port Louis. As more drivers shift to the BRT, the travel time decreases gradually.

With the BRT40 the maximum number of persons displaced is greater than for the LRT100. The travel time form Quay D will decrease by 49% while with the LRT100 it will decrease by 33%. Travel time form the City Centre for the BRT 40 decreases by 24% while for the LRT100 it increases by 46%. Hence, in terms of travel time and maximum number of persons displaced, the BRT40 outperforms the LRT100.

4.3. Carbon Dioxide Emission Analysis

In this section we provide an analysis of the difference in the amount of CO_2 emitted by the three proposed solutions. In Mauritius the average CO_2 emissions from cars is of 158 g/km [6]. The amount of CO_2 emission from buses has been taken as 1015.4 g/km while the CO_2

Table 3: Hourly CO_2 emission from the 3 proposed solutions.

	Quay D to Ring road entry point			City Centre to Ring road rntry point			Ring road		Hourly CO_2 emission/tons
Simulation	Cars	Bus	CO_2/tons	Cars	Bus	CO_2/tons	Cars	CO_2/tons	
Actual	982	121	1.68	952	121	1.48	0	0	3.16
Ring road	116	121	0.85	908	121	1.44	880	1.46	3.75
LRT20	1074	121	1.77	808	121	1.35	0	0	3.32
LRT40	1232	121	1.92	656	121	1.22	0	0	3.34
LRT60	1400	121	2.08	484	121	1.08	0	0	3.36
LRT80	1596	121	2.26	314	121	0.93	0	0	3.39
LRT100	1756	121	2.42	154	121	0.79	0	0	3.41
BRT20	774	138	1.59	774	138	1.42	0	0	3.01
BRT40	580	202	1.79	580	202	1.60	0	0	3.39
BRT60	388	294	2.18	394	294	1.95	0	0	4.13
BRT80	194	342	2.28	194	342	2.04	0	0	4.32
BRT100	0	394	2.41	0	394	2.16	0	0	4.57

emission resulting from electricity generation for the LRT is of 2970.2 g/km [13]. Using these figures and data obtained from the simulations performed, the total amount of CO_2 emitted for each network has been calculated. Vehicles traveling from Quay D to the Ring road will cover a distance of 6.045 km while those coming from the City Centre will travel 5.400 km. Vehicles taking the Ring road will travel 10.500 km. Table 3 summarises the hourly amount of CO_2 emission from the different situations investigated.

Table 3 suggests that, compared to the actual case, a net improvement in the hourly CO_2 emission is achieved only by the BRT20. The emission of the LRT, however, compares favourably with BRT40.

5. Conclusions

The aim of this paper was to analyse three different solutions for traffic congestion relief in Port Louis. TCA simulations were performed to investigate the impact on travel time and the maximum number of persons that will be displaced in the three different alternatives. Our study has shown that Ring road option will not lead to any reduction in the congestion level at Port Louis. On the contrary it will lead to further congestion and will have higher CO_2 emissions compared to the actual case, the LRT and the BRT. This will be caused mainly by the fact that commuters using the ring road will travel an additional 5 km before reaching their destination and the additional delay created at the point where vehicles from the Ring road merge with the motorway. This second inconvenience will result in a decreased capacity of both the motorway and the Ring Road.

The LRT can be envisaged as a long-term solution because of its lower CO_2 emission. It, however, suffers from longer travel times and lower carrying capacity than the BRT. Thus, our studies reveal that the BRT40 can be set as the target that authorities should go for.

Acknowledgments

This work has been realised with the financial support of the Mauritius Research Council. The University of Mauritius is gratefully acknowledged for providing the necessary facilities and logistics for this work. The authors also wish to thank the anonymous reviewer for the valuable comments provided which helped to improve the work.

References

[1] GM (Government of Mauritius), 2011, http://www.gov.mu.
[2] MRDP (Mauritius Road Decongestion Program), 2011, http://www.mauritiustollproject.net/.
[3] B. Jia, R. Jiang, and Q. S. Wu, "A realistic two-lane cellular automaton model for traffic flow," *International Journal of Modern Physics C*, vol. 15, no. 3, pp. 381–392, 2004.
[4] C. Mallikarjuna and K. R. Rao, "Cellular Automata model for heterogeneous traffic," *Journal of Advanced Transportation*, vol. 43, no. 3, pp. 321–345, 2009.
[5] S. F. Hafstein, R. Chrobok, A. Pottmeier, M. Schreckenberg, and F. C. Mazur, "A high-resolution cellular automata traffic simulation model with application in a freeway traffic information system," *Computer-Aided Civil and Infrastructure Engineering*, vol. 19, no. 5, pp. 338–350, 2004.
[6] MFG (Ministry of Flemish Government), Design mobility plan Flanders, Brussels, Belgium, 2001, http://viwc.lin.vlaanderen.be/mobiliteit/.
[7] L. Gilbert, M. Angel, A. M. Juan, and P. Federico, "Designing robust rapid transit networks with alternative routes," *Journal of Advanced Transportation*, vol. 45, no. 1, pp. 54–65, 2011.
[8] Origin Destination Survey For Port Louis, 2004.
[9] K. Nagel and M. Schreckenberg, "A cellular automaton model for freeway traffic," *Journal de Physique I*, vol. 2, no. 12, pp. 2221–2229, 1992.
[10] R. Barlovic, L. Santen, A. Schadschneider, and M. Schreckenberg, "Metastable states in cellular automata for traffic flow," *European Physical Journal B*, vol. 5, no. 3, pp. 793–800, 1998.
[11] C. Fowdur and S. D. D. V. Rughooputh, "Traffic cellular automata simulation of a congested roundabout in mauritius," *International Journal of Modern Physics C*, vol. 20, no. 3, pp. 459–468, 2009.
[12] http://www.gov.mu/portal/goc/file/Mauritius_web.pdf.
[13] AEA Group, "Carbon Footprinting of Policies," Programmes and Projects, Oxfordshire, 2009.

Hindawi Publishing Corporation
Journal of Applied Mathematics
Volume 2012, Article ID 857824, 12 pages
doi:10.1155/2012/857824

Research Article

GMM Estimator: An Application to Intraindustry Trade

Nuno Carlos Leitão

Polytechnic Institute of Santarém and CEFAGE, Évora University, Complexo Andaluz Apt. 295, 2001-904 Santarém, Portugal

Correspondence should be addressed to Nuno Carlos Leitão, nunocarlosleitao@gmail.com

Received 16 December 2011; Revised 3 February 2012; Accepted 3 February 2012

Academic Editor: Shuyu Sun

This paper investigates the determinants of intraindustry trade (IIT), horizontal IIT (HIIT), and Vertical IIT (VIIT) in the automobile industry in Portugal. The trade in this sector between Portugal and the European Union (EU-27) was examined, between 1995 and 2008, using a dynamic panel data. We apply the GMM system to solve the problems of serial correlation and the endogeneity of some explanatory variables. The findings are consistent with the literature. The difference between per capita incomes and factor endowments present a positive sign. These results are according to Heckscher-Ohlin predictions. The economic dimension has a positive impact on trade. A negative effect of the distance on bilateral trade was expected and the results confirm this, underlining the importance of neighbour partnerships for all trade.

1. Introduction

The intraindustry trade (IIT) or two-way trade is explained by product differentiation and the existence of products belonging to the same category. The big push in the literature emerged with the work of Grubel and Lloyd [1]. The pioneering models of IIT, especially the horizontal differentiation as in Krugman [2], Lancaster [3], and Helpman and Krugman [4], explained this type of trade based on monopolistic competition and economies of scale. In fact, the models of horizontal intraindustry trade (HIIT) do not predict the advantages theory as explanatory factor. HIIT is explained by consumers with similar characteristics and similar types of income.

In this respect, the vertical intraindustry trade (VIIT) admits different types of quality, that is, different types of preferences. The consumers have different types of income per capita, which emphasize the theoretical models of Falvey and Kierzkowski [5] and Shaked and Sutton [6].

In 1990s the intermediate goods led to interest in the academic community [7]. In recent years, the empirical studies [8–11] have focused primarily on vertical specialization, and this linked to the concept of fragmentation or outsourcing. This paper evaluates the vertical intraindustry trade as well as the horizontal intraindustry trade and intraindustry trade.

This paper presents two contributions. First we use the GMM system estimator because we intended to evaluate the long-term effects. Second, this study contributes to the discussion of the development of automobile industry and fragmentation theory.

The results presented in this paper for this specific industrial sector are generally consistent with the expectations of intraindustry trade studies. The remainder of the paper is organised as follows: Section 2 presents the theoretical background; Section 3 presents the indexes of intraindustry trade used in this study. Section 4 displays the econometrical model; Section 5 presents the estimation results, and the final section provides the conclusions.

2. Literature Review

In recent years, emerged in the literature an explanation of international trade based on the transaction of intermediate goods. Fragmentation also called outsourcing of production has received attention from many scholars especially starting in the 1990s.

In fact, the conceptual model of Jones and Kierzkowski [7] demonstrated that the location of multinational firms was associated with economies of scale and factor endowments. In other words, a multinational company may have several branches located in several regional blocks. As Faustino and Leitão [11] referred, the term fragmentation has taken various forms (outsourcing by Feenstra and Hanson [12] and vertical specialization by Hummels and Skiba [13].

Globalisation promotes regional clusters in the international economics. As Eiteam et al. [14] demonstrated, we have some countries as India, Russia, and Mexico that developed highly efficiently. The sector of parts and components for vehicles, aircraft, and software are generally referenced in the literature. According to Kol and Rayment [15] the exchange of intermediate goods may take two forms: horizontal intraindustry trade and vertical intraindustry trade. In fact horizontal intraindustry trade in intermediate goods cannot be explained by different types of quality. However, vertical intraindustry trade helps to explain the various stages of international production, since there are economies abundant in capital (K) and other factors in labour (L). Thus, it is understood that the vertical intraindustry trade is explained by different types of quality. The application of the index of Grubel and Lloyd [1] and the methodology of Abd-el-Rahman [16] and Greenaway et al. [17] have allowed validating the conceptual model of Jones and Kierzkowski [7]. Empirical studies [8–11] have focused primarily on vertical products differentiation (vertical intraindustry trade).

The research of Ando [8] and Kimura et al. [9] validated the fragmentation and vertical intraindustry trade (VIIT) in East Asian countries. Leitão et al. [10] used a static panel data (OLS with time dummies and Tobit model) to explain the phenomena of fragmentation. The article of Leitão et al. [10] concluded that vertical specialization is explained by dissimilarities of per capita GDP, factor endowments and geographical distance. The last few years in the literature is emerging new and important developments on the intraindustry trade (IIT). The dynamic analysis (GMM system) for intraindustry trade was introduced by Faustino and Leitão [18]. This analysis was also used by Faustino and Leitão [18] and Leitão [19].

The study of Faustino and Leitão [18] examined the determinants of VIIT in the automobile components between Portugal and European Union countries and BRIC (Brazil,

Russia, India, and China) for the period 1995–2006. The authors applied a dynamic panel data (GMM System). Faustino and Leitão [18] demonstrated that the differences in per capita and transaction costs are the main determinants of fragmentation.

Leitão [19] examines the long-term effects of IIT and its components—horizontal and vertical IIT, applied to the study case of the United States. Using GMM system, the study shows a negative correlation between factor endowments, and IIT. The findings also illustrate that there is no positive correlation between HIIT and HO (Heckscher-Ohlin) model.

3. Grubel and Lloyd Indexes

Grubel and Lloyd [1] define IIT as the difference between the trade balance of industry i and the total trade of this same industry. In order to make comparisons easier between industries or countries, the index is presented as a ratio, where the denominator is total trade:

$$\mathrm{IIT}_{\mathrm{it}} = 1 - \frac{|X_i - M_i|}{(X_i + M_i)} \Longleftrightarrow \mathrm{IIT}_{\mathrm{it}} = \frac{(X_i + M_i) - |X_i - M_i|}{(X_i + M_i)}, \tag{3.1}$$

where X_i and M_i are export and import to partner country i.

The index is equal to 1 if all trade is intraindustry. If $\mathrm{IIT}_{\mathrm{it}}$ is equal to 0, all trade is inter-industry trade.

Grubel and Lloyd [1, page 22] proposed an adjustment measure to the country IIT index (IIT calculated for all individual industries), introducing the aggregate trade imbalance.

Aquino [20, page 280] also considered that an adjustment measure is required, but to a more disaggregated level, but for this, the Grubel and Lloyd method is inadequate. Following Aquino, we require an appropriate imbalance effect. The imbalancing effect must be equi-proportional in all industries. So, the Aquino at the 5-digit level estimates "what the values of exports and imports of each commodity would have been if total exports had been equal to total imports."

3.1. HIIT and VIIT Indexes

To determine the horizontal ($\mathrm{HIIT}_{\mathrm{it}}$) and vertical intraindustry trade ($\mathrm{VIIT}_{\mathrm{it}}$), Grubel and Lloyd [1] indexes and the methodology of Abd-el-Rahaman [16] and Greenaway et al. [17] are used, that is, the relative unit values of exports ($\mathrm{UV}_{\mathrm{it}}^{X}$), and imports ($\mathrm{UV}_{\mathrm{it}}^{m}$).

Where $\mathrm{HIIT}_{\mathrm{it}}$:

$$1 - \alpha \leq \frac{\mathrm{UV}_{\mathrm{it}}^{X}}{\mathrm{UV}_{\mathrm{it}}^{m}} \leq 1 + \alpha \tag{3.2}$$

and $\mathrm{VIIT}_{\mathrm{it}}$ is

$$\frac{\mathrm{UV}_{\mathrm{it}}^{X}}{\mathrm{UV}_{\mathrm{it}}^{m}} \leq 1 - \alpha \quad \text{or} \quad \frac{\mathrm{UV}_{\mathrm{it}}^{X}}{\mathrm{UV}_{\mathrm{it}}^{m}} > 1 + \alpha, \tag{3.3}$$

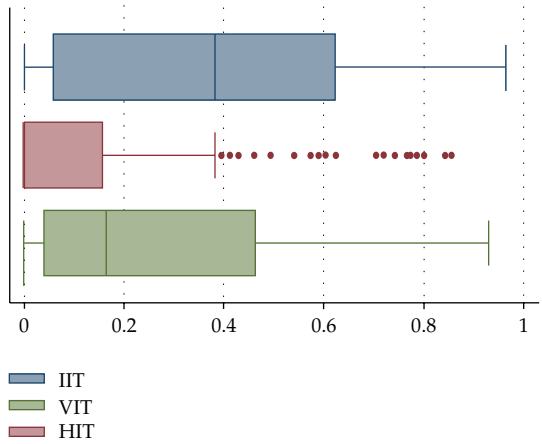

Figure 1: Trade between Portugal and European Countries for the period 1995–2008.

where $\alpha = 0.15$. When the relative unit values of exports and imports are less than 15%, the trade flows are horizontally differentiated (HIIT). The HIIT and VIIT indexes are also calculated with disaggregation at 5-digit Portuguese Economic Activity Classification from INE-Trade Statistics.

In Figure 1, the intraindustry trade between Portugal and the European Union (EU) is over 50% for the period 1995–2008. For all of the period in analysis, the VIIT is much higher than the HIIT. These values are in accordance with the fragmentation theory.

4. Econometric Model

The dependent variable used is the IIT Grubel and Lloyd [1] index, HIIT and VIIT indexes at five-digit level of the Standard International Trade Classification (SITC). The explanatory variables are country-specific characteristics. The data sources for the explanatory variables are the World Bank Development Indicators (2011). The source used for the dependent variable was data from INE, the Portuguese National Institute of Statistics.

This study uses a dynamic panel data (GMM system). In static panel data models, Pooled OLS, fixed effects (FEs), and random effects (REs) estimators have some problems like serial correlation, heteroskedasticity, and endogeneity of some explanatory variables.

The estimator GMM system (GMM-SYS) permits the researchers to solve the problems of serial correlation, heteroskedasticity and endogeneity for some explanatory variables. These econometric problems were solved by Arellano and Bond [21], Arellano and Bover [22], and Blundell and Bond [23, 24], who developed the first-differenced GMM (GMM-DIF) estimator and the GMM system (GMM-SYS) estimator. The GMM-SYS estimator is a system containing both first differenced and levels equations. The GMM-SYS estimator is an alternative to the standard first differenced GMM estimator. To estimate the dynamic model, we applied the methodology of Blundell and Bond [23, 24] and Windmeijer [25] to small sample correction to correct the standard errors of Blundell and Bond [23, 24]. The GMM system estimator is consistent if there is no second-order serial correlation in the residuals (m2 statistics). The dynamic panel data model is valid if the estimator is consistent and the instruments are valid.

4.1. Hypotheses and Definition of Explanatory Variables

Hypothesis 1. There is a negative (positive) correlation between differences in per capita income and IIT and HIIT (VIIT).

LogDGDP is the logarithm of absolute difference in per capita GDP (PPP, in current international dollars) between Portugal and the trading partner. Loertscher and Wolter [26] suggested a negative sign for the IIT model. Hypothesis 1, was formulated based the Linder [27] theory. Linder [27] considers that countries with similar demands have similar products. So, the Linder hypothesis suggests a negative sign for the IIT model (Helpman [28]; and Hummels and Levinsohn [29]).

Regarding Hypothesis 1, Loertscher and Wolter [26] and Balassa [30] estimated a negative coefficient. The recent study of Leitão [19] also found a negative sign. The model of Falvey and Kierzkowski [5] suggests a positive impact between income difference and VIIT. The empirical works of Loertscher and Wolter [26] and Greenaway et al. [17] provide empirical support for a negative relation between difference in per capita income and HIIT.

Hypothesis 2. IIT and HIIT occurs more frequently among countries that are similar in terms of factor endowments.

(a) VIIT predominate among countries that are dissimilar in terms of factor endowments.

LogEP is a proxy for differences in physical endowments. It is the logarithm of the absolute difference in electric power consumption (Kwh per capita) between Portugal and its partners. Considering Hypothesis 2, the models of Helpman and Krugman [4] and Hummels and Levinsohn [29] suggest a negative effect of physical endowment on IIT. Zhan et al. [31] use the absolute difference in electric power consumption in examining IIT for China. Zhang et al. [31] found a negative sign to IIT. The findings of Leitão [19] show a positive sign to VIIT.

Hypothesis 3. The economic dimension influences the volume of trade positively.

LogDIM is the logarithm of average GDP of the two trading partners. Usually the studies utilized this proxy to evaluate the potential economies of scales and the variety of differentiated product. A positive sign is expected for the coefficient of this variable (see, e.g, Greenaway et al. [17], Hummels and Levinsohn, [29], and Leitão et al. [10]).

Hypothesis 4. Trade increases when partners are geographically close.

LogDIST is the logarithm of geographical distance between Portugal and the partner country. Following the most empirical studies, we use kilometres between the capital cities of the trading partners. According to the literature, we expect a negative sign (Badinger and Breuss [32], Blanes [33], Cieślik [34], and Faustino and Leitão [11]).

4.2. Model Specification

We consider that

$$\mathrm{IIT}_{\mathrm{it}} = \beta_0 + \beta_1 X_{\mathrm{it}} + \delta t + \eta_i + \varepsilon_{\mathrm{it}}, \tag{4.1}$$

where $\mathrm{IIT}_{\mathrm{it}}$ stands for IIT, HIIT, or VIIT, meaning Total, Vertical, or Horizontal Portuguese IIT index, and X is a set of explanatory variables. All variables are in the logarithm form; η_i is the unobserved time-invariant specific effects; δt captures a common deterministic trend; $\varepsilon_{\mathrm{it}}$ is a random disturbance assumed to be normal, and identically distributed with $E(\varepsilon_{\mathrm{it}}) = 0$; Var $(\varepsilon_{\mathrm{it}}) = \sigma^2 > 0$.

Following the empirical work of Hummels and Levinsohn [29], we apply a logistic transformation to IIT, HIIT, and VIIT because these indexes vary between zero and one. LOGISTIC IIT = Ln[IIT/(1 − IIT)]. The same transformation is made for HIIT and VIIT.

The model can be rewritten in the following dynamic representation:

$$\mathrm{IIT}_{\mathrm{it}} = \mathrm{IIT}_{\mathrm{it-1}} + \beta_0 + \beta_1 X_{\mathrm{it}} - \rho\beta_1 X_{\mathrm{it-1}} + \delta t + \eta_i + \varepsilon_{\mathrm{it}}. \tag{4.2}$$

5. Estimation Results

Table 1 presents summary statistics for each variable. LogDGDP, LogEP, LogDIM, and LogDIST appear to have only little differences. However, this is not the case for the indexes of LogIIT, LogHIIT and LogVIIT.

Before estimating the panel regression model, we have conducted a test for unit root of the variable. Table 2 presents the results of panel unit root test (ADF-Fischer Chi square).

The most important variables such as the intraindustry trade (LogIIT), horizontal intraindustry trade (LogHIIT), vertical intraindustry trade (LogVIIT), electric power consumption (LogEP), economic dimension (LogDIM) do not have unit roots, that is, are stationary with individual effects and individual specifications.

In Figure 2 we can observe the distribution of intraindustry trade.

Table 3 reports the determinants of IIT using a GMM system estimator. All explanatory variables are significant at 1% level (LogIIT_{t-1}, LogDGDP, LogEP, LogDIM, and LogDIST). Our model presents consistent estimates, with no serial correlation (m2 statistics). The specification Sargan test shows that there are no problems with the validity of instruments used. As expected for the Lagged dependent variable (LogIIT_{t-1}) the result presents a positive sign, showing the changes in IIT have a significant impact on long-term effects. The difference between per capita incomes, in logs (LogDGDP), presents a positive sign. We can infer that countries have dissimilar demand. Following Falvey and Kierzkowski [5], we introduced one proxy for the difference in factor endowments (electric power). The variable, electric power in logs (LogEP) presents a positive sign. As Portuguese IIT is mainly vertical intraindustry trade (VIIT), this is consistent with the neo-Heckscher-Ohlin trade theory, that is, the differences in physical endowments promote the IIT.

The coefficient economic dimension (LogDIM) has a significant and a positive effect on IIT. This result confirms the importance of scale economy and product differentiation. We can conclude that economic dimension influences the volume of intraindustry trade. The geographical distance (LogDIST) has been used as a typical gravity model variable. A negative effect of the distance on bilateral IIT was expected and the results confirm this, underlining the importance of neighbour partnerships for all trade.

The Table 4 presents the results using the horizontal intraindustry trade equation. The model presents consistent estimates, with no serial correlation (m2 statistics). The specification Sargan test shows that there are no problems with the validity of instruments used. As expected for the Lagged dependent variable ($\mathrm{LogHIIT}_{t-1}$) the result presents

Table 1: Summary statistics.

Variables	Mean	Std. dev	Min	Max
LogIIT	−0.56	0.56	−2.56	−0.01
LogHIIT	−2.22	1.42	−6.14	−0.07
LogVIIT	−0.92	0.63	−2.87	−0.05
LogDGDP	4.13	0.38	2.18	4.93
LogEP	3.37	0.46	1.60	4.12
LogDIM	4.31	0.20	3.77	4.82
LogDIST	3.33	0.18	2.70	3.59

Table 2: Panel unit root test results.

	Intercept and trend	
ADF-Fischer Chi square	Statistic	Probability
LogIIT	131.19	0.0000
LogHIIT	65.31	0.0319
LogVIIT	97.67	0.0000
LogEP	88.60	0.0006
LogDIM	65.63	0.0682

a positive sign. So we can infer that the changes in horizontal intraindustry trade have a a significant impact on the long-term effects.

The absolute difference in electric power consumption (LogEP) is statistically significant, with positive sign. We can conclude that countries have dissimilar factor endowment. As expected, the variable LogDIM (average of per capita GDP) between Portugal and the partner consider) has a significant and positive effect on trade. Therefore, the intensity of HIIT is positively correlated with the similarity in per capita income between trading partners. The coefficient of LogDIST (geographical distance) is negative as expected. The studies of Balassa and Bauwens [35], Badinger and Breuss, [32], Blanes [33], Cieślik [34], H. Egger and P. Egger [36] also found a negative sign.

In Figure 3 we present the distribution of horizontal intraindustry trade.

Vertical intraindustry trade estimates are report in Table 5. All explanatory variables are significant. The results are according to previous studies. The model present consistent estimates, with no serial correlation and Sargan test validates the instruments used.

The hypothesis for economic differences between countries (DGDP) in logs presents a positive sign and is significant at 1% level. Falvey and Kierzkowski [5] suggest a positive effect of income difference on VIIT model. Kimura et al. [9] found positive relationship between income difference and VIIT for parts and components trade. We can conclude that VIIT occurs more frequently among economies that are dissimilar, that is, differentiation by quality of products.

In Figure 4 we can observe the distribution of vertical intraindustry trade.

The coefficients electric power consumption (EP) and the economic dimension (DIM) are consistent with the expected sign. The result confirms that VIIT can be explained by Heckscher-Ohlin theory.

The difference in electric power consumption per capita (LEP) reflects the difference in endowments between Portugal and its trade partners. Regarding the hypothesis for

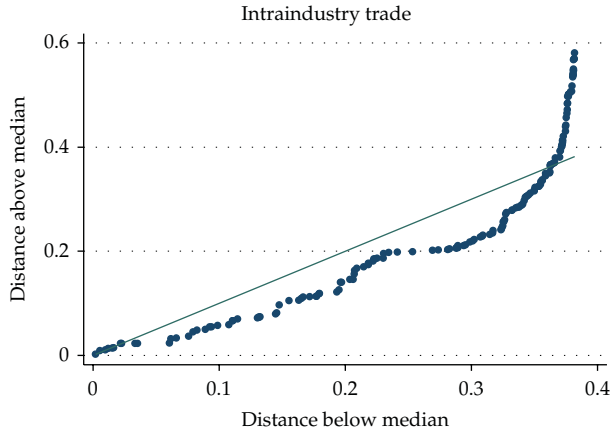

Figure 2: Distribution of intraindustry trade (IIT).

Table 3: Determinants of intraindustry trade.

Variables	GMM system	t-statistics	Significance	Expected sign
LogIIT_{t-1}	0.10	(6.25)	***	(+)
LogDGDP	0.29	(3.55)	***	(−)
LogEP	0.38	(10.49)	***	(−)
LogDIM	0.21	(3.09)	***	(+)
LogDIST	−1.53	(−3.09)	***	(−)
C	2.59	(1.69)	*	
Ar(2)	−0.69 [0.49]			
Sargan Test	20.96 [1.00]			
Observations	289			

The null hypothesis that each coefficient is equal to zero is tested using one-step robust standard error. t-statistics (heteroskedasticity corrected) are in round brackets. P values are in square brackets; ***/*statistically significant at the 1 percent and 10 percent levels. Ar(2) is tests for second-order serial correlation in the first-differenced residuals, asymptotically distributed as $N(0,1)$ under the null hypothesis of no serial correlation (based on the efficient two-step GMM estimator). The Sargan test addresses the overidentifying restrictions, asymptotically distributed X^2 under the null of the instruments' validity (with the two-step estimator).

Table 4: Determinants of Horizontal Intraindustry Trade.

Variables	GMM system	t-statistics	Significance	Expected sign
LogHIIT_{t-1}	0.33	(21.1)	***	(+)
LogDGDP	2.06	(2.44)	*	(−)
LogEP	1.09	(3.33)	***	(−)
LogDIM	2.69	(4.19)	***	(+)
LogDIST	−1.92	(−1.79)	*	(−)
C	3.94	(0.90)		
Ar(2)	2.09 [0.36]			
Sargan Test	18.54 [1.00]			
Observations	138			

The null hypothesis that each coefficient is equal to zero is tested using one-step robust standard error. t-statistics (heteroskedasticity corrected) are in round brackets. P values are in square brackets; ***/*statistically significant at the 1, and 10 percent levels. Ar(2) is tests for second-order serial correlation in the first-differenced residuals, asymptotically distributed as $N(0,1)$ under the null hypothesis of no serial correlation (based on the efficient two-step GMM estimator). The Sargan test addresses the overidentifying restrictions, asymptotically distributed X^2 under the null of the instruments' validity (with the two-step estimator).

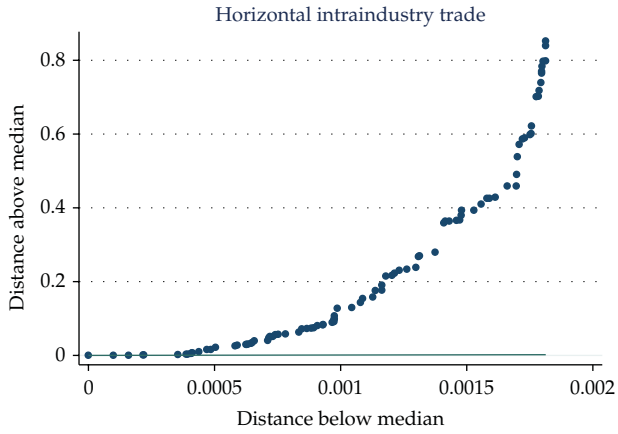

Figure 3: Distribution of horizontal intraindustry trade (HIIT).

Table 5: Determinants of vertical intraindustry trade.

Variables	GMM system	t-statistics	Significance	Expected sign
LogVIIT_{t-1}	0.32	(15.63)	***	(+)
LogDGDP	0.19	(4.18)	***	(+)
LogEP	0.01	(1.78)	*	(+)
LogDIM	0.55	(5.13)	***	(+)
LogDIST	−0.44	(−4.25)	***	(−)
C	0.24	(0.69)		
Ar(2)	0.39 [0.70]			
Sargan Test	21.14 [1.00]			
Observations	267			

The null hypothesis that each coefficient is equal to zero is tested using one-step robust standard error. t-statistics (heteroskedasticity corrected) are in round brackets. P values are in square brackets; ***/*statistically significant at the 1 percent, 5 percent, and 10 percent levels. Ar(2) is tests for second-order serial correlation in the first-differenced residuals, asymptotically distributed as $N(0,1)$ under the null hypothesis of no serial correlation (based on the efficient two-step GMM estimator). The Sargan test addresses the overidentifying restrictions, asymptotically distributed X^2 under the null of the instruments' validity (with the two-step estimator).

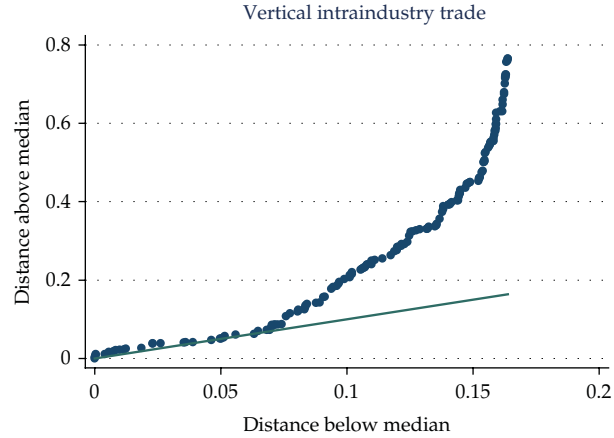

Figure 4: Distribution of vertical intraindustry trade (VIIT).

the geographical distance on VIIT, the empirical result support the idea that the gravity model is important to explain vertical intraindustry trade between partners.

6. Conclusion

The objective of this paper was to analyze the main determinants of intraindustry trade in automobile sector. The IIT between Portugal and the European Union countries is over 50% for the period 1995–2008. For all of the period in analysis, the VIIT is much higher than the HIIT. These values are in accordance with the fragmentation theory.

The Lagged dependent variables (LogIIT_{t-1}, LogHIIT_{t-1}, and LogVIIT_{t-1}) are positive and less than one. So we can infer that the changes in intraindustry trade, horizontal and vertical IIT have a significant impact on the long-term effects.

The Linder theory considers that a difference in per capita incomes explains intraindustry trade and their components (HIIT and VIIT). The variable (LogDGDP) used to evaluate the relative factor endowments presents a positive impact on IIT, HIIT and VIIT. In fact the decision of multinational corporations is associated with different factors as in localization, skilled labour and economies of scales.

In relationship to the variable differences in physical capital endowments (LogEP), our results validate the hypothesis: VIIT occurs more frequently among countries that are dissimilar in terms of factor endowments. Our research confirms that fragmentation of production in the automobile sector is explained by the Heckscher-Ohlin. The difference in factor endowment allows showing that fragmentation is associated with vertical differentiation of products. This reveals that the decision-making of multinational corporations are based in reducing production costs; showing the importance of globalization to explain the phenomenon of fragmentation or outsourcing.

For the variable size of the market (average of GDP), the study suggests that Portugal has size to attract this type of industry. In fact, the Euro Zone countries considered in the econometric analysis show that the removal of tariff and nontariff barriers promoted the increase of intraindustry trade with special focus on the VIIT. In future studies it will be interesting to extend our sample.

According to the literature we expected a negative sign to geographical distance. Usually the literature attributes a negative sign to geographical distance, that is, trade increases if the partners are geographically close. The findings support this hypothesis, that is, the gravity model are important to explain the composition of trade (IIT, HIIT and VIIT) within partners.

Acknowledgment

The author is indebted to the anonymous referees for greatly improving is paper from the previous version.

References

[1] H. Grubel and P. Lloyd, *Intra-Industry Trade. The Theory and Measurement of International Trade in Di erentiation Products*, The Mcmillian Press, London, UK, 1975.

[2] P. R. Krugman, "Increasing returns, monopolistic competition, and international trade," *Journal of International Economics*, vol. 9, no. 4, pp. 469–479, 1979.

[3] K. Lancaster, "Intra-industry trade under perfect monopolistic competition," *Journal of International Economics*, vol. 10, no. 2, pp. 151–175, 1980.
[4] E. Helpman and P. Krugman, *Market Structure and Foreign Trade*, Harvester Wheatsheaf, Brighton, UK, 1985.
[5] R. Falvey and H. Kierzkowski, "Product quality, Intra-industry trade (Im) Perfect competition," in *Protection and Competition in International Trade. Essays in Honour of W. M.Corden*, H. Kierzkowki, Ed., pp. 143–161, Basil Blackwell, Oxford, Miss, USA, 1987.
[6] A. Shaked and J. Sutton, "Natural oligopolies and international trade," in *Monopolistic Competition and International Trade*, H. Kierzkowski, Ed., pp. 34–50, Oxford University Press, Oxford, Miss, USA, 1984.
[7] R. Jones and H. Kierzkowski, "The role of services in production and international trade: a theoretical framework," in *The Political Economy of International Trade*, R. W. Jones and A. Krueger, Eds., chapter 3, pp. 31–48, Basil Blackwell, Oxford, Miss, USA, 1990.
[8] M. Ando, "Fragmentation and vertical intra-industry trade in East Asia," *North American Journal of Economics and Finance*, vol. 17, no. 3, pp. 257–281, 2006.
[9] F. Kimura, Y. Takahashi, and K. Hayakawa, "Fragmentation and parts and components trade: Comparison between East Asia and Europe," *North American Journal of Economics and Finance*, vol. 18, no. 1, pp. 23–40, 2007.
[10] N. C. Leitão, H. C. Faustino, and Y. Yoshida, "Fragmentation, vertical intra-industry trade, and automobile components," *Economics Bulletin*, vol. 30, no. 2, pp. 1006–1015, 2010.
[11] H. C. Faustino and N. C. Leitão, "Fragmentation in the automobile manufacturing industry: Evidence from Portugal," *Journal of Economic Studies*, vol. 38, no. 3, pp. 287–300, 2011.
[12] R. C. Feenstra and G. H. Hanson, "Globalization, outsourcing, and wage inequality," *American Economic Review*, vol. 86, no. 2, pp. 240–245, 1996.
[13] D. Hummels and A. Skiba, "Shipping the good apples out? An empirical confirmation of the Alchian-Allen conjecture," *Journal of Political Economy*, vol. 112, no. 6, pp. 1384–1402, 2004.
[14] D. Eiteam, I. Stonehill, and H. Moffett, *Comparative Corporate Governance and Financial Goals*, Multinational Business Finance, Pearson Education, Boston, Mass, USA, 2007.
[15] J. Kol and P. Rayment, "Allyn-Young specialization and intermediate goods in intra-industry trade," in *Intra-Industry Trade: Theory and Extensions*, P. K. M. Tharakan and J. Kol, Eds., St Martin's Press, New York, NY, USA, 1989.
[16] K. Abd-el-Rahman, "Firms' competitive and national comparative advantages as joint determinants of trade composition," *Weltwirtschaftliches Archiv*, vol. 127, no. 1, pp. 83–97, 1991.
[17] D. Greenaway, R. Hine, and C. Milner, "Country-specific factors and the pattern of horizontal and vertical intra-industry trade in the UK," *Weltwirtschaftliches Archiv*, vol. 130, no. 1, pp. 77–100, 1994.
[18] H. C. Faustino and N. C. Leitão, "Intra-industry trade: A static and dynamic panel data analysis," *International Advances in Economic Research*, vol. 13, no. 3, pp. 313–333, 2007.
[19] N. C. Leitão, "Long-term effects in intra-industry trade," *Actual Problems of Economics*, vol. 122, no. 8, pp. 390–398, 2011.
[20] A. Aquino, "Intra-industry trade and inter-industry specialization as concurrent sources of international trade in manufactures," *Weltwirtschaftliches Archiv*, vol. 114, no. 2, pp. 275–296, 1978.
[21] M. Arellano and S. Bond, "Some tests of specification for panel data: Monte Carlo evidence and an application to employment equations," *The Review of Economic Studies*, vol. 5, no. 2, pp. 277–297, 1991.
[22] M. Arellano and O. Bover, "Another look at the instrumental variable estimation of error-components models," *Journal of Econometrics*, vol. 68, no. 1, pp. 29–51, 1995.
[23] R. Blundell and S. Bond, "Initial conditions and moment restrictions in dynamic panel data models," *Journal of Econometrics*, vol. 87, no. 1, pp. 115–143, 1998.
[24] R. Blundell and S. Bond, "GMM estimation with persistent panel data: an application to production functions," *Econometric Reviews*, vol. 19, no. 3, pp. 321–340, 2000.
[25] F. Windmeijer, "A finite sample correction for the variance of linear efficient two-step GMM estimators," *Journal of Econometrics*, vol. 126, no. 1, pp. 25–51, 2005.
[26] R. Loertscher and F. Wolter, "Determinants of intra-industry trade: Among countries and across industries," *Weltwirtschaftliches Archiv*, vol. 116, no. 2, pp. 280–293, 1980.
[27] S. Linder, *An Essay on Trade and Transformation*, Wiley, New York, NY, USA, 1961.
[28] E. Helpman, "Imperfect competition and international trade: Evidence from fourteen industrial countries," *Journal of The Japanese and International Economies*, vol. 1, no. 1, pp. 62–81, 1987.
[29] D. Hummels and J. Levinsohn, "Monopolistic competition and international trade: reconsidering the evidence," *Quarterly Journal of Economics*, vol. 110, no. 3, pp. 799–836, 1995.

[30] B. Balassa, "The determinants of intra-industry specialization in United States trade," *Oxford Economic Papers*, vol. 38, no. 2, pp. 220–233, 1986.

[31] J. Zhang, A. Van Witteloostuijn, and C. Zhou, "Chinese bilateral intra-industry trade: a panel data study for 50 countries in the 1992–2001 period," *Review of World Economics*, vol. 141, no. 3, pp. 510–540, 2005.

[32] H. Badinger and F. Breuss, "Trade and productivity: an industry perspective," *Empirica*, vol. 35, no. 2, pp. 213–231, 2008.

[33] J. Blanes, "Does immigration help to explain intra-industry trade? Evidence for Spain," *Review of World Economics*, vol. 141, no. 2, pp. 244–270, 2006.

[34] A. Cieślik, "Intraindustry trade and relative factor endowments," *Review of International Economics*, vol. 13, no. 5, pp. 904–926, 2005.

[35] B. Balassa and L. Bauwens, "Intra-industry specialization in multi-country and multi- industry framework," *The Economic Journal*, pp. 923–939, 1987.

[36] H. Egger, P. Egger, and D. Greenaway, "Intra-industry trade with multinational firms," *European Economic Review*, vol. 51, no. 8, pp. 1959–1984, 2007.

Hindawi Publishing Corporation
Journal of Applied Mathematics
Volume 2012, Article ID 287271, 12 pages
doi:10.1155/2012/287271

Research Article

Airflow and Heat Transfer in the Slot-Vented Room with Radiant Floor Heating Unit

Xiang-Long Liu,[1,2] Guang-Cai Gong,[1] Heng-Sheng Cheng,[3] and Li-Xing Ding[4]

[1] *School of Civil Engineering, Hunan University, Hunan, Changsha 410082, China*
[2] *Department of Building Engineering, Hunan Institute of Engineering, Hunan, Xiangtan 411104, China*
[3] *Soochow University, Jiangsu, Suzhou 215137, China*
[4] *Institute of Built Environment and Control, Zhongkai University of Agriculture and Engineering, Guangdong, Guangzhou 510225, China*

Correspondence should be addressed to Xiang-Long Liu, xianglongliu1@163.com

Received 13 January 2012; Accepted 20 February 2012

Academic Editor: M. F. El-Amin

Radiant floor heating has received increasing attention due to its diverse advantages, especially the energy saving as compared to the conventional dwelling heating system. This paper presents a numerical investigation of airflow and heat transfer in the slot-vented room with the radiant floor heating unit. Combination of fluid convection and thermal radiation has been implemented through the thermal boundary conditions. Spatial distributions of indoor air temperature and velocity, as well as the heat transfer rates along the radiant floor and the outer wall, have been presented and analyzed covering the domains from complete natural convection to forced convection dominated flows. The numerical results demonstrate that the levels of average temperature in the room with lateral slot-ventilation are higher than those without slot-ventilation, but lower than those in the room with ceiling slot-ventilation. Overall, the slot-ventilation room with radiant floor heating unit could offer better indoor air quality through increasing the indoor air temperature and fresh air exchanging rate simultaneously. Concerning the airborne pollutant transports and moisture condensations, the performance of radiant floor heating unit will be further optimized in our future researches.

1. Introduction

Radiant floor heating is a novel indoor heating technique that has received increasing attention in recent years. In the conventional heating methods, such as the air convection by radiators and the hot air supply by air conditioners, the hot air is always located in the upside or middle upside of the room instead of the occupied zone, leading to the obvious

temperature differences between the upside and underside of the room. Under such condition, occupants usually feel uncomfortable. In the radiant floor heating, however, the effective temperature of the floor is higher than the temperature in the upside of the room, which can supply more heat to the underside of the room for warming the occupants' feet instead of their heads that follows the rule of human's physiologic adjustment. Therefore, the radiant floor heating improves the thermal comfort condition for the occupants as compared to the conventional heating methods. In addition, the radiant system has the advantages of energy saving, long life, wide selection of the heat sources, low cost, and environmental friendliness. The theoretical and experimental research [1, 2] showed that radiant floor system can decrease more than 30% of the energy consumption. The radiant floor system is also used for indoor cooling in summer only by changing the heat source to the cool source. In recent years, the indoor radiant heating or cooling system has been receiving increasing utilization in residential and commercial buildings. For example, among the newly built European buildings, many of them have been equipped with the radiant heating/cooling systems.

Radiant heating system is such a complex system that involves the various heat transfer mechanisms, including the heat conduction in the floor, the radiative heat transfer between radiant surface and other surfaces, convective heat transfer between the radiant surface and its neighboring air, and the buoyancy's effects. The numerical method provides a convenient way to solve such problem. Ghaly and Elbarbary [3] and Shateyi [4] numerically studied the convection coupled with radiative heat transfer and buoyancy's effects. Ma et al. [5] numerically studied the characteristics of the temperature and velocity distribution in the room, and their results showed that radiant heat flux accounted for 50–60% of the total heat flux. Sattari and Farhanieh [6] studied the effects of design parameters on performance of a typical radiant floor heating system using finite element method. Bozkir and Canbazoğlu [7] carried out the experimental and numerical research on the radiant heating system with an attempt to find the characteristics. In practice, the adequate fresh air supply is usually required to ensure indoor air quality. As a result, the floor radiant heating system is usually combined with the slot-ventilation system. However, few of the research works focuses on the air flow and heat transfer in the slot-vented room with radiant floor heating unit.

This paper presents the numerical simulation of floor radiant heating system with three types of slot-ventilation, that is, lateral slot-ventilation (LSV), ceiling slot-ventilation (CSV) and no slot-ventilation (NSV). The indoor temperature, velocity, and heat flux distributions are calculated. This work is of great significance for the design and wider application of the floor radiant heating system.

2. Mathematical Model

The steady 2D model of the turbulent airflow and heat transfer in the room is developed in this study. The schematic of radiant heating system and coordinate system is shown in Figure 1. The radiant floor is assumed as the constant temperature T_{fl}; the outside wall is cooled at the constant heat flux q_{ow}; other walls are adiabatic. The air velocity at the inlet is u_{in}, and the inflow temperature is t_{in}. The standard K-ε two equations are used to describe the turbulent flow and the governing equations are given as follows.
Continuity equation:

$$\frac{\partial(\rho u)}{\partial x} + \frac{\partial(\rho v)}{\partial y} = 0. \tag{2.1}$$

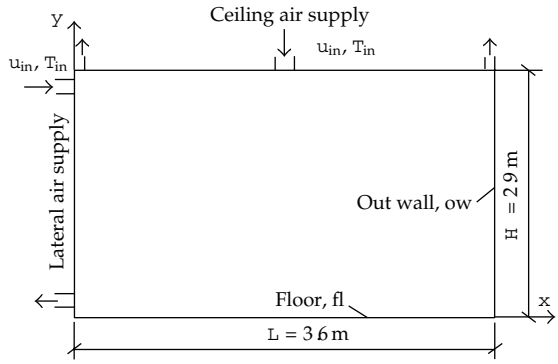

Figure 1: Schematic of radiant heating system and coordinate system.

Momentum equations:

$$\begin{aligned}\frac{\partial(\rho uu)}{\partial x}+\frac{\partial(\rho vu)}{\partial y}&=\frac{\partial}{\partial x}\left(\mu_{\text{eff}}\frac{\partial u}{\partial x}\right)+\frac{\partial}{\partial y}\left(\mu_{\text{eff}}\frac{\partial u}{\partial y}\right)-\frac{\partial p}{\partial x}\\&\quad+\frac{\partial}{\partial x}\left(\mu_{\text{eff}}\frac{\partial u}{\partial x}\right)+\frac{\partial}{\partial y}\left(\mu_{\text{eff}}\frac{\partial v}{\partial x}\right)\\\frac{\partial(\rho uv)}{\partial x}+\frac{\partial(\rho vv)}{\partial y}&=\frac{\partial}{\partial x}\left(\mu_{\text{eff}}\frac{\partial v}{\partial x}\right)+\frac{\partial}{\partial y}\left(\mu_{\text{eff}}\frac{\partial v}{\partial y}\right)-\frac{\partial p}{\partial y}\\&\quad-\rho g+\frac{\partial}{\partial x}\left(\mu_{\text{eff}}\frac{\partial u}{\partial y}\right)+\frac{\partial}{\partial y}\left(r\mu_{\text{eff}}\frac{\partial v}{\partial y}\right),\end{aligned}\tag{2.2}$$

where u, v are the fluid velocities in x- and y-directions respectively; p is the pressure of the fluid; g represents the acceleration of gravity. μ_{eff} is effective viscosity coefficient, which is equal to the sum of molecular viscosity μ and turbulent eddy viscosity μ_{t}. Turbulent eddy viscosity μ_{t} is determined by the local turbulent kinetic energy K and the dissipation rate ε:

$$\mu_{\text{t}}=\frac{c_\mu\rho K^2}{\varepsilon}.\tag{2.3}$$

Energy equation in terms of temperature T is given below

$$\frac{\partial(\rho uT)}{\partial x}+\frac{\partial(\rho vT)}{\partial y}=\frac{\partial}{\partial x}\left(\left(\frac{\lambda}{c_p}+\frac{\mu_t}{\sigma_T}\right)\frac{\partial T}{\partial x}\right)+\frac{\partial}{\partial y}\left(\left(\frac{\lambda}{c_p}+\frac{\mu_t}{\sigma_T}\right)\frac{\partial T}{\partial r}\right).\tag{2.4}$$

Transport equations for turbulent kinetic energy K and dissipation rate equations ε are

$$\begin{aligned}
\frac{\partial(\rho u K)}{\partial x} + \frac{\partial(\rho v K)}{\partial y} &= \frac{\partial}{\partial x}\left(\left(\mu + \frac{\mu_t}{\sigma_k}\right)\frac{\partial K}{\partial x}\right) + \frac{\partial}{\partial r}\left(\left(\mu + \frac{\mu_t}{\sigma_k}\right)\frac{\partial K}{\partial y}\right) + G - \rho\varepsilon, \\
\frac{\partial(\rho u \varepsilon)}{\partial x} + \frac{\partial(\rho v \varepsilon)}{\partial y} &= \frac{\partial}{\partial x}\left(\left(\mu + \frac{\mu_t}{\sigma_\varepsilon}\right)\frac{\partial \varepsilon}{\partial x}\right) + \frac{\partial}{\partial r}\left(\left(\mu + \frac{\mu_t}{\sigma_\varepsilon}\right)\frac{\partial \varepsilon}{\partial y}\right) + \left(c_1 G - c_2 \rho\varepsilon\right)\frac{\varepsilon}{K},
\end{aligned} \tag{2.5}$$

G in (2.5) is the production term given by

$$G = \mu_t \left\{ 2\left[\left(\frac{\partial u}{\partial x}\right)^2 + \left(\frac{\partial v}{\partial y}\right)^2 + \left(\frac{v}{r}\right)^2\right] + \left(\frac{\partial u}{\partial y} + \frac{\partial v}{\partial x}\right)^2 \right\}. \tag{2.6}$$

The closure coefficients c_μ, c_1, c_2, σ_T, σ_K, and σ_ε in the above turbulent model are set as constants 0.09, 1.44, 1.92, 1.0, 1.0, and 1.3, respectively [8].

The DO radiation model is employed to handle the radiative heat transfer, and the absorbing and scattering of air are omitted:

$$\frac{dI(\vec{r},\vec{s})}{ds} + aI(\vec{r},\vec{s}) = a\frac{\sigma T^4}{\pi}, \tag{2.7}$$

where $\vec{s}$ is the distance between the two points of different wall surfaces and a is the absorption coefficient. Each of the wall surfaces is assumed as grey-body radiation surfaces, and the radiation emissivity at the floor is $\varepsilon_{\mathrm{fl}} = 0.6$, and are taken as 0.8 at the other surfaces.

3. Numerical Method

Based on the control volume and SIMPLEC method [9], the governing equations (2.1)–(2.7) subject to the boundary conditions are solved in the iterative manner. The grid is $x \times y = 200 \times 180$, with the depressed mesh at near the wall to match the high velocity and temperature gradients. In the calculation, the Boussinesq assumption is used to consider the buoyancy's effect, and the thermal expansion coefficient β is 0.0033. The thermophysical properties of air are constant except the density. The converged solution is obtained when the following convergence criteria are satisfied for the dependent variables:

$$\left|\frac{\phi^{n+1} - \phi^n}{\phi^n}\right| \le 10^{-5}, \quad \text{where } \phi = u, v, \text{and } T. \tag{3.1}$$

4. Results and Discussion

The calculation conditions are as follows: the constant wall temperature $T_{\mathrm{fl}} = 30°\mathrm{C}$; the inlet velocity $u_{in} = 0.3$, 0.6 and 0.9 m/s; the cooling heat flux of the outside wall $q_{\mathrm{ow}} = -100\,\mathrm{W/m^2}$. The air temperature at the inlet is equal to the mass-averaged temperature without slot-ventilation so that no additional heat load is induced into the room. The indoor air temperature and velocity distributions, as well as the radiative and convective heat flux

between radiant floor and outside wall, are calculated under the different slot-ventilation modes (i.e., LSV, CSV, and NSV).

4.1. Velocity and Temperature Distributions

Figure 2 shows the temperature and velocity distributions for the three slot ventilation modes at $T_{fl} = 30°C$, $q_{ow} = -100\,W/m^2$, and $u_{in} = 0.6\,m/s$. The air temperature in the room is quite uniform (the temperature difference is less than 1°C), except in the area near the floor. The air temperature is lower in the area near outside wall. As no fresh air is supplied for NSV (Figure 2(a)), the air near outside wall is firstly cooled down and then moves downward due to the density difference in the vertical direction. The cooled air flows along the floor due to the stagnation effect as it touches the floor and is warmed up at the floor. Then the heated air moves upwards along the inside wall due to the buoyancy' effect. As a result, the clockwise natural convection of indoor air is formed. It is clearly seen that only in the region near the wall the obvious air flow is observed, and the velocity is quite low elsewhere. As shown in Figure 2(b), the indoor air temperature is higher under LSV mode as compared to the case with NSV. Because both the air inlet and air outlet are installed at the same inside wall (one is near the ceiling and the other is near the floor), the attaching jet flow is formed along the ceiling as the air is supplied. The air is then cooled near the outside wall and goes downwards so that the flow pattern similar to the natural convection is formed, but the air velocity is higher for LSV. Due to the higher air velocity along the walls, the convective heat transfer between the air and the wall is enhanced for LSV. Under CSV, (Figure 2(c)), the indoor air temperature is further increased, and the air flow pattern is quite different from those under above-mentioned two modes. As the air is supplied from the middle of ceiling, the air from the inlet is continuously expanded and decelerated along the flow direction. The supplied air is divided into two parts; one flows towards the outlet and is exhausted, and the other flows towards to the outside wall which is cooled and goes down, forming the same flow pattern as the natural convection. As the magnitude of the air velocity is close to that of natural convection velocity, the flow pattern is the combined result of the forced convection and the natural convection.

Figure 3 shows the temperature distribution at the different locations for the cases shown in Figure 2. In this figure, X, Y are dimensionless distance $X = x/L$, $Y = y/H$. It is found that the average temperature for CSV is highest, while the average temperature for NSV is lowest. For all the cases, the temperature gradients along the height direction are quite small except in the area near the floor and ceiling, which indicates the uniform temperature distribution in most of the area. The temperature gradients near the floor are quite large, especially in the area closer to outside wall (e.g., $X = 0.8$). This is because the air cooled at the outside wall produces the greater temperature difference as it is passing along the floor. Near the ceiling, because of the influences of the radiation, convection, cooling from the outside wall, heat transfer mechanism is complex. As a result, the obvious temperature gradient is also observed near the ceiling.

Figure 4 shows the velocity distribution at different locations for the cases shown in Figure 2. It is clearly found that the influence of the slot-ventilation on the flow pattern is obvious. Under these three conditions, air velocity in the occupied zone is all less than $0.2\,m/s$, while the air velocity of the area near the ceiling and floor is as high as $0.5\,m/s$. Compared to NSV, the velocity near the floor and the ceiling for LSV and CSV is much higher, and CSV leads to the more complex flow pattern.

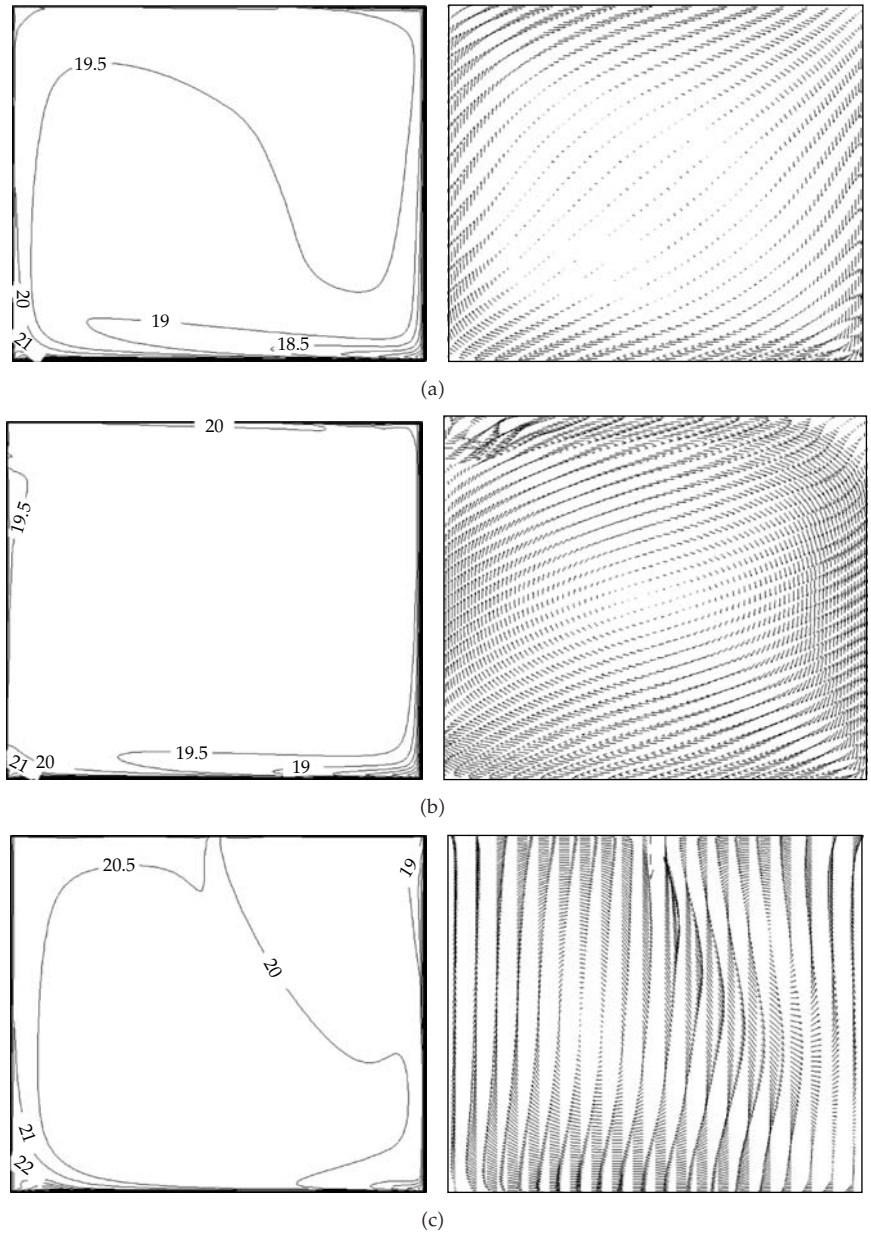

Figure 2: The temperature and velocity distribution at $T_{fl} = 30°C$, $q_{ow} = -100\ W/m^2$ and $u_{in} = 0.3\,m/s$ for (a) no slot-ventilation (NSV), (b) lateral slot-ventilation (LSV), and (c) ceiling slot-ventilation (CSV).

Figure 5 shows the temperature and velocity distributions for LSV at $T_{fl} = 30°C$, $q_{ow} = -100\,W/m^2$, and $u_{in} = 0.3$, and $0.9\,m/s$. It is clear that the airflow pattern and temperature distributions are similar to the case shown in Figure 2(b). As the inlet velocity increases ($u_{in} = 0.9\,m/s$), (Figure 5(a)), more air flows towards the outside wall, leading to the more intensive convective heat transfer between the indoor air and the outside wall. As a result, the air is cooled to the lower temperature. For this reason, the bulk temperature of the indoor air

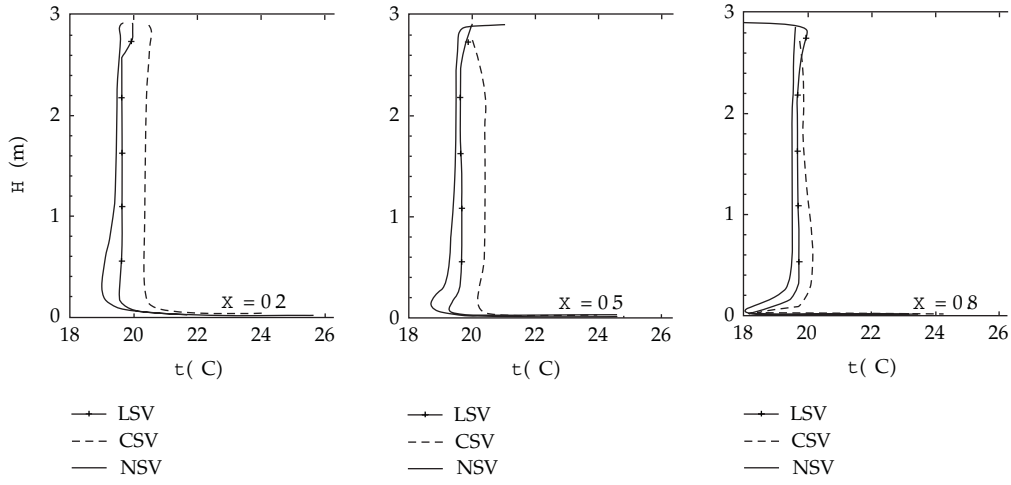

Figure 3: The temperature distributions at different X locations for the cases shown in Figure 2.

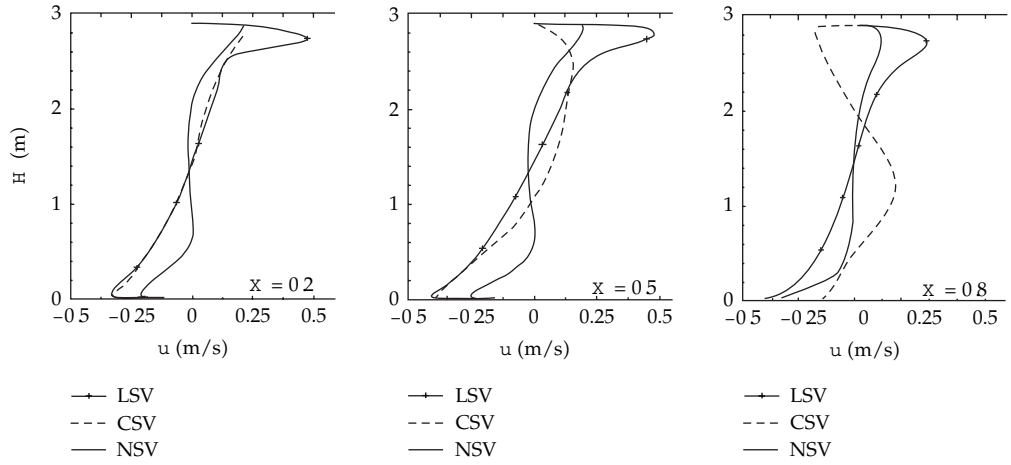

Figure 4: The velocity distributions at different X locations for the cases shown in Figure 2.

is lower. In reverse, as the inlet velocity is lower ($u_{in} = 0.3\,m/s$) (Figure 5(b)), less air reaches the outside wall, and the bulk temperature of the indoor air is higher because of the weaker convective heat transfer along the outside wall.

Figure 6 shows the temperature and velocity distributions for CSV at $T_{fl} = 30°C$, $q_{ow} = -100\,W/m^2$, and $u_{in} = 0.3$ and $0.9\,m/s$. The airflow pattern and temperature distributions are similar to the case shown in Figure 2(c). As the inlet velocity increases ($u_{in} = 0.9\,m/s$) (Figure 6(a)), more air flows are supplied, leading to the more intensive convective heat transfer between the air and the outside wall and the floor. However, because the direction of the inlet velocity is towards the floor, the convective and radiative heat transfer along the floor are dominant. As a result, the bulk temperature of the air in the room is higher. In reverse, as the inlet velocity is lower ($u_{in} = 0.3\,m/s$) (Figure 6(b)), the convective heat transfer along both the outside wall and the floor decreases, which decreases the bulk air temperature in the room as compared to the case of $u_{in} = 0.9\,m/s$. However, the air temperature at $u_{in} = 0.3\,m/s$

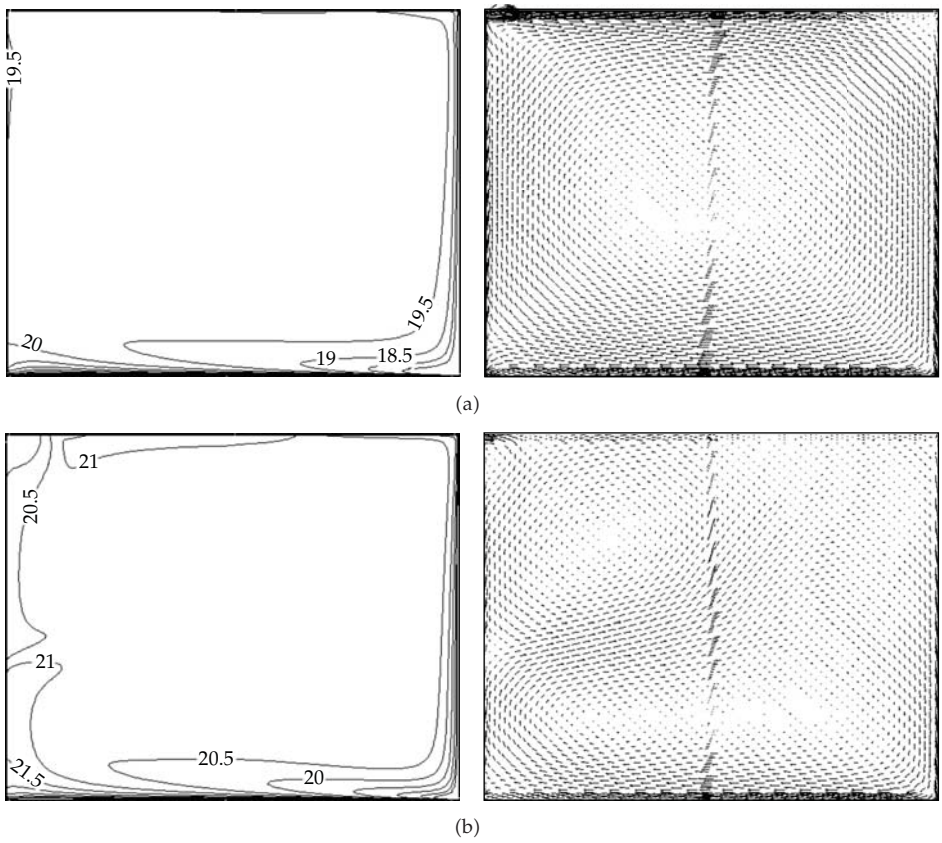

Figure 5: The velocity and temperature distributions for LSV at $T_{fl} = 30°C$, $q_{ow} = -100\,W/m^2$, (a) $u_{in} = 0.3\,m/s$, and (b) $u_{in} = 0.9\,m/s$.

is higher than that for $u_{in} = 0.6\,m/s$. Therefore, the air temperature is related to the intensities of the convective heat transfer along the outside wall and the floor. There exists an optimal inlet velocity for CSV to increase the bulk temperature of the indoor air.

4.2. Characteristics of Radiative and Convective Heat Transfer

The different behaviors of the indoor air temperature under the different conditions are the combined results of the different heat transfer mechanisms. The heat fluxes along the floor and outside wall are studied and the Nusselt numbers for the convective heat transfer Nu_c and the radiative heat transfer Nu_r along the wall surface are given. Radiative heat flux q_r and convective heat flux q_c are defined as

$$q_r = \int_{\Omega} \sigma\left(\varepsilon_{w'} T_{w'}^4 - \alpha_w T_w^4\right) \frac{\cos\theta_1 \cos\theta_2}{\pi s^2} dA_{w'}$$
$$q_c = -\lambda \left.\frac{\partial T}{\partial r}\right|_W, \tag{4.1}$$

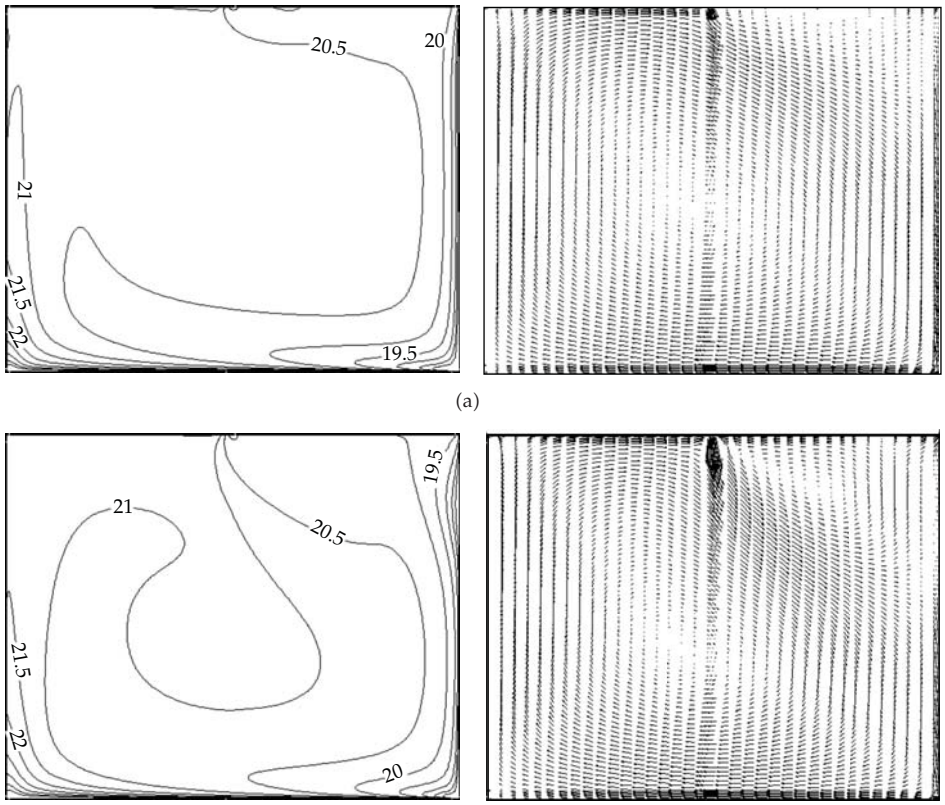

Figure 6: The velocity and temperature distributions for CSV at $T_{fl} = 30°C$, $q_{ow} = -100\,W/m^2$, (a) $u_{in} = 0.3\,m/s$, and (b) $u_{in} = 0.9\,m/s$.

where q_r is net radiative heat flux between the cells w at the outside wall or floor and w' at other walls; s is the distance of two points; θ_1 and θ_2 are the angles to the surface normal, and λ is heat conductivity. The radiative and convective heat transfer coefficients are defined as α_r and α_c:

$$\alpha_c = \frac{q_c}{(T_w - T_b)},$$
$$\alpha_r = \frac{q_r}{(T_w - T_b)}, \tag{4.2}$$

where T_b is the bulk temperature of indoor air, Nu can be calculated through $Nu = \alpha l_e/\lambda$, in which l_e is characteristic length, which is taken as 3.6 m for the floor and 2.9 m for the outside wall.

Figures 7 and 8, respectively, present the distributions of Nu_c and Nu_r distribution along with floor and outside wall for the cases shown in Figure 2. It is found that Nu_r is greater than Nu_c in most of the areas under the different conditions, which indicates that the radiative heat transfer is stronger than the convective heat transfer. For NSV, the radiative heat flux accounts for about 56% of the total heat flux. For LSV and CSV, the percentages of the

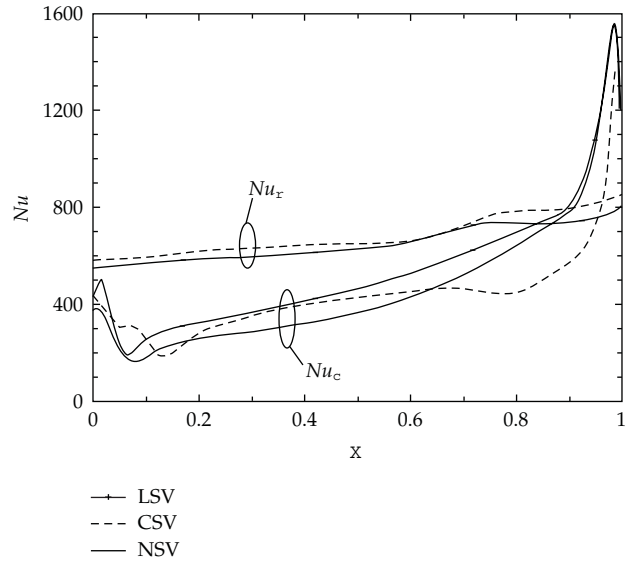

Figure 7: Nu_c and Nu_r distributions along the floor for the cases shown in Figure 2.

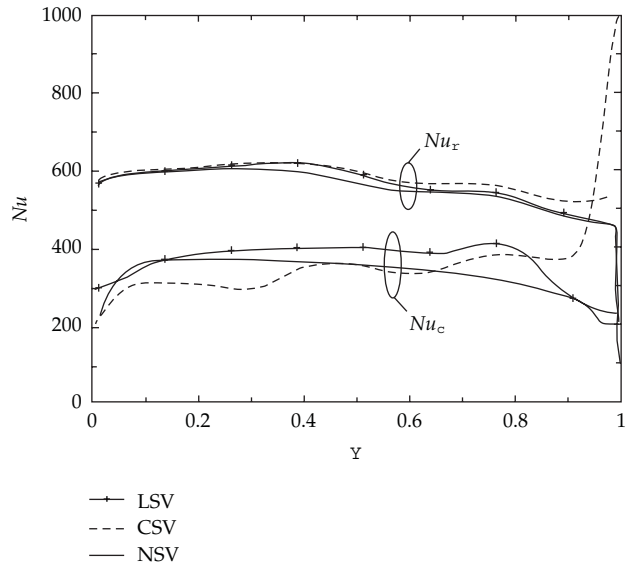

Figure 8: Nu_c and Nu_r distribution along the outside wall for the cases shown in Figure 2.

radiative heat transfer are about 54% and 61%, respectively. In the area near the outside wall, the intense convection is observed due to the local vortex and higher temperature gradients (Figure 3) and thus Nu_c is greater Nu_r, indicating the stronger convective heat transfer in this area. The magnitude of the radiative heat flux increases with the increased X; therefore, the radiation is more significant in the area closer to the low-temperature outside wall. Under LSV and NSV, the air velocity and hence Nu_c decrease with the decreased X. The velocity under CSV increases firstly and then decreases along X, and Nu_c has the same tendency.

Near the inside wall, the local vortex is formed that increases the convective heat transfer and thus Nu_c increases to some extent. There is no significant difference between Nu_r under the three conditions. For LSV, Nu_c is of the largest magnitude as the result of the strongest convective heat transfer. As $X < 0.67$, Nu_c for CSV is greater than that for NSV. It is also found from Figure 8 that Nu_r is greater than Nu_c for all the three conditions except in the area near air inlet for the CSV ($Y > 0.95$), which suggests that the radiation dominates the heat transfer mechanism. Under LSV, Nu_c is larger as $Y < 0.85$ as compared to the two other cases, indicating the strongest convection heat transfer in this area. As $Y > 0.85$, for CSV, the air velocity significantly increases near the inlet, which increases the convection heat transfer.

5. Conclusions

The numerical stimulations of the airflow and heat transfer in the slot-vented room with radiant floor heating unit, including LSV, CSV, and NSV, are performed. The temperature, velocity, and the behaviors of the radiative and convective heat transfer are calculated. The results show that the air temperatures in the room are quite uniform under these three air-supply modes and the average temperature difference is less than 1°C. Under LSV, the forced ventilation has the same moving direction with the natural convection and thus increases the air velocity. Under CSV, the flow pattern is more complex as the combined result of the forced ventilation and natural convection. Radiation is main heat transfer mechanism at the floor and the outside wall under all the three conditions. Radiative heat flux accounts for 50–60% of the total heat flux, which is largest under CSV. LSV offers the strongest convection along the floor and outside wall, which increases the convective heat transfer, especially at cold outside wall. Therefore, the average temperature for LSV is lower than that for CSV.

Concerning the airborne pollutant transports and moisture condensations, the performance of radiant floor heating unit will be further optimized in our future researches.

Acknowledgments

The authors gratefully acknowledge the funding for this project provided by International Science and Technology Cooperative Project of China (2010DFB63830), Major Science and Technology Project of Hunan Province (2010FJ1013), and National Natural Science Foundation of China (51178477).

References

[1] I. B. Kilkis, S. S. Sager, and M. Uludag, "A simplified model for radiant heating and cooling panels," *Simulation Practice and Theory*, vol. 2, no. 2, pp. 61–76, 1994.

[2] A. K. Athienitis and T. Y. Chen, "Experimental and theoretical investigation of floor heating with thermal storage," *ASHRAE Transactions*, vol. 99, no. 1, pp. 1049–1057, 1993.

[3] A. Y. Ghaly and E. M. E. Elbarbary, "Radiation effect on MHD free-convection flow of a gas at a stretching surface with a uniform free stream," *Journal of Applied Mathematics*, vol. 2, no. 2, pp. 93–103, 2002.

[4] S. Shateyi, "Thermal radiation and buoyancy effects on heat and mass transfer over a semi-infinite stretching surface with suction and blowing," *Journal of Applied Mathematics*, vol. 2008, Article ID 414830, 2008.

[5] L. D. Ma, W. Q. Tao, Y. Dai, and D. X. Sun, "Numerical simulation of temperature distribution and turbulent flow in the radiant floor heating room," *Journal of Engineering Thermophysics*, vol. 26, no. 3, pp. 501–503, 2005 (Chinese).

[6] S. Sattari and B. Farhanieh, "A parametric study on radiant floor heating system performance," *Renewable Energy*, vol. 31, no. 10, pp. 1617–1626, 2006.
[7] O. G. Bozkir and S. Canbazoğlu, "Unsteady thermal performance analysis of a room with serial and parallel duct radiant floor heating system using hot airflow," *Energy and Buildings*, vol. 36, no. 6, pp. 579–586, 2004.
[8] N. C. Markatos, "The mathematical modelling of turbulent flows," *Applied Mathematical Modelling*, vol. 10, no. 3, pp. 190–220, 1986.
[9] S. V. Partankar, *Numerical Heat Transfer and Fluid Flow*, McGraw–Hill, 1980.

Hindawi Publishing Corporation
Journal of Applied Mathematics
Volume 2012, Article ID 546203, 20 pages
doi:10.1155/2012/546203

Research Article

Upscaling of Permeability Field of Fractured Rock System: Numerical Examples

Kai Bao, Amgad Salama, and Shuyu Sun

Computational Transport Phenomena Laboratory, Division of Mathematics and Computer Science and Engineering, King Abdullah University of Science and Technology, Thuwal 23955-6900, Saudi Arabia

Correspondence should be addressed to Shuyu Sun, shuyu.sun@kaust.edu.sa

Received 4 January 2012; Revised 19 February 2012; Accepted 19 February 2012

Academic Editor: M. F. El-Amin

When the permeability field of a given porous medium domain is heterogeneous by the existence of randomly distributed fractures such that numerical investigation becomes cumbersome, another level of upscaling may be required. That is such complex permeability field could be relaxed (i.e., smoothed) by constructing an effective permeability field. The effective permeability field is an approximation to the real permeability field that preserves certain quantities and provides an overall acceptable description of the flow field. In this work, the effective permeability for a fractured rock system is obtained for different coarsening scenarios starting from very coarse mesh all the way towards the fine mesh simulation. In all these scenarios, the effective permeability as well as the pressure at each cell is obtained. The total flux at the exit boundary is calculated in all these cases, and very good agreement is obtained.

1. Introduction

The first level of upscaling encountered when studying phenomena occurring in porous media is related to adopting the continuum hypothesis to such complex formations. That is moving from pore scale simulations in which variables are only defined within the fluid region to the continuum description in which macroscopic variables are defined everywhere in the simulation domain. In doing so, certain conditions and length scale constraints need to be fulfilled in order to generate macroscopic quantities that are scale independent [1]. While these length scale constraints may be easily adopted in statistically homogeneous porous media, it may be difficult to satisfy particularly closer to the interface boundaries between media with very different textures [2]. Unfortunately, these sharp interface boundaries are ubiquitous in rock systems which apparently contain several fractures and fissures. These fractures have significant effects on both flow and transport in porous media. They provide fluids and solutes with significantly less resistance paths compared with the surrounding

matrix and therefore can lead solutes to reach further distances than what simulations ignoring them would normally predict. There are two approaches to dealing with these fractures depending on their density and distributions in rock systems. For rock systems with few penetrating fractures, it is customary to consider the discrete fracture model (e.g., [3, 4]). In this model, fractures are assumed as two-dimensional surfaces impeded within the given rock matrix domain. These fracture surfaces have their own properties and equations which include interaction terms between the rock matrix and the fractures. When the numbers of the fractures are large and their geometrical distributions are complex such that it becomes exceedingly difficult to consider them in simulation, another alternative is to construct an equivalent porous medium domain by further increasing the averaging representative volume. In this approach, one abandons the fractures and considers another continuum, coarser in nature, but may be acceptable for our engineering application and design.

In terms of simulation, although the discrete fracture model provides an elegant way to deal with fractures when their density is manageable, the drawback of this approach, however, is the fact that the interaction term between the fracture and the surrounding rock matrix is, in most cases, not known and ends up as a fitting parameter. The other approach is to refine the mesh all the way to the fractures level, which apparently poses enormous difficulties in large systems particularly when modeling complex transport problems like multiphase compositional flows. It has been, therefore, proposed that an even higher level of upscaling may be required to generate field properties to reduce the required computing resources and provide certain requirements satisfaction. These requirements are related to the fact that the solution of the upscaled system should produce approximately close results to those obtained from simulating the real system. That is if the permeability field may be relaxed such that the sharp interface boundaries may be smoothed, in a sense, the requirements for denser mesh closer to the sharp interface boundaries may be abandoned, and it may be possible to significantly decrease the number of degrees of freedom of the system. Different approaches have been considered in the literatures based on either deterministic approaches (e.g., [5–13], etc.) or stochastic approaches (e.g., [14–18], etc.). In the next section we introduce a quick review of the previous work emphasizing on two methods which are related to this work closely.

2. Investigation of the Upscaling Techniques

A review on the upscaling of hydraulic conductivities in heterogeneous media may be found in the work of Farmer [11] and in the work of Wen and Gomez-Hernandez [8]. In both reviews the authors pointed out that the need for upscaling stems from the fact that the scales at which measurements are taken and the scale at which reservoirs are discretized are usually different. Therefore, it is suggested that a transformation of hydraulic conductivities from the scale of the measurements into a coarser grid of block conductivity tensors amenable for input to a numerical flow simulator may be needed. Holden and Nielsen [19] pointed out that the scale at which permeability in a reservoir may change is much finer than what is possible to use in a reservoir simulator. They proposed a methodology in which permeability is formulated as a minimization problem. In the method, the upscaled permeability is defined as that which minimizes the difference between the pressure and the velocity fields generated by the fine and coarse scale pressure equations. In this work, however, we apply an averaging over a coarser grid of the porous media domain such that certain quantities are conserved. The problem may be casted as follows: consider a three-dimensional rectangular domain, Ω with boundary $\partial\Omega$, if $\mathbf{v}$ represents Darcy's velocity and p the pressure field of the fluid

saturating the porous medium domain, the governing equations describing this system may be written as

$$\nabla \cdot \mathbf{v} = q, \tag{2.1}$$

$$\mathbf{v} = -\mathbf{K}\nabla p. \tag{2.2}$$

From which one obtains an equation only in the pressure given as

$$-\nabla \cdot \mathbf{K}\nabla p = q. \tag{2.3}$$

The upscaling problem, as described in [11], is to find a corresponding coarse hydraulic conductivity field, $\tilde{\mathbf{K}}$ such that the new velocity and pressure fields, $\tilde{\mathbf{v}}$, $\tilde{p}$ obtained from solving the equivalent system of equations, are close, in some sense, to the fine scale velocity and pressure fields, $\mathbf{v}$, p. The system of equations that need to be solved in this case takes the form

$$\begin{aligned} \nabla \cdot \tilde{\mathbf{v}} &= \tilde{q}, \\ \tilde{\mathbf{v}} &= -\tilde{\mathbf{K}}\nabla \tilde{p}. \end{aligned} \tag{2.4}$$

The general methodology is to seek an equivalent (effective) hydraulic conductivity field $\tilde{\mathbf{K}}$, calculated from a set of boundary conditions, and it may be used afterwards to yield accurate results with different boundary conditions. To do so, the rectangular domain is divided into a number of segments in each direction, that is, N_x, N_y, and N_z to form boxes of sizes, H_x, H_y, and H_z. These cells are called the coarse cells. Furthermore, each of the boxes is divided into n_x, n_y, and n_z finer boxes with sizes h_x, h_y, and h_z. The hydraulic conductivity tensor field $\mathbf{K}$, generally, takes a different value in each of the fine cells. There have been two approaches highlighted by Farmer [11], which may be used to construct the coarser hydraulic conductivity field, namely, the global (overall) strategy and the local methods. The first technique is performed in two stages. In the first stage one needs to perform one or more fine grid experiment which may cover the whole domain or at least most of it. Three test cases for each scenario are performed, one in each coordinate direction on the fine grid within each of the coarse cells. In the second stage, the fine grid simulations are used to extract the coarse scale permeability, $\tilde{\mathbf{K}}$. In the second method, which is sometimes called the local-local or the subdomain method, each coarse cell is considered separately, as shown in Figure 1, and the three independent flow experiments in the three directions are performed. In each of these experiments, no flow conditions are assigned to the four surfaces parallel to the flow direction and constant pressure conditions on the two surfaces normal to the flow direction. If the total flux may be computed through one of the faces that were assigned pressure boundary condition, an equivalent permeability for this cell may be computed [20, 21].

There are, however, certain requirements for the correct upscaling as defined in [1, 2]. For the case of single phase incompressible fluids, it suffices to require that the flux across any area in the domain should be the same for all levels of upscaled description. This requirement

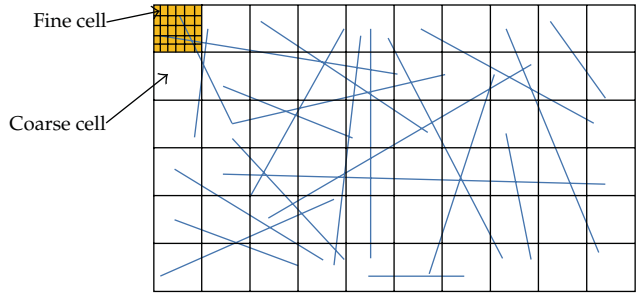

Figure 1: Representative coarse and fine mesh.

ensures a divergence-free flow field in case there is no source/sink term. This condition can be defined as

$$\int_A \tilde{\mathbf{v}}(\mathbf{r}) \cdot \mathbf{n}\, dA = \int_A \mathbf{v}(\mathbf{r}) \cdot \mathbf{n}\, dA, \tag{2.5}$$

where $\tilde{\mathbf{v}}$ and $\mathbf{v}$ are the velocity vectors at different level of upscaling, and $\mathbf{r}$ is the position vector which scans the area A. Applying this requirement on the local-local method mentioned earlier in which each coarse cell is considered separately, the above equation reduces to

$$\tilde{\mathbf{v}}(\mathbf{x}) \cdot \mathbf{n} A = \int_A \mathbf{v}(\mathbf{r}) \cdot \mathbf{n}\, dA, \tag{2.6}$$

where $\tilde{\mathbf{v}}(\mathbf{x})$ represents the velocity vector at the center of the coarse cell face, and $\mathbf{x}$ is the position vector which defines the center of the cell face. Likewise for volumetric quantities (e.g., the source/sink term, q), Salama and Van Geel [1] pointed out that

$$\int_v \tilde{q}(\mathbf{r}) dv = \int_v q(\mathbf{r}) dv = \tilde{q}(\mathbf{x}) v. \tag{2.7}$$

3. The Subdomain Technique

We apply the local-local method to obtain the effective permeability field for a given complex permeability field in fractured rock system. The simulation domain represents a rectangular two-dimensional area with a set of randomly generated fractures. We use the cell-centered finite difference scheme (CCFD) to approximate the governing equations because it satisfies mass conservation law locally. Furthermore, we consider the fractures oriented horizontally and vertically, as shown schematically in Figure 2. The local-local method deals with each macroscopic cell separately. For this purpose, we define two different meshes; the first mesh is the coarse mesh and it is defined globally over the whole simulation domain, and the second mesh is fine according the complexity of the permeability field within each coarse cell. That is we construct the coarse rectangular mesh over the whole simulation domain, $\{X_0, X_1, X_2, \ldots, X_i, \ldots, X_m\} \times \{Y_0, Y_1, Y_2, \ldots, Y_j, \ldots, Y_n\}$, and for each coarse mesh we construct a finer mesh given as $\{x_0, x_1, x_2, \ldots, x_i, \ldots, x_p\} \times \{y_0, y_1, y_2, \ldots, y_j, \ldots, y_q\}$.

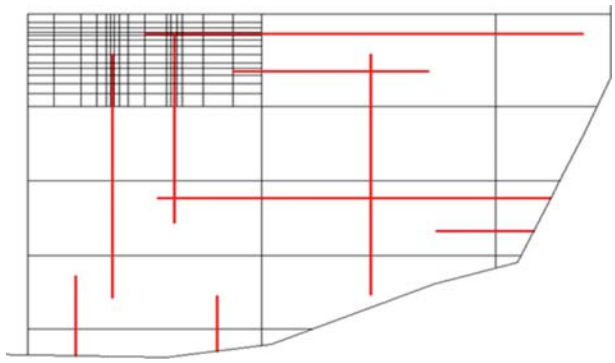

Figure 2: The fine and the coarse mesh used with the fractures.

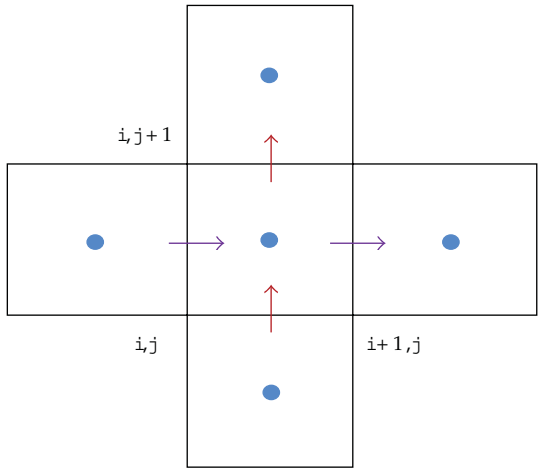

Figure 3: A generic cell for finite difference approximation.

4. Discretization of the Governing Equations

For the generic cell shown in Figure 3, the governing equations for this problem may be approximated using the cell-centered finite difference scheme with the various velocity components at the mid edges of the cell obtained as follows:

$$u_x\left(i, j+\frac{1}{2}\right) = -K_{xx}\left(i, j+\frac{1}{2}\right)\frac{P(i+1/2, j+1/2) - P(i-1/2, j+1/2)}{x(i+1/2) - x(i-1/2)}, \tag{4.1}$$

$$u_x\left(i+1, j+\frac{1}{2}\right) = -K_{xx}\left(i+1, j+\frac{1}{2}\right)\frac{P(i+3/2, j+1/2) - P(i+1/2, j+1/2)}{x(i+3/2) - x(i+1/2)}, \tag{4.2}$$

$$u_y\left(i+\frac{1}{2}, j\right) = -K_{yy}\left(i+\frac{1}{2}, j\right)\frac{P(i+1/2, j+1/2) - P(i+1/2, j-1/2)}{y(j+1/2) - y(j-1/2)}, \tag{4.3}$$

$$u_y\left(i+\frac{1}{2}, j+1\right) = -K_{yy}\left(i+\frac{1}{2}, j+1\right)\frac{P(i+1/2, j+3/2) - P(i+1/2, j+1/2)}{y(j+3/2) - y(j+1/2)}. \tag{4.4}$$

Equation (2.2) is discretized, likewise, in the following form:

$$\frac{u_x(i+1,j+1/2)-u_x(i,j+1/2)}{x(i+1)-x(i)}+\frac{u_y(i+1/2,j+1)-u_y(i+1/2,j)}{y(j+1)-y(j)}=q\left(i+\frac{1}{2},j+\frac{1}{2}\right). \tag{4.5}$$

Now substituting (2.7)–(4.3) into (4.4), one obtains an equation in the pressure only, as explained earlier, which may be solved to obtain the pressure field from which the velocity field may be determined. The permeability at cell edges is obtained based on the harmonic mean relationship which is given as

$$\begin{aligned} &k_{xx}\left(i,j+\frac{1}{2}\right)\\ &\quad=\frac{x(i+1)-x(i-1)}{(x(i)-x(i-1))/\left(k_{xx}(i-1/2,j+1/2)\right)+(x(i+1)-x(i))/\left(k_{xx}(i+1/2,j+1/2)\right)},\\ &k_{yy}\left(i+\frac{1}{2},j\right)\\ &\quad=\frac{y(i+1)-y(i)}{(y(i)-y(i-1))/\left(k_{yy}(i+1/2,j-1/2)\right)+(y(i+1)-y(i))/\left(k_{yy}(i+1/2,j+1/2)\right)}. \end{aligned} \tag{4.6}$$

5. Application of the Local Upscaling Technique to Fractured Rock System

In this work we consider the local-local upscaling technique to generate an effective permeability field which would require less computational load and in the same time would result in reasonable match with the fine scale modeling. As explained earlier the scheme follows the following steps.

(i) Discretize the whole domain with the appropriate fine mesh based on the complexity of the permeability field and fractures structure.

(ii) Discretize the whole domain with the required coarse mesh that conforms with the fine mesh (i.e., the mesh coincides with the fine mesh).

(iii) For each coarse cell, solve the boundary value problem given by (2.3) over the finer cells subject to predefined boundary conditions. That is to get the effective permeability in the x and y-directions, K_{xx} and K_{yy}, we consider two cases as shown in Figure 4. For example, in Figure 4(a), we consider a no-flow boundary condition at the top and bottom boundaries and prescribed pressure boundary condition (say $p_1 = 1$ and $p_2 = 0$) at the other two sides. Similar boundary conditions are suggested in Figure 4(b). The velocity at the finer scale could then be calculated.

(iv) Using (2.6), one may calculate the x and y-velocity at the center of the faces of the coarse cell which encompass the finer mesh.

(v) These velocities can then be used to calculate the effective permeability components in x and y directions with the Darcy's equation (2.2).

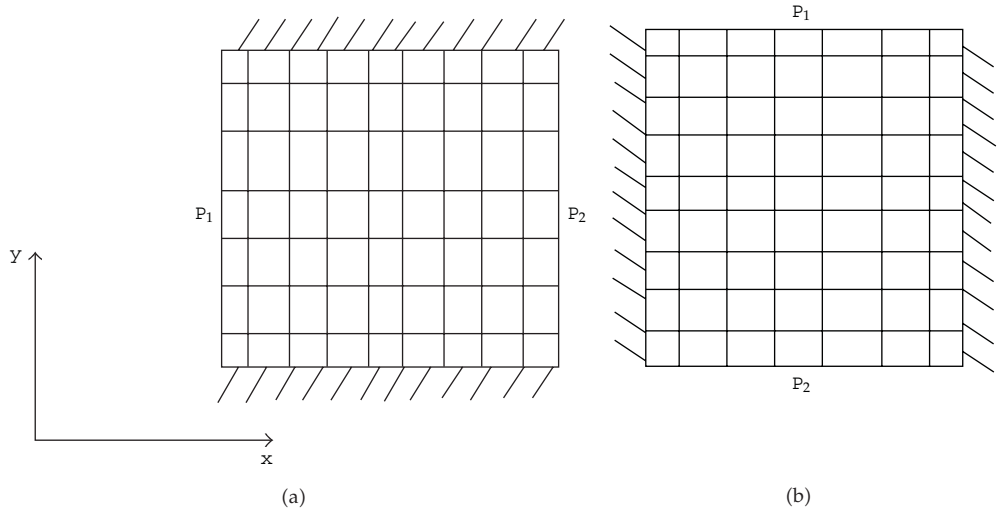

Figure 4: The boundary condition for each coarse cell.

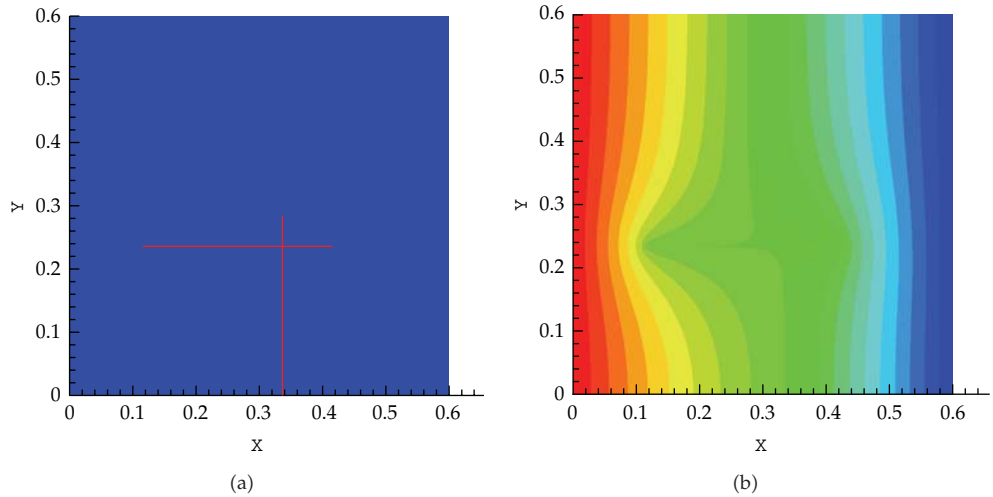

Figure 5: Fractures orientations (2 fractures) and pressure contours based on the fine mesh.

6. Numerical Examples

Several scenarios with different fractures numbers and distributions have been considered. The simulation domain in all these scenarios is $[0, 0.6] \times [0, 0.6]$. For the sake of simplicity, the width and the length of the fractures in all the simulation scenarios are considered identical as 0.00015 and 0.12, respectively (i.e., 0.2 times the length of the domain). In the 2-fracture scenario, the length of the fractures is chosen 0.3, 0.5 times of the size of the domain. The locations of the fractures are random. The flow rate in the fracture is usually described with

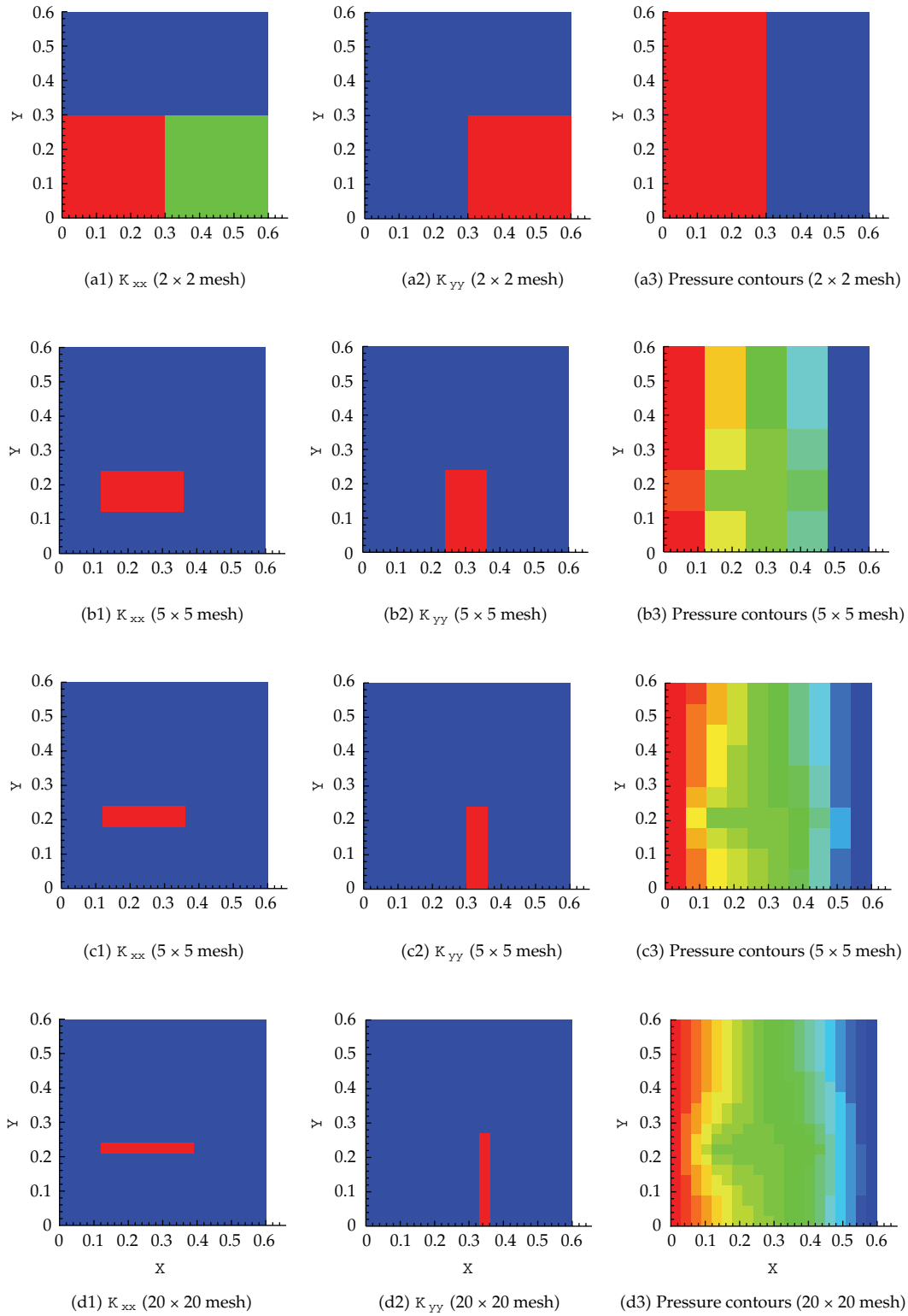

(a1) K_{xx} (2 × 2 mesh) (a2) K_{yy} (2 × 2 mesh) (a3) Pressure contours (2 × 2 mesh)

(b1) K_{xx} (5 × 5 mesh) (b2) K_{yy} (5 × 5 mesh) (b3) Pressure contours (5 × 5 mesh)

(c1) K_{xx} (5 × 5 mesh) (c2) K_{yy} (5 × 5 mesh) (c3) Pressure contours (5 × 5 mesh)

(d1) K_{xx} (20 × 20 mesh) (d2) K_{yy} (20 × 20 mesh) (d3) Pressure contours (20 × 20 mesh)

Figure 6: Continued.

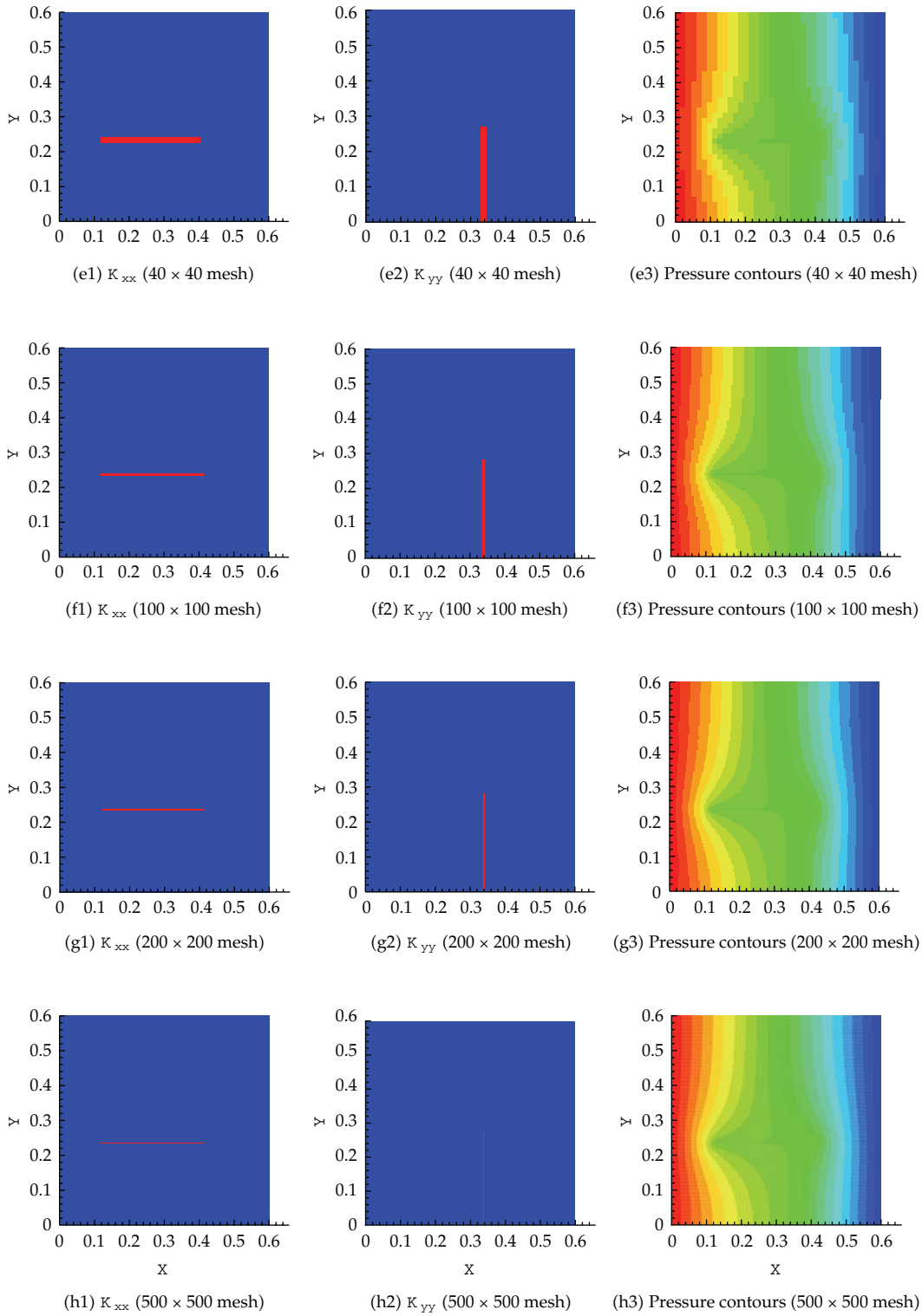

Figure 6: Effective permeability and pressure contours for the 2 fractures scenarios for different degrees of resolutions.

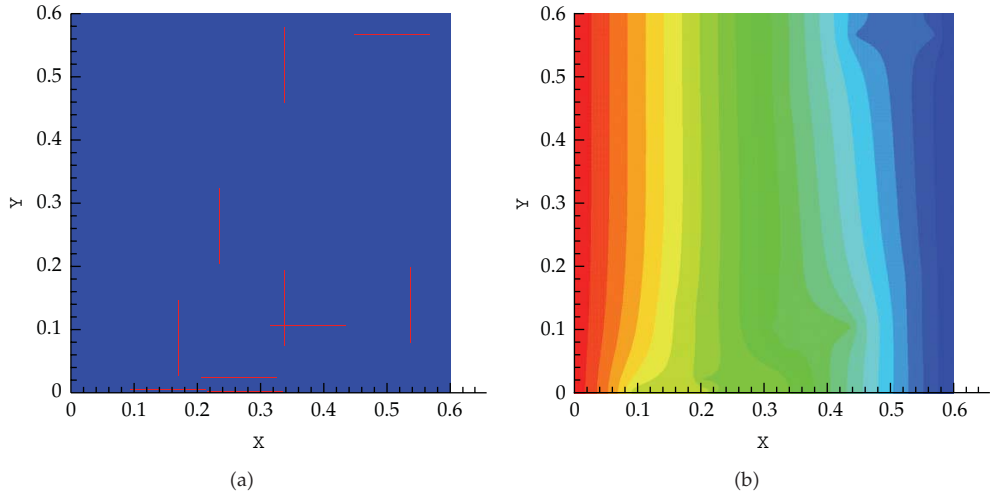

Figure 7: Fractures orientations (10 fractures) and pressure contours based on the fine mesh.

the cubic law [22] in which the flux through the fracture is given as a cubic function of the fracture aperture, therefore

$$Q = -\frac{\rho g b^3}{12\mu}\frac{\Delta h}{\Delta L}, \tag{6.1}$$

where Q is the flux across the fracture section, ρ is the density, μ is the viscosity, g is the gravity, and b is the fracture aperture. Generally, the hydraulic conductivity in the fracture region will be much higher than that in the matrix and plays a dominant role in the flow in the fracture-matrix system. In the paper, the hydraulic conductivity of the fracture region is specified as 3×10^5 times that of the matrix. The mesh size of the fine mesh is 0.0006 for the matrix and 0.00015 for the fractures. Four scenarios with different number of fractures are considered. In the first scenario, only one fracture in the horizontal direction and one fracture in the vertical direction, respectively, are assumed. The other three scenarios consider, respectively, 5, 20 and 400 fractures in both the horizontal and vertical directions. At first, fine meshes are generated with the number of the mesh cells in horizontal and vertical directions are respectively as follows: 1002×1002 for the 2-fracture scenario, 1008×1008 for the 10-fracture scenario, 1032×1035 for the 40-fracture scenario, and 1480×1500 for the 800-fracture scenario. The flow equations are solved with the fine mesh, and the pressure distribution is obtained for each scenario. As will be seen later, the flow in the whole domain is very much affected by the fractures. To consider different levels of upscaling, the domain is discretized with a coarse mesh of different resolutions. In this work we consider very coarse resolutions and moderately fine resolutions. In all these levels of resolutions, effective permeability is obtained based on (2.2).

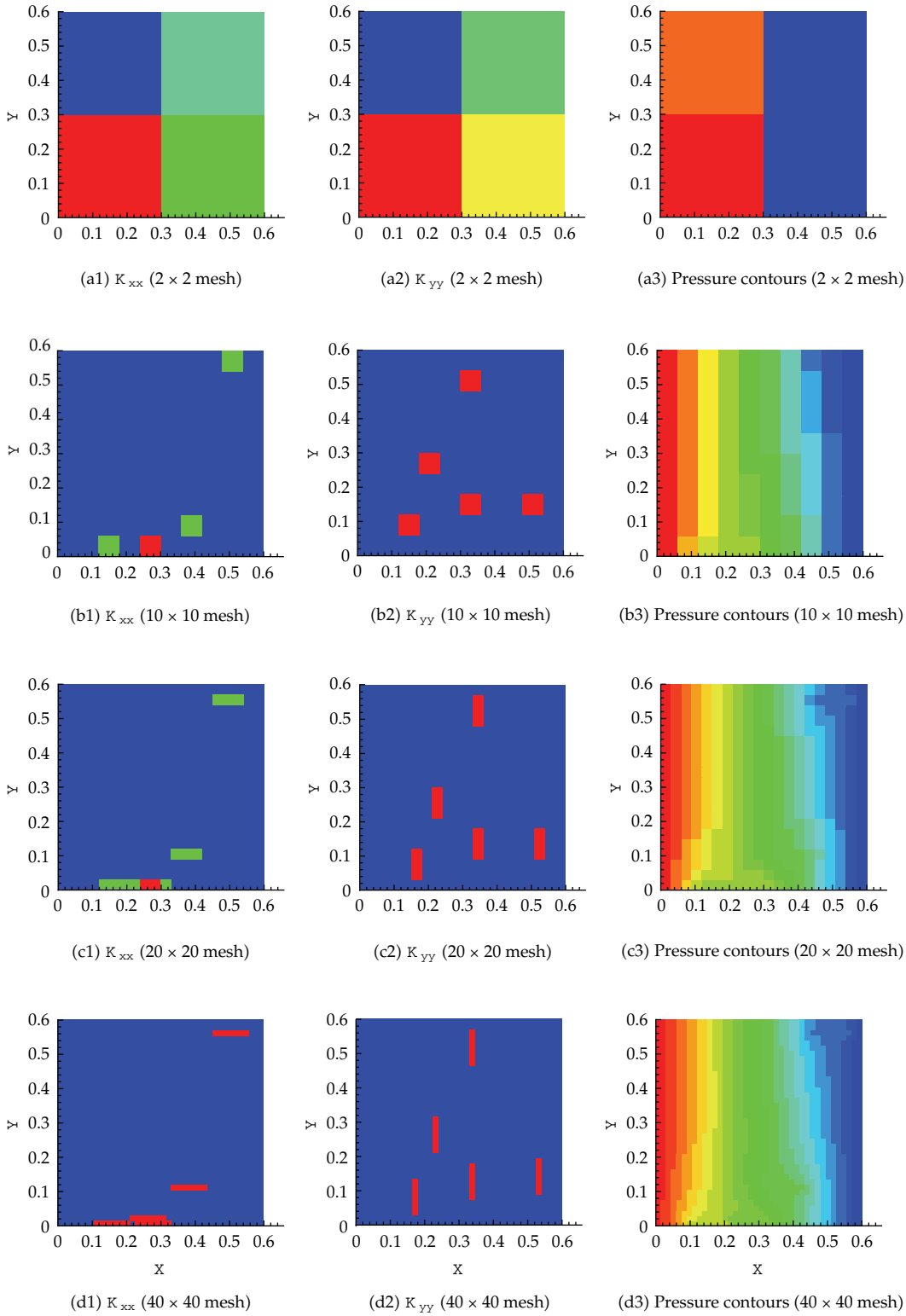

(a1) K_{xx} (2 × 2 mesh) (a2) K_{yy} (2 × 2 mesh) (a3) Pressure contours (2 × 2 mesh)

(b1) K_{xx} (10 × 10 mesh) (b2) K_{yy} (10 × 10 mesh) (b3) Pressure contours (10 × 10 mesh)

(c1) K_{xx} (20 × 20 mesh) (c2) K_{yy} (20 × 20 mesh) (c3) Pressure contours (20 × 20 mesh)

(d1) K_{xx} (40 × 40 mesh) (d2) K_{yy} (40 × 40 mesh) (d3) Pressure contours (40 × 40 mesh)

Figure 8: Continued.

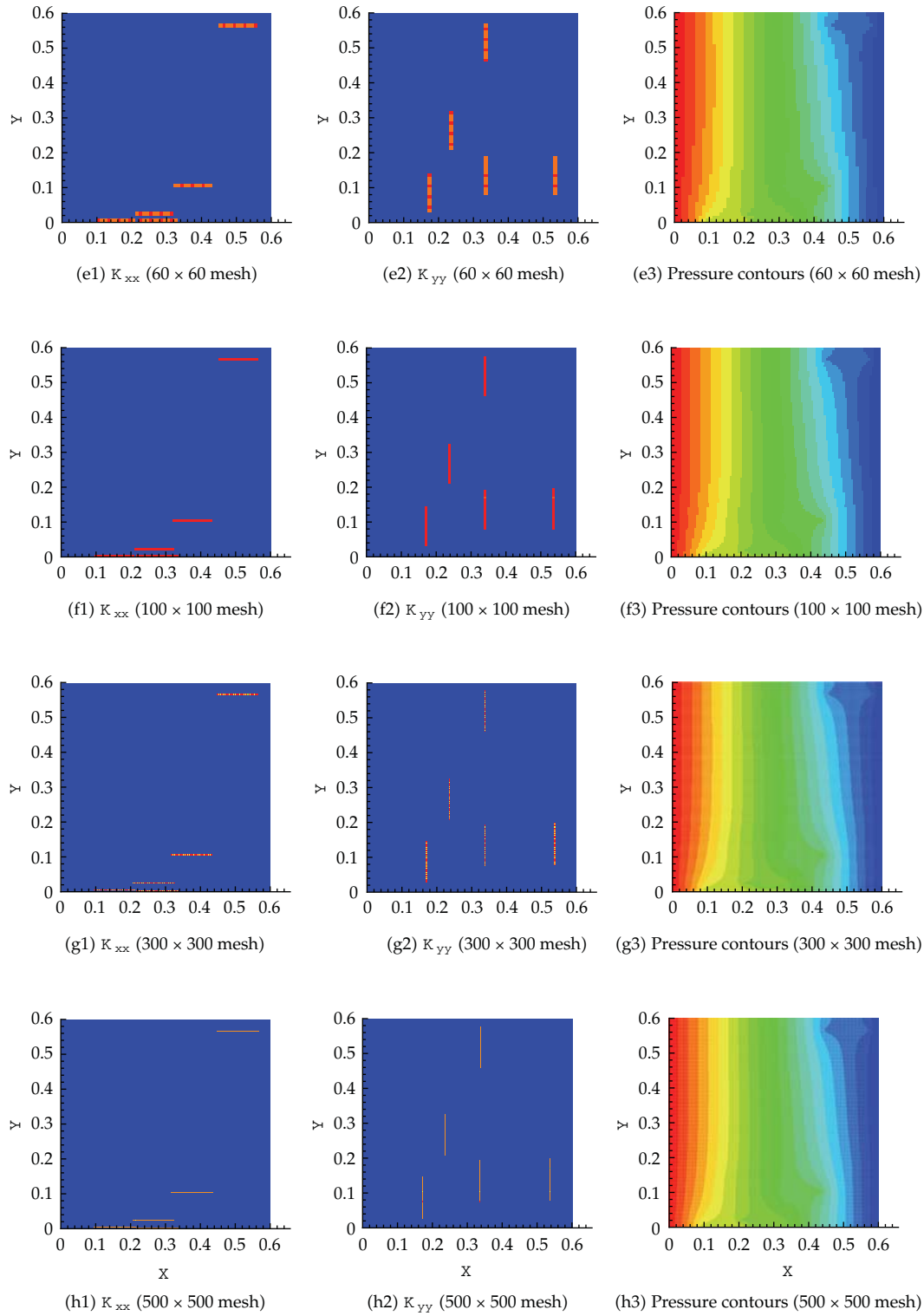

Figure 8: Effective permeability and pressure contours for the 10 fractures scenarios for different degrees of resolutions.

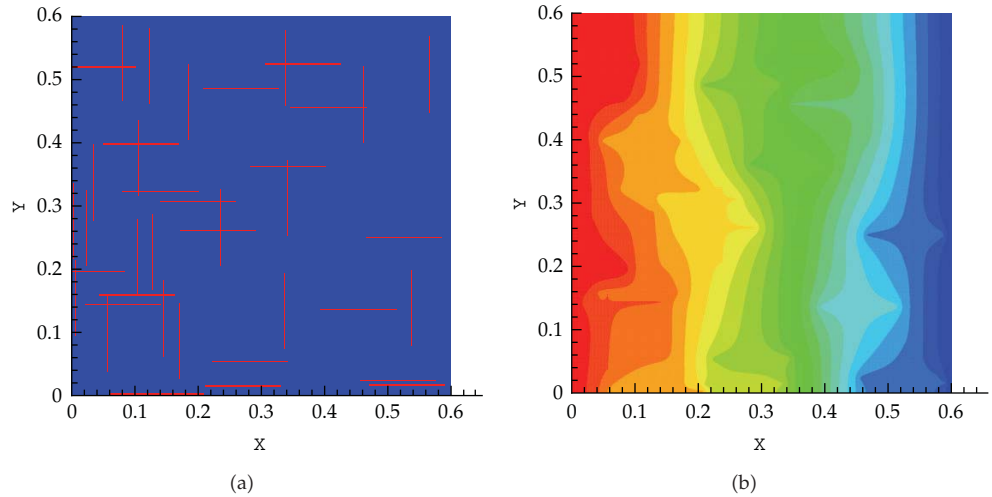

Figure 9: Fractures orientations (40 fractures) and pressure contours based on the fine mesh.

6.1. Example 1: One Fracture in Both the Horizontal and Vertical Directions

In this scenario, two fractures are generated randomly as shown in Figure 5(a). The pressure field for this system obtained by solving the governing equations using the fine mesh is shown in Figure 5(b), from which we can see the apparent influence of the fractures in distorting the pressure field.

Several coarsening scenarios are considered, namely, 2×2, 5×5, 20×20, 40×40, 100×100, and 500×500. In all these scenarios, the requirement that the flux across any surface calculated using the fine mesh and any other coarse mesh is the same. The generated effective hydraulic conductivity of each cell, $\widetilde{k}_{xx}$ and $\widetilde{k}_{yy}$, for different resolution scenarios is shown in Figure 6. Apparently, the permeability of the cells containing fractures is larger. Furthermore, as the resolution of the mesh increases, the permeability contrast sharpens around the fractures. Figure 6 also shows the pressure at the center of each cell for the different resolution scenarios. It is apparent that the pressure field gets closer to the fine scale simulation as the resolution increases. On comparing the flux at the exit boundary (Table 1), it is clear that the flux for different coarsening scenario is close to one another.

6.2. Example 2: Five Fracture in Both the Horizontal and Vertical Directions

In this scenario, five fractures are generated randomly in both the horizontal and vertical directions (i.e., 10 fractures in total), as shown in Figure 7(a). The pressure field for this system as obtained by solving the governing equations using the very fine mesh is shown in Figure 7(b). Again, the influence of the fractures in distorting the pressure field is significant.

Effective permeability in each cell is shown in Figure 8, which shows that the effective permeability approaches that of the fine mesh simulation as the number of grid cells increase. Again the flux at the exit boundary is very close to the different coarsening scenarios as depicted in Table 1.

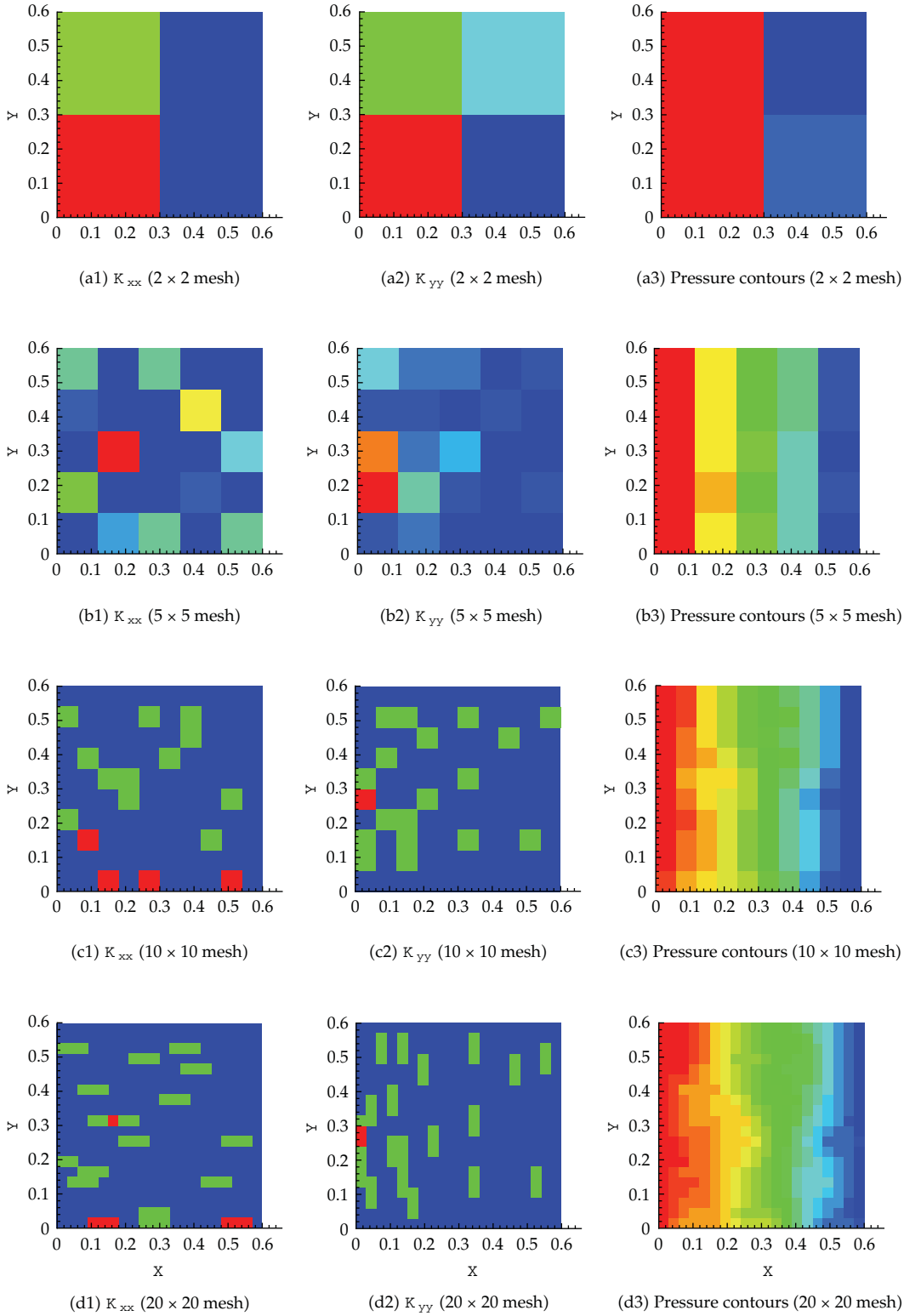

(a1) K_{xx} (2 × 2 mesh) (a2) K_{yy} (2 × 2 mesh) (a3) Pressure contours (2 × 2 mesh)

(b1) K_{xx} (5 × 5 mesh) (b2) K_{yy} (5 × 5 mesh) (b3) Pressure contours (5 × 5 mesh)

(c1) K_{xx} (10 × 10 mesh) (c2) K_{yy} (10 × 10 mesh) (c3) Pressure contours (10 × 10 mesh)

(d1) K_{xx} (20 × 20 mesh) (d2) K_{yy} (20 × 20 mesh) (d3) Pressure contours (20 × 20 mesh)

Figure 10: Continued.

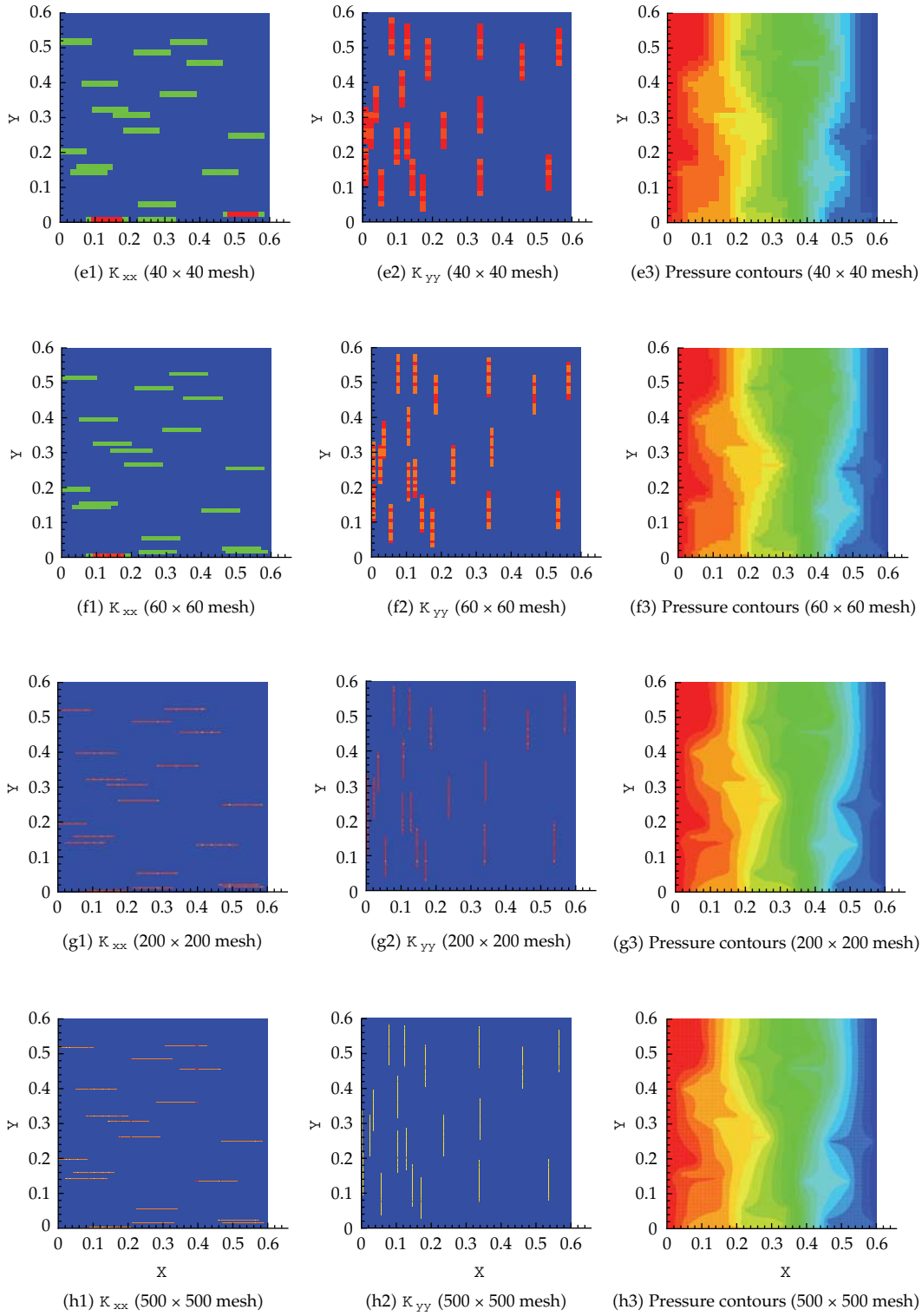

Figure 10: Effective permeability and pressure contours for the 40 fractures scenarios for different degrees of resolutions.

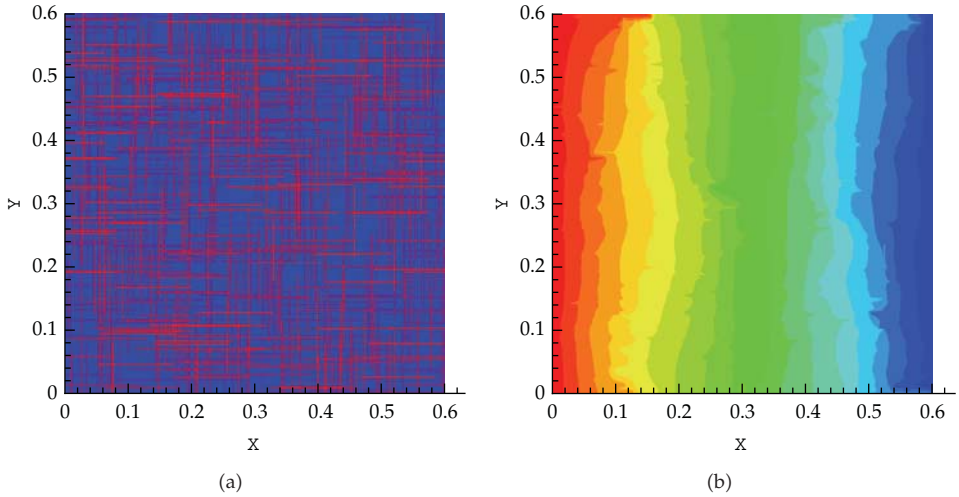

Figure 11: Fractures orientations (800 fractures) and pressure contours based on the fine mesh.

6.3. *Example 3: Twenty Fractures in Both the Horizontal and Vertical Directions*

In this scenario, 20 fractures in x and 20 in the y directions are considered, as shown in Figure 9(a). The pressure field obtained by solving the governing equations based on the actual permeability field is shown in Figure 9(b). The effect of the fractures on the pressure field is apparent.

On the other hand, the effective permeability field obtained from solving the equivalent equations as explained earlier is shown in Figure 10. It is clear that as the number of grid cells increases, the system approach that based on the actual permeability field. Table 1 confirms again that the flux at the exit boundary is almost identical for the different coarsening scenarios.

6.4. *Example 4: 400 Fractures in Both the Horizontal and Vertical Directions*

As shown in Figures 11 and 12, similar behavior is obtained for this scenario which assumes 400 fractures in both the horizontal and vertical directions for both the effective permeability and the pressure fields. In this scenario, we consider several degrees of coarsening including, 2×2, 10×10, 20×20, 40×40, 300×300, and 500×500.

Apparently in this scenario, the large number of fractures will increase the overall effective hydraulic conductivity field which will result in a significantly larger flux compared with the other scenarios. Indeed this is the case as shown in Table 1.

7. Conclusions

In this work several numerical examples have been considered to calculate effective hydraulic properties for a given fractured porous medium domain. Several scenarios of fractured systems have been considered starting with two fractures up to 800 fractures. Cell-centered

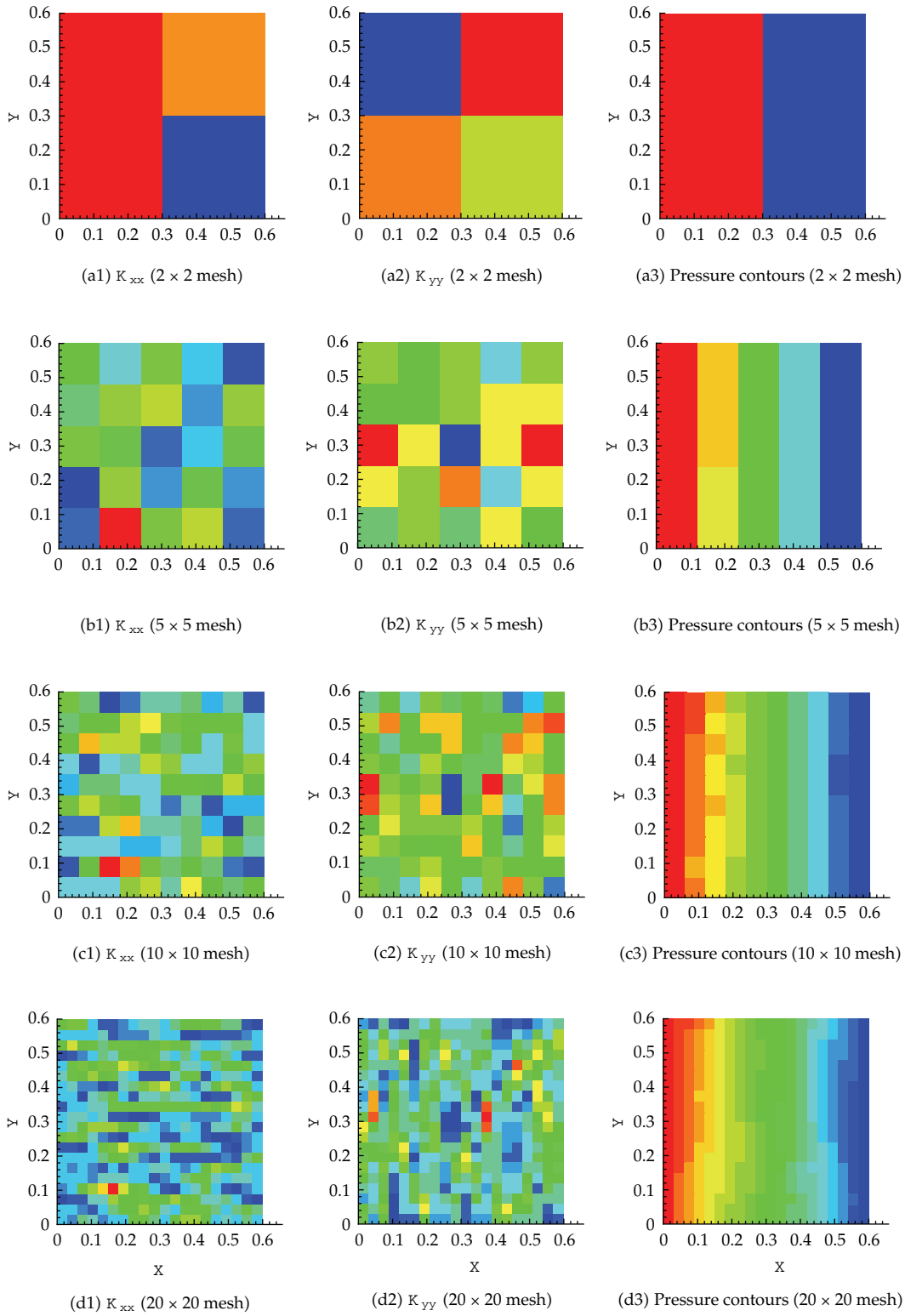

(a1) K_{xx} (2 × 2 mesh) (a2) K_{yy} (2 × 2 mesh) (a3) Pressure contours (2 × 2 mesh)

(b1) K_{xx} (5 × 5 mesh) (b2) K_{yy} (5 × 5 mesh) (b3) Pressure contours (5 × 5 mesh)

(c1) K_{xx} (10 × 10 mesh) (c2) K_{yy} (10 × 10 mesh) (c3) Pressure contours (10 × 10 mesh)

(d1) K_{xx} (20 × 20 mesh) (d2) K_{yy} (20 × 20 mesh) (d3) Pressure contours (20 × 20 mesh)

Figure 12: Continued.

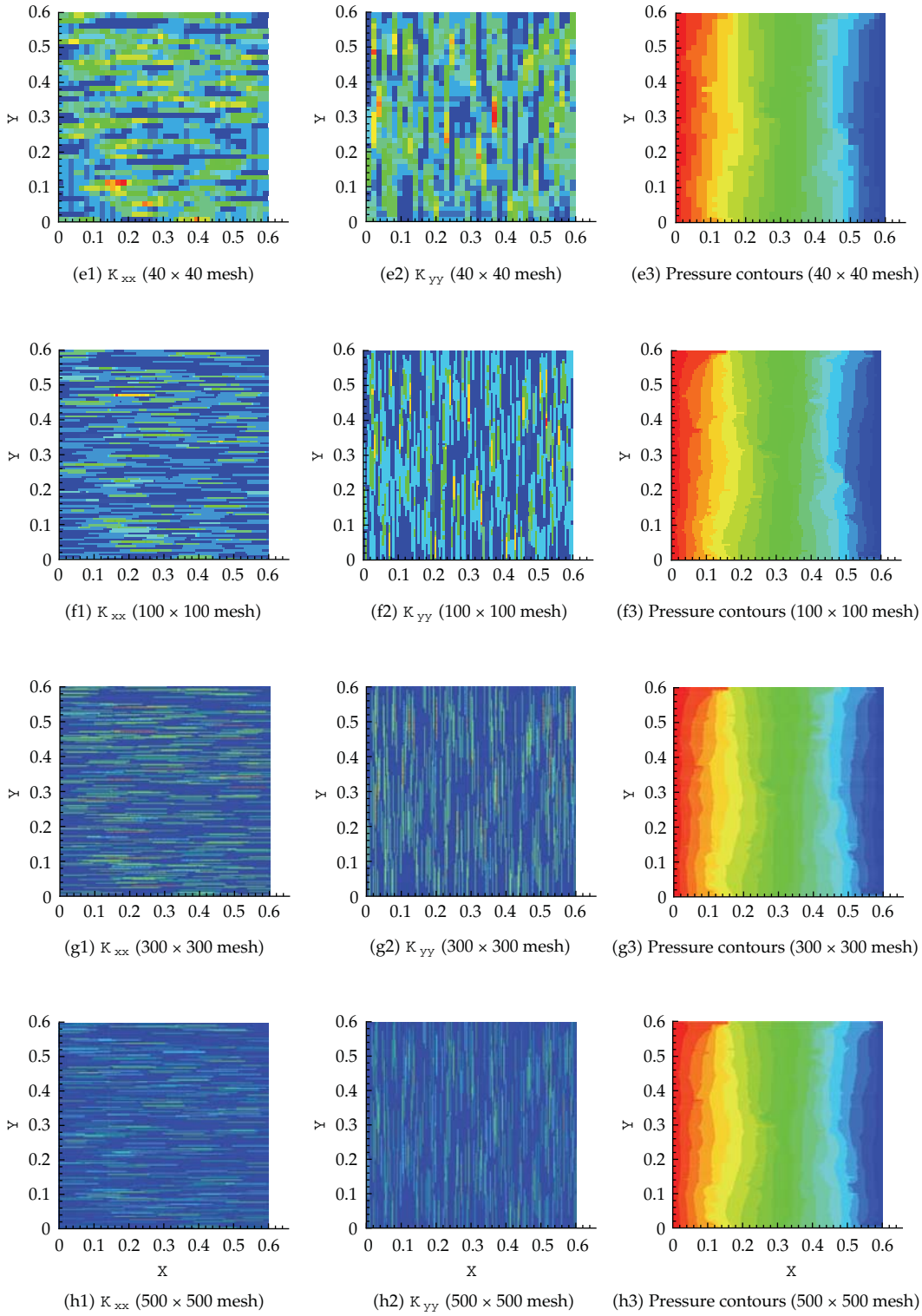

Figure 12: Effective permeability and pressure contours for the 800 fractures scenarios for different degrees of resolutions.

Table 1: Flux across the exit boundary for the different fractures and mesh scenarios.

	2 fractures	10 fractures	40 fractures	800 fractures
Reference (fine mesh)	1.238536e − 03	1.140093e − 03	1.784033e − 03	4.037607e + 00
Upscaled (2 × 2)	1.2060398e − 03	1.1671849e − 03	1.7678765e − 03	4.0482439e + 00
Upscaled (5 × 5)	1.2279665e − 03	1.1480335e − 03	1.6639357e − 03	4.0201914e + 00
Upscaled (10 × 10)	1.2305291e − 03	1.1357165e − 03	1.6719508e − 03	4.0624327e + 00
Upscaled (20 × 20)	1.2377141e − 03	1.1567826e − 03	1.7251369e − 03	4.0636998e + 00
Upscaled (40 × 40)	1.2329549e − 03	1.1414539e − 03	1.7356198e − 03	4.0958317e + 00
Upscaled (60 × 60)	1.2330102e − 03	1.1364853e − 03	1.7344252e − 03	3.9842654e + 00
Upscaled (80 × 80)	1.2312922e − 03	1.1368569e − 03	1.7406374e − 03	4.0324003e + 00
Upscaled (100 × 100)	1.2368716e − 03	1.1353105e − 03	1.7651864e − 03	4.0198896e + 00
Upscaled (160 × 160)	1.2354428e − 03	1.1366243e − 03	1.7682102e − 03	3.9614817e + 00
Upscaled (200 × 200)	1.2376183e − 03	1.1376407e − 03	1.7735081e − 03	4.0495773e + 00
Upscaled (240 × 240)	1.2366092e − 03	1.1380291e − 03	1.7735767e − 03	3.9653353e + 00
Upscaled (300 × 300)	1.2393249e − 03	1.1413561e − 03	1.7762217e − 03	3.9176552e + 00
Upscaled (400 × 400)	1.2368358e − 03	1.1370930e − 03	1.7671836e − 03	3.7225614e + 00
Upscaled (500 × 500)	1.2378015e − 03	1.1405213e − 03	1.7877663e − 03	4.0850977e + 00

finite different method has been used, and therefore the fractures orientations are considered only in the horizontal and vertical directions. Different coarsening scenarios have been considered for each fracture scenario starting with very coarse mesh (2 × 2) all the way to the fine mesh. The fine mesh used in this work is that associated with the actual permeability field of both the matrix and the rock. Effective permeability for each cell is obtained for each coarsening scenario based on the requirement that the flux at the face of each cell is the same as that considered with the actual permeability field. It is found that the spatial distribution of effective permeability of the medium changes with the change in the degree of coarsening. That is for coarser mesh the effective permeability spans a larger domain while it reduces to the actual permeability field as the mesh approaches the fine mesh. The usefulness of this approach stems from the significantly less computational effort and memory requirement that would be required when using the upscaled permeability field and in the same time the satisfaction of conservation laws at the new scale.

Acknowledgment

The work is funded by KAUST's GRP-CF (Global Research Partnership Collaborative Fellows) Program, and KAUST-UTAustin AEA project (7000000058).

References

[1] A. Salama and J. van Geel, "Flow and solute transport in saturated porous media: 1. The continuum hypothesis," *Journal of Porous Media*, vol. 11, no. 4, pp. 403–413, 2008.

[2] A. Salama and J. van Geel, "Flow and solute transport in saturated porous media: 2. Violating the continuum hypothesis," *Journal of Porous Media*, vol. 11, no. 5, pp. 421–441, 2008.

[3] M. Karimi-Fard and A. Firoozabadi, "Numerical simulation of water injection in fractured media using the discrete-fracture model and the Galerkin method," *SPE Reservoir Evaluation and Engineering*, vol. 6, no. 2, pp. 117–126, 2003.

[4] J. Kou, S. Sun, and B. Yu, "Multiscale time splitting strategy for multi-scale multi-physics processes of two-phase flow in fractured media," *Journal of Applied Mathematics*, vol. 2011, Article ID 861905, 24 pages, 2011.
[5] A. Rodriguez, H. Klie, S. Sun, X. Gai, and M. Wheeler, "Upscaling of hydraulic properties of fractured porous media: full permeability tensor and continuum scale simulations," in *Proceedings of the SPE Symposium on Improved Oil Recovery*, Tulsa, Okla, USA, 2006.
[6] B. Noetinger, T. Estebenet, and M. Quintard, "Up-scaling flow in fractured media: equivalence between the large scale averaging theory and the continuous time random walk method," *Transport in Porous Media*, vol. 43, no. 3, pp. 581–596, 2001.
[7] M. Kfoury, R. Ababou, B. Noetinger, and M. Quintard, "Upscaling fractured heterogeneous media: permeability and mass exchange coefficient," *Journal of Applied Mechanics*, vol. 73, no. 1, pp. 41–46, 2006.
[8] X. Wen and J. Gomez-Hernandez, "Upscaling hydraulic conductivities in heterogeneous media: an overview," *Journal of Hydrology*, vol. 183, no. 1-2, pp. 9–32, 1996.
[9] M. Crotti and R. Cobenas, "Upscaling of relative permeability curves for reservoir simulation: an extension to areal simulations based on realistic average water saturations," in *Proceedings of the SPE Latin American and Caribbean Petroleum Engineering Conference*, Port-of-Spain, Trinidad & Tobago, 2003.
[10] G. Narsilio, O. Buzzi, S. Fityus, T. Yun, and D. Smith, "Upscaling of Navier-Stokes equations in porous media: theoretical, numerical and experimental approach," *Computers and Geotechnics*, vol. 36, no. 7, pp. 1200–1206, 2009.
[11] C. Farmer, "Upscaling: a review," *International Journal for Numerical Methods in Fluids*, vol. 40, no. 1-2, pp. 63–78, 2002.
[12] P. Mayur and M. Edwards, "Effective upscaling using a family of flux-continuous, finite-volume schemes for the pressure equation," in *Proceedings of the 14th Association of Computational Mechanics in Engineering (ACME '06)*, Queen's University, Belfast, UK, 2006.
[13] T. Samardzioska and V. Popov, "Numerical comparison of the equivalent continuum, non-homogeneous and dual porosity models for flow and transport in fractured porous media," *Advances in Water Resources*, vol. 28, no. 3, pp. 235–255, 2005.
[14] Y. Zhang, C. W. Gable, and B. Sheets, "Equivalent hydraulic conductivity of three-dimensional heterogeneous porous media: an upscaling study based on an experimental stratigraphy," *Journal of Hydrology*, vol. 388, no. 3-4, pp. 304–320, 2010.
[15] S. Painter and V. Cvetkovic, "Upscaling discrete fracture network simulations: an alternative to continuum transport models," *Water Resources Research*, vol. 41, no. 2, pp. 1–10, 2005.
[16] J. Öhman and A. Niemi, "Upscaling of fracture hydraulics by means of an oriented correlated stochastic continuum model," *Water Resources Research*, vol. 39, no. 10, p. 13, 2003.
[17] S. P. MacLachlan and J. D. Moulton, "Multilevel upscaling through variational coarsening," *Water Resources Research*, vol. 42, no. 2, Article ID W02418, p. 9, 2006.
[18] X. Sanchez-Vila, J. P. Girardi, and J. Carrera, "A synthesis of approaches to upscaling of hydraluic conductivities," *Water Resources Research*, vol. 31, no. 4, pp. 867–882, 1995.
[19] L. Holden and B. F. Nielsen, "Global upscaling of permeability in heterogeneous reservoirs; the Output Least Squares (OLS) method," *Transport in Porous Media*, vol. 40, no. 2, pp. 115–143, 2000.
[20] J. Warren and H. Price, "Flow in heterogeneous porous media," *Society of Petroleum Engineers Journal*, vol. 1, no. 3, pp. 153–169, 1961.
[21] S. Begg, R. Carter, and P. Dranfield, "Assigning effective values to simulator gridblock parameters for heterogeneous reservoirs," *Society of Petroleum Engineers*, vol. 4, no. 4, pp. 455–463, 1989.
[22] P. A. Witherspoon, J. S. Y. Wang, K. Iwai, and J. E. Gale, "Validity of cubic law for fluid flow in a deformable rock fracture," *Water Resources Research*, vol. 16, no. 6, pp. 1016–1024, 1980.

Hindawi Publishing Corporation
Journal of Applied Mathematics
Volume 2012, Article ID 783101, 30 pages
doi:10.1155/2012/783101

Research Article

The Technique of MIEELDLD in Computational Aeroacoustics

A. R. Appadu

Department of Mathematics and Applied Mathematics, University of Pretoria, Pretoria 0002, South Africa

Correspondence should be addressed to A. R. Appadu, rao.appadu@up.ac.za

Received 3 January 2012; Accepted 14 February 2012

Academic Editor: M. F. El-Amin

The numerical simulation of aeroacoustic phenomena requires high-order accurate numerical schemes with low dispersion and low dissipation errors. A technique has recently been devised in a Computational Fluid Dynamics framework which enables optimal parameters to be chosen so as to better control the grade and balance of dispersion and dissipation in numerical schemes (Appadu and Dauhoo, 2011; Appadu, 2012a; Appadu, 2012b; Appadu, 2012c). This technique has been baptised as the Minimized Integrated Exponential Error for Low Dispersion and Low Dissipation (MIEELDLD) and has successfully been applied to numerical schemes discretising the 1-D, 2-D, and 3-D advection equations. In this paper, we extend the technique of MIEELDLD to the field of computational aeroacoustics and have been able to construct high-order methods with Low Dispersion and Low Dissipation properties which approximate the 1-D linear advection equation. Modifications to the spatial discretization schemes designed by Tam and Webb (1993), Lockard et al. (1995), Zingg et al. (1996), Zhuang and Chen (2002), and Bogey and Bailly (2004) have been obtained, and also a modification to the temporal scheme developed by Tam et al. (1993) has been obtained. These novel methods obtained using MIEELDLD have in general better dispersive properties as compared to the existing optimised methods.

1. Introduction

Computational aeroacoustics (CAA) has been given increased interest because of the need to better control noise levels from aircrafts, trains, and cars due to increased transport and stricter regulations from authorities [1]. Other applications of CAA are in the simulation of sound propagation in the atmosphere to the improved design of musical instruments.

In computational aeroacoustics, the accurate prediction of the generation of sound is demanding due to the requirement for preservation of the shape and frequency of wave propagation and generation. It is well known [2, 3] that, in order to conduct satisfactory computational aeroacoustics, numerical methods must generate the least possible dispersion

and dissipation errors. In general, higher order schemes would be more suitable for CAA than the lower-order schemes since, overall, the former are less dissipative [4]. This is the reason why higher-order spatial discretisation schemes have gained considerable interest in computational aeroacoustics.

The field of CAA has grown rapidly during the last decade and there has been a resurgence of interest in aeroacoustic phenomena characterised by harsher legislation and increasing environmental awareness. CAA is concerned with the accurate numerical prediction of aerodynamically generated noise as well as its propagation and far-field characteristics. CAA involves mainly the development of numerical methods which approximate derivatives in a way that better preserves the physics of wave propagation unlike typical aerodynamic computations [1].

Since multidimensional finite-volume algorithms are generally more expensive in terms of numerical cost than finite-difference algorithms, the majority of CAA codes are based on the finite-difference methodology [5]. The trend within the field of CAA has been to employ higher-order accurate numerical schemes that have in some manner been optimized for wave propagation in order to reduce the number of grid points per wavelength while ensuring tolerable levels of numerical error. Apart from acoustics and aeroacoustics, low amplitude wave propagation takes place over distances characterized by large multiples of wavelength in other areas such as [6]

(1) electromagnetics, for microcircuit design,

(2) elastodynamics, for nondestructive testing,

(3) seismology, for oil exploration,

(4) medical Imaging, for accurate diagnosis,

(5) hyperthermia, for noninvasive surgery.

Aerodynamics and other areas of fluid mechanics have benefitted immensely from the development of CFD [7]. The numerical analysis of flows around full aircraft configurations has become feasible with advances in both numerical techniques and computing machines. The temptation to apply effective CFD methods to aeroacoustic problems has been unavoidable and has been met with some success, but, in some cases, it has been observed that there is a necessity for some numerical protocols specific to problems involving disturbance propagation over long distances. The difference between aerodynamic and aeroacoustic problems lies mainly in the fact that for aeroacoustic computations, the solution is desired at some large distance from the aerodynamic source, but, in the case of aerodynamic problems, flow properties are required accurately only on the body itself [7]. Most aerodynamics problems are time independent, whereas aeroacoustics problems are, by definition, time dependent [8]. There are computational issues that are unique to aeroacoustics. Thus, computational aeroacoustics requires somewhat independent thinking and development.

At specific Courant numbers and angles of propagation, the perfect-shift property can be obtained, leading to exact propagation for all wavenumbers [9]. The perfect shift property refers to the situation when the error from the spatial discretisation precisely cancels that from the temporal discretisation. Several numerical schemes which combine the spatial and temporal discretisation produce the perfect shift property at specific Courant numbers [9]. Often this perfect cancellation of temporal and spatial errors occurs at cfl = 1.0. For such methods, the sum of the spatial and temporal error increases when the cfl number is decreased as the temporal error no longer cancels the spatial error. As the cfl number tends to zero, so does the temporal error and thus only spatial error remains. For most schemes,

a low cfl represents the worst case associated with large dispersion or large dissipation errors as there is no cancellation of temporal and spatial errors [9]. Thus it is important to assess numerical methods over a range of Courant numbers [9]. However, this is not an issue for schemes built up from a high-accuracy spatial discretisation with a high-accuracy time-marching method. These schemes generally do not rely on cancellation to achieve high accuracy and thus the error does not increase as the Courant number is reduced.

The imaginary part of the numerical wavenumber represents numerical dissipation only when it is negative [10]. Due to the difference between the physical and numerical wavenumber, some wavenumbers propagate faster or slower than the wave speed of the original partial differential equation [11]. This is how dispersion errors are induced. The real part of the modified wavenumber determines the dispersive error while the imaginary part determines the dissipative error [9]. The group velocity of a wavepacket governs the propagation of energy of the wavepacket. The group velocity is characterised by $\mathrm{Re}((d/(d(\theta h)))(\theta^* h)) - 1.0$ which must be almost one in order to reproduce exact result [12]. Otherwise, dispersive patterns appear. When $\mathrm{Re}((d/(d(\theta h)))(\theta^* h)) = 1.0$, the scheme has the same group velocity or speed of sound as the original governing equations and the numerical waves are propagated with correct wave speeds.

2. Organisation of Paper

This paper is organised as follows. In Section 3, we briefly describe the technique of Minimised Integrated Exponential Error for Low Dispersion and Low Dissipation (MIEELDLD) when used to optimise parameters in numerical methods. We also describe how this technique can be extended to construct high order methods with low dispersive and low dissipative properties in computational aeroacoustics. In Sections 4–8, we use MIEELDLD to obtain some optimized spatial methods based on a modification of the methods constructed by Tam and Webb [3], Lockard et al. [13], Zingg et al. [14], Zhuang and Chen [15], Bogey and Bailly [16]. Section 9 introduces an optimised temporal scheme which is obtained using MIEELDLD and based on a modification of the temporal discretisation method constructed by Tam et al. [17]. In Section 10, we construct numerical methods based on blending each of the five new spatial schemes with the new time discretisation scheme when used to discretise the 1-D linear advection equation and obtain rough estimates of the range of stability of these methods. Section 12 highlights the salient features of the paper.

3. The Concept of Minimised Integrated Exponential Error for Low Dispersion and Low Dissipation

In this section, we describe briefly the technique of Minimized Integrated Exponential Error for Low Dispersion and Low Dissipation (MIEELDLD). This technique have been introduced in Appadu and Dauhoo [18] and Appadu and Dauhoo [19]. We now give a resume of how we have derived this technique of optimisation.

Suppose the amplification factor of the numerical scheme when applied to the 1-D linear advection equation:

$$\frac{\partial u}{\partial t} + \beta \frac{\partial u}{\partial x} = 0 \tag{3.1}$$

is

$$\xi = A + IB. \tag{3.2}$$

Then the modulus of the Amplification Factor (AFM) and the relative phase error (RPE) are calculated as

$$\begin{aligned} \text{AFM} &= |\xi|, \\ \text{RPE} &= -\frac{1}{rw}\tan^{-1}\frac{B}{A}, \end{aligned} \tag{3.3}$$

where r and w are the cfl number and phase angle, respectively.

For a scheme to have Low Dispersion and Low Dissipation, we require

$$|1 - \text{RPE}| + (1 - \text{AFM}) \longrightarrow 0. \tag{3.4}$$

The quantity, $|1-\text{RPE}|$ measures dispersion error while $(1-\text{AFM})$ measures dissipation error. Also when dissipation neutralises dispersion optimally, we have

$$||1 - \text{RPE}| - (1 - \text{AFM})| \longrightarrow 0. \tag{3.5}$$

Thus on combining these two conditions, we get the following condition necessary for dissipation to neutralise dispersion and for low dispersion and low dissipation character to be satisfied:

$$\text{eldld} = ||1 - \text{RPE}| - (1 - \text{AFM})| + (|1 - \text{RPE}| + (1 - \text{AFM})) \longrightarrow 0. \tag{3.6}$$

Similarly, we expect

$$\text{eeldld} = \exp(||1 - \text{RPE}| - (1 - \text{AFM})|) + \exp(|1 - \text{RPE}| + (1 - \text{AFM})) - 2 \longrightarrow 0, \tag{3.7}$$

in order for Low Dispersion and Low Dissipation properties to be achieved.

The measure, eeldld, denotes the exponential error for low dispersion and low dissipation. The reasons why we prefer eeldld over eldld is because the former is more sensitive to perturbations.

We next explain how the integration process is performed in order to obtain the optimal parameter(s).

Only One Parameter Involved

If the cfl number is the only parameter, we compute

$$\int_0^{w_1} \text{eeldld}\, dw, \tag{3.8}$$

for a range of $w \in [0, w_1]$, and this integral will be a function of r. The optimal cfl is the one at which the integral quantity is closest to zero.

Two Parameters Involved

We next consider a case where two parameters are involved and whereby we would like to optimise these two parameters.

Suppose we want to obtain an improved version of the Fromm's scheme which is made up of a linear combination of Lax-Wendroff (LW) and Beam-Warming (BW) schemes. Suppose we apply BW and LW in the ratio $\lambda : 1 - \lambda$. This can be done in two ways.

In the first case, if we wish to obtain the optimal value of λ at any cfl, then we compute

$$\int_0^{r_1} \int_0^{w_1} \text{eeldld}\, dw\, dr, \tag{3.9}$$

which will be in terms of λ.

The value of r_1 is chosen to suit the region of stability of the numerical scheme under consideration while w_1 is chosen such that the approximated RPE ≥ 0 for $r \in [0, r_1]$. In cases where phase wrapping phenomenon does not occur, we use the exact RPE instead of the approximated RPE and in that case, $w \in [0, \pi]$.

The second way to optimise a scheme made up of a linear combination of Beam-Warming and Lax-Wendroff is to compute the IEELDLD as $\int_0^{w_1}$ eeldld dw and the integral obtained in that case will be a function of r and λ. Then a 3-D plot of this integral with respect to $r \in [0, r_1]$ and $\lambda \in [0, 1]$ enables the respective optimal values of r and λ to be located. The optimised scheme obtained will be defined in terms of both a cfl number and the optimal value of λ to be used.

Considerable and extensive work on the technique of Minimised Integrated Exponential Error for Low Dispersion and Low Dissipation has been carried out in Appadu and Dauhoo [18], Appadu and Dauhoo [19], Appadu [20–22].

In Appadu and Dauhoo [18], we have obtained the optimal cfl for some explicit methods like Lax-Wendroff, Beam-Warming, Crowley, Upwind Leap-Frog, and Fromm's schemes. In Appadu and Dauhoo [19], we have combined some spatial discretisation schemes with the optimised time discretisation method proposed by Tam and Webb [3] in order to approximate the linear 1-D advection equation. These spatial derivatives are a standard 7-point and 6th-order central difference scheme (ST7), a standard 9-point and 8th-order central difference scheme (ST9) and optimised spatial schemes designed by Tam and Webb [3], Lockard et al. [13], Zingg et al. [14], Zhuang and Chen [15] and Bogey and Bailly [16]. The results from some numerical experiments were quantified into dispersion and dissipation errors and we have found that the quality of the results is dependent on the choice of the cfl number even for optimised methods, though to a much lesser degree as compared to standard methods.

Moreover, in Appadu [20], we obtain the optimal cfl of some multilevel schemes in 1-D. These schemes are of high order in space and time and have been designed by Wang and Liu [23]. We have also optimised the parameters in the family of third-order schemes proposed by Takacs [24]. The optimal cfl of the 2-D CFLF4 scheme which is a composite method made up of Corrected Lax-Friedrichs and the two-step Lax-Friedrichs developed by Liska and Wendroff [25] has been computed and some numerical experiments have been performed such as 2-D solid body rotation test [26], 2-D acoustics [27], and 2-D circular Riemann problem [26]. We have shown that better results are obtained when the optimal parameters obtained using MIEELDLD are used.

Some more interesting features of MIEELDLD are detailed in Appadu [21]. In that paper, we extend the measures used by Tam and Webb [3], Bogey and Bailly [16], Berland et al. [28] in a computational aeroacoustics framework to suit them in a computational fluid dynamics framework such that the optimal cfl of some known numerical methods can be obtained. Thus, we define the following integrals: integrated error from Tam and Webb [3], (IETAM), integrated error from Bogey and Bailly [16] ((IEBOGEY), and integrated error from Berland et al. [28] (IEBERLAND) as follows:

$$\begin{aligned}
\text{IETAM} &= \int_0^{w_1} |1 - \text{RPE}|^2 dw, \\
\text{IEBOGEY} &= \int_0^{w_1} |1 - \text{RPE}| dw, \\
\text{IEBERLAND} &= \int_0^{w_1} (1-\alpha)|1 - \text{RPE}| + \alpha(1 - \text{AFM}) dw.
\end{aligned} \tag{3.10}$$

The optimal cfl is obtained by plotting the respective integral with respect to the cfl number and locating the cfl at which the integral is least. The techniques used to obtain the quantities IETAM, IEBOGEY, and IEBERLAND are named Minimised Integrated Error from Tam and Webb [3] (MIETAM), Minimised Integrated Error from Bogey and Bailly [16] (MIEBOGEY), and Minimised Integrated Error from Berland et al. [28] (MIEBERLAND) respectively. It is shown that MIEELDLD has an upper hand over the other techniques of optimisation: MIETAM, MIEBOGEY, and MIEBERLAND.

The work in Appadu [22] helps us to understand why not all composite schemes can be effective to capture shocks with minimum dispersion and dissipation. The findings concluded are that some efficient composite methods to approximate the 1-D linear advection equation are as follows: composite methods using Lax-Wendroff and Beam-Warming as either predictor or corrector steps, a linear combination of either Lax-Wendroff and Beam-Warming schemes or MacCormack and two-step Lax-Friedrichs and the composite MacCormack/Lax-Friedrichs schemes [29].

4. Modification to Space Discretisation Scheme Proposed by Tam and Webb [3]

Tam and Webb [3] constructed a 7-pt and 4th-order central difference method based on a minimization of the dispersion error.

They approximated $\partial u/\partial x$ at x_0 as

$$\frac{\partial u}{\partial x} = \frac{1}{h} \sum_{i=-3}^{3} a_i u(x_0 + ih), \tag{4.1}$$

where h is the spacing of a uniform mesh and the coefficients a_i are such that $a_i = -a_{-i}$, providing a scheme without dissipation. On applying spatial Fourier Transform to (4.1), the effective wavenumber $\theta^* h$ of the scheme is obtained and it is given by

$$\theta^* h = 2 \sum_{i=1}^{3} a_i \sin(i\theta h). \tag{4.2}$$

Taylor expansion of $\theta^* h$ about θh from (4.2) gives the following:

$$2a_1\left(\theta h - \frac{1}{6}(\theta h)^3 + \frac{1}{120}(\theta h)^5\right) + 2a_2\left(2\theta h - \frac{1}{6}(2\theta h)^3 + \frac{1}{120}(2\theta h)^5\right) + 2a_3\left(3\theta h - \frac{1}{6}(3\theta h)^3 + \frac{1}{120}(3\theta h)^5\right) + \cdots . \tag{4.3}$$

To obtain a 4th-order accurate method, we must have

$$\begin{aligned} 2a_1 + 4a_2 + 6a_3 &= 1, \\ a_1 + 8a_2 + 27a_3 &= 0. \end{aligned} \tag{4.4}$$

Since, we have 2 equations and 3 unknowns, we can choose, for instance, say a_1 as a free parameter. Thus,

$$\begin{aligned} a_2 &= \frac{9}{20} - \frac{4}{5}a_1, \\ a_3 &= \frac{1}{5}\left(a_1 - \frac{2}{3}\right). \end{aligned} \tag{4.5}$$

Hence, the numerical wavenumber can be expressed as

$$\theta^* h \approx 2a_1 \sin(\theta h) + 2\left(\frac{9}{20} - \frac{4}{5}a_1\right)\sin(2\theta h) + 2\left(\frac{1}{5}a_1 - \frac{2}{15}\right)\sin(3\theta h). \tag{4.6}$$

The optimisation procedure used by Tam and Webb [3] is to find a_1 which minimizes the integrated error, E defined as

$$E = \int_0^{1.1} |\theta^* h - \theta h|^2 d(\theta h). \tag{4.7}$$

The value obtained for a_1 is 0.7708823806. The corresponding values for a_2 and a_3 are -0.1667059045 and 0.0208431428.

Hence, the scheme developed by Tam and Webb [3] has numerical wavenumber, $\theta^* h$, and group velocity given by

$$\theta^* h = 1.5417647612 \sin(\theta h) - 0.3334118090 \sin(2\theta h) + 0.0416862856 \sin(3\theta h), \tag{4.8}$$

$$\text{groupvelocity} = 1.5417647612 \cos(\theta h) - 0.6668236180 \cos(2\theta h) + 0.1250588568 \cos(3\theta h) \tag{4.9}$$

and is termed as "TAM" method.

We next consider the numerical wavenumber in (4.2) and use the technique of MIEELDLD to find optimal values of a_1, a_2, and a_3. The integrated error using MIEELDLD is given by

$$E = \int_0^{1.1} \left(\exp(|\Re(\theta^* h) - \theta h| + |\Im(\theta^* h)|) + \exp||\Re(\theta^* h) - \theta h| - |\Im(\theta^* h)|| - 2\right) d(\theta h). \tag{4.10}$$

Since we are considering a 7-point and 4th-order central difference method, the numerical wavenumber, $\theta^* h$, does not have an imaginary part, that is, $\Im(\theta^* h) = 0$. Hence, (4.10) simplifies to

$$E = \int_0^{1.1} \left(2\ \exp|\Re(\theta^* h) - \theta h| - 2\right) d(\theta h), \tag{4.11}$$

and on minimising this integral using the function NLPSolve in maple, we obtain a_1 as 0.7677206709. Corresponding values for a_2 and a_3 are 0.1641765367 and 0.0202108009, respectively.

Hence we have obtained a modified method which is 7-point and of 4th-order which we term as "TAM-NEW" method. Expressions for the numerical wavenumber and the group velocity of the "TAM-NEW" method are given by

$$\theta^* h = 1.5354413418 \sin(\theta h) - 0.3283530734 \sin(2\theta h) + 0.0404216018 \sin(3\theta h), \tag{4.12}$$

$$\text{groupvelocity} = 1.5354413418 \cos(\theta h) - 0.6567061468 \cos(2\theta h) + 0.1212648054 \cos(3\theta h). \tag{4.13}$$

We next perform a spectral analysis of the two methods. We compare the variation of numerical wavenumber versus the exact wavenumber in Figure 1. A plot of the dispersion error versus the exact wavenumber is depicted in Figure 2. The dispersion error for TAM-NEW is slightly less than that for TAM for $0 < \theta h \leq 1$, but for $1 \leq \theta h \leq \pi/2$, the dispersion error from TAM is slightly less than that for TAM-NEW.

We now compare quantitatively these two methods: TAM and TAM-NEW. We use four accuracy limits [5, 16] defined as follows:

$$\begin{aligned} \frac{|\theta^* h - \theta h|}{\pi} &\leq 5 \times 10^{-3}, \\ \frac{|\theta^* h - \theta h|}{\pi} &\leq 5 \times 10^{-4}, \\ \left| \frac{d}{d(\theta h)} (\theta^* h) - 1.0 \right| &\leq 5 \times 10^{-3}, \\ \left| \frac{d}{d(\theta h)} (\theta^* h) - 1.0 \right| &\leq 5 \times 10^{-4} \end{aligned} \tag{4.14}$$

and compute the minimum number of points per wavelength needed to resolve a wave for each of the four accuracy limits. The results are summarised in Table 1.

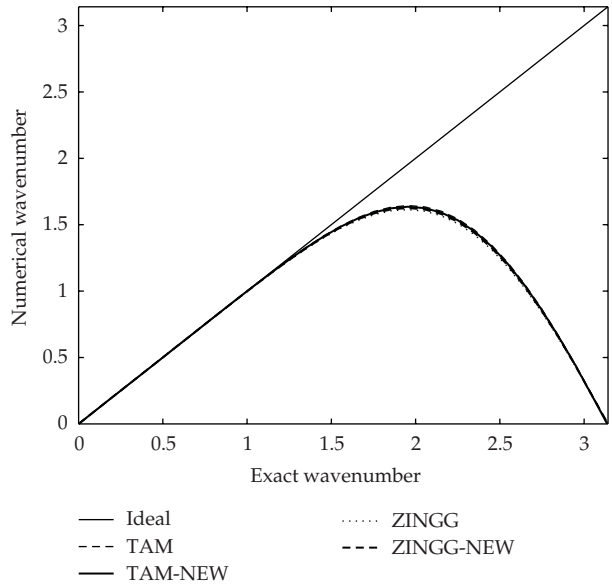

Figure 1: Plot of the variation of numerical wavenumber versus exact wavenumber for the methods: TAM, TAM-NEW, ZINGG, and ZINGG-NEW.

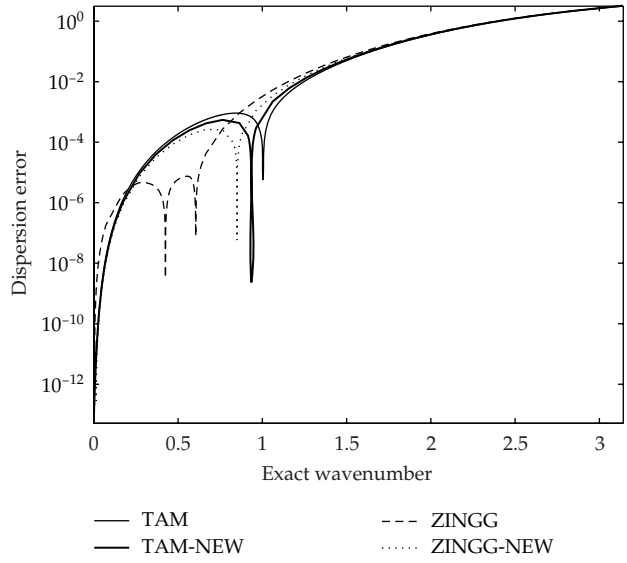

Figure 2: Plot of the dispersion error on a logarithmic scale versus exact wavenumber for the methods: TAM, TAM-NEW, ZINGG, and ZINGG-NEW.

It is seen that the scheme "TAM-NEW" is not superior to the TAM method as for a given accuracy it requires more points per wavelength in regard to the dispersive and group velocity properties. This is because the technique of MIEELDLD aims to minimize both dispersion and dissipation in numerical methods but here our aim is to construct a 7-point and 4th-order central difference method with no dissipation.

Table 1: Comparing the dispersive and group velocity properties for two spatial discretisation methods "TAM" and "TAM-NEW" in terms of number of points per wavelength (to 4 d.p).

Accuracy	Method	Max. value of θh	No. of pts per wavelength
$\frac{\lvert\theta^* h-\theta h\rvert}{\pi} \le 5\times 10^{-3}$	TAM	1.3068	4.8081
$\frac{\lvert\theta^* h-\theta h\rvert}{\pi} \le 5\times 10^{-3}$	TAM-NEW	1.2830	4.8974
$\frac{\lvert\theta^* h-\theta h\rvert}{\pi} \le 5\times 10^{-4}$	TAM	1.0820	5.8073
$\frac{\lvert\theta^* h-\theta h\rvert}{\pi} \le 5\times 10^{-4}$	TAM-NEW	1.0365	6.0617
$\left\lvert \frac{d}{d(\theta h)}(\theta^* h)-1.0\right\rvert \le 5\times 10^{-3}$	TAM	0.9239	6.8007
$\left\lvert \frac{d}{d(\theta h)}(\theta^* h)-1.0\right\rvert \le 5\times 10^{-3}$	TAM-NEW	0.8870	7.0835
$\left\lvert \frac{d}{d(\theta h)}(\theta^* h)-1.0\right\rvert \le 5\times 10^{-4}$	TAM	0.8533	7.3636
$\left\lvert \frac{d}{d(\theta h)}(\theta^* h)-1.0\right\rvert \le 5\times 10^{-4}$	TAM-NEW	0.8002	7.8517

5. Modification to Space Discretisation Scheme Developed by Lockard et al. [13]

Lockard et al. [13] constructed a 7-point and 4th-order difference method by approximating $\partial u/\partial x$ at x_0 as

$$\frac{\partial u}{\partial x} = \frac{1}{h}\sum_{i=-4}^{3} a_i u(x_0 + ih), \tag{5.1}$$

and therefore the real and imaginary parts of the numerical wavenumber are obtained as follows:

$$\begin{aligned}\Re(\theta^* h) = {} & -a_{-4}\sin(4\theta h) - a_{-3}\sin(3\theta h) - a_{-2}\sin(2\theta h) - a_{-1}\sin(\theta h)\\ & + a_1\sin(\theta h) + a_2\sin(2\theta h) + a_3\sin(3\theta h),\end{aligned} \tag{5.2}$$

$$\begin{aligned}\Im(\theta^* h) = {} & -(a_{-4}\cos(4\theta h) + a_{-3}\cos(3\theta h) + a_{-2}\cos(2\theta h) + a_{-1}\cos(\theta h) + a_0\\ & + a_1\cos(\theta h) + a_2\cos(2\theta h) + a_3\cos(3\theta h)).\end{aligned} \tag{5.3}$$

To obtain a 4th-order method, we require 4 conditions based on the real and imaginary parts of $\theta^* h$, namely,

$$\begin{aligned} a_1 + 2a_2 + 3a_3 - 4a_{-4} - 3a_{-3} - 2a_{-2} - a_{-1} &= 1,\\ -a_1 - 8a_2 - 27a_3 + 64a_{-4} + 27a_{-3} + 8a_{-2} + a_{-1} &= 0,\\ a_0 + a_1 + a_2 + a_3 + a_{-4} + a_{-3} + a_{-2} + a_{-1} &= 0,\\ -a_1 - 4a_2 - 9a_3 - 16a_{-4} - 9a_{-3} - 4a_{-2} - a_{-1} &= 0.\end{aligned} \tag{5.4}$$

The coefficients obtained by Lockard et al. [13] are

$$a_{-4} = 0.0103930209, \quad a_{-3} = -0.0846974943, \quad a_{-2} = 0.3420311831,$$
$$a_{-1} = -1.0526812838, \quad a_0 = 0.2872741244, \quad a_1 = 0.5861624738, \quad a_2 = -0.0981442817, \quad a_3 = 0.0096622576. \tag{5.5}$$

Hence, the real and imaginary parts of $\theta^* h$ for LOCKARD scheme are given as follows:

$$\Re(\theta^* h) = 1.63884375 \sin(\theta h) - 0.44017538 \sin(2\theta h) + 0.09433201 \sin(3\theta h) - 0.01039020 \sin(4\theta h), \tag{5.6}$$

$$\Im(\theta^* h) = -0.28727412 + 0.46651881 \cos(\theta h) - 0.24388682 \cos(2\theta h) + 0.07500749 \cos(3\theta h) - 0.01039020 \cos(4\theta h), \tag{5.7}$$

respectively.

We now obtain a modification to the scheme developed by Lockard et al. [13]. We consider the numerical wavenumber in (5.2) and (5.3) and replace a_{-1}, a_0, a_1, a_2, and a_3 in terms of a_{-2}, a_{-3}, a_{-4}, and θh. Our aim is to minimise the following integral:

$$E = \int_0^{1.1} \left(\exp(|\Re(\theta^* h) - \theta h| + |\Im(\theta^* h)|) + \exp||\Re(\theta^* h) - \theta h| - |\Im(\theta^* h)|| - 2\right) d(\theta h). \tag{5.8}$$

The integral is a function of a_{-2}, a_{-3}, and a_{-4}. We use the function NLPSolve and obtain optimal values for a_{-4}, a_{-3}, and a_{-2} as 0.0113460667, −0.0891980000, and 0.3499980000. Then the values of the other unknowns can be obtained and we are out with

$$a_{-1} = -1.0582666667, \quad a_0 = 0.2866010000, \quad a_1 = 0.5895196001, \quad a_2 = -0.1, \quad a_3 = 0.01. \tag{5.9}$$

The modified method is termed as "LOCKARD-NEW" and has real and imaginary parts of its numerical wavenumber described by

$$\Re(\theta^* h) = 1.6477862670 \sin(\theta h) - 0.4499980000 \sin(2\theta h) + 0.0991980000 \sin(3\theta h) - 0.0113460667 \sin(4\theta h), \tag{5.10}$$

$$\Im(\theta^* h) = -0.2866010000 + 0.4687470669 \cos(\theta h) - 0.2499980000 \cos(2\theta h) + 0.0791980000 \cos(3\theta h) - 0.0113460667 \cos(4\theta h), \tag{5.11}$$

respectively.

We next perform a spectral analysis of the two methods: LOCKARD and LOCKARD-NEW. We compare the variation of numerical wavenumber versus the exact wavenumber

Table 2: Comparing the dispersive and group velocity properties for two spatial methods LOCKARD and LOCKARD-NEW in terms of number of points per wavelength (to 4 d.p).

Accuracy	Method	Max. value of θh	No. of pts per wavelength
$\frac{\lvert\theta^* h - \theta h\rvert}{\pi} \leq 5 \times 10^{-3}$	LOCKARD	1.4910	4.2140
$\frac{\lvert\theta^* h - \theta h\rvert}{\pi} \leq 5 \times 10^{-3}$	LOCKARD-NEW	1.5197	4.1344
$\frac{\lvert\theta^* h - \theta h\rvert}{\pi} \leq 5 \times 10^{-4}$	LOCKARD	1.2204	5.1485
$\frac{\lvert\theta^* h - \theta h\rvert}{\pi} \leq 5 \times 10^{-4}$	LOCKARD-NEW	1.2596	4.9881
$\left\lvert \frac{d}{d(\theta h)} (\theta^* h) - 1.0 \right\rvert \leq 5 \times 10^{-3}$	LOCKARD	1.0964	5.7309
$\left\lvert \frac{d}{d(\theta h)} (\theta^* h) - 1.0 \right\rvert \leq 5 \times 10^{-3}$	LOCKARD-NEW	1.1395	5.5142
$\left\lvert \frac{d}{d(\theta h)} (\theta^* h) - 1.0 \right\rvert \leq 5 \times 10^{-4}$	LOCKARD	0.9655	6.5077
$\left\lvert \frac{d}{d(\theta h)} (\theta^* h) - 1.0 \right\rvert \leq 5 \times 10^{-4}$	LOCKARD-NEW	1.0240	6.1359

in Figure 3 and in Figure 4, we have the plot of the dispersion error versus the exact wavenumber.

We now compare quantitatively the two methods by computing the minimum number of points per wavelength needed to resolve a wave for each of the four accuracy limits and the results are summarized in Table 2.

Clearly, LOCKARD-NEW has appreciably better phase and group velocity properties as compared to LOCKARD scheme.

6. Modification to Spatial Discretisation Scheme Developed by Zingg et al. [14]

Zingg et al. [14] constructed a 4-point and 4th-order difference method. They approximated $\partial u/\partial x$ at x_0 by

$$\frac{\partial u}{\partial x} = \frac{1}{h}\sum_{i=1}^{3} a_i (u(x_0 + ih) - u(x_0 - ih)) + \frac{1}{h}\left(d_0 u(x_0) + \sum_{i=1}^{3} d_i (u(x_0 + ih) + u(x_0 - ih)) \right). \tag{6.1}$$

The real and imaginary parts of the numerical wavenumber are obtained as

$$\Re(\theta^* h) = 2(a_1 \sin(\theta h) + a_2 \sin(2\theta h) + a_3 \sin(3\theta h)), \tag{6.2}$$

$$\Im(\theta^* h) = -(d_0 + 2d_1 \cos(\theta h) + 2d_2 \cos(2\theta h) + 2d_3 \cos(3\theta h)). \tag{6.3}$$

The conditions to have a 4th-order difference method are as follows.

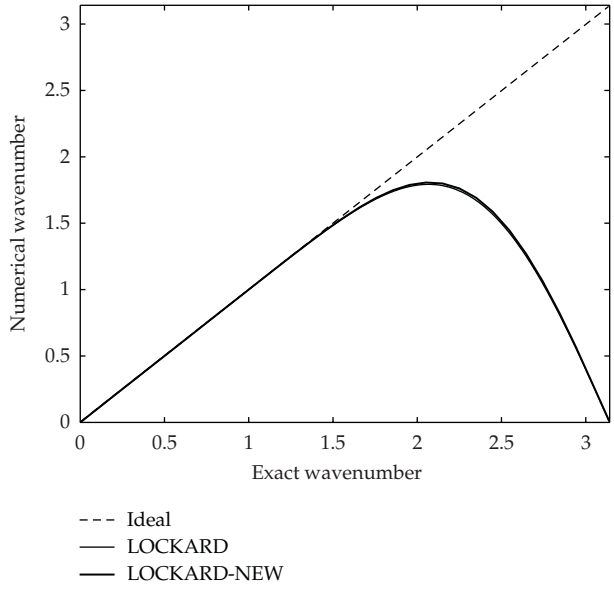

Figure 3: Plot of the variation of numerical wavenumber versus exact wavenumber for the methods LOCKARD and LOCKARD-NEW.

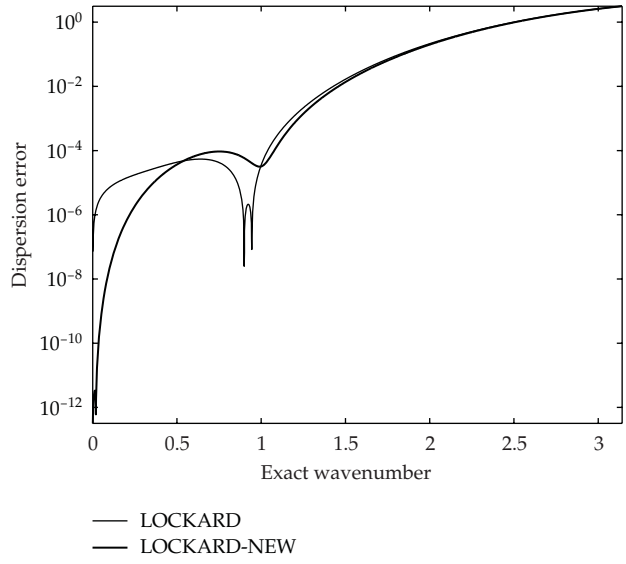

Figure 4: Plot of the variation of dispersion error in logarithmic scale versus exact wavenumber for LOCKARD and LOCKARD-NEW schemes.

(i) If we consider $\Re(\theta^* h)$, then

$$\begin{aligned} 2a_1 + 4a_2 + 6a_3 &= 1, \\ -\frac{1}{6}a_1 - \frac{8}{6}a_2 - \frac{27}{6}a_3 &= 0, \end{aligned} \tag{6.4}$$

and these two conditions give

$$a_2 = \frac{9}{20} - \frac{4}{5}a_1, \tag{6.5}$$

$$a_3 = \frac{1}{5}\left(a_1 - \frac{2}{3}\right). \tag{6.6}$$

(ii) If we consider $\Im(\theta^* h)$, then

$$\begin{aligned} d_0 + 2d_1 + 2d_2 + 2d_3 &= 0, \\ -d_1 - 4d_2 - 9d_3 &= 0, \end{aligned} \tag{6.7}$$

and this gives

$$d_0 = 6d_2 + 16d_3, \tag{6.8}$$

$$d_1 = -4d_2 - 9d_3. \tag{6.9}$$

Based on the optimisation performed by Zingg et al. [14], the following values are obtained:

$$\begin{aligned} a_1 &= 0.75996126, \quad a_2 = -0.15812197, \quad a_3 = 0.01876090, \quad d_0 = 0.1, \\ d_1 &= -0.07638462, \quad d_2 = 0.03228962, \quad d_3 = -0.00590500. \end{aligned} \tag{6.10}$$

We now obtain a modification to the scheme proposed by Zingg et al. [14] using MIEELDLD. We consider

$$\Im(\theta^* h) = -(d_0 + 2\ d_1 \cos(\theta h) + 2\ d_2 \cos(2\theta h) + 2d_3 \cos(3\theta h)). \tag{6.11}$$

Since $\mathrm{Im}(\theta^* h)$ must be negative and the method must have sufficient dissipation, we can choose $d_0 = 0.1$ and hence obtain

$$\begin{aligned} d_1 &= -\frac{5}{8}d_2 - 0.05625, \\ d_3 &= 0.00625 - \frac{3}{8}d_2. \end{aligned} \tag{6.12}$$

We next plot $\mathrm{Im}(\theta^* h)$ versus d_2 versus $\theta h \in [0, 2\pi]$ and obtain the range of d_2 such that $\mathrm{Im}(\theta^* h) < 0$. The maximum value of d_2 is 0.0323. Having fixed the values of d_0 as 0.1 and d_2 as 0.0323, now we can compute the values of d_1 and d_3. We are out with $d_1 = -0.0764375$ and $d_3 = -5.8625 \times 10^{-3}$. Hence, we minimize the following integral:

$$\int_0^{1.1} \exp(|\Re(\theta^* h) - \theta h| + |\Im(\theta^* h)|) + \exp||\Re(\theta^* h) - \theta h| - |\Im(\theta^* h)|| - 2.0\ d(\theta h) \tag{6.13}$$

which is a function of a_1, using NLPSolve.

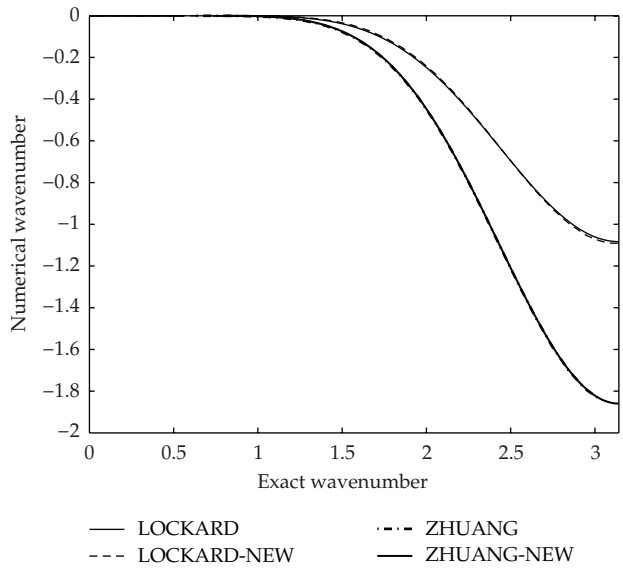

Figure 5: Plot of the imaginary part of numerical wavenumber versus exact wavenumber for the methods: LOCKARD, LOCKARD-NEW, ZHUANG, and ZHUANG-NEW.

We obtain $a_1 = 0.7643155206$, and therefore, using (6.5) and (6.6), we obtain $a_2 = -0.1614524165$ and $a_3 = 0.0195297708$.

Hence, the real and imaginary parts of the real and imaginary parts of the numerical wavenumber of the scheme ZINGG-NEW are as follows:

$$\Re(\theta^* h) = 1.5286310410 \sin(\theta h) - 0.3229048330 \sin(2\theta h) + 0.0390595416 \sin(3\theta h), \tag{6.14}$$

$$\Im(\theta^* h) = -0.1 + 0.1528750000 \cos(\theta h) - 0.0646000000 \cos(2\theta h) + 0.0117250000 \cos(3\theta h). \tag{6.15}$$

Plots of $\Re(\theta^* h)$ versus θh and also for $\Im(\theta^* h)$ versus θh for ZINGG and ZINGG-NEW schemes are depicted in Figures 1 and 6, respectively. It is observed based on Figure 6 that the two methods have almost the same dissipation error for $\theta h \in [0, \pi]$. Based on (Figure 1), we observe that for $\theta h < 0.2$ and $0.8 < \theta h < \pi/2$, the dispersion error from ZINGG-NEW is less than that for ZINGG. For $0.2 < \theta h < 0.8$, the dispersion error from ZINGG is less than ZINGG-NEW.

Based on Table 3, for the four accuracy limits tested, we can conclude that the new scheme developed is superior to the ZINGG method in terms of both dispersive and group velocity properties as it requires less points per wavelength in all the four cases.

7. Modification to Spatial Scheme Developed by Zhuang and Chen [15]

Zhuang and Chen [15] constructed a 7-point and 4th-order difference method by approximating $\partial u/\partial x$ at x_0 as

$$\frac{\partial u}{\partial x} = \frac{1}{h} \sum_{i=-4}^{2} a_i u(x_0 + ih), \tag{7.1}$$

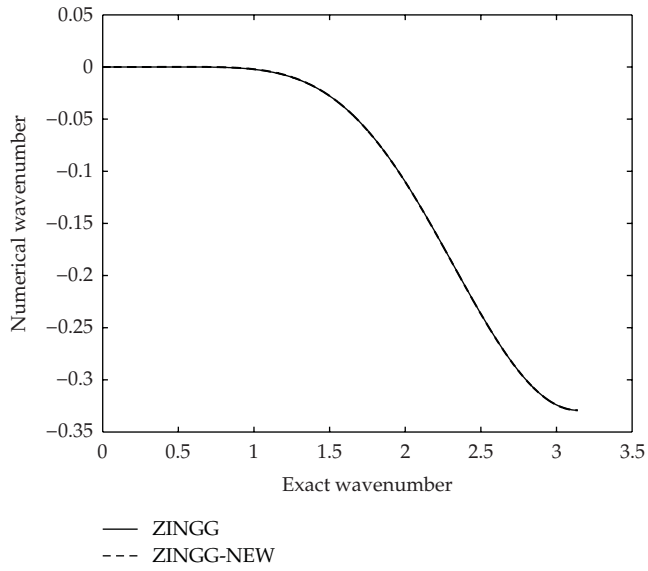

Figure 6: Plot of the imaginary part of numerical wavenumber versus exact wavenumber for ZINGG and ZINGG-NEW.

Table 3: Comparing the dispersive and group velocity properties for two spatial methods ZINGG and ZINGG-NEW in terms of number of points per wavelength (to 4 d.p).

Accuracy	Method	Max. value of θh	No. of pts per wavelength
$\frac{\lvert\theta^* h - \theta h\rvert}{\pi} \leq 5 \times 10^{-3}$	ZINGG	1.2239	5.1339
$\frac{\lvert\theta^* h - \theta h\rvert}{\pi} \leq 5 \times 10^{-3}$	ZINGG-NEW	1.2579	5.1258
$\frac{\lvert\theta^* h - \theta h\rvert}{\pi} \leq 5 \times 10^{-4}$	ZINGG	0.9163	6.8575
$\frac{\lvert\theta^* h - \theta h\rvert}{\pi} \leq 5 \times 10^{-4}$	ZINGG-NEW	0.9988	6.2904
$\left\lvert \frac{d}{d(\theta h)} (\theta^* h) - 1.0 \right\rvert \leq 5 \times 10^{-3}$	ZINGG	0.7885	7.9686
$\left\lvert \frac{d}{d(\theta h)} (\theta^* h) - 1.0 \right\rvert \leq 5 \times 10^{-3}$	ZINGG-NEW	0.8471	7.4176
$\left\lvert \frac{d}{d(\theta h)} (\theta^* h) - 1.0 \right\rvert \leq 5 \times 10^{-4}$	ZINGG	0.6200	10.1341
$\left\lvert \frac{d}{d(\theta h)} (\theta^* h) - 1.0 \right\rvert \leq 5 \times 10^{-4}$	ZINGG-NEW	0.7379	8.5152

and therefore the real and imaginary parts of the numerical wavenumber are obtained as

$$\begin{aligned} \Re(\theta^* h) = {} & a_1 \sin(\theta h) + a_2 \sin(2\theta h) - a_{-4} \sin(4\theta h) - a_{-3} \sin(3\theta h) \\ & - a_{-2} \sin(2\theta h) - a_{-1} \sin(\theta h), \end{aligned} \tag{7.2}$$

$$\begin{aligned} \Im(\theta^* h) = {} & -(a_{-4} \cos(4\theta h) + a_{-3} \cos(3\theta h) + a_{-2} \cos(2\theta h) + a_{-1} \cos(\theta h) + a_0 \\ & + a_1 \cos(\theta h) + a_2 \cos(2\theta h)). \end{aligned} \tag{7.3}$$

To obtain a 4th-order method, we require 4 conditions based on the real and imaginary parts of $\theta^* h$:

$$\begin{aligned} a_1 + 2a_2 - 4a_{-4} - 3a_{-3} - 2a_{-2} - a_{-1} &= 1, \\ -a_1 - 8a_2 + 64a_{-4} + 27a_{-3} + 8a_{-2} + a_{-1} &= 0, \\ a_0 + a_1 + a_2 + a_{-4} + a_{-3} + a_{-2} + a_{-1} &= 0, \\ -a_1 - 16a_{-4} - 4a_{-2} - a_1 - 4a_2 - 9a_{-3} &= 0. \end{aligned} \tag{7.4}$$

These simplify to the following if we let $a_{-4},\ a_{-3},\ a_{-2}$ as free parameters:

$$\begin{aligned} a_2 &= 10a_{-4} + 4a_{-3} + a_{-2} - \frac{1}{6}, \\ a_{-1} &= -20a_{-4} - 10a_{-3} - 4a_{-2} - \frac{1}{3}, \\ a_0 &= 45a_{-4} + 20a_{-3} + 6a_{-2} - \frac{1}{2}, \\ a_1 &= -36a_{-4} - 15a_{-3} - 4a_{-2} + 1. \end{aligned} \tag{7.5}$$

On plugging a_2, a_{-1}, a_0, and a_1 in terms of functions of a_{-4}, a_{-3}, a_{-2} in (7.2) and (7.3), we get

$$\begin{aligned} \Re(\theta^* h) &= -5\left(\frac{16}{5}\ a_{-4} + a_{-3} - \frac{4}{15}\right)\sin(\theta h) + \frac{1}{6}(60a_{-4} + 24a_{-3} - 1)\sin(2\theta h) \\ &\quad - a_{-3}\sin(3\theta h) - a_{-4}\sin(4\theta h), \end{aligned} \tag{7.6}$$

$$\begin{aligned} \Im(\theta^* h) &= \frac{1}{2} - 45a_{-4} - 20a_{-3} - 6a_{-2} + \frac{1}{6}\ \cos(\theta h)(336a_{-4} + 150a_{-3} + 48a_{-2} - 4) \\ &\quad - a_{-3}\cos(3\theta h) - a_{-4}\cos(4\theta h) + \frac{1}{6}(-60a_{-4} - 24a_{-3} - 12a_{-2} + 1)\cos(2\theta h). \end{aligned} \tag{7.7}$$

The coefficients obtained by Zhuang and Chen [15] are

$$\begin{aligned} &a_{-4} = 0.0161404967, \quad a_{-3} = -0.1228212790, \quad a_{-2} = 0.4553322778, \\ &a_{-1} = -1.2492595883, \quad a_0 = 0.5018904380, \quad a_1 = 0.4399321927, \\ &a_2 = -0.0412145379, \end{aligned} \tag{7.8}$$

and, therefore, the real and imaginary parts of $\theta^* h$ are given as follows:

$$\begin{aligned}\Re(\theta^* h) &= 1.689191781\sin(\theta h) - 0.4965468157\sin(2\theta h) + 0.1228212790\sin(3\theta h)\\ &\quad - 0.0161404967\sin(4\theta h),\end{aligned} \tag{7.9}$$

$$\begin{aligned}\Im(\theta^* h) &= -0.5018904390 + 0.8093273950\cos(\theta h) - 0.4141177399\cos(2\ \theta h)\\ &\quad + 0.1228212790\cos(3\theta h) - 0.0161404967\cos(4\theta h),\end{aligned} \tag{7.10}$$

respectively.

We now obtain a modification to the scheme developed by Zhuang and Chen [15]. We consider the numerical wavenumber in (7.6) and (7.7) and minimise the following integral

$$E = \int_0^{1.1} \left(\exp(|\Re(\theta^* h) - \theta h| + |\Im(\theta^* h)|) + \exp||\Re(\theta^* h) - \theta h| - |\Im(\theta^* h)|| - 2\right) d(\theta h). \tag{7.11}$$

The integral is a function of a_{-4}, a_{-3}, and a_{-2}. We use the function NLPSolve and obtain optimal values for a_{-4}, a_{-3}, and a_{-2} as 0.01575, −0.122, and 0.4553 respectively. Corresponding values for a_2, a_{-1}, a_0, and a_1 are then obtained as −0.0418666600, −1.2495333300, 0.5005500000, and 0.4418000000, respectively.

The modified method is termed as ZHUANG-NEW and has real and imaginary parts of its numerical wavenumber described by

$$\begin{aligned}\Re(\theta^* h) &= 1.6913333333\sin(\theta h) - 0.4971666667\sin(2\theta h) + 0.1220000000\sin(3\theta h)\\ &\quad - 0.0157500000\sin(4\theta h),\end{aligned} \tag{7.12}$$

$$\begin{aligned}\Im(\theta^* h) &= -0.5005500000 + 0.8077333330\cos(\theta h) - 0.4134333333\cos(2\theta h)\\ &\quad + 0.1220000000\cos(3\theta h) - 0.0157500000\cos(4\theta h),\end{aligned} \tag{7.13}$$

respectively.

We next perform a spectral analysis of the two methods: ZHUANG and ZHUANG-NEW. We compare the variation of real part and imaginary parts of the numerical wavenumber versus the exact wavenumber in Figures 7 and 5, respectively. We have the plot of the dispersion error versus the exact wavenumber in Figure 8 and we observe that, for $0 < \theta h < 1$, ZHUANG-NEW is slightly better than ZHUANG in terms of dispersive properties.

We now compare quantitatively these two methods. We compute the minimum number of points per wavelength needed to resolve a wave for each of the four accuracy limits. The results are summarized in Table 4.

ZHUANG-NEW requires fewer points per wavelength than ZHUANG scheme for $|(\theta^* h - \theta h)/\pi| \leq 0.005$.

Table 4: Comparing the dispersive and group velocity properties for two spatial methods ZHUANG and ZHUANG-NEW in terms of number of points per wavelength (to 4 d.p).

Accuracy	Method	Max. value of θh	No. of pts per wavelength
$\frac{\lvert\theta^* h - \theta h\rvert}{\pi} \leq 5 \times 10^{-3}$	ZHUANG	1.6755	3.7501
$\frac{\lvert\theta^* h - \theta h\rvert}{\pi} \leq 5 \times 10^{-3}$	ZHUANG-NEW	1.6957	3.7175
$\frac{\lvert\theta^* h - \theta h\rvert}{\pi} \leq 5 \times 10^{-4}$	ZHUANG	1.3315	4.7190
$\frac{\lvert\theta^* h - \theta h\rvert}{\pi} \leq 5 \times 10^{-4}$	ZHUANG-NEW	1.1417	5.5030
$\left\lvert \frac{d}{d(\theta h)} (\theta^* h) - 1.0 \right\rvert \leq 5 \times 10^{-3}$	ZHUANG	1.0484	5.9932
$\left\lvert \frac{d}{d(\theta h)} (\theta^* h) - 1.0 \right\rvert \leq 5 \times 10^{-3}$	ZHUANG-NEW	0.9620	6.3865
$\left\lvert \frac{d}{d(\theta h)} (\theta^* h) - 1.0 \right\rvert \leq 5 \times 10^{-4}$	ZHUANG	0.9029	6.9593
$\left\lvert \frac{d}{d(\theta h)} (\theta^* h) - 1.0 \right\rvert \leq 5 \times 10^{-4}$	ZHUANG-NEW	0.8052	7.5176

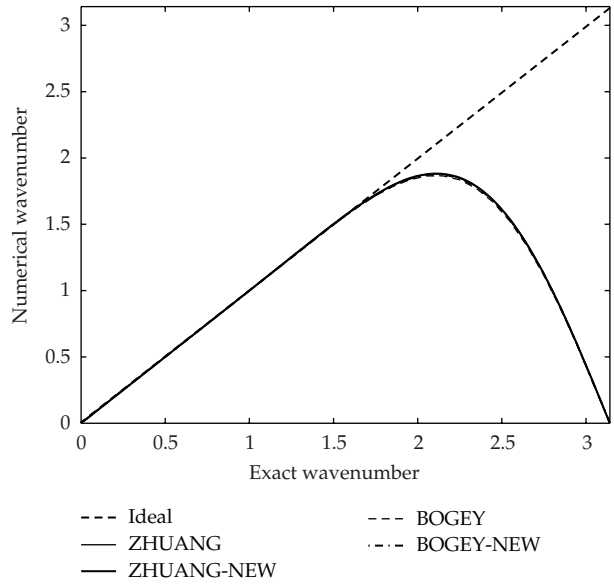

Figure 7: Plot of the variation of numerical wavenumber versus exact wavenumber for the methods: ZHUANG, ZHUANG-NEW, BOGEY, and BOGEY-NEW.

8. Modification to Spatial Discretisation Scheme Developed by Bogey and Bailly [16]

Bogey and Bailly [16] modified the measure used by Tam and Webb [3] by minimizing the relative difference between θh and $\theta^* h$. They define the integrated error, E, as

$$E = \int_{\pi/16}^{\pi/2} \frac{\lvert\theta^* h - \theta h\rvert}{\theta h} d(\theta h). \tag{8.1}$$

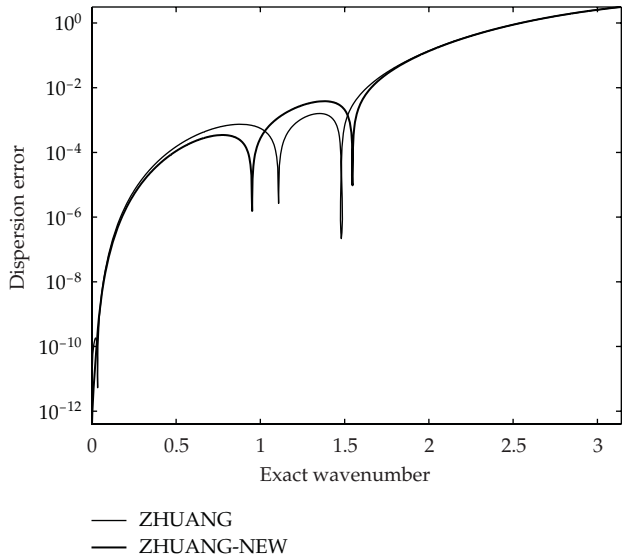

Figure 8: Plot of the variation of dispersion error in logarithmic scale versus exact wavenumber for the methods ZHUANG and ZHUANG-NEW.

Bogey and Bailly [3] use a 9-point stencil with coefficients a_{-4}, a_{-3}, a_{-2}, a_{-1}, a_0, a_1, a_2, a_3, a_4 and choose $a_0 = 0$, $a_{-1} = -a_1$, $a_{-2} = -a_2$, $a_{-3} = -a_3$, and $a_{-4} = -a_4$ and therefore the numerical wavenumber can be written as

$$\theta^* h = 2(a_1 \sin(\theta h) + a_2 \sin(2\theta h) + a_3 \sin(3\theta h) + a_4 \sin(4\theta h)). \tag{8.2}$$

To obtain a 4th-order method, a_1 and a_2 are chosen such as

$$\begin{aligned} a_1 &= \frac{2}{3} + 5a_3 + 16a_4, \\ a_2 &= -\frac{1}{6}\left(\frac{1}{2} + 24a_3 + 60a_4\right), \end{aligned} \tag{8.3}$$

respectively.

The coefficients a_3 and a_4 are chosen to minimize the integrated error defined in (8.1), and the values which Bogey and Bailly [16] have obtained are as follows:

$$a_1 = 0.841570125, \qquad a_2 = -0.2446786318, \qquad a_3 = 0.0594635848, \qquad a_4 = -0.0076509040. \tag{8.4}$$

We now construct a method based on a 9-point stencil using MIEELDLD. The wavenumber is set as follows:

$$\theta^* h = 2\left(\frac{2}{3} + 5a_3 + 16a_4\right)\sin(\theta h) + 2\left(-\frac{1}{12} - 4a_3 - 10a_4\right)\sin(2\theta h) + 2a_3 \sin(3\theta h). \tag{8.5}$$

The integrated error using MIEELDLD is defined as

$$\int_{\pi/16}^{\pi/2} \left(2\exp|\Re(\theta^* h) - \theta h| - 2\right) d(\theta h), \tag{8.6}$$

which is a function of a_3 and a_4. Using NLPSolve, we obtain the optimal values of a_3 and a_4 as 0.0613000000 and −0.0080500000, respectively. Hence, we obtain a_1 and a_2 as 0.8443666667 and −0.2480333333, respectively.

Using MIEELDLD, a new scheme is obtained and is termed as BOGEY-NEW with its numerical wavenumber given by

$$\begin{aligned}\theta^* h = {} & 1.6887333332 \sin(\theta h) - 0.4960666667 \sin(2\theta h) \\ & + 0.1226000000 \sin(3\theta h) 0.0161000000 \sin(4\theta h).\end{aligned} \tag{8.7}$$

We next perform a spectral analysis of the two methods: BOGEY and BOGEY-NEW. We compare the variation of numerical wavenumber versus the exact wavenumber in Figures 7 and 9; we have the plot of the dispersion error versus the exact wavenumber.

We now compare quantitatively these two methods. We compute the minimum number of points per wavelength needed to resolve a wave for each of the four accuracy limits.

Table 5 indicates that BOGEY-NEW has appreciably better phase and group velocity properties as compared to BOGEY scheme.

9. Optimized Time Discretisation Schemes

9.1. Time Discretisation Scheme by Tam et al. [17]

Tam et al. [17] have developed a time-marching scheme which is four-level and accurate up to k^3. They expressed

$$U^{(n+1)} - U^{(n)} \approx k \sum_{j=0}^{3} b_j \left(\frac{dU}{dt}\right)^{(n-j)}. \tag{9.1}$$

We next summarize how the coefficients have been obtained.

The effective angular frequency of the time discretisation method is obtained as

$$\varpi = \frac{I\left(\exp(-I\omega k) - 1\right)}{k \sum_{j=0}^{3} b_j \exp\left(I j \omega k\right)}. \tag{9.2}$$

For ϖk to approximate ωk to order $(\omega k)^4$, we must have

$$\begin{aligned} b_0 + b_1 + b_2 + b_3 &= 1, \\ b_1 + 2b_2 + 3b_3 &= -\frac{1}{2}, \\ b_1 + 4b_2 + 9b_3 &= \frac{1}{3}. \end{aligned} \tag{9.3}$$

Table 5: Comparing the dispersive and group velocity properties for two spatial methods BOGEY and BOGEY-NEW in terms of number of points per wavelength (to 4 d.p).

Accuracy	Method	Max. value of θh	No. of pts per wavelength
$\frac{\lvert\theta^* h - \theta h\rvert}{\pi} \leq 5 \times 10^{-3}$	BOGEY	1.4875	4.2240
$\frac{\lvert\theta^* h - \theta h\rvert}{\pi} \leq 5 \times 10^{-3}$	BOGEY-NEW	1.5175	4.1405
$\frac{\lvert\theta^* h - \theta h\rvert}{\pi} \leq 5 \times 10^{-4}$	BOGEY	1.6529	3.8013
$\frac{\lvert\theta^* h - \theta h\rvert}{\pi} \leq 5 \times 10^{-4}$	BOGEY-NEW	1.6733	3.7550
$\left\lvert \frac{d}{d(\theta h)} (\theta^* h) - 1.0 \right\rvert \leq 5 \times 10^{-3}$	BOGEY	1.0572	5.9433
$\left\lvert \frac{d}{d(\theta h)} (\theta^* h) - 1.0 \right\rvert \leq 5 \times 10^{-3}$	BOGEY-NEW	1.0523	5.9710
$\left\lvert \frac{d}{d(\theta h)} (\theta^* h) - 1.0 \right\rvert \leq 5 \times 10^{-4}$	BOGEY	0.8784	7.1533
$\left\lvert \frac{d}{d(\theta h)} (\theta^* h) - 1.0 \right\rvert \leq 5 \times 10^{-4}$	BOGEY-NEW	0.9049	6.9437

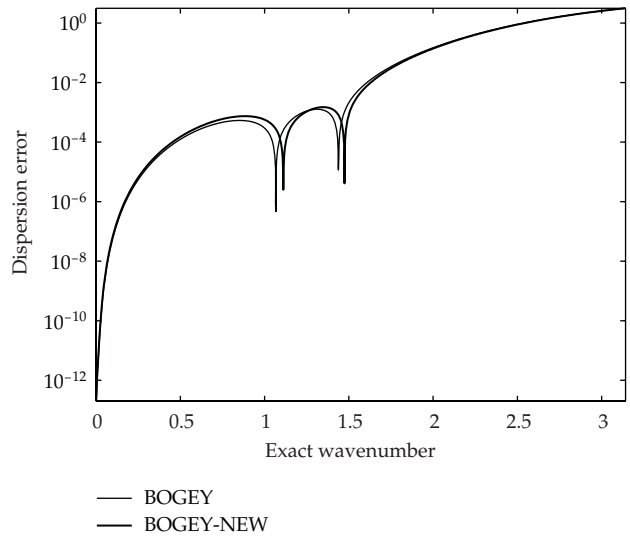

Figure 9: Plot of the variation of dispersion error in logarithmic scale versus exact wavenumber.

Since we have 4 equations and 3 unknowns, we can choose b_0 as a free parameter, and hence we have

$$b_1 = \frac{53}{12} - 3b_0, \qquad b_2 = 3b_0 - \frac{16}{3}, \qquad b_3 = \frac{23}{12} - b_0. \tag{9.4}$$

Hence, we can express ϖ as follows:

$$\varpi k = \frac{AC + BD_1 + I(BC - AD_1)}{C^2 + (D1)^2}, \tag{9.5}$$

where

$$A = \sin(\omega k),$$
$$B = \cos(\omega k) - 1,$$
$$C = b_0 + \left(\frac{53}{12} - 3b_0\right)\cos(\omega k) + \left(3b_0 - \frac{16}{3}\right)\cos(2\omega k) + \left(\frac{23}{12} - b_0\right)\cos(3\omega k), \tag{9.6}$$
$$D_1 = \left(\frac{53}{12} - 3b_0\right)\sin(\omega k) + \left(3b_0 - \frac{16}{3}\right)\sin(2\omega k) + \left(\frac{23}{12} - b_0\right)\sin(3\omega k).$$

The weighted integral error incurred by using ϖ to approximate ω, used by Tam et al. [17], is computed as

$$E_T = \int_{-0.5}^{0.5} \left[\sigma(\Re(\varpi k) - \omega k)^2 + (1-\sigma)(\Im(\varpi k))^2\right] d(\omega k), \tag{9.7}$$

and σ is chosen as 0.36.

On minimizing E_T, the value of b_0 is obtained as 2.30255809 and therefore the corresponding values for b_1, b_2, and b_3 are −2.49100760, 1.57434094, and −0.38589142, respectively.

9.2. Modified Temporal Discretisation Scheme Using MIEELDLD

We consider the equation in (9.5) which expresses ϖk in terms of ωk and define the quantity, eeldld as

$$\exp(|\Re(\varpi k) - \omega k| + |\Im(\varpi k)|) + \exp(|\Re(\varpi k) - \omega k| - |\Im(\varpi k)|) - 2. \tag{9.8}$$

We minimize

$$\int_{-0.5}^{0.5} \text{eeldld } d(\omega k) \tag{9.9}$$

and this integral is a function of b_0. Using NLPSolve, we obtain the value of b_0 as 2.2796378228. A plot of E_T versus b_0 is shown in Figure 10.

Corresponding values of b_1, b_2, b_3 are obtained as −2.4222468020, 1.5055801360, and −0.3629711560. This modified temporal discretisation scheme obtained by modifying the temporal scheme of Tam et al. [17] is termed as "TAM-MODIFIED" scheme. Plots of $\Re(\varpi k)$ versus ωk and $\Im(\varpi k)$ versus ωk for the TAM-MODIFIED scheme are shown in Figures 11 and 12, respectively.

For $|\Im(\varpi k)| \leq 3 \times 10^{-3}$, we require $\omega k \leq 0.42$.

9.3. Comparison between Temporal Discretisation Schemes: TAM and TAM-MODIFIED

Plots of $\Re(\varpi k)$ versus ωk for the two methods are shown in Figure 13. We also compare their dispersive properties at two different levels of accuracy in terms of number of points

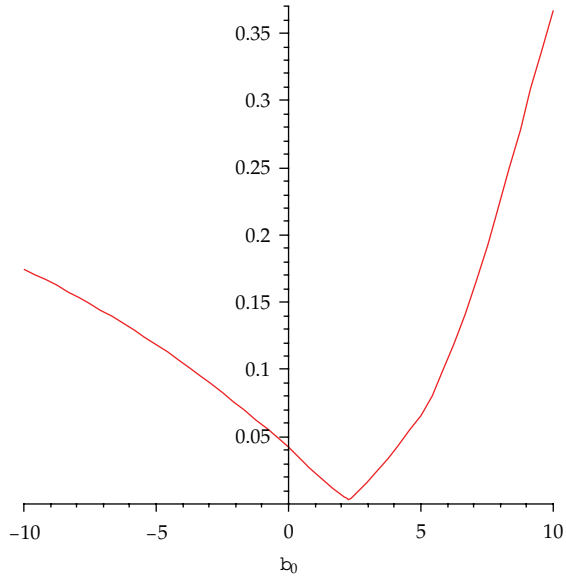

Figure 10: Plot of IEELDLD versus b_0.

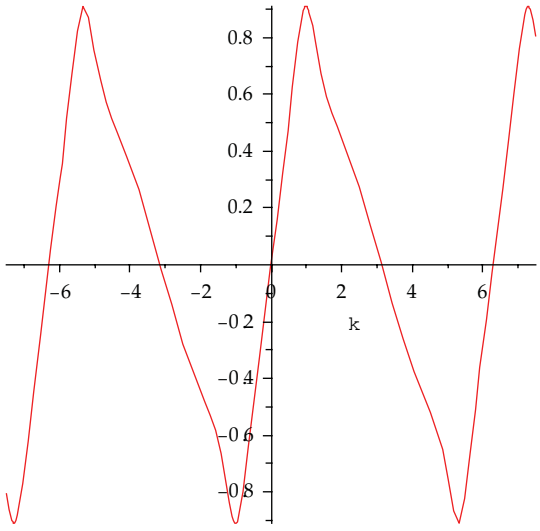

Figure 11: Plot of $\Re(\varpi k)$ versus ωk.

per wavelength and the results are tabulated in Table 6. Clearly, TAM-MODIFIED is more superior as it requires less points per wavelength for the same accuracy.

10. Stability of Some Multilevel Optimized Combined Spatial-Temporal Finite Difference Schemes

The stability of the combined spatial and temporal finite difference scheme developed by Tam and Webb [3] and Tam et al. [17], which is 7-point in space and 4-point in time and which

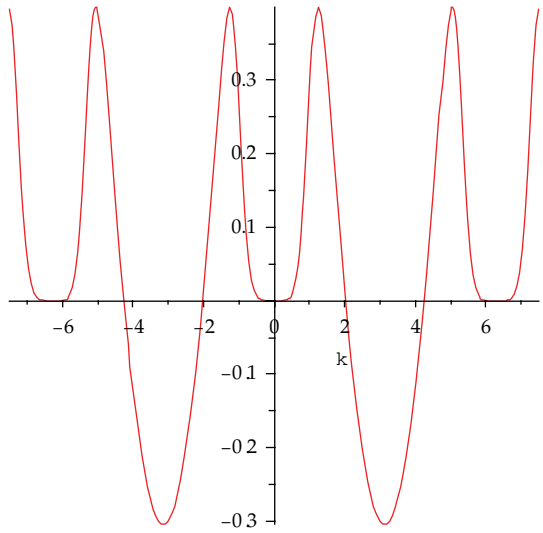

Figure 12: Plot of $\Im(\varpi k)$ versus ωk.

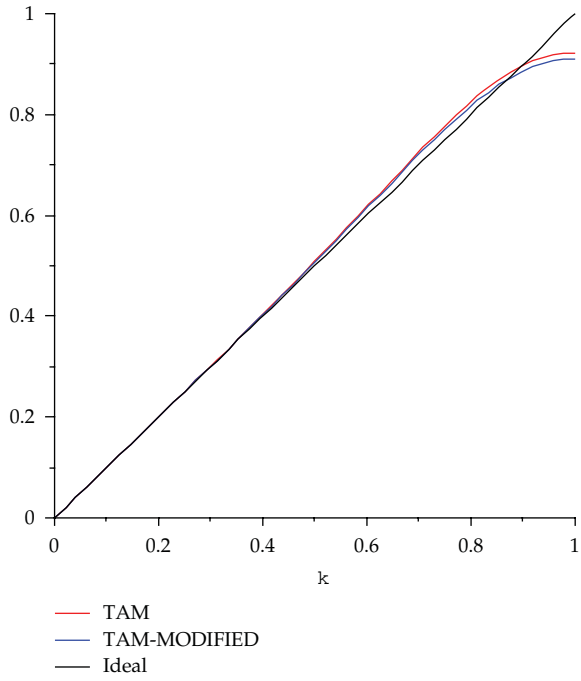

Figure 13: Plot of $\Re(\varpi k)$ versus ωk for TAM and TAM-MODIFIED schemes.

is referred to as the Dispersion-Relation-Preserving (DRP) scheme, satisfies the stability condition, $r \leq 0.229$ [3]. The condition on the spatial discretisation is that $|(\theta^* h - \theta h)/\pi| \leq 0.05$ and this gives $\theta h \leq 1.76$. The interval $0 < \varpi k \leq 0.4$ has been chosen in order to maintain satisfactory temporal resolution and this interval is obtained by requiring the condition: $\Im(\varpi k) \leq 0.003$.

Table 6: Comparing the dispersive properties for two temporal discretisation methods TAM and TAM-MODIFIED in terms of number of points per wavelength (to 4 d.p).

Method	Accuracy	Max. value of ωk	No. of pts per wavelength
TAM	$\frac{\lvert\Re(\varpi k)-\omega k\rvert}{\pi} \leq 5\times 10^{-3}$	0.5913	10.6267
TAM-MODIFIED	$\frac{\lvert\Re(\varpi k)-\omega k\rvert}{\pi} \leq 5\times 10^{-3}$	0.6280	10.0050
TAM	$\frac{\lvert\Re(\varpi k)-\omega k\rvert}{\pi} \leq 5\times 10^{-4}$	0.3461	18.1565
TAM-MODIFIED	$\frac{\lvert\Re(\varpi k)-\omega k\rvert}{\pi} \leq 5\times 10^{-4}$	0.3570	17.6002

Since

$$\varpi k = (\beta\theta)k, \tag{10.1}$$

we also have

$$\varpi k = r\ \theta h. \tag{10.2}$$

Since, we require $\varpi k \leq 0.4$, this implies that $r\ (\theta h) \leq 0.4$. Also, we have $\theta h \leq 1.76$ and thus $r \leq 0.4/1.76$.

The stability of the DRP scheme therefore satisfies the condition: $r \leq 0.23$.

Using the approach just described in the preceding paragraph, the ranges of stability of some methods are obtained, namely, TAM-NEW, ZINGG-NEW, ZHUANG-NEW, LOCKARD-NEW, and BOGEY-NEW when combined with TAMMODIFIED. We also obtain the range of stability for the methods: ZINGG, ZINGG, ZHUANG, LOCKARD, and BOGEY when they are combined with the temporal discretisation scheme of Tam et al. [17]. The results are tabulated in Table 7. It is seen that the new combined spatial-temporal methods constructed using MIEELDLD have a slightly greater region of stability than the existing combined spatial-temporal methods.

11. Comparison of Some Metric Measures

Spatial Scheme of Tam and Webb [3]

The integrated error is defined as

$$\int_0^{1.1} |\theta^* h - \theta h|^2 d(\theta h). \tag{11.1}$$

The quantity, $|\theta^* h - \theta h|^2$ is equivalent to $|1 - \mathrm{RPE}|^2$ in a computational fluid dynamics framework. A plot of $|1 - \mathrm{RPE}|^2$ versus $\mathrm{RPE} \in [0, 2]$ is shown in Figure 14(a).

Table 7: Region of stability for some combined spatial-temporal discretisation schemes.

Spatial scheme	Temporal scheme	Range of θh required	Range of ωk required	max. value of r
TAM	TAM	1.76	0.40	0.23
TAM-NEW	TAM-MODIFIED	1.75	0.42	0.24
ZINGG	TAM	1.72	0.40	0.23
ZINGG-NEW	TAM-MODIFIED	1.73	0.42	0.24
ZHUANG	TAM	2.03	0.40	0.20
ZHUANG-NEW	TAM-MODIFIED	2.03	0.42	0.21
LOCKARD	TAM	1.97	0.40	0.20
LOCKARD-NEW	TAM-MODIFIED	1.92	0.42	0.22
BOGEY	TAM	2.01	0.40	0.20
BOGEY-NEW	TAM-MODIFIED	2.02	0.42	0.21

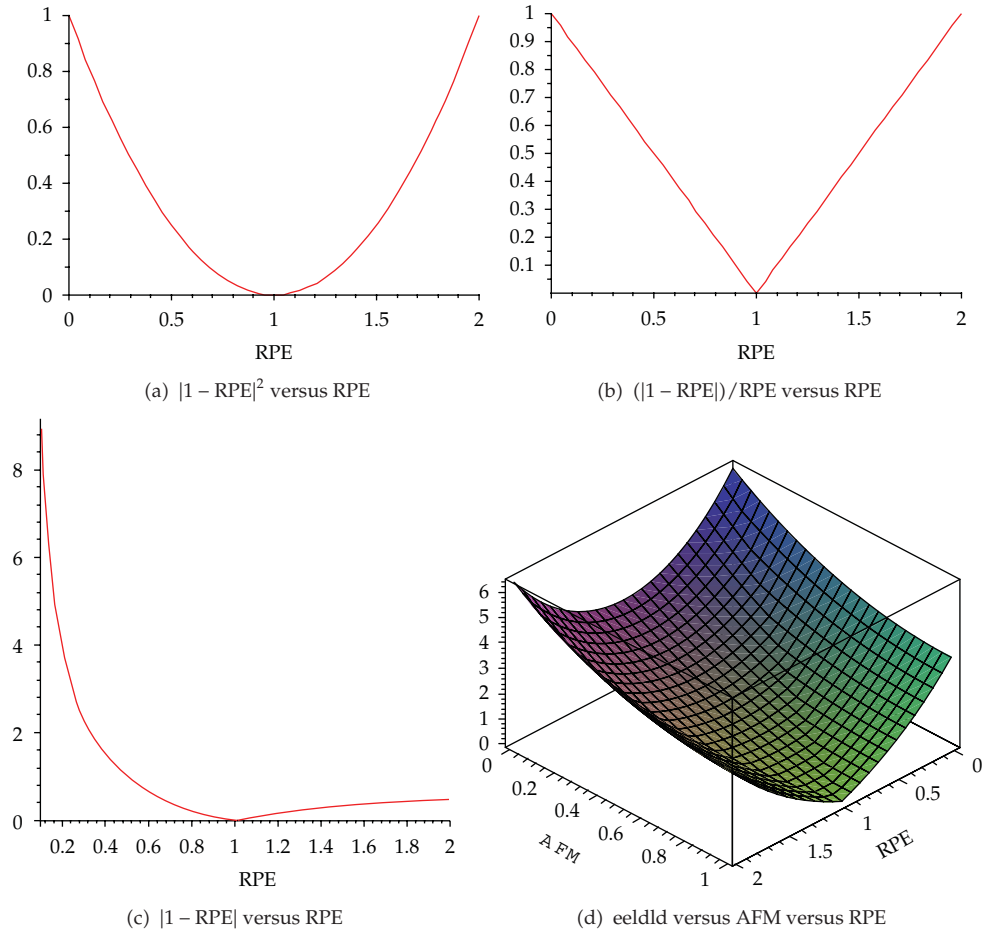

(a) $|1 - \text{RPE}|^2$ versus RPE

(b) $(|1 - \text{RPE}|)/\text{RPE}$ versus RPE

(c) $|1 - \text{RPE}|$ versus RPE

(d) eeldld versus AFM versus RPE

Figure 14: Plot of different metrics from Tam and Webb [3], Bogey and Bailly [16] and Appadu and Dauhoo [18].

Spatial Scheme of Bogey and Bailly [16]

In this case, the integrated error is defined as

$$\int_{\pi/16}^{\pi/2} \frac{|\theta^* h - \theta h|}{\theta h} d(\theta h), \tag{11.2}$$

or

$$\int_{\ln \pi/16}^{\ln \pi/2} |\theta^* h - \theta h| d(\ln(\theta h)). \tag{11.3}$$

The quantity $(|\theta^* h - \theta h|)/\theta h$ is equivalent to $(|1 - \text{RPE}|)/\text{RPE}$ while $|\theta^* h - \theta h|$ is equivalent to $|1 - \text{RPE}|$. Plots of $(|1 - \text{RPE}|)/\text{RPE}$ and $|1 - \text{RPE}|$, both versus RPE $\in [0, 2]$, are shown in Figures 14(b) and 14(c).

Spatial Scheme Using MIEELDLD

A plot of eeldld $= \exp((|1 - \text{RPE}| - (1 - \text{AFM})|) + \exp(|1 - \text{RPE}| + (1 - \text{AFM})) - 2)$ versus RPE $\in [0, 2]$ versus AFM $\in [0, 1]$ is shown in Figure 14(d).

We observe from Figures 14(a), 14(b), and 14(c) that the measure is zero when RPE = 1 whereas, in Figure 14(d), the measure is zero provided RPE = 1 and AFM = 1.

12. Conclusions

In this work, we have used the technique of Minimised Integrated Exponential Error for Low Dispersion and Low Dissipation (MIEELDLD) in a computational aeroacoustics framework to obtain modifications to optimized spatial schemes constructed by Tam and Webb [3], Zingg et al. [14], Lockard et al. [13], Zhuang and Chen [15], and Bogey and Bailly [16], and also a modification to the optimized temporal scheme devised by Tam et al. [17] is obtained. It is seen that, in general, improvements can be made to the existing spatial discretisation schemes, using MIEELDLD. The new temporal scheme obtained using MIEELDLD is superior in terms of dispersive properties as compared to the one constructed by Tam et al. [17]. The region of stability has also been obtained. In a nutshell, we conclude that MIEELDLD is an efficient technique to construct high order methods with low dispersion and dissipative properties. An extension of this work will be to use the new spatial discretisation schemes and the novel temporal discretisation method constructed to solve 1-D wave propagation experiments and quantify the errors into dispersion and dissipation. Moreover, MIEELDLD can be used to construct low dispersive and low dissipative methods which approximate 2-D and 3-D scalar advection equation suited for computational aeroacoustics applications.

Nomenclature

$I = \sqrt{(-1)}$
k: Time step
h: Spatial step
n: Time level

β: Advection velocity
$\theta^* h$: Numerical wavenumber
θh: Exact wavenumber
r: cfl/courant number
$r =$ $\beta k/h$
w: Phase angle in 1-D
$w =$ θh
ω: Exact angular frequency
ϖ: Effective angular frequency of time discretization scheme
RPE: Relative phase error per unit time step
AF: Amplification factor
AFM = $|AF|$
LDLD: Low Dispersion and Low Dissipation
IEELDLD: Integrated Exponential Error for Low Dispersion and Low Dissipation
MIEELDLD: Minimised Integrated Exponential Error for Low Dispersion and Low Dissipation.

Acknowledgment

This work was funded through the Research Development Programme of the University of Pretoria.

References

[1] S. Johansson, *High Order Finite Di erence Operators with the Summation by Parts Property Based on DRP Schemes*, Division of Scientific Computing, Department Information Technology, Uppsala University, Sweden, 2007.
[2] J. Hardin and M. Y. Hussaini, *Computational Aeroacoustics*, Springer, New-York, NY, USA, 1992.
[3] C. K. W. Tam and J. C. Webb, "Dispersion-relation-preserving finite difference schemes for computational acoustics," *Journal of Computational Physics*, vol. 107, no. 2, pp. 262–281, 1993.
[4] R. Hixon, "Evaluation of high-accuracy MacCormack-type scheme using benchmark problems," NASA Contractor Report 202324, ICOMP-97-03-1997.
[5] G. Ashcroft and X. Zhang, "Optimized prefactored compact schemes," *Journal of Computational Physics*, vol. 190, no. 2, pp. 459–477, 2003.
[6] P. Roe, "Linear bicharacteristic schemes without dissipation," *SIAM Journal on Scientific Computing*, vol. 19, no. 5, pp. 1405–1429, 1998.
[7] V. L. Wells and R. A. Renault, "Computing aerodynamically generated noise," *Annual Review Fluid Mechanics*, vol. 29, pp. 161–199, 1997.
[8] C. K. W. Tam, "Computational aeroacoustics: issues and methods," *AIAA Journal*, vol. 33, no. 10, pp. 1788–1796, 1995.
[9] D. W. Zingg, "Comparison of high-accuracy finite-difference methods for linear wave propagation," *SIAM Journal on Scientific Computing*, vol. 22, no. 2, pp. 476–502, 2001.
[10] T. K. Sengupta, G. Ganeriwal, and S. De, "Analysis of central and upwind compact schemes," *Journal of Computational Physics*, vol. 192, no. 2, pp. 677–694, 2003.
[11] W. De Roeck, W. Desmet, M. Baelmans, and P. Sas, "An overview of high-order finite difference schemes for computational aeroacoustics," in *Proceedings of the International Conference on Noise and Vibration Engineering*, pp. 353–368, Katholieke Universiteit Leuven, Belgium, September 2004.
[12] M. Popescu, W. Shyy, and M. Garbey, "Finite-volume treatment of dispersion-relation- preserving and optimized prefactored compact schemes for wave propagation," Tech. Rep. UH-CS-05-03.
[13] D. P. Lockard, K. S. Brentner, and H. L. Atkins, "High-accuracy algorithms for computational aeroacoustics," *AIAA Journal*, vol. 33, no. 2, pp. 246–251, 1995.
[14] D. W. Zingg, H. Lomax, and H. Jurgens, "High-accuracy finite-difference schemes for linear wave propagation," *SIAM Journal on Scientific Computing*, vol. 17, no. 2, pp. 328–346, 1996.

[15] M. Zhuang and R. F. Chen, "Applications of high-order optimized upwind schemes for computational aeroacoustics," *Aiaa Journal*, vol. 40, no. 3, pp. 443–449, 2002.
[16] C. Bogey and C. Bailly, "A family of low dispersive and low dissipative explicit schemes for flow and noise computations," *Journal of Computational Physics*, vol. 194, no. 1, pp. 194–214, 2004.
[17] C. K. W. Tam, J. C. Webb, and Z. Dong, "A study of the short wave components in computational acoustics," *Journal of Computational Acoustics*, vol. 1, no. 1, pp. 1–30, 1993.
[18] A. R. Appadu and M. Z. Dauhoo, "The concept of minimized integrated exponential error for low dispersion and low dissipation schemes," *International Journal for Numerical Methods in Fluids*, vol. 65, no. 5, pp. 578–601, 2011.
[19] A. R. Appadu and M. Z. Dauhoo, "An overview of some high order and multi-level finite difference schemes in computational aeroacoustics," *Proceedings of World Academy of Science, Engineering and Technology*, vol. 38, pp. 365–380, 2009.
[20] A. R. Appadu, "Some applications of the concept of minimized integrated exponential error for low dispersion and low dissipation," *International Journal for Numerical Methods in Fluids*, vol. 68, no. 2, pp. 244–268, 2012.
[21] A. R. Appadu, "Comparison of some optimisation techniques for numerical schemes discretising equations with advection terms," *International Journal of Innovative Computing and Applications*, vol. 4, no. 1, pp. 12–27, 2012.
[22] A. R. Appadu, "Investigating the shock-capturing properties of some composite numerical schemes for the 1-D linear advection equation," *International Journal of Computer Applications in Technology*, vol. 43, no. 2, pp. 79–92, 2012.
[23] J. Wang and R. Liu, "A new approach to design high-order schemes," *Journal of Computational and Applied Mathematics*, vol. 134, no. 1-2, pp. 59–67, 2001.
[24] L. L. Takacs, "A two-step scheme for the advection equation with minimized dissipation and dispersion errors," *Monthly Weather Review*, vol. 113, no. 6, pp. 1050–1065, 1985.
[25] R. Liska and B. Wendroff, "Composite schemes for conservation laws," *SIAM Journal on Numerical Analysis*, vol. 35, no. 6, pp. 2250–2271, 1998.
[26] M. Lukacova, "Finite volume schemes for multi-dimensional hyperbolic systems based on the use of bicharacteristics," *Applications of Mathematics*, vol. 51, no. 3, pp. 205–228, 2006.
[27] C. Kim, *Multi-dimensional Upwind Leapfrog Schemes and their Applications*, Ph.D. thesis, Aerospace Engineering, University of Michigan, 1997.
[28] J. Berland, C. Bogey, O. Marsden, and C. Bailly, "High-order, low dispersive and low dissipative explicit schemes for multiple-scale and boundary problems," *Journal of Computational Physics*, vol. 224, no. 2, pp. 637–662, 2007.
[29] A. R. Appadu, M. Z. Dauhoo, and S. D. D. V. Rughooputh, "Control of numerical effects of dispersion and dissipation in numerical schemes for efficient shock-capturing through an optimal Courant number," *Computers & Fluids*, vol. 37, no. 6, pp. 767–783, 2008.

Hindawi Publishing Corporation
Journal of Applied Mathematics
Volume 2012, Article ID 489269, 14 pages
doi:10.1155/2012/489269

Research Article

1D and 2D Numerical Modeling for Solving Dam-Break Flow Problems Using Finite Volume Method

Szu-Hsien Peng

Department of Spatial Design, Chienkuo Technology University, Number 1, Chieh Shou N. Road, Changhua City 500, Taiwan

Correspondence should be addressed to Szu-Hsien Peng, shpeng@cc.ctu.edu.tw

Received 6 January 2012; Accepted 13 February 2012

Academic Editor: Shuyu Sun

The purpose of this study is to model the flow movement in an idealized dam-break configuration. One-dimensional and two-dimensional motion of a shallow flow over a rigid inclined bed is considered. The resulting shallow water equations are solved by finite volumes using the Roe and HLL schemes. At first, the one-dimensional model is considered in the development process. With conservative finite volume method, splitting is applied to manage the combination of hyperbolic term and source term of the shallow water equation and then to promote 1D to 2D. The simulations are validated by the comparison with flume experiments. Unsteady dam-break flow movement is found to be reasonably well captured by the model. The proposed concept could be further developed to the numerical calculation of non-Newtonian fluid or multilayers fluid flow.

1. Introduction

Earthquakes or heavy rainfall usually caused more than a dozen landslide dams to form across Taiwan streams, temporarily impounding large volumes of water after the Chichi Earthquake in 1999 and Typhoon Morakot in 2009 [1]. Once formed, these natural dams were highly exposed to catastrophic failure. Partial or complete failure can lead to severe flooding downstream and possibly trigger further floods or debris flows such as Shiaolin landslide events in 2009 [2]. For realizing the dam formation process and evaluate the potential consequences of subsequent failure, it is important to be able to model the dynamics of dam-break flows, such as computational hydraulics and laboratory experiments.

Computational Hydraulics is regarded as an important technology, which utilizes numerical methods for solving the governing equations and discusses the relationship

between the flow field and the change of water depth. The commonly used numerical methods such as finite difference method, finite element method, method of characteristics, and finite volume method have been studied.

The first computer-based simulation model for shallow water flows was finite difference method (FDM), which is still widely applied at present [3]. According to Taylor series, FDM is an approximate numerical solution directly turning shallow water equations into algebra questions. Based on the typical numerical theory, FDM was developed early and presented high processing efficiency that it was simple and easily accepted. In order to enhance the calculation accuracy, FDM requires more simulated time for calculation and is rather unstable. According to the past research applying various numerical methods to solving such problems, Liao et al. [4] also applied the commonly used finite difference method (FDM). When catching shock wave, discontinuous numerical oscillation appeared in the numerical processing that the total variation diminishing scheme (TVD) was utilized as the research method [5, 6]. It remained two-order accuracy of time and space for the optimal solution for unsteady flows.

Finite element method (FEM) was first applied to structural mechanics. With the development of computers in 1970s, it was applied to computational hydraulics [3]. In finite element method, the computing zone is divided into several nonoverlapping and connected individuals; basis functions are selected from each element for linear combinations so as to approach the true solution of elements. A large system of linear equations is required for each time-point (standard FEM is implicit) so that the explicit FEM could be utilized for enhancing the efficiency. In spite of the fact that finite element method could solve irregular zones, it requires more time to solve matrix equations. In this case, parallel computing or specific solutions are required for saving the calculation time. FEM therefore has not been widely applied to hydraulics computing. Idelsohn et al. [7] suggested applying meshless finite element method (MFEM) and particle finite element method (PFEM) to the approximate partial differential equation of fluid, where MFEM covered irregular shapes to approach the real situation. It therefore continuously disperses the moving particles (due to gravity) and the surface energy (owing to the interaction with the contiguous particles), as well as density, viscosity, conductivity, and so on. The changes of particle velocity and position are also defined. For this reason, PFEM is considered as an advantageous and effective model to solve the surface problem and simplify the interaction between fluid structures in the papers [7, 8].

Wu and Chen [9] applied method of characteristics (MOC) to the calculation of kinematic wave equation. Method of characteristics does not show the drawback of numerical diffusion as in finite difference method, and the accuracy and convenience are better than other numerical methods. But the mathematical deduction of MOC is more complicated and it merely shows more restrictions on the side flow term. However, it makes more definitely physical meaning of the algorithm for method of characteristics. Shi and Liu [10] regarded method of characteristics as the most accurate numerical solution for hyperbolic partial differential equations. The basic theory was the one-order simulation of linear hyperbolic partial differential equations with two-dimensional characteristics space. The curves of the two characteristics and the correspondent characteristic arithmetic expressions are deducted. In terms of characteristic arithmetic expressions, they are proceeded by the numerical solutions (such as velocity and water depth) to discretize characteristic equations. The physical concept of MOC is definite, and the calculation accuracy of numerical analyses is high. The discontinuity of dam-break flows is rather difficult to solve with general difference method. However, the characteristic line still exists

and can be solved with method of characteristics. Nevertheless, the ratio of time-space is restricted by stable conditions that the minimum time is obtained. When the analysis is abundant, it would require longer calculation time.

Finite volume method (FVM) used to be applied to aviation and aerodynamics. For hydraulics, finite difference method and finite element method were more widely applied [3, 11]. However, unstructured grids are utilized for the grid computing with both finite volume method and finite element method that they are acceptable in irregularly natural channels. Besides, finite volume method and finite difference method present similar calculating speed, but faster than finite element method. The application of finite volume method has therefore been emphasized in recent years. With distinct directions, characters, and coordinates or different grids being the numerical calculation, each method would show different advantages. Both FVM and FEM divide calculation zone into several regular or irregular shapes of elements or control volume, but the calculating speed of FVM is faster than it of FEM. Bellos et al. [12] utilized finite volume method for calculation simulation and verified by the dam-break test and observe the surges generated by the dam-break in an extreme-wide flume.

In this paper, a numerical model by using the finite volume method is presented for simulating the dam-break flows. Meanwhile, the model uses a splitting to deal with the source term. The advantage of this approach is that it can develop more other computations, for example, mudflows, debris flows, or the aggradation and degradation of sediment-laden flows [13], in the future.

2. Numerical Model

2.1. Governing Equations

The Saint Venant equations are used to describe unsteady one-dimensional open-channel flow. Continuity and momentum balance are, respectively, written as [14, 15]:

$$\begin{aligned} \frac{\partial h}{\partial t} + \frac{\partial q}{\partial x} &= 0, \\ \frac{\partial q}{\partial t} + \frac{\partial}{\partial x}\left(\frac{q^2}{h} + \frac{1}{2}gh^2\right) &= gh(S_0 - S_f), \end{aligned} \tag{2.1}$$

where h is the depth of flow above the rigid bed, $q = hu$ is the unit width discharge, and u is the mean velocity in the longitudinal flow direction. Letting z_b denote the bed elevation above a reference datum, the slope S_0 can be written as

$$\frac{\partial z_b}{\partial x} = -S_0. \tag{2.2}$$

The friction slope S_f can also be also expressed with a relationship established for uniform flow, by using the Manning-Strickler formula [16] as follows:

$$S_f = \frac{q^2 n^2}{h^{10/3}}, \tag{2.3}$$

where n is the Manning coefficient, recalling that, for a very wide channel, the hydraulic radius is equal to the flow depth.

2.2. Hyperbolic Term

In this study, the above shallow water equations are solved numerically using a finite volume approach, well suited for transient problems such as dam-break flows. An operator-splitting approach [17] is used to separately treat the hyperbolic and source components. The hyperbolic operator solves the homogeneous equations:

$$\begin{aligned} \frac{\partial h}{\partial t} + \frac{\partial q}{\partial x} &= 0, \\ \frac{\partial q}{\partial t} + \frac{\partial}{\partial x}\left(\frac{q^2}{h} + \frac{1}{2}gh^2\right) + gh\frac{\partial z_b}{\partial x} &= 0, \\ \frac{\partial z_b}{\partial t} &= 0. \end{aligned} \tag{2.4}$$

The source operator, on the other hand, deals with the nonhomogeneous part in the absence of flux terms:

$$\begin{aligned} \frac{\partial h}{\partial t} &= 0, \\ \frac{\partial q}{\partial t} &= -ghS_f, \\ \frac{\partial z_b}{\partial t} &= 0. \end{aligned} \tag{2.5}$$

For both operators, the procedure outlined by documents [18–20] is adapted for the computation of geomorphic dam-break surges. In the hyperbolic operator, two schemes, including Roe and HLL, are used to deal with the partial differential equations, and an implicit backward Euler scheme to treat the source term which will be illustrated in the next section.

2.2.1. Roe Scheme

Consider first the hyperbolic operator. The corresponding equations can be cast in the following matrix form:

$$\frac{\partial \mathbf{U}}{\partial t} + \frac{\partial}{\partial x}\mathbf{F}(\mathbf{U}) + \mathbf{H}(\mathbf{U})\frac{\partial \mathbf{U}}{\partial x} = 0, \tag{2.6}$$

where

$$\mathbf{U} = \begin{bmatrix} h \\ q \\ z_b \end{bmatrix}, \qquad \mathbf{F}(\mathbf{U}) = \begin{bmatrix} q \\ \dfrac{q^2}{h} + \dfrac{1}{2}gh^2 \\ 0 \end{bmatrix}, \qquad \mathbf{H}(\mathbf{U}) = \begin{bmatrix} 0 & 0 & 0 \\ 0 & 0 & gh \\ 0 & 0 & 0 \end{bmatrix}. \tag{2.7}$$

Fluxes at the interfaces between finite volumes are evaluated using the Roe scheme. Let $\mathbf{U}_L$ and $\mathbf{U}_R$ denote the cell states to the left and right of a given interface. A decomposition of the flux difference $\Delta\mathbf{F} = \mathbf{F}_R - \mathbf{F}_L$ is sought and simultaneously satisfies

$$\Delta\mathbf{U} = \sum_{k=1}^{3} \tilde{\alpha}_k \tilde{\mathbf{K}}^{(k)}, \tag{2.8}$$

$$\Delta\mathbf{F} + \overline{\mathbf{H}}\Delta\mathbf{U} = \sum_{k=1}^{3} \tilde{\alpha}_k \tilde{\lambda}_k \tilde{\mathbf{K}}^{(k)}, \tag{2.9}$$

where the $\tilde{\alpha}_k$, $\tilde{\lambda}_k$, and $\tilde{\mathbf{K}}^{(k)}$ are the surge strengths, eigenvalues, and right eigenvectors of the Roe linearisation of Jacobian matrix $\partial\mathbf{F}/\partial\mathbf{U}$. Following the Roe-Pike procedure, the eigenvalues and the eigenvectors are first written in terms of the averaged variables $\tilde{h}$, $\tilde{u}$, and $\overline{gh}$:

$$\begin{gathered}
\tilde{\lambda}_1 = \tilde{u} - \sqrt{g\tilde{h}}, \qquad \tilde{\lambda}_2 = \tilde{u} + \sqrt{g\tilde{h}}, \qquad \tilde{\lambda}_3 = 0, \\
\tilde{\mathbf{K}}^{(1)} = \begin{bmatrix} 1 \\ \tilde{u} - \sqrt{g\tilde{h}} \\ 0 \end{bmatrix}, \qquad \tilde{\mathbf{K}}^{(2)} = \begin{bmatrix} 1 \\ \tilde{u} + \sqrt{g\tilde{h}} \\ 0 \end{bmatrix}, \qquad \tilde{\mathbf{K}}^{(3)} = \begin{bmatrix} 1 \\ 0 \\ \dfrac{\tilde{u}^2 - g\tilde{h}}{g\tilde{h}} \end{bmatrix}.
\end{gathered} \tag{2.10}$$

The surge strengths $\tilde{\alpha}_k$ are then obtained by linearising (2.8):

$$\begin{gathered}
\tilde{\alpha}_1 = \frac{1}{2}\left[\Delta h - \frac{\sqrt{g\tilde{h}}}{\tilde{u} - \sqrt{g\tilde{h}}}\Delta z_b - \frac{\tilde{h}}{\sqrt{g\tilde{h}}}\Delta u\right], \qquad \tilde{\alpha}_2 = \frac{1}{2}\left[\Delta h + \frac{\sqrt{g\tilde{h}}}{\tilde{u} + \sqrt{g\tilde{h}}}\Delta z_b + \frac{\tilde{h}}{\sqrt{g\tilde{h}}}\Delta u\right], \\
\tilde{\alpha}_3 = \frac{g\tilde{h}}{\tilde{u}^2 - g\tilde{h}}\Delta z_b.
\end{gathered} \tag{2.11}$$

Finally, the substitution of these expressions in (2.9) yields a set of algebraic equations which can be solved for the averages of $\tilde{h}$, $\tilde{u}$, and $\overline{gh}$:

$$\tilde{h} = \sqrt{h_L h_R}, \qquad \tilde{u} = \frac{\sqrt{h_R}}{\sqrt{h_R} + \sqrt{h_L}}u_R + \frac{\sqrt{h_L}}{\sqrt{h_R} + \sqrt{h_L}}u_L, \qquad \overline{gh} = \frac{1}{2}(gh_R + gh_L). \tag{2.12}$$

This decomposition is exploited as follows in a finite volume framework. Let Δt be the time step and Δx the size of each cell of a one-dimensional grid. Denoting by $\mathbf{U}_i^n$ the state of cell i at time $n\Delta t$, the state $\mathbf{U}_i^{n+1}$ at the next time step is computed using the finite volume statement:

$$\mathbf{U}_i^{n+1} = \mathbf{U}_i^n + \frac{\Delta t}{\Delta x}(\mathbf{F}_{i-1/2} - \mathbf{F}_{i+1/2}) + \frac{\Delta t}{\Delta x}\frac{1}{4}(\mathbf{H}_{i-1} + \mathbf{H}_{i+1})(\mathbf{U}_{i-1} - \mathbf{U}_{i+1}), \tag{2.13}$$

where $\mathbf{F}_{i-1/2}$ and $\mathbf{F}_{i+1/2}$ are the fluxes across the left and right interfaces of the cell. Based on the Roe wave decomposition derived previously, these fluxes are evaluated using the expression

$$\mathbf{F}_{i+1/2} = \frac{1}{2}(\mathbf{F}_i + \mathbf{F}_{i+1}) - \frac{1}{2}\sum_{k=1}^{3} \widetilde{\alpha}_k \left|\widetilde{\lambda}_k\right| \widetilde{\mathbf{K}}^{(k)}, \tag{2.14}$$

hence the hyperbolic operator is fully specified by the Roe scheme.

2.2.2. HLL Scheme

Another scheme of hyperbolic operator adopted in the present work is an extension of the HLL scheme [20] widely used for shallow flows. Whereas the original HLL scheme applies to the equations in full conservation form, the momentum equation feature nonconservative product associated with pressure along the slope bed. This term is treated following the approach [19]. The source term associated with friction along the bed is further treated in the next section.

Adopting a finite volume point of view, each depth $h(x)$ is discretised into piecewise constant segments h_i over finite intervals $x_{i-1/2} < x < x_{i+1/2}$ of constant length Δx. The corresponding discharges $q(x)$ are represented by fluxes $q_{i+1/2}$ sampled at the boundaries $x_{i+1/2}$ of the intervals. For the continuity equation, time step from t to $t + \Delta t$ is achieved using the classical finite volume statement

$$h_i^{t+\Delta t} = h_i^t + \frac{\Delta t}{\Delta x}\left(q_{i-1/2}^{\mathrm{HLL}} - q_{i+1/2}^{\mathrm{HLL}}\right), \tag{2.15}$$

where

$$q_{i+1/2}^{\mathrm{HLL}} = \frac{S_R}{S_L - S_R} q_i^t - \frac{S_L}{S_L - S_R} q_{i+1}^t + \frac{S_L S_R}{S_L - S_R}\left(h_{i+1}^t - h_i^t\right) \tag{2.16}$$

is the standard HLL flux function [20, 21]. In the above formula, the left and the right surge speeds S_L and S_R are estimated from

$$S_L = \min(S_{\min,i}, S_{\min,i+1}, 0), \qquad S_R = \max(S_{\max,i}, S_{\max,i+1}, 0), \tag{2.17}$$

where $S_{\min}$ and $S_{\max}$ are the surge speed bounds.

Besides, the LHLL scheme [19] is used to discretize the momentum equation, which associates with the nonconservative product $gh\partial z_b/\partial x$:

$$q_i^{t+(1/2)\Delta t} = q_i^t + \frac{\Delta t}{\Delta x}\left(\sigma_{i-1/2}^R - \sigma_{i+1/2}^L\right), \tag{2.18}$$

where

$$\sigma_{i+1/2}^{L} = \sigma_{i+1/2}^{\mathrm{HLL}} - \frac{S_L}{S_R - S_L}\frac{g\left(h_i^t + h_{i+1}^t\right)}{2}\left((z_b + h)_{i+1}^t - (z_b + h)_i^t\right), \tag{2.19}$$

$$\sigma_{i+1/2}^{R} = \sigma_{i+1/2}^{\mathrm{HLL}} - \frac{S_R}{S_R - S_L}\frac{g\left(h_i^t + h_{i+1}^t\right)}{2}\left((z_b + h)_{i+1}^t - (z_b + h)_i^t\right) \tag{2.20}$$

are lateralised corrections to the standard HLL flux:

$$\sigma_{i+1/2}^{\mathrm{HLL}} = \frac{S_R}{S_L - S_R}\sigma_i^t - \frac{S_L}{S_L - S_R}\sigma_{i+1}^t + \frac{S_L S_R}{S_L - S_R}\left(q_{i+1}^t - q_i^t\right), \tag{2.21}$$

in which $\sigma = (q^2/h) + (1/2)gh^2$. In the above formulas, the surge speeds S_L and S_R are again estimated from (2.17). The "lateralised flux correction" approach leading to the statements (2.18)–(2.20) is presented by Fraccarollo et al. [19].

2.3. Source Term

Consider now the source term operator. Using the Manning-Strickler formula to specify the friction slope S_f for the computation of clear water, the equation for the momentum source term can be written as:

$$\frac{\partial q}{\partial t} = -gh\frac{q^2 n^2}{h^{10/3}}. \tag{2.22}$$

Using an implicit backward Euler scheme, (2.22) is discretised as:

$$q_i^{t+\Delta t} = q_i^{t+(1/2)\Delta t} - \Delta t\left(gh^{-7/3}n^2\left(q_i^{t+\Delta t}\right)^2\right). \tag{2.23}$$

Using the first component of the source operator, $\partial h/\partial t = 0$ hence $h_i^{t+\Delta t} = h_i^t$. Thus, one can solve (2.23) for the unit width discharge of clear water at the next time step.

To advance the solution at each time step, the hyperbolic operator is first applied to obtain a partial update. These results are then used as the initial conditions for the source operator to yield the complete update. Since the hyperbolic update is explicit, stability of the scheme is subject to the CFL condition on the time step:

$$\Delta t = \mathrm{CFL}\frac{\Delta x}{\max(|u| + c)}, \tag{2.24}$$

where c is the wave celerity and u the velocity at any given grid point, and CFL is the Courant number. The value CFL should be smaller than 1 and it is found to be satisfactory in our case.

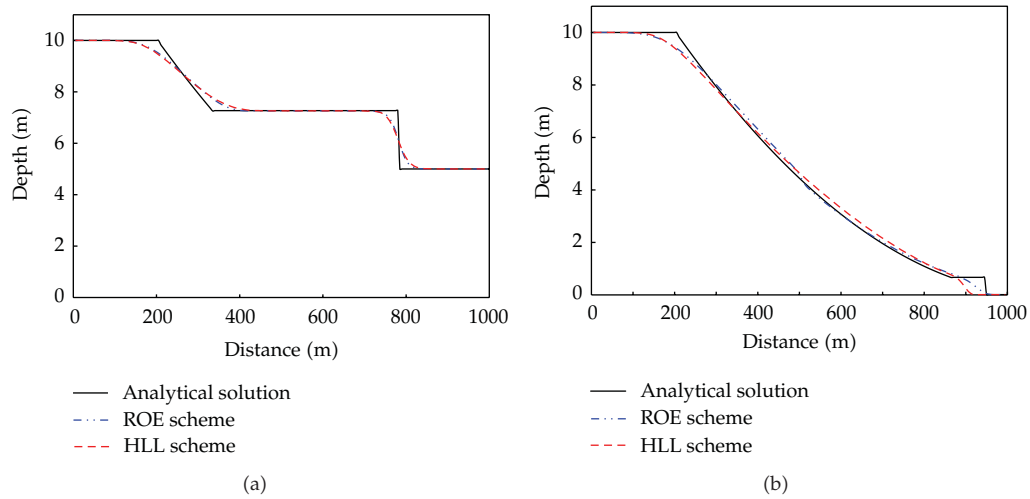

Figure 1: Idealized dam-break problem: (a) initial depth ratio $H_r/H_t = 2$; (b) initial depth ratio $H_r/H_t = 1000$.

2.4. Extend to Two-Dimensional Model

The numerical method of two-dimensional model in this study applies the explicit square grid to discrete governing equations in finite volume method. It also applies the approach of one-dimensional model which deals with the Riemann solutions and with the Godunov-type scheme [20]. The calculations of numerical fluxes apply to HLL scheme, and LHLL scheme is utilized for calculating the nonconservative term including the slope bed [19]. Finally, Strang splitting is applied to calculate the source term with frictions [17].

Since this study applies conservative finite volume method, the hyperbolic term and the source term in differential equations are separately processed so that the numerical model is largely improved. For example, the promotion of one-dimensional to two-dimensional grids utilizes dimensional splitting that it first calculates x-sweeps and then applies the result as the initial conditions to calculate y-sweeps [22]. Similarly, Strang splitting is also applied to the calculation of bed shear stress. In each time step, the hyperbolic term of shallow water equations is first calculated; the result is applied as the initial conditions for friction calculations. In this case, it is easy to expand, such as expanding from one-dimensional model to two-dimensional model, or expanding from clear water flows to mudflows or debris flows; merely the geometric mesh or source term is regulated.

3. Results and Discussions

3.1. Idealized Dam-Break Problem

To test the computation of the hyperbolic term, calculations for the clear water are first compared with the classical analytical solution of Stoker [23] for the sudden breach of a dam over a horizontal frictionless bed. The initial data used by Tseng et al. [24] are adopted: the ratios of water depths at the left (H_r) and the right (H_t) of the dam are set equal to $H_r/H_t = 2$ and $H_r/H_t = 1000$, respectively; the total length of the channel is 1000 m; the discretisation

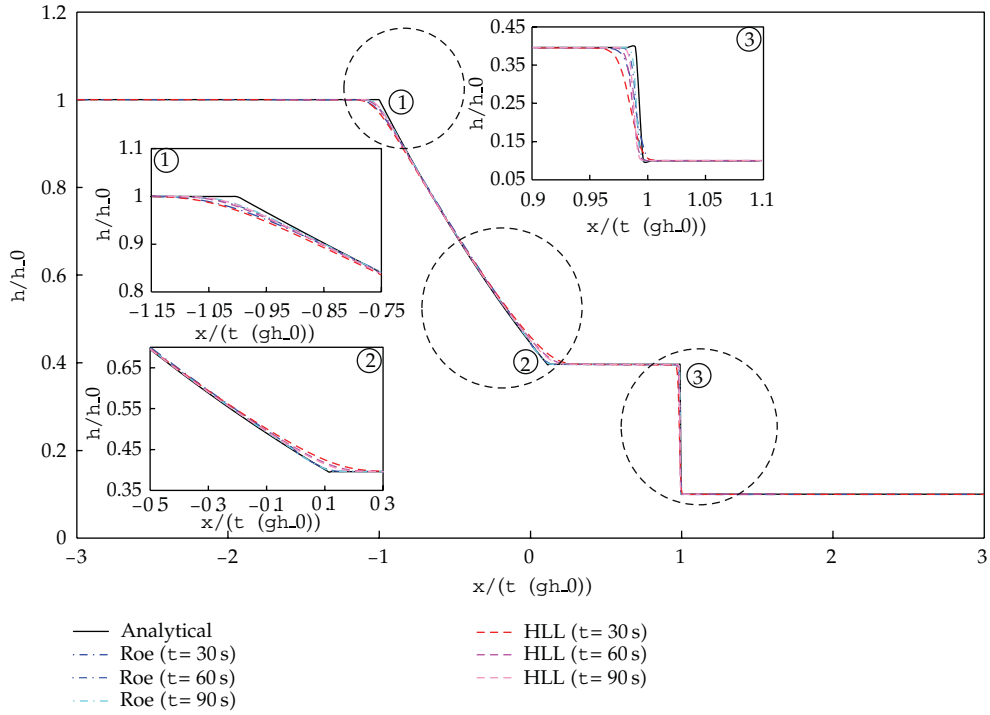

Figure 2: Increasing accuracy by decreasing the grid size to $\Delta x = 2\,\text{m}$.

interval is $\Delta x = 10\,\text{m}$; the Courant number is set to CFL = 0.9. The results for the Roe and HLL schemes at time $t = 30\,\text{s}$ are plotted in Figure 1. It is clearly shown in Figure 1 that the Roe and HLL schemes can capture the shock wave but not accurate enough. Hence, the second test refers to Wang and Shen [25] and uses the conditions: water depths to the left and the right of the dam are set equal to $h = 10\,\text{m}$ and $h_0 = 1\,\text{m}$, respectively; the total length of the channel is 2000 m; $\Delta x = 2\,\text{m}$, and CFL = 0.9. Figure 2 indicates the reasonable results for $t = 30\,\text{s}$, 60 s, and 90 s, respectively, in nondimensional form. The accuracy can be increased by decreasing the grid size from these two figures.

3.2. *Dam-Break Experiment in Rigid Channel*

To test the numerical model for clear water, the simulation is compared with the laboratory experiments of the US Army Engineer Waterways Experiment Station [26] in Figure 3. The WES' experiments were conducted in a rectangular channel 122 m long and 1.22 m wide, with a bottom slope of 0.005 and Manning's coefficient of 0.009. The dam was placed at the middle of the channel, giving the initial water depth upstream of the dam $H_1 = 0.305\,\text{m}$ and downstream of the dam $H_2 = 0.0\,\text{m}$. In this simulation, the uniform grid spacing Δx is 1.0 m and the Courant number CFL = 0.9. The agreement between the simulation and experimental results is satisfactory. The results also indicate that the finite volume method can capture the surges well and the numerical model has a good ability to deal with the "contact points" at locations where the depth reaches zero.

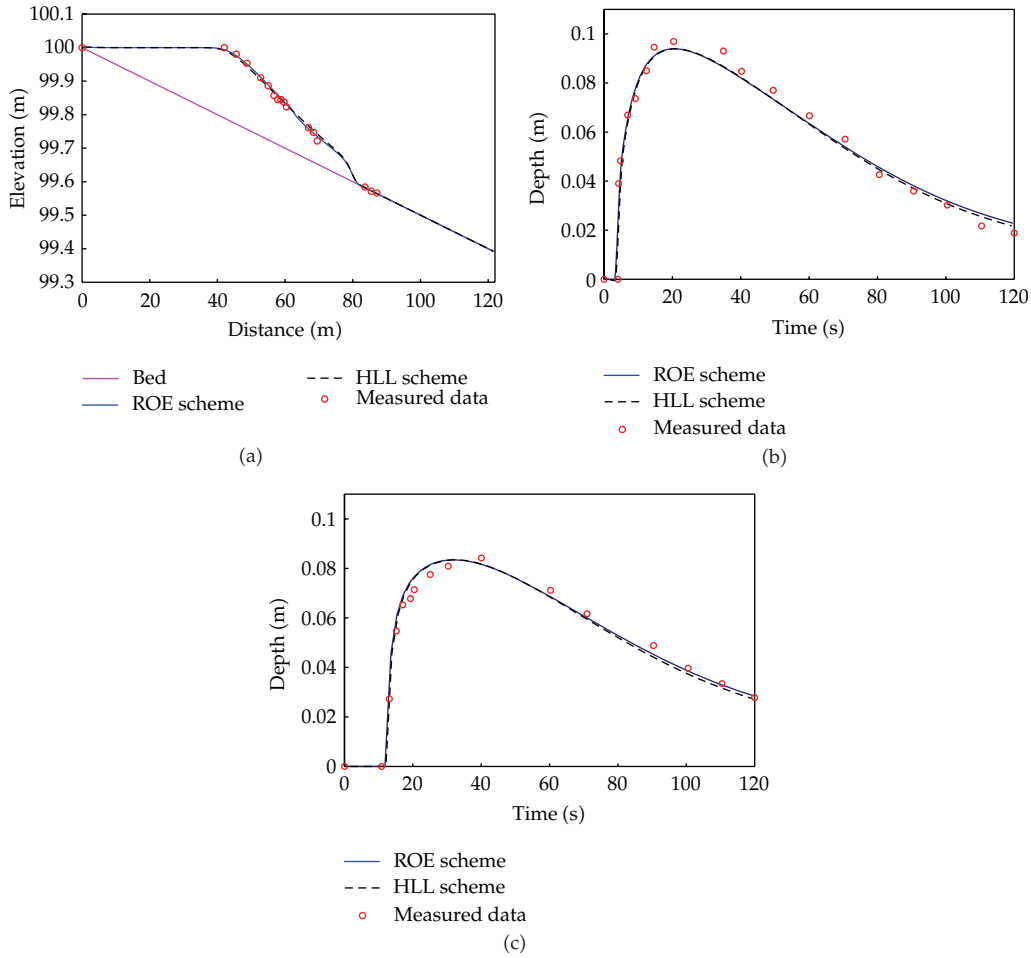

Figure 3: Comparisons with WES experiment: (a) water surface profile along the channel at $t = 10$ sec; (b) time evolution of water depth at $x = 70.1$ m; (c) time evolution of water depth at $x = 85.4$ m.

3.3. Comparison of 2D Numerical Simulation and Experiment

In order to prove the two-dimensional numerical model, this study designs a rectangular flume, which is a closed tank of 1.6 m (Length) × 0.6 m (Width) × 0.6 m (Height). A gate, located on the longitudinal $x = 0.4$ m, could be quickly removed for simulating the dam-break flow. The initial depth before gate is 0.15 m and the downstream depth is 0.01 m. Two square columns (of the length and width being 0.1 m and the height being 0.3 m) are placed on $x = 1.2$ m and are paralleled placed in the middle (with the distance 0.1 m) shown as Figure 4. Besides, in consideration of the natural channel not being as flat as the artificial construction, six small obstacles are placed on both sides for simulating the irregular banks. They are placed on the side walls at longitudinal $x = 0.4$ m, 0.8 m, and 1.2 m. The simulated grid number is 160 × 60 ($\Delta x = \Delta y = 0.01$ m) that there are 9600 cells. The Manning coefficient is $n = 0.01$. The boundary conditions are considered as closed boundary, that is, there is

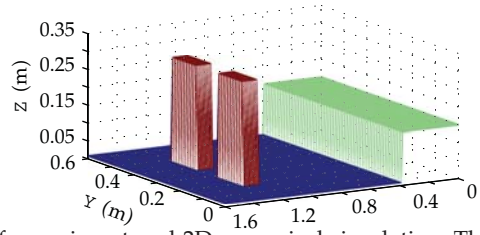

Figure 4: Initial conditions of experiment and 2D numerical simulation. The gate is located at $x = 0.4$ m, the dam-break modeling initial water depth 0.15 m, the downstream water depth 0.01 m, and 2 square columns (0.1 m × 0.1 m × 0.3 m) paralleled placed at $x = 1.2$ m with the distance 0.1 m.

(a)

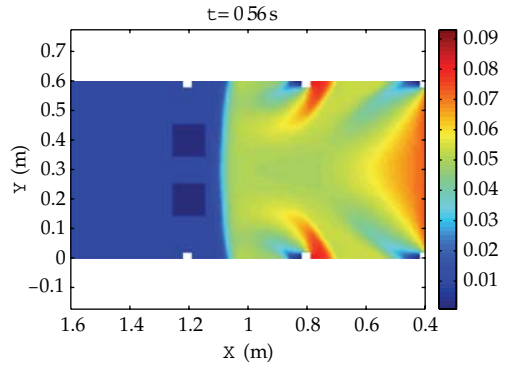

(b)

(c)

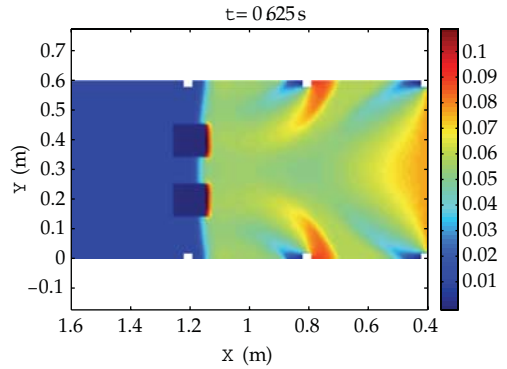

(d)

(e)

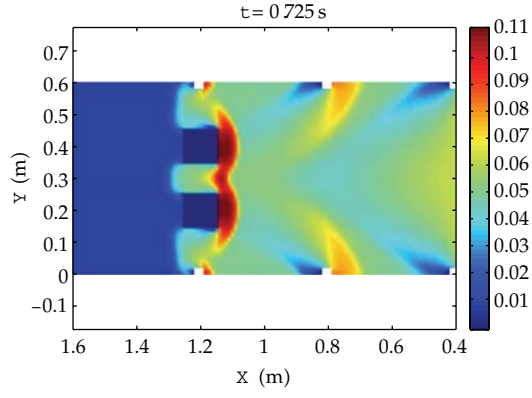

(f)

Figure 5: Continued.

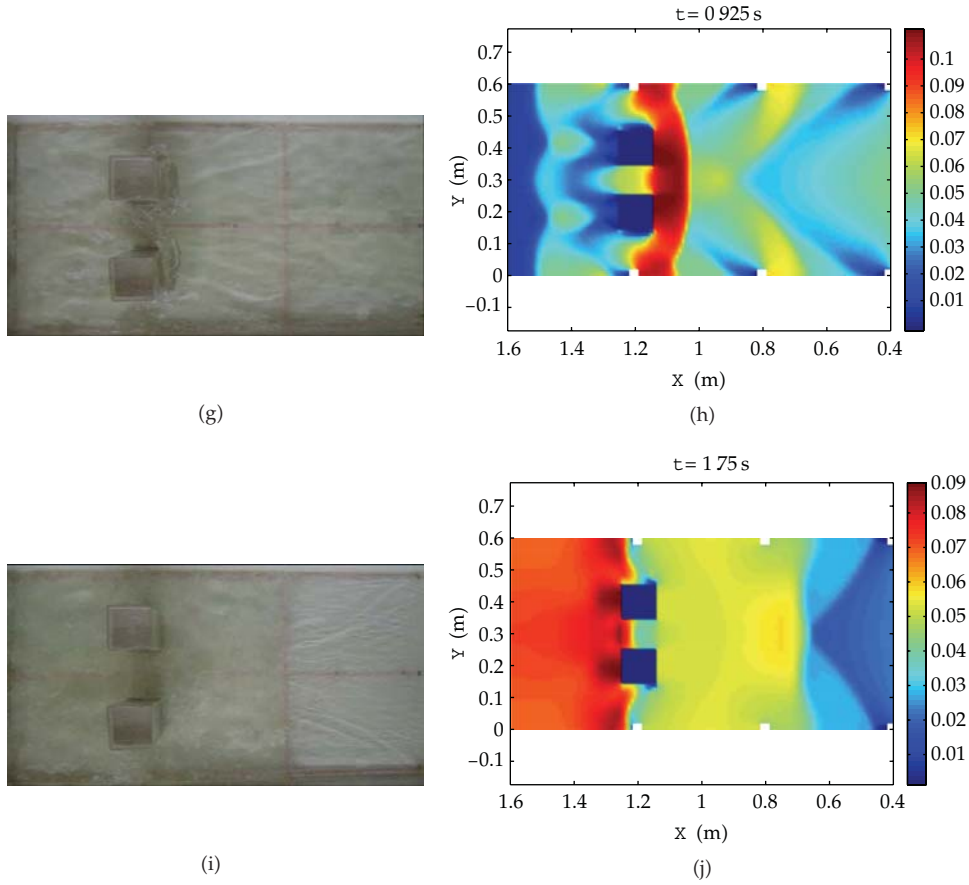

Figure 5: Comparisons of experiments and numerical simulations—(a) and (b) when $t = 0.56$ sec, dam-break flow arrives to the columns; (c) and (d) when $t = 0.625$ sec, dam-break flow moves to the middle of the columns; (e) and (f) when $t = 0.725$ sec, dam-break flow surrounds the columns and forms vortexes; (g) and (h) when $t = 0.925$ sec, dam-break flow touches the boundary of tank; (i) and (j) when $t = 1.75$ sec, the flow returns to the location of gate.

no flow-out at the sides. With the total simulation time 2 sec, it is simulated the water flow crashes the boundary after gate opening and returns to the initial location.

The experimental results show that it takes about 0.56 sec that dam-break flow touches the square columns when the distance between the columns and the gate is 0.8 m. It presents the same time as the simulation time of the numerical model in Figures 5(a) and 5(b). With the flow movement of the small obstacles on both sides, it could also be simulated in the numerical model. When the time is 0.625 sec, the time of dam-break flow moving to the center of two columns is similar to it simulated in the model (see Figures 5(c) and 5(d)). The time of dam-break flow surrounding the two columns and forming vortexes ($t = 0.725$ sec) also corresponds to the simulated result, Figures 5(e) and 5(f). Finally, the water flow reaches the boundary of the tank at $t = 0.925$ sec, which then forms surges crashing the columns and returning to the gate at $t = 1.75$ sec. In the entire simulation, the water crashing obstacles and forming surges as well as the flow movement due to small obstacles could be captured well by the present model.

4. Conclusions

This paper proposes the one-dimensional and two-dimensional numerical model with the finite volume method based on the shallow water equations. A key feature of the model is the use of an operator-splitting method to divide the governing equations into hyperbolic and source terms. This approach provides an easy method for using different numerical schemes such as the Roe and HLL schemes. With the conservative finite volume method, the model can be applied to various numerical methods or spatial dimensions. As described in the study, one-dimensional model could be easily developed into two-dimensional model so as to save the time for programming the codes. The comparisons between the experimental results and the model simulation are matched. In addition, it is very easy to develop another computation, for example, non-Newtonian fluid or multilayers fluid flows, from the present model in the future.

Acknowledgments

Thanks for the parts of support from the Project (NSC 98-2622-B-270-001-CC3) of National Science Council. Special thanks are due to Dr. H. Capart, Professor of Civil Engineering at National Taiwan University, for reading the parts of the paper and making a number of helpful suggestions.

References

[1] S. C. Chen, "Failure mechanism and disaster mitigation on landslide-dammed lakes," *Journal of Chinese Soil and Water Conservation*, vol. 30, no. 4, pp. 299–311, 1999.
[2] Z. Y. Feng, "The seismic signatures of the surge wave from the 2009 Xiaolin landslide-dam breach in Taiwan," *Hydrological Processes*, 2011. In press.
[3] W. Y. Tan, *Shallow Water Hydrodynamics*, Elsevier, New York, NY, USA, 1992.
[4] C. B. Liao, M. S. Wu, and S. J. Liang, "Numerical simulation of a dam break for an actual river terrain environment," *Hydrological Processes*, vol. 21, no. 4, pp. 447–460, 2007.
[5] D. Liang, R. A. Falconer, and B. Lin, "Comparison between TVD-MacCormack and ADI-type solvers of the shallow water equations," *Advances in Water Resources*, vol. 29, no. 12, pp. 1833–1845, 2006.
[6] M. H. Tseng, "Improved treatment of source terms in TVD scheme for shallow water equations," *Advances in Water Resources*, vol. 27, no. 6, pp. 617–629, 2004.
[7] S. R. Idelsohn, E. Oñate, F. Del Pin, and N. Calvo, "Fluid-structure interaction using the particle finite element method," *Computer Methods in Applied Mechanics and Engineering*, vol. 195, no. 17-18, pp. 2100–2123, 2006.
[8] T. W. H. Sheu, C. Chiao, and C. Huang, "Development of a particle interaction kernel function in MPS method for simulating incompressible free surface flow," *Journal of Applied Mathematics*, Article ID 793653, 16 pages, 2011.
[9] C. M. Wu and S. C. Chen, "Simulating runoff using the method of characteristics with unsteady rainfall events," *Journal of Mechanics*, vol. 21, no. 3, pp. 171–178, 2005.
[10] H. D. Shi and Z. Liu, "Review and progress of research in numerical simulation of dam-break water flow," *Advances in Water Science*, vol. 17, no. 1, pp. 129–135, 2006.
[11] C. Hirsch, *Numerical Computation of Internal and External Flows, Fundamentals of Numerical Discretization*, vol. 2, John Wiley & Sons, New York , NY, USA, 1988.
[12] C. V. Bellos, J. V. Soulis, and J. G. Sakkas, "Experimental investigation of two-dimensional dam-break induced flows," *Journal of Hydraulic Research*, vol. 30, no. 1, pp. 47–75, 1992.
[13] G. Simpson and S. Castelltort, "Coupled model of surface water flow, sediment transport and morphological evolution," *Computers and Geosciences*, vol. 32, no. 10, pp. 1600–1614, 2006.
[14] M. B. Abbott, *Computational Hydraulics Elements of the Theory of Free Surface Flows*, vol. 1 of *Monographs and Surveys in Water Resource Engineering*, Pitman Publishing, London, UK, 1979.

[15] M. H. Chaudhry, *Open-Channel Flow*, Prentice-Hall, Englewood Cliffs, NJ, USA, 1993.
[16] W. H. Graf, *Fluvial Hydraulics*, John Wiley & Sons, Chichester, UK, 1998.
[17] E. F. Toro, *Riemann Solvers and Numerical Methods for Fluid Dynamics*, Springer, Berlin, Germany, 2nd edition, 1999.
[18] H. Capart, *Dam-break induced geomorphic flows and the transition from solid- to fluid-like behaviour across evolving interfaces*, Ph.D. thesis, University of Louvain, Belgium, 2000.
[19] L. Fraccarollo, H. Capart, and Y. Zech, "A Godunov method for the computation of erosional shallow water transients," *International Journal for Numerical Methods in Fluids*, vol. 41, no. 9, pp. 951–976, 2003.
[20] A. Harten, P. D. Lax, and B. van Leer, "On upstream differencing and Godunov-type schemes for hyperbolic conservation laws," *SIAM Review*, vol. 25, no. 1, pp. 35–61, 1983.
[21] L. Fraccarollo and E. F. Toro, "Experimental and numerical assessment of the shallow water model for two-dimensional dam-break type problems," *Journal of Hydraulic Research*, vol. 33, no. 6, pp. 843–864, 1995.
[22] R. J. LeVeque, *Finite volume methods for hyperbolic problems*, Cambridge Texts in Applied Mathematics, Cambridge University Press, Cambridge, 2002.
[23] J. J. Stoker, *Water Waves*, Interscience, New York, NY, USA, 1957.
[24] M. H. Tseng, C. A. Hsu, and C. R. Chu, "Channel routing in open-channel flows with surges," *Journal of Hydraulic Engineering*, vol. 127, no. 2, pp. 115–122, 2001.
[25] Z. Wang and H. T. Shen, "Lagrangian simulation of one-dimensional dam-break flow," *Journal of Hydraulic Engineering*, vol. 125, no. 11, pp. 1217–1221, 1999.
[26] USACE, *Flood Resulting from Suddenly Breached Dams*, US Army Engineer Waterways Experiment Station, Vicksburg, Miss, USA, 1960.

Hindawi Publishing Corporation
Journal of Applied Mathematics
Volume 2012, Article ID 714973, 10 pages
doi:10.1155/2012/714973

Research Article

A New Direct Method for Solving Nonlinear Volterra-Fredholm-Hammerstein Integral Equations via Optimal Control Problem

M. A. El-Ameen[1] and M. El-Kady[2]

[1] *Faculty of Engineering, Umm Al-Qura University, P.O. Box 5555, Mecca, Saudi Arabia*
[2] *Faculty of Science, Helwan University, Helwan, Egypt*

Correspondence should be addressed to M. A. El-Ameen, kearmossa@yahoo.com

Received 28 December 2011; Accepted 28 January 2012

Academic Editor: Shuyu Sun

A new method for solving nonlinear Volterra-Fredholm-Hammerstein (VFH) integral equations is presented. This method is based on reformulation of VFH to the simple form of Fredholm integral equations and hence converts it to optimal control problem. The existence and uniqueness of proposed method are achieved. Numerical results are given at the end of this paper.

1. Introduction

The nonlinear integral equations arise in the theory of parabolic boundary value problems, engineering, various mathematical physics, and theory of elasticity [1–3]. In recent years, several analytical and numerical methods of this kind of problems have been presented [4, 5]. Analytically, the decomposition methods are used in [6, 7]. The classical method of successive approximations was introduced in [8], while some kind of appropriate projection such as Galerkin and collocation methods have been applied in [9–13]. These methods often transform integral or integrodifferential equations into a system of linear algebraic equations which can be solved by direct or iterative methods. In [14], the authors used Taylor series to solve the following nonlinear Volterra-Fredholm integral equation:

$$y(x) = f(x) + \lambda_1 \int_0^x k_1(x,t)\left[y(t)\right]^p dt + \lambda_2 \int_0^1 k_2(x,t)\left[y(t)\right]^q dt, \quad p,q \in R, \tag{1.1}$$

whereas the Legendre wavelets method for a special type was applied in [15] for solving the nonlinear Volterra-Fredholm integral equation of the form

$$y(x) = f(x) + \lambda_1 \int_0^x k_1(x,t)\left[F\left(y(t)\right)\right]dt + \lambda_2 \int_0^1 k_2(x,t)G\left(y(t)\right)dt, \tag{1.2}$$

where $f(x)$ and the kernels $k_1(x,t)$ and $k_2(x,t)$ are assumed to be in $L^2(R)$ on the interval $0 \le x,t \le 1$. The nonlinear Volterra-Fredholm-Hammerstein integral equation is given in [16] as follows:

$$y(t) = f(t) + \lambda_1 \int_0^t k_1(t,s)\left[g_1\left(s,y(s)\right)\right]ds + \lambda_2 \int_0^1 k_2(t,s)g_2\left(s,y(s)\right)ds, \quad 0 \le t,s \le 1. \tag{1.3}$$

In this paper, we introduce a method to find the numerical solution of a nonlinear Volterra-Fredholm-Hammerstein integral equation of the form:

$$\phi(t) = f(t) + \lambda_1 \int_0^t V\left(t,s,\phi(s)\right)ds + \lambda_2 \int_a^b F\left(t,s,\phi(s)\right)ds, \quad 0 \le t,\ s \le 1, \tag{1.4}$$

where $f(t)$, $V(t,s,\phi(s))$, and $F(t,s,\phi(s))$ are assumed to be in $L^2(R)$ and satisfy the Lipschitz condition

$$\left|K\left(t,s,\phi_1(s)\right) - K\left(t,s,\phi_2(s)\right)\right| \le N(t,s)\left|\phi_1(s) - \phi_2(s)\right|. \tag{1.5}$$

This paper is organized as follows. In Section 2, we present a form of (1.4) by Fredholm type integral equation, which can convert it into optimal control problem (OC). In Section 3, the existence and uniqueness are presented. The computational results are shown in Section 4.

2. Problem Reformulation

Let the VFH given in (1.4) be written in the form

$$\phi(t) = f(t) + \lambda \int_a^b k\left(t,s,\phi(s)\right)ds, \tag{2.1}$$

such that

$$\begin{aligned} k\left(t,s,\phi(s)\right) &= G\left(t,s,\phi(s)\right) + F\left(t,s,\phi(s)\right), \\ G\left(t,s,\phi(s)\right) &= e\left(t,s,\phi(s)\right)V\left(t,s,\phi(s)\right), \\ e\left(t,s,\phi(s)\right) &= \begin{cases} 1 & a < s < t < b, \\ 0 & s > t, \end{cases} \end{aligned} \tag{2.2}$$

and the kernel $k(t,s,\phi(s)) \in C[a,b] \times [a,b]$ satisfyies

$$\left|k(t,s,\phi(s))\right| \leq M, \qquad \left|f(t)\right| \leq K, \tag{2.3}$$

where M, K are arbitrary constants.

It is easy to see that (2.1) can be written as follows:

$$\begin{aligned}\phi(t) - f(t) &= \int_a^t \left[\dot{\phi}(s) - \dot{f}(s)\right] ds + \left[\phi(a) - f(a)\right] \\ &= \int_a^b \delta\left[\dot{\phi}(s) - \dot{f}(s)\right] ds + \left[\phi(a) - f(a)\right], \qquad \text{where } \delta = \begin{cases} 1 & a < s < t < b, \\ 0 & s > t, \end{cases}\end{aligned} \tag{2.4}$$

then

$$\int_a^b \delta\left[\dot{\phi}(s) - \dot{f}(s)\right] ds + \left[\phi(a) - f(a)\right] = \lambda \int_a^b k(t,s,\phi(s)) ds. \tag{2.5}$$

Since

$$\phi(a) - f(a) = \lambda \int_a^b k(a,s,\phi(s)) dt, \tag{2.6}$$

therefore,

$$\int_a^b \delta\left[\dot{\phi}(s) - \dot{f}(s)\right] ds + \lambda \int_a^b \left[k(a,s,\phi(s)) - k(t,s,\phi(s))\right] ds = 0. \tag{2.7}$$

Let

$$G(t) = \int_a^b \left\{\delta\left[\dot{\phi}(s) - \dot{f}(s)\right] + \lambda\left[k(a,s,\phi(s)) - k(t,s,\phi(s))\right]\right\} ds = 0, \tag{2.8}$$

that is, if

$$|G(t)| = 0. \tag{2.9}$$

By integrating (2.9), we have

$$\int_a^b |G(t)| dt = 0. \tag{2.10}$$

On the other hand, one can define the following equality:

$$F(t,s,\phi(t),u(t)) = \delta\left[\dot{\phi}(s) - \dot{f}(s)\right] + \lambda\left[k(a,s,\phi(s)) - k(t,s,\phi(s))\right]. \tag{2.11}$$

This will lead us to the following inequality:

$$\int_a^b |G(t)|dt \leq \iint_a^b \left|F(t,s,\phi(t),u(t))\right| ds dt, \tag{2.12}$$

where

$$\dot{\phi}(s) = u(s), \quad s \in [a,b]. \tag{2.13}$$

With the boundary conditions

$$\phi(a) = f(a) + \int_a^b k(a,s,\phi(s))ds, \qquad \phi(b) = f(b) + \int_a^b k(b,s,\phi(s))ds. \tag{2.14}$$

At the end, we have the following OC problem:

minimize

$$I = \int_\Omega \left|F(t,s,\phi(t),u(t))\right| ds dt \tag{2.15}$$

subject to

$$\dot{\phi}(s) = u(s), \quad s \in [a,b], \tag{2.16}$$

$\phi(a)$ and $\phi(b)$ are defined in (2.14) where $\Omega = [a,b] \times [a,b]$.

The existence and uniqueness of (2.1) will be considered in the next section by using the successive approximation method.

3. Existence and Uniqueness

The solution $\phi(t)$ of (2.1) can be approximated successively as follows:

$$\phi_1(t) - \lambda \int_a^b k(t,s,\phi_0(s))ds = f(t). \tag{3.1}$$

Thus, we obtain sequence of functions $\phi_0(t), \phi_1(t), \ldots, \phi_n(t)$, such that

$$\phi_n(t) - \lambda \int_a^b k(t,s,\phi_{n-1}(s))ds = f(t), \quad n \geq 1, \tag{3.2}$$

with $\phi_0(t) = f(t)$.

It is convenient to introduce

$$\varphi_n(t) = \phi_n(t) - \phi_{n-1}(t), \quad n \geq 1, \tag{3.3}$$

with $\varphi_0(t) = f(t)$.

Subtracting from (3.2), the same equation with replacing n by $n-1$, we get

$$\phi_n(t) - \phi_{n-1}(t) = \lambda \int_a^b k\big(t, s, \phi_{n-1}(s)\big)ds - \lambda \int_a^b k\big(t, s, \phi_{n-2}(s)\big)ds. \tag{3.4}$$

Using (3.3), we have

$$\varphi_n(t) = \lambda \int_a^b k\big(t, s, \varphi_{n-1}(s)\big)ds \quad n \geq 1. \tag{3.5}$$

Also, from (3.3), we deduce that

$$\phi_n(t) = \sum_{i=0}^{n} \varphi_i(t). \tag{3.6}$$

The existence and uniqueness of the solution can be followed.

Theorem 3.1. *If the kernel $k(t, s, \phi(s))$ and the function $f(t)$ are continuous and satisfy condition* (2.3) *in $a < s < t < b$, then the integral equation* (2.1) *possesses a unique continuous solution.*

Proof. From (3.5), we get

$$\begin{aligned} \big|\varphi_n(t)\big| &= \left|\lambda \int_a^b k\big(t, s, \varphi_{n-1}(s)\big)ds\right| \\ &\leq \lambda \big|k\big(t, s, \varphi_{n-1}(s)\big)\big| \int_a^b ds \\ &\leq \lambda(b-a)M. \end{aligned} \tag{3.7}$$

We now show that this $\phi(t)$ satisfies (2.1).

The series (3.6) is uniformly convergent since the term $\varphi_i(t)$ is dominated by $\lambda(b-a)M$. Then,

$$\begin{aligned} \lambda \int_a^b k\left(t, s, \sum_{i=0}^{\infty} \varphi_i(s)\right)ds &= \sum_{i=0}^{\infty} \lambda \int_a^b k\big(t, s, \varphi_i(s)\big)ds \\ &= \sum_{i=0}^{\infty} \varphi_{i+1}(t) = \sum_{i=0}^{\infty} \varphi_{i+1}(t) + \varphi_0(t) - \varphi_0(t). \end{aligned} \tag{3.8}$$

Hence, we have

$$\lambda \int_a^b k\left(t, s, \sum_{i=0}^{\infty} \varphi_i(s)\right) ds = \sum_{i=0}^{\infty} \varphi_i(t) - f(t). \tag{3.9}$$

This proves that $\phi(t)$, defined in (3.6), satisfies (2.1). Since each of the $\varphi_i(t)$ is clearly continuous, therefore $\phi(t)$ is continuous, where it is the limit of a uniformly convergent sequence of continuous functions.

To show that $\phi(t)$ is a unique continuous solution, suppose that there exists another continuous solution $\tilde{\phi}(t)$ of (2.1), Then,

$$\tilde{\phi}(t) - \lambda \int_a^b k\left(t, s, \tilde{\phi}(s)\right) ds = f(t). \tag{3.10}$$

Subtracting (3.10) from (2.1), we get

$$\phi(t) - \tilde{\phi}(t) = \lambda \int_a^b k\left(t, s, \left\{\phi(s) - \tilde{\phi}(s)\right\}\right) ds. \tag{3.11}$$

Since $\phi(t)$ and $\tilde{\phi}(t)$ are both continuous, there exists a constant B such that

$$\left|\phi(t) - \tilde{\phi}(t)\right| \leq B. \tag{3.12}$$

By using the condition of (2.3), the inequality (3.12) becomes

$$\left|\phi(t) - \tilde{\phi}(t)\right| \leq \lambda(b-a)MB. \tag{3.13}$$

For the large enough n, the right-hand side is arbitrary small, then

$$\phi(t) = \tilde{\phi}(t). \tag{3.14}$$

This completes the proof. □

4. Computational Results

In this section, some numerical experiments will be carried out in order to compare the performances of the new method with respect to the classical collocation methods. The method has been applied to the following three test problems [16, 17].

Example 4.1. Consider the Volterra-Fredholm-Hammerstein integral equation

$$x(s) = 2\cos(s) - 2 + 3\int_0^s \sin(s-t)x^2(t)dt + \frac{6}{7 - 6\cos(1)} \int_0^1 (1-t)\cos^2(s)(t + x(t))dt. \tag{4.1}$$

The exact solution is given by $x(s) = \cos(s)$.

Table 1: Maximum errors for collocation and OC methods.

N	Errors in collocation method	Errors in optimal control method
8	3.17E – 11	2.22E – 13
12	1.11E – 12	1.11E – 15
16	4.03E – 13	3.33E – 16
20	7.93E – 15	2.22E – 16
24	2.22E – 16	2.22E – 16

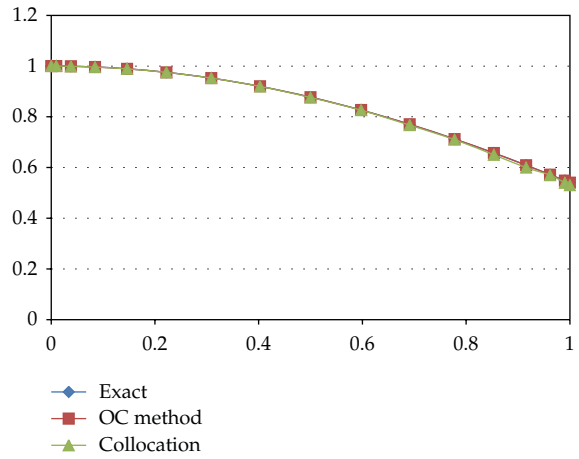

Figure 1: Observed results for Example 4.1 ($N = 16$).

The computational maximum absolute errors for different values of N are shown in Table 1. It is clear that the optimal control method is more accurate for small values of N. It seems that the errors for $N = 16$, in case of OC method, are caused by machine error. The numerical solutions are computed by two methods and summarized in Figure 1, and it seems that our method compared very well with those obtained via the collocation method.

Example 4.2. Consider the following VIE:

$$x(s) = 1 + \sin^2(s) - 3\int_0^s \sin(s-t)x^2(t)dt, \quad s \in [0,10]. \tag{4.2}$$

The exact solution is $x(s) = \cos(s)$. This example can be solved by using the proposed OC method. The numerical results together with computational effort of errors in boundaries and CPU time/iteration are given in Table 2.

The computational efforts presented here proved that we could rearrange in a way to avoid the rounding errors in collocation and reducing the CPU time/iteration processes. Furthermore, this rearrangement of the computation leads to a much more accurate and robust method.

Table 2: Observed results for Example 4.2.

Methods	N	CPU time/iteration	Errors in boundaries
Chebyshev collocation method	8	0.74 sec.	3.7E – 02
	12	1.43 sec.	1.9E – 04
	16	1.89 sec.	2.0E – 06
	20	2.01 sec.	7.7E – 07
	24	2.11 sec.	3.1E – 09
Optimal control method	8	0.03 sec.	1.1E – 05
	12	0.28 sec.	7.6E – 07
	16	0.86 sec.	5.0E – 09
	20	1.01 sec.	3.2E – 11
	24	1.19 sec.	4.1E – 13

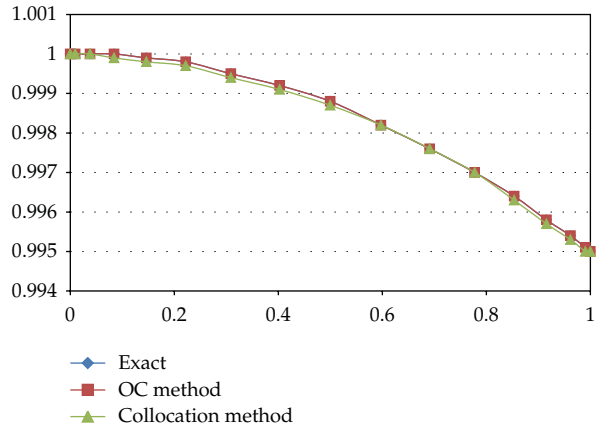

Figure 2: Observed results for Example 4.2 ($N = 16$).

In Figure 2, the proposed OC method shows the observed results for Example 4.2 for $N = 16$. It seems also that OC method is more accurate than collocation methods.

Example 4.3. Consider the nonlinear Volterra-Fredholm integral equation

$$x(s) = y(s) + \int_0^s (s-t)x^2(t)dt + \int_0^1 (s+t)x(t)dt, \tag{4.3}$$

with $y(s) = (-1/30)s^6 + (1/3)s^4 - s^2 + (5/3)s - (5/4)$. We applied the OC method presented in this paper and solved (4.3). The computational results together with the exact solution $x(s) = s^2 - 2$ are given in Figure 3.

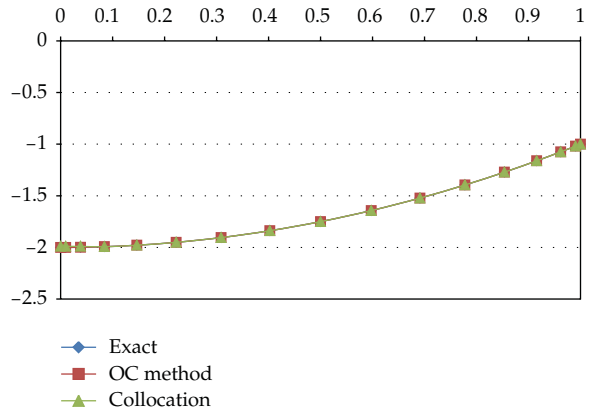

Figure 3: Observed results for Example 4.3 ($N = 16$).

5. Conclusion

In this paper, the optimal control method is introduced to simplify the implementation of general nonlinear integral equations of the second kind. We have shown, in numerical examples, that this method is fast and gains better results compared with collocation method. The important thing to note is that the control-state constraint is satisfied everywhere. Furthermore, the structure of the optimal control agrees with the results obtained in [16].

References

[1] A. K. Khamis and M. A. El-Ameen, "Volterra-fredholm integral equation with carlman kernel in position and time," *Journal of Engineering and Applied Sciences*, vol. 4, no. 5-6, pp. 288–294, 2009.
[2] E. V. Kovalenko, "Some approximate methods for solving integral equations for mixed problems," *Journal of Applied Mathematics and Mechanics*, vol. 53, no. 1, pp. 85–92, 1989.
[3] B. I. Smetanin, "On an integral equation of axisymmetric problems for an elastic body containing an inclusion," *Journal of Applied Mathematics and Mechanics*, vol. 55, no. 3, pp. 371–375, 1991.
[4] M. A. El-Ameen, "Approximate solutions of nonlinear Fredholm integral equations," *Applied Mathematics & Information Sciences*, vol. 5, no. 1, pp. 122–131, 2011.
[5] P. Linz, *Analytical and Numerical Methods for Volterra Equations*, vol. 7, Society for Industrial and Applied Mathematics, Philadelphia, Pa, USA, 1985.
[6] K. Maleknejad and M. Hadizadeh, "The numerical analysis of Adomian's decomposition method for nonlinear Volterra integral and integro-differential equations," *International Journal of Engineering Science*, vol. 8, no. 2a, pp. 33–48, 199.
[7] A.-M. Wazwaz, *A First Course in Integral Equations*, World Scientific, Singapor, 1997.
[8] F. G. Tricomi, *Integral Equations*, Dover, New York, NY, USA, 1982.
[9] A. A. Daşcıoglu, "A Chebyshev polynomial approach for linear Fredholm-Volterra integro-differential equations in the most general form," *Applied Mathematics and Computation*, vol. 181, no. 1, pp. 103–112, 2006.
[10] H. Brunner, *Collocation Methods for Volterra Integral and Related Functional Di erential Equations*, vol. 15, Cambridge University Press, Cambridge, UK, 2004.
[11] L. M. Delves and J. L. Mohamed, *Computational Methods for Integral Equations*, Cambridge University Press, Cambridge, UK, 1985.
[12] K. Maleknejad and H. Derili, "The collocation method for Hammerstein equations by Daubechies wavelets," *Applied Mathematics and Computation*, vol. 172, no. 2, pp. 846–864, 2006.
[13] K. Maleknejad, M. Karami, and M. Rabbani, "Using the Petrov-Galerkin elements for solving Hammerstein integral equations," *Applied Mathematics and Computation*, vol. 172, no. 2, pp. 831–845, 2006.

[14] S. Yalcinbas, "Taylor polynomial solutions of nonlinear Volterra-Fredholm integral equations," *Applied Mathematics and Computation*, vol. 127, no. 2-3, pp. 195–206, 2002.
[15] S. Yousefi and M. Razzaghi, "Legender wavelet method for the nonlinear Volterra- Fredholm integral equations," *Mathematics and Computers in Simulation*, vol. 70, no. 1, pp. 1–8, 2005.
[16] Y. Ordokhani and M. Razzaghi, "Solution of nonlinear Volterra-Fredholm-Hammerstein integral equations via a collocation method and rationalized Haar functions," *Applied Mathematics Letters*, vol. 21, no. 1, pp. 4–9, 2008.
[17] E. Babolian, F. Fattahzadeh, and E. G. Raboky, "A Chebyshev approximation for solving nonlinear integral equations of Hammerstein type," *Applied Mathematics and Computation*, vol. 189, no. 1, pp. 641–646, 2007.

Hindawi Publishing Corporation
Journal of Applied Mathematics
Volume 2012, Article ID 259284, 18 pages
doi:10.1155/2012/259284

Research Article

Numerical Investigation of Nanofluid Forced Convection in Channels with Discrete Heat Sources

Payam Rahim Mashaei, Seyed Mostafa Hosseinalipour, and Mehdi Bahiraei

CAE Lab & CFD Center, Mechanical Engineering Department, Faculty of Engineering, Iran University of Science & Technology (IUST), Tehran, Iran

Correspondence should be addressed to Mehdi Bahiraei, bahira@iust.ac.ir

Received 6 January 2012; Revised 21 January 2012; Accepted 22 January 2012

Academic Editor: M. F. El-Amin

Numerical simulation is performed to investigate the laminar force convection of Al_2O_3/water nanofluid in a flow channel with discrete heat sources. The heat sources are placed on the bottom wall of channel which produce much thermal energy that must be evacuated from the system. The remaining surfaces of channel are kept adiabatic to exchange energy between nanofluid and heat sources. In the present study the effects of Reynolds number (Re = 50, 100, 200, 400, and 1000), particle volume fraction (ϕ = 0 (distilled water), 1 and 4%) on the average heat transfer coefficient (h), pressure drop (ΔP), and wall temperature (T_w) are evaluated. The use of nanofluid can produce an asymmetric velocity along the height of the channel. The results show a maximum value 38% increase in average heat transfer coefficient and 68% increase in pressure drop for all the considered cases when compared to basefluid (i.e., water). It is also observed that the wall temperature decreases remarkably as Re and ϕ increase. Finally, thermal-hydraulic performance (η) is evaluated and it is seen that best performance can be obtained for Re = 1000 and ϕ = 4%.

1. Introduction

Localized areas of high temperature on microprocessors and various electronic components produce hot spots that have an unfavorable effect on their performance and operating conditions. With increasing of power density of these electronic components, good attempts have been carried out to enhance the heat exchanger rate of them by active as well as passive methods. While the former usually offers higher augmentation, it requires additional external forces that can increase the capital and operating cost of the system. In contrast, passive heat transfer enhancement can be obtained by changing the geometry or modifying thermal properties of working fluid [1]. In recent years, the advances in manufacturing technology

have caused the production of nanoparticles and created a special class of fluids, called "nanofluids". The term "nanofluid" refers to a two-phase mixture where the continuous phase is usually a liquid and the dispersed phase is created of extremely fine metallic particles of size about 50 nm, called "nanoparticles" [2].

Many researchers experimentally showed nanofluids have higher thermal conductivity than those of the base fluids and a lot of correlations were reported. For example Lee et al. [3] evaluated Al_2O_3-water/ethylene glycol with particle diameters 24.4 and 38.4 nm as well as CuO-water/ethylene glycol with particle diameters 18.6 and 23.6 nm and showed that thermal conductivity increases to 20% as particle volume fraction increases from 0 to 4%. Chopkar el al. [4] measured thermal conductivity of Ag_2Al-water nanofluids and Al_2Cu-water nanofluids and found that it increases about 130% with a volume fraction less than 1%. Some researchers [5–7] investigated the thermal conductivity of nanofluids as a function of volume fraction and temperature. They showed that the thermal conductivity of nanofluids remarkably increases as temperature rises. Wang and Mujumdar [8] listed a large number of correlations, which are available in the literatures, for thermal conductivity of nanofluids.

Santra et al. [11] numerically studied the effect of CuO-water nanofluid as a cooling medium to simulate the heat transfer behavior in a two-dimensional (infinite depth) horizontal rectangular duct, where top and bottom walls were two isothermal symmetric heat sources. They considered the fluid Newtonian as well as non-Newtonian for a wide range of Reynolds numbers and solid volume fractions. These authors observed that the heat transfer enhancement is possible using nanofluid in comparison with conventional fluid for the both cases. Maiga et al. [12] numerically investigated the flow and thermal behavior of water-Al_2O_3 and Ethylene Glycol-Al_2O_3 mixtures for a system of parallel, coaxial, and heated disks. A remarkable augmentation of heat transfer coefficient has been observed with increasing of the volume fraction of nanoparticles for both nanofluids. They have reported that the rate of increase of heat transfer is more for Ethylene Glycol-Al_2O_3 nanofluid in comparison with the water-Al_2O_3 nanofluid. However, the wall shear stress also increases considerably with increasing of volume fraction of nanoparticles. Feng and Kleinstreuer [13] executed a numerical simulation for alumina-water nanofluid flow with heat transfer between parallel disks. They reported that nanofluid produce smoother flow fields and temperature distributions and heat transfer rate increases with higher volume fraction, smaller nanoparticle diameter, reduced disk spacing, and larger inlet Reynolds number.

With respect the problem under study, that is, heat transfer of discrete heat sources in channel flows, there are numerous works [14–17], both numerical and experimental, which consider such a problem.

Bhowmik et al. [14] performed steady-state experiments to investigate general heat transfer from an in-line four simulated electronic chips in a vertical rectangular channel employing water as the fluid working. They evaluated the effects of heat fluxes, flow rate, and geometrical parameters on heat transfer coefficient and illustrated heat transfer rate strongly depends on flow rate. da Silva et al. [15] employed two different analytical approaches to determine how to arrange discrete heat sources on wall cooled by force convection: (i) large number of small heat sources and (ii) small number of heat sources with finite length, which are mounted on a flat wall. Both analyses proved that heat sources should be placed nonuniformly on the wall. Arquis et al. [16] numerically examined the fluid flow and heat transfer characteristics associated with cooling an in-line array of discrete heated blocks in a channel by using a single laminar slot air jet. They studied the effects of various values such as channel height, slot weight, jet Reynolds number, spacing between blocks, block height, and block thermal conductivities. In general, the heat transfer rate increases with the increase

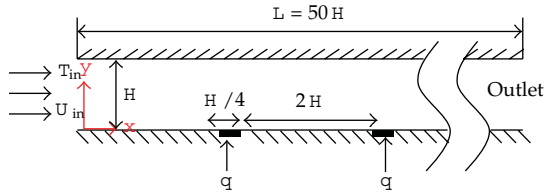

Figure 1: Parallel plates channel with discrete heat sources.

of Reynolds number and the decrease of channel weight. The effective cooling of blocks is observed to increase for shorter and widely spaced heated blocks. Jassim and Muzychka [17] studied the problem how to allocate discrete heat source to the space on a wall of a convergent flow. They showed that the heat sources should be distributed nonuniformly. Furthermore, the optimal spacing between heat sources depends on both Reynolds number and channel shape factor.

In the present paper, the flow and heat transfer characteristics of channel flow with discrete heat sources for base fluid (distilled water) and a nanofluid that is composed of distilled water and Al_2O_3 nanoparticles are numerically investigated. The main aim of this study is how the nanofluid affects on the heat transfer rate and pressure drop of flow in a channel with hot spots.

2. Mathematical Formulation

2.1. Geometry Configuration

In this study the velocity and temperature fields are determined in a parallel plates channel with height H and Length L, as shown in Figure 1. The length of duct is 50 times more than height. Nineteen heat sources of q of length $H/4$ are placed on the bottom wall of the channel. The remaining bottom wall and whole top wall are isolated. The spacing between heat sources is $2H$.

2.2. Governing Equations and Boundary Conditions

Since nanofluids are composed of extremely small particles, it is assumed that the nanoparticles and basefluid are in thermal equilibrium and they flow at same velocity. In the present work, the nanofluid is considered incompressible with temperature-dependent properties. The compression work and viscous dissipation terms were considered negligible in the energy equation. Under such assumptions, the general governing equations written are as the followings.

Conservation of mass:

$$\nabla\left(\rho_{\mathrm{nf}} V\right) = 0. \tag{2.1}$$

Conservation of momentum:

$$\nabla \cdot \left(\rho_{\mathrm{nf}} VV\right) = -\nabla P + \mu_{\mathrm{nf}} \nabla^2 V. \tag{2.2}$$

Conservation of energy:

$$\nabla \cdot \left(\rho_{\mathrm{nf}} V (C_p)_{\mathrm{nf}} T\right) = \nabla \cdot (k_{\mathrm{nf}} \nabla T). \tag{2.3}$$

Equations (2.1)–(2.3) must be solve by using appropriate boundary conditions. The flow boundary conditions are a uniform velocity at the channel inlet, equal to V_0, no-slip at the channel walls and zero relative pressure at channel outlet. The thermal boundary conditions are a uniform temperature at the channel entrance, equal to T_0 and an adiabatic condition at channel walls, except along the heat sources, in which a uniform heat flux is applied.

2.3. Nanofluid Thermophysical Properties

The thermophysical properties of nanofluid are chiefly functions of particle volumetric concentration and temperature. In the absence of experimental data, nanofluid density and specific heat are defined only as a function of volume fraction as follow.

Density:

$$\rho_{\mathrm{nf}} = (1 - \phi)\rho_{\mathrm{bf}} + \phi\rho_p. \tag{2.4}$$

Specific heat:

$$(C_P)_{\mathrm{nf}} = (1 - \phi)(C_P)_{\mathrm{bf}} + \phi(C_p)_p. \tag{2.5}$$

In above equations, subscripts "bf", "p" and "nf" refer to basefluid, nanoparticle and the nanofluid, respectively.

Viscosity:

$$\begin{aligned} \mu_{\mathrm{nf}} &= 2.9 \times 10^{-7} T^2 - 2.0 \times 10^{-4} T + 0.034 \quad \text{for } \phi = 1\%, \\ \mu_{\mathrm{nf}} &= 3.4 \times 10^{-7} T^2 - 2.3 \times 10^{-4} T + 0.039 \quad \text{for } \phi = 4\%. \end{aligned} \tag{2.6}$$

Thermal conductivity:

$$k_{\mathrm{nf}} = 0.003352 \times T - 0.3708 \quad \text{for } \phi = 1\%, \tag{2.7}$$

$$k_{\mathrm{nf}} = 0.004961 \times T - 0.8078 \quad \text{for } \phi = 4\%. \tag{2.8}$$

Equations (2.6) to (2.8) were presented by Roy et al. [18] for water-Al_2O_3 nanofluid based on available experimental results published by Putra et al. [19].

3. Numerical Method

The governing differential equations are solved using the control volume method. A second order upwind method is used for energy and momentum equations. The SIMPLE procedure

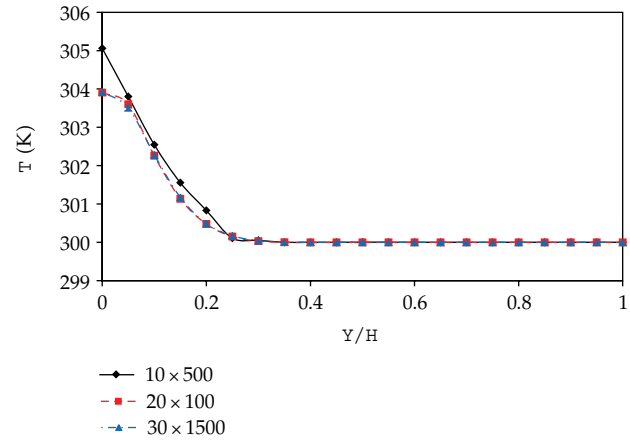

Figure 2: Effect of grid density on the temperature of channel outlet (Re = 1000, ϕ = 4%, q = 6000).

is chosen to couple pressure and velocity. The solution converge was met when the normalized residuals for all equations reached to the 10^{-7}. The algebraic discretized equations throughout the physical domain are solved by means of well-known TDMA techniques.

In order to assess the grid independent of numerical solution, three grid densities are checked. Figure 2 illustrates the effect of grid size on the predicted temperature at outlet channel for Re = 1000 and ϕ = 4%. As it can be seen a grid density of 20 × 1000 provides satisfactory solution for the shown example.

4. Results and Discussion

The thermal performance of the channel is characterized in terms of average heat transfer coefficient along the heat sources, h_{ave}, defined as:

$$h_{\text{ave}} = \frac{\int h_s \, ds}{19(H/4)}, \tag{4.1}$$

where s is the coordinate along the heat sources and h_s is given by

$$h_s = \frac{q''}{(T_0 - T_w)}, \tag{4.2}$$

where q'' and T_w are heat flux of heat sources and wall temperature, respectively.

Thermalhydraulic performance factor is defined as:

$$\eta = \frac{h_r}{(\Delta P)_r^{1/3}}, \tag{4.3}$$

where h_r and ΔP_r are, respectively, average heat transfer coefficient and pressure drop ratio, referred to values obtained for basefluid.

The heat transfer performance of cooling channel is discussed in term of the figure of merit, FoM, which is given by [1]

$$\mathrm{FoM} = \frac{W}{W_{\mathrm{pump}}}. \tag{4.4}$$

Here W_{pump} is the pumping power, which is given as:

$$W_{\mathrm{pump}} = \frac{1}{\eta_{\mathrm{pump}}} \dot{m} \Delta p, \tag{4.5}$$

where η_{pump} is pump efficiency which assumed to be 70%. The total heat transfer rate is calculated as:

$$W = \dot{m} \left(C_p\right)_{\mathrm{nf}} \left(T_{m,\mathrm{in}} - T_{m,\mathrm{out}}\right), \tag{4.6}$$

where, $\dot{m}$ is mass flow rate and $T_{m,\mathrm{in}}$ and $T_{m,\mathrm{out}}$ are mean temperature at inlet and outlet, respectively. Mean temperature is obtained by

$$T_m = \frac{1}{HU_{\mathrm{in}}} \int_0^H VT dy. \tag{4.7}$$

4.1. Code Validation

In order to show the validity and also accuracy of the model and numerical method, two comparisons with the available data are carried out. The first comparison is related to a parallel plates channel that all its walls are heated with a constant heat flux and the water is used as fluid working. In this case, the Nusselt number is compared which is given by the following definitions:

$$\mathrm{Nu} = \frac{qH}{k(T_w - T_m)}, \tag{4.8}$$

where T_m is bulk temperature of fluid. The comparison is depicted in Figure 3. It is seen that the results of the present study are in good agreement with previous data [9].

The second comparison is concerned with experimental data of nanofluid heat transfer in a circular tube with diameter (D) equal to 4.75 mm and Length of 1.2 m, given by Anoop et al. [10]. The nanofluid is water-Al_2O_3 with $\phi = 4\%$ at a constant Reynolds number 1588. Figure 4 shows remarkable agreement between the present results on local heat transfer coefficient and those provided by [10].

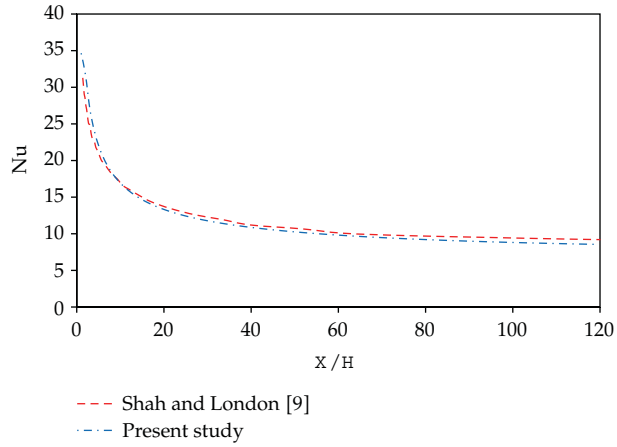

Figure 3: Comparison of present numerical results with those obtained by Shah and London [9].

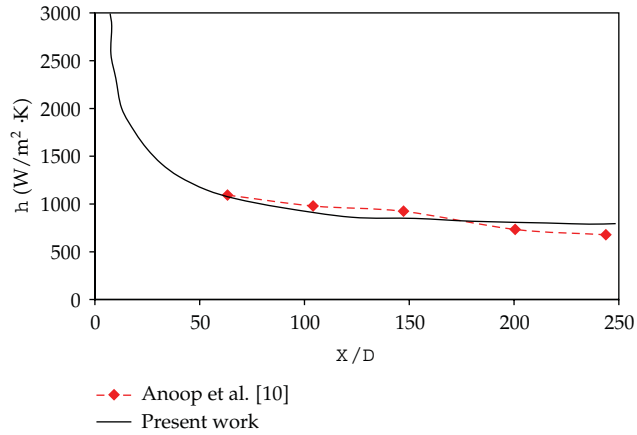

Figure 4: Comparison of heat transfer coefficient between present simulation and experimental data [10] for water-Al_2O_3 nanofluid with $\phi = 4\%$ in the circular tube.

4.2. Velocity Field

The values of velocity at channel outlet for Re = 50 and Re = 1000 are depicted in Figures 5(a) and 5(b), respectively, for considered volume fractions. It can be seen that trend of velocity profile is affected by adding the nanoparticle in basefluid for both Reynolds numbers. However, with the increase of nanoparticle loading, as it is expected, the peak of velocity profile will increase. This produces larger velocity gradient near the wall which can lead to increase wall shear stress and pressure drop. Another interesting issue, which one can perceive in Figure 5, is the asymmetric profile for $\phi = 1\%$ and $\phi = 4\%$ because of temperature-depended viscosity. The magnitude of velocity near the bottom wall is lower due to decreased viscosity. This is because of higher temperature near the bottom wall that decreases the viscosity according to (2.6). The velocity profile is more asymmetric for Re = 50 and $\phi = 1\%$. The values of velocity at $Y/H = 0.05$ and $Y/H = 0.95$ (i.e., near the bottom and top walls) are, respectively, 0.00083 m/s and 0.00069 m/s for Re = 1000 and $\phi = 4\%$ which indicate about

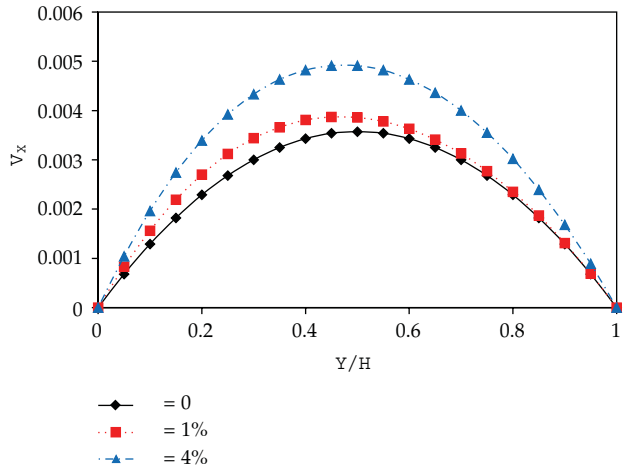

(a)

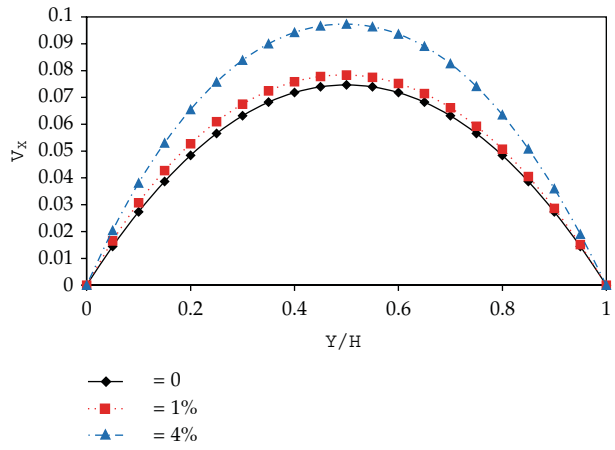

(b)

Figure 5: Effect of particle loading parameter ϕ on velocity profile at channel outlet for: (a) Re = 50, (b) Re = 1000.

20% difference, while this value is equal to 0 (symmetric) and 16% for $\phi = 0$ (distilled water) and $\phi = 4\%$, respectively.

4.3. Local Nanofluid Properties

Figures 6(a) and 6(b) show temperature effects on local nanofluid conductivity which is computed inside the numerical model with (2.7) and (2.8). Since the whole top wall is adiabatic and there is no heat transfer, the nanofluid conductivity is only illustrated on bottom wall. One can easily notice that the behavior of nanofluid conductivity is periodic along the channel. This is due the fact that heat sources increase wall temperature and nanofluid conductivity. Furthermore, the remaining bottom wall, which is adiabatic, has lower temperature that leads to lower nanofluid conductivity. With comparison of

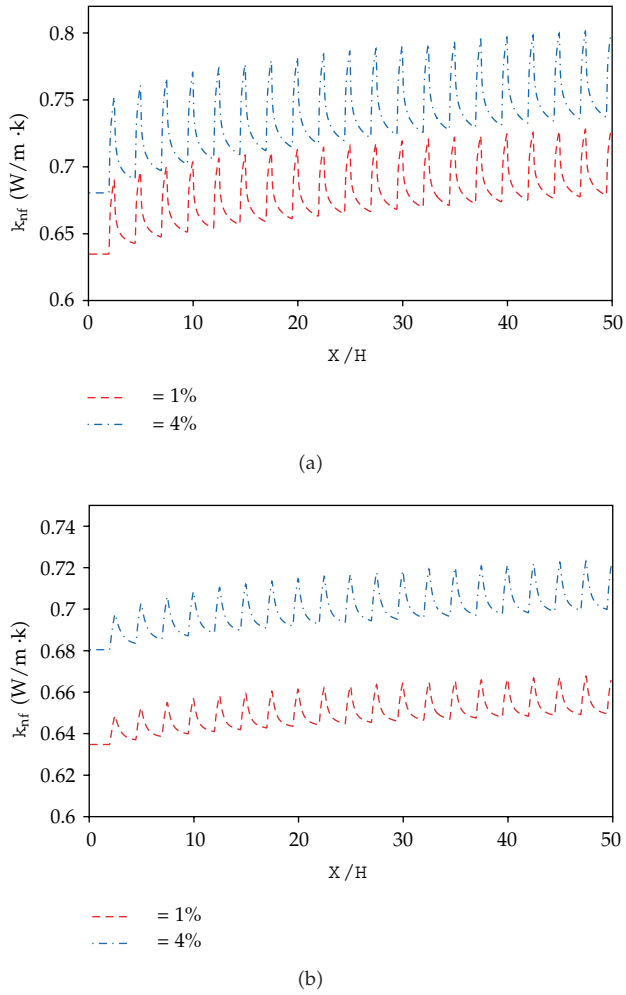

Figure 6: Effect of particle loading parameter ϕ on nanofluid conductivity profile along the channel for: (a) Re = 50, (b) Re = 1000.

Figures 6(a) and 6(b), It can be seen that Re = 50 presents higher conductivity when compared to Re = 1000. The reason is explained as flows. Although the higher Reynolds number increases the heat transfer rate, but, it is not allowed fluid particles to residence for a long time in channel because of its higher mass flow rate. So, for Re = 50 the nanofluid temperature rises more in comparison with Re = 1000 and presents higher conductivity.

Since the variations of temperature on the top wall is negligible (less than 2 K), the local viscosity is illustrated in Figures 7(a) and 7(b) for Re = 50 and Re = 1000, respectively, only for bottom wall. It can be observed that the local viscosity has a decreasing periodic behavior on bottom wall because of the growing temperature along the channel. As shown in Figure 7, similar to the conductivity profile, the amplitude of variations in a period of local viscosity is higher for Re = 50 in comparison with Re = 1000. This is due this fact that the lower Reynolds number increases the residence time distribution (RTD) of nanofluid in a period of channel and causes more temperature difference.

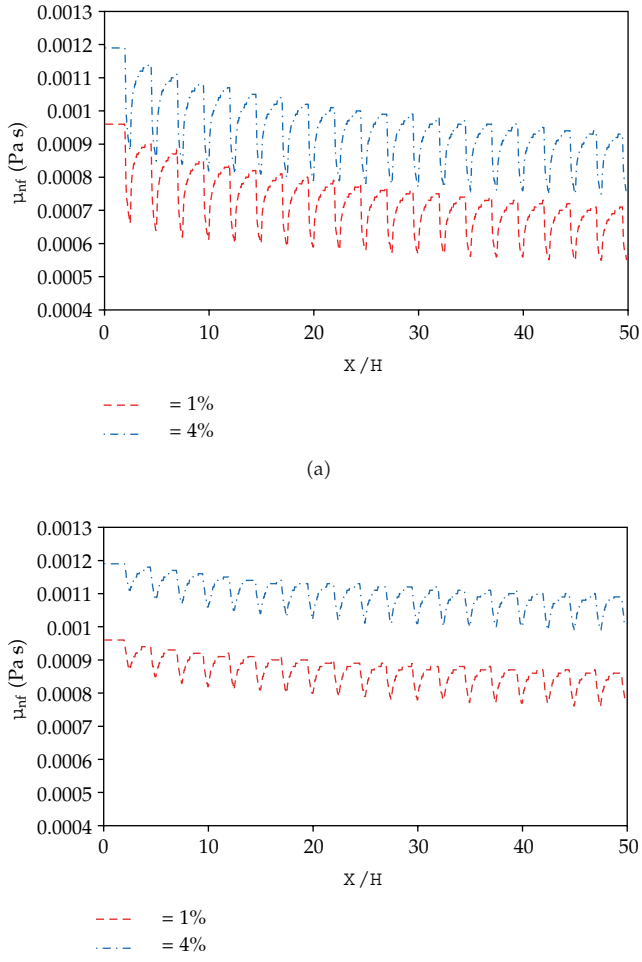

Figure 7: Effect of particle loading parameter ϕ on nanofluid viscosity along the channel for: (a) Re = 50, (b) Re = 1000.

4.4. Effect of Particle Volume Fraction on Heat Transfer and Temperature Field

Results reveal that the presence of nanoparticles has a remarkable effect on heat transfer enhancement. The average heat transfer coefficient profiles on the heat sources as a function of Reynolds number are depicted in Figure 8(a) for $\phi = 0, 1$, and 4. In general, the average heat transfer coefficient increases as Reynolds number is increased. It is also observed that as ϕ increases h_{ave} becomes higher for a fixed value of Re. Thus, passing from $\phi = 0\%$ to $\phi = 4\%$, the maximum value of about 2366 W/m^2 k for h_{ave} is found at Re = 1000 and $\phi = 4$.

Figure 8(b) illustrates the average heat transfer coefficient ratio (h_r), referred to the values obtained for basefluid, as a function of Reynolds number for $\phi = 0, 1$ and 4%. It can be seen that the h_r is greater than one for all considered cases and rises slightly as Reynolds number increases from 200 to 1000 for both volume fractions $\phi = 1$ and 4%. Furthermore,

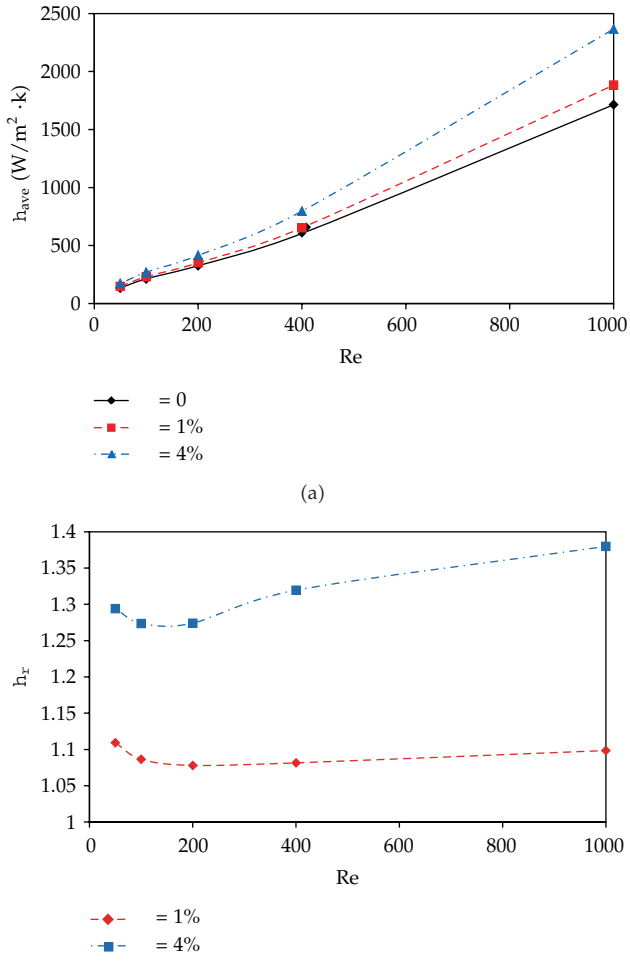

Figure 8: Effect of parameters ϕ and Re on: (a) average heat transfer coefficient and (b) average heat transfer coefficient ratio.

there is a considerable augmentation for higher volume fraction, in fact the highest value of 1.38 is detected at Re = 1000 and ϕ = 4%.

As we are also interested to analysis the cooling benefits of nanofluid on bottom wall, Figures 9(a) and 9(b) show the wall temperature for various volume fractions for Re = 50 and 1000, respectively. Due to a nonuniform heat flux on bottom wall, an increasing periodic behavior is detected in Figure 9. One can see that the wall temperature is more for Re = 50 in comparison with Re = 1000. As mentioned earlier, this is due this fact that the fluid particles spend more time in channel. The peak values of bottom wall temperature are related to the heat sources, while the minimum values belong to adiabatic part of bottom wall. It is also observed that among the considered particle volume fractions, the lowest minimum and maximum values of wall temperature in each period belong to ϕ = 4%. It can also be noted the effect of volume fraction on wall cooling becomes more within the farther distance from inlet, that is, greater X/H.

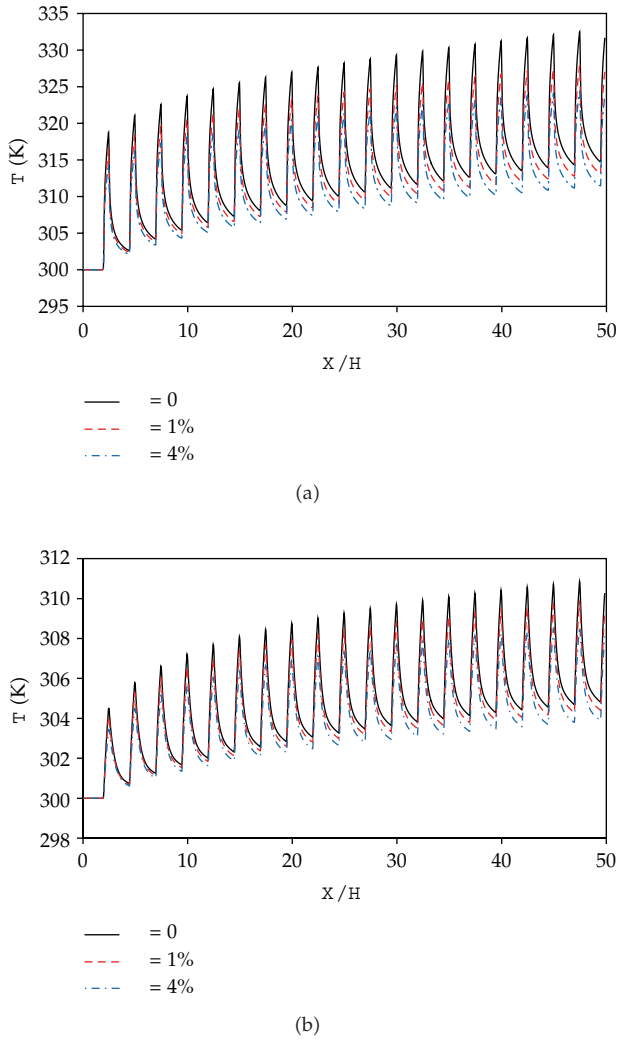

Figure 9: Effect of particle loading parameter ϕ on bottom wall temperature at: (a) Re = 50, (b) Re = 1000.

The effect of particle volume fraction on temperature along the channel height can be seen on Figures 10(a) and 10(b), depicting the temperature profile at the first of the last heat source for Re = 50 and 1000, respectively. It is observed that the values of temperature are higher for Re = 50. On the bottom wall, that is, $Y/H = 0$, passing from Re = 50 to Re = 1000 the temperature gradient increases which presents a better heat transfer enhancement. By comparison of Figures 10(a) and 10(b), it is noted that the effect of the use of nanofluid on the temperature along the height of channel is greater for lower Reynolds.

4.5. Effect of Particle Volume Fraction on Pressure Drop

It will be predictable that the use of nanoparticles in basefluid can have an adverse influence on pressure drop because of increased viscosity. The pressure drop profiles as a function of

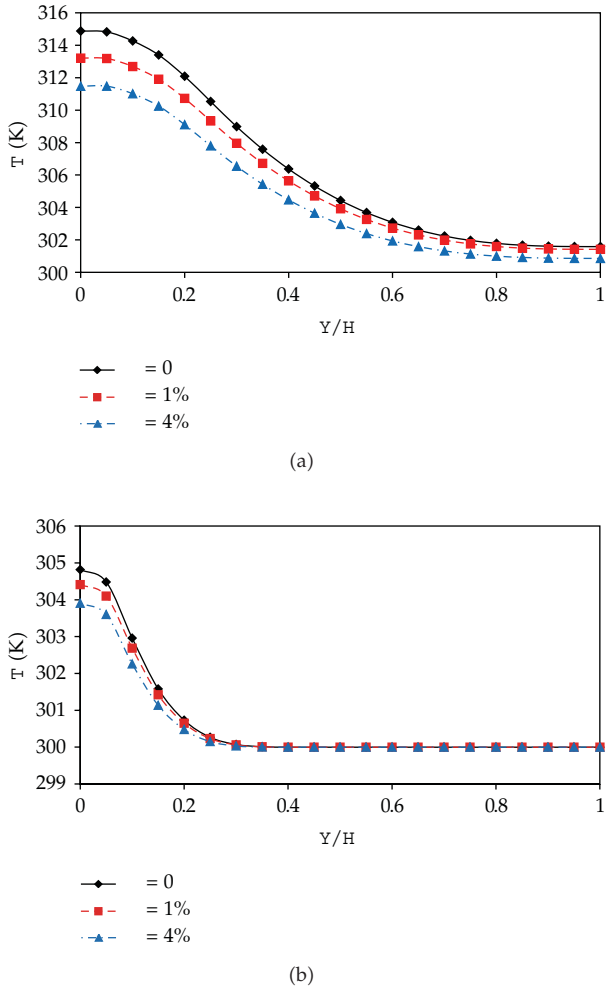

Figure 10: Effect of volume fraction ϕ on temperature profile along channel height at the first of last heat source for: (a) Re = 50, (b) Re = 1000.

Reynolds number are depicted in Figure 11(a) for $\phi = 0, 1$, and 4%. As it can be noted, the pressure drop increases as Reynolds number and particle volume fraction increase and the highest value is found at Re = 1000 and $\phi = 4\%$. By comparison $\phi = 0$, and $\phi = 1\%$, it is observed that the difference between the values of pressure drop is less at lower Reynolds number, while it will be more considerable at higher Reynolds number. This can be explained by the temperature-dependent viscosity of nanofluid.

The pressure drop ratio (ΔP_r), referred to the base fluid is described in Figure 11(b). It is observed that the ΔP_r is greater than one for all considered cases, similar to h_r, and rises slightly as Reynolds number increases from 200 to 1000 for both volume fractions $\phi = 1$ and 4%. In fact the highest value of pressure drop ratio is equal to 1.68 that is dedicated at Re = 1000 and $\phi = 4\%$.

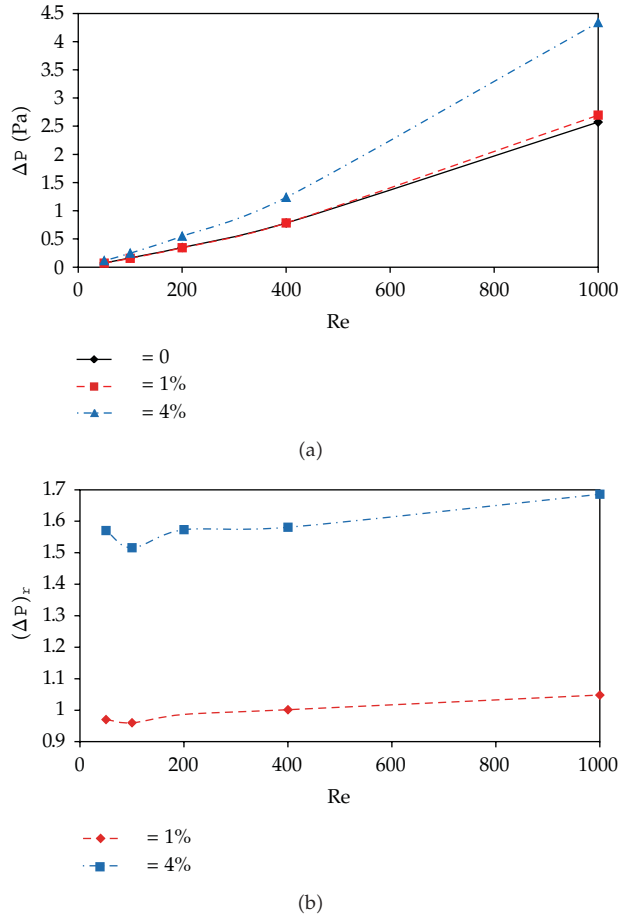

Figure 11: Effect of parameters ϕ and Re on: (a) pressure drop and (b) pressure drop ratio.

4.6. Effect of Heat Flux of Heat Sources on Heat Transfer and Pressure Drop

Since we use temperature-dependent properties, it is interesting to determine the effect of heat sources heat flux (q) on heat transfer coefficient and pressure drop. The effects of (q) on the average heat transfer and pressure drop can be seen in Figures 12(a) and 12(b), depicting, respectively, the heat transfer coefficient and pressure drop for $\phi = 1$ and 4%. It can easily be seen in Figure 12(a) that the average heat transfer coefficient increases as (q) is increased because of increased nanofluid conductivity. On the other hand, as shown in Figure 12(b), the pressure drop decreases as (q) increases because of decreased nanofluid viscosity. Thus, the augmentation of (q) has a good effect on thermal-hydraulic performance of channel.

4.7. Thermal Hydraulic and Overall Heat Transfer Performance

As discussed in previous sections, the use of nanofluids increases the heat transfer rate as well as pressure drop. In order to investigate the order of magnitude of augmentation of heat transfer and pressure drop for various Reynolds number and volume fraction, the thermal

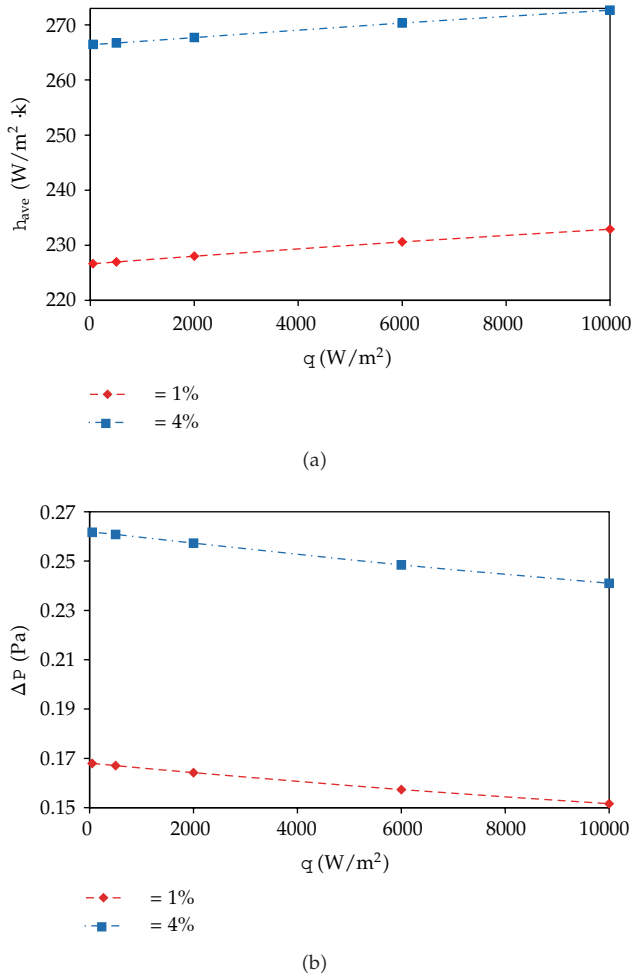

Figure 12: Effect of parameters ϕ and q on (a) averaged heat transfer coefficient and (b) pressure drop. (Re = 100).

hydraulic performance factor as a function of Reynolds number is depicted in Figure 13 for $\phi = 1$ and 4%.

It is observed that the thermal hydraulic performance has different behaviors for $\phi = 1$ and 4%. For $\phi = 1$, thermal hydraulic performance decreases as Reynolds number increases from 50 to 200 and after it, the profile will be unchangeable. For $\phi = 4\%$, thermal hydraulic performance decreases as Reynolds number increases from 50 to 200, similar to $\phi = 1\%$, but there is a remarkable augmentation as Reynolds number increases from 200 to 1000 and the best performance of 1.16 is found at Re = 1000 and $\phi = 4\%$.

In order to have a comparison between ratio of output (heat transfer rate) to the input (pumping power), the overal heat transfer performance of channel in term of figure of merit (FoM) as a function of Reynolds number is illustrated in Figure 14 for $\phi = 1$ and 4%. It can be seen that FoM decreases as volume fraction increases. This is due this fact that specific heat decreases as volume fraction increases. Furthermore, the increase of volume fraction leads to increased inlet velocity, which decreases residence time distribution of nanofluid.

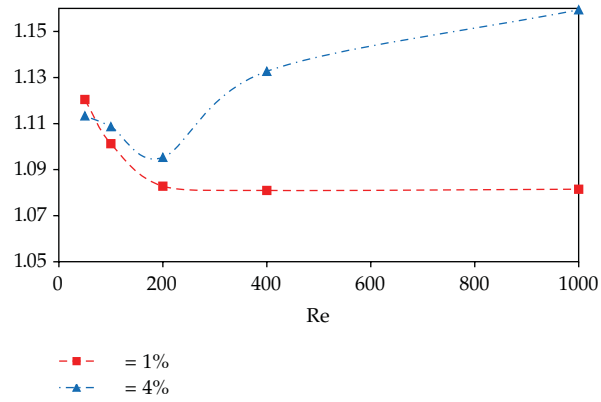

Figure 13: Effect of parameters ϕ and Re on η.

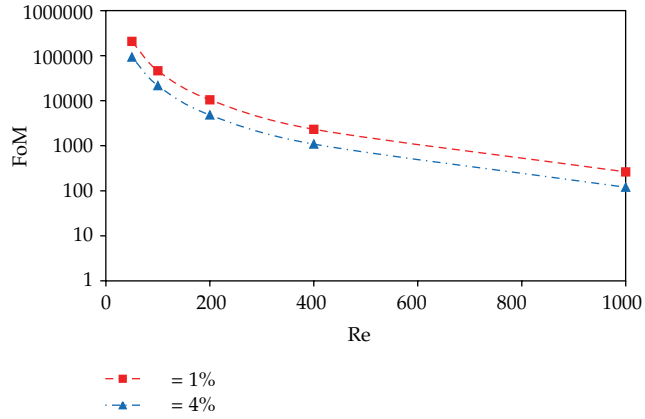

Figure 14: Effect of parameters ϕ and Re on FoM.

So, although the heat transfer coefficient increases, but overall heat transfer performance decreases as volume fraction increases. As Figure 14 indicates, the FoM remarkably decreases as Reynolds number increases and the best value of 207347 is found at Re = 50 and ϕ = 1%.

5. Conclusion

A numerical analysis of flow and heat transfer characteristics of nanofluid in a parallel plates channel with discrete heat sources has been presented. The heat sources are placed on bottom wall at a constant heat flux and remaining channel surfaces are considered adiabatic. The basefluid is water and three volume fractions of Al_2O_3 nanoparticles (ϕ = 0 (distilled water) 1 and 4%) are taken into account with a single-phase model. Furthermore, different Reynolds numbers in the range 50–1000 are considered. The use of nanofluid can cause an asymmetric profile velocity along the height of channel. Results clearly show that the use of nanofluid can remarkably increase heat transfer rate and decrease the wall temperature. Furthermore, for increasing volume fraction, nanofluid can produce lower wall temperature and higher heat transfer rate. The average heat transfer coefficient and pressure profiles present that heat

transfer rate increases as applied heat flux of heat sources is increased while the pressure drop decreases.

Nomenclature

Symbols

∇: nabla operatoe (1/m)
C_p: specific heat of the fluid (J/kg K)
FoM: figure of merit
H: channel height (m)
h_{ave}: average heat transfer coefficient along heat sources (W/m^2 K)
k: thermal conductivity (W/m K)
$\dot{m}$: mass flow rate (Kg/s)
Nu: local Nusselt number (Nu = $qH/(k(T_w - T_m))$)
P: pressure (Pa)
q: heat flux of heat sources (W/m^2)
Re: reynolds number (Re = $(\rho_{\text{nf}}\ HU_{\text{in}})/\mu_{\text{nf}}$)
s: coordinate along heat sources (m)
T: temperature (K)
V: velocity vector (m/s)
W: total heat transfer rate (J/s)
U_{in}: inlet velocity (m/s).

Greeks

η: thermal hydraulic performance factor
η_{pump}: pump efficiency
μ: dynamic viscosity (Pa·s)
ρ: density (kg/m^3)
ϕ: particle volume fraction (%).

Subscripts

w: refers to the wall conditions
bf: refers to the base fluid
nf: refers to the nanofluid
p: refers to particles
r: refers to a ratio
0: refers to the inlet conditions.

Acknowledgments

First, the authors would like to thank Editor Dr. M. F. El-Amin and two anonymous referees for their useful suggestions, which greatly improve the paper. We also would like to express

our appreciation to the Iran nanotechnology initiative council for their financial support for this project.

References

[1] A.P. Saamito, J.C. Kurnia, and A. S. Mujumdar, "Numerical evaluation of laminar heat transfer enhancement in nanofluid flow in coiled square tube," *Nanoscale Research Letter*, vol. 6, p. 376, 2011.
[2] G. Roy, S. J. Palm, and C. T. Nguyen, "Heat transfer and fluid flow of nanofluids in laminar radial flow cooling systems," *Journal of Thermal Science*, vol. 14, no. 4, pp. 362–367, 2005.
[3] S. Lee, S. U. S. Choi, S. Li, and J. A. Eastman, "Measuring thermal conductivity of fluids containing oxide nanoparticles," *Journal of Heat Transfer*, vol. 121, no. 2, pp. 280–288, 1999.
[4] I. Chopkar, S. Sudarshan, P. K. Das, and I. Manna, "Effect of particle size on thermal conductivity of nanofluid," *Metallurgical and Materials Transactions A*, vol. 39, no. 7, pp. 1535–1542, 2008.
[5] C. H. Li and G. P. Peterson, "Experimental investigation of temperature and volume fraction variations on the effective thermal conductivity of nanoparticle suspensions (nanofluids)," *Journal of Applied Physics*, vol. 99, no. 8, Article ID 084314, 2006.
[6] S. K. Das, N. Putra, P. Thiesen, and W. Roetzel, "Temperature dependence of thermal conductivity enhancement for nanofluids," *Journal of Heat Transfer*, vol. 125, no. 4, pp. 567–574, 2003.
[7] T. P. Teng, Y. H. Hung, T. C. Teng, and J. H. Chen, "Performance evaluation on an air-cooled heat exchanger for alumina nanofluid under laminar flow," *Nanoscale Research Letter*, vol. 6, p. 488, 2011.
[8] X. Q. Wang and A. S. Mujumdar, "Heat transfer characteristics of nanofluids: a review," *International Journal of Thermal Sciences*, vol. 46, no. 1, pp. 1–19, 2007.
[9] R. K. Shah and A. L. London, *Laminar Flow Forced Convection in Ducts*, Academic Press, New York, NY, USA, 1978.
[10] K. B. Anoop, T. Sundararajan, and S. K. Das, "Effect of particle size on the convective heat transfer in nanofluid in the developing region," *International Journal of Heat and Mass Transfer*, vol. 52, no. 9-10, pp. 2189–2195, 2009.
[11] A. K. Santra, S. Sen, and N. Chakraborty, "Study of heat transfer due to laminar flow of copper-water nanofluid through two isothermally heated parallel plates," *International Journal of Thermal Sciences*, vol. 48, no. 2, pp. 391–400, 2009.
[12] S. E. B. Maiga, S. J. Palm, C. T. Nguyen, G. Roy, and N. Galanis, "Heat transfer enhancement by using nanofluids in forced convection flows," *International Journal of Heat and Fluid Flow*, vol. 26, no. 4, pp. 530–546, 2005.
[13] Y. Feng and C. Kleinstreuer, "Nanofluid convective heat transfer in a parallel-disk system," *International Journal of Heat and Mass Transfer*, vol. 53, no. 21-22, pp. 4619–4628, 2010.
[14] H. Bhowmik, C. P. Tso, K. W. Tou, and F. L. Tan, "Convection heat transfer from discrete heat sources in a liquid cooled rectangular channel," *Applied Thermal Engineering*, vol. 25, no. 16, pp. 2532–2542, 2005.
[15] A. K. da Silva, S. Lorente, and A. Bejan, "Optimal distribution of discrete heat sources on a plate with laminar forced convection," *International Journal of Heat and Mass Transfer*, vol. 47, no. 10-11, pp. 2139–2148, 2004.
[16] E. Arquis, M. A. Rady, and S. A. Nada, "A numerical investigation and parametric study of cooling an array of multiple protruding heat sources by a laminar slot air jet," *International Journal of Heat and Fluid Flow*, vol. 28, no. 4, pp. 787–805, 2007.
[17] E. Jassim and Y. S. Muzychka, "Optimal distribution of heat sources in convergent channels cooled by laminar forced convection," *Journal of Heat Transfer*, vol. 132, no. 1, pp. 1–8, 2010.
[18] G. Roy, S. J. Palm, and C. T. Nguyen, "Heat transfer and fluid flow of nanofluids in laminar radial flow cooling systems," *Journal of Thermal Science*, vol. 14, no. 4, pp. 362–367, 2005.
[19] N. Putra, W. Roetzel, and S. K. Das, "Natural convection of nano-fluids," *Heat and Mass Transfe*, vol. 39, no. 8-9, pp. 775–784, 2003.

Hindawi Publishing Corporation
Journal of Applied Mathematics
Volume 2012, Article ID 420189, 15 pages
doi:10.1155/2012/420189

Research Article

Viscoelastic Flow through an Axisymmetric Contraction Using the Grid-by-Grid Inversion Method

H. M. Park

Department of Chemical and Biomolecular Engineering, Sogang University, Seoul 121-742, Republic of Korea

Correspondence should be addressed to H. M. Park, hmpark@sogang.ac.kr

Received 1 December 2011; Revised 5 January 2012; Accepted 15 January 2012

Academic Editor: M. F. El-Amin

The newly developed algorithm called the grid-by-grid inversion method is a very convenient method for converting an existing computer code for Newtonian flow simulations to that for viscoelastic flow simulations. In this method, the hyperbolic constitutive equation is split such that the term for the convective transport of stress tensor is treated as a source which is updated iteratively. This allows the stress tensors at each grid point to be expressed in terms of velocity gradient tensor at the same location, and the set of stress tensor components is found after inverting a small matrix at each grid point. To corroborate the robustness and accuracy of the grid-by-grid inversion method, we apply it to the $4:1$ axisymmetric contraction problem. This algorithm is found to be robust and yields accurate results as compared with other finite volume methods. Any commercial CFD packages for Newtonian flow simulations can be easily converted to those for viscoelastic fluids exploiting the grid-by-grid inversion method.

1. Introduction

Contrary to the techniques of computational fluid dynamics for Newtonian fluids, the numerical algorithms for viscoelastic flows are not so matured. The hyperbolic nature of the constitutive equation incurs peculiar flow phenomena such as rod-climbing and extrudate swell as well as causes difficulties in numerical simulation [1–3]. Since the momentum balance equation is elliptic in steady state and parabolic in unsteady state, the complete set for viscoelastic flows is a mixed type, hyperbolic-elliptic, or hyperbolic-parabolic. This situation is difficult to treat numerically since it is difficult to devise a numerical algorithm that works for mixed systems. Another difficulty associated with the hyperbolic constitutive equation is the choice of appropriate boundary conditions for the stress field at the boundary

of computational domain. One can impose nonslip boundary condition on the walls for the velocity field but there exist no apparent or natural boundary conditions for the stress components at the wall. Various numerical techniques for solving viscoelastic flows, such as finite volume methods, finite element methods, and spectral methods, are well documented in the references cited [4–9].

In the present investigation, a newly developed algorithm called the grid-by-grid inversion method [10] is employed to solve the viscoelastic flows through an axisymmetric contraction. Figure 1 shows the flow geometry for the axisymmetric contraction. Viscoelastic fluid passes from one circular tube into the other tube of smaller radius and generates a complex flow having a strong shear near the walls and uniaxial extension along the centerline. The existence of strong shearing zones and uniaxial extension zone makes this flow geometry a good test bed for numerical algorithms of viscoelastic fluids. Many investigators of rheology adopt this flow geometry as an important benchmark problem, especially the $4:1$ contraction geometry [11]. We shall solve the $4:1$ axisymmetric contraction problem employing the newly developed "grid-by-grid inversion method" [10], which is implemented based on a finite volume method [10].

The hyperbolic constitutive equations of viscoelastic fluids have a nonlocal character because of the term representing convective transport of stress tensor. If this term is assumed to be known, the constitutive equation becomes local and the stress tensor is easily evaluated for a given velocity gradient tensor at the same location. The six stress tensor components for the cases of a three-dimensional flow are found after inverting a six by six matrix at each grid point and are substituted into the Navier-Stokes equation as a source term. In this way, the numerical solution of viscoelastic flows becomes as straightforward as that of Newtonian fluids. We call this algorithm the grid-by-grid inversion method since the viscoelastic stress tensor is obtained by the grid-by-grid inversion of a matrix equation at each grid point. This algorithm can easily be implemented using finite volume methods, finite element methods and spectral methods. When applied to the $4:1$ axisymmetric contraction problem, it is found that the grid-by-grid inversion method yields accurate results efficiently in comparison with numerical results of traditional algorithms.

2. Governing Equations and the Grid-by-Grid Inversion Method

We consider incompressible isothermal flows of viscoelastic fluids. The governing equations may be written in dimensionless variables as follows:

$$\nabla \cdot \mathbf{v} = 0, \tag{2.1}$$

$$\mathrm{Re}\left(\frac{\partial \mathbf{v}}{\partial t} + \mathbf{v} \cdot \nabla \mathbf{v}\right) = \nabla \cdot \boldsymbol{\sigma}, \tag{2.2}$$

$$\boldsymbol{\sigma} = -P\mathbf{I} + 2\beta\mathbf{D} + \boldsymbol{\tau}, \tag{2.3}$$

$$\lambda\left(\frac{\partial \boldsymbol{\tau}}{\partial t} + \mathbf{v} \cdot \nabla \boldsymbol{\tau}\right) = 2(1-\beta)\mathbf{D} + \lambda\left((\nabla \mathbf{v})^T \cdot \boldsymbol{\tau} + \boldsymbol{\tau} \cdot \nabla \mathbf{v}\right) - \boldsymbol{\tau}. \tag{2.4}$$

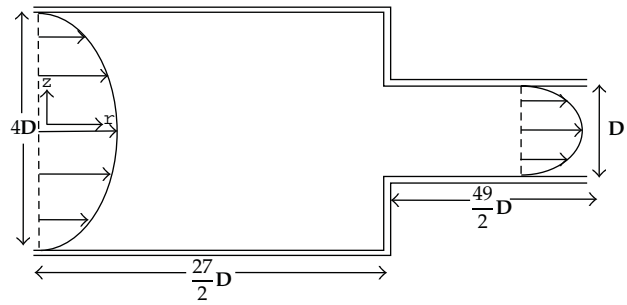

Figure 1: The 4 : 1 axisymmetric contraction.

In the above equations, P is pressure, $\mathbf{D}$ is the rate of deformation tensor, $\boldsymbol{\tau}$ is the viscoelastic part of the stress tensor. The parameter β is the ratio of the retardation and relaxation times of the fluid. Equation (2.4) is the constitutive equation of the Oldroyd-B model [9], λ is the dimensionless relaxation time or the Deborah number, and Re is the Reynolds number. The superscript T in (2.4) is the transpose. The Reynolds number and the dimensionless Deborah number are defined by

$$\mathrm{Re} = \frac{\rho U L}{\eta}, \qquad \lambda = \frac{\lambda_1 U}{L}, \tag{2.5}$$

where ρ is the density, λ_1 the dimensional relaxation time, U the characteristic speed, and L is the characteristic length. The characteristic velocity U and the characteristic length L are taken as the average velocity in the downstream tube and the radius of the downstream tube, respectively. To compare with the results of other investigators [9, 11], we take the value of β to be $1/9$.

Next, we consider the grid-by-grid inversion method as applied to the set of equations (2.1)–(2.4). Contrary to the Newtonian fluids where the stress field $\boldsymbol{\tau}$ depends on the velocity gradient tensor $\nabla\mathbf{v}$ locally, the stress depends on the velocity gradient tensor nonlocally due to the fact that constitutive equation is hyperbolic partial differential equation. The convective transport of the stress tensor, represented by $\mathbf{v}\cdot\nabla\boldsymbol{\tau}$ in (2.4), takes care of the memory effect of $\boldsymbol{\tau}$ in its dependence on $\nabla\mathbf{v}$ and causes the functional dependence of $\boldsymbol{\tau}$ on $\nabla\mathbf{v}$ to be nonlocal. In the grid-by-grid inversion method, $\mathbf{v}\cdot\nabla\boldsymbol{\tau}$ is assumed to be a known source term which shall be updated iteratively in the process. Then the constitutive equation (2.4) can be converted such that $\boldsymbol{\tau}$ is represented as a local function of $\nabla\mathbf{v}$ as in the case of Newtonian fluids. This arrangement renders the numerical solution of viscoelastic fluids as straightforward as that of Newtonian fluids. The steps for obtaining the velocity and the stress at time step $n+1$, $\mathbf{v}^{n+1}$ and $\boldsymbol{\tau}^{n+1}$, using known velocity and stress at time step n, $\mathbf{v}^n$ and $\boldsymbol{\tau}^n$, proceed in an iterative manner as follows. First, define

$$\mathbf{C} \equiv \mathbf{v}^{n+1(it)}\cdot\nabla\boldsymbol{\tau}^{n+1(it)}, \tag{2.6}$$

where the superscript $n+1(it)$ indicates variable at time step $n+1$ in the itth iteration. Discretizing (2.4) in time implicitly and representing $\mathbf{D}$ in terms of the velocity gradient $\nabla\mathbf{v}$, we find the following local matrix equations defined at each grid point.

$$\left(\frac{\lambda}{\Delta t}+1.0\right)\boldsymbol{\tau}^{n+1(it+1)}-\lambda(\nabla\mathbf{v})^{T^{n+1(it)}}\cdot\boldsymbol{\tau}^{n+1(it+1)}-\lambda\boldsymbol{\tau}^{n+1(it+1)}\cdot(\nabla\mathbf{v})^{n+1(it)}$$
$$=\frac{\lambda}{\Delta t}\boldsymbol{\tau}^{n}-\lambda\mathbf{C}+(1-\beta)\left[(\nabla\mathbf{v})^{n+1(it)}+(\nabla\mathbf{v})^{T^{n+1(it)}}\right]. \tag{2.7}$$

Once $\mathbf{C}$ is evaluated using variables at $n+1(it)$, (2.7) can be solved for $\boldsymbol{\tau}^{n+1(it+1)}$ by inverting a six-by-six matrix at each grid point for the six independent stress components for the case of three-dimensional flows. Equation (2.7) is also solved at the boundary grid points to find the boundary stress field. This suggests a natural method of imposing boundary conditions for the hyperbolic constitutive equations at all boundaries of the computational domain. This method had been employed to impose outflow boundary conditions by Papanastasiou et al. [12] and is called the open boundary condition. Using $\boldsymbol{\tau}^{n+1(it+1)}$ obtained from (2.7), the velocity at the $n+1$ th time step in the $it+1$ th iteration, $\mathbf{v}^{n+1(it+1)}$, is found by solving (2.1)–(2.3) as follows:

$$\nabla\cdot\mathbf{v}^{n+1(it+1)}=0, \tag{2.8}$$

$$\mathrm{Re}\left(\frac{\mathbf{v}^{n+1(it+1)}-\mathbf{v}^{n}}{\Delta t}+\mathbf{v}^{n+1(it+1)}\cdot\nabla\mathbf{v}^{n+1(it+1)}\right)=-\nabla P^{n+1(it+1)}+2\beta\nabla^{2}\mathbf{v}^{n+1(it+1)}+\nabla\cdot\boldsymbol{\tau}^{n+1(it+1)}. \tag{2.9}$$

Although (2.8)-(2.9) can be solved using any numerical methods for incompressible Navier-Stokes equations, we employ a finite volume method based on the SIMPLE algorithm [13, 14]. To stabilize the numerical scheme for large values of λ, (2.6) is evaluated using one of the various upwind schemes. In the present work, we adopt a higher-order upwind scheme, MinMod [14], to evaluate $\mathbf{C}$.

The case of $\beta=0$ requires a special deliberation before employing standard algorithms for incompressible Navier-Stokes equations in the grid-by-grid inversion technique. When $\beta=0$, we decompose the total stress $\boldsymbol{\sigma}$ into pure viscous and elastic parts $-P\mathbf{I}+2\mathbf{D}$ and $\boldsymbol{\Sigma}$, respectively, such that

$$\boldsymbol{\sigma}=-P\mathbf{I}+2\mathbf{D}+\boldsymbol{\Sigma}, \tag{2.10}$$

where

$$\boldsymbol{\Sigma}\equiv\boldsymbol{\tau}-2\mathbf{D}. \tag{2.11}$$

Then the momentum and constitutive equations for the case of $\beta = 0$ may be written as

$$\nabla \cdot \mathbf{v} = 0, \tag{2.12}$$

$$\mathrm{Re}\left(\frac{\partial \mathbf{v}}{\partial t} + \mathbf{v} \cdot \nabla \mathbf{v}\right) = -\nabla P + \nabla^2 \mathbf{v} + \nabla \cdot \boldsymbol{\Sigma}, \tag{2.13}$$

$$\lambda\left(\frac{\partial \boldsymbol{\Sigma}}{\partial t} + \mathbf{v} \cdot \nabla \boldsymbol{\Sigma} - (\nabla \mathbf{v})^T \cdot \boldsymbol{\Sigma} - \boldsymbol{\Sigma} \cdot (\nabla \mathbf{v})\right) + \boldsymbol{\Sigma} = -2\lambda\left(\frac{\partial \mathbf{D}}{\partial t} + \mathbf{v} \cdot \nabla \mathbf{D} - (\nabla \mathbf{v})^T \cdot \mathbf{D} - \mathbf{D} \cdot \nabla \mathbf{v}\right). \tag{2.14}$$

This decomposition is called the EVSS formulation and was proposed by Perera and Walters [15]. The implementation of grid-by-grid inversion method to the set of (2.12)–(2.14) is straightforward. First, we evaluate

$$\mathbf{E} \equiv \mathbf{v}^{n+1(it)} \cdot \nabla \boldsymbol{\Sigma}^{n+1(it)}. \tag{2.15}$$

Next, convert (2.14) to the following local matrix equations for $\boldsymbol{\Sigma}$ decoupled at each grid point:

$$\begin{aligned}\left(\frac{\lambda}{\Delta t} + 1.0\right)\boldsymbol{\Sigma}^{n+1(it+1)} - \lambda(\nabla \mathbf{v})^{T^{n+1(it)}} \cdot \boldsymbol{\Sigma}^{n+1(it+1)} - \lambda \boldsymbol{\Sigma}^{n+1(it+1)} \cdot (\nabla \mathbf{v})^{n+1(it)} \\ = \frac{\lambda}{\Delta t}\boldsymbol{\Sigma}^n - \lambda \mathbf{E} - 2\lambda\left(\frac{1}{\Delta t}\mathbf{D}^{n+1(it)} - \frac{1}{\Delta t}\mathbf{D}^n + \mathbf{v} \cdot \nabla \mathbf{D} - (\nabla \mathbf{v})^T \cdot \mathbf{D} - \mathbf{D} \cdot \nabla \mathbf{v}\right)^{n+1(it)}.\end{aligned} \tag{2.16}$$

Then, (2.12) and (2.13) are discretized as follows:

$$\nabla \cdot \mathbf{v}^{n+1(it+1)} \tag{2.17}$$

$$\mathrm{Re}\left(\frac{\mathbf{v}^{n+1(it+1)} - \mathbf{v}^n}{\Delta t} + \mathbf{v}^{n+1(it+1)} \cdot \nabla \mathbf{v}^{n+1(it+1)}\right) = -P^{n+1(it+1)} + \nabla^2 \mathbf{v}^{n+1(it+1)} + \nabla \cdot \boldsymbol{\Sigma}^{n+1(it+1)}. \tag{2.18}$$

The structure of (2.16) is the same as that of (2.7) and can be solved for $\boldsymbol{\Sigma}^{n+1(it+1)}$ by inverting a six-by-six matrix at each grid point for a three-dimensional flow once $(\nabla \mathbf{v})^{n+1(it)}$ is given. After obtaining $\boldsymbol{\Sigma}^{n+1(it+1)}$, $\mathbf{v}^{n+1(it+1)}$ is found by solving (2.17)-(2.18) using the SIMPLE algorithm [13]. The second-order derivative terms appearing in $\mathbf{v} \cdot \nabla \mathbf{D}$ of (2.14) are evaluated using a one-sided finite difference formula at the boundaries.

The overall solution procedure for the grid-by-grid inversion method may be summarized as follows.

(1) $\mathbf{v}^n$ and $\boldsymbol{\tau}^n$ have obtained in the previous time step n.

The procedure for the time step $n + 1$ begins as follows.

(2) Assume $\mathbf{v}^{n+1(it)}$ and $\boldsymbol{\tau}^{n+1(it)}$. For the first iteration ($it = 1$), $\mathbf{v}^{n+1(it)} = \mathbf{v}^n$ and $\boldsymbol{\tau}^{n+1(it)} = \boldsymbol{\tau}^n$.

(3) Evaluate $\mathbf{C}$ of (2.6) ($\beta \neq 0$) or $\mathbf{E}$ of (2.15) ($\beta = 0$) using an upwind scheme.

(4) Using $\mathbf{v}^{n+1(it)}$, solve (2.7) ($\beta \neq 0$) or (2.16) ($\beta = 0$) for $\boldsymbol{\tau}^{n+1(it+1)}$ by inverting a six-by-six matrix at each grid point including the boundary grids.

(5) Using $\boldsymbol{\tau}^{n+1(it+1)}$,

($\beta \neq 0$) solve the momentum equation, (2.9), and continuity equation to find $\mathbf{v}^{n+1(it+1)}$.
($\beta = 0$) solve the momentum equation, (2.18), and continuity equation to find $\mathbf{v}^{n+1(it+1)}$.

(6) Convergence check for $\boldsymbol{\tau}^{n+1}$ and $\mathbf{v}^{n+1}$. If not converged, go to step (2). Otherwise, update the time step and go to step (1).

Usually convergence is attained in two or three iterations. The novelty of the grid-by-grid inversion method is its easiness of numerical implementation. As noted in the above procedure, one can easily convert any existing computer code for Newtonian flow simulations to that for viscoelastic flow simulation by adding a subroutine that solves the viscoelastic constitutive equation using the grid-by-grid inversion method, summarized as steps (3)~(4), to evaluate the viscoelastic source terms in the Navier-Stokes equation, $\nabla \cdot \boldsymbol{\tau}$. Adding a source term to the Navier-Stokes equation is an easy procedure whether we employ a finite volume method or a finite element method. In the subroutine for the viscoelastic constitutive equation, one inverts a small matrix at each grid point, which can be performed cheaply. Therefore, one can easily convert any commercial CFD package for Newtonian fluid flows to that for viscoelastic fluids employing the grid-by-grid inversion method. Its robustness and accuracy are corroborated in the next section, where the grid-by-grid inversion method is employed to solve the 4 : 1 viscoelastic axisymmetric contraction problem. Although Phillips and Williams [16] solve the viscoelastic constitutive equation by converting small matrix equations in their semi-Lagrange method, it is very difficult to convert an existing Newtonian code to a viscoelastic code using the semi-Lagrange method since it treats the momentum and the constitutive equation simultaneously.

3. Viscoelastic Flow through an Axisymmetric Contraction

In this section, we solve the flow of an Oldroyd-B fluid through a 4 : 1 axisymmetric contraction geometry using the grid-by-grid inversion method. The schematic representation of the flow geometry is depicted in Figure 1. The viscoelastic flow through the circular contraction geometry has served as a standard benchmark problem for numerical algorithms for viscoelastic fluids. The presence of a singularity in the entry-flow geometry as well as regions of high shear and extension in the flow have been a significant challenge for a long time, and many investigators have struggled to develop accurate and robust algorithms for viscoelastic flows through contraction geometries [17, 18]. The contraction ratio 4 : 1 is the standard one in this benchmark problem. A good review of old works may be Trebotich et al. [18]. Recently, Phillips and Williams [11, 16] used a finite volume method to solve the flow of an Oldroyd-B fluid through planar and axisymmetric contractions. Among these two geometries, the axisymmetric contraction yields more dramatic viscoelastic effects. In the present investigation, we will solve the flow of Oldroyd-B fluid through the axisymmetric geometry using the grid-by-grid inversion method based on the SIMPLE algorithm to corroborate the accuracy and robustness of the grid-by-grid inversion method. When solving (2.8)-(2.9) or (2.17)-(2.18) using the SIMPLE algorithm, we adopt a collocated mesh and

the pressure oscillation induced by the collocated mesh is eliminated using the Rhie-Chow method [19], and a higher-order upwind scheme, MinMod [14], is used to treat the inertia force term in the momentum equation and the convective transport of stress tensor in the constitutive equation. For the 4 : 1 axisymmetric contraction geometry depicted in Figure 1, the number of relevant components of stress tensor is four because the $\nabla \cdot \boldsymbol{\tau}$ term in (2.9) contains a circular stress component $\tau^{\theta\theta}$ as follows:

$$\begin{aligned}(\nabla \cdot \boldsymbol{\tau})_r &= \frac{1}{r}\frac{\partial}{\partial r}(r\tau^{rr}) + \frac{\partial}{\partial z}\tau^{rz} - \frac{\tau^{\theta\theta}}{r},\\ (\nabla \cdot \boldsymbol{\tau})_z &= \frac{1}{r}\frac{\partial}{\partial r}(r\tau^{rz}) + \frac{\partial}{\partial z}\tau^{zz}.\end{aligned} \tag{3.1}$$

Although the relevant velocity components for axisymmetric flows are (v^r, v^z), it is necessary to find the four stress components, $\tau^{rr}, \tau^{rz}, \tau^{zz}$, and $\tau^{\theta\theta}$ which appear in (3.1). The constitutive equation (2.4) may be written for an axisymmetric geometry as follows:

$$\lambda\left(\frac{\partial \tau^{rr}}{\partial t} + v^r\frac{\partial \tau^{rr}}{\partial r} + v^z\frac{\partial \tau^{rr}}{\partial z}\right) = 2(1-\beta)\frac{\partial v^r}{\partial r} + \lambda\left(2\frac{\partial v^r}{\partial r}\tau^{rr} + 2\frac{\partial v^r}{\partial z}\tau^{rz}\right) - \tau^{rr}, \tag{3.2}$$

$$\begin{aligned}&\lambda\left(\frac{\partial \tau^{rz}}{\partial t} + v^r\frac{\partial \tau^{rz}}{\partial r} + v^z\frac{\partial \tau^{rz}}{\partial z}\right)\\ &\quad= (1-\beta)\left(\frac{\partial v^z}{\partial r} + \frac{\partial v^r}{\partial z}\right) + \lambda\left(\frac{\partial v^r}{\partial r}\tau^{rz} + \frac{\partial v^r}{\partial z}\tau^{zz} + \tau^{rr}\frac{\partial v^z}{\partial r} + \tau^{rz}\frac{\partial v^z}{\partial z}\right) - \tau^{rz},\end{aligned} \tag{3.3}$$

$$\lambda\left(\frac{\partial \tau^{zz}}{\partial t} + v^r\frac{\partial \tau^{zz}}{\partial r} + v^z\frac{\partial \tau^{zz}}{\partial z}\right) = 2(1-\beta)\frac{\partial v^z}{\partial z} + \lambda\left(2\frac{\partial v^z}{\partial r}\tau^{rz} + 2\frac{\partial v^z}{\partial z}\tau^{zz}\right) - \tau^{zz}, \tag{3.4}$$

$$\lambda\left(\frac{\partial \tau^{\theta\theta}}{\partial t} + v^r\frac{\partial \tau^{\theta\theta}}{\partial r} + v^z\frac{\partial \tau^{\theta\theta}}{\partial z}\right) = 2(1-\beta)\frac{v^r}{r} + \lambda\left(2\frac{v^r}{r}\tau^{\theta\theta}\right) - \tau^{\theta\theta}. \tag{3.5}$$

It is to be noted that equations for $(\tau^{rr}, \tau^{rz}, \tau^{zz})$ are coupled with each other, while that for $\tau^{\theta\theta}$ is decoupled. The relevant components of $\mathbf{C}$ of (2.6) are

$$C^{IJ} = v^r\frac{\partial \tau^{IJ}}{\partial r} + v^z\frac{\partial \tau^{IJ}}{\partial z}, \tag{3.6}$$

where $IJ = rr,\ rz,\ zz,\ \theta\theta$. Assuming known values of C^{IJ}, (3.2)–(3.4) may be represented as a set of matrix equations at each grid point including the boundary grids as follows:

$$\begin{bmatrix} \dfrac{\lambda}{\Delta t}+1-2\lambda\dfrac{\partial v^r}{\partial r} & -2\lambda\dfrac{\partial v^r}{\partial z} & 0 \\ -\lambda\dfrac{\partial v^z}{\partial r} & \dfrac{\lambda}{\Delta t}+1-\lambda\left(\dfrac{\partial v^r}{\partial r}+\dfrac{\partial v^z}{\partial z}\right) & -\lambda\dfrac{\partial v^r}{\partial z} \\ 0 & -2\lambda\dfrac{\partial v^z}{\partial r} & \dfrac{\lambda}{\Delta t}+1-2\lambda\dfrac{\partial v^z}{\partial z} \end{bmatrix}_{ik}^{n+1(it)} \begin{bmatrix} \tau^{rr} \\ \tau^{rz} \\ \tau^{zz} \end{bmatrix}_{ik}^{n+1(it+1)}$$
$$= \begin{bmatrix} \dfrac{\lambda\tau^{rr(n)}}{\Delta t}-\lambda C^{rr}+2(1-\beta)\dfrac{\partial v^r}{\partial r} \\ \dfrac{\lambda\tau^{rz(n)}}{\Delta t}-\lambda C^{rz}+(1-\beta)\left(\dfrac{\partial v^z}{\partial r}+\dfrac{\partial v^r}{\partial z}\right) \\ \dfrac{\lambda}{\Delta t}\tau^{zz(n)}-\lambda C^{zz}+2(1-\beta)\dfrac{\partial v^z}{\partial z} \end{bmatrix}_{ik}^{n+1(it)}. \tag{3.7}$$

On the other hand, from (3.5), $\tau_{ik}^{\theta\theta}$ can be found at each grid point within the computational domain and on the boundary as follows:

$$\left(\tau^{\theta\theta}\right)_{ik}^{n+1(it+1)} = \frac{\left(\dfrac{\lambda}{\Delta t}\left(\tau^{\theta\theta}\right)^n-\lambda C^{\theta\theta}+2(1-\beta)\dfrac{v^r}{r}\right)_{ik}^{n+1(it)}}{\left(\dfrac{\lambda}{\Delta t}+1-2\lambda\dfrac{v^r}{r}\right)_{ik}^{n+1(it)}}. \tag{3.8}$$

Once $(\tau_{ik}^{rr}, \tau_{ik}^{rz}, \tau_{ik}^{zz}, \tau_{ik}^{\theta\theta})^{n+1(it+1)}$ are obtained from (3.7)-(3.8), they are used to solve (2.8)-(2.9) to find $(v^r, v^z)_{ik}^{n+1(it+1)}$ in the 4 : 1 axisymmetric contraction geometry.

4. Results

In this section, we compare the results from the grid-by-grid inversion method with those of Phillips and Williams [11] to corroborate the accuracy and robustness of the grid-by-grid inversion method. To make the comparison meaningful, we adopt the same flow geometry and inlet conditions as those employed by Phillips and Williams [11]. Namely, the contraction

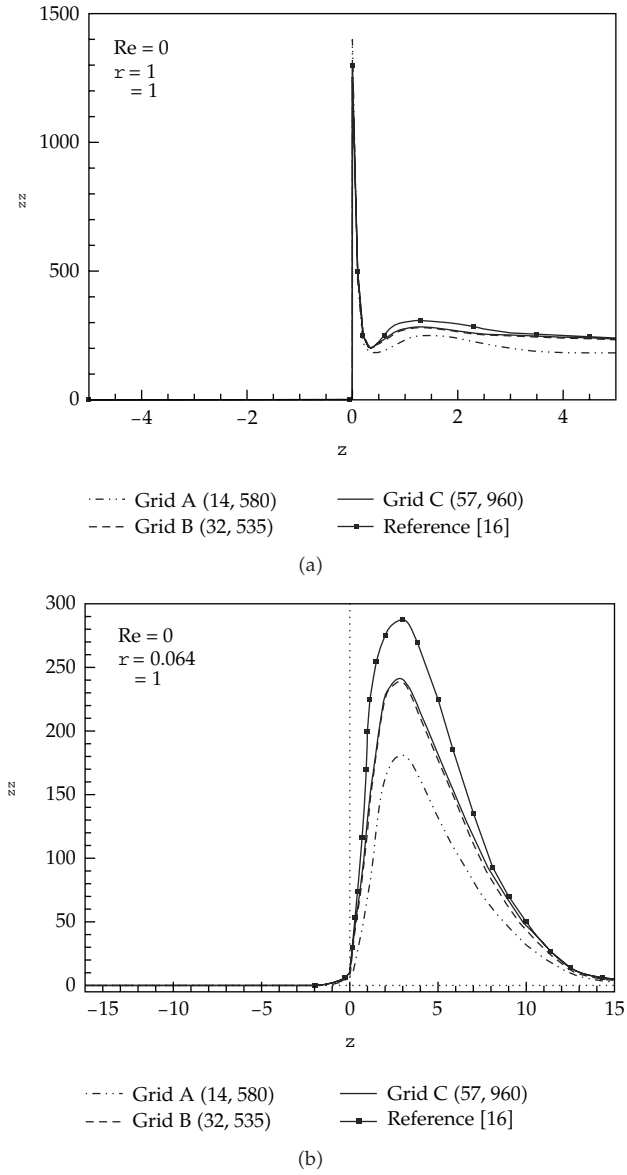

Figure 2: Confirmation of grid convergence of the grid-by-grid inversion method when Re = 0.0 and $\lambda = 1.0$ (a) along $r = 1.0$ (b) along $r = 0.064$.

ratio is 4 : 1, the length of the larger channel is $27R$, and that of smaller channel is $49R$ when R is the radius of the smaller channel (cf. Figure 1). At the inlet, the parabolic Poiseuille flow is adopted as Phillips and Williams [11] have done.

(-) inlet velocity

$$v^z(r) = \frac{1}{64}\left(16 - r^2\right), \quad v^r = 0, \ 0 \le r \le 4, \tag{4.1}$$

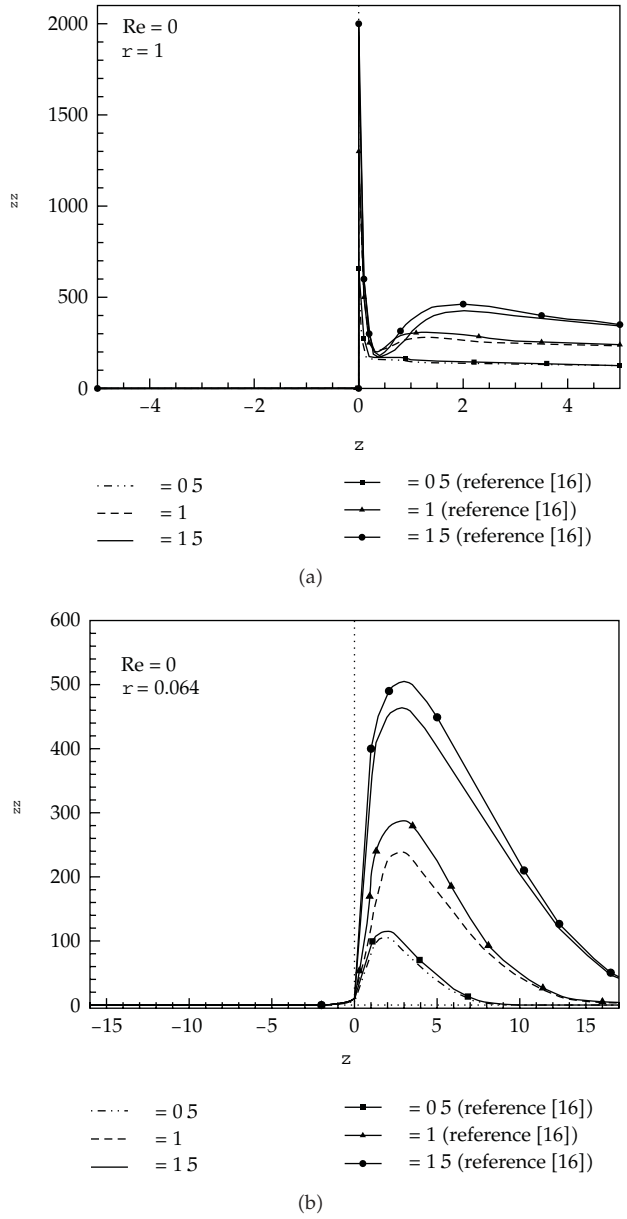

Figure 3: Stress overshoot at various λ when Re = 0.0 (a) along $r = 1.0$ (b) along $r = 0.064$.

where $r \equiv r'/R$ and r' is the dimensional radial distance. Contrary to Phillips and Williams [11], we do not impose inlet boundary conditions for the stress field, since the grid-by-grid inversion method does not require them and simply solve (3.7)-(3.8) at the inlet grid points to find the stress field at the inlet location. This is also an important merit of the grid-by-grid inversion method over other algorithms for the viscoelastic flows. Although Papanastasiou et al. [12] employed this method of imposing open outflow boundary conditions previously and named it open boundary condition method or free boundary condition method, it appears very naturally in the grid-by-grid inversion method.

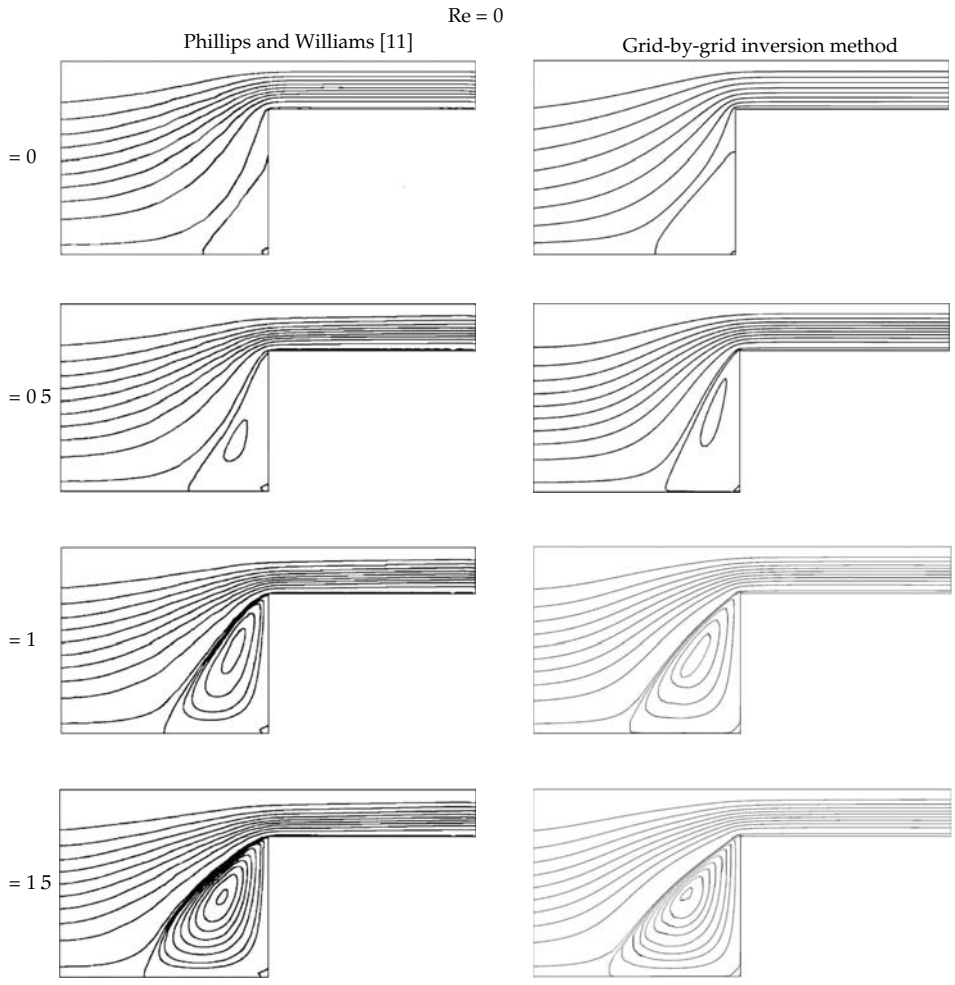

Figure 4: Comparison of streamlines for $\lambda = 0.0$, $\lambda = 0.5$, $\lambda = 1.0$, and $\lambda = 1.5$ when Re = 0.0.

We have employed three sets of grid system to ensure grid convergence of numerical results. For the three sets of grids, that is, 14,580 (Grid A), 32,535 (Grid B), and 57,960 (Grid C), the extrastress component τ^{zz} is plotted when $\lambda = 1.0$ for Re = 0.0 along $r = 1$ in Figure 2(a), and along $r = 0.064$ in Figure 2(b). For there three mesh systems, the numbers of cells along r in the small tube are 30, 45, and 60, respectively. For Grid A, the minimum Δr is 0.005 at the wall and it grows gradually until it becomes 5.1×10^{-2} at the center. For Grid B, $(\Delta r)_{\min}$ is 0.003 and $(\Delta r)_{\max}$ is 3.4×10^{-2} at the center, and for Grid C, $(\Delta r)_{\min} = 0.002$ at the wall and $(\Delta r)_{\max} = 2.3 \times 10^{-2}$ at the center. The results of the present work are also compared with those of Phillips and Williams [11]. Though the grid number increases from 32,535 to 57,960, there is not appreciable change in τ^{zz}. Therefore, we adopt Grid B in the subsequent computations. Figure 3 shows the extrastress component τ^{zz} at Re = 0.0 for $\lambda = 0.5, 1.0,$ and 1.5 along $r = 1.0$ (Figure 2(a)) and along $r = 0.064$ (Figure 2(b)). The grid-converged data for τ^{zz} obtained from the grid-by-grid inversion method are somewhat smaller than the benchmark data of Phillips and Williams [11]. At the corner of the contractor, τ^{zz} has a sharp overshoot, which increases with respect to λ, and it settles down to a downstream

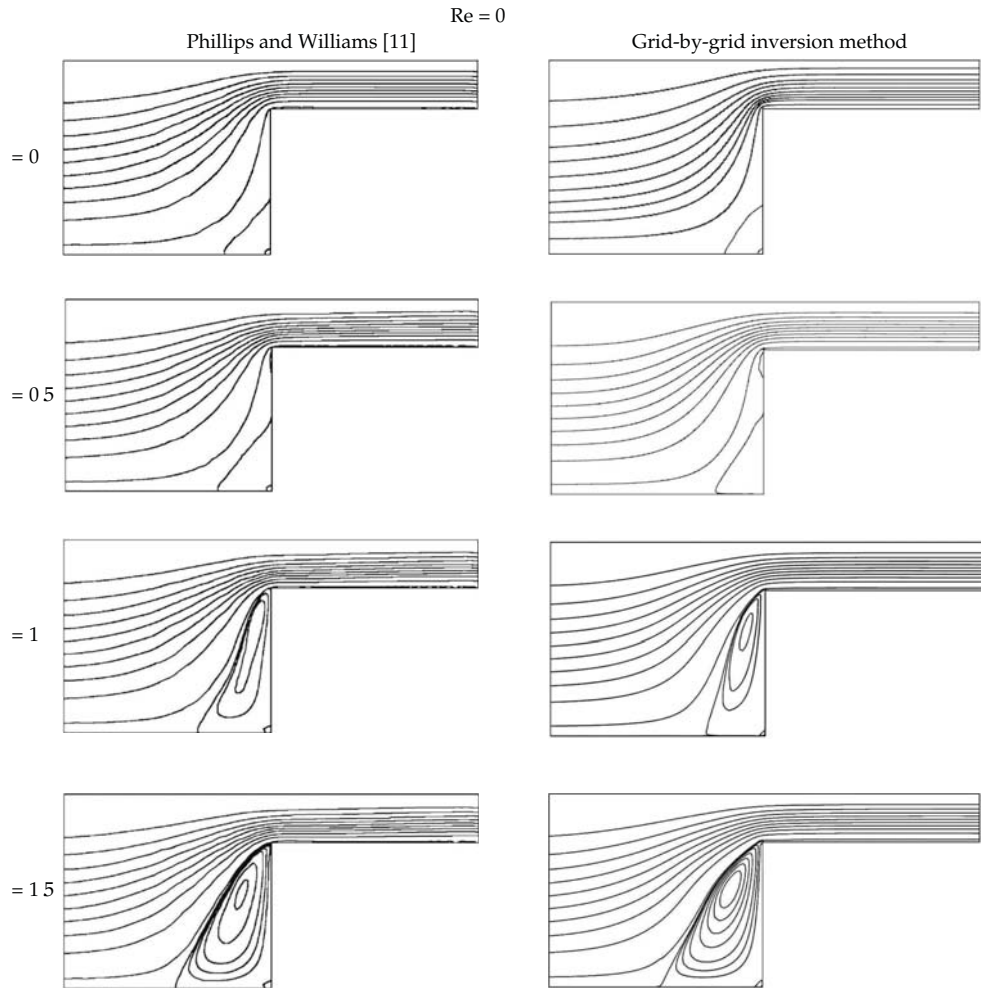

Figure 5: Comparison of streamlines for $\lambda = 0.0$, $\lambda = 0.5$, $\lambda = 1.0$, and $\lambda = 1.5$ when Re = 1.0.

value rapidly. Near the center of the contracted channel ($r = 0.064$), a smaller overshoot of τ^{zz} appears, which increases as λ increases, and it settles down to a downstream value much slowly as compared to that at the wall ($r = 1.0$).

Figure 4 shows comparison of streamlines for $\lambda = 0.0$, 0.5, 1.0, and 1.5 obtained from the grid-by-grid inversion method with those from the Phillips and Williams [11] when Re = 0.0. The grid-by-grid inversion method yields accurate results as compared with the benchmark data for the range of λ values considered. The size of the corner vortex increases as λ increases. Figure 5 depicts comparison of streamlines at various values of λ when Re = 1.0. The predictions of the grid-by-grid inversion method are also in good agreement with those of the benchmark data [11]. Comparing with the streamlines of Re = 0.0, it is found that the vortex sizes are diminished due to the inertia effect [11]. The size of the corner vortex can be measured using a parameter L_1, as suggested by Phillips and Williams [11] and Oliveira et al.[8], which is the distance of the upstream separation point from the salient corner. Figure 6 shows the variation of L_1 with respect to λ for Re = 0.0 and Re = 1.0.

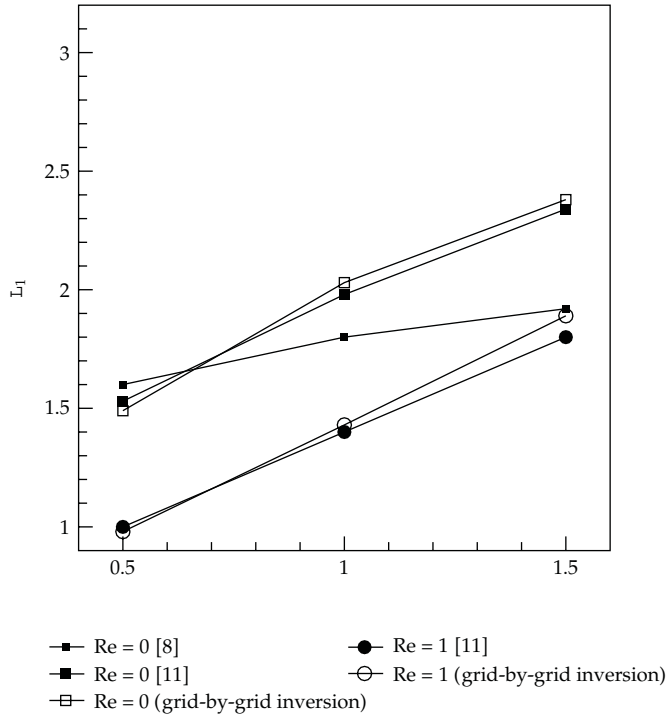

Figure 6: Variation of the size of corner vortex L_1 with respect to λ when Re = 0.0 and Re = 1.0.

For Re = 1.0, the grid-by-grid inversion method is found to yield results similar to those of the benchmark data of Phillips and Williams [11]. For Re = 0.0, the results of the grid-by-grid inversion method are compared with those of Oliveira et al. [8] as well as those of Phillips and Williams [11]. It is shown that both the grid-by-grid inversion and Phillips and Williams [11] yield L_1 somewhat larger than those of Oliveira et al. [8]. Since Oliveira et al. [8] do not consider the case Re = 1.0, we cannot compare the grid-by-grid inversion method with Oliveira et al. when Re = 1.0. To corroborate the accuracy of the grid-by-grid inversion method further, we compare the results for the vortex intensity Ψ_R, which is defined as the flow rate in recirculation divided by inlet flow rate, in Figure 7 when Re = 0.0. As in previous comparison, the grid-by-grid inversion method yields results similar to those of Phillips and Williams [11], while Oliveira et al. [8] predicts results somewhat smaller than the grid-by-grid inversion method. The grid-by-grid inversion method yields results for λ larger than 1.5 and Re larger than 1.0, which demonstrates the robustness of the grid-by-grid inversion method as compared to other finite volume methods or finite element methods [9, 11, 16, 18].

5. Conclusion

The grid-by-grid inversion method [10] has been applied to the 4 : 1 circular contraction problem in the present investigation. Viscoelastic flows through the contraction generate complex flows exhibiting strong shear and uniaxial extension, which is a good test bed for the robustness and accuracy of a new numerical algorithms. In the grid-by-grid inversion

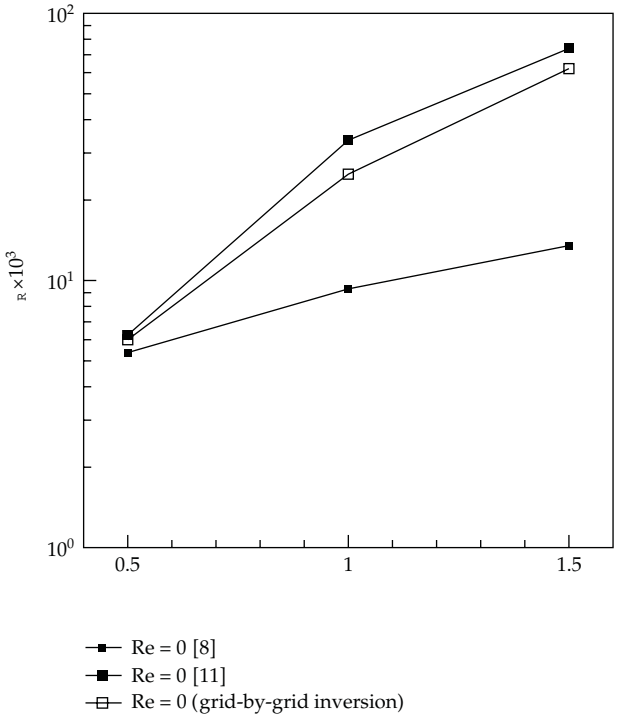

Figure 7: Variation of the dimensionless vortex intensity Ψ_R with respect to λ when Re = 0.0.

method [10], the hyperbolic constitutive equation is split such that the term for the convective transport of stress tensor is treated as a source, which is updated iteratively. This allows the stress tensor at each grid point to be expressed in terms of velocity gradient tensor at the same location, and the set of stress tensor components is found after inverting a small matrix at each grid point. The grid-by-grid inversion method can be implemented easily in any commercial CFD packages for Newtonian fluid flows to convert them to be used for viscoelastic fluid flows. The grid-by-grid inversion method is found to yield accurate results as compared with the benchmark data of Phillips and Williams [11]. It predicts accurately the variation of corner vortex size and the τ^{zz} overshoot with respect to λ at Re = 0.0 and Re = 1.0.

Acknowledgment

This paper was supported by the Human Resources Development of the Korea Institute of Energy Technology Evaluation and Planning (KETEP) Grant funded by the Korea Government Ministry of Knowledge and Economy (no. 20114010203090).

References

[1] R. B. Bird, R. C. Amstrong, and O. Hassager, *Dynamics of Polymeric Liquids*, vol. 1, Wiley, New York, NY, USA, 1987.

[2] R. R. Huilgol and N. Phan-Thien, *Fluid Mechanics of Viscoelasticity*, Elsevier, Amsterdam, The Netherlands, 1997.

[3] D. D. Joseph, *Fluid Dynamics of Viscoelastic Liquids*, vol. 84 of *Applied Mathematical Sciences*, Springer, 1990.
[4] M. A. Alves, F. T. Pinho, and P. J. Oliveira, "The flow of viscoelastic fluids past a cylinder: finite-volume high-resolutions method," *Journal of Non-Newtonian Fluid Mechanics*, vol. 97, no. 2-3, pp. 207–232, 2001.
[5] M. J. Crochet, A. R. Davis, and K. Walters, *Numerical Simulation of Non-Newtonian Flow*, Elsevier, Amsterdam, The Netherlands, 1984.
[6] F. Yurun and M. J. Crochet, "High-order finite element methods for steady viscoelastic flows," *Journal of Non-Newtonian Fluid Mechanics*, vol. 57, no. 2-3, pp. 283–311, 1995.
[7] B. Khomami, K. K. Talwar, and H. K. Ganpule, "A comparative study of higher- and lower-order finite element techniques for computation of viscoelastic flows," *Journal of Rheology*, vol. 38, no. 2, pp. 255–289, 1994.
[8] M. S. N. Oliveira, P. J. Oliveira, F. T. Pinho, and M. A. Alves, "Effect of contraction ratio upon viscoelastic flow in contractions: the axisymmetric case," *Journal of Non-Newtonian Fluid Mechanics*, vol. 147, no. 1-2, pp. 92–108, 2007.
[9] R. G. Owens and T. N. Phillips, *Computational Rheology*, Imperial College Press, London, UK, 2002.
[10] H. M. Park and J. Y. Lim, "A new numerical algorithm for viscoelastic fluid flows: the grid-by-grid inversion method," *Journal of Non-Newtonian Fluid Mechanics*, vol. 165, no. 5-6, pp. 238–246, 2010.
[11] T. N. Phillips and A. J. Williams, "Comparison of creeping and inertial flow of an Oldroyd B fluid through planar and axisymmetric contractions," *Journal of Non-Newtonian Fluid Mechanics*, vol. 108, no. 1–3, pp. 25–47, 2002.
[12] T. C. Papanastasiou, N. Malamataris, and K. Ellwood, "A new outflow boundary condition," *International Journal for Numerical Methods in Fluids*, vol. 14, no. 5, pp. 587–608, 1992.
[13] S. V. Patankar, *Numerical Heat Transfer and Fluid Flow*, Hemisphere, New York, NY, USA, 1980.
[14] H. K. Versteeg and W. Malalasekera, *An Introduction to Computational Fluid Dynamics*, Pearson Education Limited, Essex, UK, 2007.
[15] M. G. N. Perera and K. Walters, "Long-range memory effects in flows involving abrupt changes in geometry: part1. Flows associated with L-shaped and T-shaped geometries," *Journal of Non-Newtonian Fluid Mechanics*, vol. 2, no. 2, pp. 191–204, 1977.
[16] T. N. Phillips and A. J. Williams, "Viscoelastic flow through a planar contraction using a semi-Lagrangian finite volume method," *Journal of Non-Newtonian Fluid Mechanics*, vol. 87, no. 2-3, pp. 215–246, 1999.
[17] R. Keunings and M. J. Crochet, "Numerical simulation of the flow of a viscoelastic fluid through an abrupt contraction," *Journal of Non-Newtonian Fluid Mechanics*, vol. 14, pp. 279–299, 1984.
[18] D. Trebotich, P. Colella, and G. H. Miller, "A stable and convergent scheme for viscoelastic flow in contraction channels," *Journal of Computational Physics*, vol. 205, no. 1, pp. 315–342, 2005.
[19] C. M. Rhie and W. L. Chow, "Numerical study of the turbulent flow past an airfoil with trailing edge separation," *AIAA Journal*, vol. 21, no. 11, pp. 1525–1532, 1983.

Hindawi Publishing Corporation
Journal of Applied Mathematics
Volume 2012, Article ID 727839, 13 pages
doi:10.1155/2012/727839

Research Article

A Platoon Dispersion Model Based on a Truncated Normal Distribution of Speed

Ming Wei, Wenzhou Jin, and Lvou Shen

Department of Transportation Engineering, South China University of Technology, Guangzhou 510640, China

Correspondence should be addressed to Ming Wei, oscar.weiming@gmail.com

Received 24 November 2011; Revised 31 December 2011; Accepted 31 December 2011

Academic Editor: M. F. El-Amin

Understanding platoon dispersion is critical for the coordination of traffic signal control in an urban traffic network. Assuming that platoon speed follows a truncated normal distribution, ranging from minimum speed to maximum speed, this paper develops a piecewise density function that describes platoon dispersion characteristics as the platoon moves from an upstream to a downstream intersection. Based on this density function, the expected number of cars in the platoon that pass the downstream intersection, and the expected number of cars in the platoon that do not pass the downstream point are calculated. To facilitate coordination in a traffic signal control system, dispersion models for the front and the rear of the platoon are also derived. Finally, a numeric computation for the coordination of successive signals is presented to illustrate the validity of the proposed model.

1. Introduction

At an intersection, lights change from red to green permitting drivers to proceed straight through the intersection. On urban roads these cars will be traveling at different speeds. While moving downstream, the platoon spreads out in a long segment and cars do not uniformly arrive at the next intersection; this is called platoon dispersion. As a platoon moves downstream from an upstream intersection at green phase end time, the cars in the platoon become segmented due to compression and splitting at the downstream intersection's signal lights. It is obvious that using platoon dispersion theory to optimize signal timing plans for traffic signal control could effectively reduce the number of stops and thereby lead to a sharp decline in pollution emissions and fuel consumption.

However, platoon dispersion makes signal coordination more complicated [1–17]. Previous studies on the diffusion of traffic platoons have adopted one of three standard

approaches: the wave theory of Lighthill and Whitham [1–3], Pacey's diffusion theory [4–9], and Robertson's recursive platoon dispersion model [10–12]. The first model, also called the LWR model in the literature of traffic flow theory, needs to have an accurate representation of the equilibrium flow-density relationship, which makes it unsuitable for practical applications [13]. The second approach firstly proposes a purely kinematical model to describe the diffusion of traffic platoons by assuming that the speed of traffic follows a normal distribution [4]. Its invalid input parameters (viz. the average speed of vehicles and standard deviation of speed) to calibrate the model make it suitable only for the study of small changes in traffic cycles [6]. The final model uses field data to derive an empirical method for predicting platoon behavior and has been widely used in the well-known TRANSYT software model, because of its simplicity and good explanatory power for understanding the qualitative behavior of road traffic [12]. Both Pacey's and Robertson's models are probability-based models with different probability density functions. Seddon [14, 15] concluded in his series of studies on different models of platoon dispersion that there is little difference between the Pacey and Robertson methods with regards to accuracy or efficiency. However, a study by Wang et al. [16] concluded that the recursive model gives good results for short distances, while models using lognormal and normal distributions are better for longer distances.

As mentioned previously, Pacey's model is the most successful combination of theoretical and experimental work on traffic platoons. Most current research based on this model assumes that platoon speed follows a normal distribution, spreading from negative infinity to positive infinity. This does not properly reflect the field situation. Grace and Potts [5] further investigated the density aspect of Pacey's model. Liu and Yang [6–8] proposed a method to correct the vehicle startup time loss of Grace's model. Wang et al. [9] also further refined Pacey's model by considering travel time following a nontransformed normal distribution.

To address the defects of Pacey's model, the authors of this paper propose a more realistic platoon dispersion model, which assumes that the velocity of cars follows a truncated normal distribution, ranging from a minimum speed to a maximum speed [17]. On the basis of the authors' previous research, this paper analyzes platoon dispersion characteristics as the platoon moves down from an upstream intersection at green phase end time. Finally, numeric computation applying the model to signal coordination is presented to confirm the model's validity.

2. Platoon Dispersion Model

2.1. Assumptions of the Speed Density Function

In Pacey's model, the cars in a platoon are assumed to move with unchanged speeds (i.e., it is ideally treated as the average speed of vehicles measured between adjacent intersections). It is assumed that (a) all the vehicles behind the stop lines uniformly start up after the signal turns from red to green, (b) a car's speed is independent of its position in a platoon, and (c) there is no interaction between cars and a faster car can pass a slower one without hindrance.

A definite value is assigned to the probability that certain cars will have positive speed. Pacey's research has proven that car speeds in a platoon are normally distributed with mean μ and variance σ^2, which accounts for the spread of platoons. However, the proportion of cars with $v < v_m$ and $v > v_f$ is zero in reality (v_m and v_f denote minimum speed and maximum

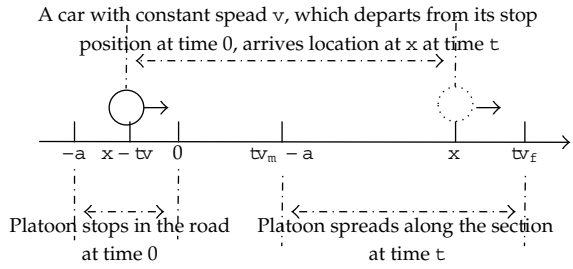

Figure 1: Spreading of platoon.

speed, resp.). Hence, a speed range in a truncated normal distribution extending from v_m to v_f is a much more reasonable assumption. In this case, the speed density function is as follows:

$$f'(v) = \begin{cases} c\dfrac{1}{\sqrt{2\pi}\sigma}e^{-0.5((v-\mu)/\sigma)^2}, & v_m \le v \le v_f, \\ 0, & \text{others.} \end{cases} \tag{2.1}$$

Its calculation formula can be expressed as follows:

(a) for $v < v_m : F'(v) = \int_{-\infty}^{v_m} f'(v)dx = 0$;

(b) for $v_m \le v \le v_f : F'(v) = \int_{-\infty}^{v} f'(v)dx = \int_{v_m}^{v} f'(v)dx = c[\int_{-\infty}^{v}(1/(\sqrt{2\pi}\sigma))e^{-0.5((v-\mu)/\sigma)^2}dx - \int_{-\infty}^{v_m}(1/(\sqrt{2\pi}\sigma))e^{-0.5((v-\mu)/\sigma)^2}dx] = c[F(v) - F(v_m)]$;

(c) for $v > v_f : F'(v) = \int_{v_m}^{v} f'(v)dx = \int_{v_m}^{v_f} f'(v)dx = c[F(v_f) - F(v_m)] = 1$.

As the constant c ensures that the accumulated probability of $f'(v)$ in the range $[v_m, v_f]$ equals 1, then $1/c = F(v_m \le v \le v_f) = \phi(v_f/\sigma - \mu/\sigma) - \phi(v_m/\sigma - \mu/\sigma)$.

2.2. Development of the Platoon Dispersion Model

Assuming that the start time of the upstream signal green phase t equals 0, and the stop bar location x is 0, then the initial density distribution function $k(x,0)$ of the queuing vehicles behind the stop bar at time $t = 0$ is

$$k(x,0) = \begin{cases} 0, & x \ge 0, \\ k_j, & -a \le x \le 0, \\ 0, & x < -a, \end{cases} \tag{2.2}$$

where a is the queue length and k_j is the jam density within the queue length.

This paper studies the movement of a platoon from the beginning of a green phase, until it passes a downstream intersection. As illustrated in Figure 1, the queuing vehicles at the upstream intersection start traveling at constant speed v from their stop position $x - vt \in [-a, 0]$ at the start time of the green phase $t = 0$. After time t, the number of vehicles having passed the downstream intersection (real or virtual) and the number that have not past the

downstream intersection are $A(x,t)$ and $B(x,t)$, respectively. The computation formula is derived according to the aforementioned physical definition and presented as follows:

$$\begin{aligned} A(x,t) &= \int_{x}^{t\cdot v_f} k(y,t)\,dy, \\ B(x,t) &= k_j a - A(x,t) = \int_{tv_m - a}^{x} k(y,t)\,dy, \end{aligned} \tag{2.3}$$

where $k(y,t)$ is the density of the platoon past y at time t. The density distribution function $k(x,t)$, at downstream location x at time t, is calculated using the following piecewise function:

$$k(x,t) = \int_{v_m}^{v_f} f'(v)k(x - vt, 0)\,dv = \begin{cases} 0, & x > tv_f \vee x < tv_m - a, \\ k_j \displaystyle\int_{v_m}^{x/t+a/t} f'(v)\,dv, & tv_m - a \le x < tv_m, \\ k_j \displaystyle\int_{x/t}^{x/t+a/t} f'(v)\,dv, & tv_m \le x \le tv_f - a, \\ k_j \displaystyle\int_{x/t}^{v_f} f'(v)\,dv, & tv_f - a < x \le tv_f. \end{cases} \tag{2.4}$$

Let $u = (v - \mu)/\sigma$, and the variation coefficient $\alpha = \sigma/\mu$, as follows:

$$\int_{v_1}^{v_2} f'(v)\,dv = c\int_{(v_1-\mu)/\sigma}^{(v_2-\mu)/\sigma} \frac{1}{\sqrt{2\pi}} e^{-0.5u^2}\,du = c\int_{(tv_1/\mu - t)/\alpha t}^{(tv_2/\mu - t)/\alpha t} \frac{1}{\sqrt{2\pi}} e^{-0.5u^2}\,du = \frac{c}{2}[F(z)]_{z_1}^{z_2}, \tag{2.5}$$

where $z_2 = (tv_2/\mu - t)/\sqrt{2}\alpha t$, $z_1 = (tv_1/\mu - t)/\sqrt{2}\alpha t$, v_1 and v_2 are constants, and $F(z) = 2\int_0^{\sqrt{2}z}(1/\sqrt{2\pi})e^{-0.5u^2}\,du = (2/\sqrt{\pi})\int_0^z e^{-u^2}\,du$ is the standard normal distribution.

Following (2.4) and (2.5), the calculation formula of $k(x,t)$ is as follows:

$$k(x,t) = \begin{cases} 0, & x > tv_f \vee x < tv_m - a, \\ \dfrac{ck_j}{2}[F(z)]_{(tv_m/\mu - t)/\sqrt{2}\alpha t}^{(x/\mu + a/\mu - t)/\sqrt{2}\alpha t}, & tv_m - a \le x < tv_m, \\ \dfrac{ck_j}{2}[F(z)]_{(x/\mu - t)/\sqrt{2}\alpha t}^{(x/\mu + a/\mu - t)/\sqrt{2}\alpha t}, & tv_m \le x \le tv_f - a, \\ \dfrac{ck_j}{2}[F(z)]_{(x/\mu - t)/\sqrt{2}\alpha t}^{(tv_f/\mu - t)/\sqrt{2}\alpha t}, & tv_f - a < x \le tv_f. \end{cases} \tag{2.6}$$

Let $G(z) = \int F(z)dz = zF(z) + (1/\sqrt{\pi})\exp(-z^2)$; then, based on (2.6), the number of vehicles $\int_{x_1}^{x_2} k(y,t)dy$ distributed along the road segment $[x_1, x_2]$ can be calculated as follows:

$$\begin{aligned}\int_{x_1}^{x_2} k(y,t)dy &= \frac{c\cdot k_j}{2}\int_{x_1}^{x_2}\left[F(z_2(y)) - F(z_1(y))\right]dy \\ &= \frac{ck_j\mu\sqrt{2}\alpha t}{2}\left[\int_{z_2(x_1)}^{z_2(x_2)} F(y)dy - \int_{z_1(x_1)}^{z_1(x_2)} F(y)dy\right] \\ &= \frac{ck_j\mu\sqrt{2}\alpha t}{2}\left([G(z)]_{z_2(x_1)}^{z_2(x_2)} - [G(z)]_{z_1(x_1)}^{z_1(x_2)}\right).\end{aligned} \tag{2.7}$$

Using (2.6) and (2.7), $A(x,t)$ and $B(x,t)$ can be calculated under the following five scenarios:

(a) for $x > tv_f$: $A(x,t) = 0$ and $B(x,t) = \int_{t\cdot v_m - a}^{t\cdot v_m} k(y,t)dy + \int_{t\cdot v_m}^{t\cdot v_f - a} k(y,t)dy + \int_{t\cdot v_f - a}^{t\cdot v_f} k(y,t)dy$;

(b) for $tv_f - a < x \le tv_f$: $A(x,t) = \int_{x}^{t\cdot v_f} k(y,t)dy$ and $B(x,t) = \int_{t\cdot v_m - a}^{t\cdot v_m} k(y,t)dy + \int_{t\cdot v_m}^{t\cdot v_f - a} k(y,t)dy + \int_{t\cdot v_f - a}^{x} k(y,t)dy$;

(c) for $tv_m \le x \le tv_f - a$: $A(x,t) = \int_{x}^{t\cdot v_f - a} k(y,t)dy + \int_{t\cdot v_f - a}^{t\cdot v_f} k(y,t)dy$ and $B(x,t) = \int_{t\cdot v_m - a}^{t\cdot v_m} k(y,t)dy + \int_{t\cdot v_m}^{x} k(y,t)dy$;

(d) for $tv_m - a \le x < tv_m$: $A(x,t) = \int_{t\cdot v_m}^{t\cdot v_f - a} k(y,t)dy + \int_{x}^{t\cdot v_m} k(y,t)dy + \int_{t\cdot v_f - a}^{t\cdot v_f} k(y,t)dy$ and $B(x,t) = \int_{t\cdot v_m - a}^{x} k(y,t)dy$;

(e) for $x < tv_m - a$: $A(x,t) = \int_{t\cdot v_m - a}^{t\cdot v_m} k(y,t)dy + \int_{t\cdot v_m}^{t\cdot v_f - a} k(y,t)dy + \int_{t\cdot v_f - a}^{t\cdot v_f} k(y,t)dy$ and $B(x,t) = 0$.

The platoon dispersion model proposed in this paper is described in the previous section. If x is set as the upstream and downstream signal location, then how dispersion characteristics of the queuing vehicles at the upstream intersection influence the downstream green phase start time setup can be quantitatively analyzed, as the platoon moves down from an upstream intersection at green phase end time to downstream intersection. The results can be used to calculate the traffic flow parameters used in signal coordination, such as delay stop and queue length.

3. The Front and Rear of a Platoon in the Dispersion Model

In general, only dispersion behavior at the front and rear of the platoon is important in traffic signal coordination. When adjacent intersections are not too far apart, fast cars at the rear of the platoon are unable to get to the front and the slower cars at the front do not have time to filter back to the rear. Hence, the front and rear of the platoons may be treated separately.

3.1. Front of the Platoon

A good design of coordinated lights aims at reducing the number of platoon leaders stopped at the second intersection before its light turns green. The rear does not significantly affect the front, which helps in the mathematical analysis of the behavior of the front of the platoon. Using Pacey's assumptions, the initial density function $k(x,0)$ of the front of the platoon is defined by

$$k(x,0) = \begin{cases} 0, & x > 0, \\ k_j, & x \le 0. \end{cases} \tag{3.1}$$

The density of the front of the platoon past x at time t, as obtained from (2.4) and (2.5), is

$$\begin{aligned} k(x,t) &= ck_j \int_{(x/\mu - t)/\alpha t}^{(tv_f/\mu - t)/\alpha t} \frac{1}{\sqrt{2\pi}} e^{-0.5y^2} dv \\ &= \frac{ck_j}{2}\left[F\left(z_2 = \frac{tv_f/\mu - t}{\sqrt{2}\alpha t}\right) - F\left(z_1 = \frac{x/\mu - t}{\sqrt{2}\alpha t}\right)\right] \\ &= \frac{ck_j}{2}[F(z)]_{z_1}^{z_2}. \end{aligned} \tag{3.2}$$

As mentioned previously, cars at the front travel at a range of speeds $[\mu, v_f]$, leading to the spread of cars along the section $[t\mu, tv_f]$. Hence, the number of cars $A(x,t)$ from the front of the platoon that have passed the downstream location x at time t can be calculated under the following three scenarios:

(a) for $x \le t\mu$: $A(x,t) = ((ck_j\mu\sqrt{2}\ \alpha t)/2)[zF((tv_f/\mu - t)/\sqrt{2}\alpha t) - G(z)]_0^{(tv_f/\mu - t)/\sqrt{2}\alpha t)}$;

(b) for $t\mu < x \le tv_f$: $A(x,t) = (ck_j/2)F((tv_f/\mu - t)/\sqrt{2}\alpha t)(tv_f - x) - ((ck_j\mu\sqrt{2}\ \alpha t)/2)[G(z)]_{(x/\mu - t)/\sqrt{2}\alpha t)}^{(tv_f/\mu - t)/\sqrt{2}\alpha t)}$;

(c) for $x > tv_f$: $A(x,t) = 0$.

3.2. Rear of the Platoon

Another goal of signal coordination is to reduce the number of stragglers at the rear who miss the green phase. Assuming the upstream signal green time ends at time 0, the initial density function $k(x,0)$ of the rear of the platoon, according to Pacey's assumptions, is defined by

$$k(x,0) = \begin{cases} 0, & x < 0, \\ k_2, & x \ge 0, \end{cases} \tag{3.3}$$

where $k_2 \le k_j$ is the density near the rear of the platoon.

Applying a similar limit process to (3.2) to calculate the proportion of the rear of platoon that has past x at time t, we obtain

$$k(x,t) = ck_2 \int_{(tv_m/\mu - t)/\alpha t}^{(x/\mu - t)/\alpha t} \frac{1}{\sqrt{2\pi}} e^{-0.5y^2} dv = \frac{ck_2}{2}\left[F\left(z_2 = \frac{x/\mu - t}{\sqrt{2}\alpha t}\right) - F\left(z_1 = \frac{tv_m/\mu - t}{\sqrt{2}\alpha t}\right)\right] = \frac{ck_2}{2}[F(z)]_{z_1}^{z_2}. \tag{3.4}$$

The previous calculations show that the speed of vehicles in the rear of the platoon is less than μ, which means that these vehicles are spread out along the section $[tv_m, t\mu]$. Hence, the number of cars $B(x,t)$ from the rear that have not passed the downstream location x at time t can be calculated under the following three scenarios:

(a) for $x \le tv_m : B(x,t) = 0$;

(b) for $tv_m < x \le t\mu : B(x,t) = ((ck_2\mu\sqrt{2}\alpha t)/2)[G(z)]_{(tv_m/\mu - t)/\sqrt{2}\alpha t}^{(x/\mu - t)/\sqrt{2}\alpha t} - (ck_2/2)(x - tv_m)F((tv_m/\mu - t)/\sqrt{2}\alpha t)$;

(c) for $x > t\mu : B(x,t) = ((ck_2\mu\sqrt{2}\alpha t)/2)[-zF((tv_m/\mu - t)/\sqrt{2}\alpha t) + G(z)]_{(tv_m/\mu - t)/\sqrt{2}\alpha t}^{0}$.

4. Numerical Calculation

Form proposed model, k_j and k_2 are not related with diffusion of platoons, which arises only from the differences in speed between vehicles (k_j and k_2 only decide how many cars are spreading along road). Wei et al.'s study shows that the initial flow is approximately a rectangular pulse with maximum flow $Q = k_j\mu = k_2\mu$ [17]. Hence, $k(x,t)$, $A(x,t)$, and $B(x,t)$ could be replaced by $k(x,t)/Q$, $A(x,t)/Q$, and $B(x,t)/Q$ to calibrate the model. Using test data in Grace and Potts's paper [5], upstream intersection $x = 0$ and downstream intersection $x = x_d$ have the following parameters: $v_m = 10.1\,\text{m/s}$, $v_f = 33.5\,\text{m/s}$, $\mu = 13.4\,\text{m/s}$, and $\sigma = 2\,\text{m/s}$. Generally, if the offset of the downstream intersection is set as $t_0 = x_d/\mu$, then the queuing vehicles at the upstream intersection, travelling at an average speed, can pass downstream intersection at the time.

To verify the validity of the proposed model, this paper compares the difference between the front and rear platoon dispersion characteristics in the proposed model and in Pacey's model. Furthermore, the effect of changing parameter α is examined hereinafter, to quantify how it affects the spreading of the platoon.

4.1. Platoon Density Distribution Function

The difference in the density distribution function between proposed model and Pacey's model decides that our model is more realistic than Pacey's model. In order to prove that, $k(x,t)/Q$, which denotes the ratio to the maximum initial flow of density of platoon past x at time t, is calculated for both the proposed model and Pacey's model at three time points $t = t_o\mu/v_f$, t_o, $(t_o\mu + a)/v_m$ under $x_d = 45\,\mu$, and the results are shown in Figure 2.

The following can be concluded based on Figure 2.

(a) The speed density of both Pacey's model and proposed model follows a normal distribution, which lead to a situation that there are more vehicles traveling

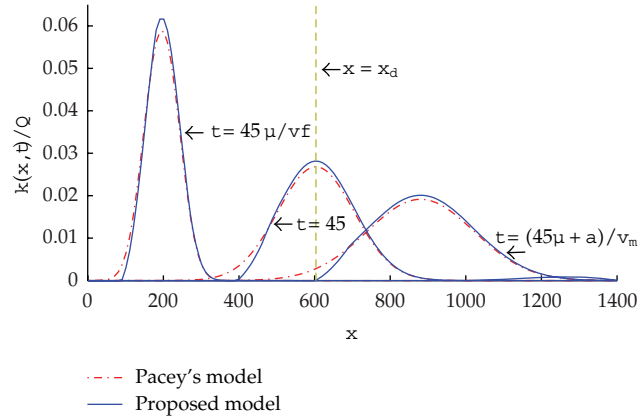

Figure 2: Comparison of the proposed model's and Pacey's density distribution function $k(x,t)$ under $x_d = 45\,\mu$.

around the mean speed, and fewer vehicles at higher or lower speeds. The speed distribution determines the platoon density distribution function. Therefore, the density in the middle of the platoon is higher than that in the front or rear of the platoon. As time passes, the platoon becomes more dispersed along the road, and the hump of the platoon density distribution function becomes less significant.

(b) In the proposed model, the queuing vehicles traveling at different speed v depart from their stop positions at time 0, and these cars are spreading along the section $x \in [tv_m - a, tv_f]$ at time t. There are the following three stages: if time is $t \in [0, t_0\mu/v_f]$, the front of platoon has not arrived at the downstream intersection $x = x_d$, then $tv_f < x_d$, and $k(x_d,t) = 0$; if time is $t \in [t_0\mu/v_f, (t_0\mu + a)/v_m]$, some vehicles are starting to pass the downstream intersection $x = x_d$, and $tv_m - a \le x_d \le tv_f$ and $k(x_d,t) \neq 0$; if time is $t \in [(t_0\mu + a)/v_m, +\infty]$, the rear of the platoon has passed the downstream intersection location $x = x_d$, and $tv_m - a > x_d$ and $k(x_d,t) = 0$.

(c) In Pacey's model, the spread of vehicles in the speed range $[v_m, v_f]$ during time period $t \in [t_0\mu/v_f, (t_0\mu + a)/v_m]$ is same as proposed model. However, Pacey's model assumes that speed is extending within the range $[-\infty, +\infty]$. It is impossible for a vehicle to have a positive infinity speed to travel to downstream infinity or a negative infinity speed to travel backwards to upstream infinity, which obviously does not match the field observations. Therefore, the application of Pacey's model is limited.

(d) The difference in the speed density between proposed model and Pacey's model decides that there are also more cars in the middle of the platoon and fewer cars in the two tails in the former, compared to the latter.

4.2. *Number of Cars at the Front That Have Passed the Downstream Intersection*

If the green phase of the downstream intersection is started at $t_0 = x_d/\mu$, as cars in the front of the platoon travel at a speed greater than μ, then the downstream signal needs to turn green t_h in advance of t_0 to allow more vehicles to pass during the green phase. That is to say,

the number of cars stopped at the front of platoon is $A(x_d, t_o - t_h)$. For $t_0 = 30, 60, 90, 120$ and $t_h = 0, 1, 2, 10$, $A(x_d, t_o - t_h)/Q$, which denotes the ratio to the maximum initial flow of the average number of cars stopped at the front of the platoon, is calculated for both the proposed model and Pacey's model, and the results are presented in Table 1.

Table 1 shows that as the distance between the successive intersections increases, the speed range of the front of the platoon $[\mu + a/t_0, v_f]$ increases and $A(x_d, t_o)$ also increases. Therefore, a higher preset t_h is needed to allow more cars at the front of platoon to pass the downstream intersection. The difference in $A(x_d, t_o - t_h)$ between the proposed model and Pacey's model is 4.78%, that is, $((c-1)/c)100\%$. The difference is a result of the assumption in Pacey's model that the speed spreads from negative infinity to positive infinity, which results in an accumulated probability in the area of $[v_m, v_f]$ less than 1.

4.3. Number of Cars at the Rear That Have Not Passed the Downstream Intersection

It is assumed that the downstream signal green time ends at time $t_0 = (x_d + a)/\mu$. According to the platoon dispersion model, the cars at the rear of the platoon are traveling at a speed lower than μ. Therefore, the green phase needs to be postponed to time t_t to allow more vehicles at the rear of platoon to pass, which means that the number of vehicles not having passed the downstream signal location is $B(x_d, t_t + t_0)$. For $t_0 = 30, 60, 90, 120$ and $t_t = 0, 1, 2, 10$, $B(x_d, t_t + t_0)/Q$, which denotes the ratio to the maximum initial flow of the average number of cars stopped at the rear of the platoon, is calculated for both the proposed model and Pacey's model, and the results are presented in Table 2.

The data in Table 2 show that as the distance between the successive intersections increases, the speed range of the rear of the platoon, $[v_m, \mu - a/t_0,]$, increases, and $B(x_d, t_o)$ also increases. Therefore, a higher preset t_t is needed to allow more cars at the rear of platoon to pass the downstream intersection. As in the analysis of the front of the platoon, the difference in $B(x_d, t_t + t_0)$ between the proposed model and Pacey's model is 4.78%, that is, $((c-1)/c)100\%$.

4.4. Impact Analysis for Variation Coefficient α

It can be concluded from the previous results that c also determines the deviation of Pacey's model from the real situation. $f'(v)$ of v is affected by σ. As mentioned previously, σ, relative to c, is affected by α. Hence, α has some influence on the accumulated probability for speed range $[v_m, v_f]$. As α increases, the speed range becomes smaller. This is why the deviation of Pacey's model increases with larger values of α.

In addition, α influences the platoon dispersion. A larger α leads to a flatter shape, and a smaller probability around the average speed area; at the same time, the probability for both tails becomes larger. As shown in the derivation process of $k(x, t)$, this is determined by the speed distribution. Thus, the same phenomenon can be seen in the platoon density distribution. To assess the impact of α on $k(x, t)$, $A(x, t)/Q$ of the front and $B(x, t)/Q$ of the rear are calculated separately for $\alpha = 0.15$ and $\alpha = 0.20$ under $x_d = 30\,\mu$ and the results are shown in Figures 3 and 4. From these figures, we can conclude that as α increases, longer preset and extension times are separately required to allow the cars at the front and the rear of the platoon to pass the downstream intersection. These results are consistent with visual analysis.

Table 1: The ratio to the maximum initial flow of the average number of cars having passed the downstream point at the front of platoon under $\alpha = 0.15$.

t_0/s	t_h/s										
	0	1	2	3	4	5	6	7	8	9	10
30	1.89/1.79	1.35/1.28	0.91/0.86	0.57/0.54	0.32/0.31	0.17/0.16	0.08/0.07	0.03/0.02	0/0	0/0	0/0
60	3.77/3.59	3.21/3.05	2.69/2.56	2.23/2.12	1.81/1.72	1.45/1.38	1.13/1.08	0.87/0.83	0.65/0.62	0.47/0.45	0.33/0.32
90	5.66/5.39	5.08/4.84	4.54/4.33	4.04/3.84	3.56/3.39	3.12/2.97	2.72/2.59	2.34/2.23	2.01/1.91	1.70/1.62	1.43/1.36
120	7.54/7.18	6.97/6.63	6.41/6.11	5.88/5.60	5.38/5.12	4.90/4.67	4.45/4.24	4.02/3.83	3.62/3.45	3.24/3.09	2.89/2.76

Note: from the proposed model/from Pacey's model.

Table 2: The ratio to the maximum initial flow of the average number of cars not having passed the downstream point at the rear of platoon under $\alpha = 0.15$.

t_0/s	t_t/s										
	0	1	2	3	4	5	6	7	8	9	10
30	1.42/1.35	1.03/0.98	0.73/0.70	0.50/0.48	0.33/0.31	0.21/0.20	0.12/0.11	0.06/0.05	0.02/0.02	0.01/0.01	0/0
60	2.83/2.70	2.43/2.31	2.06/1.97	1.75/1.66	1.46/1.39	1.22/1.16	1.00/0.96	0.82/0.78	0.66/0.63	0.52/0.50	0.41/0.40
90	4.25/4.04	3.83/3.65	3.45/3.29	3.10/2.95	2.77/2.64	2.47/2.35	2.20/2.09	1.94/1.85	1.71/1.63	1.51/1.43	1.32/1.25
120	5.66/5.39	5.24/4.99	4.85/4.62	4.48/4.27	4.13/3.93	3.80/3.62	3.49/3.32	3.20/3.05	2.93/2.79	2.67/2.55	2.43/2.32

Note: from the proposed model/from Pacey's model.

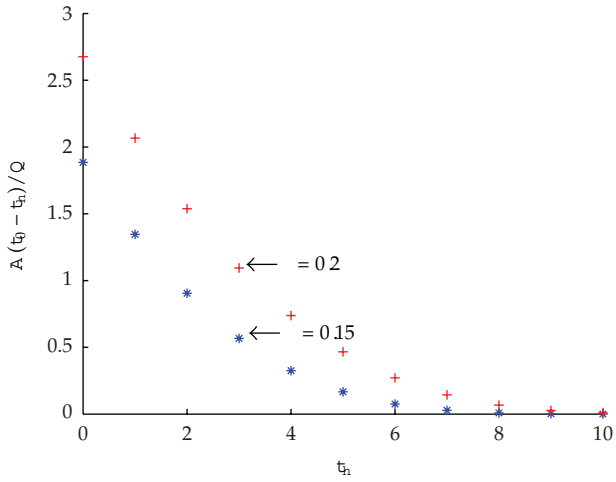

Figure 3: Influence of α on $A(x,t)$ for the front of the platoon.

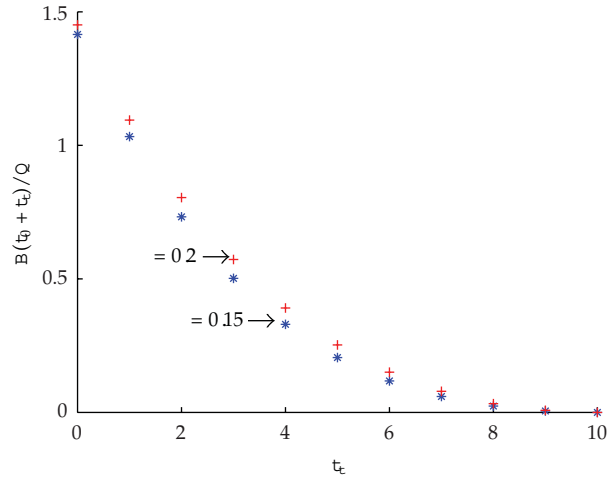

Figure 4: Influence of α on $B(x,t)$ for the rear of the platoon.

5. Conclusion

Platoon dispersion is the foundation of coordinating traffic signal control in an urban traffic network. This paper proposes a new platoon dispersion model which assumes that speed density follows a truncated normal distribution. This addresses the main defect of Pacey's model and matches the field situation. To calibrate proposed model, values of four parameters, namely, the average speed of vehicles, the standard deviation of speed, minimum speed, and maximum speed, are quantified. Using test data in Grace and Potts's paper [5] in the numerical example, there are 4.78% fewer cars travelling in the front and the rear of the platoon between the proposed model and Pacey's model, and we interpret the results for application of coordination of two traffic lights distance x_d apart to prove the validity of the proposed model. Future work needs to focus on proposed model with nonsynchronous

start-up of all vehicles, validating the model using field data, and on simulation program development for the application of the proposed model in the timing of signal coordination.

Acknowledgments

This work was supported by the High-Technology Research and Development Program of China (863 program) under contract no. 2007AA11Z201 and the National Science Foundation of China under contract no. 61174188. This support is gratefully acknowledged. However, all facts, conclusions, and opinions expressed here are solely the responsibility of the authors. The authors thank the anonymous referee for her/his helpful comments.

References

[1] M. J. Lighthill and G. B. Whitham, "On kinematic waves:a theory of traffic flow on long crowded roads," *Proceedings of the Royal Society of London A*, vol. 229, no. 1178, pp. 317–345, 1955.

[2] S. C. Wong and G. C. K. Wong, "An analytical shock-fitting algorithm for LWR kinematic wave model embedded with linear speed-density relationship," *Transportation Research B*, vol. 36, no. 8, pp. 683–706, 2002.

[3] P. Zhang, S. C. Wong, and S. Q. Dai, "A conserved higher-order anisotropic traffic flow model: description of equilibrium and non-equilibrium flows," *Transportation Research B*, vol. 43, no. 5, pp. 562–574, 2009.

[4] G. M. Pacey, "The progress of a bunch of vehicles released from a traffic signal," Research Note RN/2665/GMP, Road Research Laboraroty, Crowthorne, Berkshire, UK, 1956.

[5] M. J. Grace and R. B. Potts, "A theory of the diffusion of traffic platoons," *Operation Research*, vol. 12, no. 2, pp. 255–275, 1964.

[6] C. Q. Liu and P. K. Yang, "Diffusion models of traffic platoon on signal-intersection and control of coordinated signals," *Journal of Tongji University*, vol. 24, no. 6, pp. 636–641, 1996.

[7] C. Q. Liu and P. K. Yang, "Diffusion model of density of traffic platoon and signal coordinated control," *China Journal of Highway and Transport*, vol. 14, no. 1, pp. 89–91, 2001.

[8] C. Q. Liu and P. K. Yang, "Modification of Grace's density diffusion model and its application," *Journal of Highway and Transportation Research and Development*, vol. 18, no. 1, pp. 62–64, 2001.

[9] D. H. Wang, F. Li, and X. M. Song, "Modification of Grace's density diffusion model and its application," *Journal of Jilin University*, vol. 39, no. 4, pp. 891–896, 2009.

[10] D. I. Robertson, "TRANSYT—a traffic network study tool," RRL Report LR 253, Road Research Laboratory, England, UK, 1969.

[11] R. A. Vincent, A. I. Mitchell, and D.I. Robertson, "User Guide to TRANSYT version 8," RRL Report LR 888, Road Research Laboratory, Crowthorne, Berkshire, UK, 1980.

[12] M. Maher, "A comparison of the use of the cell transmission and platoon dispersion models in TRANSYT 13," *Transportation Planning and Technology*, vol. 34, no. 1, pp. 71–85, 2011.

[13] P. A. Seddon, "Another look at platoon dispersion: the Kinematic wave theory," *Tra c Engineering and Control*, vol. 13, no. 8, pp. 332–336, 1971.

[14] P. A. Seddon, "Another look at platoon dispersion: the diffusion theory," *Tra c Engineering and Control*, vol. 13, no. 9, pp. 388–390, 1972.

[15] P. A. Seddon, "Another look at platoon dispersion: the recurrence relationship," *Tra c Engineering and Control*, vol. 13, no. 10, pp. 442–444, 1972.

[16] D. Wang, Y. Zhang, and W. Zhitao, "Study of platoon dispersion models," *Transportation Research Board Annual Meeting*, pp. 3563–3571, 2003.

[17] M. Wei, W. Z. Jin, and L.O. Shen, "A platoon dispersion model considering the speed range limits," *Journal of Jilin University*. In press.

Hindawi Publishing Corporation
Journal of Applied Mathematics
Volume 2012, Article ID 710172, 12 pages
doi:10.1155/2012/710172

Research Article

Theoretical Analysis and Semianalytical Solutions for a Turbulent Buoyant Hydrogen-Air Jet

M. F. El-Amin,[1,2] Shuyu Sun,[1] and Amgad Salama[1]

[1] *Computational Transport Phenomena Laboratory (CTPL), Physical Sciences and Engineering Division (PSE), King Abdullah University of Science and Technology (KAUST), Thuwal, Jeddah 23955-6900, Saudi Arabia*
[2] *Department of Mathematics, Aswan Faculty of Science, South Valley University, Aswan 81528, Egypt*

Correspondence should be addressed to M. F. El-Amin, mohamed.elamin@kaust.edu.sa

Received 1 October 2011; Revised 16 November 2011; Accepted 28 November 2011

Academic Editor: Hiroshi Kanayama

Semianalytical solutions are developed for turbulent hydrogen-air plume. We derived analytical expressions for plume centerline variables (radius, velocity, and density deficit) in terms of a single universal function, called plume function. By combining the obtained analytical expressions of centerline variables with empirical Gaussian expressions of the mean variables, we obtain semianalytical expressions for mean quantities of hydrogen-air plume (velocity, density deficit, and mass fraction).

1. Introduction

One of the important safety issues of hydrogen energy is the hydrogen leakage into ambient air and the associated risk of fire or explosion. In fact, industry has already produced several prototype products using hydrogen as a fuel. Unfortunately, these products are not yet available for commercial use because of safety concerns related to hydrogen leakage. So studying hydrogen-air behavior is very important in order to estimate expected hazards from leakage as well as to propose recommendations when designing hydrogen-related facilities.

Recently, El-Amin and coauthors [1–6] studied the problem of hydrogen leakage in air. In [1–3], they introduced boundary layer theory approach to model the concentration layer adjacent to a ceiling wall at the impinging and far regions in both planar and axisymmetric cases for small-scale hydrogen leakage. While in [4–6], they studied the turbulent hydrogen-air jet/plume resulted from hydrogen leakage in open air. The laminar hydrogen jet is analyzed by Sánchez–Sanz et al. [7]. Also, experimental measurements for turbulent hydrogen jet have been performed by Schefer and coauthors (e.g., [8–10]). On the other hand, CFD simulations of the problem have been done by many researcher such as Matssura and coauthors [11–14], Kikukawa [15], Agarant et al. [16], and Swain et al. [17, 18].

Hydrogen-air jet is an example of non-Boussinesq plume; since the initial fractional density difference is high. The initial fractional density difference is defined as $\Delta\rho_0/\rho_\infty = (\rho_\infty - \rho_0)/\rho_\infty$, where ρ_0 is the initial centerline density (density at the source) and ρ_∞ is the ambient density. As an example, the initial fractional density differences for selected binary low-density gases at temperature 15°C are 0.93 for H_2-Air, 0.86 for He-Air, 0.43 for CH_4-Air, and 0.06 for C_2H_2-N_2. Crapper and Baines [19] suggested that the upper bound of applicability of the Boussinesq approximation is that the initial fractional density difference $\Delta\rho_0/\rho_\infty$ does not exceed 0.05. In general, one can say that the Boussinesq approximation is valid for small initial fractional density difference, $\Delta\rho_0/\rho_\infty \ll 1$ (e.g., El-Amin and Kanayama [5]). This is correct only for the case of a plume produced by a positive source of buoyancy, that is, a plume composed of fluid less dense than the ambient. For the cases where this criterion is not met, Boussinesq approximation may not be used and a density equation needs to be incorporated. El-Amin [6] introduced a numerical investigation of a non-Boussinesq, low-density gas jet (hydrogen) leaking into a high-density ambient (air). The integral models of jet fluxes are obtained and transformed into a set of ordinary differential equations of the mean centerline quantities. Therefore, mean quantities are obtained in addition to cross-stream velocity, Reynolds stresses, and turbulent Schmidt number. Furthermore, the normalized jet-feed material density and momentum flux density are correlated.

It is worth mentioning that theoretical developments and analysis of jet/plume theory were studied by a number of authors since 1950s (see, e.g., Morton et al. [20]; Morton [21]; Morton and Middleton [22]; Delichatsios [23]; Rooney and Linden [24]; Hunt and Kaye [25, 26]; Carlotti and Hunt [27]). Recently, Michaux and Vauquelin [28] developed analytical solutions for centerlines quantities of turbulent plumes rising from circular sources of positive buoyancy in a quiescent environment of uniform density for both Boussinesq and non-Boussinesq cases.

In this paper, semianalytical solution and theoretical analysis are developed for round hydrogen jet leaking into air based on Michaux and Vauquelin [28]. It is assumed that the rate of entrainment is a function of the plume centerline velocity and the ratio of the mean plume and ambient densities. Analytical expressions for all plume variables (radius, velocity, and density deficit) in terms of plume function for a given source parameter are derived.

2. Mathematical Analysis and Similarity Solutions

2.1. Governing Equations

Consider a vertical axisymmetric hydrogen-air buoyant jet resulting from a small-scale hydrogen leakage in the air with a finite circular source. Using cylindrical polar coordinates (z, r) with the z-axis vertical, the source is located at $z = 0$. The continuity, momentum, and concentration equations in cylindrical coordinate system (Figure 1) for the steady vertical axisymmetric buoyant free jet can be written as [29]:

$$\frac{\partial(r\rho V)}{\partial r} + \frac{\partial(r\rho U)}{\partial z} = 0, \tag{2.1}$$

$$\frac{\partial(r\rho UV)}{\partial r} + \frac{\partial(r\rho U^2)}{\partial z} + \frac{\partial(r\rho\overline{uv})}{\partial r} = gr(\rho - \rho_\infty), \tag{2.2}$$

$$\frac{\partial(r\rho VC)}{\partial r} + \frac{\partial(r\rho UC)}{\partial z} + \frac{\partial(r\rho\overline{vc})}{\partial r} = 0, \tag{2.3}$$

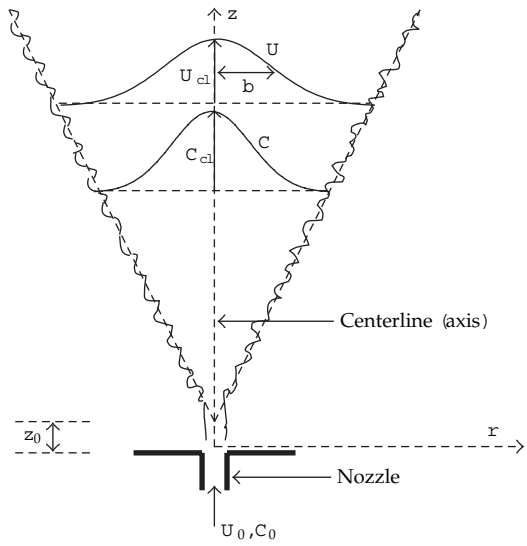

Figure 1: Schematic diagram of turbulent hydrogen-air jet.

where U is the mean streamwise velocity, and V is the mean cross-stream velocity, and C is the hydrogen concentration (mass fraction). The overbar denotes the time-averaged quantities, u, v are the components of velocity fluctuations in z, r directions, respectively, c is the concentration fluctuation, and ρ is the mixture density.

On the other hand, from the experimental observations, the equations for the vertical velocity, density deficiency, and mass fraction profiles, assuming that the hydrogen-air mixture behaves as an ideal gas, are as follows (Fisher et al. [30], Hussein et al. [31], Shabbir and George [32], and Schefer et al. [9, 10]):

$$U(r,z) = U_{cl}(z)\exp\left(-\frac{r^2}{b^2(z)}\right), \tag{2.4}$$

$$\rho_\infty - \rho(r,z) = \left(\rho_\infty - \rho_{cl}(z)\right)\exp\left(-\lambda^2\frac{r^2}{b^2(z)}\right), \tag{2.5}$$

$$\rho(r,z)C(r,z) = \rho_{cl}(z)C_{cl}(z)\exp\left(-\lambda^2\frac{r^2}{b^2(z)}\right), \tag{2.6}$$

$$\rho = \frac{1}{\left(\left[(1/\rho_0) - (1/\rho_\infty)\right]C + (1/\rho_\infty)\right)}, \tag{2.7}$$

where $U(r,z)$ and $\rho(r,z)$ are the mean velocity and mean density at any point of the jet body; $U_{cl}(z)$ and $\rho_{cl}(z)$ are the centerline velocity and density. $b(z) = c_m(z - z_0)$ is the jet/plume width which increases linearly with z, c_m is the momentum spread rate of the jet. z_0 is the virtual origin, which is the distance above/below the orifice where the flow appears to originate. The experimentally measured spread rate c_m varies in the range 0.1–0.13. The buoyancy spreading factor $\lambda = c_m/c_c$ expresses the ratio of spreading rates between

the velocity and density deficiency profiles. The corresponding streamwise concentration for the axisymmetric hydrogen-air, free jet as detected experimentally by Schefer et al. [10] is given as $C = C_{cl}\exp(-0.693\, r^2/b^2)$. In general, the spread rate for the concentration c_c is given in the formula $C = C_{cl}\exp(-r^2/{c_c}^2\,(z-z_0)^2)$. In the work of Schefer et al. [10], the momentum spread rate for the case of hydrogen jet was estimated as $c_m = 0.103$, from which one can find $c_c = 0.124$, and $\lambda = 0.832$. It is well known that $c_C \neq c_m$, that is, velocity and density spread at different rates.

2.2. Similarity Solutions

Integrating the continuity (2.1) radially gives

$$\frac{d}{dz}\int_0^\infty rU(r,z)\rho(r,z)dr = -r\rho V(r,z)\big|_{r=\infty} = -rV(r,z)|_{r=\infty}\rho_\infty. \tag{2.8}$$

Since $U(r,z)$ is negligible for $r > b$, then integrating (2.1) for $b < r < \infty$ gives

$$\int_b^\infty \frac{\partial}{\partial r}\big(rV(r,z)\rho(r,z)\big)dr = 0. \tag{2.9}$$

This implies that

$$-rV(r,z)|_{r=\infty} = bV_e, \tag{2.10}$$

where V_e denotes the inflow velocity at the plume edge which is known as the entrainment velocity. Therefore, we have

$$\frac{d}{dz}\int_0^\infty rU(r,z)\rho(r,z)dr = bV_e\rho_\infty. \tag{2.11}$$

This equation indicates that the increase in plume volume flux is supplied by a radial influx from the far field which in turn implies a flow across the plume boundary b. Batchelor [33] concluded that a vigorous entrainment of the ambient will be obtained as the density ratio tends to unity, $\rho_{cl}/\rho_\infty \to 1$. While as the density ratio tends to zero, $\rho_{cl}/\rho_\infty \to 0$, the entrainment falls to zero. Between these two limits, there will be a smooth transition of entrainment pattern. The experiments by Ricou and Spalding [34] suggest that the entrainment velocity may be obtained using the following formula

$$V_e = \alpha\left(\frac{\rho_{cl}}{\rho_\infty}\right)^{1/2}U_{cl}, \qquad V_e\left(\frac{\rho_{cl}}{\rho_\infty}\longrightarrow 1\right) = \alpha U_{cl}, \qquad V_e\left(\frac{\rho_{cl}}{\rho_\infty}\longrightarrow 0\right) = 0, \tag{2.12}$$

where α is the entrainment coefficient.

Also, Morton [35] assumed that the rate of entrainment into a strongly buoyant plume is a function of both density ratio ρ_{cl}/ρ_∞ and Reynolds stresses which have a magnitude proportional to $\rho_{cl}U_{cl}^2$. Therefore, the local entrainment velocity may be obtained

as $\alpha(\rho_{cl}/\rho_\infty)^{1/2}U_{cl}$, which has also been suggested by Thomas [36], Steward [37], and Townsend [38]. Therefore, (2.11) can be written in the form

$$\frac{d}{dz}\int_0^\infty 2\pi\ rU(r,z)\rho(r,z)dr = 2\pi\ b\rho_\infty\alpha\left(\frac{\rho_{cl}(z)}{\rho_\infty}\right)^{1/2}U_{cl}(z). \tag{2.13}$$

For calculating the momentum flux, let us integrate (2.2) with respect to r, from $r = 0$ to $r = \infty$, noting that $|r\rho UV|_0^\infty = 0$ and $|r\rho\overline{uv}|_0^\infty = 0$, we get

$$\frac{d}{dz}\int_0^\infty 2\pi r U^2(r,z)\rho(r,z)dr = \int_0^\infty 2\pi r g\big(\rho_\infty - \rho(r,z)\big)dr. \tag{2.14}$$

Similarly, for concentration flux, integrating (2.3) with respect to r from $r = 0$ to $r = \infty$, noting also that $|r\rho CV|_0^\infty = 0$ and $|r\rho\overline{uc}|_0^\infty = 0$, we get

$$\frac{d}{dz}\int_0^\infty 2\pi r U(r,z)\rho(r,z)C(r,z)dr = 0. \tag{2.15}$$

This equation may be equivalent to the buoyancy flux equation which can be written in the following form [19]:

$$\frac{d}{dz}\int_0^\infty 2\pi r U(r,z)\big(\rho_\infty - \rho(r,z)\big)dr = 0. \tag{2.16}$$

Substituting (2.4)–(2.6) into (2.16), one obtains

$$\frac{d}{dz}\left(b^2U_{cl}(z)\left(1-\frac{\rho_{cl}(z)}{\rho_\infty}\right)\right) = 0. \tag{2.17}$$

Substituting (2.5), (2.6), and (2.17) into (2.13), (2.14), and (2.15) gives

$$\frac{d}{dz}\left(b^2(z)U_{cl}(z)\frac{\rho_{cl}(z)}{\rho_\infty}\right) = 2bV_e, \tag{2.18}$$

$$\frac{d}{dz}\left(b^2(z)U_{cl}^2\ (z)\frac{\rho_{cl}(z)}{\rho_\infty}\right) = \frac{\rho_\infty - \rho_{cl}(z)}{\rho_\infty}gb^2(z). \tag{2.19}$$

In homogeneous surroundings of density ρ_∞, the density deficit flux, (2.17), is equivalent to

$$B = \pi g b^2(z)U_{cl}(z)\left(1-\frac{\rho_{cl}(z)}{\rho_\infty}\right), \tag{2.20}$$

which has the dimension of a buoyancy flux.

Recently, Michaux and Vauquelin [28] developed analytical solutions for centerlines quantities of turbulent plumes. Now, let us introduce a modified radius β and a dimensionless density deficit η [28]:

$$\beta(z) = \left(\frac{\rho_{cl}(z)}{\rho_\infty}\right)^{1/2} b(z),$$
$$\eta(z) = \frac{\rho_\infty - \rho_{cl}(z)}{\rho_{cl}(z)}. \tag{2.21}$$

Therefore, (2.17)–(2.19) can be rewritten in the following form:

$$\frac{d}{dz}\left(\beta^2 \eta U_{cl}\right) = 0,$$
$$\frac{d}{dz}\left(\beta^2 U_{cl}\right) = 2\alpha\beta U_{cl}, \tag{2.22}$$
$$\frac{d}{dz}\left(\beta^2 U_{cl}^2\right) = \eta g \beta^2.$$

In the previous work of El-Amin and Kanayama [5] and El-Amin [6], they developed the similarity formulation and numerical solutions of the centerline quantities such as velocity and concentration.

In the current work, we follow the work of Michaux and Vauquelin [28] to obtain analytical/semianalytical solutions for centerline plume quantities. Using $\beta(z) = C_\beta z^m$, $U_{cl}(z) = C_{U_{cl}} z^n$, and $\eta(z) = C_\eta z^p$, the constants C_β, $C_{U_{cl}}$, and C_η; exponents m, n, p can be determined to obtain similarity solutions for β, U_{cl}, and η as

$$\beta(z) = \frac{6\alpha}{5} z\ ,$$
$$w(z) = \left(\frac{3}{4}\right)^{1/3}\left(\frac{6\alpha}{5}\right)^{-2/3}\left(\frac{B}{\pi}\right)^{1/3} z^{-1/3}\ , \tag{2.23}$$
$$\eta(z) = \frac{1}{g}\left(\frac{3}{4}\right)^{-1/3}\left(\frac{6\alpha}{5}\right)^{-4/3}\left(\frac{B}{\pi}\right)^{2/3} z^{-5/3},$$

z in these expressions may be replaced by $z - z_0$ to adapt solutions at near-source region and z_0 is virtual origin.

2.3. Plume Function and Source Parameter

Now, let us introduce the plume function as [28]:

$$\Gamma(z) = \frac{5}{8\alpha}\frac{g}{}\frac{\eta\beta}{U_{cl}^2}. \tag{2.24}$$

At source ($z = 0$), $\Gamma(0) = \Gamma_0$, corresponding to the source parameter initially introduced by Morton [21] and defined as [26]:

$$\Gamma_0 = \frac{5Q^2 B_f}{4\alpha M^{5/2}}, \tag{2.25}$$

where Q, M, and B_f are the initial values of specific mass flux, specific momentum flux, and specific buoyancy flux, respectively, defined as

$$\begin{aligned} Q &= \frac{1}{4}\pi d^2 u_0, \\ M &= \frac{1}{4}\pi d^2 u_0^2, \\ B_f &= gQ\frac{\Delta\rho_\infty}{\rho_\infty}, \end{aligned} \tag{2.26}$$

d is the inlet diameter, U_0 is velocity at source, and $\Delta\rho_\infty$ is the difference in density between the receiving fluid and the fluid being discharged. Based on source parameter value Morton and Middleton [22] have categorized plumes with positive buoyancy as simple (pure) plume ($\Gamma_0 = 1$), forced plume ($\Gamma_0 < 1$), and lazy plume ($\Gamma_0 > 1$). Other possibilities (Hunt and Kaye [25]) for $\Gamma_0 = 0$, flow is pure jet without buoyancy, and, for $\Gamma_0 < 0$, flow is weak fountains (negative buoyancy).

For hydrogen-air plume the source parameter is $\Gamma_0 \ll 1$ (of order 10^{-4}), so, based on Morton et al. [20] classification, it is a forced plume.

Equation (2.22) can be rewritten in terms of Γ as follow:

$$\frac{d\beta}{dz} = \frac{4\alpha}{5}\left(\frac{5}{2} - \Gamma\right), \tag{2.27}$$

$$\frac{dU_{cl}}{dz} = -\frac{8\alpha}{5}\left(\frac{U_{cl}}{\beta}\right)\left(\frac{5}{4} - \Gamma\right), \tag{2.28}$$

$$\frac{d\eta}{dz} = -\frac{16\alpha^2}{5g}\left(\frac{U_{cl}}{\beta}\right)^2 \Gamma. \tag{2.29}$$

Using plume function Γ, (2.24), and (2.27)–(2.29), we may write

$$\frac{d\Gamma}{dz} = \frac{4\alpha\Gamma}{\beta}(1 - \Gamma). \tag{2.30}$$

One can deduce that for $\Gamma_0 < 1$, Γ increases monotonically with height and tends asymptotically toward unity.

Using (2.27) and (2.30), one may get

$$\frac{d\beta}{\beta} = \frac{1}{2}\frac{d\Gamma}{\Gamma} + \frac{3}{10}\frac{d\Gamma}{1 - \Gamma}. \tag{2.31}$$

Integrating this equation subject to the source conditions, one obtains

$$\frac{\beta}{\beta_0} = \left(\frac{\Gamma}{\Gamma_0}\right)^{1/2}\left(\frac{1-\Gamma_0}{1-\Gamma}\right)^{3/10}, \tag{2.32}$$

therefore,

$$\frac{b}{b_0} = \left(\frac{\rho_0}{\rho_{cl}}\right)^{1/2}\left(\frac{\Gamma}{\Gamma_0}\right)^{1/2}\left(\frac{1-\Gamma_0}{1-\Gamma}\right)^{3/10}. \tag{2.33}$$

Similarly, we can find that

$$\frac{dU_{cl}}{U_{cl}} = -\frac{1}{2}\frac{d\Gamma}{\Gamma} - \frac{1}{10}\frac{d\Gamma}{1-\Gamma}, \tag{2.34}$$

therefore,

$$\frac{U_{cl}}{U_0} = \left(\frac{\Gamma_0}{\Gamma}\right)^{1/2}\left(\frac{1-\Gamma}{1-\Gamma_0}\right)^{1/10}. \tag{2.35}$$

Finally, using (2.24), (2.32), and (2.34), we get

$$\frac{\eta}{\eta_0} = \left(\frac{\Gamma_0(1-\Gamma)}{\Gamma(1-\Gamma_0)}\right)^{1/2}, \tag{2.36}$$

or

$$\frac{\rho_0(\rho_\infty - \rho_{cl})}{(\rho_\infty - \rho_0)\rho_{cl}} = \left(\frac{\Gamma_0(1-\Gamma)}{\Gamma(1-\Gamma_0)}\right)^{1/2}. \tag{2.37}$$

Now, Γ is a function of z to relate each plume variable to z. Substituting (2.32) into (2.30), one gets

$$\frac{d\Gamma}{dz} = \frac{1}{\Lambda_0}\Gamma^{1/2}(1-\Gamma)^{13/10}, \tag{2.38}$$

where $\Lambda_0 = (\beta_0/4\alpha)(|1-\Gamma_0|^{3/10}/\Gamma_0^{1/2})$, and $\beta_0 = (\rho_0/\rho_\infty)^{1/2}\, b_0$ is the characteristic length defined from initial plume condition. For the case under consideration, we find $\Lambda_0 = 0.17$.

Integrating (2.38), one obtains

$$\frac{z}{\Lambda_0} = \int_{\Gamma_0}^{\Gamma} \gamma^{-1/2}(1-\gamma)^{-13/10}\, d\gamma = \Im(\Gamma) - \Im(\Gamma_0). \tag{2.39}$$

The above integration function has no explicit form, so Michaux and Vauquelin [28] computed and tabulated the integral function $\Im(X)$ for several values of X. Unfortunately,

they did not provide very small values as we find in this investigation when the source parameter is $\Gamma_0 \ll 1$ (of order 10^{-4}). Alternatively, we can write the integration function as

$$\begin{aligned}\Im(\Gamma) &= \int_{\Gamma_0}^{\Gamma} \gamma^{-1/2}(1-\gamma)^{-13/10}\,d\gamma \\ &= \frac{3}{4}\Gamma^{1/2}\,{}_2F_1\left(\frac{3}{10},\frac{1}{2};\frac{3}{2};\Gamma\right) - \frac{10}{3}\frac{\Gamma^{1/2}}{\Gamma-1}(1-\Gamma)^{7/10},\end{aligned} \tag{2.40}$$

where ${}_2F_1$ is the hypergeometric function defined by

$${}_2F_1(a,b;\ c;\Gamma) = \sum_{k=0}^{\infty}\frac{(a)_k(b)_k}{(c)_k}\frac{\Gamma^k}{k!}. \tag{2.41}$$

But $\Gamma \ll 1$ is very small (of order 10^{-4}) for the case of hydrogen-air plume, so two terms of the above series can approximate the function. Thus,

$${}_2F_1(a,b;c;\Gamma) = 1 + \frac{ab}{c}\Gamma. \tag{2.42}$$

This may lead to

$$\Im(\Gamma) \ = \frac{3}{4}\Gamma^{1/2}\left(1+\frac{\Gamma}{10}\right) + \frac{10}{3}\frac{\Gamma^{1/2}}{(1-\Gamma)^{3/10}}. \tag{2.43}$$

According to this relation, $\Im(\Gamma_0) = 0.039294$, therefore,

$$\Im(\Gamma) = 0.039294 + \frac{z}{0.17}. \tag{2.44}$$

From (2.43) and (2.44), one gets

$$\frac{z}{0.17} \ = \frac{3}{4}\Gamma^{1/2}\left(1+\frac{\Gamma}{10}\right) + \frac{10}{3}\frac{\Gamma^{1/2}}{(1-\Gamma)^{3/10}} - 0.039294. \tag{2.45}$$

Again from (2.43), we can determine values of Γ from $\Im(\Gamma)$ given by (2.44). It is clear that Γ decreases as $\Im(\Gamma)$ increases and $\Im(\Gamma)$ increases as z increases. Thus, Γ decreases as z increases and the maximum value of Γ is located at $z = 0$, which is equal to Γ_0. Therefore, using (2.36), one can find $U_{cl}/U_0 = 1$, and the maximum velocity is $U_{cl} = U_0$.

Finally, by combining (2.4)–(2.6) with (2.33), (2.36), and (2.37), one can obtain analytical expressions for vertical velocity, density deficiency, and mass fraction for hydrogen-air mixture in terms of the universal variable Γ as follows:

$$U(r,z) = U_0\left(\frac{\Gamma_0}{\Gamma}\right)^{1/2}\left(\frac{1-\Gamma}{1-\Gamma_0}\right)^{1/10} \times \exp\left(-r^2\frac{(\Gamma_0/\Gamma)((1-\Gamma)/(1-\Gamma_0))^{3/5}}{b_0^2\rho_\infty/\rho_0\left((\rho_\infty/\rho_0-1)(\Gamma_0/\Gamma)^{1/2}((1-\Gamma)/(1-\Gamma_0))^{1/2}+1\right)}\right), \tag{2.46}$$

$$\rho(r,z) = \rho_\infty - \left(\rho_\infty - \frac{\rho_\infty}{\left((\rho_\infty/\rho_0-1)(\Gamma_0/\Gamma)^{1/2}((1-\Gamma)/(1-\Gamma_0))^{1/2}+1\right)}\right) \times \exp\left(-\lambda^2 r^2\frac{(\Gamma_0/\Gamma)((1-\Gamma)/(1-\Gamma_0))^{3/5}}{\frac{b_0^2\rho_\infty}{\rho_0}\left((\rho_\infty/\rho_0-1)(\Gamma_0/\Gamma)^{1/2}((1-\Gamma)/(1-\Gamma_0))^{1/2}+1\right)}\right), \tag{2.47}$$

$$C(r,z) = -\frac{\rho_0}{\rho_\infty-\rho_0} + \frac{\rho_0\rho_\infty}{\rho(r,z)(\rho_\infty-\rho_0)}. \tag{2.48}$$

3. Conclusion

This paper introduces the reader to a set of features of hydrogen-air plume, which is very important to assess the potential hazard resulting from hydrogen sources upon leakage into the ambient atmosphere. Throughout this work, we derived profiles of the mean quantities for a turbulent hydrogen-air plume. These mean quantities, such as plume radius, velocity, and density deficit, are expressed in terms of the plume function for a given source parameter. These quantities are determined by integral relations and by analysis using similarity variables. Therefore, mean quantities are expressed solely in terms of the plume function and the source parameter. The plume function is valid for a range of small values of Γ as required for hydrogen-air plume. The hypergeometric function is exploited, and the profiles of the mean quantities are obtained. These results may be generalized and extended in a future work to cover more complex flow types found in a prober accident of hydrogen leaks such as leakage in hydrogen station.

References

[1] M. F. El-Amin and H. Kanayama, "Boundary layer theory approach to the concentration layer adjacent to a ceiling wall at impinging region of a hydrogen leakage," *International Journal of Hydrogen Energy*, vol. 33, no. 21, pp. 6393–6400, 2008.

[2] M. F. El-Amin, M. Inoue, and H. Kanayama, "Boundary layer theory approach to the concentration layer adjacent to a ceiling wall of a hydrogen leakage: far region," *International Journal of Hydrogen Energy*, vol. 33, no. 24, pp. 7642–7647, 2008.

[3] M. F. El-Amin and H. Kanayama, "Boundary layer theory approach to the concentration layer adjacent to the ceiling wall of a hydrogen leakage: axisymmetric impinging and far regions," *International Journal of Hydrogen Energy*, vol. 34, no. 3, pp. 1620–1626, 2009.

[4] M. F. El-Amin and H. Kanayama, "Integral solutions for selected turbulent quantities of small-scale hydrogen leakage: a non-buoyant jet or momentum-dominated buoyant jet regime," *International Journal of Hydrogen Energy*, vol. 34, no. 3, pp. 1607–1612, 2009.

[5] M. F. El-Amin and H. Kanayama, "Similarity consideration of the buoyant jet resulting from hydrogen leakage," *International Journal of Hydrogen Energy*, vol. 34, no. 14, pp. 5803–5809, 2009.

[6] M. F. El-Amin, "Non-Boussinesq turbulent buoyant jet resulting from hydrogen leakage in air," *International Journal of Hydrogen Energy*, vol. 34, no. 18, pp. 7873–7882, 2009.

[7] M. Sánchez-Sanz, M. Rosales, and A. L. Sánchez, "The hydrogen laminar jet," *International Journal of Hydrogen Energy*, vol. 35, no. 8, pp. 3919–3927, 2010.

[8] W. G. Houf and R. W. Schefer, "Analytical and experimental investigation of small-scale unintended releases of hydrogen," *International Journal of Hydrogen Energy*, vol. 33, no. 4, pp. 1435–1444, 2008.

[9] R. W. Sehefer, W. G. Houf, and T. C. Williams, "Investigation of small-scale unintended releases of hydrogen: momentum-dominated regime," *International Journal of Hydrogen Energy*, vol. 33, no. 21, pp. 6373–6384, 2008.

[10] R. W. Schefer, W. G. Houf, and T. C. Williams, "Investigation of small-scale unintended releases of hydrogen: buoyancy effects," *International Journal of Hydrogen Energy*, vol. 33, no. 17, pp. 4702–4712, 2008.

[11] K. Matsuura, "Effects of the geometrical configuration of a ventilation system on leaking hydrogen dispersion and accumulation," *International Journal of Hydrogen Energy*, vol. 34, no. 24, pp. 9869–9878, 2009.

[12] K. Matsuura, M. Nakano, and J. Ishimoto, "Forced ventilation for sensing-based risk mitigation of leaking hydrogen in a partially open space," *International Journal of Hydrogen Energy*, vol. 35, no. 10, pp. 4776–4786, 2010.

[13] K. Matsuura, M. Nakano, and J. Ishimoto, "The sensing-based adaptive risk mitigation of leaking hydrogen in a partially open space," *International Journal of Hydrogen Energy*, vol. 34, no. 20, pp. 8770–8782, 2009.

[14] K. Matsuura, H. Kanayama, H. Tsukikawa, and M. Inoue, "Numerical simulation of leaking hydrogen dispersion behavior in a partially open space," *International Journal of Hydrogen Energy*, vol. 33, no. 1, pp. 240–247, 2008.

[15] S. Kikukawa, "Consequence analysis and safety verification of hydrogen fueling stations using CFD simulation," *International Journal of Hydrogen Energy*, vol. 33, no. 4, pp. 1425–1434, 2008.

[16] V. Agarant, Z. Cheng, and A. Tchouvelev, "CFD modeling of hydrogen releases and dispersion in hydrogen energy station," in *Proceedings of the 15th World Hydrogen Energy Conference*, 2004.

[17] M. R. Swain and M. N. Swain, "Passive ventilation systems for the safe use of hydrogen," *International Journal of Hydrogen Energy*, vol. 21, no. 10, pp. 823–835, 1996.

[18] M. R. Swain, P. Filoso, E. S. Grilliot, and M. N. Swain, "Hydrogen leakage into simple geometric enclosures," *International Journal of Hydrogen Energy*, vol. 28, no. 2, pp. 229–248, 2003.

[19] P. F. Crapper and W. D. Baines, "Non Boussinesq forced plumes," *Atmospheric Environment*, vol. 11, pp. 415–420, 1977.

[20] B. R. Morton, G. Taylor, and J. S. Turner, "Turbulent gravitational convection from maintained and instantaneous sources," *Proceedings of the Royal Society A*, vol. 234, pp. 1–23, 1956.

[21] B. R. Morton, "Forced plumes," *Journal of Fluid Mechanics*, vol. 5, pp. 151–163, 1959.

[22] B. R. Morton and J. Middleton, "Scaling diagram for forced plumes," *The Journal of Fluid Mechanics*, vol. 58, pp. 165–176, 1973.

[23] M. A. Delichatsios, "Strong turbulent buoyant plumes. I. Similarity," *Combustion Science and Technology*, vol. 24, pp. 191–195, 1981.

[24] G. G. Rooney and P. F. Linden, "Similarity considerations for non-Boussinesq plumes in an unstratified environment," *The Journal of Fluid Mechanics*, vol. 318, pp. 237–250, 1996.

[25] G. R. Hunt and N. G. Kaye, "Virtual origin correction for lazy turbulent plumes," *The Journal of Fluid Mechanics*, vol. 435, pp. 377–396, 2001.

[26] G. R. Hunt and N. B. Kaye, "Lazy plumes," *The Journal of Fluid Mechanics*, vol. 533, pp. 329–338, 2005.

[27] P. Carlotti and G. R. Hunt, "Analytical solutions for turbulent non-Boussinesq plumes," *The Journal of Fluid Mechanics*, vol. 538, pp. 343–359, 2005.

[28] G. Michaux and O. Vauquelin, "Solutions for turbulent buoyant plumes rising from circular sources," *Physics of Fluids*, vol. 20, no. 6, Article ID 066601, 2008.

[29] M. F. El-Amin and S. Sun, "Turbulent buoyant jet of a low-density gas leaks into a high-density ambient: hydrogen leakage in air," in *Advanced Topics in Mass Transfer*, M. F. El-Amin, Ed., INTECH, 2011.

[30] H. B. Fischer, E. J. List, R. C. Y. Koh, J. Imberger, and N. H. Brooks, *Mixing in Inland and Coastal Waters*, Academic Press, 1979.

[31] H. J. Hussein, S. P. Capp, and W. K. George, "Velocity measurements in a high-Reynolds-number, momentum-conserving, axisymmetric, turbulent jet," *The Journal of Fluid Mechanics*, vol. 258, pp. 31–75, 1994.

[32] A. Shabbir and W. K. George, "Experiments on a round turbulent buoyant plume," *The Journal of Fluid Mechanics*, vol. 275, pp. 1–32, 1994.

[33] G. K. Batchelor, "Heat convection and buoyancy effects in fluids," *Quarterly Journal of the Royal Meteorological Society*, vol. 80, pp. 339–358, 1954.

[34] F. P. Ricou and D. B. Spalding, "Measurements of entrainment by axisymmetrical turbulent jets," *The Journal of Fluid Mechanics*, vol. 8, pp. 21–32, 1961.

[35] B. R. Morton, "Modelling fire plumes," in *Proceedings of the 10th International Symposium on Combustion*, pp. 973–982, 1965.

[36] P. H. Thomas, "The size of flames from natural fires," in *Proceedings of the 9th Symposium on Combustion*, pp. 844–859, 1963.

[37] F. R. Steward, "Prediction of the height of turbulent diffusion buoyant flames," *Combustion Science and Technology*, vol. 2, pp. 203–212, 1970.

[38] A. A. Townsend, "The mechanism of entrainment in free turbulent flows," *The Journal of Fluid Mechanics*, vol. 26, pp. 689–715, 1966.